



SUSTAINABLE DEVELOPMENT GOALS

## REPORT 2023

6 CLEAN WATER AND SANITATION





SDG6 For environmental sustainability, economic development, and access to clean water and sanitation, freshwater ecosystem management is crucial. The goal of SDG 6 is to "ensure access to water, its sustainable management, and proper sanitation for all." Manipal University Jaipur captures progressive improvements from surface water and use of unimproved water to using an improved water source helps protect against contamination. The Water Management Centre at Manipal University Jaipur addresses several of these concerns in the Indian and global contexts.



# ACADEMICS



MANIPAL UNIVERSITY  
JAIPUR

**FACULTY OF SCIENCE**

**SCHOOL OF BASIC SCIENCES**

**DEPARTMENT OF BIOSCIENCES**

**Invitation for Expert Lecture**

**On**

**Nature-based technologies for treatment and recycling  
wastewater**

**28 July, 2023 ~ 11.00AM**

**Room No 020, 1 AB, MUJ**



Content of Report (index)

(Page number may not be required)

(Delete entries which are not applicable)

1. Introduction of the Event
2. Objective of the Event
3. Beneficiaries of the Event
4. Details of the Guests
5. Brief Description of the event
6. Geo-tagged Photographs
7. Brochure or creative of the event
8. Schedule of the Event
9. Attendance of the Event

## 1. Introduction of the Event

Expert Lecture On Nature-based technologies for treatment and recycling wastewater by Dr. Sanjeev Prajapati, Department of Hydro and Renewable Energy (HRED) Indian Institute of Technology, Roorkee

## 2. Objective of the Event (bullet points or about 50 words)

The lecture was designed to provide insight into the processes and techniques that are applied in the wastewater treatment field, where the focus is laid on the basic principles, local conditions, basic circumstances, and performance of constructed wetlands integrated with the algae-based process which aimed towards the resource recycling.

## 3. Beneficiaries of the Event (Student/Faculty/Community etc) (25 words)

The lecture was the starting stage for the students to learn about the integrated constructed wetlands and learn about the design of various industrial components. This is thus meant to bring about a general understanding of the research illustrated and explained by the expert.

## 4. Details of the Guests (Chief Guests, speakers etc Designation, organization, contact details if any please give them in sr no)

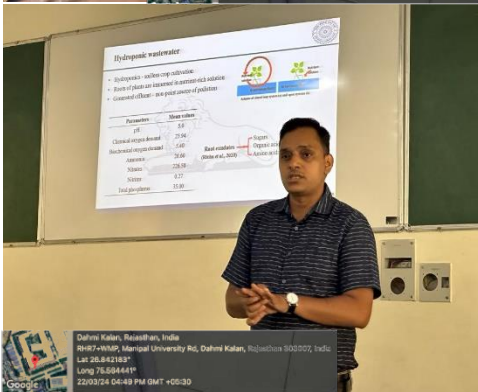
Dr. Sanjeev Prajapati, Department of Hydro and Renewable Energy (HRED)  
Indian Institute of Technology, Roorkee

## 5. Brief Description of the event (about 200 words)


Expert Lecture on the Nature-based technologies for treatment and recycling wastewater. The lecture was designed to provide insight into the processes and techniques that are applied in the wastewater treatment field, where the focus is laid on the basic principles, local conditions, essential circumstances, and performance of constructed wetlands integrated with the algae-based process, which is aimed towards resource recycling.

## 6. Photographs

3 to 5 geotagged photographs of the event or screenshots of the



7. Brochure or creative of the event (insert in the document only )



The brochure features a light blue background with a central graphic of a water treatment plant. At the top left is the Manipal University Jaipur logo. To its right are the NAAC A+ accreditation logo and the G20 India 2023 logo. The main text is centered, starting with 'Department of Biosciences' in bold red, followed by 'Invitation for Expert Lecture' in italics. Below this, it says 'On' followed by the lecture title 'Nature-based technologies for treatment and recycling wastewater' in large bold red font. The speaker's name 'Dr. Sanjeev Prajapati' is in bold red, with his affiliation 'Department of Hydro and Renewable Energy (HRED) Indian Institute of Technology, Roorkee' below it. A portrait of Dr. Sanjeev Prajapati is on the right. A yellow box on the left contains the date '28<sup>th</sup> July, 2023', time '11.00AM', and location 'Room No 020, 1 AB'. Below this, the convener 'Dr. Monika Sogani' is listed with her title and department. At the bottom is a photograph of the Manipal University Jaipur building.

 MANIPAL UNIVERSITY  
JAIPUR

 ACCREDITED WITH GRADUATE  
A+  
NAAC

 G20  
भारत 2023 INDIA

**Department of Biosciences**  
*Invitation for Expert Lecture*

On

**Nature-based technologies for treatment  
and recycling wastewater**


By

**Dr. Sanjeev Prajapati**  
Department of Hydro and Renewable Energy (HRED)  
Indian Institute of Technology, Roorkee



**28<sup>th</sup> July, 2023**  
**11.00AM**  
**Room No 020, 1 AB**

Convenor  
**Dr. Monika Sogani**  
Associate Professor  
Department of Biosciences  
Manipal University Jaipur





## 8. Schedule of the event (insert in the report)

28 July, 2023 ~ 11.00AM

Room No O20, 1 AB

Manipal University Jaipur

## 9. Attendance of the Event (insert in the document only)

**Total attendee - Approx 20 (15 in list plus few more students)**

Sr. No	Name of Institution	Place of Institution	Name of Attendee	Name of Dept
1.	Manipal University Jaipur	Jaipur	Dr. Monika Sogani	Biosciences
2.	Manipal University Jaipur	Jaipur	Dr. Sandeep K Srivatava	Biosciences
3.	Manipal University Jaipur	Jaipur	Dr. Rakesh Sharma	Biosciences
4.	Manipal University Jaipur	Jaipur	Dr. Anand Chakinala	Chemical Engineering
5.	Manipal University Jaipur	Jaipur	Dr. Nitesh Kumar Poddar	Biosciences
6.	Manipal University Jaipur	Jaipur	Dr. Anil Dutt Vyas	Civil Engineering
7.	Manipal University Jaipur	Jaipur	Dr. Karishma Sharma	Chemical Engineering
8.	University of Mannheim	Germany	Rosy	Biology
8.	Manipal University Jaipur	Jaipur	Priyanka Sharma	Biosciences
9.	Manipal University Jaipur	Jaipur	Bhanu Kushwaha	Biosciences
10.	Manipal University Jaipur	Jaipur	Sandesh Telang	Biosciences
11.	Manipal University Jaipur	Jaipur	Himanshi Sen	Biosciences
12.	Manipal University Jaipur	Jaipur	Nishaan Sen Gupta	Biosciences
13.	Manipal University Jaipur	Jaipur	Jayana Rajvanshi	Biosciences
14.	Manipal University Jaipur	Jaipur	Sapna Kumari	Biosciences
15.	Manipal University Jaipur	Jaipur	Nandana Chakinala	Chemical Engineering



28-07-2023

**Seal and Signature of Head with date**



# RESEARCH

# Summary for Manipal University Jaipur 6



Manipal University Jaipur

2021 to 2023 ▼

## Research performance within SDG 6: Clean Water and Sanitation (2023)

Entity: Manipal University Jaipur · Within: All subject areas (ASJC) · Year range: 2021 to 2023 · Data source: Scopus, up to 30 Oct 2024

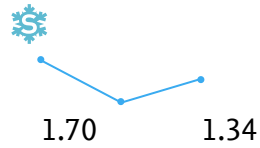
102

Scholarly Output



1.28

Field-Weighted Citation Impact



13

International Collaboration



2,161

Views Count

1,134

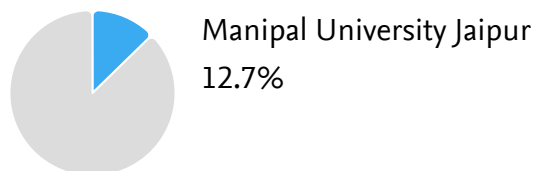
Citation Count

## Collaboration summary within SDG 6: Clean Water and Sanitation (2023)

Entity: Manipal University Jaipur · Within: All subject areas (ASJC) · Year range: 2021 to 2023 · Data source: Scopus, up to 30 Oct 2024

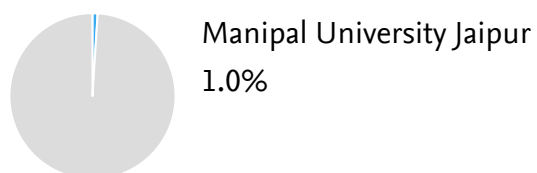
### International Collaboration

Publications co-authored with Institutions in other countries/regions



### Academic-Corporate Collaboration

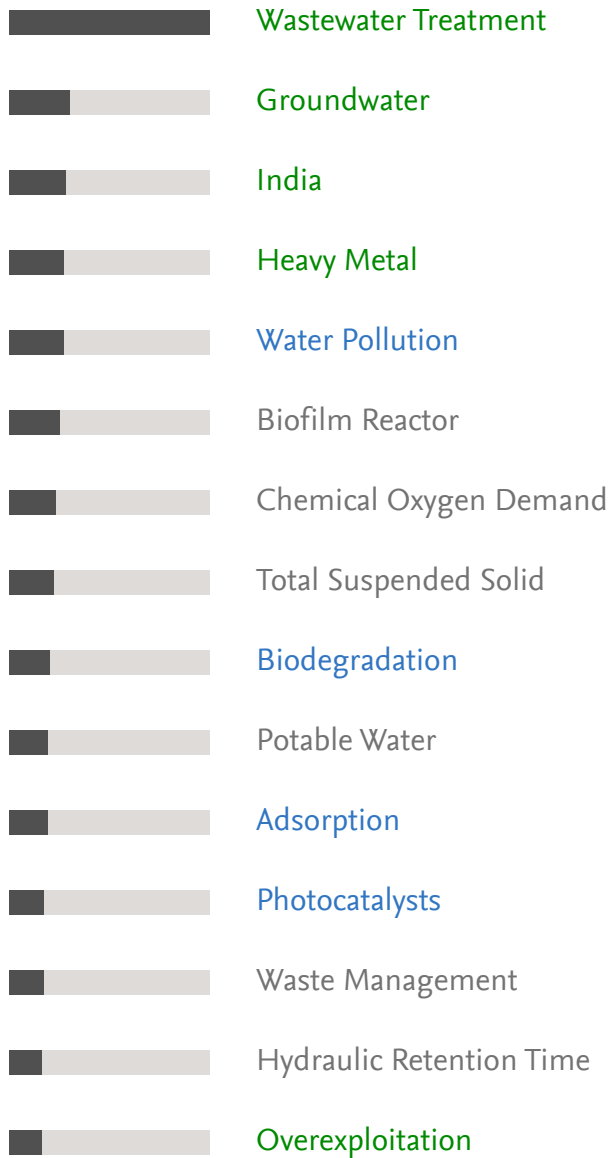
Publications with both academic and corporate affiliations



## Top keyphrases within SDG 6: Clean Water and Sanitation (2023)

Entity: Manipal University Jaipur · Within: All subject areas (ASJC) · Year range: 2021 to 2023 · Data source: Scopus, up to 30 Oct 2024

Top keyphrases by  relevance





# Contents

---

1. Academics
2. Research
3. Events
4. Collaborations



MANIPAL UNIVERSITY  
JAIPUR



# EVENTS



MUJ/DSW/Society Connect/ 31 Oct 2023

**DIRECTORATE OF STUDENT'S WELFARE**

**(SOCIETY CONNECT)**

**And**

**Faculty of Management and Commerce**

**Department of Business Administration**

**Activity on**

**SWACH BHARAT**

**OCTOBER 31, 2023**



## 1. Introduction of the Event

School of Business and Commerce in collaboration with Directorate of Student Welfare (NCC, NSS) and Rotaract Club (Rotary Bapu Nagar) organized a “Awareness on Environment Protection” on October 31, 2023. 40 students and 2 faculty members participated in the campaign. The event took place in Dehmi Kalan hamlet.

## 2. Objective of the Event

The aim of the campaign was to raise awareness about plantation and Environmental Protection.

## 3. Beneficiaries of the Event

Through this initiative, students and villagers had better communication and understanding of the situation.

## 4. Details of the Guests

The event was laid by the students of BBA, BBA(BA), IMBA and Club Members of Rotaract Club MUJ

## 5. Brief Description of the event

School of Business and Commerce, Department of Business Administration in collaboration with Directorate of Student Welfare, Directorate of sports and NCC, NSS organized a plantation drive for creating awareness on environment protection on 31st October 2023. 20 students and 2 faculty members participated in the drive. The group visited various houses in the Begas Village Road and planted saplings and encouraged villagers to take care about environment and newly planted saplings. Students also learned various communication skills and interactive skills with the villagers.

## 6. Photographs



Fig 1 Students at Begus Village for Plantation



Fig 2 Students doing Plantation.



Fig 2 Students & Faculty doing Plantation.



Fig 4 Students & Faculty doing Plantation.

## 7. Brochure or creative of the event



## 8. Schedule of the Event

The event took place on October 31, 2023

## 9. Attendance of the Event (60 student)

Sr. No	Registration No	Attendee Name	Name of Institution
1	23FM10BBA00197	VIPUL SHARMA	Manipal University Jaipur
2	23FM10BBA00198	MUKUND MAHESHWARI	Manipal University Jaipur
3	23FM10BBA00199	ROSHAN GUPTA	Manipal University Jaipur
4	23FM10BBA00200	VANSH MULCHANDANI	Manipal University Jaipur
5	23FM10BBA00227	PAWAN POTALIYA	Manipal University Jaipur
6	23FM10BBA00232	AKSHAT KUMARCHOUDHARY	Manipal University Jaipur
7	23FM10BBA00233	DHAIRYA BANSAL	Manipal University Jaipur
8	23FM10BBA00230	YASH ARORA	Manipal University Jaipur
9	23FA10BSP00028	Anupama Rustagi	Manipal Univesrity Jaipur
10	23FE10CCE00085	Siddhartha tiwari	Manipal Univesrity Jaipur
11	23FA10BAP00002	Tanisha Mathur	Manipal Univesrity Jaipur
12	23FD10BFD00009	Mariya Shabbir Baiwala	Manipal Univesrity Jaipur
13	23FE10CDS00224	Harsh Ajmera	Manipal Univesrity Jaipur
14	23fe10cds00125	Suryanshi Singh	Manipal Univesrity Jaipur
15	23fs10mat00009	Malavika ramdas	Manipal Univesrity Jaipur
16	221007021	Arshi Jain	Manipal Univesrity Jaipur
17	23FE10CSE00137	Stuti Dixit	Manipal Univesrity Jaipur
18	23fe10cii00094	Aarohi Tyagi	Manipal Univesrity Jaipur
19	23FE10CSE00152	Gautam Kakkar	Manipal Univesrity Jaipur



20	23FE10CSE00318	Krish Ray	Manipal Univesrity Jaipur
21	23FE10CII00076	Kriissh Marwaha	Manipal Univesrity Jaipur
22	229310321	Shiv Rajput	Manipal Univesrity Jaipur
23	23FS10BIO00051	Ragini Singh Thakur	Manipal Univesrity Jaipur
24	23FS10BIO00052	Anukriti sharma	Manipal Univesrity Jaipur
25	220901073	Diya Mittal	Manipal Univesrity Jaipur
26	23FE10CSE00081	Smmayan Gupta	Manipal Univesrity Jaipur
27	229309083	Raghav Gupta	Manipal Univesrity Jaipur
28	23FE10CDS00397	Hrishita Singh Timaney	Manipal Univesrity Jaipur
29	23FE10ITE00203	Sarah Sharda	Manipal Univesrity Jaipur
30	23fa10bsp00025	Jasleen kaur	Manipal Univesrity Jaipur
31	23FA10BSP00039	Jiya Kumar	Manipal Univesrity Jaipur
32	23FA10BSP00004	Aarya Mahale	Manipal Univesrity Jaipur
33	220606020	Chaarvi Kumar	Manipal Univesrity Jaipur
34	23fa10bsp00058	Kashvi Mahajan	Manipal Univesrity Jaipur
35	229301095	Shaurya Singh	Manipal Univesrity Jaipur
36	23fe10ece00024	Kushagra agrawal	Manipal Univesrity Jaipur
37	23FA10BSP00017	Megha Sharma	Manipal Univesrity Jaipur
38	23FM10BBA00162	Alina Nadeem	Manipal Univesrity Jaipur
39	23FM10BBA00178	Avishi Akhaury	Manipal Univesrity Jaipur
40	221007004	Urvi Thakare	Manipal Univesrity Jaipur
41	23FA10BAP00027	Natasha Joan Menezes	Manipal Univesrity Jaipur
42	23FA10BLE00004	Tanisha chaturvedi	Manipal Univesrity Jaipur
43	23fe10cai00579	Arjun Malhotra	Manipal Univesrity Jaipur
44	23FE10CAI00352	Maanyata Aul	Manipal Univesrity Jaipur
45	220901322	Divyanshi Singh	Manipal Univesrity Jaipur
46	229310412	Jatin Verma	Manipal Univesrity Jaipur
47	229301094	Yashovardhan Pratap Singh	Manipal Univesrity Jaipur
48	23FM10BBA00348	Niska kedia	Manipal Univesrity Jaipur
49	221105005	Dhruv Nair	Manipal Univesrity Jaipur
50	23FM10BBA00170	Shambhavi Agrawal	Manipal Univesrity Jaipur
51	23FE10CDS00241	Armaan Setia	Manipal Univesrity Jaipur
52	23FE10CAI00105	Mritunjay Singh	Manipal Univesrity Jaipur
53	229311075	Aarna Tyagi	Manipal Univesrity Jaipur
54	229302051	Prince jindal	Manipal Univesrity Jaipur
55	23FA10BHE00035	Taneesha puri	Manipal Univesrity Jaipur
56	220903033	Suhani Jain	Manipal Univesrity Jaipur
57	220901391	Dipika Agarwal	Manipal Univesrity Jaipur
58	229310222	Aayush Sharma	Manipal Univesrity Jaipur
59	221003007	Yachna Jain	Manipal Univesrity Jaipur
60	220901002	Anshu jangir	Manipal Univesrity Jaipur



Dr Narendra Singh Bhati Ho

HOD, BBA

(Hemant Kumar)  
Assistant Director, Society Connect  
Directorate of Student's Welfare

DIRECTOR STUDENT WELFARE & PROCTOR  
MANIPAL UNIVERSITY, JAIPUR

(Prof. AD Vyas)

**Director, Directorate of Student's Welfare**



MUJ/DSW/Student Clubs/2023/Biotech Club MUJ/8<sup>th</sup>November'23



MANIPAL UNIVERSITY  
JAIPUR

## **DIRECTORATE OF STUDENTS' WELFARE**

# **RANGOLI COMPETITION ON BACTERIAL AND VIRAL DISEASES**

**Department of Biosciences,  
Biotech Club of MUJ,  
&  
Microbiologists Society, India (MBSI)**

## **OFFLINE EVENT**

**Date of Event (8<sup>th</sup> November 2023)  
(10:00 AM- 01:30 PM)**



## Index

<b>S.No.</b>	<b>Activity Heads</b>	<b>Page no.</b>
1.	Introduction of the Event	3
2.	Objective of the Event	3
3.	Beneficiaries of the Event	3
4.	Brief Description of the event	3
5.	Photographs	4
6.	Brochure or creative of the event	5
7.	Schedule of the Event	6
8.	Attendance of the Event	6
9.	Event link	8

## 1. Introduction of the Event

In collaboration with the Department of Biosciences at Manipal University Jaipur, the Biotech Club, and the **Microbiologists Society India**, organized a **Rangoli Competition on Bacterial and Viral Diseases on November 8<sup>th</sup>, 2023**. This unique event converged the traditional artistry of Rangoli with the scientific world of microbial pathogens, offering participants a creative platform to explore and express their insights into the intricate realm of bacterial and viral diseases.

## 2. Objectives of the Event

- To foster a sense of community within the university and beyond by bringing students, faculty, and the local community together.
- To encourage participation from diverse backgrounds, promoting inclusivity and knowledge sharing.
- Promote interdisciplinary discussions, allowing individuals from various academic backgrounds to explore the intersections of art and science.
- Highlight the pervasive influence of biotechnology in everyday life, with a specific focus on how it impacts disease prevention and treatment.
- Enhance public understanding of the importance of biotechnological advancements in addressing global health challenges and the development of innovative solutions.

## 3. Beneficiaries of the Event

- MUJ students

## 4. Brief Description of the event

The **Rangoli Competition on the theme of Bacterial and Viral Diseases** began with an exciting inaugural ceremony at 10 AM attended by the esteemed faculty members. Total registered students for the competition was 20. Each participating student group, creatively named after aspects of the topic, brought their unique perspective to life on the colorful canvas. The groups, included

***Petridish Picassos (G1) – Lavanya Tiwari, Roma Joishi, Shipra Rathi, Jenifer Laimayum***

***Gene Code Conqueror (G2) – Kanushree Rathore***

***Microbe Master (G3) – Thati Ameta***

***SARS (G4) – Vanisha Sharma, Prashant Pradhan, Ananya Khanna, Ankita Singh***

***Nain Naksh Group (G5)- Simran Maharshi, Simran Duggal, Pallavi Anand, Radhika Rathore***

***Viro Path Explorers (G6)- Sakshi***

***Vax Guardian (G7)- Shreya Ganvir***

***Bacterial Pioneer (G8)- Riddhima Gupta, Priyanka Chatterjee***

***Biotech Innovators (G9)- Vaishali Shahi, Aishwarya Rai Saxena***

who showcased their artistic talents and their understanding of the subject matter. As the event unfolded, curious students observed the intricate designs and symbolic representations. The rangoli creations were later evaluated and graded by the faculty, and deserving students were honored with certificates and mementos, making it a memorable and educational event.



The results of the rangoli competition were compiled as a total score per group on the criteria of presentation, concept, and defense. Placeholders were as follows-  
**Winners- Petridish Picassos (G1) 1st Runner-up- Microbe Master (G3)**  
**2nd Runner-up – Nain Naksh (G5)**  
**Consolation prizes- Viro Path Exploror (G6), SARS (G4), Vax Guardian (G7)**

### 5. Photographs



Images 1-9: Rangoli entries by each of the participating groups (in order of the groups G1 to G9)



Images 10-12: Dr. Praveen Surolia (HoD, Chemistry) in conversation with our participant Sakshi; Dr. Saurabh Srivastava and Dr. Lalita Ledwani (Dean, FOS) along with Dr. Mousumi Debnath reviewing our participants' designs

## RESULTS



*Group photograph of all our participants along with the faculty members, guests and executive members of Biotech Club*



### WINNERS

*Petridish Picassos (G1) – Lavanya Tiwari, Roma Joishi, Shipra Rathi, Jenifer Laimayum*



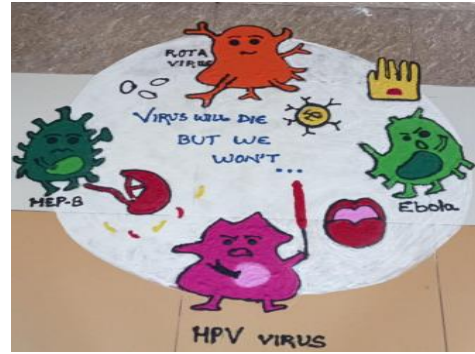
### 1<sup>ST</sup> RUNNER UP

*Microbe Master (G3) – Thati Ameta*



### 2<sup>ND</sup> RUNNER UP

*Nain Naksh Group (G5)- Simran Maharshi, Simran Duggal, Pallavi Anand, Radhika Rathore*



*Consolation prize- Viro Path Explorer (G6)- Sakshi*



*Consolation prize- SARS (G4) – Vanisha Sharma, Prashant Pradhan, Ananya Khanna, Ankita Singh*



*Consolation prize- Vax Guardian (G7)- Shreya Ganvir*

## 6. Brochure or creative of the event



The brochure is for a Rangoli Competition on Bacterial and Viral Diseases. It features logos for Manipal University Jaipur, Biotech Club, and MBSI. The event is presented by the Department of Biosciences and MBSI. The competition is on 8th November 2023, from 10 AM onwards in the AB1 corridor. A QR code is provided for registration. The faculty coordinator is Dr. Mousumi Debnath. Contact information for the organizing committee is also listed.

MANIPAL UNIVERSITY  
JAIPUR

Biotech Club

DEPARTMENT OF BIOSCIENCES  
Biotech Club & Microbiologists Society, India (MBSI)

PRESENTS

**rangoli**  
COMPETITION

ON

**BACTERIAL AND VIRAL DISEASES**

**8th November, 2023**  
10 AM ONWARDS, AB1 corridor (towards Dome)

how to participate?



Scan to register yourself as a participant now!

ઘટના શુભેદોનેદે

- All rangoli designs should align in accordance to the theme of the event.
- We request all participants to be present on time at the venue of the event.

faculty coordinator

**Dr. Mousumi Debnath**  
Associate Professor (Senior Scale),  
Department of Biosciences, MUJ  
State President (Rajasthan), MBSI

for any queries, contact:

Anshulika Saxena (President)-  
7080114443  
Prachi Jain (Vice President)-  
9602087842  
Arindam Yadav (Exec Member)-  
8302673699  
Or mail us at-  
biotech@mu.j.manipal.edu

## 7. SCHEDULE OF THE EVENT:

The event was conducted on 8<sup>th</sup> November 2023 from 10:00 AM- 1:30 PM at the allotted venue- AB1 Corridor facing old mess.



## 8. ATTENDANCE OF THE EVENT:

TOTAL PARTICIPANTS IN THE COMPETITION: 20

S.No.	Name	Course/Year	Registration No.	Signature
1	Laxanya Timari	M.Sc biotech / 1 <sup>st</sup> yr	23FS20MBD00008	Laxanya
2	Roma Jaiski	M.Sc biotech / 1 <sup>st</sup> yr	23FS20MB000023	Roma Jaiski
3	Shruti Kothari	M.Sc biotech / 1 <sup>st</sup> yr	23FS20MB000030	Shruti Kothari
4	Jennifer Laimayum	M.Sc biotech / 1 <sup>st</sup> yr	23FS20MB000005	Jennifer L
5	Kamushree Rathore ]G2	B.Sc biotech / 1 <sup>st</sup> yr	23FS10BID00055	Kamushree
6	Thati Ameta ]G3	B.Sc biotech / 1 <sup>st</sup> yr	23FS10BID00031	Thati
7	Vanisha Sharma	M.Sc biotech / 1 <sup>st</sup> yr	23FS20MB000039	Vanisha
8	Prashant Pradhan	M.Sc biotech / 1 <sup>st</sup> yr	23FS20MB000015	Prashant
9	Ananya Kaanna	M.Sc biotech / 1 <sup>st</sup> yr	23FS20MB000024	Ananya
10	Ankita Singh	M.Sc biotech / 1 <sup>st</sup> yr	23FS20MB000001	Ankita
11	Simran Maharchi	M.Sc Biotech	23FS20MB000022	Simran
12	Simran Duggal	M.Sc Biotech	23FS20MB000009	Simran Duggal
13	Pallavi Anand	M.Sc biotech	23FS20MB000025	Pallavi
14	Radhika Rathore	M.Sc Biotech 1 <sup>st</sup> yr	23FS20MB000008	Radhika
15	Sakshi ]G6	B.Sc Biotech / 2 <sup>nd</sup> yr	221002057	Sakshi
16	Anshulika Sorune	B.Sc biotech / 3 <sup>rd</sup> yr	221002053	Anshulika
17	Prachi Jain	B.Sc biotech / 2 <sup>nd</sup> yr	221002076	Prachi
18	Divyanshu Joshi	B.Sc biotech / 2 <sup>nd</sup> yr	221002056	Divyanshu
19	Aditi Rathore	B.Sc biotech / 2 <sup>nd</sup> yr	221002036	Aditi
20	Shruti Gannir	B.Sc biotech / 1 <sup>st</sup> yr	23FS10BID000054	Shruti
21	Vaishali Shakti	B.Sc biotech / 1 <sup>st</sup> yr	23FS10BID000035	Vaishali
22	Aishwarya Rai Saxena	B.Sc biotech / 1 <sup>st</sup> yr	" 65	Aishwarya
23	Riddhima Gupta	Bcom hono	23FM10BCM000044	Riddhima
24	Priyanka Chatterjee	Bcom hono	23FM10BCM000021	Priyanka
25	Tushar Parulkar	B.Sc biotech / 1 <sup>st</sup> yr	23FS10BID000040	Tushar
26				



MANIPAL UNIVERSITY  
JAIPUR



**DEPARTMENT OF BIOSCIENCES**  
**biotech Club & Microbiologists Society, India (MBSI)**  
**rangoli Competition on Bacterial and Viral Diseases**

November 8th, 2023

**ATTENDANCE**

S.No.	Name	Course/Year	Registration No.	Signature
1	Dr. Sandip B. Hirakote	Faculty	Biosciences	[Signature]
2	Dr. Abhyud Singh	- do -	Biosciences	[Signature]
3	Dr. Kavita	- do -	I.T	[Signature]
4	Dr. Neha	- do -	DSE	[Signature]
5	Shatowjai	- do -	Bio Sciences	[Signature]
6	Dr. Sarabh Srivastava	- do -	Chemistry	[Signature]
7	Dr. Sripama Ray	- do -	Chemistry	[Signature]
8	Dr. Praveen K. Surolia	- do -	Chemistry	[Signature]
9	Dr. Mousumi Debnath	- do -	Bio sciences	[Signature]
10	Priya Agarwal	Biotech I <sup>st</sup> year	23FS10BI000042	[Signature]
11	Akshara Alex	Biotech 1 <sup>st</sup>	23FS10BI000022	[Signature]
12	Pragya Chauhan	Biotech I <sup>st</sup>	23FS10BI000006	[Signature]
13	Aryam	BAUB	23FL10IBL00081	[Signature]
14	Aayushi	Msc. Clinical Psy	23FA20MCP00005	[Signature]
15	Ektta	Msc. Clinical Psy	23FA20MCP00025	[Signature]
16	Narvika Choudhary	Biotech II <sup>nd</sup> year	221002040	[Signature]
17	Anindhan Yadav	Micro Biotech 2 <sup>nd</sup> year	221002015	[Signature]
18	Ritik Mittal	MCA II <sup>nd</sup> year	221020007	[Signature]
19	Saranst Sharma	BFA II year	220603022	[Signature]
20	Nikita Thakur	Bsc. biotech 2 <sup>nd</sup> year	221002045	[Signature]
21	Jushan Pareek	Bsc biotech 1 <sup>st</sup> year	23FS10BI000040	[Signature]
22	Aishwarya Rai Senera	"	23FS10BI000065	[Signature]
23	Vaishali Shahi	"	23FS10BI000056	[Signature]
24				
25	Charvi Solanki	BCA	221015168	[Signature]
26	Simran Chhipa	BCA	221015104	[Signature]
27				

**9. POST EVENT LINK:**

Registration Form: <https://forms.gle/bQTpySKTgXzm9BnHA>  
All media related to the event: [https://mu.jmanipal-my.sharepoint.com/:f:/g/personal/anshulika\\_211002053\\_mu\\_jmanipal\\_edu/Evtb6qt\\_fiYFDt0bMFbgnIX4BcF9OYXtxcowmUqMqj0drNg?e=krd05e](https://mu.jmanipal-my.sharepoint.com/:f:/g/personal/anshulika_211002053_mu_jmanipal_edu/Evtb6qt_fiYFDt0bMFbgnIX4BcF9OYXtxcowmUqMqj0drNg?e=krd05e)

[Signature]

Anshulika Saxena  
President, Biotech Club MUJ  
Signature of the Student Coordinator

[Signature]

Dr. Mousumi Debnath  
Faculty Coordinator, Biotech Club  
Signature of the Faculty Coordinator



MANIPAL UNIVERSITY  
JAIPUR

## FACULTY OF DESIGN

### International Conference on Sustainable Development for Heritage and Built Environment

22/06/2023 – 23/06/2023

Head, Department of Interior Design  
SD&A, Faculty of Design  
Manipal University Jaipur



## **Content of Report**

1. Introduction of the Event
2. Objective of the Event
3. Beneficiaries of the Event
4. Brief Description of the event
5. Photographs
6. Poster of an Event
7. Schedule of the Event
8. Attendance of the Event





## 1. Introduction of the Event

The conference is inspired from the critical challenge of human, environmental, heritage and built sustainability concerning the present and future generations in a global-scale context. This theme emphasizes the strong foundation that is provided by using research to inform our everyday practices, policies, and analytical approaches. This interdisciplinary forum is for scholars, teachers, and practitioners from the built environment professional discipline who share an interest in—and concern for— sustainability in an holistic perspective, where environmental, cultural, economic and social concerns intersect. It will provide a platform for various individuals to connect the past and present and develop solutions to a more universal and environmentally friendly approach towards built environment.

The conference will include topics such as

- (i) Sustainable approach to design in built environment,
- (ii) Sustainability & built Heritage,
- (iii) Conserving Built Heritage,
- (iv) Sustainable Policies for Environmental and Infrastructure Planning,
- (v) Earth and Environmental Planning & Design

## 2. Objective of the Event

This conference was a gathering of minds dedicated to addressing the pressing challenges of sustainability that affect our world today and tomorrow. It recognized that sustainability is a multifaceted concept that requires interdisciplinary collaboration and rigorous research. By bringing together scholars, educators, and practitioners, the conference facilitated the exchange of ideas and the development of solutions that promote a more sustainable, resilient, and environmentally friendly built environment.

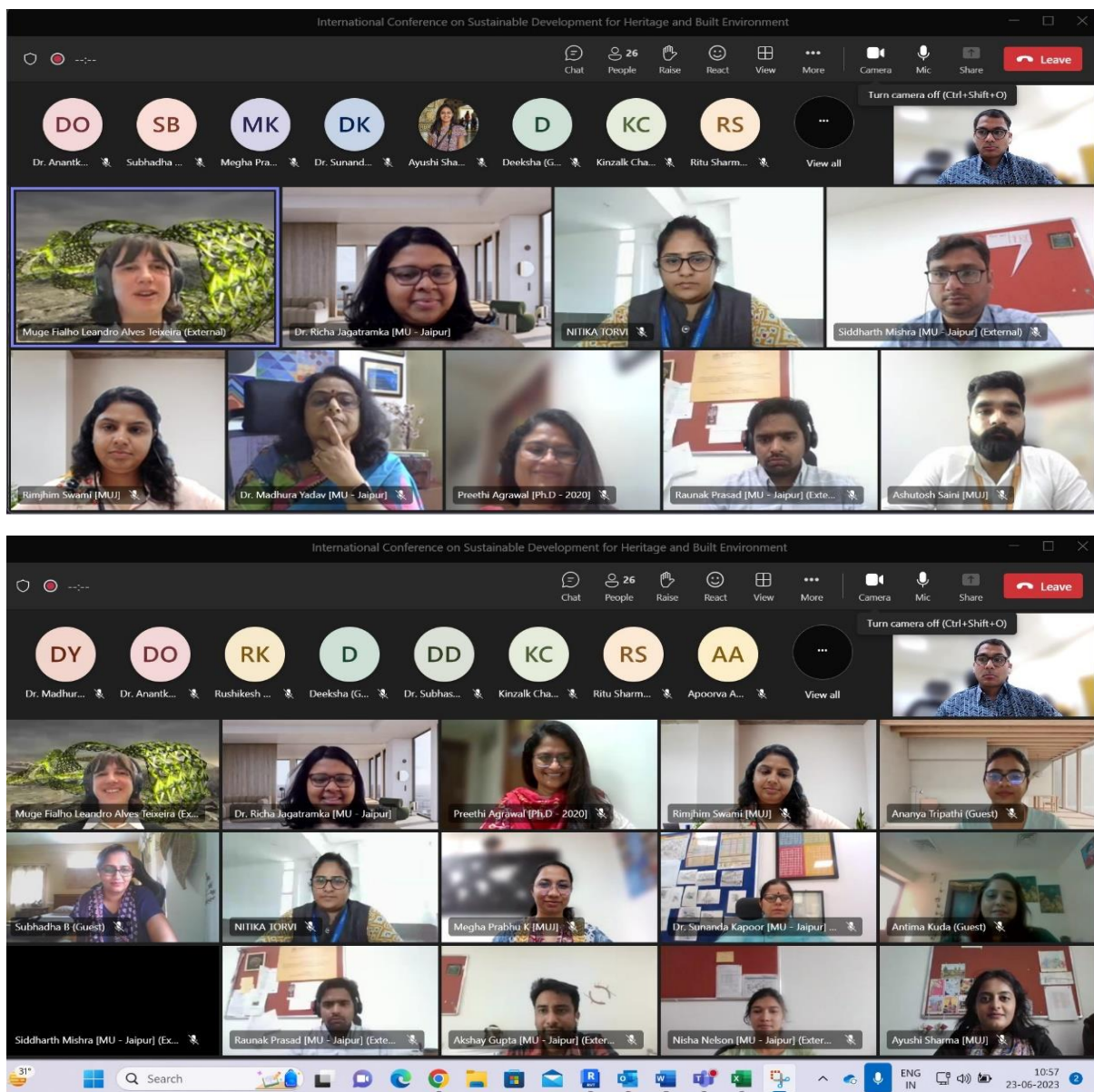
## 3. Beneficiary of the event

This interdisciplinary forum is for scholars, teachers, and practitioners from the built environment professional discipline who share an interest in—and concern for— sustainability in an holistic perspective, where environmental, cultural, economic and social concerns intersect.

#### 4. Brief Description of the event

The conference was hosted by Department of Interior Design and School of Architecture and Design, Faculty of Design at Manipal University Jaipur. This interactive and engaging event is tailored exclusively for our researchers, as part of our commitment to foster continuous learning, future research opportunities. The presentations focused on sustainability as the prime agenda and paved way for the researchers to present their work at an international level.

#### 5. Photographs of the Event



Snippets of the Conference

## 6. Poster of the event



**MANIPAL UNIVERSITY  
JAIPUR**  
(University under Section 2(f) of the UGC Act)

School of Architecture and  
Design and Department of  
Interior Design

International Conference  
on  
**“Sustainable  
Development for  
Heritage and Built  
Environment”**

**22<sup>nd</sup> June – 23<sup>rd</sup> June 2023**

Venue:  
Manipal University Jaipur/ Hybrid  
Mode

**About the University**  
The Manipal Education Group, with its heritage of excellence in higher education for over 60 years, launched Manipal University Jaipur (MUJ) in 2011. MUJ is affiliated by University Grants Commission, Association of Indian Universities, Council of Architecture, Bar Council of India and All India Council of Technical Education. MUJ is the first university in the state of Rajasthan, accredited as A+ (3.28) grade by NAAC. The university offers courses in different disciplines like Architecture, Interior Design, Fashion Design, Applied arts, Engineering, Management, Hospitality, Humanities & Social Sciences, Journalism and Mass communication, Basic Sciences, Law, Business & Commerce.

**Organizing Committee**  
**Patron**  
Dr. G. K. Prabhu (President, MUJ)  
**Co - Patrons**  
Dr. Thammaiah Chekkera (Pro-President, MUJ)  
Dr. Nitu Bhatnagar (Registrar, MUJ)  
**Chair:**  
Dr. Madhura Yadav (Dean, FoD, MUJ)  
Dr. J.P. Sampath Kumar (Director, SD&A, MUJ)  
**Convenors:**  
Dr. Richa Jagatramka (Assist. Prof., ID-SD&A)  
Ar. Raunak Prasad (Assist. Prof., SA&D)  
**Coordinators:**  
Ar. Megha Prabhu (Assist. Prof., ID-SD&A)  
Ar. Himangshu Kedia (Assist. Prof., ID-SD&A)  
Ar. Akshay Gupta (Assist. Prof., SA&D)  
Ar. Ashutosh Saini (Assist. Prof., SA&D)

**About the Conference**  
The conference will include topics such as

- (i) Sustainable approach to design in built environment,
- (ii) Sustainability & built Heritage,
- (iii) Conserving Built Heritage,
- (iv) Sustainable Policies for Environmental and Infrastructure Planning,
- (v) Earth and Environmental Planning & Design.

Participants will gain exposure and insight To various sustainable approaches to sustain the heritage as well as define the built environment. It will provide a platform for various individuals to connect the past and present and develop solutions to a more universal and environmentally friendly approach towards built environment.

**Submission Deadline:**  
**Call for Papers – 23<sup>rd</sup> Feb 2023**  
**Abstract Submission – 30<sup>th</sup> March 2023**  
**Acceptance Notification – 7<sup>th</sup> April 2023**  
**Full paper Submission – 23<sup>rd</sup> April 2023**

**Publication –**  
**Conference proceedings with IOP**  
**Conference Series: Earth and Environmental Science (SCOPUS Indexed)**

**Notable Speakers**

1. Dr Ranjith Dayaranthe , Associate Professor, Asian School of Architecture, Australia
2. Dr Muge Belek Fialho Teixeira, Queensland University of Technology.
3. Dr. Shikha Jain, Director, DRONAH
4. Dr Rajat Gupta, Oxford Brookes, Director, Dept. of sustainable development
5. Ar. Chitra Vishwanath, Biome Bangalore.

**Conference Fees :**  
Students 9500 INR  
Academics & professional 10500 INR

For International Participants  
Students - 150 USD  
Academics & professional – 180 USD

For additional information contact –  
[richa.jagatramka@jaipur.manipal.edu](mailto:richa.jagatramka@jaipur.manipal.edu)  
[raunak.prasad@jaipur.manipal.edu](mailto:raunak.prasad@jaipur.manipal.edu)

## 7. Schedule of the event

Time	Event	Speaker
11:00 – 11:30 AM	Opening speech	Dr Richa Jagatramka
11: 30 – 11:35 AM	Welcome address	Dr Madhura Yadav
11: 35 – 11:45 AM	Introduction of international speaker	Ar Himangshu Kedia
11: 45 AM – 12:45 PM	Presentation by Dr Muge	Dr Muge
12: 45 – 01:00 PM	Q & A session	
01:00 – 01:05PM	Vote of Thanks	Ar. Himangshu Kedia



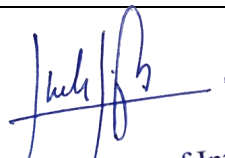
## Meeting Link :

[https://teams.microsoft.com/l/meetup-join/19%3ameeting\\_MmRjNjZiN2ltMTc1NS00YmJlLTkwMTItMzBiYTVjNTIOYTRh%40thread.v2/0?context=%7b%22Tid%22%3a%227d0726e8-bf4b-4ac1-99f1-010fb11f1d3f%22%2c%22Oid%22%3a%2216be8839-914f-456c-9836-e6b3ba8fa2f9%22%7d](https://teams.microsoft.com/l/meetup-join/19%3ameeting_MmRjNjZiN2ltMTc1NS00YmJlLTkwMTItMzBiYTVjNTIOYTRh%40thread.v2/0?context=%7b%22Tid%22%3a%227d0726e8-bf4b-4ac1-99f1-010fb11f1d3f%22%2c%22Oid%22%3a%2216be8839-914f-456c-9836-e6b3ba8fa2f9%22%7d)

## 8. Attendance of the Event

Total attendees – 28 participants from MUJ and outside

Sl.no	Name	Organisation
1	Dr. Richa Jagatramka	FOD
2	Megha Prabhu K	FOD
3	Dr. Sampath Kumar Padmanabha Jinka	FOD
4	Dr. Madhura Yadav	FOD
5	Dr. Anantkumar Dada Ozarkar	FOD
6	Dr. Subhash Chandra Devrath	FOD
7	Nisha Nelson	FOD
8	Preethi Agrawal	Practicing Architect and PhD scholar
9	NITIKA TORVI	Christ University
10	Subhadha B	Christ University
11	Himangshu Kedia	FOD
12	Rushikesh Kolte	MNIT
13	Dr. Sunanda Kapoor	FOD
14	Ananya Tripathi	AKTU - GCA
15	Kinzalk Chauhan	FOD
16	Ritu Sharma	FOS – Phd Scholar
17	Rimjhim Swami	FOD
18	Ayushi Sharma	FOD
19	Apoorva Agarwal	FOD
20	Muge Fialho Leandro Alves Teixeira	QUT Australia
21	Deeksha	MNIT
22	Siddharth Mishra	FOD
23	Akshay Gupta	FOD
24	Ritu Sharma	FOD
25	Neha Saxena	FOD
26	Antima Kuda	MAHE Dubai
27	Raunak Prasad	FOD
28	Ashutosh Saini	FOD

  
Head, Department of Interior Design  
SD&A, Faculty of Design  
Manipal University Jaipur



MUJ/Q&C/22/F/1.01

Event Report Format



MANIPAL UNIVERSITY  
JAIPUR

**FACULTY OF SCIENCE**

**SCHOOL OF BASIC SCIENCES**

**DEPARTMENT OF BIOSCIENCES**

**Invitation for Expert Lecture**

**On**

**Nature-based technologies for treatment and recycling  
wastewater**

**28 July, 2023 ~ 11.00AM**

**Room No 020, 1 AB, MUJ**



## Content of Report (index)

(Page number may not be required)

(Delete entries which are not applicable)

1. Introduction of the Event
2. Objective of the Event
3. Beneficiaries of the Event
4. Details of the Guests
5. Brief Description of the event
6. Geo-tagged Photographs
7. Brochure or creative of the event
8. Schedule of the Event
9. Attendance of the Event



## 1. Introduction of the Event

Expert Lecture On Nature-based technologies for treatment and recycling wastewater by Dr. Sanjeev Prajapati, Department of Hydro and Renewable Energy (HRED) Indian Institute of Technology, Roorkee

## 2. Objective of the Event (bullet points or about 50 words)

The lecture was designed to provide insight into the processes and techniques that are applied in the wastewater treatment field, where the focus is laid on the basic principles, local conditions, basic circumstances, and performance of constructed wetlands integrated with the algae-based process which aimed towards the resource recycling.

## 3. Beneficiaries of the Event (Student/Faculty/Community etc) (25 words)

The lecture was the starting stage for the students to learn about the integrated constructed wetlands and learn about the design of various industrial components. This is thus meant to bring about a general understanding of the research illustrated and explained by the expert.

## 4. Details of the Guests (Chief Guests, speakers etc Designation, organization, contact details if any please give them in sr no)

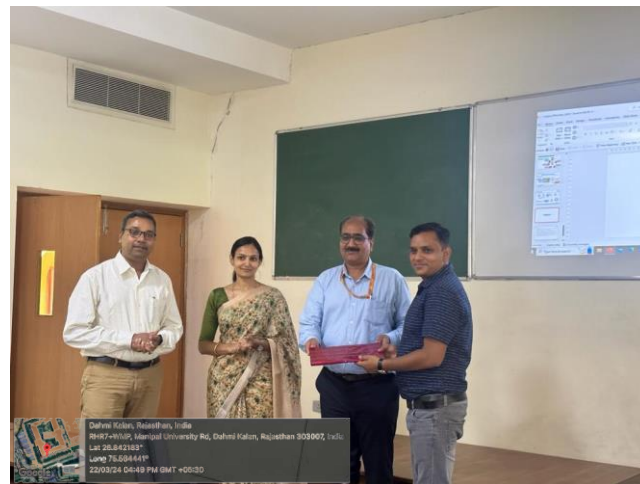
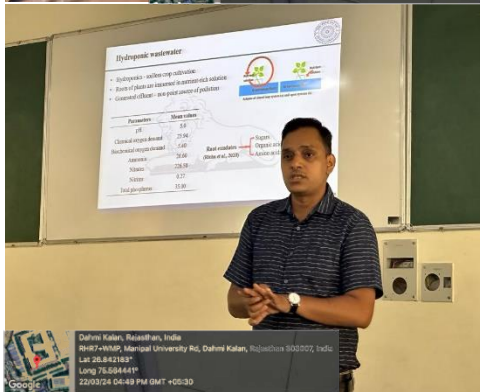
Dr. Sanjeev Prajapati, Department of Hydro and Renewable Energy (HRED)  
Indian Institute of Technology, Roorkee

## 5. Brief Description of the event (about 200 words)

Expert Lecture on the Nature-based technologies for treatment and recycling wastewater. The lecture was designed to provide insight into the processes and techniques that are applied in the wastewater treatment field, where the focus is laid on the basic principles, local conditions, essential circumstances, and performance of constructed wetlands integrated with the algae-based process, which is aimed towards resource recycling.

## 6. Photographs

3 to 5 geotagged photographs of the event or screenshots of the







7. Brochure or creative of the event (insert in the document only )

 **MANIPAL UNIVERSITY  
JAIPUR**

**Department of Biosciences**  
*Invitation for Expert Lecture*

On

**Nature-based technologies for treatment  
and recycling wastewater**


By

**Dr. Sanjeev Prajapati**  
Department of Hydro and Renewable Energy (HRED)  
Indian Institute of Technology, Roorkee



**28<sup>th</sup> July, 2023**  
**11.00AM**  
**Room No 020, 1 AB**

Convenor  
**Dr. Monika Sogani**  
Associate Professor  
Department of Biosciences  
Manipal University Jaipur





### 8. Schedule of the event (insert in the report)

28 July, 2023 ~ 11.00AM

Room No O20, 1 AB

Manipal University Jaipur

### 9. Attendance of the Event (insert in the document only)

**Total attendee - Approx 20 (15 in list plus few more students)**

Sr. No	Name of Institution	Place of Institution	Name of Attendee	Name of Dept
1.	Manipal University Jaipur	Jaipur	Dr. Monika Sogani	Biosciences
2.	Manipal University Jaipur	Jaipur	Dr. Sandeep K Srivatava	Biosciences
3.	Manipal University Jaipur	Jaipur	Dr. Rakesh Sharma	Biosciences
4.	Manipal University Jaipur	Jaipur	Dr. Anand Chakinala	Chemical Engineering
5.	Manipal University Jaipur	Jaipur	Dr. Nitesh Kumar Poddar	Biosciences
6.	Manipal University Jaipur	Jaipur	Dr. Anil Dutt Vyas	Civil Engineering
7.	Manipal University Jaipur	Jaipur	Dr. Karishma Sharma	Chemical Engineering
8.	University of Mannheim	Germany	Rosy	Biology
8.	Manipal University Jaipur	Jaipur	Priyanka Sharma	Biosciences
9.	Manipal University Jaipur	Jaipur	Bhanu Kushwaha	Biosciences
10.	Manipal University Jaipur	Jaipur	Sandesh Telang	Biosciences
11.	Manipal University Jaipur	Jaipur	Himanshi Sen	Biosciences
12.	Manipal University Jaipur	Jaipur	Nishaan Sen Gupta	Biosciences
13.	Manipal University Jaipur	Jaipur	Jayana Rajvanshi	Biosciences
14.	Manipal University Jaipur	Jaipur	Sapna Kumari	Biosciences
15.	Manipal University Jaipur	Jaipur	Nandana Chakinala	Chemical Engineering

28-07-2023

**Seal and Signature of Head with date**



**FACULTY OF SCIENCE**

**SCHOOL OF BASIC SCIENCES**

**Department of Computer Applications**

**International Seminar Report**

**14<sup>th</sup> March, 2023**

## Event Report

### A Global Conclave for Circular Economy and Sustainability (CORE-2023)

#### International Seminar on Fireside Chat on Global Business Opportunities: Unlimited (Clean Water and Sanitation)

**Title:** International Seminar on Fireside Chat on Global Business Opportunities: Unlimited

**Date:** 14<sup>th</sup> March, 2023

**Venue:** Smt Sharda Pai Auditorium, Manipal University Jaipur

**Panelist:**

1. Mr. Bjorn Appelqvist, Scientific and Technical Committee Chair
2. Ms. Carolina Urmeneta, Circular Economy Program Director and America's regional lead for the Global Methane Hub
3. Mr. Siddhant Agrawal, CEO, CDC and Chair – circular economy ICWM.
4. Mr. Siddhartha Srivastava, Dy. General Manger – Sales and Marketing, Blue Planet Group

**Core Committee of the Club:**

**Convener:** Dr. Devershi Pallavi Bhatt

**Student Coordinator:**

Muskan Goyal (211015077)

Sanchit Sardana (211015036)

#### 1. Introduction of the Event:

International Seminar, Fireside Chat on Global Business Opportunities: Unlimited, organized by Department of Computer Applications, in Association with International Solid Waste Association (ISWA) & The Institute of Chartered Waste Managers (ICWM). Students from different disciplines of MUJ were attended the international seminar to get an exposure about clean water and Sanitation.

#### 2. Objective of the Event:

- a. To provide the students of MUJ with Global business opportunities to learn and be aware about clean water and sanitation.
- b. To learn about how business increases focus on can leveraging circular strategies to achieve climate goals.
- c. To learn how the transition to a circular economy can benefit our economy.
- d. To learn about Nationally Determined Contribution (NDC), the first long-term climate strategy.

#### 3. Beneficiaries of the Event:

Students of MUJ across several disciplines like BCA, B.Sc. Chemistry, B.Sc. Bio Technology, B.Sc. Micro Biology actively participated in panel discussion.

#### **4. Details of Panelists:**

##### **I) Mr. Bjorn Appelqvist**

Björn Appelqvist has worked in the waste management sector for more than 20 years and has worked in consultancy, municipalities, intermunicipal companies and with private contractors. Since 2016, he works as Department Manager for Waste & Resource Management at Ramboll, a global engineering, architecture and consultancy company founded in Denmark in 1945. Björn is also a member of the Technical Committee of DAKOFA – Waste and Resource Network Denmark.

Mr. Appelqvist has been an active member of ISWA since 2006. In 2013 he was elected Chair of the Working Group on Recycling and Waste Minimisation and part of the Scientific and Technical Committee of ISWA. Since 2018, Björn is the Chair of the Scientific and Technical Committee of ISWA and member of the ISWA Board of Executives.

##### **II) Ms. Carolina Urmeneta**

Ms. Carolina Urmeneta is the Circular Economy Program Director, and Americas Regional Lead for The Global Methane Hub. A Civil Engineer in Biotechnology, from University of Chile, International Master in Sustainability Sciences, Diploma in Disaster Risk Management and Adaptation to Climate Change. She holds 15 years of work experience in public policy development, studies, projects, and consulting on climate change and sustainability. For the last 4 years, she was the head of Climate Change for the Government of Chile, leading transformative public policy as the Climate Change Framework Law, approved unanimously in the congress, the ambitious update of the NDC, and the first Long Term Strategy of Chile. Chile was one of the first countries to include circular economy concrete goals in their climate change commitments. Previously she worked supporting the design and implementation of methane capture projects in the agriculture and waste sector and the regular and voluntary carbon market.

##### **III) Mr. Siddhant Agrawal**

Mr. Siddhant Agrawal is the Head of Innovations and Operations at the Centre for Development Communication and is the Founder Member of the Young Professionals Group – India Chapter of ISWA. He is also the Director of Global Public School in Jharana which caters to the students in the rural area of Jharana, Madhorajpura, etc. He holds a Master's Degree in Development Management from S.P. Jain Institute of Management and Research, Mumbai, a Master's in International Development from the University of Denver, and a Bachelor's degree in Economics from the University of Sussex. He has more than 7 years of experience in the Waste Management Sector and has been actively involved in the Management of various projects. He had also initiated a project for managing textile waste at the consumer end (REVIRE) and has engaged 1132 customers to date; more than 20 women as self-entrepreneurs in textile waste management.

##### **IV) Mr. Siddhartha Srivastava**

Mr. Siddharth Srivastava is carrying a decade of experience in green energy and waste management industry. He has been instrumental in penetrating the Asian market for waste management projects under the Brand name of Blue Planet Group. With an engineering background Siddharth is working with different stakeholders like policy makers, local project teams and multiple clients for development of projects and developing new opportunities in the South East Asian market.

5. **Brief Description of the event:** UG and PG students across different bachelor courses were attended the Panel Discussion.

- **Prof. Thammaiah CS - Pro-President, MUJ** welcomed the panellist Mr. Bjorn Appelqvist and Ms. Carolina Urmeneta.
- **Prof. Lalita Ledwani- Dean, FoS, MUJ** welcomed the panellist Mr. Siddhant Agrawal.
- **Prof. Devershi Pallavi Bhatt, HoD - Department of Computer Applications** welcomed the panellist Mr. Siddhartha Srivastava.

During the discussion, panellists' brain-stormed on following topics-

1. **Bjorn-** there is an increasing buzz about circular economy, what do you think are the global opportunities around it, how can businesses increase focus on leveraging circular strategies to achieve climate goals.

2. **Siddhant** - Continue talking about circular economy How will the transition to a circular economy benefit our economy and contribute to reach the target of climate-neutrality by 2050? Being a second generation entrepreneur in the waste management sector have you observed any shift or transitions

3. **Siddhartha-** Biomaterials will be a hot topic but also a polarising one. They will be scrutinised in a holistic lens, do you think they are a part of the solution?

4. **Carolina-** Chile implemented the Nationally Determined Contribution (NDC), the first long-term climate strategy, the Climate Risk Atlas at the community level, the first regional action plans against climate change, what should other nations learn from this while designing their own action plan

5. **Siddhartha.** While doing multiple projects on Waste Management in Asia what difference have you noticed in India and other countries in terms of execution

6. **Siddhant-** you're a hardcore operations person, what do you think are your biggest challenges when executing in different parts of India.

7. **Carolina-** Do you think more businesses should focus on mitigating methane or reducing methane emissions, is there a way to incentivise it as a business opportunity?

8. **Siddhartha-** what do you think are the most exciting new business opportunities in the waste management that you are coming across during your expansion in the south East Asian market

9. **Bjorn** - galvanising action as the treaty takes shape and what kind of changes will they bring in the global business landscape

During the session students also asked relevant questions from panellists and got answered.

Finally, Vote of Thanks was given by Convener – Prof. Devershi Pallavi Bhatt, HoD - Department of Computer Applications

6. Photographs of the event:



Seminar Pictures



7. Brochure :

**MANIPAL UNIVERSITY JAIPUR**

**G20** भारत 2023

**ISWA** INTERNATIONAL SOLID WASTE ASSOCIATION

**ICWM** INSTITUTE OF CHARTED WASTE MANAGERS

**ENSOL** **GreenTech** **CDC**

## INTERNATIONAL SEMINAR

on

### Fireside Chat on Global Business Opportunities : Unlimited (Clean Water and Sanitation)

In Association with  
**International Solid Waste Association (ISWA)**  
&  
**The Institute of Chartist Waste Managers (ICWM)**

**March 14, 2023**  
Venue: Smt. Sharada Pai Auditorium | Time: 2:00 PM onwards

**Panelist**



**Björn Appelqvist**  
StG Chair  
ISWA



**Rene Moller Rosendal**  
Vice Chair ISWA Working  
Group on Landfill



**Carolina Urmeneta**  
Circular Economy Program  
Director and Americas' Regional Lead  
for The Global Methane Hub



**Dr. Krishna Mohan**  
Scientist at Birla Institute  
of Scientific Research



**Siddhant Agrawal**  
Head of Innovations and  
Operations at the Centre for  
Development Communication

Convener  
**Dr. Devershi Pallavi Bhatt**  
Head of Department  
Department of Computer Applications

Organized by  
Department of Computer Applications  
Faculty of Science  
Manipal University Jaipur







9. Attendance of the Event

**Total attendee- 78**

**List:**

Preside Chat on Global Business opportunity

S.No	Attendee Name	Organization	Phone Number	Email	Signature
1	Khushi Sharma	B.C.A [A]	9414353058	Khushiacharya180	
2	Tanmay Rasthore	B.C.A (A)	7019269940	Tanmay_rasthore1763	
3	Harshvardhan Singh	B.C.A (A)	9024342576	Harshvardhan_0808	
4	Sunny Chauhan	B.C.A (H)	9521799167	Sunny_04194	
5	Dinesh Suthar	B.C.A (A)	9645661354	Sutadinesh35	
6	Raghav Raj Arora	BCA (B)	8302933458	Raghavraj_31820	
7	Keshav Bhogat	BCA (A)	8529570229	Keshavbhogat01	
8	Nakul	BCA (A)	968052295	nakul09012001@gmail.com	
9	Mohit	BCA (A)	061903755	mohitjayal08	
10	Ronit	BCA (A)	810236495	ronitmur@gmail.com	
11	Vaibhav Raj	BCA (A)	9523371767	vibhavraj615@gmail.com	
12	Aushan	BCA (A)	820997409	gushan_21015050	
13	Vishaldeep Seniwat	B.Sc Maths	9729432227	seniwatvishal2001@gmail.com	
14	Dhnyraj	B.Sc Maths	9509400513	dhnyraj_21105008	
15	Sushil Madhavi	B.Sc Maths	6778858061	Sushilmadhavi0909@gmail.com	
16	Vansh Gupta	B.Sc Maths	961081650	ivishvan180	
17	Manish Jain	BCA (A)	9955161427	Saini Manish 410	
18	Divanshu	BCA (A)	7412088065	Divanshu@gmail.com	
19	Tushar	BCA (A)	9079706721	Tushar_129@gmail.com	
20	Sunil	BCA (A)	9587981027	Sunil_22@gmail.com	
21	Yagya Goel	BCA (A)	8272024813	yagyagoel87@gmail.com	
22	Harshit Kumar	BCA (A)	8562804798	HK8562804798@gmail.com	
23	Masood Khan	BCA (A)	9079558836	Masoodkhan0805@gmail.com	
24	Gursharan	BCA (A)	8267901487	gursharan10@gmail.com	

Event: Preside Chat on Global Business opportunity

Attendee Name	Organization	Phone No	E-mail	Signature	
25	Keshav Sharma	BCA - (B)	8290421602	Keshav_221015166	
26	Ajaya Kumawat	BCA - (B)	8094986522	ajaya_221015157	
27	Jayant Singh Rathore	BCA - (B)	9829967772	Jayant_221015127	
28	Rakesh Singh	BCA - (A)	9024907794	Rakesh_221015083	
29	Nitesh Pradyapat	BCA (A)	7414827170	Nitesh_221015060	
30	Mohit Sharma	BCA - (A)	8005561989	mohit_221015080	
31	Vikash Jolhi	BCA - (A)	63753383128	Vikashjohal6375	
32	Prin Sharma	BCA - (A)	7339882156	Prinsharma0244@gmail.com	
33	Mohit Pratap	BCA - (A)	9352072238	mohitpratap12@gmail.com	
34	Gaurav Agarwal	BCA - (A)	790306658	Gaurav_22625038	
35	Ashish Kumar Yadav	BCA - (A)	6202094983	Ashish_221015010	
36	Hemant Saini	BCA - (A)	6378419005	hemant80saini@gmail.com	
37	Mohit Kumar	BCA - (A)	9667176813	Mohit_221015004	
38	Praveer Singh	BCA - (A)	8094645040	askpraveerchauhan@gmail.com	
39	Sunny Chauhan	BCA - (A)	9521799167	Sunnychauhan62916	
40	Aditya Rawat	BCA - (A)	9130589130	Adityarawat1144556	
41	Krishna Bhani	BCA - (A)	9828051261	Krishna_221015085	
42	Ahaana Verma	BCA - (A)	9315421451	Ahaana_221015001	
43	Dhnyraj	BCA - (A)	9079246533	dhnyraj_221015057	
44	Mohammad Faiz	BCA - (A)	9024133338	Mohammadfaiz03@gmail.com	
45	Balsham Jais	BCA - (A)	9829034343	Serisobhan_soni@pttdl.com	
46	Vishal Anand Mishra	BCA - (A)	9145466789	Vishal_221015011	
47	Ayan Ahmed	BCA - (A)	8233700000	ayan_221015017@gmail.com	
48	Satgagan Kam Patni	BCA - (A)	8851838558	Satgagan_221015015@gmail.com	
49	Smriti Gupta	BCA - (A)	9004502129	smritigupta20@gmail.com	
50	Anshika Kumawat	BCA - (A)	9412534471	anshika_221015082@gmail.com	
51	Ritika Sharma	BCA - (B)	6350217709	ritika_221015137	
52					



	Attendee Name	Organisation	Phone No.	E-mail	Signature
53	MAYANK PURI	BCA - (B)	9928837760	Mohank280@gmail.com	
54	Abhishek Pillai	BCA - B	7231837527	Abhishekpillai95@gmail.com	
55	Simran Chhipa	BCA - B	9376564871	chhipasimran2005@gmail.com	
56	Poojyoti Bhatnagar	BCA - B	741400876	jainpoojyoti15@gmail.com	
57	Chirvi Salunki	BCA - (B)	9460186087	chirvisalunki444@gmail.com	
58	Ramnik Gulati	BCA - B	7232840102	gulatiRamnik32@gmail.com	
59	Manvendra Singh	BCA - B	9652115990	manvendra233@gmail.com	
60	Muhammad Bilal	BCA - B	6900607971	Muhammadbilal@gmail.com	
61	Pratyaksh Bhandari	BCA - 2nd year	7733025541	PratyakshA	
62	Varishka Kapi	BCA - 1st year	7990832129	Varishka.kapi@gmail.com	
63	OMSHREYA	BCA - 1st year	9508146145	omshreyabhatnagar@gmail.com	
64	DIYA SHARMA	BCA - 1st year	8302556333	sharmadiya267@gmail.com	
65	Raksha Agarwal	BCA - 1st year	9339451018	agarwalraksha0625@gmail.com	
66	Rohit Agarwal	BCA - IV sem	9929786267	rohitagrawal0602@gmail.com	
67	Bhuvan Maheshwari	BCA - IV sem	8448447410	bhuvan.211015027@gmail.com	
68	Namisha	BCA IV sem	811280849	Namishakb2	
69	Amit	BCA IV sem	9636882797	AmitHuniker	
70	ROHIT SOLANKI	MCA IT sem	785501721	Rohit22102004@gmail.com	
71	Jay Sharma	MCA IT sem	792206570	Jay221020076	
72	Anshu Bhatnagar	BCA IV sem	102023123	Anshubhatnagar	
73	Vishal Gupta	BCA IV sem	9929119295	vishalgupta46@gmail.com	
74	Tanishka Gupta	BCA IV Sem	9603632156	TanishkaGupta	
75	Tanya Jain	EL	8806106548	Tanyajain36@gmail.com	
76	Prity Jain	BCA II Sem	81		
77	Shreya	BCA II Sem			
78	Hitesh Jain	BCA IV Sem			
79					
80					



MANIPAL UNIVERSITY  
JAIPUR



MUJ/DSW/Society Connect/ Oct2023/03



MANIPAL UNIVERSITY  
JAIPUR

## **DIRECTORATE OF STUDENT'S WELFARE**

**(SOCIETY CONNECT)**

**#DAANUTSAV 2023**

**Plantation Drive**

**3<sup>rd</sup> October 2023**

**Date: 3<sup>rd</sup> October 2023**



## Index

<b>S.No.</b>	<b>Activity Heads</b>	<b>Page no.</b>
1.	Introduction of the Event	1
2.	Objective of the Event	1
3.	Beneficiaries of the Event	1
4.	Brief Description of the event	1
5.	Photographs	2-4
6.	Brochure or creative of the event	5-6
7.	Schedule of the Event	6
8.	Attendance of the Event	6-9
9.	Feedback of the Event	9
10.	Link of MUJ website	9

## 1. Introduction of the Event

“A nation that destroys its soils destroys itself. Forests are the lungs of our land, purifying the air and giving fresh strength to our people. ” Trees are indispensable for life. Man can't live without trees. However, the present condition of forests in the world, especially developing countries is pathetic and miserable. Forests are the source of life. They are the giving angels. They give man oxygen, rains, wood, fruit, make the world look so beautiful, yet the sinister man kills them! Who will be more inhumane than man himself? Cutting of forests ultimately endangers man's own existence. Trees are important to the environment; they recycle water and process carbon dioxide in the atmosphere through photosynthesis. They are the world's full-time purifiers of air and water. Their cutting will disturb the natural water cycles which will lead to the shortage of fresh water in the water reserves of the world.

Rotaract Green Club under Society Connect organized a Plantation Drive on account of DAAN UTSAV 2031. It took place on the 3<sup>rd</sup> of October from 10 a.m. Students were taken to the Mahatma Gandhi School, Begus for the drive. The drive aimed to instill a sense of discipline and respect for the environment while doing our part.

## 2. Objective of the Event

- Spread awareness on the importance of afforestation
- Direct students' mind in constructive activities
- Contribution to the society
- Promote tree planting
- Create awareness regarding importance of ecology
- Attempt at reducing pollution and improve green ambience

## 3. Beneficiaries of the Event

Community

## 4. Brief Description of the event

Rotaract Green Club organized the Plantation Drive on the 3<sup>rd</sup> October at 9 a.m. on account of DAAN UTSAV 2023. The drive's main aim was to direct student's mind

in constructive activities with the positive outcome through the facilitation of contributing to the nature and environment.

It also aimed at spreading awareness about the effects of global warming and the positive effects of planting trees. The students gathered on campus to go to the Mahatma Gandhi School, Begus.

The students participated in the drive enthusiastically and helped each other in planting the saplings. All the saplings were planted in the school ground by students. Participants were highly energetic to make the event a big success. A spirit of teamwork, exchange of ideas and enthusiasm of the participants especially among the students could be seen. Pictures were taken. The drive was successfully conducted by planting 40-50 saplings.

## 5. Photographs of the event



Image 1. Students and Faculty planting saplings



Image 2 Students participating in the Drive.



Students participating in the Drive.



Image 4 Giving the manure to the newly plant samplings

6. Brochure or creative of the event



MANIPAL UNIVERSITY  
JAIPUR















**Directorate of Students' Welfare**  
**Society Connect**

**ROTARACT CLUB**

*Presents*

**#DAANUTSAV2023**

# PLANTATION DRIVE

Date: 3<sup>rd</sup> October, 2023      Time: 10:00 AM

Venue: Govt. Senior Secondary School, Sanjhariya, Jaipur

Plantation Drive



## 7. Schedule of the event

S.NO.	Name of the Event	Time	Place
1.	Plantation Drive	10:00 AM	Mahatma Gandhi School (English Medium) Begus.

A bus from MUJ was taken to the school in the morning.

## 8. Attendance of the Event

**Total attendee- 67**

S.No.	Reg. NO.	Name of Students	Institute Name
1	23FE10ITE00079	Amisha anand	Manipal University Jaipur
2	23FE10CAI00360	shaivi adesh	Manipal University Jaipur
3	23FE10CSE00060	Amay Garg	Manipal University Jaipur
4	23FE10CDS00177	Manas Mathur	Manipal University Jaipur
5	23fe10bte00029	Saloni kamal	Manipal University Jaipur
6	23FE10CSE00508	Dev Dhawan	Manipal University Jaipur
7	23fe10cii00035	Bhargavi Anand	Manipal University Jaipur
8	220606004	Pranjal Puri	Manipal University Jaipur
9	23FA10BSP00028	Anupama Rustagi	Manipal University Jaipur
10	23FE10CCE00085	Siddhartha tiwari	Manipal University Jaipur
11	23FA10BAP00002	Tanisha Mathur	Manipal University Jaipur
12	23FD10BFD00009	Mariya Shabbir Baiwala	Manipal University Jaipur
13	23FE10CDS00224	Harsh Ajmera	Manipal University Jaipur
14	23fe10cds00125	Suryanshi Singh	Manipal University Jaipur
15	23fs10mat00009	Malavika ramdas	Manipal University Jaipur
16	221007021	Arshi Jain	Manipal University Jaipur
17	23FE10CSE00137	Stuti Dixit	Manipal University Jaipur
18	23fe10cii00094	Aarohi Tyagi	Manipal University Jaipur
19	23FE10CSE00152	Gautam Kakkar	Manipal University Jaipur
20	23FE10CSE00318	Krish Ray	Manipal University Jaipur
21	23FE10CII00076	Kriissh Marwaha	Manipal University Jaipur
22	229310321	Shiv Rajput	Manipal University Jaipur
23	23FS10BIO00051	Ragini Singh Thakur	Manipal University Jaipur
24	23FS10BIO00052	Anukriti sharma	Manipal University Jaipur
25	220901073	Diya Mittal	Manipal University Jaipur
26	23FE10CSE00081	Smmayan Gupta	Manipal University Jaipur
27	229309083	Raghav Gupta	Manipal University Jaipur
28	23FE10CDS00397	Hrishita Singh Timaney	Manipal University Jaipur
29	23FE10ITE00203	Sarah Sharda	Manipal University Jaipur
30	23fa10bsp00025	Jasleen kaur	Manipal University Jaipur

31	23FA10BSP00039	Jiya Kumar	Manipal University Jaipur
32	23FA10BSP00004	Aarya Mahale	Manipal University Jaipur
33	220606020	Chaarvi Kumar	Manipal University Jaipur
34	23fa10bsp00058	Kashvi Mahajan	Manipal University Jaipur
35	229301095	Shaurya Singh	Manipal University Jaipur
36	23fe10ece00024	Kushagra agrawal	Manipal University Jaipur
37	23FA10BSP00017	Megha Sharma	Manipal University Jaipur
38	23FM10BBA00162	Alina Nadeem	Manipal University Jaipur
39	23FM10BBA00178	Avishi Akhaury	Manipal University Jaipur
40	221007004	Urvi Thakare	Manipal University Jaipur
41	23FA10BAP00027	Natasha Joan Menezes	Manipal University Jaipur
42	23FA10BLE00004	Tanisha chaturvedi	Manipal University Jaipur
43	23fe10cai00579	Arjun Malhotra	Manipal University Jaipur
44	23FE10CAI00352	Maanyata Aul	Manipal University Jaipur
45	220901322	Divyanshi Singh	Manipal University Jaipur
46	229310412	Jatin Verma	Manipal University Jaipur
47	229301094	Yashovardhan Pratap Singh	Manipal University Jaipur
48	23FM10BBA00348	Niska kedia	Manipal University Jaipur
49	221105005	Dhruv Nair	Manipal University Jaipur
50	23FM10BBA00170	Shambhavi Agrawal	Manipal University Jaipur
51	23FE10CDS00241	Armaan Setia	Manipal University Jaipur
52	23FE10CAI00105	Mritunjay Singh	Manipal University Jaipur
53	229311075	Aarna Tyagi	Manipal University Jaipur
54	229302051	Prince jindal	Manipal University Jaipur
55	23FA10BHE00035	Taneesha puri	Manipal University Jaipur
56	220903033	Suhani Jain	Manipal University Jaipur
57	220901391	Dipika Agarwal	Manipal University Jaipur
58	229310222	Aayush Sharma	Manipal University Jaipur
59	221003007	Yachna Jain	Manipal University Jaipur
60	220901002	Anshu jangir	Manipal University Jaipur
61	23FE10CDS00284	Anant Barjatya	Manipal University Jaipur
62	221015074	Rupal Sharma	Manipal University Jaipur
63	23fa10bsp00047	Vartika Agarwal	Manipal University Jaipur
64	23FA10BSP00041	Kali Vithlani	Manipal University Jaipur
65	23FM10BBA00030	Harshal Saini	Manipal University Jaipur
66	23FE10CSE00746	Daksh Sharma	Manipal University Jaipur
67	23FS10BIO00034	PC Rahul	Manipal University Jaipur

## 9. Feedback of the Event:- The students participated enthusiastically.



**(Hemant Kumar)**

**Assistant Director, Society Connect  
Directorate of Student's Welfare**

**(Prof. AD Vyas)**

**Director, Directorate of Student's Welfare**

DIRECTOR STUDENT WELFARE & PROCTOR  
MANIPAL UNIVERSITY, JAIPUR



MANIPAL UNIVERSITY  
JAIPUR



MANIPAL UNIVERSITY  
JAIPUR

**FACULTY OF ARTS**

**SCHOOL OF HUMANITIES AND SOCIAL SCIENCES**

**DEPARTMENT OF ECONOMICS**

**COMMUNITY OUTREACH VISIT**

**Date of Event- October 31, 2023**



Content of Report (index)

1. Introduction of the Event
2. Objective of the Event
3. Beneficiaries of the Event
4. Details of the Guests
5. Brief Description of the event
6. Geo-tagged Photographs
7. Brochure or creative of the event
8. Schedule of the Event
9. Attendance of the Event
10. News Publication
11. Feedback of the Event
12. Link of MUJ website

## 1. Introduction of the Event

The practical knowledge about the subject is of immense importance for the students of B.A, Economics (Hons.), M.A. Economics (Hons.), and as such apart from regular classroom teaching there is a strong case for exposing them to innovative and practical outdoor sessions/visits to the nearby areas & projects. Taking this pedagogy of teaching, a one day visit to the renowned Laporiya village and interaction with **Padma Shree Laxman Singh** was planned to closely to observe how the water stressed Laporiya village became self-sufficient in water with all the efforts of **Laxman Singh Ji**. He has been awarded the Padma Shree for his significant contribution to the field of saving water and the environment for the last 40 years. He changed the picture of more than 50 villages with the technique of saving water and the campaign launched for it. He recharged the ponds with the Chowka technique to save water and pastures.

To take insights into his dedication, efforts, and commitments, this visit was planned for students to interact with him so that the **environmental sustainability** thought will sustain forever with **Gen-Z** and they will transfer the same to **Gen-Alpha**.

## 2. Objective of the Event

Water is a finite and shared resource. As well as being a basic human right and fundamental to healthy ecosystems, water is vital to the functioning of the global economy. However, increasing demand and competition, climate change and pollution are putting pressure on global water resources, creating risks for business and society. To experience the outstanding achievements and gain practical knowledge about environmental economics, an academic visit to “Laporiya village, near Dudu” is organized for the betterment and knowledge enhancement of the students.

## 3. Beneficiaries of the Event

Students and faculty members of Manipal University Jaipur.

## 4. Details of the Guests

The President of India has awarded Shri Laxman Singh Ji Padma Shree for his commendable work of reviving the Chowka system, a traditional water harvesting method in Rajasthan. He has founded the NGO Gram Vikas Navyuvak Mandal Laporiya (GVNML). The efforts of Sh. Laxman Singh Ji has borne fruits in a drought-ridden small village (Lapodiya), 80 km from Jaipur.

## 5. Brief Description of the event

It was an expert lecture on Syllogism of knowledge of economics, entrepreneurial and data skills: Unpack the Why? by Mr. Abhishek Jain, EY, Senior project consultant E & Y. The aim of the lecture is to provide economic knowledge, entrepreneurial skill with basic data analytics knowledge and skills when it comes to leveraging data while growing their businesses, regardless of their respective industries. Student's always be in prisoners dilemma of Why?

**Photographs**

**3 to 5 geotagged photographs of the event or screenshots of the event (if online) with captions**



*Mr Laxaman Singh Ji discussing the importance of ecosystem*



*Mr Laxaman Singh Ji Addressing the students*



The Village well



*Taking a short break, Mr Lakshman Singh Ji, faculties and students*



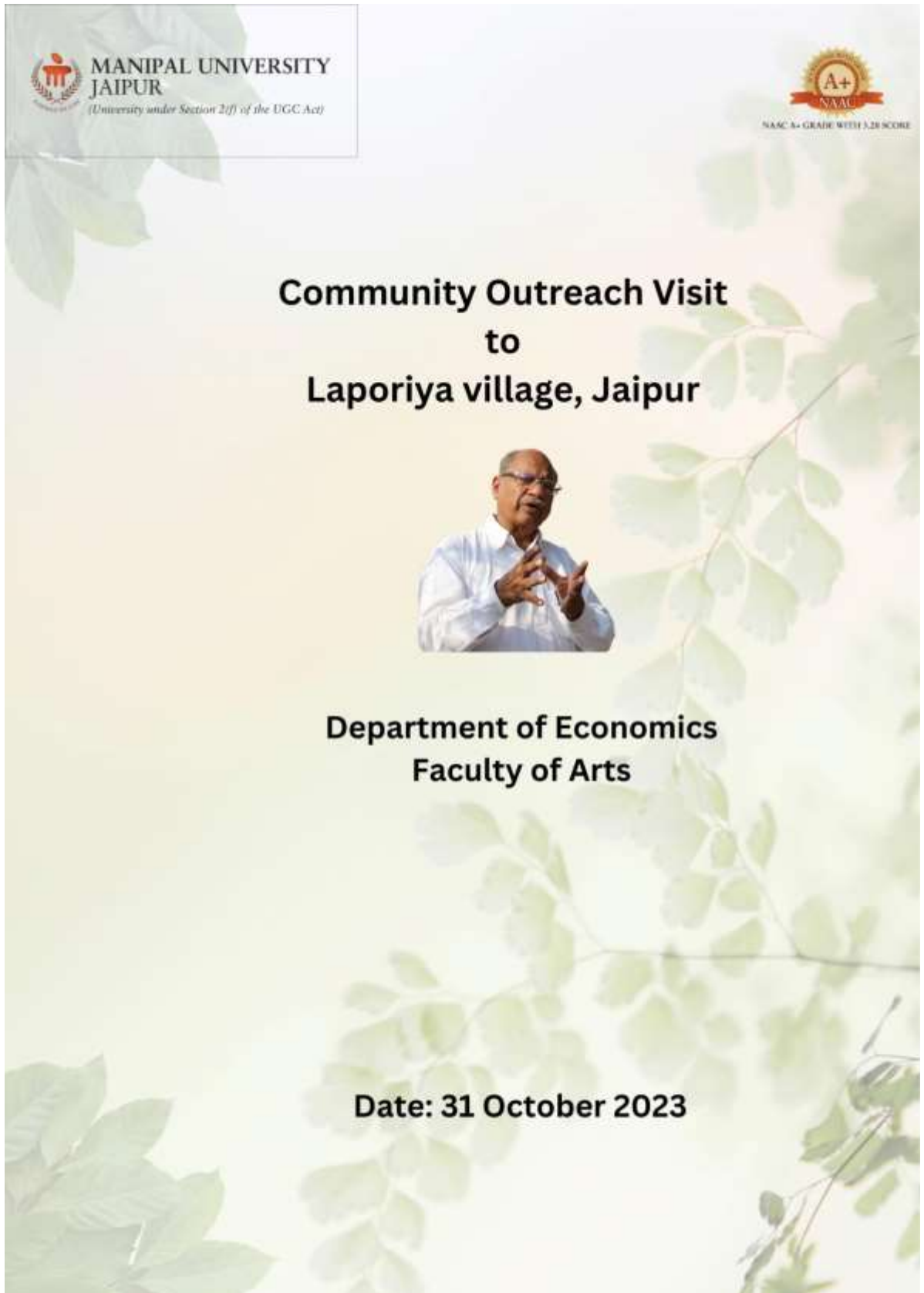


*Mr Singh (centre) discussing the young mind's learnings and impressions in his house at the end of the visit.*



*The students, Mr Lakshman Singh (towards right in white) and Dr Shilpi Gupta, outside his house.*

6. Brochure or creative of the event (insert in the document only)



The brochure cover features a light green background with a faint pattern of leaves. In the top left corner, there is a white box containing the Manipal University Jaipur logo and the text "MANIPAL UNIVERSITY JAIPUR (University under Section 2(f) of the UGC Act)". In the top right corner, there is a gold NAAC A+ logo with the text "NAAC A+ GRADE WITH 3.28 SCORE". The main title is centered in bold black text: "Community Outreach Visit to Lajoriya village, Jaipur". Below the title is a photograph of a man in a white shirt and glasses, gesturing with his hands. Underneath the photo, the text "Department of Economics Faculty of Arts" is centered. At the bottom, the date "Date: 31 October 2023" is centered.

## 7. Schedule of the event (insert in the report)

Date of the event –October 31, 2023 7:30 AM

## 8. Attendance of the Event (insert in the document only)

### Total attendee-

Registration No.	Name of the Students	Column1	Column2
211101046	Akshay	P	
211101035	Anubhav	p	
211101003	Dakshita	P	
211101043	Gaurav basniwal	P	
211101050	Gaurav kumar	P	
211101013	Saarthak tiwari	P	
211101042	Praseeda	P	
211101004	Rishita	P	
211101006	Shivangi	P	
211101015	Sumriddhi	P	
211101040	Yash	P	
211101041	Yashi	P	
211101039	Anushka	P	
211101007	Utkarsh	P	
211101044	Riti	P	
211101021	Paritosh	P	
211101028	Divya surana	P	
211101025	Atharv	P	
23FA20MEA00004	Santanu Bhowmick	P	
23FA20MEA00007	Anubhav Joshi	P	
23FA20MEA00005	Bhumita Yadav	P	
23FA20MEA00006	Shweta Choudhary	P	
23FA20MEA00003	Medini Choudhary	A	Unwell
23FA20MEA00002	Nisha Choudhary	A	Unwell
231151001	Devanshi Kapoor	P	
Dr. Shilpi Gupta	Associate professor - Department of Economics	P	
Mr. Apoorva Saxena	Head, community Radio Station	P	
Mr. Parul Kanwar	Jr. Assistant SHSS	P	

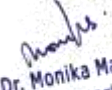
**News Publication-** News printed in newspaper or online links (if any) for news – insert images)

NA

**9. Feedback report of the Event**

Students experienced Padam Shree Laxman Singh Ji's dedication, efforts, and commitments, and take away from him the **environmental sustainability** thought which will sustain forever with **Gen-Z** and they will transfer the same to **Gen-Alpha**.

**10. Link of MUJ website stating the event is uploaded on website**



Dr. Monika Mathur  
Head, Department of Economics  
Manipal University Jaipur

**Seal and Signature of Head with date**



MANIPAL UNIVERSITY  
JAIPUR

MUJ/Q&C/021/F/1.03



MANIPAL UNIVERSITY  
JAIPUR

**FACULTY OF ENGINEERING**

**School of Civil & Chemical Engineering**

**Department of Civil Engineering**

**Societal Connect Activity**

**On**

**Toilet Training for GHS Staff**

**Date of Event 19<sup>th</sup> Oct. 2023**



1. Introduction of the Event
2. Objective of the Event
3. Beneficiaries of the Event
4. Details of the Guests
5. Brief Description of the event
6. Photographs
7. Brochure or creative of the event
8. Schedule of the Event
9. Attendance of the Event
10. News Publication
11. Feedback of the Event
12. Link of MUJ website

## 1. Introduction of the Event

Department of Civil Engineering SCCE, Conducted Toilet management training for GHS staff on 19<sup>th</sup> Oct. 2023. The planned and coordinated by Mr Sagar Gupta, Assistant Professor, Civil Engineering Department.

## 2. Objective of the Event

- The activity was designed to raise conscious related to behaviour of toilet users and consensus building.
- Understanding essential component of toilet cleaning and management

## 3. Beneficiaries of the Event

The beneficiaries of event where GHS house keeping staff and students of MUJ.

## 4. Details of Speaker

Sr.No.	Name of Guest	Designation
1.	Animesh Kumar, Good Host Spaces	Operations Manager
2.	Sagar Gupta, MUJ	Assistant Professor

## 5. Brief Description of the event

The activity includes video lecture and active question and answer sessions . The planned and coordinated by Mr Sagar Gupta, Assistant Professor, Civil Engineering Department.

### Brochure of the Event



MANIPAL UNIVERSITY  
JAIPUR

GHS  
Good Host Spaces



G20  
INDIA 2023

SUSTAINABLE  
DEVELOPMENT  
GOALS

## Toilet Management Training

Trainer  
Mr Sagar Gupta  
Assistant Professor  
Department of Civil Engineering  
Manipal University Jaipur

Trainer  
Mr Animesh Kr Dubey  
Assistant Manager  
Good Host Spaces

## 6. Attendance of the Event

Manipal University Jaipur
School of Civil & Chemical Engineering
Department of Civil Engineering



Toilet Training for GHS Staff		
Date	Oct. 19, 2023	
Attendance List		
S. NO.	Name	Reg.No.
1.	AKSHIT CHAURASIA	219102001
2.	PRINCE KUMAR	219102002
3.	HARSHIT GOTHWAL	219102005
4.	AAKARSH RANJAN RAI	219102009
5.	ARMAAN VERMA	219102010
6.	TANYA SINGH THAKUR	219102011
7.	DIVYA PRAKASH DUBEY	219102014
8.	RAVISH DEG	219102015
9.	MAYANK CHOUDHARY	219102016
10.	SUPRIYA CHATTOPADHYAY	219102017
11.	JASVEER DEWASI	219301128
12.	HEMANT MEDATWAL	209102009
13.	ADNAN SHEIKH	209102010
14.	PIYUSH SHARMA	209102013
15.	SANKET SANDEEP KARPE	209102014
16.	KHADKE SUYASH SHAILENDRA	209102015
17.	SPARSH KHARE	209102016
18.	ANURAG MEERAL	209102017
19.	SAGAR CHOUHAN	209102018
20.	MAYANK SHARMA	209102019
21.	HIMANSHU MANDRAI	209102021
22.	MAYANK TOMAR	209102023

## 7. List of Participants

Manipal University Jaipur		
School of Civil & Chemical Engineering		
Department of Civil Engineering		
Toilet Training for GHS Staff		
Date	Oct. 19, 2023	
Attendance List		
S.No	Employee Code	Employee Name
1	2000860612	Meera Devi Mundotiya
2	2000860626	Kamla Devi
3	2000860635	Santosh
4	2000860649	Geeta Verma
5	2000860699	Seeta Kumawat
6	2000860726	Chanda Devi
7	2000860731	Vimla Devi
8	2000860734	Vinod







9	2000860741	Jitendra Kumar Pareek
10	2000860767	Manju Devi
11	2000860770	Manju Devi
12	2000860773	Manju Devi
13	2000860794	Nagendra Singh
14	2000860797	Nand Kishore
15	2000860835	Sita
16	2000860874	Guddi Devi Balai
17	2000860904	Sugan Meena
18	2000860913	Suman Devi
19	2000860939	Shanti Kumawat
20	2000860963	Deepak Bariwa
21	2000860981	Lali Barai
22	2000861082	Tara Kumawat
23	2000861094	Gopali
24	2000861138	Prem Devi
25	2000861150	Radha Devi
26	2000861170	Guddi Devi
27	2000861192	Prem Devi
28	2000861286	Jagdish
29	2000861302	Usha
30	2000861307	Babli Harijan
31	2000861359	Rakesh Kumar Raikwar
32	2000861384	Koyal Devi
33	2000861404	Manisha Devi
34	2000861426	Anita Devi
35	2000939490	Gita Devi
36	2000939503	Naina
37	2000939515	Santosh Devi
38	2000939527	Vimla Devi Bairwa
39	2000954160	Minakshi Devi
40	2000982536	Ramesh
41	2000996175	Kavita Kumari Raigar
42	2001043602	Pinky Yogi
43	2001113764	Somoti Lal Bairwa
44	2001194725	Anju Devi
45	2001289599	Ramswrup

## 8. Photograph



Pic no.1 active session on toilet management training



Pic no.2 Participant at Event

Link of event posted on university Website -



Head  
Civil Engrg. Dept.  
MLU, Dehriwala, Jaipur





**FACULTY OF DESIGN**

**SCHOOL OF ARCHITECTURE AND DESIGN**

**“SAMSARA” at Nehru Children Secondary School, Dehmi Kalan**

**ON 30<sup>th</sup> Sep 2023**

**Date of Event 30th Sep 2023**



## Index

<b>S.No.</b>	<b>Activity Heads</b>
1.	Introduction of the Event
2.	Objective of the Event
3.	Beneficiaries of the Event
4.	Brief Description of the event
5.	Photographs
6.	Brochure or creative of the event
7	Attendance of the Event
8	Link of MUJ website

## 1. Introduction of the Event

At **Nehru Children Academy Secondary School in Dehmi Kalan**, a pioneering initiative unfolded. This inventive project aims to transform discarded materials into a vibrant space, meeting the school's assembly requirements while emphasizing resource efficiency and community engagement.

With approximately 300 students, the school grappled with challenges like the lack of a dedicated assembly area and inadequate facilities for artistic activities. The selected site within the school grounds proved perfect for this transformative endeavor, aiming to integrate cultural practices, such as shoe removal, into its design seamlessly.

## 2. Objective of the Event

To create an architectural design that showcases the potential of utilizing pre-used, discarded, or waste material in a new building. To raise public awareness about building sustainability through functional efficacy, resource frugality, and sensory appeal of the design.

To demonstrate the above attributes through a built example that can be used, experienced, and emotionally engaged with by the common public.

To create a functional space using waste material for the betterment of the community, the space can be used for any activity for any age group with a minimum capacity of 6 people.

- Site Selection:

### **Location-Nehru Children Academy Secondary School, Dehmi Kalan**

We visited a private school named 'Nehru Children Academy Secondary School', Dehmi Kalan, with holding capacity of approximately 300 students with no functional area for assembly gatherings and poor amenities for the students ranging from KG to Grade 10. There is a need to design versatile spaces that can accommodate various artistic disciplines, to create an environment that inspires creativity and promotes a well-rounded education. According to Indian culture, students remove their shoes while entering the premises without any proper arrangement.

## 3. Beneficiaries of the Event

The beneficiaries of the stage at Nehru Children Academy include students and staff with improved learning and assembly spaces, the local community with a multi-functional gathering area, and the environment through waste reduction and increased awareness of sustainability.

#### 4. Details of the Participants

1. Prof. Raunak Prasad (Asst. Prof.)
2. Divyesh Shankla
3. Chirag Gurnani
4. Kartik Gehlot
5. Riddhi Sorte
6. Aishmeen Kaur
7. Vaishnavi Shukla
8. Aishwarya Singh Rathore
9. Sahib Chagger
10. Khushi Chowdhary
11. Bhavesh Khemka
12. Harsh Srivastava
13. Abhinav Kumar Singh
14. Ikshita Bagla
15. Pranat Kothari
16. Sajal Panwar
17. Rijul Chaudhary
18. Daksh Rupani
19. Arghya Bhagwat
20. Harshita Mundhra
21. Aarya Chandiramani
22. Moulesh
23. Shriya Panwar
24. Yash Dhingra
25. Ridhi Arora
26. Bhoomica Mittal
27. Tanmay Gupta
28. Nalin Sharma
29. Subhrajyoti Dutta Choudhary
30. Aditi Payne
31. Aadhya Mahajan
32. Raghav Mahajan
33. Palak Chawla
34. Abhijeet Yadav
35. Ritwiza

## 5. Photographs of the event or screenshots of the event with captions



Students performing on the stage created



Image showing the structure created



Utilization of space created during school event



Tree plantation during the event

## 6. Brochure or creative of the event



## 7. Attendance of the Event

1. Prof. Raunak Prasad (Asst. Prof.)
2. Divyesh Shankla
3. Chirag Gurnani
4. Kartik Gehlot
5. Riddhi Sorte
6. Aishmeen Kaur
7. Vaishnavi Shukla
8. Aishwarya Singh Rathore
9. Sahib Chagger
10. Khushi Chowdhary
11. Bhavesh Khemka
12. Harsh Srivastava
13. Abhinav Kumar Singh
14. Ikshita Bagla
15. Pranat Kothari
16. Sajal Panwar
17. Rijul Chaudhary
18. Daksh Rupani
19. Arghya Bhagwat
20. Harshita Mundhra
21. Aarya Chandiramani
22. Moulesh
23. Shriya Panwar
24. Yash Dhingra
25. Ridhi Arora
26. Bhoomica Mittal
27. Tanmay Gupta
28. Nalin Sharma
29. Subhrajyoti Dutta Choudhary
30. Aditi Payne
31. Aadhya Mahajan
32. Raghav Mahajan
33. Palak Chawla
34. Abhijeet Yadav
35. Ritwiza





8. Post event link:

<https://jaipur.manipal.edu/content/dam/manipal/muj/fod/Document/eventlist/NSS%20REPORT.pdf>

**Ar. Raunak Prasad**

School of Architecture & Design

Signature of the Faculty Coordinator

**Ar. Siddharth Mishra**

School of Architecture & Design

Signature of the Faculty Coordinator

**Prof. (Dr.) Sunanda Kapoor**

School of Architecture & Design

HOD, SA&D

Faculty of Design

स्थापित 1998

रजि. क्र. 561/जय./96-97

मान्यता क्रमांक: शिविरा माध्य/माध्य/अ-4/21313/848



(राजस्थान सरकार व माध्यमिक शिक्षा बोर्ड, राज. द्वारा मान्यता प्राप्त)  
**नेहरु चिल्ड्रन एकेडमी माध्यमिक विद्यालय**

दहमी कलाँ, बगरू, जयपुर (राज.) 303007

मो. 9252121178, 8952857486

प्रेषक :

प्रधानाध्यापक/सचिव/निदेशक

नेहरु चिल्ड्रन एकेडमी माध्यमिक विद्यालय

दहमी कलाँ, बगरू, जयपुर (राज.)

प्रेषित/सेवामें,

श्रीमान् ..... *Manipal University Jaipur* .....

.....

.....

क्रमांक: ने. चि. ए. मा. वि./

दिनांक ...*18/12/23*.....

विषय:

प्रसंग:

### Letter of Appreciation

On 30th September 2023, Manipal University Jaipur organized SAMSARA (the Stage Design) in association with NSS (National Service Scheme), DSW (Directorate of Student Welfare, MUJ), and SA&D (School of Architecture & Design) in the campus of Nehru Children Secondary School, Dehmi Kalan.

SAMSARA was conducted by Ar. Siddharth Mishra & Ar. Raunak Prasad, MUJ along with students of 1<sup>st</sup>, 2<sup>nd</sup>, and 3<sup>rd</sup> year Architecture and Students from Nehru Children Secondary School.

We highly appreciate the efforts of Manipal University Jaipur for conducting SAMSARA (the stage design) in the campus of Nehru Children Secondary School, Dehmi Kalan.

  
HEADMASTER *18/12/23*

NEHRU CHILDREN ACADEMY  
SECONDARY SCHOOL

DEHMI KALAN, BARGARU, JAIPUR

Phone: 9252121178

**Nehru Children Secondary School, Dehmi Kalan**



MANIPAL UNIVERSITY  
JAIPUR

**FACULTY OF ENGINEERING**

**SCHOOL OF ELECTRICAL, ELECTRONICS AND COMMUNICATION  
ENGINEERING**

**DEPARTMENT OF ELECTRONICS AND COMMUNICATIONS  
ENGINEERING**

**CLEAN WATER AND SANITATION DRIVE**

***at Sri Sri Krishna Balaram Mandir***

**in collaboration with MUJ NCC & Abhigya Club, MUJ**

**Visit to: Sri Sri Krishna Balaram Mandir,  
Jagatpura, Jaipur, 302017, Rajasthan, India.**

**Date of Event: 17/08/2023**



## Content of Report

1. Introduction of the Event
2. Objective of the Event
3. Beneficiaries of the Event
4. Details of the Guests
5. Brief Description of the event
6. Geo-tagged Photographs
7. Brochure or creative of the event
8. Schedule of the Event
9. Attendance of the Event
10. News Publication
11. Feedback of the Event
12. Link of MUJ website

*Praveen*

## 1. Introduction of the Event

Water and sanitation are at the core of sustainable development, and the range of services they provide underpin poverty reduction, economic growth and environmental sustainability. However, in recent decades overexploitation, pollution, and climate change have led to severe water stress in locales across the world. Today, 2.2 billion people lack access to safely managed drinking water, and more than 4.2 billion people lack safely managed sanitation.

This drive aims to educate people about the importance of CLEAN WATER AND SANITATION.

## 2. Objective of the Event (bullet points or about 50 words)

To bring awareness about CLEAN WATER AND SANITATION sustainable development goals.

## 3. Beneficiaries of the Event (Student/Faculty/Community etc) (25 words)

General Public & MUJ students.

## 4. Details of the Guests (Chief Guests, speakers etc Designation, organization, contact details if any please give them in sr no)

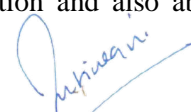
- a) Dept of ECE, NCC & Abhigya Club Students.
- b) Raghav Charan Das ji, is a Civil Engineer by education and has worked in the industry for few years. He has been a national cricket player. From the past 10 years he is a full time volunteer in The Akshaya Patra foundation. He is a spiritualist, a youth mentor and is also Unit Head at FOLK programme offered by The Akshaya Patra foundation. He has been associated with Abhigya Club MUJ from last 4 years.

## 5. Brief Description of the event

Water and sanitation are at the core of sustainable development, and the range of services they provide underpins poverty reduction, economic growth and environmental sustainability. However, in recent decades overexploitation, pollution, and climate change have led to severe water stress in locales across the world. Today, 2.2 billion people lack access to safely managed drinking water, and more than 4.2 billion people lack safely managed sanitation.

Looking at this grave situation students of Dept of ECE, NCC and Abhigya Club MUJ decided to collaborate and conduct an awareness session for general public. It was decided to conduct this event at a prominent temple, Sri Sri Krishna Balaram Mandir, Jagatpura, Jaipur. As temple attracts good footfall and general public does not emphasise enough on importance of clean water and sanitation in general.

Shri Raghav Charan Das ji engaged students to develop Krishna Consciousness. After offering prayers ECE, NCC & Abhigya Club students educated general public and visiting school students at the temple about the importance of clean water and sanitation and also about necessary actions to be taken at individual level.



**6. Photographs**

**3 to 5 geotagged photographs of the event or screenshots of the event (if online) with captions**



**HoD ECE Flagging of the students**



**Students Offering Prayers**



**Students Participating in the Kirtan**



**Session on Krishna Consciousness**



**Students Meditating**



**ECE, NCC & Abhigya Club Students conducting awareness session on CLEAN WATER AND SANITATION**



*Rupinagiri*

**7. Brochure or creative of the event:**




**MANIPAL UNIVERSITY**  
**JAIPUR**  
*(University under Section 2(f) of the UGC Act)*




**DEPT. OF ELECTRONICS AND COMMUNICATION ENGG., SEEC, MUJ**  
**IN COLLABORATION WITH NCC & ABHIGYA CLUB, MUJ**

**INVITES YOU TO BE PART OF CLEAN WATER AND SANITATION DRIVE AT SRI SRI KRISHNA BALARAM MANDIR, JAGATPURA**

**17 AUGUST 2023**

**CONVENER:**  
**DR. ROHIT MATHUR**  
**DR. ABHISHEK SHRIVASTAVA**  
 More information : **+91-8527118621**

**8. Schedule of the event (insert in the report)**

S.No.	Timing	Event
1)	09:15 AM – 10:30 AM	MUJ to Sri Sri Krishna Balaram Mandir
2)	10:30 AM – 12:00 NOON	Visit Sri Sri Krishna Balaram Mandir
3)	12 NOON – 12:30 PM	Session on Krishna Consciousness
4)	12:30 PM – 02:00 PM	Awareness Drive by ECE, NCC & Abhigya Club Students
5)	02:00 PM – 03:30 PM	Back to MUJ

*Rupin*

## 9. Attendance of the Event (insert in the document only)

**Total attendee: 53**

S. No.	Registration No.	Student Name
1	229202019	VINEET PATEL
2	229202064	YUVRAJ SINGH SIKARWAR
3	229202068	KARTIK SHARMA
4	229202007	AYUSH KUMAR SINGH
5	229202008	ASHISH SHAMRAO GAIKWAD PATIL
6	229202048	ABIR GAUTAM
7	229202042	ADITYA KUMAR
8	229202052	SACHIN YADAV
9	229202045	SOUMIL HALLAN
10	229202066	AAGMAN SHUKLA
11	229202054	DILLI SHANMUKHA PRANAYA
12	229202001	DEVANG VIKRAM SINGH
13	229202044	SASHIV ASHISH BHATNAGAR
14	229202036	SHAIHAM SRIVASTAVA
15	229202062	VIKRANT KUMAR
16	229202033	JAYANT KUMAR
17	229202070	MOHD RAMIN ZAHEER
18	229202059	SARTHAK JAIN
19	229202067	GARV YADAV
20	229202017	AYUSH RAGHUDATHA PAI PANANDIKAR
21	229202039	BHARVI JAYDEEP PATEL
22	229202004	ANUSHKA SHARMA
23	229202016	HARSHVARDHAN ADIL
24	229202058	TANAY MALHAN
25	229301167	VIVEK SHEKHAWAT
26	229202077	KANISHKA GOYAL
27	229202072	HIMANSHU
28	229202055	SAKSHAM ARORA
29	229202015	SIDDHANT SHRENIK KOLE
30	229202023	RUGVED PRASAD PANSE
31	229202079	YUVRAJ SINGH
32	229302495	AYUSH GUPTA
33	229202020	SHREYASH
34	229202026	JASANJOT SINGH
35	229202029	PRATYUSH TAK
36	229202076	DINESH SARAN
37	229202078	POORVAKSHI BARGOTI

*Prishu*



S. No.	Registration No.	Student Name
38	229202047	JAIDEEP PATEL
39	229202010	KANISHKA CHAUDHARY
40	229303006	SAKSI ADHIKARI
41	229202002	KAMAL KISHOR PRAJAPATH
42	229202041	ANSH YADAV
43	229202043	UJJAWAL SHARMA
44	229202061	KANAV JAIN
45	229202071	JAYAN GUPTA
46	229202053	GARV MISHRA
47	229202069	DIVYANSHU RAI
48	229202073	AADARSH PAL
49	229202063	MAYANK JAWLA
50	229202014	ADITYA GUPTA
51	229202005	TANMOY PODDER
52	229205005	MAYAANK Shailesh Bambardekar
53	229202081	Harshad Sharma

**10. News Publication- News printed in newspaper or online links (if any) for news – insert images)**

**11. Feedback report of the Event**

■ Excellent   
 ■ Good   
 ■ Satisfactory

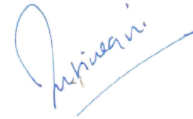


Would you be interested in attending sessions on similar topics?



*Rupin*

**12. Link of MUJ website stating the event is uploaded on website**



Dept. of E & C Engineering  
School of Engineering  
Manipal University, JAIPUR

**17<sup>th</sup> August 2023**

**Dr. Manish Tiwari**

**HEAD OF DEPARTMENT**

**Seal and Signature of Head with date**



MUJ/DSW/Society Connect/Oct 2023/02



MANIPAL UNIVERSITY  
JAIPUR

## **DIRECTORATE OF STUDENT'S WELFARE**

**(SOCIETY CONNECT)**

**#DAANUTSAV 2023**

**CLEANLINESS DRIVE**

**(GANDHI JAYANTI)**

**2<sup>nd</sup> October 2023**

## Index

<b>S.No.</b>	<b>Activity Heads</b>	<b>Page no.</b>
1.	Introduction of the Event	1
2.	Objective of the Event	1
3.	Beneficiaries of the Event	1
4.	Brief Description of the event	1
5.	Photographs	2-3
6.	Brochure or creative of the event	4-5
7.	Schedule of the Event	6
8.	Attendance of the Event	6-8
9.	Feedback of the Event	8
10.	Link of MUJ website	8



## 1. Introduction of the Event

A clean India would be the best tribute India could pay to Mahatma Gandhi on his 150-birth anniversary in 2019,” said Shri Narendra Modi as he launched the Swachh Bharat Mission at Rajpath in New Delhi. On 2nd October 2014, Swachh Bharat Mission was launched throughout the length and breadth of the country as a national movement. The campaign aims to achieve the vision of a ‘Clean India’. In this direction, “*Cleanliness Drive*” is organized on 2<sup>nd</sup> October 2023 at the nearby village called Dehmi kalan at 9 Am morning. The importance of Swachh Bharat Abhiyan has been discussed with local people and vendor. The whole team of Faculty and students advised the local people and vendors to put dustbin near the village. Team also interacted with the students at school and discussed the swachhatha hi seva and Swachh Bharat Mission. This drive is organized by Rotaract Club of MUJ on the auspicious occasion of Gandhi Jayanti and DAAN UTSAV 2023 i.e 2nd October from 9 in the morning. The drive was conducted to help clean our surroundings and the betterment of the environment.

## 2. Objective of the Event

- Promote the value of cleanliness
- Discipline and respect for the environment
- Spreading word about the need for cleanliness and hygiene
- Sensitizing people about the importance of cleanliness

## 3. Beneficiaries of the Event

Community, students of MUJ

## 4. Brief Description of the event

The Cleanliness Drive took place on 2<sup>nd</sup> October, the birth anniversary of Mahatma Gandhi and the 4<sup>th</sup> anniversary of Swachh Bharat Abhiyan. On the account of DAAN UTSAV 2023, Rotaract Club organized this event in Dahmi Kalan Village. Students participated with enthusiasm throughout the drive. Everyone gathered at 9 a.m. to depart for the drive. Everyone helped each other to clean up the area and dispose the waste properly.

The drive helped instill the importance of cleanliness and hygiene in the environment and how we, as regular people, can help maintain it.

## 5. Photographs of the event



Image 1 Cleanliness Drive at Dahmi Kalan



Image 2 Cleaning drive at near School

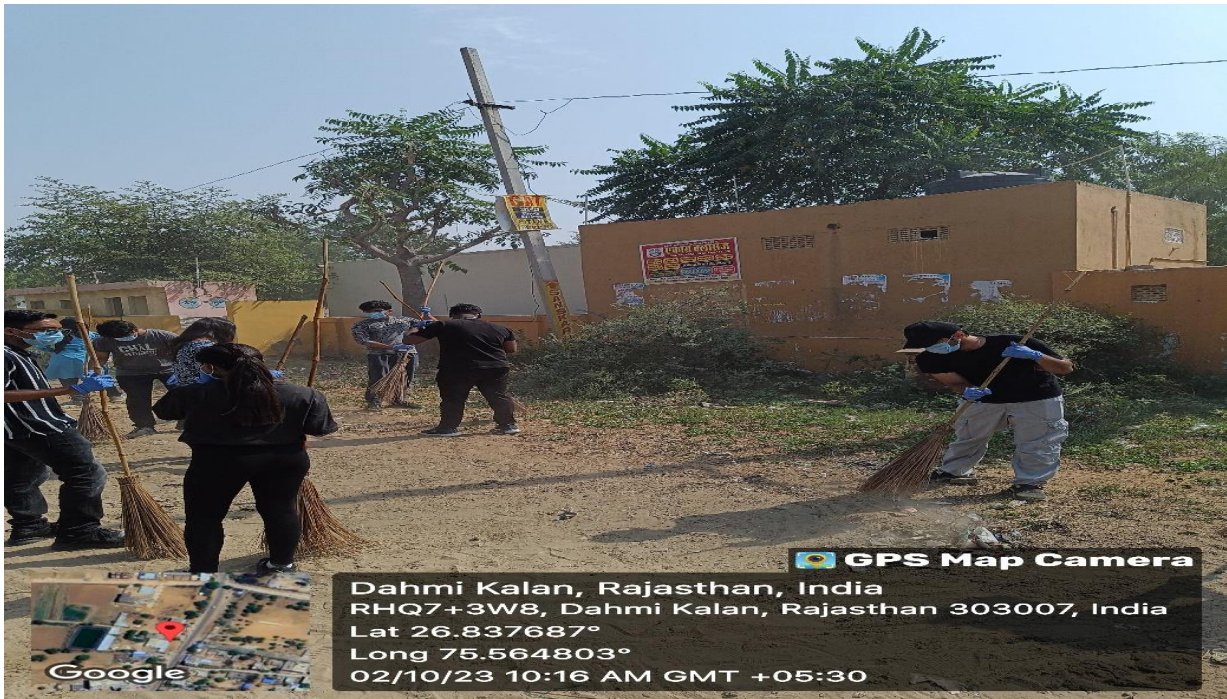
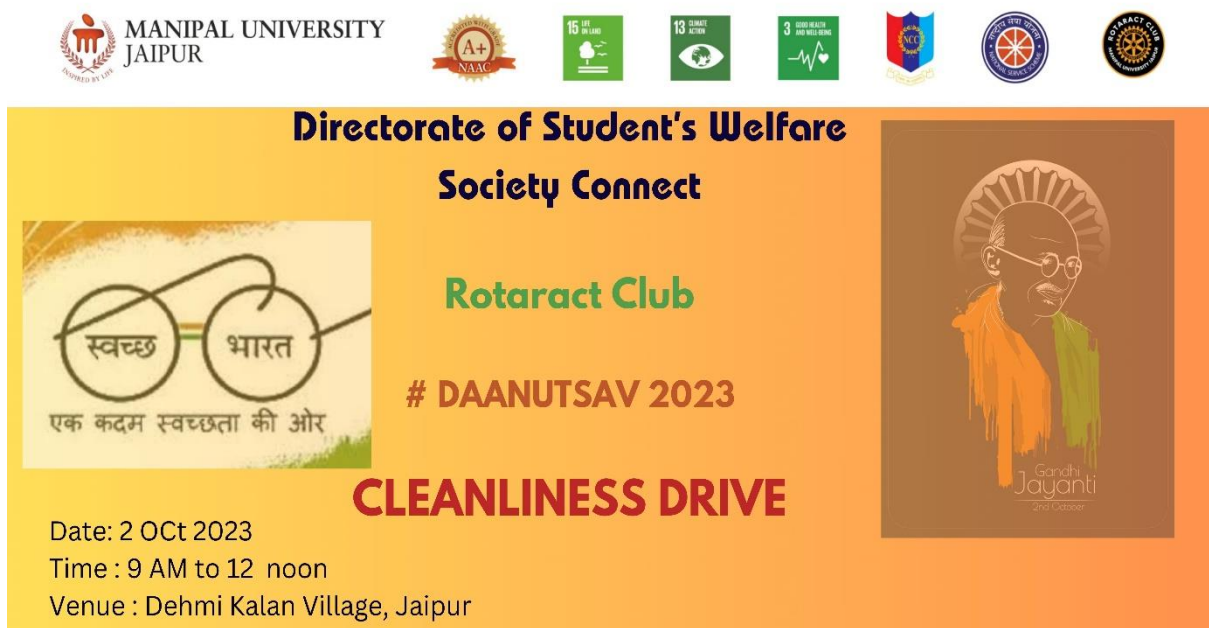


Image 3 Rotaract Club Srtuents participating in the drive



Image 4 Students participating in the drive.

## 6. Brochure or creative of the event



The brochure features the Manipal University Jaipur logo and NAAC A+ accreditation. It includes icons for Sustainable Development Goals 16 (Life in Land), 13 (Climate Action), and 3 (Good Health and Well-being). The text reads: "Directorate of Student's Welfare Society Connect", "Rotaract Club", "# DAANUTSAV 2023", and "CLEANLINESS DRIVE". It also features a graphic of Mahatma Gandhi with the text "Gandhi Jayanti and Utsav".

**Directorate of Student's Welfare  
Society Connect**

**Rotaract Club**

**# DAANUTSAV 2023**

**CLEANLINESS DRIVE**

Date: 2 Oct 2023  
Time : 9 AM to 12 noon  
Venue : Dehmi Kalan Village, Jaipur

#DAANUTSAV 2023- Cleanliness Drive

## 7. Schedule of the event

S.NO.	Name of the Event	Time	Place
1.	Cleanliness Drive	9:00 AM	Dehmi Kalan Village

## 8. Attendance of the Event (insert in the document only)

**Total attendee- 70**

S.NO.	Registration Number	Name	Institute Name
1	229302644	Ankur kumar	Manipal University Jaipur
2	229311104	Shashwat Kumar	Manipal University Jaipur
3	229301221	Rubhav Bahirwani	Manipal University Jaipur
4	229302571	Shreya Kumari	Manipal University Jaipur
5	23FE10CAI00360	shaivi adesh	Manipal University Jaipur
6	23FE10CAI00487	Dev Sharma	Manipal University Jaipur
7	229310059	Aditya Yadav	Manipal University Jaipur
8	23FS20MBO00001	Ankita Singh	Manipal University Jaipur
9	23FA20MCP00005	Ayushi Pushkarna	Manipal University Jaipur
10	23FE10CSE00186	Akshita Sai Pery	Manipal University Jaipur
11	23FE10CSE00766	Akshat Tiwari	Manipal University Jaipur





12	23FE10CSE00435	HARSHIT ATTRI	Manipal University Jaipur
13	229310269	Sneha Bhatia	Manipal University Jaipur
14	229303005	Nidhi Verma	Manipal University Jaipur
15	221007075	Preetika Sharma	Manipal University Jaipur
16	23FE10CAI00028	VALLURI SRI AASRITHA	Manipal University Jaipur
17	23FE10CDS00483	Kritika Magnani	Manipal University Jaipur
18	23FE10CDS00528	VANSHIKA VISHNAWAT	Manipal University Jaipur
19	23FE10CSE00043	KRITI RASTOGI	Manipal University Jaipur
20	23FE10CII00034	Trisha shanvi	Manipal University Jaipur
21	23FE10ITE00199	Ayush Singh	Manipal University Jaipur
22	23FE10CCE00034	KRISHNA GOEL	Manipal University Jaipur
23	23FE10AEE00008	Kisna Rana	Manipal University Jaipur
24	23FE10CSE00077	Akriti Chauhan	Manipal University Jaipur
25	23FE10CAI00548	Poorti Swarup	Manipal University Jaipur
26	23FE10CSE00005	Suhana Kaushik	Manipal University Jaipur
27	23FA10BSP00024	Lavanya Choudhary	Manipal University Jaipur
28	23FA10BSP00046	Rafia	Manipal University Jaipur
29	23FA10BHE00012	Nausheen broca	Manipal University Jaipur
30	221007020	Ayushi Mittal	Manipal University Jaipur
31	23FE10CCE00057	Mohit kumhar	Manipal University Jaipur
32	23fe10cse00395	Samriddhi Sharma	Manipal University Jaipur
33	23FE10CSE00699	Nancy	Manipal University Jaipur
34	23FE10ITE00015	Janhvi Soni	Manipal University Jaipur
35	23FE10ITE00185	Aryaman Singh	Manipal University Jaipur
36	23FE10CSE00039	Priyal Kansal	Manipal University Jaipur
37	221002064	shweta mishra	Manipal University Jaipur
38	23FE10CSE00643	KSHITIJ VERMA	Manipal University Jaipur
39	23FE10CDS00235	Anika sharma	Manipal University Jaipur
40	23FE10CII00109	Satvik Ahuja	Manipal University Jaipur
41	23FE10CDS00208	Ananya Srivastava	Manipal University Jaipur
42	23FE10CSE00222	Taarunya Aggarwal	Manipal University Jaipur
43	23FM10IBA00010	Harshit singh	Manipal University Jaipur
44	23FE10ITE00277	Aayushi Singh	Manipal University Jaipur
45	229302160	Parth johar	Manipal University Jaipur
46	23FM10BBA00341	Pallavi Dhaibhai	Manipal University Jaipur
47	23fd10bar00004	Aadhya mahajan	Manipal University Jaipur
48	23FE10CDS00423	Purvi Sharma	Manipal University Jaipur
49	23FE10ITE00021	Mounil Kankhara	Manipal University Jaipur
50	23FE10ITE00178	Pranav Prakash	Manipal University Jaipur
51	23FE10ITE00079	Amisha anand	Manipal University Jaipur
52	23FE10CAI00360	shaivi adesh	Manipal University Jaipur
53	23FE10CSE00060	Amay Garg	Manipal University Jaipur
54	23FE10CDS00177	Manas Mathur	Manipal University Jaipur
55	23fe10bte00029	Saloni kamal	Manipal University Jaipur
56	23FE10CSE00508	Dev Dhawan	Manipal University Jaipur

57	23fe10cii00035	Bhargavi Anand	Manipal University Jaipur
58	220606004	Pranjal Puri	Manipal University Jaipur
59	23FA10BSP00028	Anupama Rustagi	Manipal University Jaipur
60	23FE10CCE00085	Siddhartha tiwari	Manipal University Jaipur
61	23FA10BAP00002	Tanisha Mathur	Manipal University Jaipur
62	23FD10BFD00009	Mariya Shabbir Baiwala	Manipal University Jaipur
63	23FE10CDS00224	Harsh Ajmera	Manipal University Jaipur
64	23fe10cds00125	Suryanshi Singh	Manipal University Jaipur
65	23fs10mat00009	Malavika ramdas	Manipal University Jaipur
66	221007021	Arshi Jain	Manipal University Jaipur
67	23FE10CSE00137	Stuti Dixit	Manipal University Jaipur
68	23fe10cii00094	Aarohi Tyagi	Manipal University Jaipur
69	23FE10CSE00152	Gautam Kakkar	Manipal University Jaipur
70	23FE10CSE00318	Krish Ray	Manipal University Jaipur

### 9. Feedback of the Event

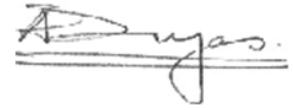
The students participated enthusiastically and helped to spread message for cleanliness.



**(Hemant Kumar)**

**Assistant Director, Society Connect**

**Directorate of Student's Welfare**



**(Prof. AD Vyas)**

**Director, Directorate of Student's Welfare**

**DIRECTOR STUDENT WELFARE & PROCTOR  
MANIPAL UNIVERSITY, JAIPUR**



MANIPAL UNIVERSITY  
JAIPUR

**FACULTY OF LAW**

**SCHOOL OF LAW**

**DEPARTMENT OF LAW**

**HEALTH AND SANITATION AWARENESS CAMPAIGN**

**- AASHRAY CARE HOME, JAIPUR**

**Awareness attempt to teach girls about hygiene and sanitation**

**20<sup>th</sup> February, 2023**



## **Contents of Report**

1. Introduction of Report
2. Objective of the Report
3. Beneficiaries of the Event
4. Brief Description of the Event
5. Geo- tagged Photographs
6. Attendance of the Event



## 1. Introduction of the Event

A small NGO visit was organised on 20<sup>th</sup> February, 2023 at Aashray Help and Care Foundation, Nirman Nagar, Brijlapura, Jaipur. It was organised for First Year students so that they get encouraged to be a supportive part of LAC to help people who are in need. We visited there to explain and teach girls about sanitisation and cleanliness which is very important for proper health as they are the most important element of this new emerging generation.

## 2. Objectives of the Event

- To spread awareness.
- Making children feel comfortable to share any problem they face while staying in the NGO, studying, hygiene provided by the NGO, etc.
- Promoting Legal Aid Clinic (LAC) work and make them understand that they can approach us whenever they need.

## 3. Beneficiaries of the Event

- The beneficiaries of the event included the Students of the School of Law of Manipal University, Jaipur.
- Students of First and Second year.

## 4. Brief Description of the Event

The volunteers were asked to report at the Old Mess of the University at 1:30 PM. We all collected there and headed towards the University bus to leave for Brijlapura. Exactly at 2:00 PM after the President of LAC- Navendu Vijayvergia and our Sensitisation Team Head Shivanshi Sharma addressed, the group left for the greatest experience to talk with the children, one can have.

After reaching the NGO, we asked girls to gather and taught them basic rights they have and should exercise when in need. We interacted with them in the best way a mentor could. We explained the importance of proper sanitation and hygiene and education.

All girls interacted beautifully and cooperated with us with all respect, love and care.

Therefore, we had a very successful visit and achieved our goal.

## 6. Photographs



6. Attendance of the Event

STUDENT LIST	
Reg No	Name
211301108	ABHISHEK CHOMAL
221305047	ADARSH NISHAD
201301001	ADHIP NARAYAN BANERJEE
211301100	AMAN PRAKASH
201301025	AMANPREET SINGH
221305052	AMISHI BASNOTRA
201301009	ARIYANT SINGH
211301098	ASHAY APURV
201301022	ASKRIT TIWARI
201301008	ATUL MISHRA
221305050	BAIBHAV BHANU NAITHANI
201301015	CHAITANYA SINGH
221305044	CHINMAY VISHAL SHARMA
221305045	DAKSH SHARMA
201301029	DAMINI CHAUHAN
211301107	DEEPANKAR SINGH
201301023	DEEPENDER SHEKHAWAT
201301017	DHRUV POTLIA
201301032	DIYA YADAV
201301021	ISHWAR JAISWAL
201301005	KASIM PATEL
221305053	KAUSTUBH VERMA
201301002	KOMAL MATHUR
221305049	LUBHANI GUPTA
201301020	MANVENDRA SINGH RATHORE
221305046	MAYAN RAJ
211301099	MEHWISH KHAN
201301028	MRITYUNJAY PAREEK
221305051	NISHIT KUMAR JAIN
201301030	PEEYUSH RAJ TRIVEDI
211301104	PRANAV MATHUR
211301106	PRATIBHA KARNOT
211301102	PUNJIKA SHEKHAWAT
201301003	RAKSHIT SHARMA
201301010	RAVIKANT DUBEY
201301012	ROHIT SINGH
221305048	RONAK CHANDORA
201301019	SACHIN LAMBA
201301016	SHASHANK FAUZDAR
211301103	SUNIL MEHRIYA
201301027	TANISHQ SAHARAN
221305054	TAVESH GUPTA
201301011	TEESHA ARORA
211301105	TITHI GUPTA
201301031	VANSHIKA LAKHANOT
211301101	VIVEK RAJ SINGH
201301026	YASHWANT SINGH SHEKHAWAT

HEAD  
SCHOOL OF LAW  
MANIPAL UNIVERSITY JAIPUR

*Sony Gulshrestha*

Seal and Signature of Head with Date



MANIPAL UNIVERSITY  
JAIPUR

**FACULTY OF ARTS**

**SCHOOL OF HUMANITIES AND SOCIAL SCIENCES**

**DEPARTMENT OF ARTS**

**Tree plantation Drive**

**Social outreach event in collaboration with DSW and NCC**

**06/09/2023**





## Index

1. Introduction of the Event
2. Objective of the Event
3. Beneficiaries of the Event
4. Details of the Guests
5. Brief Description of the event
6. Geo-tagged Photographs
7. Brochure or creative of the event
8. Schedule of the Event
9. Attendance of the Event
10. News Publication
11. Feedback of the Event
12. Link of MUJ website



**1. Introduction of the Event**

The Department of Arts in collaboration with the DSW (NCC and NSS) organized a tree plantation drive with a number of BA(Liberal Arts) students.

**2. Objective of the Event (bullet points or about 50 words)**

To make the students aware of the importance of tree plantation.

**3. Beneficiaries of the Event**

Government school, Begas, an adopted school of MUJ

**4. Brief Description of the event**

The Department of Arts in collaboration with the DSW (NCC and NSS) organized a tree plantation drive with a number of BA(Liberal Arts) students. The objective of the event was to make the students aware of the importance of tree plantation.

## 5. Photographs



Students engaged in a tree plantation drive in the government school, Begas



MUJ students with the government school students



MUJ department students during the plantation drive

## 6. Brochure or creative of the event (insert in the document only)

8x4.5 feet



## 7. Schedule of the event (insert in the report)

6<sup>th</sup> September, 11:00 a.m. to 12:00 p.m.

## 8. Attendance of the Event (insert in the document only)

**Total attendee-16**

Sr. No	Name of Institution	Place of Institution	Name of Attendee	Name of Dept
1.	MUJ	Jaipur	Chandravardhan	Arts
2.	MUJ	Jaipur	Kumesh Mishra	Arts
3.	MUJ	Jaipur	Soumya Pareek Dhanushree	Arts
4.	MUJ	Jaipur		Arts
5.	MUJ	Jaipur	Karan Mallick	Arts
6.	MUJ	Jaipur	Vanshika Agarwal	Arts
7.	MUJ	Jaipur	Prithviraj	Arts
8.	MUJ	Jaipur	Akshatt Singh	Arts
9.	MUJ	Jaipur	Dhruv Nair	Arts
10.	MUJ	Jaipur	Krishna	Arts
11.	MUJ	Jaipur	Gaury	Arts
12.	MUJ	Jaipur	Sudeepti Dhruv Dahiya	Arts
13.	MUJ	Jaipur	Aditi Panigrahi	Arts
14.	MUJ	Jaipur	Aradhya Khandelwal	Arts
15.	MUJ	Jaipur	Komal Chadha	Arts
16.	MUJ	Jaipur	Kkritika Khandelwal Pragya Sharma	Arts
17.	MUJ	Jaipur	Prachi Randhawa	Arts
18.	MUJ	Jaipur	Gurmehr Singh	Arts
19.	MUJ	Jaipur	Himmat di Charan	Arts
20.	MUJ	Jaipur	Sameer Khan	Arts
21.	MUJ	Jaipur	Ananya Thakur	Arts
22.	MUJ	Jaipur	Harshita Das	Arts
23.	MUJ	Jaipur	Manan Sharma	Arts

24.	MUJ	Jaipur	Surendra Singh	Arts
25.	MUJ	Jaipur	Joy Tak	Arts
26.	MUJ	Jaipur	Soumya harma	Arts
27.	MUJ	Jaipur	Deepak	Arts
28.	MUJ	Jaipur	Anup Choudhary	Arts
29.	MUJ	Jaipur	Prithviraj Hada	Arts
30.	MUJ	Jaipur	Tanisha Vashisht	Arts



**9. Link of MUJ website stating the event is uploaded on website**

<https://jaipur.manipal.edu/muj/news-events/events-list.html>

**Dr. Mani Sachdev  
Head, Department of Arts  
Manipal University Jaipur**

15.9.23

**Seal and Signature of HOD**





MANIPAL UNIVERSITY  
JAIPUR

**FACULTY OF ARTS**

**SCHOOL OF HUMANITIES AND SOCIAL SCIENCES**

**DEPARTMENT OF ARTS**

**Tree plantation Drive**

**Social outreach event in collaboration with DSW and NCC**

**06/09/2023**



## **Index**

1. Introduction of the Event
2. Objective of the Event
3. Beneficiaries of the Event
4. Details of the Guests
5. Brief Description of the event
6. Geo-tagged Photographs
7. Brochure or creative of the event
8. Schedule of the Event
9. Attendance of the Event
10. News Publication
11. Feedback of the Event
12. Link of MUJ website



### 1. Introduction of the Event

The Department of Arts in collaboration with the DSW (NCC and NSS) organized a tree plantation drive with a number of BA(Liberal Arts) students.

### 2. Objective of the Event (bullet points or about 50 words)

To make the students aware of the importance of tree plantation.

### 3. Beneficiaries of the Event

Government school, Begas, an adopted school of MUJ

### 4. Brief Description of the event

The Department of Arts in collaboration with the DSW (NCC and NSS) organized a tree plantation drive with a number of BA(Liberal Arts) students. The objective of the event was to make the students aware of the importance of tree plantation.

## 5. Photographs



Students engaged in a tree plantation drive in the government school, Begas

MUJ students with the government school students



MUJ department students during the plantation drive



6. Brochure or creative of the event (insert in the document only )

8x4.5 feet



### 7. Schedule of the event (insert in the report)

6<sup>th</sup> September, 11:00 a.m. to 12:00 p.m.

### 8. Attendance of the Event (insert in the document only)

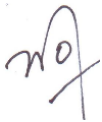
**Total attendee-16**

Sr. No	Name of Institution	Place of Institution	Name of Attendee	Name of Dept
1.	MUJ	Jaipur	Chandravardhan	Arts
2.	MUJ	Jaipur	Kumesh Mishra	Arts
3.	MUJ	Jaipur	Soumya Pareek Dhanushree	Arts
4.	MUJ	Jaipur		Arts
5.	MUJ	Jaipur	Karan Mallick	Arts
6.	MUJ	Jaipur	Vanshika Agarwal	Arts
7.	MUJ	Jaipur	Prithviraj	Arts
8.	MUJ	Jaipur	Akshatt Singh	Arts
9.	MUJ	Jaipur	Dhruv Nair	Arts
10.	MUJ	Jaipur	Krishna	Arts
11.	MUJ	Jaipur	Gaury	Arts
12.	MUJ	Jaipur	Sudeepti Dhruv Dahiya	Arts
13.	MUJ	Jaipur	Aditi Panigrahi	Arts
14.	MUJ	Jaipur	Aradhya Khandelwal	Arts
15.	MUJ	Jaipur	Komal Chadha	Arts
16.	MUJ	Jaipur	Kkritika Khandelwal Pragya Sharma	Arts
17.	MUJ	Jaipur	Prachi Randhawa	Arts
18.	MUJ	Jaipur	Gurmehr Singh	Arts
19.	MUJ	Jaipur	Himmat di Charan	Arts
20.	MUJ	Jaipur	Sameer Khan	Arts
21.	MUJ	Jaipur	Ananya Thakur	Arts
22.	MUJ	Jaipur	Harshita Das	Arts
23.	MUJ	Jaipur	Manan Sharma	Arts

24.	MUJ	Jaipur	Surendra Singh	Arts
25.	MUJ	Jaipur	Joy Tak	Arts
26.	MUJ	Jaipur	Soumya harma	Arts
27.	MUJ	Jaipur	Deepak	Arts
28.	MUJ	Jaipur	Anup Choudhary	Arts
29.	MUJ	Jaipur	Prithviraj Hada	Arts
30.	MUJ	Jaipur	Tanisha Vashisht	Arts

9. Link of MUJ website stating the event is uploaded on website

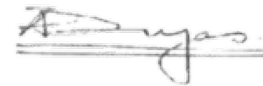
<https://jaipur.manipal.edu/muj/news-events/events-list.html>



Dr. Mani Sachdev  
Head, Department of Arts  
Manipal University Jaipur

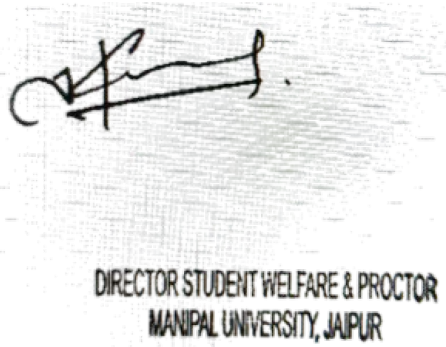
15.9.23

Seal and Signature of HOD



(Prof. AD Vyas)

Director, Directorate of Student's Welfare



DIRECTOR STUDENT WELFARE & PROCTOR  
MANIPAL UNIVERSITY, JAIPUR



MUJ/Q&C/DSW/SC/1.01



MANIPAL UNIVERSITY  
JAIPUR

**DIRECTORATE OF STUDENT'S WELFARE**

**(SOCIETY CONNECT)**

And

**Faculty of Science**

**Department of Chemistry**

Presents

**Plantation Drive**

**OCTOBER 26, 2023**

**Venue : Dabar Ki Dhani**





## 1. Introduction of the Event

School of Basic science in collaboration with Directorate of Student Welfare, NCC, NSS organized a “Plantation Drive” on October 26, 2023. The societal connect outreach activity on by planting the small plants. Program is organized by the Department of Chemistry in collaboration with Department of Student welfare (DSW) under the guidance of Mr. Hemant Kumar (Assistant Director, DSW), Dr. Rahul Shrivastava (Head, Department of Chemistry) and Dr Meenakshi Pilia (Departmental coordinator, DSW). The mention activity held at a Government School, Dabar ki Dhani, near Manipal University Jaipur on Thursday, 26<sup>th</sup> October 2023.

## 2. Objective of the Event

The focal point of this event was to spread awareness among school students with respect to their environment and also motivate the students towards to work their endeavors via the power of knowledge and education.

## 3. Beneficiaries of the Event

Through this initiative, students and villagers had better communication and understanding of the situation.

## 4. Details of the Guests

The event was laid by the students of BBA, BBA(BA), IMBA

### **Rotary Club Jaipur Bapu Nagar**

Rotary started with the vision of one man — Paul Harris. The Chicago attorney formed the Rotary Club of Chicago on 23 February 1905, so professionals with diverse backgrounds could exchange ideas and form meaningful, lifelong friendships.

Over time, Rotary’s reach and vision gradually extended to humanitarian service. Members have a long track record of addressing challenges in their communities and around the world.

Rotary is a global network of 1.4 million neighbors, friends, leaders, and problem-solvers who see a world where people unite and take action to create lasting change – across the globe, in our communities, and in ourselves. They provide service to others, promote integrity, and advance world understanding, goodwill, and peace through our fellowship of business, professional, and community leaders. We collaborate with community leaders who want to get to work on projects that have a real, lasting impact on people’s lives. We connect passionate people with diverse perspectives to exchange

ideas, forge lifelong friendships, and, above all, take action to change the world.

## 5. Brief Description of the event

The Department of Chemistry organized a societal connect outreach activity on Plantation in collaboration with the Department of Student Welfare (DSW) under the supervision of Mr. Hemant Kumar (Assistant Director, DSW), Dr. Rahul Shrivastava (Head, Department of Chemistry) and Dr. Meenakshi Pilia (Departmental coordinator, DSW). The mentioned activity was held at a Govt. school, Dabar ki Dhani, near Manipal University Jaipur on Thursday, 26th October 2023.

## 6. Photographs



Image 1 : Students with faculty at School for the Career Awareness



Image 2: Students of school during the plantation drive



Image 3: Team of MUJ Students at DABAR ki Dani School

## 7. Brochure or creative of the event



## 8. Schedule of the Event

The event took place on October 26, 2023

## 9. Attendance of the Event (50)

S. No.	Name	Registration No	Name of Institution
1	Rakshanda Singhal	211051012	Manipal University Jaipur
2	Vartika Vaishya	211051015	Manipal University Jaipur
3	Shakir Sisodia	201022604	Manipal University Jaipur
4	Govind Gupta	170703601	Manipal University Jaipur
5	Kanika Taneja	211004002	Manipal University Jaipur
6	Avani Kothari	221004004	Manipal University Jaipur
7	Pranjalee Ghosh	221004002	Manipal University Jaipur
8	Kishika Arora	221004003	Manipal University Jaipur
9	Aman Kumar	221004001	Manipal University Jaipur



10	Khushi Verma	211004006	Manipal University Jaipur
11	Karunya Papney	211004004	Manipal University Jaipur
12	Ankita Kumawat	211004003	Manipal University Jaipur
13	Supriyo	23FS20MCH00004	Manipal University Jaipur
14	Anjali Yadav	23FS20MCH00001	Manipal University Jaipur
15	Divya Sharma	23FS20MCH00003	Manipal University Jaipur
16	Vaibhav Anand	221013001	Manipal University Jaipur
17	Dipesh Gehlot	221013002	Manipal University Jaipur
18	Suman Yadav	221013003	Manipal University Jaipur
19	Ashish Sharma	221013004	Manipal University Jaipur
20	Ishan Jain	229310159	Manipal University Jaipur
21	Ishika Jain	229310410	Manipal University Jaipur
22	Aditi Singh Parihar	219311171	Manipal University Jaipur
23	Utkarsh Shukla	229301763	Manipal University Jaipur
24	Vedika	221007014	Manipal University Jaipur
25	Honey Trivedi	229302207	Manipal University Jaipur
26	Shaurya Nandwani	229301726	Manipal University Jaipur
27	Shreyas Bhati	229301374	Manipal University Jaipur
28	Aditya Mishra	229310237	Manipal University Jaipur
29	Aaryan kale	229303031	Manipal University Jaipur
30	Mustansir kanchwala	220903021	Manipal University Jaipur
31	Sahil Kalra	229303321	Manipal University Jaipur
32	Krishang Goel	229309035	Manipal University Jaipur
33	Anand Mandlik	229310162	Manipal University Jaipur
34	Aryan Sachdeva	229301438	Manipal University Jaipur
35	Ansh manawat	229301712	Manipal University Jaipur
36	Utkarsh Jha	220901009	Manipal University Jaipur
37	ria chauhan	229301253	Manipal University Jaipur
38	Ishita Sharma	229303237	Manipal University Jaipur
39	Ajinkya wagh	229310003	Manipal University Jaipur
40	Kritika Pahuja	229310048	Manipal University Jaipur
41	Ishan Aaditya	229303314	Manipal University Jaipur
42	Jiya Thakur	229309176	Manipal University Jaipur
43	Utsav Acharjya	229301358	Manipal University Jaipur
44	Kanishka Chaudhary	229202010	Manipal University Jaipur
45	Sameeksha	229310311	Manipal University Jaipur
46	Taarush Kathuria	229301462	Manipal University Jaipur
47	Ankit Kumar Tiwari	229309098	Manipal University Jaipur
48	Hanis Gori	229310131	Manipal University Jaipur
49	Aditya Prakash Sinha	229310189	Manipal University Jaipur
50	Lakshita Agrawal	229301455	Manipal University Jaipur

(Hemant Kumar)  
Assistant Director, Society Connect  
Directorate of Student's Welfare

DIRECTOR STUDENT WELFARE & PROCTOR  
MANIPAL UNIVERSITY, JAIPUR

(Prof. AD Vyas)

Director, Directorate of Student's Welfare



MUJ/DSW/Society Connect/ Oct2023/03



MANIPAL UNIVERSITY  
JAIPUR

## **DIRECTORATE OF STUDENT'S WELFARE**

### **(SOCIETY CONNECT)**

### **#DAANUTSAV 2023**

### **Plantation Drive**

### **3<sup>rd</sup> October 2023**

**Date: 3<sup>rd</sup> October 2023**

## Index

<b>S.No.</b>	<b>Activity Heads</b>	<b>Page no.</b>
1.	Introduction of the Event	1
2.	Objective of the Event	1
3.	Beneficiaries of the Event	1
4.	Brief Description of the event	1
5.	Photographs	2-4
6.	Brochure or creative of the event	5-6
7.	Schedule of the Event	6
8.	Attendance of the Event	6-9
9.	Feedback of the Event	9
10.	Link of MUJ website	9



## 1. Introduction of the Event

“A nation that destroys its soils destroys itself. Forests are the lungs of our land, purifying the air and giving fresh strength to our people. ” Trees are indispensable for life. Man can't live without trees. However, the present condition of forests in the world, especially developing countries is pathetic and miserable. Forests are the source of life. They are the giving angels. They give man oxygen, rains, wood, fruit, make the world look so beautiful, yet the sinister man kills them! Who will be more inhumane than man himself? Cutting of forests ultimately endangers man's own existence. Trees are important to the environment; they recycle water and process carbon dioxide in the atmosphere through photosynthesis. They are the world's full-time purifiers of air and water. Their cutting will disturb the natural water cycles which will lead to the shortage of fresh water in the water reserves of the world.

Rotaract Green Club under Society Connect organized a Plantation Drive on account of DAAN UTSAV 2031. It took place on the 3<sup>rd</sup> of October from 10 a.m. Students were taken to the Mahatma Gandhi School, Begus for the drive. The drive aimed to instill a sense of discipline and respect for the environment while doing our part.

## 2. Objective of the Event

- Spread awareness on the importance of afforestation
- Direct students' mind in constructive activities
- Contribution to the society
- Promote tree planting
- Create awareness regarding importance of ecology
- Attempt at reducing pollution and improve green ambience

## 3. Beneficiaries of the Event

Community

## 4. Brief Description of the event

Rotaract Green Club organized the Plantation Drive on the 3<sup>rd</sup> October at 9 a.m. on account of DAAN UTSAV 2023. The drive's main aim was to direct student's mind



in constructive activities with the positive outcome through the facilitation of contributing to the nature and environment.

It also aimed at spreading awareness about the effects of global warming and the positive effects of planting trees. The students gathered on campus to go to the Mahatma Gandhi School, Begus.

The students participated in the drive enthusiastically and helped each other in planting the saplings. All the saplings were planted in the school ground by students. Participants were highly energetic to make the event a big success. A spirit of teamwork, exchange of ideas and enthusiasm of the participants especially among the students could be seen. Pictures were taken. The drive was successfully conducted by planting 40-50 saplings.

## 5. Photographs of the event



Image 1. Students and Faculty planting saplings



Image 2 Students participating in the Drive.



Students participating in the Drive.



Image 4 Giving the manure to the newly plant samplings

**6. Brochure or creative of the event**



**MANIPAL UNIVERSITY  
JAIPUR**







**Directorate of Students' Welfare  
Society Connect**

**ROTARACT CLUB**

*Presents*

**#DAANUTSAV2023**

# PLANTATION DRIVE

**Date: 3<sup>rd</sup> October, 2023**      **Time: 10:00 AM**

**Venue: Govt. Senior Secondary School, Sanjhariya, Jaipur**



Plantation Drive

## 7. Schedule of the event

S.NO.	Name of the Event	Time	Place
1.	Plantation Drive	10:00 AM	Mahatma Gandhi School (English Medium) Begus.

A bus from MUJ was taken to the school in the morning.

## 8. Attendance of the Event

**Total attendee- 67**

S.No.	Reg. NO.	Name of Students	Institute Name
1	23FE10ITE00079	Amisha anand	Manipal University Jaipur
2	23FE10CAI00360	shaivi adesh	Manipal University Jaipur
3	23FE10CSE00060	Amay Garg	Manipal University Jaipur
4	23FE10CDS00177	Manas Mathur	Manipal University Jaipur
5	23fe10bte00029	Saloni kamal	Manipal University Jaipur
6	23FE10CSE00508	Dev Dhawan	Manipal University Jaipur
7	23fe10cii00035	Bhargavi Anand	Manipal University Jaipur
8	220606004	Pranjal Puri	Manipal University Jaipur
9	23FA10BSP00028	Anupama Rustagi	Manipal University Jaipur
10	23FE10CCE00085	Siddhartha tiwari	Manipal University Jaipur
11	23FA10BAP00002	Tanisha Mathur	Manipal University Jaipur
12	23FD10BFD00009	Mariya Shabbir Baiwala	Manipal University Jaipur
13	23FE10CDS00224	Harsh Ajmera	Manipal University Jaipur
14	23fe10cds00125	Suryanshi Singh	Manipal University Jaipur
15	23fs10mat00009	Malavika ramdas	Manipal University Jaipur
16	221007021	Arshi Jain	Manipal University Jaipur
17	23FE10CSE00137	Stuti Dixit	Manipal University Jaipur
18	23fe10cii00094	Aarohi Tyagi	Manipal University Jaipur
19	23FE10CSE00152	Gautam Kakkar	Manipal University Jaipur
20	23FE10CSE00318	Krish Ray	Manipal University Jaipur
21	23FE10CII00076	Kriish Marwaha	Manipal University Jaipur
22	229310321	Shiv Rajput	Manipal University Jaipur
23	23FS10BIO00051	Ragini Singh Thakur	Manipal University Jaipur
24	23FS10BIO00052	Anukriti sharma	Manipal University Jaipur
25	220901073	Diya Mittal	Manipal University Jaipur
26	23FE10CSE00081	Smmayan Gupta	Manipal University Jaipur
27	229309083	Raghav Gupta	Manipal University Jaipur
28	23FE10CDS00397	Hrishita Singh Timaney	Manipal University Jaipur
29	23FE10ITE00203	Sarah Sharda	Manipal University Jaipur
30	23fa10bsp00025	Jasleen kaur	Manipal University Jaipur

31	23FA10BSP00039	Jiya Kumar	Manipal University Jaipur
32	23FA10BSP00004	Aarya Mahale	Manipal University Jaipur
33	220606020	Chaarvi Kumar	Manipal University Jaipur
34	23fa10bsp00058	Kashvi Mahajan	Manipal University Jaipur
35	229301095	Shaurya Singh	Manipal University Jaipur
36	23fe10ece00024	Kushagra agrawal	Manipal University Jaipur
37	23FA10BSP00017	Megha Sharma	Manipal University Jaipur
38	23FM10BBA00162	Alina Nadeem	Manipal University Jaipur
39	23FM10BBA00178	Avishi Akhaury	Manipal University Jaipur
40	221007004	Urvi Thakare	Manipal University Jaipur
41	23FA10BAP00027	Natasha Joan Menezes	Manipal University Jaipur
42	23FA10BLE00004	Tanisha chaturvedi	Manipal University Jaipur
43	23fe10cai00579	Arjun Malhotra	Manipal University Jaipur
44	23FE10CAI00352	Maanyata Aul	Manipal University Jaipur
45	220901322	Divyanshi Singh	Manipal University Jaipur
46	229310412	Jatin Verma	Manipal University Jaipur
47	229301094	Yashovardhan Pratap Singh	Manipal University Jaipur
48	23FM10BBA00348	Niska kedia	Manipal University Jaipur
49	221105005	Dhruv Nair	Manipal University Jaipur
50	23FM10BBA00170	Shambhavi Agrawal	Manipal University Jaipur
51	23FE10CDS00241	Armaan Setia	Manipal University Jaipur
52	23FE10CAI00105	Mritunjay Singh	Manipal University Jaipur
53	229311075	Aarna Tyagi	Manipal University Jaipur
54	229302051	Prince jindal	Manipal University Jaipur
55	23FA10BHE00035	Taneesha puri	Manipal University Jaipur
56	220903033	Suhani Jain	Manipal University Jaipur
57	220901391	Dipika Agarwal	Manipal University Jaipur
58	229310222	Aayush Sharma	Manipal University Jaipur
59	221003007	Yachna Jain	Manipal University Jaipur
60	220901002	Anshu jangir	Manipal University Jaipur
61	23FE10CDS00284	Anant Barjatya	Manipal University Jaipur
62	221015074	Rupal Sharma	Manipal University Jaipur
63	23fa10bsp00047	Vartika Agarwal	Manipal University Jaipur
64	23FA10BSP00041	Kali Vithlani	Manipal University Jaipur
65	23FM10BBA00030	Harshal Saini	Manipal University Jaipur
66	23FE10CSE00746	Daksh Sharma	Manipal University Jaipur
67	23FS10BIO00034	PC Rahul	Manipal University Jaipur

**9. Feedback of the Event:- The students participated enthusiastically.**



**(Hemant Kumar)**

**Assistant Director, Society Connect**

**Directorate of Student's Welfare**

**DIRECTOR STUDENT WELFARE & PROCTOR  
MANIPAL UNIVERSITY, JAIPUR**

**(Prof. AD Vyas)**

**Director, Directorate of Student's Welfare**



MANIPAL UNIVERSITY  
JAIPUR

**FACULTY OF SCIENCES**

**SCHOOL OF BASIC SCIENCES**

**DEPARTMENT OF CHEMISTRY**

**&**

**Department of Student welfare (DSW)**

**The societal connect outreach activity on Plantation.**

**October 26, 2023**

*Fahd Shrivastava*

The societal connect outreach activity on Career Awareness Programme is organized by the Department of Chemistry in collaboration with Department of Student welfare (DSW) under the guidance of Mr. Hemant Kumar (Assistant Director, DSW), Dr. Rahul Shrivastava (Head, Department of Chemistry) and Dr Meenakshi Pilonia (Departmental coordinator, DSW). The mention activity held at a Government School, Dabar ki Dhani, near Manipal University Jaipur on Thursday, 26th October, 2023..

In order to promote a sense of concern among the students with regards to the natural environment around them we planted number of trees like peepal, neem, ashoka, babul, and meetha neem saplings on the school campus ground. Our B.Sc, M.Sc, PhD scholars and students of school campus participated in plantation activity. They would develop over the next years to shade the school's kids and create a greener, healthier environment. Refreshments were provided to the school's students, faculty, and staff after the aforementioned

Event Schedule:

Date: October 26, 2023; 12:30 PM

Venue: Govt Primary School, Dabar ki Dhani, Jaipur

Faculty Coordinator:

Dr. Meenakshi Pilonia

Number of MUJ students: 05

Number of school students: 24







Some photographs of plantation in Govt Sr. Sec. School, Dabar ki Dhani, Jaipur

## Attendance sheet

### List of Students participated the Event (Undergraduate and PhD Scholar):

S. No.	Name	Registration Number
<b>1</b>	Rakshanda Singhal	211051012
<b>2</b>	Vartika Vaishya	211051015
<b>3</b>	Shakir Sisodia	201022604
<b>4</b>	Govind Gupta	170703601
<b>5</b>	Kanika Taneja	211004002
<b>6</b>	Avani Kothari	221004004
<b>7</b>	Pranjalee Ghosh	221004002
<b>8</b>	Kishika Arora	221004003
<b>9</b>	Aman Kumar	221004001
<b>10</b>	Khushi Verma	211004006
<b>11</b>	Karunya Papney	211004004
<b>12</b>	Ankita Kumawat	211004003
<b>13</b>	Supriyo	23FS20MCH00004
<b>14</b>	Anjali Yadav	23FS20MCH00001
<b>15</b>	Divya Sharma	23FS20MCH00003
<b>16</b>	Vaibhav Anand	221013001
<b>17</b>	Dipesh Gehlot	221013002
<b>18</b>	Suman Yadav	221013003
<b>19</b>	Ashish Sharma	221013004

### List of faculties attended the event

Dr. Rahul Shrivastava

Dr Praveen K Surloia

Dr. Meenakshi Pilonia

Dr. Sriparna Ray

Dr Susruta Samanta

Dr. Saurabh



**School Students list:**

Societal connect outreach activity: Plantation  
Government School, Dabar Ki Dhani

S. No.	Name	Signature
1.	पिप्लि कुमवार	Pipli
2.	Ritik Kumawat	Ritik
3.	Robit Kumawat	Robit
4.	Maya Shya	Maya
5.	Vikram Kumawat	Vikram
6.	Vanshika Kumawat	Vanshika
7.	Kareena Kumawat	Kareena
8.	Kanishka Kumawat	Kanishka
9.	Manavi Kumawat	Manavi
10.	Nikita Kumawat	Nikita
11.	Vandana Kumawat	Vandana
12.	Bhupika Kumawat	Bhupika
13.	Abhishek Kumawat	Abhishek
14.	Abhishek	Abhishek
15.	Suman choudhary	Suman
16.	Priya Kumawat	Priya
17.	Ankita Kumawat	Ankita
18.	Yashika Kumawat	Yashika
19.	Sarika Kumawat	Sarika
20.	Priya Kumawat	Priya
21.	Harinder Kumawat	Harinder
22.	Robit saba	Robit
23.	Neeraj Kumawat	Neeraj

Neeraj Kumawat

Neeraj Kumawat



Brochure or creative of the event:

The brochure features a green and white color scheme. At the top, it displays the Manipal University Jaipur logo and several accreditation and award logos, including AACSB, ISO 9001, ISO 14001, ISO 45001, and others. The main text is centered and reads: 'Faculty of Science Department of Chemistry in collaboration with Directorate of Students' Welfare (DSW) Student Societal Outreach Activity on Plantation'. Below this, the date '26<sup>th</sup> October 2023' and the venue 'Government School, Dabar Ki Dhani' are listed. At the bottom, three names and titles are provided: Dr Hemant Kumar (Assistant Director (DSW)), Dr Rahul Shrivastava (Head, Department of Chemistry), and Dr Meenakshi Pilonia (Faculty Coordinator). The background of the brochure shows a large, classical-style building with a dome.

MANIPAL UNIVERSITY  
JAIPUR

16 AWARDS  
13 ISO CERT  
3 ISO 45001  
AACSB  
ISO 9001  
ISO 14001  
ISO 45001

Faculty of Science  
**Department of Chemistry**

*in collaboration with*  
**Directorate of Students' Welfare (DSW)**  
**Student Societal Outreach Activity**  
*on*  
**Plantation**

**26<sup>th</sup> October 2023** **Venue: Government School, Dabar Ki Dhani**

**Dr Hemant Kumar**  
Assistant Director (DSW)

**Dr Rahul Shrivastava**  
Head, Department of Chemistry

**Dr Meenakshi Pilonia**  
Faculty Coordinator

*Rahul Shrivastava*

## Appreciation Certificate


This is certified that faculty and students of Department of Chemistry, Manipal University Jaipur in collaboration with Directorate of Student Welfare (DSW)-MUJ, conducted a societal connect outreach activity on "Plantation" at Government School, Dabar ki Dhani on 26<sup>th</sup> October 2023 during 11:00 AM - 1:30 PM. The following students and faculty members participated in event:

### Students:

(1) Vaibhav Anand	221013001
(2) Dipesh Gehlot	221013002
(3) Suman Yadav	221013003
(4) Ashish Sharma	221013004
(5) Aditya Talesara	221013005

### Faculty Members:

- (1) Dr Babita Malik
- (2) Dr. Meenakshi Pilonia
- (3) Dr. Sriparna Ray

  
26/10/2023  
इतिहासकारिका  
राजकीय उच्च प्राथमिक विद्यालय  
डाबर की डाणी, दहमीकला (सांगानेर)



MUJ/DSW/Student Clubs/2023/Biotech Club MUJ/28<sup>th</sup> February

## **DIRECTORATE OF STUDENTS' WELFARE**

### **Nukkad Natak**

**ON**

### **Solid Waste Management**

**Department of Biosciences & Biotech Club, Manipal University Jaipur**

**Date of Event (28th February, 2023)**

**(Venue: TMA Pai Auditorium)**



## Index

<b>S.No.</b>	<b>Activity Heads</b>	<b>Page no.</b>
1.	Introduction of the Event	3
2.	Objective of the Event	3
3.	Beneficiaries of the Event	3
4.	Brief Description of the event	3
5.	Photographs	5
6.	Brochure or creative of the event	6
7.	Schedule of the Event	7
8.	Attendance of the Event	7



## **Introduction of the Event ,**

The Department of Biosciences & Biotech Club, Manipal University Jaipur organized a 'Nukkad Natak' on 'Solid Waste Management' on 28th Feb, 23. It was directed by 2<sup>nd</sup> year students of Department of Biosciences, Divya and Samrat and it was awe-inspiringly performed by the students. This Nukkad Natak was under the guidance of the convenor – Dr. Mousumi Debnath, Faculty Coordinator, Biotech Club.

The performers interacted with the audience and presented an informatic skit on solid waste management and the do's and don'ts of waste disposal.

This skit was a call to action, urging the audience to take responsibility for their waste and make conscious choices in their daily lives. It was an effective way to educate and engage the public on a crucial environmental issue.

## **Objectives of the Event**

- To increase awareness about solid waste management.
- To bring public awareness about the fatality caused by wastes.
- To educate about the waste disposal methods and its do's and don'ts.

## **Beneficiaries of the Event**

- MUJ Students
- Faculty

## **Brief Description of the event**

Conducted under the guidance of the Founder Faculty Coordinator, Biotech Club, Dr. Mousumi Debnath, Faculty of Biosciences, this Nukkad Natak solely aimed in bringing public awareness on solid waste management. It was well directed by students of Department of Biosciences, Divya and Samrat, who commenced from writing the scripts to directing the performers and eventually operated a successful and inspiring Nukkad Natak.

A group of brilliant and motivated performers presented the Nukkad Natak, bringing attention to the problem of solid waste management through a stirring and thought-provoking performance. The show highlighted the negative consequences of littering and the necessity of effective waste management.

The actors portrayed different characters like a litterbug, a garbage collector, and a responsible citizen who showed how the problem of solid waste management can be tackled. The audience was made conscious of the risks that incorrect garbage disposal poses to both the public's health and the environment.

The play also highlighted the role of the government and the civic bodies in managing solid waste.

In conclusion, the Nukkad Natak on Solid Waste Management held on 28th February on the occasion of National Science Day was a highly successful event that effectively highlighted the issue of solid waste management. The play succeeded in spreading awareness about the importance of proper waste management practices and the role of individuals and the government in tackling this issue.

## Photographs

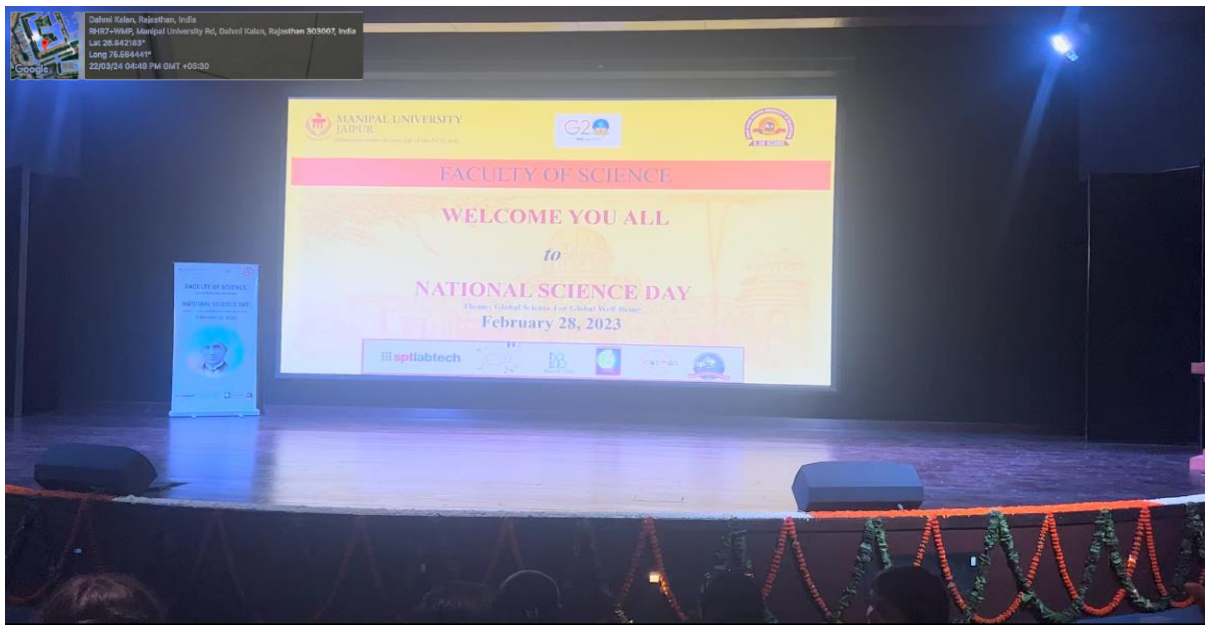


Figure 1 National Science Day; Coordinates: 26.843429; 75.566529; N26°50'36.34" E75°33'59.50"(Manipal University Jaipur)



Figure 2 Nukkad Natak performed by students.; Coordinates: 26.843429; 75.566529; N26°50'36.34" E75°33'59.50"(Manipal University Jaipur)



Figure 3 Nukkad Natak performed by students. Coordinates: 26.843429; 75.566529; N26°50'36.34" E75°33'59.50"(Manipal University Jaipur)



Figure 4 Nukkad Natak performed by students. Coordinates: 26.843429; 75.566529; N26°50'36.34" E75°33'59.50"(Manipal University Jaipur)



Figure 5 Nukkad Natak team and Dr. Mousumi Debnath, Faculty Coordinator, Biotech Club; Coordinates: 26.843429; 75.566529; N26°50'36.34" E75°33'59.50"(Manipal University Jaipur)



Brochure or Creative of the Event



MANIPAL UNIVERSITY  
JAIPUR  
*(University under Section 2(f) of the UGC Act)*



# BIOTECH CLUB OF MUJ

Presents

# NUKKAD NATAK

on

## SOLID WASTE MANAGEMENT

DATE AND TIME

28th February, 2PM onwards

VENUE

TMA PAI auditorium, MUJ



## Schedule of the event

The event was on the 28<sup>th</sup> February 2023 from 2:00 PM- 3:00 PM in TMA Pai Auditorium, Academic Block 2.

## Attendance of the event: 38

S.No.	Name	Registration No.
1.	Ananya Singh	201002002
2.	Harsh Saxena	201003004
3.	Anvarshu Gopal	211002011
4.	Anshullika Saxena	211002053
5.	Ayushi Gupta	201002029
6.	Divya	211002056
7.	Sylvia Parveen	211003009
8.	Anushka Singh	211002003
9.	Shivani Tiwari	211002002
10.	Aryan Singh	211002038
11.	Muskan Yadav	211002040
12.	Sakshi Nirmal	211002060
13.	Priyasha Paul	211002035
14.	Akash Chandra	211002036
15.	Shashank Goyal	21102043
16.	Nandini	211003001
17.	Mrunal Mangaje	211003007
18.	Sowvhik Parvej	211002007
19.	Aayushi Thakkar	211002061
20.	Manisha Verma	211002009
21.	Rahul Shrivastava	211002050
22.	Debarghya Sarkar	211002015



23.	Samrat Banerjee	211003008
24.	Sneha Srivastava	211002042
25.	Sonali Lalwani	211002041
26.	Suhani Pareek	211002062
27.	Vishnu Priya	211002028
28.	Tarushi Jain	201003001
29.	Dr. Abhijeet Singh	
30.	Dr. Mousumi Debnath	
31.	Dr. Madan Mohan Sharma	
32.	Dr. Rakesh Sharma	
33.	Dr. Nitesh Poddar	
34.	Dr. Monika Sangani	

Ananya Singh

President, Biotech Cub MUJ

**Signature of the Student Coordinator**

Dr. Mousumi Debnath

School of Basic Science

**Signature of the Faculty Coordinator**

DIRECTOR STUDENT WELFARE & PROCTOR  
MANIPAL UNIVERSITY, JAIPUR

**Dr. Arun Kumar Poonia**  
Asst. Director, DSW Clubs

MUJ/Q&C/021/F/1.01



**DIRECTORATE OF STUDENT'S WELFARE**

**(SOCIETY CONNECT)**

**And**

**Faculty of Management and Commerce**

**Department of Business Administration**

**Presents**

**SWACH BHARAT**

**OCTOBER 25, 2023**



## 1. Introduction of the Event

School of Business and Commerce in collaboration with Directorate of Student Welfare, Directorate of sports and NCC, NSS organized a “SWACH BHARAT” on October 25, 2023. 52 students participated in the campaign. The event took place in Dehmi Kalan hamlet.

## 2. Objective of the Event

The aim of the campaign was to raise awareness about Waste Segregation and encourage education on the SWACH BHARAT.

## 3. Beneficiaries of the Event

Through this initiative, students and villagers had better communication and understanding of the situation.

## 4. Details of the Guests

The event was laid by the students of BBA, BBA(BA), IMBA

### **Rotary Club Jaipur Bapu Nagar**

Rotary started with the vision of one man — Paul Harris. The Chicago attorney formed the Rotary Club of Chicago on 23 February 1905, so professionals with diverse backgrounds could exchange ideas and form meaningful, lifelong friendships.

Over time, Rotary’s reach and vision gradually extended to humanitarian service. Members have a long track record of addressing challenges in their communities and around the world.

Rotary is a global network of 1.4 million neighbors, friends, leaders, and problem-solvers who see a world where people unite and take action to create lasting change – across the globe, in our communities, and in ourselves. They provide service to others, promote integrity, and advance world understanding, goodwill, and peace through our fellowship of business, professional, and community leaders. We collaborate with community leaders who want to get to work on projects that have a real, lasting impact on people’s lives. We connect passionate people with diverse perspectives to exchange ideas, forge lifelong friendships, and, above all, take action to change the world.

## 5. Brief Description of the event

The event was initiated to make students aware of their surroundings with respect to Waste and its consequences on the local community. The students went on a rally in groups, holding posters

on Wet Waste and Dry Waste. They were chanting slogans “Alag Karo Alag Karo” Gila aur Sukha Kachara Alag Karo, to make the local community aware of the Waste Segregation process.

## 6. Photographs

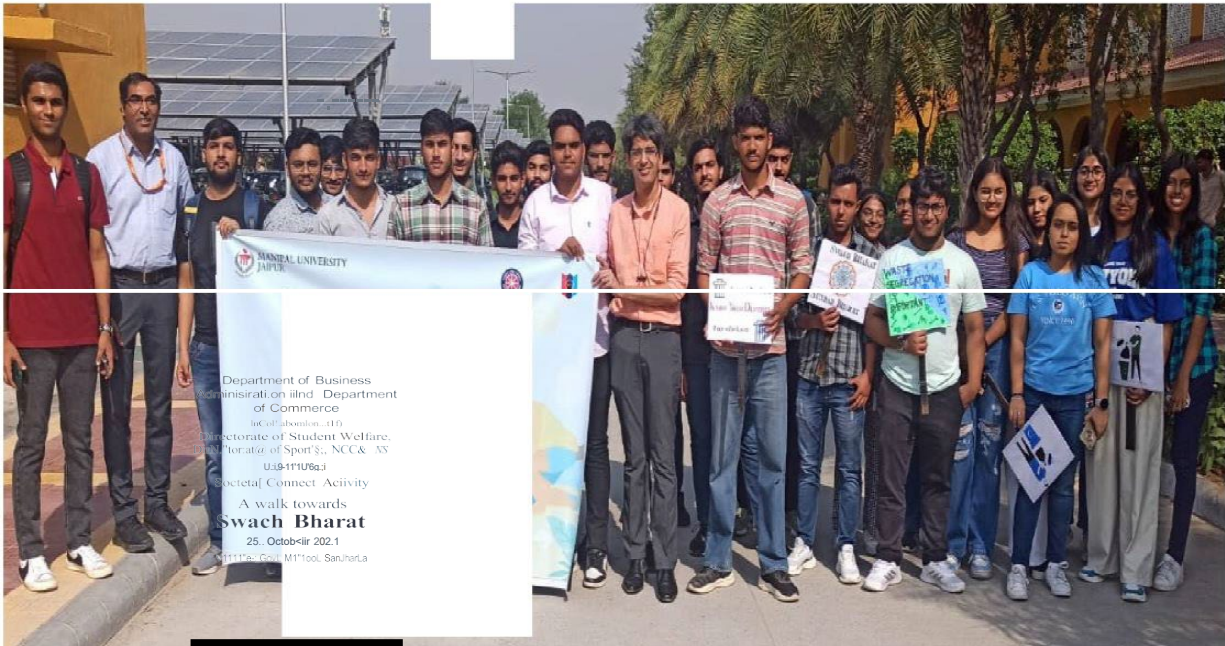


Image 1 : Students with faculty



Image 2: Students walking with the Rally through the Village



Image 3: Team of MUJ Students at Village for Rally



Image 4: Team of MUJ Students at Village for Rally

## 7. Brochure or creative of the event



## 8. Schedule of the Event

The event took place on October 25, 2023

## 9. Attendance of the Event

Sr. No	Name of Institution	Registration No	Attendee Name
1	Manipal University Jaipur	23FM10BBA00122	Naresh Choudhary
2	Manipal University Jaipur	23FM10BBA00123	Prem Singhrathore
3	Manipal University Jaipur	23FM10BBA00124	Yash Vardhansingh
4	Manipal University Jaipur	23FM10BBA00125	Krishna Snair
5	Manipal University Jaipur	23FM10BBA00126	Viyom Gupta
6	Manipal University Jaipur	23FM10BBA00127	Aditya Singh shekhawat
7	Manipal University Jaipur	23FM10BBA00128	Sheikh Tabish ahmed
8	Manipal University Jaipur	23FM10BBA00129	Bhaves Aggarwal
9	Manipal University Jaipur	23FM10BBA00130	Riddhima Gupta
10	Manipal University Jaipur	23FM10BBA00131	Ishita Sharma
11	Manipal University Jaipur	23FM10BBA00132	Akshat Sharma
12	Manipal University Jaipur	23FM10BBA00133	Preksha Sood
13	Manipal University Jaipur	23FM10BBA00134	Tanisha Agarwal
14	Manipal University Jaipur	23FM10BBA00135	Ram Avtarchouhan



15	Manipal University Jaipur	23FM10BBA00136	Sourabh Shekhawat
16	Manipal University Jaipur	23FM10BBA00137	Abhishek Jain
17	Manipal University Jaipur	23FM10BBA00138	Priyanshu Yadav
18	Manipal University Jaipur	23FM10BBA00139	Riddhi Charan
19	Manipal University Jaipur	23FM10BBA00140	Akhil
20	Manipal University Jaipur	23FM10BBA00141	Shaily Kushwaha
21	Manipal University Jaipur	23FM10BBA00142	Deep Mittal
22	Manipal University Jaipur	23FM10BBA00143	Rahul Choudhary
23	Manipal University Jaipur	23FM10BBA00144	Ronil Joshi
24	Manipal University Jaipur	23FM10BBA00145	Arihant Jaisawal
25	Manipal University Jaipur	23FM10BBA00146	Ayush Kumarthakur
26	Manipal University Jaipur	23FM10BBA00147	Angad Yadav
27	Manipal University Jaipur	23FM10BBA00148	Shashank Chaudhary
28	Manipal University Jaipur	23FM10BBA00149	Khushi Gupta
29	Manipal University Jaipur	23FM10BBA00150	Garvita Rathore
30	Manipal University Jaipur	23FM10BBA00151	Anirban Bhattacharyya
31	Manipal University Jaipur	23FM10BBA00152	Keshav Badthuniya
32	Manipal University Jaipur	23FM10BBA00153	Yash Saini
33	Manipal University Jaipur	23FM10BBA00154	Vineet Kumar
34	Manipal University Jaipur	23FM10BBA00155	Bhavuk Parashar
35	Manipal University Jaipur	23FM10BBA00156	Mohit Oshu
36	Manipal University Jaipur	23FM10BBA00157	Honey Chandnani
37	Manipal University Jaipur	23FM10BBA00158	Veer Singh
38	Manipal University Jaipur	23FM10BBA00159	Naman Kriplani
39	Manipal University Jaipur	23FM10BBA00160	Himanshu Yogesh Mittal
40	Manipal University Jaipur	23FM10BBA00161	Amogh Goyal
41	Manipal University Jaipur	23FM10BBA00162	Alina Nadeem
42	Manipal University Jaipur	23FM10BBA00163	Prince Gandhi
43	Manipal University Jaipur	23FM10BBA00164	Devansh Devansh Tiwari
43	Manipal University Jaipur	221016048	Aarohi
44	Manipal University Jaipur	229301387	Soham maskara
45	Manipal University Jaipur	229301650	Karan Kapoor
46	Manipal University Jaipur	229301552	MONIL SHAH
47	Manipal University Jaipur	229311009	Krittika Wadhawan
48	Manipal University Jaipur	229301034	Maulik Mehrotra
49	Manipal University Jaipur	229302340	Shreya Saihgal
50	Manipal University Jaipur	229302257	Yash Dhruv
51	Manipal University Jaipur	229302641	Pankaj Patel
52	Manipal University Jaipur	229310250	Amrit Raj
53	Manipal University Jaipur	220901154	Mehul rawat
54	Manipal University Jaipur	221201002	Palak chawla
55	Manipal University Jaipur	229309070	Pranav Banker
56	Manipal University Jaipur	229303128	Mahi Bhardwaj
57	Manipal University Jaipur	229303305	Karshh Divekar
58	Manipal University Jaipur	229310242	Ashmit



59	Manipal University Jaipur	229301681	Armaan Deep Singh Bedi
60	Manipal University Jaipur	229302281	Shriyam Singh Tiwari
61	Manipal University Jaipur	229301130	Shreyansh Reddy
62	Manipal University Jaipur	220901032	Raj Singh
63	Manipal University Jaipur	211103077	Sanmai Pathak
64	Manipal University Jaipur	211103075	Anvesha Shekhar
65	Manipal University Jaipur	219311129	Shubham Yadav
66	Manipal University Jaipur	221201033	Divanshi Gupta
67	Manipal University Jaipur	229310052	Lakshya Khandelwal
68	Manipal University Jaipur	229303191	Krishang Shukla
69	Manipal University Jaipur	221305050	Baibhav Bhanu Naithani
70	Manipal University Jaipur	229302371	Rishika Bhagawati
71	Manipal University Jaipur	229311168	Rudra Nayyar
72	Manipal University Jaipur	229311024	Shivam Singh
73	Manipal University Jaipur	229311289	puneet more
74	Manipal University Jaipur	229310200	Nainish Mane
75	Manipal University Jaipur	229310153	Diksha M
76	Manipal University Jaipur	221007068	Akshita Pandey
77	Manipal University Jaipur	229309068	Rahul Trivedi
78	Manipal University Jaipur	229309052	Raez Mohammed K P

Dr Narendra Singh Bhati HoD, BBA

(Hemant Kumar)  
Assistant Director, Society Connect  
Directorate of Student's Welfare

DIRECTOR STUDENT WELFARE & PROCTOR  
MANIPAL UNIVERSITY, JAIPUR

(Prof. AD Vyas)  
**Director, Directorate of Student's Welfare**



# COLLABORATIONS



## OPEN ACCESS

## EDITED BY

Sirikanjana Thongmee,  
Kasetsart University, Thailand

## REVIEWED BY

Ramzan Ahmed,  
University of Science and Technology,  
Meghalaya, India  
Mithun Kumar Ghosh,  
Govt College Hatta, India

## \*CORRESPONDENCE

Devendra Jain,  
✉ devroshan@gmail.com,  
✉ devendrajain@mpuat.ac.in

## SPECIALTY SECTION

This article was submitted to  
Nanoscience,  
a section of the journal  
Frontiers in Chemistry

RECEIVED 30 January 2023

ACCEPTED 23 March 2023

PUBLISHED 07 April 2023

## CITATION

Singh D, Jain D, Rajpurohit D, Jat G,  
Kushwaha HS, Singh A, Mohanty SR,  
Al-Sadoon MK, Zaman W and  
Upadhyay SK (2023), Bacteria assisted  
green synthesis of copper oxide  
nanoparticles and their potential  
applications as antimicrobial agents and  
plant growth stimulants.  
*Front. Chem.* 11:1154128.  
doi: 10.3389/fchem.2023.1154128

## COPYRIGHT

© 2023 Singh, Jain, Rajpurohit, Jat,  
Kushwaha, Singh, Mohanty, Al-Sadoon,  
Zaman and Upadhyay. This is an open-  
access article distributed under the terms  
of the [Creative Commons Attribution  
License \(CC BY\)](https://creativecommons.org/licenses/by/4.0/). The use, distribution or  
reproduction in other forums is  
permitted, provided the original author(s)  
and the copyright owner(s) are credited  
and that the original publication in this  
journal is cited, in accordance with  
accepted academic practice. No use,  
distribution or reproduction is permitted  
which does not comply with these terms.

# Bacteria assisted green synthesis of copper oxide nanoparticles and their potential applications as antimicrobial agents and plant growth stimulants

Deepak Singh<sup>1</sup>, Devendra Jain<sup>1\*</sup>, Deepak Rajpurohit<sup>1</sup>,  
Gajanand Jat<sup>2</sup>, Himmat Singh Kushwaha<sup>3</sup>, Abhijeet Singh<sup>4</sup>,  
Santosh Ranjan Mohanty<sup>5</sup>, Mohammad Khalid Al-Sadoon<sup>6</sup>,  
Wajid Zaman<sup>7</sup> and Sudhir K. Upadhyay<sup>8</sup>

<sup>1</sup>Department of Molecular Biology and Biotechnology, Maharana Pratap University of Agriculture and Technology, Udaipur, India, <sup>2</sup>Department of Soil Science and Agricultural Chemistry, Maharana Pratap University of Agriculture and Technology, Udaipur, India, <sup>3</sup>Material Research Centre, Malviya National Institute of Technology, Jaipur, India, <sup>4</sup>Department of Biosciences, Manipal University Jaipur, Jaipur, India, <sup>5</sup>All India Network Project on Soil Biodiversity-Biofertilizers, ICAR-Indian Institute of Soil Science, Bhopal, India, <sup>6</sup>Department of Zoology, College of Science, King Saud University, Riyadh, Saudi Arabia, <sup>7</sup>Department of Life Sciences, Yeungnam University, Gyeongsan, Republic of Korea, <sup>8</sup>Department of Environmental Science, V. B. S. Purvanchal University, Jaunpur, India

Copper oxide nanoparticles (CuO-NPs) have piqued the interest of agricultural researchers due to their potential application as fungicides, insecticides, and fertilizers. The *Serratia* sp. ZTB29 strain, which has the NCBI accession number MK773873, was a novel isolate used in this investigation that produced CuO-NPs. This strain can survive concentrations of copper as high as 22.5 mM and can also remove copper by synthesizing pure CuO-NPs. UV-VIS spectroscopy, DLS, Zeta potential, FTIR, TEM, and XRD techniques were used to investigate the pure form of CuO-NPs. The synthesized CuO-NPs were crystalline in nature (average size of 22 nm) with a monoclinic phase according to the XRD pattern. CuO-NPs were found to be polydisperse, spherical, and agglomeration-free. According to TEM and DLS inspection, they ranged in size from 20 to 40 nm, with a typical particle size of 28 nm. CuO-NPs were extremely stable, as demonstrated by their zeta potential of -15.4 mV. The ester (C=O), carboxyl (C=O), amine (NH), thiol (S-H), hydroxyl (OH), alkyne (C-H), and aromatic amine (C-N) groups from bacterial secretion were primarily responsible for reduction and stabilization of CuO-NPs revealed in an FTIR analysis. CuO-NPs at concentrations of 50  $\mu\text{g mL}^{-1}$  and 200  $\mu\text{g mL}^{-1}$  displayed antibacterial and antifungal activity against the plant pathogenic bacteria *Xanthomonas* sp. and pathogenic fungus *Alternaria* sp., respectively. The results of this investigation support the claims that CuO-NPs can be used as an efficient antimicrobial agent and nano-fertilizer, since, compared to the control and higher concentrations of CuO-NPs (100  $\text{mg L}^{-1}$ ) considerably improved the growth characteristics of maize plants.

## KEYWORDS

novel bacterial isolate, 16s-rDNA sequencing, CuO-NPs-green synthesis, confirmatory tests, antimicrobial and plant growth-promoting activity





## 1 Introduction

Nanotechnology research is the most active research region in contemporary materials science (Singh et al., 2018; Rajput et al., 2021a; Bhavyasree and Xavier, 2022). Nanomaterials synthesis through conventional physical and chemical methods has several adverse features *viz.*, critically high pressure and temperature conditions, utilization of expensive and hazardous chemicals, a longer reaction time and absorbance of toxic by-products on nanomaterial surface (Buazar et al., 2019; Sukumar et al., 2020). Properties of NPs determined by their size, shape, composition, crystalline, and structure (Sharma et al., 2020; Hidangmayum et al., 2022; Rajput et al., 2022). Recent years have seen a significant increase in the significance of green synthesis techniques for nanomaterials, making it one of the very popular methods in modern material sciences (Sukhwal et al., 2017; Mahboub et al., 2022).

Green synthesis has become one of the most preferred methods to overcome the adverse effects physical and chemical synthesis such as critical conditions of temperature and pressure, expensive and toxic chemicals, long reflux time of reaction, toxic by-products *etc.* (Sukhwal et al., 2017; Jain et al., 2020). Metal-tolerant bacteria are important nano-factories that not only accumulates and also detoxify heavy metals due to the various mechanism, *i.e.*, reductase enzymes, EPS, *etc.*, to reduce metal salts to nanomaterials (Jain et al., 2012; Jain et al., 2020; Garg et al., 2022). The nanomaterial synthesis using plant extracts may be easier than microbial synthesis however the microbial synthesis is more cost-effective and freer from any seasonal and plant growth stage variation.

Inorganic metal oxide NPs, *viz.*, CuO, ZnO, MgO, TiO<sub>2</sub>, SiO<sub>2</sub>, *etc.*, with significant antimicrobial features as well as their selective toxicity, point to potential applications of these materials in medical devices and diagnostics, therapeutics, and nanomedicine against human pathogens (Mohsen and Zahra, 2008; Sobha et al., 2010; Jain D. et al., 2022). These inorganic oxide NPs are beneficial as antibacterial agents because they are more effective against resistant pathogens. According to Makhluaf et al. (2005), crystalline structure and particle shape of nanomaterials have relatively little effect on antibacterial behavior, but a high concentration of smaller-size nanoparticles with a higher surface area does.

The simplest copper compound in the family is copper oxide, which has a variety of possibly practical physical characteristics (Buazar et al., 2019). Copper oxide (CuO) has drawn more interest than other nanomaterials because of its distinctive qualities, which include stability, conductivity, catalytic activity, and anticancer and antibacterial activities. Copper oxide nanoparticles (CuO-NPs) are receiving more attention owing to their availability and lower cost when compared to more costly and noble metals like gold and silver, as well as their effective potential for application as microbial agents (Sankar et al., 2014). Among them, CuO-NPs has drawn a lot of attention in research areas including solar cells, biodiesel, photocatalysis, water pollutant removal, supercapacitors, and electrocatalysis owing to their desired qualities, such as cheap cost, non-toxicity, and ease of manufacturing (Grigore et al., 2016).

By preventing the growth of bacteria, fungi, viruses, and algae, CuO-NPs have important antimicrobial qualities (Amin et al., 2021; Bukhari et al., 2021). Furthermore, compared to other organic antimicrobials like silver and gold, nanoscale copper oxide has a

longer shelf life. According to Keabadile et al. (2020) green synthesis of CuO-NPs with acceptable physio-chemical characteristics has previously been performed with several microbial precursors as reductants. However, very little study has been done on the synthesis of CuO-NPs employing bacteria that are copper-resistant. Hence, the current investigation was conducted to tackle this issue and build a bacteria-assisted synthesis of CuO-NPs and assessment of their antimicrobial and plant growth stimulating activities.

## 2 Materials and methods

### 2.1 Source, minimum inhibitory concentration, and molecular identification of copper-tolerant bacteria

The maximum copper tolerance concentration (MTC) was determined on LB agar medium (in triplicate) having an increased concentration of CuSO<sub>4</sub> (2.5–25 mM), and the MTCs were noted from the concentration of CuSO<sub>4</sub> at which the isolate failed to demonstrate growth. The different bacterial isolates were utilized in this study taken from our lab, which were isolated from Zn-Pb ore mine tailings areas of Zawar mines in Udaipur, Rajasthan, India (Jain et al., 2020). According to a previously illustrated method, the 16S rDNA region was amplified and sequenced to perform molecular characterization of copper-tolerant bacteria (Janda and Abbott, 2007).

### 2.2 Bacterial-assisted synthesis of copper oxide nanoparticles

The synthesis of CuO-NPs was borne out by using copper (Cu) tolerant bacterial isolate (ZTB29) with little modification technique of earlier published (John et al., 2021). The bacterial strain that showed the highest tolerance against copper ion, was inoculated in LB medium (100 mL) and incubated at 28°C with 150 rpm. After 24 h, 5 mM CuSO<sub>4</sub>·5H<sub>2</sub>O was dropped into the bacterial culture and incubated for 48 h at 28°C until the solution color changed from blue to green. This combination was then centrifuged at 4,000 rpm for 20 min at 4°C to separate the bacterial cell pellet, and the CuO-NPs were produced by centrifuging the residual supernatant at 14,000 rpm for 15 min at 4°C. The obtained CuO-NP pellet was washed twice with deionized water, dried at 80°C in an oven and used for further characterization. A control experiment without copper-tolerant bacteria was also done and upon inclusion of 5 mM CuSO<sub>4</sub>·5H<sub>2</sub>O, the color change was not seen which states no nanoparticles formation.

### 2.3 Characterization of CuO-NPs

CuO-NPs were primarily characterized using UV-Vis absorption scanning at 200–1,000 nm using a nanophotometer (Make: Implen, Germany) as the method outlined by Davaeifar et al. (2019). Dynamic Light Scattering (DLS) and Zeta potential were performed by the earlier described method (Rajput et al., 2021b) by using Malvern zeta-sizer nanoseries (United Kingdom). The FTIR spectroscopy (Perkin Elmer)

was performed for CuO-NPs (in KBr pellets) in the 4,100–400  $\text{cm}^{-1}$  range (Garg et al., 2022). Around 10  $\mu\text{L}$  of CuO-NPs dispersed in milli Q water were placed onto carbon-coated copper TEM grid for transmission electron microscopy (Tecnai G220 (FEI) S-Twin 200kv) (Sukhwal et al., 2017). The dried powder of CuO-NPs was further characterized by XRD (X'Pert Pro X-ray diffractometer, PAN analytical BV) with Cu K $\alpha$  radiation set with 40 kV and 30 mA (Sukhwal et al., 2017).

## 2.4 Antimicrobial activities of CuO nanoparticles

Antibacterial activities of bacterial-assisted CuO-NPs were studied by both disc diffusion method and well diffusion using LB agar medium against plant pathogenic bacteria *Xanthomonas* sp. Briefly, 1 mL bacterial suspension ( $>10^7$  CFU  $\text{mL}^{-1}$ ) was spread by spreader on LB agar Petri-plates, and in disc diffusion method, the sterile filter paper disk, dipped in a known concentration of CuO-NPs was placed on LB agar plates whereas, in well diffusion method, 5 mm wells (prepared by sterile cork-borer on LB agar Petri-plates) were loaded with CuO-NPs and incubated for inhibition zone development (Jain et al., 2020). The antifungal activities of CuO-NPs were investigated by using the poisoned food technique and spore germination test. The radial mycelia growth of test fungi *Alternaria* sp. was recorded on PDA containing different concentrations of CuO-NPs (50, 75, 100, 150, and 200  $\mu\text{g mL}^{-1}$ ). PDA plates without CuO-NPs were used as a control. These plates were kept for incubation at 25°C until full radical growth was observed in the control. The different concentration of CuO-NPs was used as per the CRD design in triplicate and the significant difference among treatment were determined by Turkey–Kramer HSD test at  $p = 0.05$ .

## 2.5 In vitro studies of CuO-NPs on the growth of maize

The experimental pot was filled with agricultural soil supplemented with sterile planting mixture, seeded with maize seed (PRATAP-3), and placed inside the plant growth chamber (humidity: 60%, light intensity: 750  $\mu\text{mol/m}^2\text{s}$  with 15 h light and 9 h dark conditions at 25°C–20°C). Seven days old maize seedlings were treated with CuO-NPs concentrations viz. 0, 25, 50, 75, 100, 200, and 300  $\text{mg L}^{-1}$  (in Hoagland solution) as foliar spray. The shoot length (cm), root length (cm), chlorophyll content (SPAD-502 + Chlorophyll Meter, Spectrum Technologies, India), Copper content [atomic absorption spectroscopy (AAS), Make: Electronics co. India Ltd. Modal no. AAS4141] was studied in 21 days old seedlings (Garg et al., 2022).

## 3 Result

### 3.1 Source, screening of MTC against copper and molecular identification of potent copper-tolerant bacteria

The bacterial isolates ZTB15, ZTB24, ZTB28, and ZTB29 were tested for their maximum copper ( $\text{CuSO}_4$ ) tolerance levels in

nutritional broth and observed Minimum inhibitory concentration (MIC). The bacterial isolate ZTB29 had a very maximum MIC of 22.5 mM copper in the medium and was able to withstand high doses of copper in the current experiment (Supplementary Table S1). A further selection of the ZTB29 strain was made for the bacterially aided synthesis of copper oxide CuO-NPs. The ZTB-29 isolate's 16S rRNA gene was sequenced in its entirety and put into nucleotide-nucleotide BLAST analysis. The strains' similarity and matches to previously published bacterial rDNA sequences allowed scientists to identify them as *Serratia* sp. (Figure 1). The ZTB29 nucleotide sequence was deposited to NCBI with the accession MK773873. The detailed biochemical, plant growth promoting and other physiological attributes of the ZTB29 strain were summarized in (Supplementary Table S2) which enables the ZTB29 strain to not only bioremediate excess copper but also to promote plant growth.

### 3.2 ZTB29 assisted copper oxide nanoparticles synthesis and its confirmatory examination

The easily observed synthetic bacterial growth in the bottom of the flask demonstrated the reaction between the bacterium and copper sulfate, the precursor salt. The starting solution's color changed from light blue to green when 5 mM copper sulfate was added drop by drop to the bacterial suspension, indicating the production of CuO-NPs. The greatest absorbance of 285 nm by using UV-visible spectroscopy was observed, indicating that copper sulfate (which does not produce any absorbance at 285 nm: Supplementary Figure S1), the starting material, was converted to CuO-NPs, as shown in (Figure 2).

The surface charge, size distribution, and potential stability of the nanoparticles contained in a liquid were characterized using dynamic light scattering (DLS) and zeta potential, respectively. Particles in the solution ranged in size from 15 nm to 30 nm and were homogeneous in size. The average CuO-NPs particle size was  $21 \pm 5.4$  nm which was created with a homogenous dispersion (Figure 3A). The TEM investigations provided strong support for the DLS findings. The presence of bacterial cell artifacts or the agglomeration of nanoparticles may be responsible for the second large-size distribution peak at about 1,000 nm. The zeta potential's magnitude (–30 mV to +30 mV) determines the stability and primarily depends upon the surface charge of the generated nanomaterials. The produced nanoparticles have a Zeta potential of –15.4 mV, which demonstrates that they were quite stable at ambient temperature (Figure 3B). The similar zeta potential value was observed even after 1 year of synthesis with CuO-NPs suggesting CuO-NPs were stable for 1 year or more. Zeta potential with a negative value indicates a strong repelling force between the particles, which inhibits agglomeration.

Fourier transform infrared spectroscopy (FTIR) technique was utilized to recognize the occurrence of different functional groups found in a sample. Depending on the infrared absorption range 600–4,000  $\text{cm}^{-1}$  in FTIR analysis, the absorbance range 3,200–3,550  $\text{cm}^{-1}$  is indicated for O-H stretching, 2,371  $\text{cm}^{-1}$  observance for O=C=O stretching, 1,624  $\text{cm}^{-1}$  observance for C=C stretching, 1,058  $\text{cm}^{-1}$  observance for C-OH stretching,

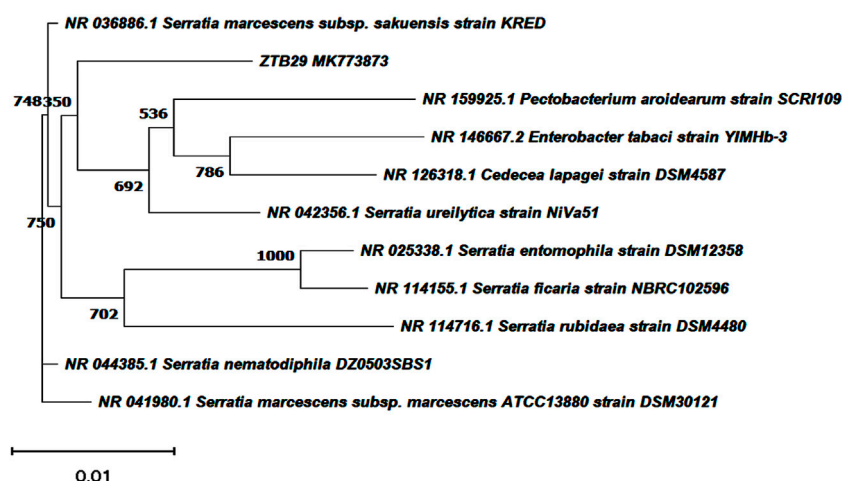


FIGURE 1

Neighbourhood joining tree showing the polygenetic relationship of copper tolerant bacterial strain ZTB29 *Serratia* sp. (NCBI Accession: MK773873).

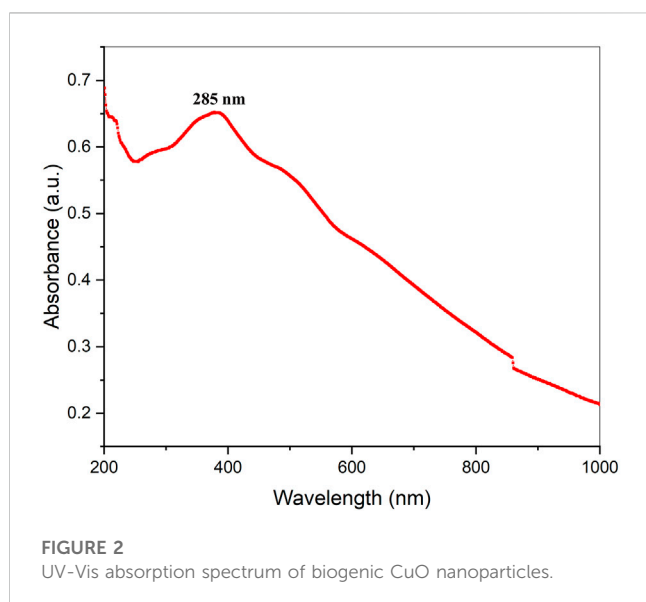


FIGURE 2

UV-Vis absorption spectrum of biogenic CuO nanoparticles.

1,377  $\text{cm}^{-1}$  observance for the existence of  $\text{CO}_2$  when compared with the standard database. The 608  $\text{cm}^{-1}$  vibration attributed to CuO formation confirms the synthesis of pure CuO nanostructures. FTIR study revealed that the carboxyl (C=O), hydroxyl (OH), amine (NH), alkyne (C-H), thiol (S-H), ester (C=O) and aromatic amine (C-N) groups from the bacterial secretion are responsible for the copper reduction and CuO-NPs stabilization (Figure 4). The details of the different FTIR peaks observed in bacteria assisted CuO-NPs and the bacterial extract used for CuO-NPs synthesis were described in the Supplementary Table S3 and Supplementary Figure S2. The CuO-NP's size and shape were studied using TEM. TEM analysis revealed the formation of different shapes of copper oxide nanostructures (Figure 5). It was evident from TEM studies that CuO-NPs were polydisperse and spherical which were free from agglomeration. The particles were in the size range of 20–40 nm with 28 nm average particles size.

X-ray diffraction (XRD) was performed to study the phase (structure) and purity (composition) of the biosynthesized CuO-NPs using copper-tolerant bacteria. The XRD pattern (Figure 6) depicted the creation of pure and crystalline CuO-NPs. The peaks at  $2\theta = 32.548, 35.466,$  and  $38.769$  were assigned to the (110) (002) and (111) reflection lines of monoclinic CuO-NPs compared to JCPDS file No. 01-080-1268. The average crystallite size calculated based on the Scherrer technique for synthesized CuO-NP was 22 nm.

### 3.3 Antimicrobial activities of CuO-NPs

The CuO-NPs ( $50 \mu\text{g mL}^{-1}$ ) showed significant antibacterial activity by generating an inhibition zone in well diffusion assay (Figure 7A). The disc contacting  $50 \mu\text{g mL}^{-1}$  CuO-NPs demonstrated antibacterial activity against *Xanthomonas* sp. as it showed a clear inhibition zone (Figure 7B), which was higher compare to Neomycin ( $30 \mu\text{g mL}^{-1}$ ) and lower compare to Rifampicin ( $5 \mu\text{g mL}^{-1}$ ). The highest inhibition of 91% in fungal mycelia and 88% spore germination was detected at the  $200 \mu\text{g mL}^{-1}$  CuO-NPs concentration (Table 1). The rate of mycelia inhibition and spore germination was proportional to CuO-NPs concentration (Figure 8). The results observed in the present study revealed CuO-NP can be used as an efficient nano fungicide against soil-born fungus.

### 3.4 Influence of CuO-NPs on maize seedling

The shoot and root length, plant biomass, total chlorophyll and copper content were considerably high in the maize plantlet (21 days old) compared to the untreated control plantlet (Table 2). The maximum shoot and root length, biomass and chlorophyll content were observed in  $100 \text{ mg L}^{-1}$  CuO-NPs application and contributed to plant growth significantly as efficient nano-fertilizers. The CuO-NPs ( $<100 \text{ mg L}^{-1}$ ) caused significant toxicity to maize seedlings and resulted in decreased growth parameters.

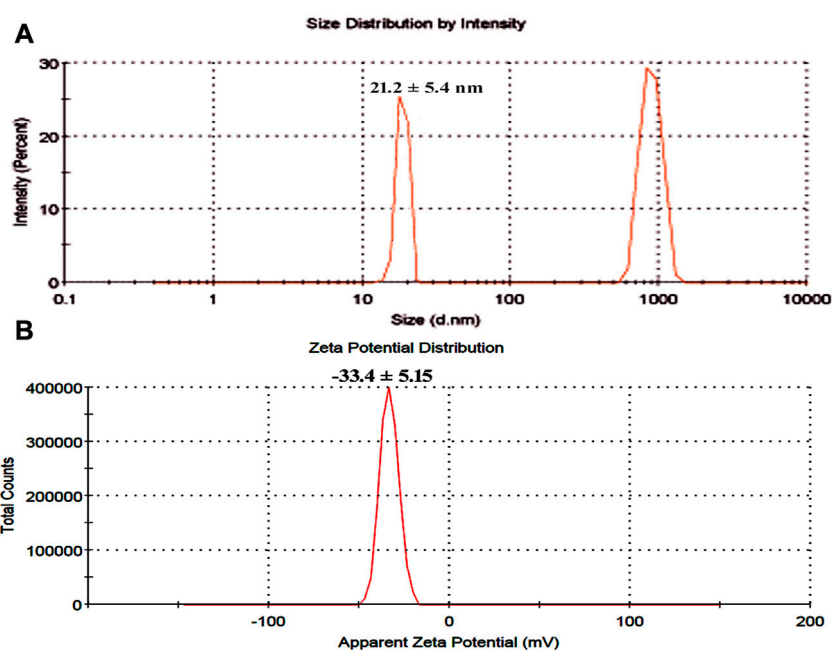


FIGURE 3

(A) Particle size determination using dynamic light scattering (B) Zeta potential analysis of bacterial assisted CuO nanoparticles.

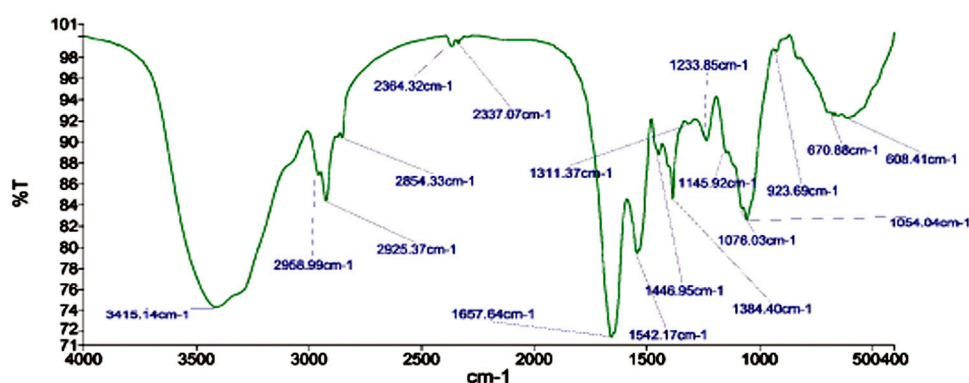


FIGURE 4

FTIR analysis of biogenic CuO nanoparticles.

## 4 Discussions

The new study could pave the way for bioprospecting for metal-tolerant microorganisms for the quick and easy synthesis of nanoparticles with a variety of applications (Jain et al., 2012; Jain et al., 2020). John et al. (2021) investigated bacterial strain copper tolerance at various CuSO<sub>4</sub> concentrations, and the bacterial strain *Marinomonas*, which tolerated 5 mM CuSO<sub>4</sub>, was employed to produce copper and CuO-NPs. Similar findings were found in the current investigation. Tiwari et al. (2016) synthesized CuO-NPs from a copper-resistant *Bacillus cereus* isolate that tolerated >10 mM of copper. The *B. cereus* isolate was able to and was identified as *B. cereus* using 16S rDNA amplification and sequencing. The change of color depends on the surface plasmon vibration of the

nanoparticles (Abdulhameed et al., 2019). Shantkriti and Rani (2014) observed that the color of the reaction changed from blue to dark green when CuSO<sub>4</sub> was added to the *Pseudomonas fluorescens* solution, which corroborated the findings. The bacteria-assisted green synthesis of metal and metal oxide nanoparticles is dependent on the bacteria's ability to remediate harmful metal concentrations by reducing metal ions to nanoparticles (Jain et al., 2020). As a result, copper-tolerant bacteria produce copper and copper oxide nanomaterials by mimicking the natural biomineralization processes that these microbes have adapted to under dangerous copper concentrations (John et al., 2021).

UV-visible absorption spectroscopy can be used to characterize metallic nanoparticles based on surface plasmon resonance (SPR) (Upadhyay et al., 2023). UV-visible spectroscopy (wavelength scan

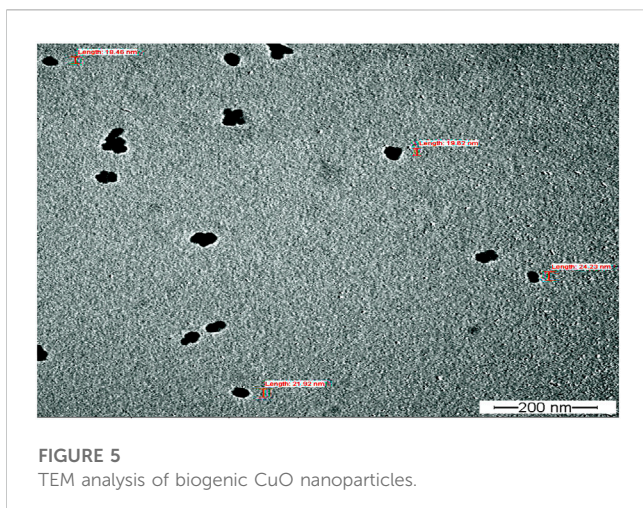


**FIGURE 5**  
TEM analysis of biogenic CuO nanoparticles.

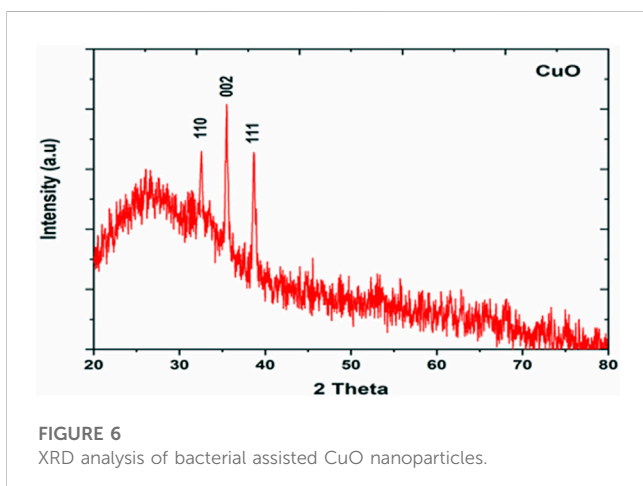


**FIGURE 6**  
XRD analysis of bacterial assisted CuO nanoparticles.

between 200 and 1,000 nm) was used to observe the solution resulting from the bluish-to-greenish color alterations of copper-tolerant bacteria (Zhao et al., 2022). The spectra of CuO-NPs generated employing copper-tolerant bacteria showed pronounced absorption at 285 nm wavelength, confirming the conversion of the starting material (copper sulfate) to the final product (CuO nanoparticles) as shown in Figure 3. Tshireletso et al. (2021) revealed that the UV-VIS absorption spectra of green-produced CuO-NPs from citrus peel extracts resulted in a notable absorbance at 290 nm. Due to surface plasmon resonance, Sankar et al. (2014) found that the UV-Vis spectra of papaya leaf extract medicated CuO-NPs spanned between 250–300 nm. In contrast, the different experiments revealed distinct absorption peaks and spectrums, which could be attributable to different forms of copper and copper oxide nanomaterials and the technology employed for nanomaterial fabrication.

DLS confirmed that the produced CuO-NPs had a homogeneous particle size distribution (15 nm–30 nm) and an average particle size of  $21 \pm 5.4$  nm (Figure 4A), which TEM investigations also validated. The CuO-NPs'  $-15.4$  mV zeta value clearly demonstrated their fairly stable character, as illustrated in Figure 4B. Nardella et al. (2022) conducted DLS investigations of biosynthesized CuO-NPs and reported a 24.4 nm Z-average diameter, while the zeta potential value, which frequently analyses the stability of nanoparticles, was found to be  $-16.1$  mV, confirming the nanoparticles' stability. Nagaraj et al. (2019) reported

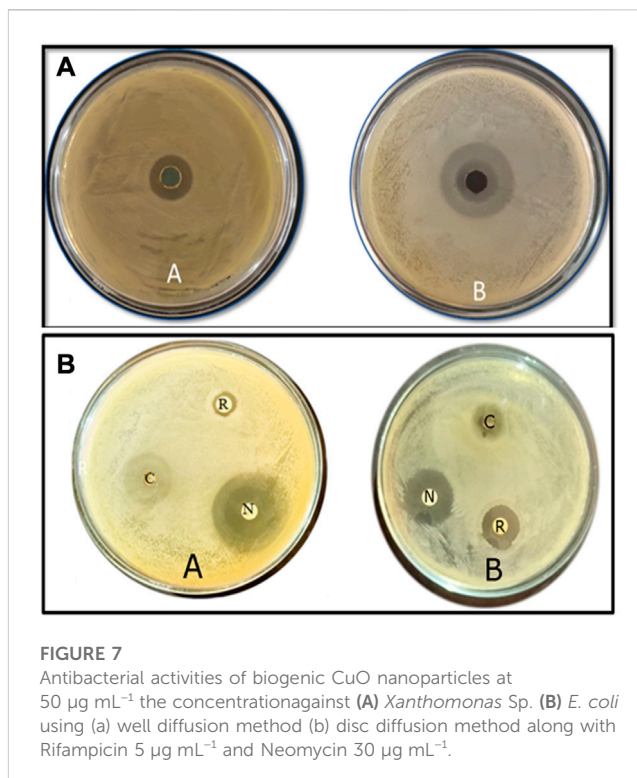


**FIGURE 7**  
Antibacterial activities of biogenic CuO nanoparticles at  $50 \mu\text{g mL}^{-1}$  the concentration against (A) *Xanthomonas* Sp. (B) *E. coli* using (a) well diffusion method (b) disc diffusion method along with Rifampicin  $5 \mu\text{g mL}^{-1}$  and Neomycin  $30 \mu\text{g mL}^{-1}$ .

the *Pterolobium hexapetalum* leaf extract-mediated synthesized CuO-NPs and the synthesized nanoparticles were extensively distributed and highly dispersed in the 10–76 nm size range, however, the associated zeta potential was  $-27.6$  mV attributed to moderate stability of nanoparticles.

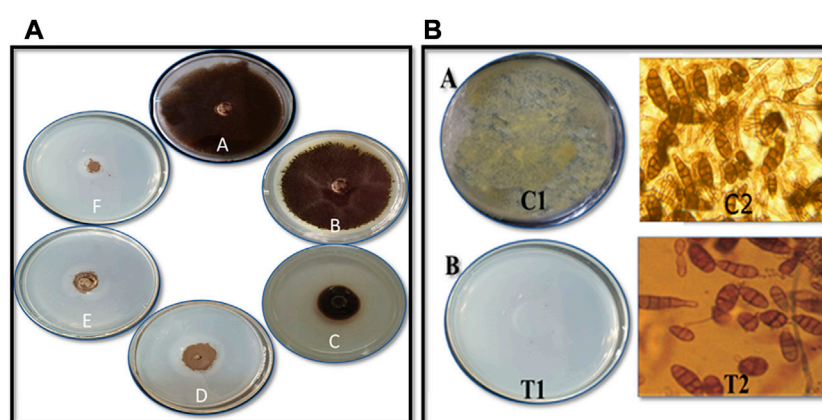
FTIR study indicated the presence of different compounds from the bacterial secretion involved in the reduction and stabilization of CuO-NPs. Amin et al. (2021) observed the FTIR peaks at  $518.4$  and  $600.1 \text{ cm}^{-1}$  (formation of CuO nanostructure and Cu–O stretching),  $1,021.14$  and  $800.58 \text{ cm}^{-1}$  (assigned to C–O and C–H bending) and  $1,412.3$  and  $1,636.4 \text{ cm}^{-1}$  (O–H bending and C=C stretching). John et al. (2021) studied FTIR spectroscopy of CuO-NPs synthesized from marine bacteria indicating the presence of  $-\text{C}=\text{O}$ ,  $-\text{OH}$ ,  $-\text{NH}$ ,  $-\text{CH}_2$  scissor vibrations of aliphatic compounds and C=C bonds inside the biomolecules suggesting the interaction of these biomolecules with CuO-NPs also observed in the present study.

TEM analysis revealed the formation of polydisperse and roughly spherical CuO-NPs which were free from agglomeration with the 20–40 nm size range (average particle size is 28 nm). The CuO-NPs as water suspension are slightly agglomerated due to their interaction with water and due to such inter-particle interactions viz. van der Waals, electrostatic and magnetic forces, etc. Previously, similar results of biogenic CuO-NPs were reported by several studies (Ida et al., 2010; Cheng and Walker, 2010; Chandra et al., 2014; Sagadevan and Koteswari, 2015; Kimber et al., 2020; Singh et al., 2019) as observed in TEM. John et al. (2021) reported the TEM micrographs of CuO-NPs from marine bacteria and reported the synthesis of monodispersed, spherical/ovoidal NPs of 10 nm–70 nm size with  $\sim 40$  nm average size. The irregular shape can be attributed to bacterial metabolites on the surface of nanoparticles as stabilizing and reducing agents. Bukhari et al. (2021) reported the *Streptomyces* sp. mediated Cu-NPs synthesis of uniform and spherical nanoparticles (1.72–13.49 nm) in the TEM

**TABLE 1** Effect of varying concentrations of CuO nanoparticles on *in vitro* mycelial growth and spore germination of phytopathogenic fungi *Alternaria* sp.

Treatment (CuO nanoparticles)	Percent inhibition mycelia growth	Percent inhibition spore germination
Control	0.0 ± 0.0 <sub>A</sub>	5.33 ± 1.52 <sub>A</sub>
50 µg mL <sup>-1</sup>	15.0 ± 1.53 <sub>B</sub>	15.0 ± 2.0 <sub>B</sub>
75 µg mL <sup>-1</sup>	70.0 ± 1.53 <sub>C</sub>	55.0 ± 2.0 <sub>C</sub>
100 µg mL <sup>-1</sup>	77.0 ± 5.7 <sub>CD</sub>	64.3 ± 2.51 <sub>D</sub>
150 µg mL <sup>-1</sup>	81.0 ± 2.0 <sub>D</sub>	74.0 ± 1.0 <sub>E</sub>
200 µg mL <sup>-1</sup>	91.0 ± 1.52 <sub>E</sub>	88.0 ± 2.0 <sub>F</sub>

\*Each value is mean of 3 replicates from 2 experiments. Mean ± SE, followed by same letter in column of each treatment is not significant difference at  $p = 0.05$  by Tukey–Kramer HSD, test, % inhibition rate was calculated compared to the germination of the control (0%).


**FIGURE 8**

Antifungal activity of CuO nanoparticles against *Alternaria* sp. on (A) mycelial growth inhibition by poisoned food technique (A) Control (B) 50 µg mL<sup>-1</sup> (C) 75 µg mL<sup>-1</sup> (D) 100 µg mL<sup>-1</sup> (E) 150 µg mL<sup>-1</sup> and (F) 200 µg mL<sup>-1</sup> CuO nanoparticles (B) Spore germination inhibition by (A) Pour plate technique C1 - Crude spore suspension and T1 - 200 µg mL<sup>-1</sup> CuO nanoparticles (B) Microscopic studies C2: Control, T2: 200 µg mL<sup>-1</sup> CuO nanoparticles.

**TABLE 2** *In vitro* studies on the effect of CuO-NPs on growth of maize seedling (Data are means of three replicates ±SD. Data are recorded after 21 days of germination).

Treatment	Average shoot length (cm)	Shoot dry weight (g)	Average root length (cm)	Chlorophyll index (SPAD)	Copper content in maize seedling (ppm)
Control	18.4 ± 1.7	4.4 ± 1.1	12.8 ± 2.1	10.03 ± 2.11	0.041 ± 0.02
T 1	24.5 ± 2.4	7.8 ± 2.3	14.8 ± 3.2	12.33 ± 2.65	0.055 ± 0.08
T 2	28.8 ± 2.8	8.3 ± 1.6	21.6 ± 2.4	13.63 ± 2.49	0.088 ± 0.06
T 3	32.4 ± 2.2	8.4 ± 2.1	24.1 ± 1.9	14.14 ± 2.43	0.092 ± 0.08
T 4	34.2 ± 3.1	10.6 ± 1.8	24.8 ± 2.3	16.86 ± 4.5	0.098 ± 0.09
T 5	29.4 ± 2.3	9.1 ± 1.5	22.7 ± 2.1	13.93 ± 2.8	0.012 ± 0.05
T 6	21.1 ± 1.9	7.5 ± 1.2	15.1 ± 1.7	11.26 ± 2.3	0.015 ± 0.05

images. Krishna et al. (2020) synthesized CuO nanoparticles from *Cinnamomum malabatum* aqueous leaf extract and the TEM revealed spherically shaped CuO-NPs with 11 nm–24 nm size range which was also in close agreement with the present study.

The XRD pattern revealed the pure CuO-NPs were crystalline in nature. Ali et al. (2021) performed XRD of CuO-NPs and the detected peaks in their study confirmed the monoclinic phase of CuO compared to JCPDS card 000021040 which was also seen in the present study. Further, the characteristic crystallite size measured



using the Scherrer equation was found to be 24.7 nm also supports the finding of the present study. Buazaret al. (2019) reported that clear and sharp peaks in XRD can be ascribed to the highly crystalline structure of nanomaterials. Similar results of the crystallite size of CuO-NPs in the range of 9–23 nm were solely dependent on the precursor conditions (Tavakoli et al., 2019).

The CuO-NPs exhibited superior antimicrobial activities and have a significant potential to control phytopathogens. Krishna et al. (2020) reported significant antibacterial activities of CuO-NPs against human pathogenic bacteria viz., *Escherichia coli*, *Staphylococcus aureus*, *Pseudomonas aeruginosa* and *Proteus mirabilis* using well diffusion method and similar results were also observed against plant pathogenic bacteria in the present study. Abboud et al. (2014) reported significant antimicrobial activities of CuO-NPs synthesized from the alga extract against *Enterobacter aerogenes* and *S. aureus* and the observed radial diameter of the inhibition zone was 14 and 16 mm, respectively. Bhavyasree and Xavier (2022) extensively reviewed the copper and CuO nanomaterial and their antimicrobial properties and demonstrated the mechanism of antibacterial action which includes mechanical damage, gene toxicity, and oxidative stress injury. The bio-molecules absorbed on the surface may also help in the antimicrobial activities of CuO-NPs.

The CuO-NPs (200 g mL<sup>-1</sup> concentration) exhibited superior antifungal activities. Qamar et al. (2020) showed reasonable results for the antifungal activity of CuO-NPs against *Trichophyton rubrum*. Rabiee et al. (2020) synthesized *Achillea millefolium* extract-mediated CuO-NPs and reported significant *in vitro* antifungal activities against four different fungi. The biosynthesized CuO-NPs showed effective antifungal activities owing to the entering of CuO-NPs on fungal membranes and negatively effect the cell divisions *via* strong interaction on the respiratory chains.

The use of CuO-NPs (100 mg L<sup>-1</sup>) resulted in the improvement of plant growth attributes as copper-based nano-fertilizer. The specific doses of CuO-NPs can play a remarkable role in plant growth promotion are advocated by several researchers (Singh et al., 2018; Rajput et al., 2022) due to the increase bio-availability of Cu<sup>2+</sup> which led to accelerating the mobilization of food reserves during germination, greater activation of copper enzymes such as cytochrome C oxidase, etc. CuO-NPs in the optimum dose can significantly influence the plant growth and act as efficient nano-fertilizers.

## 5 Conclusion

In conclusion, we present a straightforward, quick, and environmentally friendly method for producing CuO-NPs with exceptional antibacterial properties. Different approaches have been applied to clarify the size, shape, composition, and stability, and the findings demonstrate that the synthesized nanoparticles are very stable and monoclinic, with the largest particles falling within the size range of 28 nm in diameter. The CuO-NPs may function as a potent bactericide and fungicide that may be employed to combat plant infections as a result of the positive results. With the right toxicological information, the green produced CuO-NPs have a large potential and may be used for a variety of tasks, including food processing and control, biomedical forms, product packaging, and more. According to the observations of this study, CuO-NPs are a novel class of antimicrobial agents that may be developed and applied in sustainable agriculture.

## Data availability statement

The datasets presented in this study can be found in online repositories. The names of the repository/repositories and accession number(s) can be found below: <https://www.ncbi.nlm.nih.gov/>-, MK773873.

## Author contributions

DJ designed the research. DS, DR, GJ performed the experiments. SM, SU interpreted the data. HK and AS performed TEM, DLS, Zeta, FTIR and XRD. DJ and SU wrote manuscript. MS and WZ revised and proofread manuscript. All authors reviewed the manuscript.

## Funding

Gratefully acknowledge the support by Researchers Supporting Project Number (RSP2023R410), King Saud University, Riyadh, Saudi Arabia. The financial assistance from All India Network Project on soil biodiversity and Bio-fertilizer project and MPUAT, India.

## Acknowledgments

The authors would like to extend their sincere appreciation to the Researchers Supporting Project Number (RSP2023R410), King Saud University, Riyadh, Saudi Arabia. The financial assistance from All India Network Project on soil biodiversity & Bio-fertilizer project and the equipment support from IDP, NAHEP project are gratefully acknowledged.

## Conflict of interest

The authors declare that the research was conducted in the absence of any commercial or financial relationships that could be construed as a potential conflict of interest.

## Publisher's note

All claims expressed in this article are solely those of the authors and do not necessarily represent those of their affiliated organizations, or those of the publisher, the editors and the reviewers. Any product that may be evaluated in this article, or claim that may be made by its manufacturer, is not guaranteed or endorsed by the publisher.

## Supplementary material

The Supplementary Material for this article can be found online at: <https://www.frontiersin.org/articles/10.3389/fchem.2023.1154128/full#supplementary-material>



## References

- Abdoud, Y., Saffaj, T., Chagraoui, A., Bouari, A. El., Brouzi, K., and Tanane, O. (2014). Biosynthesis, characterization and antimicrobial activity of copper oxide nanoparticles (CONPs) produced using Brown alga extract (*Bifurcariabifurcata*). *Appl. Nanosci.* 4, 571–576. doi:10.1007/s13204-013-0233-x
- Abdulhameed, A. S., Jawad, A. H., and Mohammad, A. K. T. (2019). Synthesis of chitosan-ethylene glycol diglycidyl ether/TiO<sub>2</sub> nanoparticles for adsorption of reactive orange 16 dye using a response surface methodology approach. *Bioresour. Technol.* 293, 122071. doi:10.1016/j.biortech.2019.122071
- Ali, M., Ijaz, M., Ikram, M., Ul-Hamid, A., Avais, M., and Anjum, A. A. (2021). Biogenic synthesis, characterization and antibacterial potential evaluation of copper oxide nanoparticles against *Escherichia coli*. *Nanoscale Res. Lett.* 16, 148. doi:10.1186/s11671-021-03605-z
- Amin, F., Khattak, B., Alotaibi, A., Qasim, M., Ahmad, I., Ullah, R., et al. (2021). Green synthesis of copper oxide nanoparticles using *Aerjavanica* leaf extract and their characterization and investigation of *in vitro* antimicrobial potential and cytotoxic activities. *Evidence-Based Complement. Altern. Med.* 5589703, 1–12. doi:10.1155/2021/5589703
- Bhavyasree, P. G., and Xavier, T. S. (2022). Green synthesised copper and copper oxide-based nanomaterials using plant extracts and their application in antimicrobial activity: Review. *Curr. Res. Green Sustain. Chem.* 5, 100249. doi:10.1016/j.crgsc.2021.100249
- Buazar, F., Sweidi, S., Badri, M., and Kroushawi, F. (2019). Biofabrication of highly pure copper oxide nanoparticles using wheat seed extract and their catalytic activity: A mechanistic approach. *Green Process. Synthesis* 8, 691–702. doi:10.1515/gps-2019-0040
- Bukhari, S. I., Hamed, M. M., Al-Agamy, M. H., Gazwi, H. S. S., Radwan, H. H., and Youssif, A. M. (2021). Biosynthesis of copper oxide nanoparticles using *Streptomyces* MHM38 and its biological applications. *Hindawi J. Nanomater.* 6693302, 1–16. doi:10.1155/2021/6693302
- Chandra, S., Kumar, A., and Kumar, T. (2014). Synthesis and characterization of copper nanoparticles by reducing agent. *J. Saudi Chem. Soc.* 18 (2), 149–153. doi:10.1016/j.jscs.2011.06.009
- Cheng, G., and Walker, A. R. H. (2010). Transmission electron microscopy characterization of colloidal copper nanoparticles and their chemical reactivity. *Anal. Bioanal. Chem.* 396, 1057–1069. doi:10.1007/s00216-009-3203-0
- Davaeifar, S., Modarresi, M. H., Mohammadi, M., Hashemi, E., Shafiei, M., Maleki, H., et al. (2019). Synthesizing, characterizing, and toxicity evaluating of phycocyanin-ZnO nanorod composites: A back to nature approaches. *Colloids Surfaces B Biointerfaces* 175, 221–230. doi:10.1016/j.colsurfb.2018.12.002
- Garg, K. K., Jain, D., Rajpurohit, D., Kushwaha, H. S., Daima, H. K., Stephen, B. J., et al. (2022). Agricultural significance of silica nanoparticles synthesized from a silica Solubilizing Bacteria. *Comments Inorg. Chem.* 42 (4), 209–225. doi:10.1080/02603594.2021.1999234
- Grigore, M. E., Biscu, E. R., Holban, A. M., Gestal, M. C., and Grumezescu, A. M. (2016). Methods of synthesis, properties and biomedical applications of CuO nanoparticles. *Pharm. (Basel)* 9 (4), 75. doi:10.3390/ph9040075
- Hidangmayum, A., Debnath, A., Guru, A., Singh, B. N., Upadhyay, S. K., and Dwivedi, P. (2022). Mechanistic and recent updates in nano-bioremediation for developing green technology to alleviate agricultural contaminants. *Int. J. Environ. Sci. Technol.*, 1–26. doi:10.1007/s13762-022-04560-7
- Ida, K., Sugiyama, Y., YukiChujyo, Y., Tomonari, M., Tomoharu Tokunaga, T., Sasaki, K., et al. (2010). *In-situ* TEM studies of the sintering behavior of copper nanoparticles covered by biopolymer nanoskin. *J. Electron Microsc.* 59, 75–80. doi:10.1093/jmicro/dfq055
- Jain, N., Bhargava, A., Tarafdar, J. C., Singh, S. K., and Panwar, J. (2012). A biomimetic approach towards synthesis of zinc oxide nanoparticles. *Appl. Microbiol. Biotechnol.* 97 (2), 859–869. doi:10.1007/s00253-012-3934-2
- Jain, D., Kour, R., Bhojiya, A. A., Meena, R. H., Singh, A., Mohanty, S. R., et al. (2020). Zinc tolerant plant growth promoting bacteria alleviates phytotoxic effects of zinc on maize through zinc immobilization. *Sci. Rep.* 10, 13865. doi:10.1038/s41598-020-70846-w
- Jain, D., Kushwaha, H. S., Rathore, K. S., Stephen, B. J., Daima, H. K., Jain, R., et al. (2022). Fabrication of iron oxide nanoparticles from ammonia vapor and their importance in plant growth and dye degradation. *Part. Sci. Technol.* 40, 97–103. doi:10.1080/02726351.2021.1929601
- Jain, R., Bohra, N., Singh, R. K., Upadhyay, S. K., Srivastava, A. K., and Rajput, V. D. (2022). “Nanomaterials for plants: From ecophysiology to signaling mechanisms and nutrient uptake,” in *The role of nanoparticles in plant nutrition under soil pollution. Sustainable plant nutrition in a changing world*. Editors V. D. Rajput, K. K. Verma, N. Sharma, and T. Minkina (Cham: Springer). doi:10.1007/978-3-030-97389-6\_8
- Janda, J. M., and Abbott, S. L. (2007). 16S rRNA gene sequencing for bacterial identification in the diagnostic laboratory: Pluses, perils, and pitfalls. *J. Clin. Microbiol.* 45 (9), 2761–2764. doi:10.1128/JCM.01228-07
- John, M. S., Nagothi, J. A., Zannotti, M., Giovannetti, R., Mancini, A., Ramasamy, K., P., et al. (2021). Biogenic synthesis of copper nanoparticles using bacterial strains isolated from an antarctic consortium associated to a psychrophilic marine ciliate: Characterization and potential application as antimicrobial agents. *Mar. Drugs* 19 (5), 263. doi:10.3390/md19050263
- Keabadile, O. P., Aremu, A. O., Elugoke, S. E., and Fayemi, O. E. (2020). Green and traditional synthesis of copper oxide nanoparticles-comparative study. *Nanomater. (Basel)* 10 (12), 2502. doi:10.3390/nano10122502
- Kimber, R. L., Bagshaw, H., Smith, K., Buchanan, D. M., Coker, V. S., Cavet, J. S., et al. (2020). Biomineralization of Cu 2S nanoparticles by geobactersulfurreducens. *Appl. Environ. Microbiol.* 86, 009677–e1020. doi:10.1128/AEM.00967-20
- Krishna, B. A., Kumar, P. N., and Prema, P. (2020). Green synthesis of copper oxide nanoparticles using *Cinnamomum malabratrum* leaf extract and its antibacterial activity. *Indian J. Chem. Technol.* 27, 525–530.
- Mahboub, H. H., Rashidian, G., Hoseinifar, S. H., Kamel, S., Zare, M., Ghafarifarsani, H., et al. (2022). Protective effects of *Allium hirtifolium* extract against foodborne toxicity of Zinc oxide nanoparticles in Common carp (*Cyprinus carpio*). *Comp. Biochem. Physiol. Part C Toxicol. Pharmacol.* 257, 109345. doi:10.1016/j.cbpc.2022.109345
- Makhluif, S., Dror, R., Nitzan, Y., Abramovich, R. J., and Gedanken, A. (2005). Microwave-assisted synthesis of nanocrystalline MgO and its use as a bactericide. *Adv. Funct. Mater.* 15, 1708–1715. doi:10.1002/adfm.200500029
- Mohsen, J., and Zahra, B. (2008). Protein nanoparticle: A unique system as drug delivery vehicles. *Afr. J. Biotechnol.* 7, 4926.
- Nagaraj, E., Karuppannan, K., Shanmugam, P., and Venugopal, S. (2019). Exploration of biosynthesized copper oxide nanoparticles using *pterolobiumhexapetalum* leaf extract by photocatalytic activity and biological evaluations. *J. Clust. Sci.* 30, 1157–1168. doi:10.1007/s10876-019-01579-8
- Nardella, M. I., Fortino, M., Barbanente, A., Natile, G., Pietropaolo, A., and Arnesano, F. (2022). Multinuclear metal-binding ability of the N-terminal region of human copper transporter Ctr1: Dependence upon pH and metal oxidation state. *Front. Mol. Biosci.* 9, 897621. doi:10.3389/fmolb.2022.897621
- Qamar, H., Rehman, S., Chauhan, D. K., Tiwari, A. K., and Upmanyu, V. (2020). Green synthesis, characterization and antimicrobial activity of copper oxide nanomaterial derived from *momordica charantia*. *Int. J. Nanomed.* 15, 2541–2553. doi:10.2147/IJN.S240232
- Rabiee, N., Bagherzadeh, M., Kiani, M., Ghadiri, A. M., Etesamifar, F., Jaberzadeh, A. H., et al. (2020). Biosynthesis of copper oxide nanoparticles with potential biomedical applications. *Int. J. Nanomed.* 15, 3983–3999. doi:10.2147/IJN.S255398
- Rajput, V. D., Minkina, T., Fedorenko, A., Chernikova, N., Hassan, T., Mandzhieva, S., et al. (2021a). Effects of zinc oxide nanoparticles on physiological and anatomical indices in spring barley tissues. *Nanomaterials* 11, 1722. doi:10.3390/nano11071722
- Rajput, V. D., Singh, A., Minkina, T., Rawat, S., Mandzhieva, S., Sushkova, S., et al. (2021b). Nano-enabled products: challenges and opportunities for sustainable agriculture. *Plants* 10, 2727. doi:10.3390/plants10122727
- Rajput, V. D., Minkina, T., Upadhyay, S. K., Kumari, A., Ranjan, A., Mandzhieva, S., et al. (2022). Nanotechnology in the restoration of polluted soil. *Nanomaterials* 12, 769. doi:10.3390/nano12050769
- Sagadevan, S., and Koteeswari, P. (2015). Analysis of structure, surface morphology, optical and electrical properties of copper nanoparticles. *J. Nanomed. Res.* 2 (5), 133–136. doi:10.15406/jnmr.2015.02.00040
- Sankar, R., Manikandan, P., Malarvizhi, V., Fathima, T., and ShivashangariRavikumar, K. S. V. (2014). Green synthesis of colloidal copper oxide nanoparticles using *Carica papaya* and its application in photocatalytic dye degradation. *Spectrochim. Acta Part A Mol. Biomol. Spectrosc.* 121, 746–750. doi:10.1016/j.saa.2013.12.020
- Shantkriti, S., and Rani, P. (2014). Biological synthesis of Copper nanoparticles using *Pseudomonas fluorescens*. *Int. J. Curr. Microbiol. Appl. Sci.* 3 (9), 374–383.
- Sharma, M., Sharma, A., and Majumder, S. (2020). Synthesis, microbial susceptibility and anti-cancerous properties of copper oxide nanoparticles-review. *Nano Express* 1 (1), 012003. doi:10.1088/2632-959x/ab9241
- Singh, J., Dutta, T., Kim, K. H., Rawat, M., Samddar, P., and Kumar, P. (2018). ‘Green’ synthesis of metals and their oxide nanoparticles: Applications for environmental remediation. *J. Nanobiotechnol.* 16 (1), 84. doi:10.1186/s12951-018-0408-4
- Singh, J., Kumar, V., Kim, K. H., and Rawat, M. (2019). Biogenic synthesis of copper oxide nanoparticles using plant extract and its prodigious potential for photocatalytic degradation of dyes. *Environ. Res.* 177, 108569. doi:10.1016/j.envres.2019.108569
- Sobha, K., Surendranath, K., Meena, V. K., Jwala, T., Swetha, N., and Latha, K. S. M. (2010). Emerging trends in nanobiotechnology. *J. Biotechnol. Mol. Rev.* 5, 01–12.
- Sukhwai, A., Jain, D., Joshi, A., Rawal, P., and Kushwaha, H. S. (2017). Biosynthesized silver nanoparticles using aqueous leaf extract of *Tagetespatula* L. and evaluation of their antifungal activity against phytopathogenic fungi. *IET Nanobiotechnol.* 11, 531–537. doi:10.1049/iet-nbt.2016.0175
- Sukumar, S., Rudrasenan, A., and PadmanabhanNambiar, D. (2020). Green-Synthesized rice-shaped copper oxide nanoparticles using *Caesalpinia bonducella*





seed extract and their applications. *ACS-Omega* 5 (2), 1040–1051. doi:10.1021/acsomega.9b02857

Tavakoli, S., Kharaziha, M., and Ahmadi, S. (2019). Green synthesis and morphology dependent antibacterial activity of copper oxide nanoparticles. *J. Nanostruct.* 9 (1), 163–171. doi:10.22052/JNS.2019.01.018

Tiwari, M., Jain, P., Hariharapura, R., Kashinathan, N., Bhat, B., Nayanabhirama, U., et al. (2016). Biosynthesis of copper nanoparticles using copper-resistant *Bacillus cereus*, a soil isolate. *Process Biochem.* 51, 1348–1356. doi:10.1016/j.procbio.2016.08.008

Tshireletso, P., Ateba, C. N., and Fayemi, O. E. (2021). Spectroscopic and antibacterial properties of CuONPs from orange, lemon and tangerine peel

extracts: Potential for combating bacterial resistance. *Molecules* 26, 586. doi:10.3390/molecules26030586

Upadhyay, S. K., Devi, P., Kumar, V., Pathak, H. K., Kumar, P., Rajput, V. D., et al. (2023). Efficient removal of total arsenic ( $As^{3+}/5+$ ) from contaminated water by novel strategies mediated iron and plant extract activated waste flowers of marigold. *Chemosphere* 313, 137551. doi:10.1016/j.chemosphere.2022.137551

Zhao, H., Maruthupandy, M., Al-mekhlafi, F. A., Chackaravathi, G., Ramachandran, G., and Chelliah, C. K. (2022). Biological synthesis of copper oxide nanoparticles using marine endophytic actinomycetes and evaluation of biofilm producing bacteria and A549 lung cancer cells. *J. King Saud Univ. - Sci.* 34 (3), 101866. doi:10.1016/j.jksus.2022.101866



OPEN

## Climate trends and maize production nexus in Mississippi: empirical evidence from ARDL modelling

Ramandeep Kumar Sharma<sup>1</sup>, Jagmandeep Dhillon<sup>1✉</sup>, Pushp Kumar<sup>2</sup>, Raju Bheemanahalli<sup>1</sup>, Xiaofei Li<sup>3</sup>, Michael S. Cox<sup>1</sup> & Krishna N. Reddy<sup>4</sup>

Climate change poses a significant threat to agriculture. However, climatic trends and their impact on Mississippi (MS) maize (*Zea mays* L.) are unknown. The objectives were to: (i) analyze trends in climatic variables (1970 to 2020) using Mann–Kendall and Sen slope method, (ii) quantify the impact of climate change on maize yield in short and long run using the auto-regressive distributive lag (ARDL) model, and (iii) categorize the critical months for maize-climate link using Pearson's correlation matrix. The climatic variables considered were maximum temperature (Tmax), minimum temperature (Tmin), diurnal temperature range (DTR), precipitation (PT), relative humidity (RH), and carbon emissions (CO<sub>2</sub>). The pre-analysis, post-analysis, and model robustness statistical tests were verified, and all conditions were met. A significant upward trend in Tmax (0.13 °C/decade), Tmin (0.27 °C/decade), and CO<sub>2</sub> (5.1 units/decade), and a downward trend in DTR (−0.15 °C/decade) were noted. The PT and RH insignificantly increased by 4.32 mm and 0.11% per decade, respectively. The ARDL model explained 76.6% of the total variations in maize yield. Notably, the maize yield had a negative correlation with Tmax for June, and July, with PT in August, and with DTR for June, July, and August, whereas a positive correlation was noted with Tmin in June, July, and August. Overall, a unit change in Tmax reduced the maize yield by 7.39% and 26.33%, and a unit change in PT reduced it by 0.65% and 2.69% in the short and long run, respectively. However, a unit change in Tmin, and CO<sub>2</sub> emissions increased maize yield by 20.68% and 0.63% in the long run with no short run effect. Overall, it is imperative to reassess the agronomic management strategies, developing and testing cultivars adaptable to the revealed climatic trend, with ability to withstand severe weather conditions in ensuring sustainable maize production.

Maize is the most important cereal, known as the “queen of cereals<sup>1</sup>.” The United States (US) is the leading producer, followed by China, Brazil, and Argentina<sup>2</sup>. The US contributes 32% to global production, and 60% of total production is exported<sup>2</sup>. Within the US, Mississippi (MS) is the state that contributes 748.3 million USD annually to national maize revenue<sup>3</sup>. Mississippi has 0.64 million acres under maize cultivation<sup>4</sup>. Mississippi has eight of the total twelve soil types, 60% of cropland is irrigated (by center pivot and furrow), and maize is grown on raised beds<sup>5,6</sup>. Mississippi has registered its maize yield progressing at a faster annual growth rate than the US for the past two decades<sup>7</sup>. As a result, MS actual maize yield surpassed the US in 2000; the current yields for MS and the US are 12.51 and 11.87 Mg ha<sup>−1</sup>, respectively<sup>4</sup>. Over the past half-century, MS has experienced a rapid increase (173%) in the harvested acres for maize compared to the US average (47%)<sup>4</sup>. More intriguingly, MS maize still has a considerable yield gap of 2 to 5.6 Mg ha<sup>−1</sup>, or 14 to 31%, at the state level when compared to the highest achievable yield under best management practices<sup>7</sup>. Closing these yield gaps is critical for economic benefits, reducing food prices, and consequently improving food security<sup>8</sup>. Strategies to close existing yield gaps via research necessitate a broader understanding of the causal factors and their extent on variations in crop yield<sup>9</sup>.

The factors that govern crop production and its variability include genetics, environment, and management such as soil properties, and agronomic management for instance fertilization, irrigation, tillage, planting dates,

<sup>1</sup>Department of Plant and Soil Sciences, Mississippi State University, Mississippi, USA. <sup>2</sup>Department of Economics, Manipal University Jaipur, Dharam Kalan, Rajasthan, India. <sup>3</sup>Department of Agricultural Economics, Mississippi State University, Mississippi, USA. <sup>4</sup>Crop Production Systems Research Unit, United States Department of Agriculture (USDA)-Agricultural Research Service (ARS), Stoneville, MS, USA. ✉email: jagman.dhillon@msstate.edu

row-to-row width, planting population, planting time, depth, etc.,<sup>10,11</sup>. However, amongst all, the climate is noted to be the major uncontrollable contributor affecting crop production, with the proven potential to explain up to or even greater than 60% of the global crop yield variations<sup>12</sup>. Numerous studies on wheat (*Triticum aestivum* L.)<sup>13–16</sup>, maize<sup>17–19</sup> and rice (*Oryza sativa* L.)<sup>20,21</sup> has demonstrated a consensus on crop-climate link in cereals. Based on region-specific studies, the crop-climate association was found to be strong, ranging 22–60%, 40–71.3%, and 67–92% in wheat, maize, and rice, respectively. The same has been confirmed by global studies for other crops as well<sup>22–25</sup>. Specifically, in maize, Rizzo et al.<sup>26</sup> attempted to separate climate, management, and genetic factors and deduced that climate change (48%) explained most of the yield variation, followed by management (39%), and genetics (13%). Given the alarming rate of future climate warming, almost 1.5 °C upsurge, precipitation (PT) irregularities (24–40%) combined with increased carbon emissions, the coefficient of yield dependability on climate is expected to rise further by 47% in 2050<sup>27</sup>.

Climatic trends induce biotic and abiotic stresses in plants by controlling microclimates around them, and influence evapotranspiration, gas exchange, resource use efficiency, plant-microbe relations, phenological processes, crop performance, and finally yield<sup>28</sup>. The severity of crop-climate links is determined by the magnitude and trend of change of climatic variables, which vary by region, and such estimates for MS are lacking<sup>29</sup>. Mississippi is in a climatically vulnerable southeastern region of the US, and has a significant agroeconomic impact<sup>30,31</sup>. Also, Mississippi agriculture relies on reduced capital investments and infrastructural inputs, removing several choices for combating climate-related negative consequences<sup>32,33</sup>. Even so, only a few climate-crop studies were conducted so far for MS<sup>34–37</sup>, and even fewer on maize<sup>21,38,39</sup>. Therefore, the current study is aimed at calculating (i) the trend in climatic variables, namely, daily maximum temperature (Tmax), daily minimum temperature (Tmin), diurnal temperature range (DTR), precipitation (PT), carbon emissions (CO<sub>2</sub>), and relative humidity (RH) in MS during 1970–2020, and (ii) impact of change in these variables on MS maize yield. The novelty of this study lies in investigating climatic variables other than just temperatures and PT, monthly investigations of trends in climatic variables, pinpointing crucial months impacting maize and employing econometric method for the first time to explore crop-climate link in MS.

## Methodology

A detailed step-by-step outline of the various methodologies used to accomplish the study's objectives is displayed in Fig. 1. The sections below provide a detailed discussion on the various methodology components, including data, study model specifications, and the estimation procedures involved.

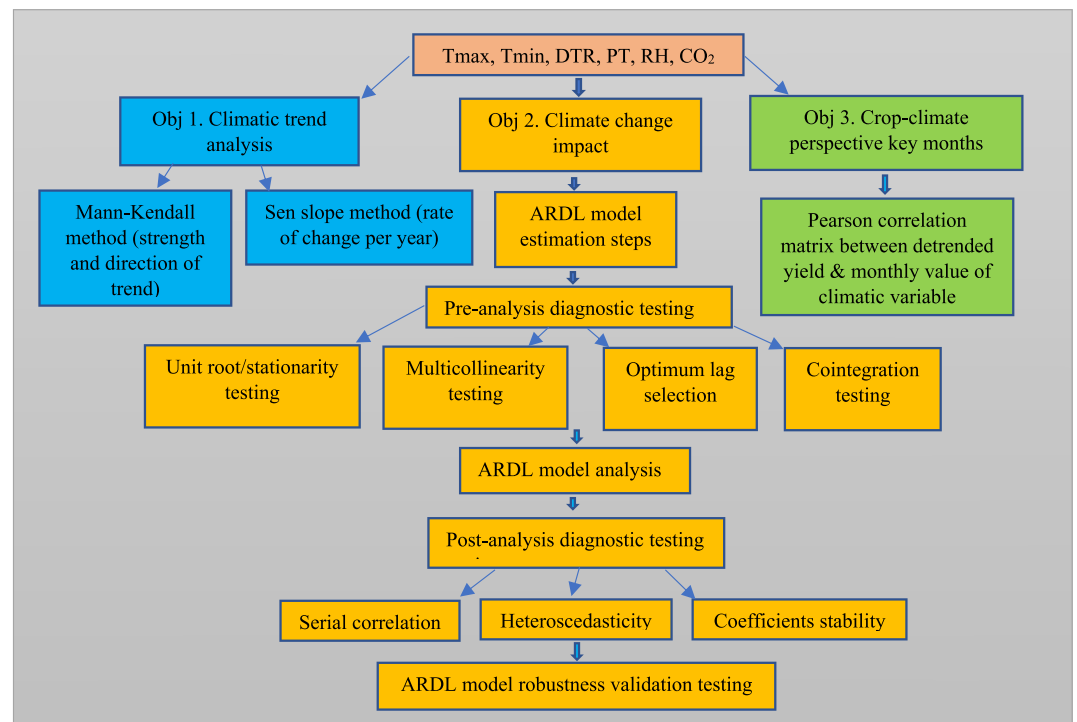


**Figure 1.** A step-by-step flowchart outlining the detailed methodology for the three different objectives. The first objective—estimating the trend for each of the six climatic variables—maximum temperature (Tmax), minimum temperature (Tmin), diurnal range (DTR), precipitation (PT), relative humidity (RH), and carbon dioxide emissions (CO<sub>2</sub>)—is shown in blue boxes on the left, the second objective—quantifying the overall impact of climatic variables on maize yield—are shown in yellow boxes in the middle, and the third objective workflow—identifying the key months for crop-climate linkage—are shown in green boxes on the right.

## Data

The present study utilized the past 50 years of time-series dataset for MS (Fig. 2), from 1970 to 2020 similarly to previous studies<sup>12,40–42</sup>.

As per World Meteorological Organization guidelines, 30 years (at minimum) dataset is recommended for climatic trend computations<sup>43</sup>. The response variable was maize yield, and the explanatory variables were Tmax, Tmin, DTR, PT, RH and CO<sub>2</sub> (Fig. 1). Harvested area (HA) was included as an input control variable as suggested by Jan et al.<sup>44</sup>. Moreover, following Chandio et al.<sup>40</sup>, the Tmax, Tmin, DTR, and RH were averaged, and PT was totaled to maize growing season (MGS) for analyzing the impact of growing season anomalies. Also, the monthly averaged data of each variable was utilized to compute the month-wise climatic impact on maize. The MGS (March–September) was taken as per the USDA harvesting and planting dates handbook. The data on CO<sub>2</sub> was available on a yearly average basis. The data were gathered from the USDA-NASS repository (<https://www.nass.usda.gov/>) for yield, National Oceanic and Atmospheric Administration (NOAA) database (<https://www.noaa.gov/>) for Tmax, Tmin, DTR, and PT, PRISM database (<https://prism.oregonstate.edu/comparisons/>) for RH, and US energy information administration (<https://www.eia.gov/environment/emissions/state/>) for CO<sub>2</sub>. There is a vast literature authenticating the use of time series data and the aforesaid data sources for crop-climate estimations<sup>45–48</sup>.

## Econometric model specification

The two-dimensional effects of climate change on crops include a short-term effect that is directly impacting the yield in the current and subsequent (residual effect) years<sup>49,50</sup>. This immediate effect accumulates to build the foundation for permanent effects, referred to as long-term effects, that ultimately influence the soil-forming processes, soil properties, microbial buildups in the soil, and nutrient-use abilities<sup>51–53</sup>. Therefore, the study evaluated both the short and long-term relationships between the variables using the widely used auto-regressive distributive lag (ARDL) bound-testing method<sup>44,54–58</sup>. The ARDL model is preferred over other statistical methods because it can efficiently run the analysis for both short-term and long-term relationships simultaneously at *ceteris paribus* keeping all other variables unchanged<sup>55</sup>. Moreover, the ARDL model accounts for previous year inputs/factors influencing the current year yield, by incorporating the “lag length” component in its functionality<sup>59</sup>. These factors could be residual effects of previous year fertilization especially if a granular form is applied, late season excessive rainfall, or maybe rollover effects of previous crop rotation<sup>60,61</sup>. By regressing the lag values of the regressors against the regressand, the lag length feature statistically advises the ARDL model on how far back in time it needs to go to capture the residual effect<sup>62,63</sup>. The ARDL model works well regardless of the integration level of the time series data *i.e.*, level (I = 0), at first difference (I = 1), or combination of I (0), and I (1)<sup>56</sup>. The ARDL approach is robust against endogeneity issues, which arises when the dependent variable tends to correlate with the error term in the regression model<sup>64</sup>, reducing residual correlation, and small sample sizes<sup>54</sup>. The ARDL has an intrinsic feature of error correction model (ECM) that estimates the pace (% per year) with which the short-term effects transfer cumulatively to form permanent basis for the long-term effects<sup>54</sup>. The following linear equation was used to evaluate short-term and long-term association of mentioned variables:

$$Y = f(Tmax, Tmin, DTR, Prec, RH, CO_2, HA) \quad (1)$$

The natural log form variables are suggested for time series data to smoothen multicollinearity and instability issues if any<sup>56</sup>.

$$\begin{aligned} \ln Y_t = & \beta_0 + \beta_1 \ln(Tmax)_t + \beta_2 \ln(Tmin)_t + \beta_3 \ln(DTR)_t + \beta_4 \ln(PT)_t \\ & + \beta_5 \ln(RH)_t + \beta_6 \ln(CO_2)_t + \beta_7 \ln(HA)_t + \varepsilon_t \end{aligned} \quad (2)$$

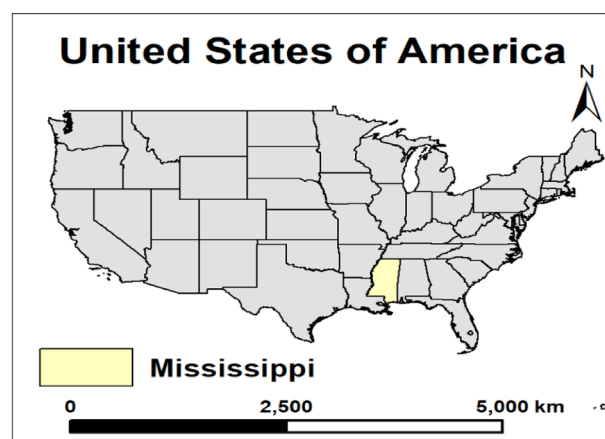


**Figure 2.** The study area (Mississippi state) highlighted on the USA map.

where,  $Y_t$  is maize yield ( $\text{Mg ha}^{-1}$ ) in year  $t$ . Tmax, Tmin, and DTR are in ( $^{\circ}\text{C}$ ), PT in (mm), RH in (%),  $\text{CO}_2$  in metric ton, HA is maize harvested in hectares,  $\beta_0$  is intercept, and  $\beta_1, \beta_2, \beta_3, \beta_4, \beta_5, \beta_6, \beta_7$  are coefficients of slopes in the function, and  $\varepsilon_t$  is error term in time  $t$ .

#### Auto-regressive distributive lag (ARDL) bound test approach

The ARDL model equation adopted in similar previous studies<sup>44,55,57</sup>, is used here as follow:

$$\begin{aligned} \Delta \ln Y_{it} = & \alpha_0 + \sum_{i=1}^n \alpha_1 \Delta \ln(Y)_{t-i} + \sum_{i=1}^n \alpha_2 \Delta \ln(\text{Tmax})_{t-i} \\ & + \sum_{i=1}^n \alpha_3 \Delta \ln(\text{Tmin})_{t-i} + \sum_{i=1}^n \alpha_4 \Delta \ln(\text{DTR})_{t-i} + \sum_{i=1}^n \alpha_5 \Delta \ln(\text{PT})_{t-i} \\ & + \sum_{i=1}^n \alpha_6 \Delta \ln(\text{CO}_2)_{t-i} + \sum_{i=1}^n \alpha_7 \Delta \ln(\text{RH})_{t-i} + \sum_{i=1}^n \alpha_8 \Delta \ln(\text{HA})_{t-i} \\ & + \sum_{i=1}^n \gamma_1 \Delta \ln(Y)_{t-i} + \sum_{i=1}^n \gamma_2 \Delta \ln(\text{Tmax})_{t-i} + \sum_{i=1}^n \gamma_3 \Delta \ln(\text{Tmin})_{t-i} \\ & + \sum_{i=1}^n \gamma_4 \Delta \ln(\text{DTR})_{t-i} + \sum_{i=1}^n \gamma_5 \Delta \ln(\text{PT})_{t-i} + \sum_{i=1}^n \delta_6 \Delta \ln(\text{CO}_2)_{t-i} \\ & + \sum_{i=1}^n \gamma_7 \Delta \ln(\text{RH})_{t-i} + \sum_{i=1}^n \gamma_8 \Delta \ln(\text{HA})_{t-i} + \emptyset(\text{ECT})_{t-i} + \varepsilon_t \end{aligned} \quad (3)$$

where  $Y$  is maize yield,  $t$  is the time in year,  $i$  is the lag order with  $n$  is the highest lag value,  $\alpha_0$  is the intercept,  $\Delta$  denotes the first differencing,  $\varepsilon_t$  is the error term,  $\alpha_1$  to  $\alpha_8$  represents coefficients of long term cointegration for different variables,  $\gamma_1$  to  $\gamma_8$  are short term coefficients for different variables, ECT is the error correction term and  $\emptyset$  is its coefficient which determines the pace (% per year) by which short term climatic impacts cumulatively transfer to form basis for permanent long term effects.

The first differencing, as suggested in previous studies<sup>23,65</sup>, was applied as a technique to detrend the maize yield to account for the other yield impacting unobserved factors such as advancement in agricultural technology, progression of the adjustments in growers according to the management recommendations, and the infrastructural developments. The data on aforesaid factors was not available. Detrending is widely used in literature to exclude (minimize) the impact of such unobserved variables and to capture the sole impact of climate variables on crop yields<sup>23,65</sup>.

#### Climatic trend analysis

The Mann-Kendall test<sup>66,67</sup> and Sen slope method<sup>68</sup> were employed to time series (1970–2020) data for all study variables to establish the trend on both monthly and growing seasonal timescale (Mar-Sep). Both these non-parametric tests are recommended by the World Meteorological Organization for climatic trend estimation<sup>69</sup>. The Kendall tau computes the direction and strength of the trend where positive sign of the coefficient indicates increasing (upward), negative sign signifies decreasing (downward) trend, and the magnitude of 0–0.25 (weak), 0.26–0.50 (fair), 0.51–0.75 (moderate), and values above 0.76 (strong) signifies the strength of the trend<sup>70–72</sup>. However, the Sen slope coefficient indicates the rate of change per year. For more detailed understanding on methodology of both these tests, readers are suggested to read Gocic and Trajkovic<sup>73</sup> or Gujree et al.<sup>74</sup> procedures.

#### Estimation procedures

##### Unit tests

Units root problem arise when the mean, variances, and co-variances are time dependent or non-constant during the study timeframe<sup>75</sup>. Usually, unit root problems (non-stationarity) exist with time series data, if it exists, can cause spurious regression<sup>76</sup>. When a single coefficient fails to accurately reflect the true relationship between the study variables, false regression occurs, and the conclusions drawn may be untrue<sup>76</sup>. Hence, the Augmented Dickey-Fuller (ADF)<sup>77</sup> and the Phillips–Perron tests (PP)<sup>78</sup> unit root tests were performed. The results revealed that all the variables were stationary at level or first differencing, fulfilling the assumption of ARDL bound testing model (Table 1A).

##### Multicollinearity testing

Analyses involving multiple variables may be susceptible to multicollinearity due to the propensity of variables to become correlated with one another<sup>79</sup>. To avoid overfitting in a regression model caused by multicollinearity, either the variables exhibiting it should be eliminated, or it needs to be verified that the data is free of multicollinearity, using tests such as the variance inflation factor (VIF) test and tolerance test<sup>80</sup>. The present study performed both these tests and found that the VIF value (3.45) and tolerance value (0.30) were within the permissible limits (Table 1B); VIF < 10 and tolerance value (TOV) > 0.1<sup>42,79,80</sup>, confirmed that multicollinearity was not an issue with the dataset (Table 1B).

Variables	ADF		PP		
	Level	First difference	Level	First difference	
(A) Unit root test results following Augmented Dickey-Fuller (ADF) and Phillips-Perron (PP) tests of variables including maximum temperature (Tmax), minimum temperature (Tmin), carbon dioxide emission (CO <sub>2</sub> ), harvested area (HA), precipitation (PT), and maize grain yield (Y)					
Tmax	-6.276***		-10.036***		
Tmin	-6.340***		-10.580***		
CO <sub>2</sub>	-2.256	-8.400***	-2.264	-8.357***	
HA	-3.237	-8.323***	-3.170	-10.284***	
PT	-6.317***		-6.287***		
Y	-7.058***		-7.054***		
Variable	Variance inflation factor (VIF)	Tolerance value (TOV)			
(B) Multicollinearity test results based on variance inflation factor (VIF) and tolerance value (TOV) tests of variables including maximum temperature (Tmax), minimum temperature (Tmin), carbon dioxide emission (CO <sub>2</sub> ), harvested area (HA), and precipitation (PT)					
Tmax	4.512	0.221			
Tmin	4.126	0.242			
CO <sub>2</sub>	3.207	0.312			
PT	2.475	0.404			
HA	2.937	0.340			
Mean value	3.451	0.304			
Lag	SMLR	FPE	AIC	SIC	HQ
(C) Model's lag selection criterion using sequential modified statistics test (SMLR), final prediction error (FPE) test, Akaike information criterion (AIC) method, Schwarz information criterion (SIC) method, and Hannan-Quinn information criterion (HQ) method					
0	NA	8.36e-13	-10.783	-10.544	-10.693
1	177.455	4.28e-14	-13.768	-12.099*	-13.142*
2	37.853	7.06e-14	-13.350	-10.249	-12.188
3	26.476*	3.42e-14*	-14.295*	-9.7631	-12.597
4	67.775	7.43e-14	-13.990	-8.0276	-11.756
Test Statistic	Value	Significance (%)	Level I (0)	First difference I (1)	
(D) The ARDL bounds cointegration test results					
F-statistic	7.228	10	2.08	3	
		5	2.39	3.38	
		1	3.06	4.15	

**Table 1.** Pre-analysis diagnostic testing. “\*\*\*” shows the significance level at 1%. \*Indicates lag order selected by the criterion, SMLR: sequential modified likelihood ratio test statistic, FPE: Final prediction error, AIC: Akaike information criterion, SC: Schwarz information criterion, HQ: Hannan-Quinn information criterion, and each test at 5% level of significance.

#### Optimum lag selection

The ARDL model can determine the number of prior years to include in the model for regressing the explanatory variables (including their lag values) against the regressand (current year yield) by using the optimal lag number, to incorporate the previous years' residual effects on current year maize yield<sup>55</sup>. The study used statistical tests such as Sequential modified likelihood ratio (SMLR) test, final prediction error (FPE) test, Akaike information criterion (AIC) method, Schwarz information criterion (SIC) method, and Hannan-Quinn information criterion (HQ) method, as guided by Agbenyo et al.<sup>57</sup>, and Warsame et al.<sup>55</sup>, to select optimum lag length for the model.

The appropriate lag length for the ARDL model was determined to be three (Table 1C), based on the minimum value generated by majority of the tests (SMLR, FPE, and AIC) utilized. The lag length of three signifies that the previous three years data needs to be considered to regress against the regressand for capturing residual effects.

#### Cointegration testing

The Wald F-test was used for the null and alternative hypotheses testing after running a regression to check for the existence of cointegration between regressors and regressand<sup>44</sup>. The two types of threshold values were produced, the upper bound threshold values were termed I (1), and the lower bound threshold values were termed I (0). The null hypothesis is accepted if the Wald F-statistics value is less than the lower bound (at I = 0) threshold value, indicating no relationship present between the regressand and regressors<sup>41</sup>. However, the null hypothesis is rejected if the Wald F-statistics value is higher than the upper bound (at I = 1) threshold value, indicating the presence of a relationship between the regressand and regressors<sup>41</sup>. The Wald F-test value (Table 1D) was estimated as 7.228, which, at the 1% significance level, was higher than the upper critical limit (4.15). The absence

of cointegration was thus ruled out as the null hypothesis, and the presence of cointegration was determined at a 1% level of significance.

#### Post analysis diagnostic tests, and sensitivity/robustness check of ARDL model

After the ARDL model estimation, the study performed Breusch–Godfrey LM test (for serial correlation check), Breusch–Pagan–Godfrey test (for heteroscedasticity check), and cumulative sum (CUSUM) and cumulative sum of squares (CUSUMSQ) of recursive residuals tests (for stability check of the model coefficients), as suggested by the previous studies<sup>58</sup>.

The results confirmed that the functional model was free from serial correlation and heteroskedasticity (mis-specifications) issues (Table 2A). The CUSUM and CUSUMSQ test graphs found that the parameter plot lines were consistent, stable, and stayed within critical bounds at the 5% level of significance (Figs. 3 and 4). Hence, confirming the accuracy and stability of short and long run model coefficients that affected the MS maize yield from 1970 to 2020. The CUSUM test can identify systematic, whereas the CUSUMSQ test identifies rapid and drastic variations from the constancy of the model coefficients<sup>81</sup>.

After confirming the ARDL model's goodness of fit and predictive effectiveness by running post-analysis diagnostic tests, the sensitivity analysis was carried out using the fully modified ordinary least square (FMOLS) model to examine the robustness of the ARDL model functionality in long run. The FMOLS model showed that Tmax and PT had a negative impact on maize yield while Tmin and CO<sub>2</sub> had a positive impact (Table 2B). These results are consistent with the long-run coefficients of the ARDL model, further validating the robustness of the model recommendations.

Test	Statistics	Probability		
(A) Diagnostic test results following Breusch–Pagan–Godfrey test, Breusch–Godfrey LM test, cumulative sum (CUSUM) and cumulative sum of squares (CUSUMSQ) of recursive residuals tests, for the error terms of the regression equation obtained based on the ARDL model output				
BPG test for Heteroskedasticity	0.532	0.919		
BG LM test for Serial Correlation	0.841	0.443		
CUSUM	Stable	Figure 3		
CUSUM Squares	Stable	Figure 4		
Variable	Coefficient	Std. error	t-Statistic	Prob
(B) Results of fully modified ordinary least square (FMOLS) model for confirming the robustness and validation of the study model				
Tmax	– 14.133	4.073	– 3.469***	0.001
Tmin	7.735	2.524	3.064***	0.004
CO <sub>2</sub>	1.374	0.574	2.396**	0.021
HA	0.252	0.115	2.180**	0.035
PT	– 1.253	0.438	– 2.858***	0.007
C	26.614	10.959	2.429**	0.019
R-square	0.828			
Adjusted R-square	0.808			

**Table 2.** Post analysis diagnostic testing. Tmax represents maximum temperature, Tmin: minimum temperature, CO<sub>2</sub>: carbon emissions, HA: harvested acres for maize, and PT: precipitation.

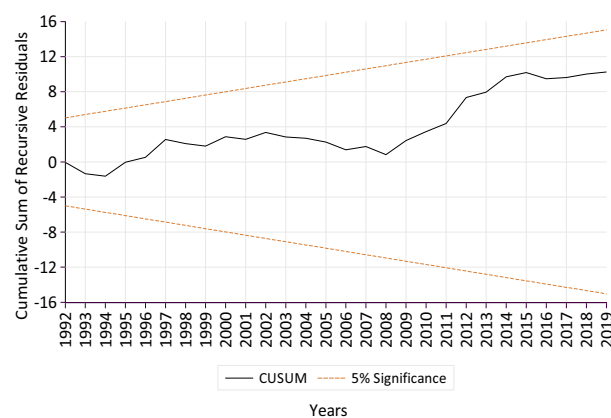


**Figure 3.** Cumulative sum (CUSUM) plot of recursive residuals of ARDL model with 95% confidence interval around the null.

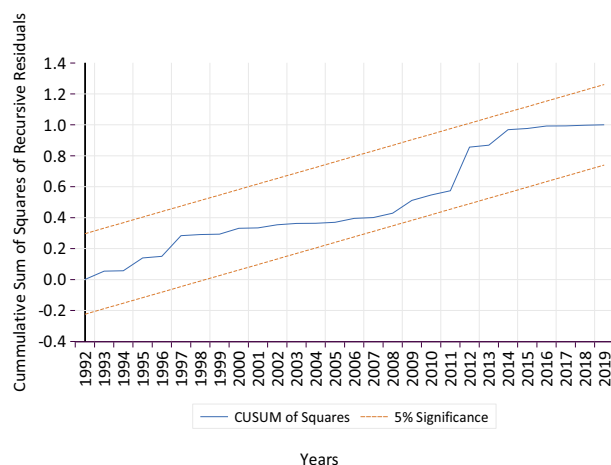


**Figure 4.** Cumulative sum (CUSUM) of squares Plot for recursive residuals of ARDL model with 95% confidence interval around the null.

### Pearson’s coefficient of correlation matrix

Pearson’s coefficient of correlation between detrended (first differenced) yield and monthly averaged value of each climatic variable, as suggested by Eck et al.<sup>82</sup>, was calculated. Based on the strength of correlation, the months that had the greatest impact on maize yield were pinpointed.

### Results and discussions

The final regression fit equation used by the ARDL was a reduced model, which excluded DTR and RH since they were found to be non-significant and reducing the overall predictive efficiency of the model. Hence, the pre and post diagnostic tests (Tables 1, 2)—all of which were based on the ARDL model’s assumptions—were only carried out for the variables that were part of the ARDL model. However, all variables were included for climatic trend analysis, and for calculating the Pearson’s correlation between detrended (first differenced) yield and monthly averaged values of climatic variables (Tables 3 and 4B).

### Climatic trend analysis

Tmax increased by 0.13 °C per decade in MGS, while Tmin increased by 0.27 °C per decade, which is 107.67% faster than Tmax (Table 3). Other studies have found similar unsymmetric Tmin-Tmax warming rates<sup>83–86</sup>.

Series\test	Tmax		Tmin		DTR		PT		RH		CO <sub>2</sub>	
	Kendall tau	Sen slope	Kendall tau	Sen slope	Kendall tau	Sen slope	Kendall tau	Sen slope	Kendall tau	Sen slope	Kendall tau	Sen slope
March	0.139	0.032	0.146	0.030	0.012	0.001	-0.095	-0.193	0.047	0.021	-	-
April	0.014	0.003	0.101	0.015	-0.078	-0.008	0.090	0.194	0.157	0.060	-	-
May	0.103	0.012	0.178	0.022	-0.092	-0.009	-0.087	-0.183	0.003	0.000	-	-
June	0.051*	0.007*	0.373***	0.035***	-0.261**	-0.028**	0.095	0.163	0.125	0.036	-	-
July	-0.006	-0.001	0.262**	0.024**	-0.401***	-0.031***	0.119	0.147	0.068	0.022	-	-
August	0.066*	0.009*	0.299**	0.027**	-0.201*	-0.019*	0.158	0.269	-0.009	-0.004	-	-
September	0.143	0.021	0.183	0.027	0.006	0.001	-0.063	-0.112	-0.110	-0.060	-	-
MGS	0.176*	0.013*	0.422***	0.027***	-0.252**	-0.015**	0.057	0.432	0.027	0.011	0.669***	0.514***
Mean	28.56 °C		16.02 °C		12.54 °C		48.49 mm		66.73%		53.58 million metric tons (Mmt)	

**Table 3.** The summarized results of the Mann–Kendall test and the Sen slope method for trend estimation of variables including maximum temperature (Tmax), minimum temperature (Tmin), diurnal temperature range (DTR), precipitation (PT), relative humidity (RH), and carbon dioxide emission (CO<sub>2</sub>) in Mississippi from 1970 to 2020. Kendall tau negative (-) value signifies downward (decreasing) trend, and positive (+) value indicates upward (increasing) trend with its value ranging between -1 and 1, and its absolute value signifies the strength of the trend. As the absolute value of Kendall tau approach 1, the strength of the trend becomes strong. The Sen slope value represents the rate of change (of variable) per year. Kendall tau is a pure number (unitless) as it is a correlation coefficient and Sen slope units are °C/year (for Tmax, Tmin, and DTR), mm/year (for PT), percentage/year (for RH), and Mmt/year (for CO<sub>2</sub>). The negative (-) value of Sen slope means the rate of decrease per year while the positive (+) value represents the rate of increase per year. Significance: “\*”  $p < 0.05$ , “\*\*”  $p < 0.01$ , and “\*\*\*”  $p < 0.001$ .



Variable	Coefficient	Std. Error	t-Statistic	Prob	
(A) Calculated ARDL model estimates for short and long run effects of Tmax, Tmin, CO <sub>2</sub> , HA, and PT on maize yield (dependent variable)					
ARDL model long run effects					
Tmax	-26.330	9.169	-2.872***	0.008	
Tmin	20.684	6.731	3.073***	0.005	
CO <sub>2</sub>	0.629	0.976	0.644**	0.032	
HA	0.155	0.154	1.007	0.323	
PT	-2.696	0.983	-2.742**	0.011	
ARDL model short run effects					
Tmax	-7.392	2.074	-3.563***	0.001	
Tmin	2.361	1.340	1.760	0.091	
CO <sub>2</sub>	-0.061	0.623	-0.098	0.922	
HA	0.018	0.093	0.198	0.844	
PT	-0.645	0.249	-2.587**	0.016	
C	44.329	25.660	1.728**	0.096	
ECM	-0.302	0.038	-7.892***	0.000	
R square	0.834				
Adjusted R square	0.766				
<b>Climatic variables</b>					
<b>Growing season months</b>	<b>Tmax</b>	<b>Tmin</b>	<b>DTR</b>	<b>PT</b>	<b>RH</b>
(B) Pearson's correlation matrix between the first differenced (detrended) yield and climatic variables (Tmax, Tmin, DTR, PT, RH) based on each month of MGS					
March	0.248	0.228	0.013	-0.251	0.103
April	0.062	0.129	-0.107	0.024	0.248
May	0.173	0.240	-0.123	-0.143	-0.024
June	-0.001**	0.485***	-0.420**	0.267	0.226
July	-0.159***	0.314*	-0.472***	0.132	0.190
August	-0.000	0.354**	-0.319*	-0.323*	0.022
September	0.213	0.231	-0.019	-0.098	-0.126

**Table 4.** Impact of climate change on maize yield. “\*”  $p < 0.05$ , “\*\*”  $p < 0.01$ , and “\*\*\*”  $p < 0.001$ . Tmax represents maximum temperature, Tmin: minimum temperature, DTR: diurnal temperature range, CO<sub>2</sub>: carbon emissions, HA: harvested acres for maize, PT: precipitation, and ECM: error correction model. Significance codes: “\*”  $p < 0.05$ , “\*\*”  $p < 0.01$ , and “\*\*\*”  $p < 0.001$ .

There was an upward trend for Tmax for MGS, specifically for June and August, but it was weak, as magnitude of correlation strength was less than 0.25 (Fig. 5A; Table 3). July was the only month that experienced a Tmax decreasing trend (Fig. 5A), yet non-significant (Table 3).

In contrast, MGS shows an upward trend for Tmin, increasing by 0.27 °C per decade in the last five decades (Fig. 5B; Table 3). Tmin warming rates ranged between 0.24 and 0.35 °C per decade in June, July, and August of MGS (Table 3). June, Tmin had the greatest rise, adding 0.35 °C per decade to global warming (Table 3). The equivalent rising trends were seen by Eck et al.<sup>82</sup> and Sharma et al.<sup>87</sup> in MGSs in the southeastern part of the US.

In recent years, the DTR (Tmax-Tmin) has been recognized as another climatic variable that is essential for diagnosis, particularly under rising unsymmetrical warming scenarios<sup>88,89</sup>. There was a downward trend for DTR in June, July, and MGS, and a weak trend for August (Fig. 5C). In MGS, the DTR decreased by 0.15 °C per decade, but in June, July, and August, it decreased by 0.19–0.31 °C per decade (Table 3). These rates are comparable with the computations of Sun et al.<sup>90</sup> for the other maize-growing regions.

Precipitation and RH, neither for MGS nor for any other month were found to indicate a significant trend line (Figs. 5D, 6A), although numerically, a negative trend was noted in March, May, and September for PT and August and September for RH (Table 3).

A moderately strong and significant upward trend and an annual increase rate of 0.51 units was noted for CO<sub>2</sub> (Fig. 6B; Table 3). The same is corroborated by Rahman<sup>91</sup> and Wu et al.<sup>92</sup> previously in the context of direction and strength, and by Ainsworth et al.<sup>93</sup> in the context of rate of increase.

### The climatic impact on maize

The Tmax was found to have a significant negative effect on maize yield in both the short and long run (Table 4A). More specifically, every 1 °C rise in Tmax reduced the maize yield by 7.39% and 26.33% in the short and long run, respectively (Table 4A).

On further downscaling the analysis to monthly basis to capture the effect of within season variability, it was noted that the monthly averaged Tmax of June and July had a significantly negative correlation with maize yield (Table 4B). This indicates that Tmax in June and July (reproductive-early grain filling stages) contributed the

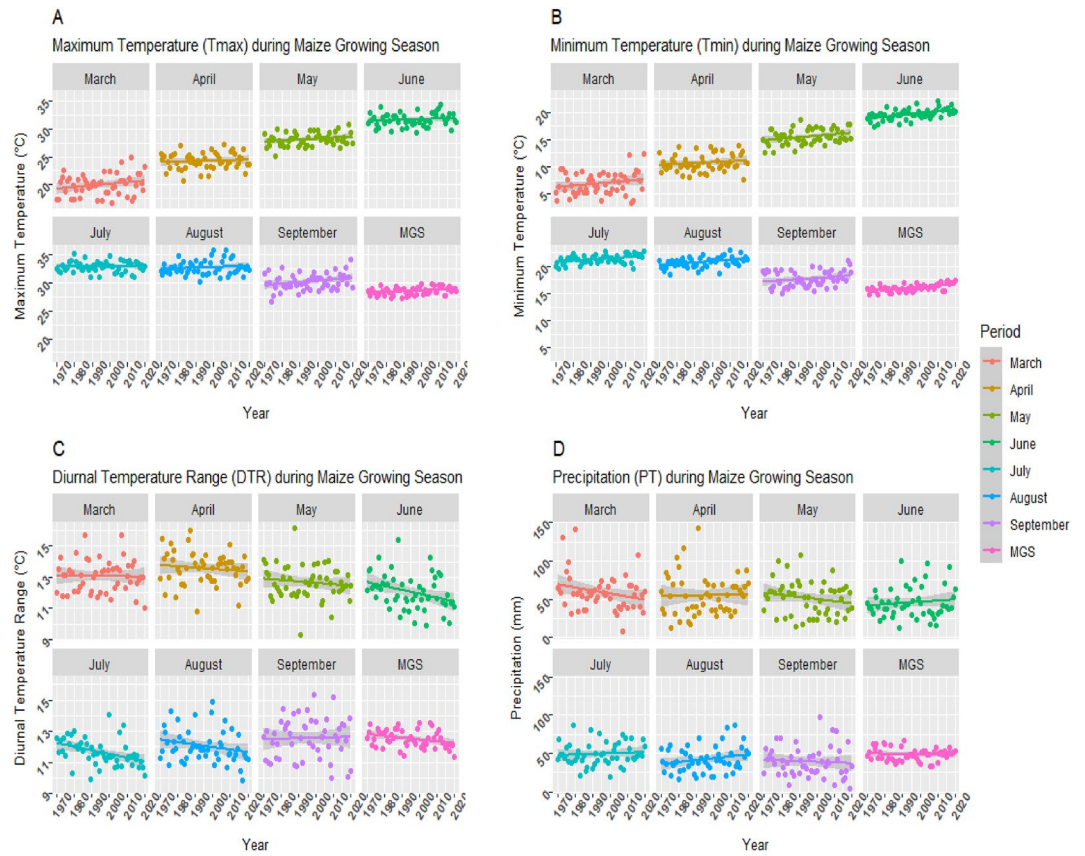


**Figure 5.** Trend lines for Tmax (A), Tmin (B), DTR (C), and precipitation (D) for maize growing season (MGS) and its individual months from 1970 to 2020 in Mississippi. Each figure is faceted by months from March to September and average of all months all together in MGS.

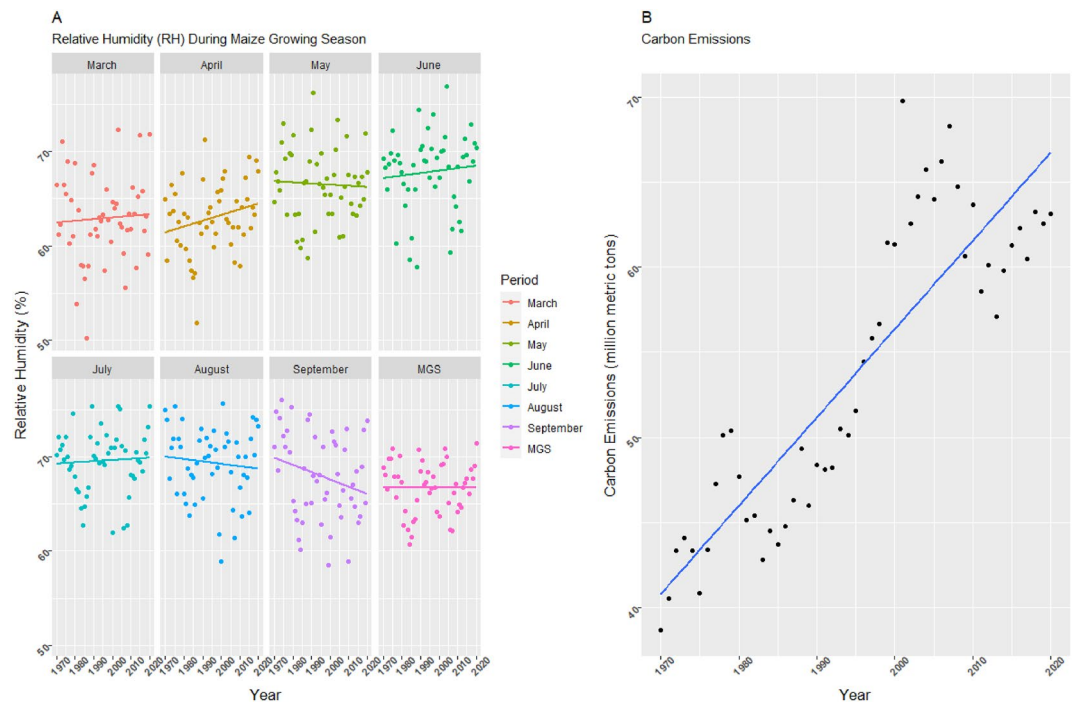


**Figure 6.** (A) Trend lines for relative humidity for maize growing season (MGS) and its individual months from 1970 to 2020 in Mississippi. (B) Trend line for CO<sub>2</sub> emissions for years from 1970 to 2020 in Mississippi. Figure A is faceted by months from March to September and average of all months all together in MGS.

most to yield loss in MS. This is because in reproductive stage, stress-induced plant dysfunction has irreparable harm on kernel development and yield which is not the case with the vegetative phase<sup>94,95</sup>. These findings are consistent with those of Kucharik and Serbin<sup>17</sup> in the context of highly correlated months with respect to maize growing season and to those of Lobell and Field<sup>23</sup>, and Wu et al.<sup>92</sup> in the context of Tmax's adverse effects. Hu and Buyanovsky<sup>96</sup> reported that maize needs both a warming trend with temperatures higher than average in April and May to provide better conditions for germination and emergence and a cooling trend with temperatures lower than average in June–August to promote reproductive success and, consequently, yield. This statement is largely agreed with by Lobell and Asner<sup>97</sup> as well. However, MS had not seen any significant warming trend in April and May; instead, it showed an unfavorable significant warming trend in June and August (Table 3). Contrary to favorable conditions, MS was observed to have temperatures that were below average (28.56 °C) in April (24.24 °C) and May (28.13 °C) and above average in June (31.66 °C) and August (32.78 °C) (Table 3). The Mid-MGS (*i.e.*, the beginning reproductive stage) coincides with June and July (hotter climate), which affects tasseling and grain filling, thereby yield, and is sensitive to additional warming<sup>98,99</sup>. Furthermore, the average Tmax (28.56 °C) noted in MS for MGS (Table 3) has already surpassed the optimal temperature (26.40 °C) for maize<sup>100</sup>, and is rapidly approaching 29 °C, which is damaging to maize<sup>101</sup>. The main reason is that after surpassing 29 °C<sup>101,102</sup> or 30 °C<sup>103</sup>, processes such as anthesis-silking, assimilates production, translocation of resources during reproductive and grain filling are hampered. Temperature beyond this range has been linked to impaired pollen structure, decreased sugar (energy) levels upon anthesis, and retarded pollen shedding, all of which negatively affect pollen germination ability and fertilization<sup>104</sup>. More recent studies found that short duration of Tmax episodes during anthesis can cause significant reduction in pollen germination (30%), kernel number (72%), kernel weight (10%), and stomatal conductivity (52%) in maize<sup>105,106</sup>. Further at the biochemical level, the activity of the enzymes involved in converting atmospheric CO<sub>2</sub> to glucose or other key photosynthesis-related molecules were found to be disrupted by elevated temperatures<sup>107</sup>. In worst case scenario at higher temperatures, a yield loss could reach 34–80%<sup>87,108</sup>.

A 1 °C rise in Tmin increased maize productivity by 20.68% over the long run, indicating a significant and positive effect on maize yield in MS (Table 4A). Several other maize-growing regions have shown that yields respond to Tmin<sup>87,109–111</sup>. Tmin warming was also shown to be advantageous to maize yield in the short run, while the impact was not significant (Table 4A). Although there has not yet been an agreement regarding the physiological effects of Tmin on plants as there is an inclination of the crop-climate research towards the Tmax or Tavg and overlooking the Tmin<sup>112,113</sup>. The current study's findings on the positive association of Tmin and maize yield were supported by evidence from the literature, which included studies using statistical modeling<sup>87,114–121</sup> as well as simulation-based studies<sup>122,123</sup>. This is attributable to the fact that the increased Tmin speeds up night-time respiration, resulting in carbohydrates losses<sup>124</sup>. However, this carbon starvation enhances the following day photosynthetic rate to more than make up for the losses brought on by the accelerated night-time respiration, increasing overall plant productivity<sup>125,126</sup>. Consequently, the amassed dry matter from various plant tissues starts remobilizing toward grain, increasing maize kernel weight, and hence, the yield<sup>127</sup>. Also, the increased Tmin is believed to impart conducive conditions for germination, emergence, seedling growth, grain filling (during night-time), and milk-maturity stage in maize<sup>110</sup>. More importantly, according to Badu-Apraku et al.<sup>127</sup>, Cairns et al.<sup>128</sup>, and Sanchez et al.<sup>100</sup>, all the beneficial mechanisms of Tmin mentioned above only prevail when the Tavg is below 25 °C or 26.40 °C. The Tavg for the current study was found to be 22.29 °C (Table 3). Furthermore, a similar case of Tavg of less than 25 °C was observed in all studies that supported the current findings, specifically at 21.2 °C and 24.4 °C in Liu et al.<sup>116</sup> and Shammil and Meng<sup>36</sup>. Contrarily, the studies that found negative effects of Tmin on maize yield were all found to have been carried out at Tavg of more than 25 °C<sup>129</sup>. For example, Wang et al.<sup>130</sup> tested at Tavg (27–31 °C), Liu et al.<sup>131</sup> tested at Tavg (25–35 °C), Suwa et al.<sup>132</sup> at Tavg (31 °C), and Wilhelm et al.<sup>133</sup> at 29.5 °C and observed negative Tmin-yield impact in maize. Furthermore, it was noted that June, July, and August demonstrated a significant and positive correlation between Tmin and detrended yield (Table 4B). This suggests that warmer nights in June, July, and August are beneficial for maize yields in MS, but there is no evidence that this beneficial effect offsets the detrimental effect of Tmax during the same months. Chen et al.<sup>110</sup> also noted 1 °C Tmin warming during May/September improved maize yield by 303/284 kg ha<sup>-1</sup>. Reilly<sup>134</sup>, Izaurralde et al.<sup>135</sup>, and Reilly et al.<sup>136</sup> also realized the positive effects of warming on maize yield. Also, according to Schlenker and Roberts<sup>137</sup>, Lobell et al.<sup>138</sup>, and Lobell et al.<sup>139</sup>, yield reductions are expected when temperature surpasses 30 °C, which was not the case with this study (Table 3). So far, the curve of Tmin has never reached the point at which it can cause the Tavg to pass above the optimal range and negatively affect maize yield.

According to the model's long-run estimation, the rising trend in CO<sub>2</sub> emissions had a positive and significant impact on maize yield (Table 4A). Ahsan et al.<sup>140</sup> and Chandio et al.<sup>40</sup> also realized similar yield improvements due to CO<sub>2</sub> emissions. However, it was discovered that the impact of CO<sub>2</sub> emissions on maize yield in the short run was not significant (Table 4A), and this is consistent with Warsame et al.<sup>55</sup> and Anapalli et al.<sup>38</sup> studies, focused on MS. Specifically, every unit increase in CO<sub>2</sub> emissions resulted in a long-term improvement in maize yield of 0.62% (Table 4A). Similar reports of 0.23% and 0.70% yield increases were noted by Asfew and Bedemo<sup>56</sup> and Mahrous<sup>141</sup> where they quantified the positive effects of increased CO<sub>2</sub> emissions. However, Islam et al.<sup>142</sup> estimated that under current climate change scenarios, these CO<sub>2</sub> emissions-driven yield increments might reach 3.5 to 12.8% at the rate of 1.80% every decade<sup>143</sup>. The upsides of elevated CO<sub>2</sub> on maize yield are due to its effects on plant physiology, growth, and biochemistry, through diminished stomatal conductivity and enhanced photosynthetic rates<sup>144–147</sup>. The decreased stomatal conductance reduces water loss thereby increasing water use efficiency, especially in drought-stress conditions<sup>148,149</sup>. The rise in atmospheric CO<sub>2</sub> levels increases the intercellular CO<sub>2</sub> concentration (Ci) and thus, photosynthetic rate (A)<sup>150</sup>. However, maize has a lower carbon saturation point than C3 plants like soybean<sup>151</sup> due to the high affinity (to CO<sub>2</sub>) of the key enzyme, phosphoenolpyruvate carboxylase<sup>152,153</sup>. These physiological and biochemical responses of maize to CO<sub>2</sub> indicated that further increases in CO<sub>2</sub> levels may not increase assimilation production<sup>150,151</sup>. Increased CO<sub>2</sub> level have been shown

to benefit other crops<sup>154–157</sup>. However, the response of C4 plants (maize) to elevated CO<sub>2</sub> levels is complex, as it is influenced by various factors such as air temperature, water availability, light intensity, vapor pressures, and nitrogen availability<sup>158,159</sup>. Nevertheless, predicted rise in CO<sub>2</sub> levels by the years 2050 and 2100 may diminish the beneficial effect of CO<sub>2</sub> in row crops, like maize<sup>150,151</sup>. Further research is therefore required to determine the influence of elevated CO<sub>2</sub> in C4 plants at different growth stages<sup>150,152,160,161</sup>.

Even though PT is a crucial crop growth factor, the current findings revealed that, at a 1% level of significance, PT patterns were determined to pose a negative and significant effect on maize yields in both the short- and long-term (Table 4A). More specifically, every 1 mm change in PT had reduced maize yield in the short- and long-term, by 0.64% and 2.70%, respectively (Table 4A). These results are consistent with the observations of Rosenzweig et al.<sup>162</sup>, Chen et al.<sup>163</sup>, and Xiang and Solaymani<sup>58</sup> who also noted the negative effect of the ongoing PT trends on maize yield. A crop yield decline due to prevailing PT trends was also documented in the study by Shammil and Meng<sup>36</sup> in MS. These results are attributable to the excessive PT (1504.44 mm annually) in MS<sup>164</sup>. Excessive PT, in addition to directly or physically harming the crop, results in prolonged wet conditions that lead to soil saturation and are averse to crop development, particularly in conditions of inadequate drainage<sup>165</sup>. This yield-reducing effect of excess moisture is attributable to (i) root growth hindrance impairing plants ability of nutrients and water uptake<sup>166,167</sup>, (ii) increased nitrate leaching, leading to nutrient depletion<sup>168</sup>, (iii) anoxic conditions in soil, leading to the risk of toxic substances development, diseases, and insect infestation<sup>169</sup>, and (iv) delayed planting or harvesting, owing to the difficulty of driving the machinery in wet fields<sup>149,170,171</sup>. On account of the aforementioned factors, the US as a whole suffers a 3% yield loss annually<sup>162,172</sup>, and significant yield decline has been seen over the past two decades in various parts of the US *i.e.*, Iowa<sup>173,174</sup>. When the analysis was further scaled down to a monthly level, it was discovered that the most significant month correlated with the MS maize yield was August, and the association was negative (Table 4B). This indicates that the August PT had the most significant negative effect on MS maize, and Eck et al.<sup>82</sup> also deduced similar results documenting increased PT to be detrimental in the latter part of the MGS. This is because the uptake of nitrogen, phosphorus, and potassium in maize plants continues up until the R3–R4 stage in August, when the plant can still transpire to the extent of 0.25–0.30 inches of water, according to Lauer<sup>175</sup>, who claimed that by this time, the two (ear and kernel number) of three key yield parameters are determined, but the kernel size/weight is still yet to be determined. Furthermore, low PT is required during the ripening period (August) of maize<sup>96</sup>, nonetheless, the current study found that the MGS month with the highest PT growth rate (2.69 mm/decade) was August (Table 3). However, Rosenzweig et al.<sup>162</sup> had a different perspective on the negative association of August–maize yield, according to them it probably has less to do with plant itself and more primarily linked with the harvesting challenges arising from overly moist conditions, for growers. Delayed harvesting degrades the quality of maize, rendering it unsalvageable, in some instances, due to rotting in the field<sup>82</sup>. Overall, such scenarios of delayed harvesting could lead to a yield loss to the extent of 10%<sup>149</sup>.

Pearson's correlation matrix revealed that the RH of any month of MGS had no correlation but DTR of June, July, and August months had negative and strong correlation with the maize yield (Table 4B). These results are consistent with those of Muhammad et al.<sup>176</sup> who found a weak correlation of RH and HA with yields, as well as with that of Lobell<sup>89</sup> who examined the impact of DTR on maize yield.

The coefficient of ECM was determined to be  $-0.302$  (Table 4A), which signifies that every year, 30.20% of the immediate climatic impact cumulatively transfers to form the permanent basis for the long-term effects. A 30.20% is equivalent to the results of Warsame et al.<sup>55</sup> and Jan et al.<sup>44</sup>. The ARDL model estimated the adjusted R<sup>2</sup> value of 0.766, indicating that 76.60% of the total variations in maize yield due to the studied variables are explained by the study model.

### Study limitations

Each research has its unique set of limitations, which forms the base for further advancement in the research field. The factors such as maize evapotranspiration, sunshine durations/hours, irrigation intensity, and vapor pressure deficit that could interact to determine the climatic effects for better insights on crop–climate link, were not included in the present study due to data unavailability. Hence, future research is suggested incorporating the aforesaid variables along with the variables considered in the present study for more practicable and accurate estimations.

### Concluding remarks

This study demonstrated a markedly rising trend in Tmax, Tmin, and CO<sub>2</sub>, with Tmin majorly contributing to the overall warming trend in the MGS of MS. The Tmin progressed at a faster rate (0.14°C decade<sup>-1</sup>) than the Tmax, causing a considerably lowering trend in the DTR. The month-wise analysis determined the most correlated month for Tmax (June and July), Tmin and DTR (June, July, and August), and PT (August) in significantly impacting maize yield in MS, indicating the varied sensitivity of maize yield to within season variability for different climatic parameters. The crop–climate link assessment revealed a significantly negative effect of Tmax and PT on maize yield in both short and long run, whereas Tmin and CO<sub>2</sub> emissions posed a significantly positive effect on maize yield in long run and no effect in short run. Overall, the study model explained the 76.60% variations in maize yield due to climate change in MS. As shown by the ECM coefficient of the study model, the short-term immediate climatic effects on maize progressively transfer to permanent long-term effects by 30.2% every year, making the crop–climate link more prominent in the long run than in the short run. As the water and nutrient usage efficiencies are climate driven and based on the current findings, it is suggested to reassess the agronomic optimum management strategies in the face of MS crop–climate link. Also, the research efforts need to be intensified to test crop varieties that might be more resistant to elevated Tmax, perform better under delayed planting circumstances, and continue to interact favorably with elevated CO<sub>2</sub> and Tmin scenarios under

the local climatic conditions of the MS. Moreover, it is recommended to test current findings at the field or in controlled settings using the locally prevalent climatic indices with a focus on agronomic optimum management strategies as they react to the climatic variations.

### Data availability

The data used in this study is accessed from National Agricultural Statistics Service's repository (USDA-NASS), US Climate Divisional Database (NOAA), PRISM database, and US energy information administration. The online links for these data sources are mentioned in Section "Data" (data) of methodology chapter. However, for more information on data, rs2564@msstate.edu (Ramandeep Kumar Sharma) can be contacted. No separate field study on plants was carried out because all the data used in the study was accessible online.

Received: 12 June 2023; Accepted: 25 September 2023

Published online: 03 October 2023

### References

- García-Lara, S., & Serna-Saldivar, S. O. Corn history and culture. *Corn*, 1–18 (2019).
- FAO. FAOSTAT—Crops and Livestock Products. *Food and Agriculture Organization (FAO)*. 2020. Available online: <https://www.fao.org/faostat/en/#data/QCL> (accessed on 14 March 2023).
- MAC 2021. <https://www.mdac.ms.gov/agency-info/mississippi-agriculture-snapshot/>
- USDA-national Agricultural Statistics Service (2021) [https://www.nass.usda.gov/Publications/Todays\\_Reports/reports/fcdat\\_e10.pdf](https://www.nass.usda.gov/Publications/Todays_Reports/reports/fcdat_e10.pdf)
- Cox, M. S. The Lancaster soil test method as an alternative to the Mehlich 3 soil test method1. *Soil Sci.* **166**(7), 484–489 (2001).
- Kebede, H., Fisher, D. K., Sui, R. & Reddy, K. N. Irrigation methods and scheduling in the Delta region of Mississippi: Current status and strategies to improve irrigation efficiency. *Am. J. Plant Sci.* **5**(20), 2917 (2014).
- Dhillon, J., Li, X., Bheemanahalli, R. & Reed, V. Mississippi state and county level yield gap in corn production. *Agric. Environ. Lett.* **7**(2), e20092 (2022).
- Snyder, K. A., Miththapala, S., Sommer, R. & Braslow, J. The yield gap: Closing the gap by widening the approach. *Expe. Agric.* **53**(3), 445–459 (2017).
- Licker, R. *et al.* Mind the gap: how do climate and agricultural management explain the 'yield gap' of croplands around the world?. *Global Ecol. Biogeogr.* **19**(6), 769–782 (2010).
- Kukal, M. S. & Irmak, S. Climate-driven crop yield and yield variability and climate change impacts on the US Great Plains agricultural production. *Sci. Rep.* **8**(1), 1–18 (2018).
- Oglesby, C. *et al.* Discrepancy between the crop yield goal rate and the optimum nitrogen rates for maize production in Mississippi. *Agron. J.* **115**(1), 340–350 (2023).
- Ray, D. K., Gerber, J. S., MacDonald, G. K. & West, P. C. Climate variation explains a third of global crop yield variability. *Nat. Commun.* **6**(1), 1–9 (2015).
- Li, S. *et al.* The observed relationships between wheat and climate in China. *Agric. For. Meteorol.* **150**(11), 1412–1419 (2010).
- de Cárcer, P. S., Sinaj, S., Santonja, M., Fossati, D. & Jeangros, B. Long-term effects of crop succession, soil tillage and climate on wheat yield and soil properties. *Soil Tillage Res.* **190**, 209–219 (2019).
- Faghih, H., Behmanesh, J., Rezaei, H. & Khalili, K. Climate and rainfed wheat yield. *Theor. Appl. Climatol.* **144**(1), 13–24 (2021).
- Schierhorn, F., Hofmann, M., Gagalyuk, T., Ostapchuk, I. & Müller, D. Machine learning reveals complex effects of climatic means and weather extremes on wheat yields during different plant developmental stages. *Clim. Change* **169**(3), 1–19 (2021).
- Kucharik, C. J. & Serbin, S. P. Impacts of recent climate change on Wisconsin maize and soybean yield trends. *Environ. Res. Lett.* **3**(3), 034003 (2008).
- Durdu, Ö. F. Evaluation of climate change effects on future maize (*Zea mays* L.) yield in western Turkey. *Int. J. Climatol.* **33**(2), 444–456 (2013).
- Sun, L., Li, H., Ward, M. N. & Moncunill, D. F. Climate variability and maize yields in semiarid Ceará, Brazil. *J. Appl. Meteorol. Climatol.* **46**(2), 226–240 (2007).
- Oguntunde, P. G., Lischeid, G. & Dietrich, O. Relationship between rice yield and climate variables in southwest Nigeria using multiple linear regression and support vector machine analysis. *Int. J. Biometeorol.* **62**(3), 459–469 (2018).
- Islam, A. R. M. *et al.* Variability of climate-induced rice yields in northwest Bangladesh using multiple statistical modeling. *Theor. Appl. Climatol.* **147**(3), 1263–1276 (2022).
- Frieler, K. *et al.* Understanding the weather signal in national crop-yield variability. *Earth's Future* **5**(6), 605–616 (2017).
- Lobell, D. B. & Field, C. B. Global scale climate–crop yield relationships and the impacts of recent warming. *Environ. Res. Lett.* **2**(1), 014002 (2007).
- Jägermeyr, J. & Frieler, K. Spatial variations in crop growing seasons pivotal to reproduce global fluctuations in maize and wheat yields. *Sci. Adv.* **4**(11), eaat4517 (2018).
- Iizumi, T. & Ramankutty, N. Changes in yield variability of major crops for 1981–2010 explained by climate change. *Environ. Res. Lett.* **11**(3), 034003 (2016).
- Rizzo, G. *et al.* Climate and agronomy, not genetics, underpin recent maize yield gains in favorable environments. *Proc. Natl. Acad. Sci.* **119**(4), e2113629119 (2022).
- Urban, D., Roberts, M. J., Schlenker, W. & Lobell, D. B. Projected temperature changes indicate significant increase in interannual variability of US maize yields. *Clim. Change* **112**(2), 525–533 (2012).
- Shen, X., Liu, B., Henderson, M., Wang, L., Jiang, M., & Lu, X. Vegetation greening, extended growing seasons, and temperature feedbacks in warming temperate grasslands of China. *J. Clim.*, 1–51 (2022).
- Apata, T. G. Effects of global climate change on Nigerian agriculture: An empirical analysis. *CBN J. Appl. Stat.* **2**(1), 31–50 (2011).
- Asseng, S. (2013). Agriculture and climate change in the southeast USA. In *Climate of the Southeast United States* (pp. 128–164). Island Press, Washington, DC.
- Sharma, R. K., Dhillon, J., Kumar, S., Vatta, K. & Reddy, K. N. Crop-climate link in the southeastern USA: A case study on Oats and Sorghum. *J. Agric. Food Res.* **12**, 100626 (2023).
- Ciscel, D. H. Creating economic growth in rural Mississippi Delta Counties. Federal Reserve Bank of St. Louis (1999).
- Sobel, R. S., & Hall, J. C. The sources of economic growth. *Promot. Prosper. Mississippi*, 15 (2018).
- Reddy, K. R. *et al.* Simulating the impacts of climate change on cotton production in the Mississippi Delta. *Clim. Res.* **22**(3), 271–281 (2002).
- Anapalli, S. S. *et al.* Vulnerabilities and adapting irrigated and rainfed cotton to climate change in the Lower Mississippi Delta Region. *Climate* **4**(4), 55 (2016).
- Shammi, S. A. & Meng, Q. Modeling the Impact of Climate Changes on Crop Yield: Irrigated vs Non-Irrigated Zones in Mississippi. *Remote Sens* **13**(12), 2249 (2021).

37. Sun, W. *et al.* Evaluation of models for simulating soybean growth and climate sensitivity in the US Mississippi Delta. *Eur. J. Agron.* **140**, 126610 (2022).
38. Anapalli, S. S., Pinnamaneni, S. R., Fisher, D. K. & Reddy, K. N. Vulnerabilities of irrigated and rainfed maize to climate change in a humid climate in the lower Mississippi delta. *Clim. Change* **164**(1), 1–18 (2021).
39. Parajuli, P. B., Jayakody, P., Sassenrath, G. F. & Ouyang, Y. Assessing the impacts of climate change and tillage practices on stream flow, crop and sediment yields from the Mississippi River Basin. *Agric. Water Manag.* **168**, 112–124 (2016).
40. Chandio, A. A., Jiang, Y., Fatima, T., Ahmad, F., Ahmad, M., & Li, J. (2022). Assessing the impacts of climate change on cereal production in Bangladesh: evidence from ARDL modeling approach. *International Journal of Climate Change Strategies and Management*.
41. Ranghuwal, S. *et al.* Quantifying the energy use efficiency and greenhouse emissions in Punjab agriculture India. *Energy Nexus* **11**, 100238 (2023).
42. Singh, P., Arora, K., Kumar, S., Gohain, N. & Sharma, R. K. Indian millets trade potential-cum-performance: Economic perspective. *Indian J. Agric. Sci.* **93**(2), 200–204 (2023).
43. Burroughs, W., & Burroughs, W. S. (Eds.). *Climate: Into the 21st century*. Cambridge University Press (2003).
44. Jan, I., Ashfaq, M. & Chandio, A. A. Impacts of climate change on yield of cereal crops in northern climatic region of Pakistan. *Environ. Sci. Pollut. Res.* **28**(42), 60235–60245 (2021).
45. Daly, C. *et al.* Physiographically sensitive mapping of climatological temperature and precipitation across the conterminous United States. *Int. J. Climatol.: A J. Royal Meteorol. Soc.* **28**(15), 2031–2064 (2008).
46. Yun, S. D. & Gramig, B. M. Agro-climatic data by county: A spatially and temporally consistent US dataset for agricultural yields, weather and soils. *Data* **4**(2), 66 (2019).
47. Marshall, M. *et al.* Field-level crop yield estimation with PRISMA and Sentinel-2. *ISPRS J. Photogramm. Remote Sens* **187**, 191–210 (2022).
48. Duan, L., Petroski, R., Wood, L. & Caldeira, K. Stylized least-cost analysis of flexible nuclear power in deeply decarbonized electricity systems considering wind and solar resources worldwide. *Nat. Energy* **7**(3), 260–269 (2022).
49. Adams, R. M., Hurd, B. H., Lenhart, S. & Leary, N. Effects of global climate change on agriculture: An interpretative review. *Clim. Res.* **11**(1), 19–30 (1998).
50. Ahmed, M. *et al.* Impact of climate change on dryland agricultural systems: A review of current status, potentials, and further work need. *Int. J. Plant Prod.* **16**(3), 341–363 (2022).
51. West, J. S., Townsend, J. A., Stevens, M. & Fitt, B. D. Comparative biology of different plant pathogens to estimate effects of climate change on crop diseases in Europe. *Eur. J. Plant Pathol.* **133**, 315–331 (2012).
52. Brevik, E. C. The potential impact of climate change on soil properties and processes and corresponding influence on food security. *Agriculture* **3**(3), 398–417 (2013).
53. Schneider, L., Rebetz, M., & Rasmann, S. The effect of climate change on invasive crop pests across biomes. *Current Opinion Insect Sci.*, 100895 (2022).
54. Pesaran, M. H., Shin, Y. & Smith, R. J. Bounds testing approaches to the analysis of level relationships. *J. Appl. Econom.* **16**(3), 289–326 (2001).
55. Warsame, A. A., Sheik-Ali, I. A., Ali, A. O. & Sarkodie, S. A. Climate change and crop production nexus in Somalia: Empirical evidence from ARDL technique. *Environ. Sci. Pollut. Res.* **28**(16), 19838–19850 (2021).
56. Asfew, M., & Bedemo, A. (2022). Impact of climate change on cereal crops production in Ethiopia. *Adv. Agric.*, 2022.
57. Agbenyo, W., Jiang, Y., Ding, Z., Titriku, J. K. & Ntim-Amo, G. Impact of climate change on cocoa production in Africa: An approach of cross-sectional ARDL. *Int. J. Environ. Res.* **16**(5), 1–12 (2022).
58. Xiang, X. & Soleymani, S. Change in cereal production caused by climate change in Malaysia. *Ecolog. Inform.* **70**, 101741 (2022).
59. Nkoro, E. & Uko, A. K. Autoregressive Distributed Lag (ARDL) cointegration technique: application and interpretation. *J. Stat. Econom. Methods* **5**(4), 63–91 (2016).
60. Babbhulkar, P. S., Wandile, R. M., Badole, W. P. & Balpande, S. S. Residual effect of long-term application of FYM and fertilizers on soil properties (Vertisols) and yield of soybean. *J. Indian Soc. Soil Sci.* **48**(1), 89–92 (2000).
61. Sieling, K., Brase, T. & Svib, V. Residual effects of different N fertilizer treatments on growth, N uptake and yield of oilseed rape, wheat and barley. *European J. Agron.* **25**(1), 40–48 (2006).
62. Chandio, A. A. *et al.* Assessment of formal credit and climate change impact on agricultural production in Pakistan: A time series ARDL modeling approach. *Sustainability* **12**(13), 5241 (2020).
63. Waiswa, D. Climate change and production of cereal crops in East Africa: Role of temperature, Precipitation, *Ecol. Carbon Footprint* (2023).
64. Nakamura, A. & Nakamura, M. Model specification and endogeneity. *J. Econom.* **83**(1–2), 213–237 (1998).
65. Wang, F., Zhan, C. & Zou, L. Risk of crop yield reduction in China under 15°C and 2°C global warming from CMIP6 models. *Foods* **12**(2), 413 (2023).
66. Mann, H. B. Nonparametric tests against trend. *Econom. J. Econom. Soc.*, 245–259 (1945).
67. Kendall, M. G. Rank correlation methods; Griffin: London, UK, 1975. Google Scholar (1975).
68. Sen, P. K. Estimates of the regression coefficient based on Kendall's tau. *J. Am. Stat. Assoc.* **63**(324), 1379–1389 (1968).
69. WMO. World Meteorological Organization 2018 Guide to climatological practices, second edition (2018).
70. Portney, L. G. Correlation. *Foundations of Clinical Research* (2000).
71. Raina, K. D., Callaway, C., Rittenberger, J. C. & Holm, M. B. Neurological and functional status following cardiac arrest: Method and tool utility. *Resuscitation* **79**(2), 249–256 (2008).
72. Prematunga, R. K. Correlational analysis. *Aust. Crit. Care* **25**(3), 195–199 (2012).
73. Gocic, M. & Trajkovic, S. Analysis of changes in meteorological variables using Mann-Kendall and Sen's slope estimator statistical tests in Serbia. *Global Planet. Change* **100**, 172–182 (2013).
74. Gujree, I., Ahmad, I., Zhang, F. & Arshad, A. Innovative trend analysis of high-altitude climatology of Kashmir Valley North-West Himalayas. *Atmosphere* **13**(5), 764 (2022).
75. DeJong, D. N., Nankervis, J. C., Savin, N. E. & Whiteman, C. H. The power problems of unit root test in time series with autoregressive errors. *J. Econom.* **53**(1–3), 323–343 (1992).
76. Patterson, K. Unit root tests in time series volume 1: Key concepts and problems. Springer (2011).
77. Dickey, D. A. & Fuller, W. A. Distribution of the estimators for autoregressive time series with a unit root. *J. Am. Stat. Assoc.* **74**(366a), 427–431 (1979).
78. Phillips, P. C. & Perron, P. Testing for a unit root in time series regression. *Biometrika* **75**(2), 335–346 (1988).
79. Gujarati, D., & Porter, D. (2003). Multicollinearity: What happens if the regressors are correlated. *Basic Econometr.*, 363.
80. Daoud, J. I. (2017). Multicollinearity and regression analysis. In *Journal of Physics: Conference Series* (Vol. 949, No. 1, p. 012009). IOP Publishing.
81. Brown, R. L., Durbin, J. & Evans, J. M. Techniques for testing the constancy of regression relationships over time. *J. Royal Stat. Soc. Ser. B (Methodol.)* **37**(2), 149–163 (1975).
82. Eck, M. A., Murray, A. R., Ward, A. R. & Konrad, C. E. Influence of growing season temperature and precipitation anomalies on crop yield in the southeastern United States. *Agric. For. Meteorol.* **291**, 108053 (2020).

83. Rosenzweig, C. & Tubiello, F. N. Effects of changes in minimum and maximum temperature on wheat yields in the central USA simulation study. *Agric. For. Meteorol.* **80**(2–4), 215–230 (1996).
84. Peng, S. *et al.* Asymmetric effects of daytime and night-time warming on Northern Hemisphere vegetation. *Nature* **501**(7465), 88–92 (2013).
85. Screen, J. A. Arctic amplification decreases temperature variance in northern mid- to high-latitudes. *Nat. Clim. Change* **4**(7), 577–582 (2014).
86. Sharma, R. K., Kumar, S., Vatta, K., Dhillon, J. & Reddy, K. N. Impact of recent climate change on cotton and soybean yields in the southeastern United States. *J. Agric. Food Res.* **9**, 100348 (2022).
87. Sharma, R. K. *et al.* Impact of recent climate change on maize, rice, and wheat in southeastern USA. *Sci. Rep.* **12**(1), 1–14 (2022).
88. Braganza, K., Karoly, D. J., & Arblaster, J. M. (2004). Diurnal temperature range as an index of global climate change during the twentieth century. *Geophys. Res. Lett.*, 31(13).
89. Lobell, D. B. Changes in diurnal temperature range and national cereal yields. *Agric. For. Meteorol.* **145**(3–4), 229–238 (2007).
90. Sun, X. *et al.* Global diurnal temperature range (DTR) changes since 1901. *Clim. Dynam.* **52**(5), 3343–3356 (2019).
91. Rahman, M. M. Environmental degradation: The role of electricity consumption, economic growth and globalisation. *J. Environ. Manag.* **253**, 109742 (2020).
92. Wu, J. Z. *et al.* Impact of climate change on maize yield in China from 1979 to 2016. *J. Integr. Agric.* **20**(1), 289–299 (2021).
93. Ainsworth, E. A., Lemonnier, P. & Wedow, J. M. The influence of rising tropospheric carbon dioxide and ozone on plant productivity. *Plant Biol.* **22**, 5–11 (2020).
94. Raju, B. R. *et al.* Root traits and cellular level tolerance hold the key in maintaining higher spikelet fertility of rice under water limited conditions. *Funct. Plant Biol.* **41**(9), 930–939 (2014).
95. Chen, J. J., Zhen, S. & Sun, Y. Estimating leaf chlorophyll content of buffaloberry using normalized difference vegetation index sensors. *HortTechnology* **31**(3), 297–303 (2021).
96. Hu, Q. & Buyanovsky, G. Climate effects on maize yield in Missouri. *J. Appl. Meteorol. Climatol.* **42**(11), 1626–1635 (2003).
97. Lobell, D. B. & Asner, G. P. Climate and management contributions to recent trends in US agricultural yields. *Science* **299**(5609), 1032–1032 (2003).
98. Wilson, J. H., Clowes, M. S. J. & Allison, J. C. S. Growth and yield of maize at different altitudes in Rhodesia. *Ann. Appl. Biol.* **73**(1), 77–84 (1973).
99. Mourtzinis, S., Ortiz, B. V. & Damianidis, D. Climate change and ENSO effects on Southeastern US climate patterns and maize yield. *Sci. Rep.* **6**(1), 1–7 (2016).
100. Sanchez, B., Rasmussen, A. & Porter, J. R. Temperatures and the growth and development of maize and rice: a review. *Global Change Biol.* **20**(2), 408–417 (2014).
101. Hoffman, A. L., Kemanian, A. R. & Forest, C. E. The response of maize, sorghum, and soybean yield to growing-phase climate revealed with machine learning. *Environ. Res. Lett.* **15**(9), 094013 (2020).
102. Butler, E. E. & Huybers, P. Adaptation of US maize to temperature variations. *Nat. Clim. Change* **3**(1), 68–72 (2013).
103. Commuri, P. D. & Jones, R. J. High temperatures during endosperm cell division in maize: A genotypic comparison under in vitro and field conditions. *Crop Sci.* **41**(4), 1122–1130 (2001).
104. Begcy, K. *et al.* Male sterility in maize after transient heat stress during the tetrad stage of pollen development. *Plant Physiol.* **181**(2), 683–700 (2019).
105. Bheemanahalli, R., Vennam, R. R., Ramamoorthy, P. & Reddy, K. R. Effects of post-flowering heat and drought stresses on physiology, yield, and quality in maize (*Zea mays* L.). *Plant Stress* **6**, 100106 (2022).
106. Bheemanahalli, R. *et al.* Effects of drought and heat stresses during reproductive stage on pollen germination, yield, and leaf reflectance properties in maize (*Zea mays* L.). *Plant Direct* **6**(8), e434 (2022).
107. Alsajri, F. A. *et al.* Morpho-physiological, yield, and transgenerational seed germination responses of soybean to temperature. *Front. Plant Sci.* **13**, 839270 (2022).
108. Hatfield, J. L. & Prueger, J. H. Temperature extremes: Effect on plant growth and development. *Weather Clim. Extremes* **10**, 4–10 (2015).
109. Stooksbury, D. E. & Michaels, P. J. Climate change and large-area Maize Yield in the Southeastern United States. *Agron. J.* **86**(3), 564–569 (1994).
110. Chen, C. *et al.* Will higher minimum temperatures increase maize production in Northeast China? An analysis of historical data over 1965–2008. *Agric. Forest Meteorol.* **151**(12), 1580–1588 (2011).
111. Zhang, Q., Zhang, J., Guo, E., Yan, D. & Sun, Z. The impacts of long-term and year-to-year temperature change on corn yield in China. *Theor. Appl. Climatol.* **119**(1), 77–82 (2015).
112. Shu, T. (2021). Soybean Phenotypic Variation Under High Night Temperature Stress.
113. Song, J. *et al.* The positive effects of increased light intensity on growth and photosynthetic performance of tomato seedlings in relation to night temperature level. *Agronomy* **12**(2), 343 (2022).
114. Magrin, G. O., Travasso, M. I. & Rodríguez, G. R. Changes in climate and crop production during the 20th century in Argentina. *Clim. Change* **72**(1), 229–249 (2005).
115. Tao, F., Yokozawa, M., Liu, J. & Zhang, Z. Climate–crop yield relationships at provincial scales in China and the impacts of recent climate trends. *Clim. Res.* **38**(1), 83–94 (2008).
116. Liu, Z., Yang, X., Hubbard, K. G. & Lin, X. Maize potential yields and yield gaps in the changing climate of northeast China. *Global Change Biol.* **18**(11), 3441–3454 (2012).
117. Ruane, A. C. *et al.* Multi-factor impact analysis of agricultural production in Bangladesh with climate change. *Global Environ. Change* **23**(1), 338–350 (2013).
118. Petersen, L. K. Impact of climate change on twenty-first century crop yields in the US. *Climate* **7**(3), 40 (2019).
119. Ding, R. & Shi, W. Contributions of climate change to cereal yields in Tibet, 1993–2017. *J. Geograph. Sci.* **32**(1), 101–116 (2022).
120. Zahoor, Z., Shahzad, K., & Mustafa, A. U. (2022). Do climate changes influence the agriculture productivity in Pakistan? Empirical Evidence from ARDL Technique. *Forman J. Econ. Stud.*, 18(1).
121. Bekuma Abdisa, T., Mamo Diga, G. & Regassa Tolessa, A. Impact of climate variability on rain-fed maize and sorghum yield among smallholder farmers. *Cogent Food Agric.* **8**(1), 2057656 (2022).
122. Cabas, J., Weersink, A. & Olale, E. Crop yield response to economic, site and climatic variables. *Clim. Change* **101**(3), 599–616 (2010).
123. Gobin, A. Modelling climate impacts on crop yields in Belgium. *Clim. Res.* **44**(1), 55–68 (2010).
124. Guo, H. *et al.* Annual ecosystem respiration of maize was primarily driven by crop growth and soil water conditions. *Agric. Ecosyst. Environ.* **272**, 254–265 (2019).
125. Paul, M. J. & Foyer, C. H. Sink regulation of photosynthesis. *J. Exp. Bot.* **52**(360), 1383–1400 (2001).
126. Wan, S., Xia, J., Liu, W. & Niu, S. Photosynthetic overcompensation under nocturnal warming enhances grassland carbon sequestration. *Ecology* **90**(10), 2700–2710 (2009).
127. Badu-Apraku, A., Hunter, R. B. & Tollenaar, M. Effect of temperature during grain filling on whole plant and grain yield in maize (*Zea mays* L.). *Can. J. Plant Sci.* **63**(2), 357–363 (1983).
128. Cairns, J. E. *et al.* Adapting maize production to climate change in sub-Saharan Africa. *Food Secur.* **5**(3), 345–360 (2013).

129. Kettler, B. A. *et al.* High night temperature during maize post-flowering increases night respiration and reduces photosynthesis, growth and kernel number. *J. Agron. Crop Sci.* **208**(3), 335–347 (2022).
130. Wang, Y. *et al.* Reduction in seed set upon exposure to high night temperature during flowering in maize. *Physiologia Plantarum* **169**(1), 73–82 (2020).
131. Liu, M. *et al.* Dissecting heat tolerance and yield stability in maize from greenhouse and field experiments. *J. Agron. Crop Sci.* **208**(3), 348–361 (2022).
132. Suwa, R. *et al.* High temperature effects on photosynthate partitioning and sugar metabolism during ear expansion in maize (*Zea mays* L.) genotypes. *Plant Physiol. Biochem.* **48**(2–3), 124–130 (2010).
133. Wilhelm, E. P., Mullen, R. E., Keeling, P. L. & Singletary, G. W. Heat stress during grain filling in maize: Effects on kernel growth and metabolism. *Crop Sci.* **39**(6), 1733–1741 (1999).
134. Reilly, J. M. (Ed.). *Agriculture: The potential consequences of climate variability and change for the United States.* Cambridge University Press (2002).
135. Izaurrealde, R. C., Rosenberg, N. J., Brown, R. A. & Thomson, A. M. Integrated assessment of Hadley Center (HadCM2) climate-change impacts on agricultural productivity and irrigation water supply in the conterminous United States: Part II. Regional agricultural production in 2030 and 2095. *Agric. For. Meteorol.* **117**(1–2), 97–122 (2003).
136. Reilly, J. *et al.* US agriculture and climate change: New results. *Clim. Change* **57**(1), 43–67 (2003).
137. Schlenker, W. & Roberts, M. J. Nonlinear temperature effects indicate severe damages to US crop yields under climate change. *Proc. Natl. Acad. Sci.* **106**(37), 15594–15598 (2009).
138. Lobell, D. B., Bänziger, M., Magorokosho, C. & Vivek, B. Nonlinear heat effects on African maize as evidenced by historical yield trials. *Nat. Clim. Change* **1**(1), 42–45 (2011).
139. Lobell, D. B. *et al.* The critical role of extreme heat for maize production in the United States. *Nat. Clim. Change* **3**(5), 497–501 (2013).
140. Ahsan, F., Chandio, A. A. & Fang, W. Climate change impacts on cereal crops production in Pakistan: Evidence from cointegration analysis. *Int. J. Clim. Change Strateg. Manag.* **12**(2), 257–269 (2020).
141. Mahrous, W. Dynamic impacts of climate change on cereal yield in Egypt: An ARDL model. *J. Econ. Financ. Res.* **5**(1), 886–908 (2018).
142. Islam, A. *et al.* Modeling the impacts of climate change on irrigated maize production in the central great plains. *Agric. Water Manag.* **110**, 94–108 (2012).
143. Lobell, D. B. & Gourdj, S. M. The influence of climate change on global crop productivity. *Plant Physiol.* **160**(4), 1686–1697 (2012).
144. Kimball, B. A. *et al.* Productivity and water use of wheat under free-air CO<sub>2</sub> enrichment. *Global Change Biol.* **1**, 429–442 (1995).
145. Tubiello, F. N. & Ewert, F. Simulating the effects of elevated CO<sub>2</sub> on crops: Approaches and applications for climate change. *Eur. J. Agron.* **18**, 57–74 (2002).
146. Ziska, L. H. Rising atmospheric carbon dioxide and plant biology: the overlooked paradigm. *DNA Cell Biol.* **27**(4), 165–172 (2008).
147. DaMatta, F. M., Grandis, A., Arenque, B. C. & Buckeridge, M. S. Impacts of climate changes on crop physiology and food quality. *Food Res. Int.* **43**(7), 1814–1823 (2010).
148. Hatfield, J. L. & Dold, C. Water-use efficiency: Advances and challenges in a changing climate. *Front. Plant Sci.* **10**, 103 (2019).
149. Urban, D. W., Sheffield, J. & Lobell, D. B. The impacts of future climate and carbon dioxide changes on the average and variability of US maize yields under two emission scenarios. *Environ. Res. Lett.* **10**(4), 045003 (2015).
150. Leakey, A. D. *et al.* Elevated CO<sub>2</sub> effects on plant carbon, nitrogen, and water relations: Six important lessons from FACE. *J. Exp. Bot.* **60**(10), 2859–2876 (2009).
151. Von Caemmerer, S. & Furbank, R. T. The C<sub>4</sub> pathway: An efficient CO<sub>2</sub> pump. *Photosynth. Res.* **77**, 191–207 (2003).
152. Bowes, G. Photosynthetic responses to changing atmospheric carbon dioxide concentration. *Photosynth. Environ.*, 387–407 (1996).
153. Wedin, D. A. C<sub>4</sub> grasses: Resource use, ecology, and global change. *Warm-season (C<sub>4</sub>) Grasses*, 45, 15–50 (2004).
154. Kimball, B. A. Carbon dioxide and agricultural yield: An assemblage and analysis of 430 prior observations 1. *Agron. J.* **75**(5), 779–788 (1983).
155. Ejemeyovwi, J., Obindah, G. & Doyah, T. Carbon dioxide emissions and crop production: Finding a sustainable balance. *Int. J. Energy Econ. Policy* **8**(4), 303 (2018).
156. Ahmed, M., & Ahmad, S. Carbon dioxide enrichment and crop productivity. *Agronomic Crops: Volume 2: Management Practices*, 31–46 (2019).
157. Rehman, A., Ma, H. & Ozturk, I. Decoupling the climatic and carbon dioxide emission influence to maize crop production in Pakistan. *Air Qual., Atmos. Health* **13**, 695–707 (2020).
158. Seneweera, S. P., Ghannoum, O. & Conroy, J. High vapour pressure deficit and low soil water availability enhance shoot growth responses of a C<sub>4</sub> grass (*Panicum coloratum* cv. Bambatsi) to CO<sub>2</sub> enrichment. *Funct. Plant Biol.* **25**(3), 287–292 (1998).
159. Ghannoum, O. & Conroy, J. P. Nitrogen deficiency precludes a growth response to CO<sub>2</sub> enrichment in C<sub>3</sub> and C<sub>4</sub> Panicum grasses. *Funct. Plant Biol.* **25**(5), 627–636 (1998).
160. Ghannoum, O., Caemmerer, S. V., Ziska, L. H. & Conroy, J. P. The growth response of C<sub>4</sub> plants to rising atmospheric CO<sub>2</sub> partial pressure: A reassessment. *Plant, Cell Environ.* **23**(9), 931–942 (2000).
161. Ziska, L. H., & Bunce, J. A. Plant responses to rising atmospheric carbon dioxide. *Plant Growth Clim. Change*, 17–47 (2006).
162. Rosenzweig, C., Tubiello, F. N., Goldberg, R., Mills, E. & Bloomfield, J. Increased crop damage in the US from excess precipitation under climate change. *Global Environ. Change* **12**(3), 197–202 (2002).
163. Chen, C., Baethgen, W. E. & Robertson, A. Contributions of individual variation in temperature, solar radiation and precipitation to crop yield in the North China Plain, 1961–2003. *Clim. Change* **116**(3), 767–788 (2013).
164. MPR. (<http://coolweather.net/staterainfall/mississippi.htm>) (2022).
165. Li, Y., Guan, K., Schnitkey, G. D., DeLucia, E. & Peng, B. Excessive rainfall leads to maize yield loss of a comparable magnitude to extreme drought in the United States. *Global Change Biol.* **25**(7), 2325–2337 (2019).
166. Wenkert, W., Fausey, N. R. & Watters, H. D. Flooding responses in *Zea mays* L. *Plant Soil* **62**(3), 351–366 (1981).
167. Parent, C., Capelli, N., Berger, A., Crèvecoeur, M. & Dat, J. F. An overview of plant responses to soil waterlogging. *Plant Stress* **2**(1), 20–27 (2008).
168. Jabloun, M., Schelde, K., Tao, F. & Olesen, J. E. Effect of temperature and precipitation on nitrate leaching from organic cereal cropping systems in Denmark. *Eur. J. Agron.* **62**, 55–64 (2015).
169. Evans, R. O. & Fausey, N. R. Effects of inadequate drainage on crop growth and yield. In *Agricultural drainage* Vol. Monograph 9 (eds Skaggs, R. W. & van Schilfhaar, J.) 13–54 (The American Society of Agronomy and Academic Press, 1999).
170. Ashraf, M. Interactive effects of nitrate and long-term waterlogging on growth, water relations, and gaseous exchange properties of maize (*Zea mays* L.). *Plant Sci.* **144**(1), 35–43 (1999).
171. Kozdrój, J. & van Elsas, J. D. Response of the bacterial community to root exudates in soil polluted with heavy metals assessed by molecular and cultural approaches. *Soil Biol. Biochem.* **32**(10), 1405–1417 (2000).
172. FEMA. Federal Emergency Management Agency. <https://www.fema.gov/emergency-managers/risk-management/risk-capability-assessment> (2021).



173. Herbold, J. New approaches to agricultural insurance in developing economies. In: D. Köhn (ed.), *Finance for food: Towards new agricultural and rural finance*, pp. 199–217. [https://doi.org/10.1007/978-3-642-54034-9\\_9](https://doi.org/10.1007/978-3-642-54034-9_9) (2014).
174. RHIS. Rain and Hail Insurance Service, Inc. historic database, <http://www.rainhail.com> 2023.
175. Lauer, J. Integrated pest and crop management. News and resources for Wisconsin agriculture from the university of Wisconsin-Madison <https://ipcm.wisc.edu/blog/2016/08/what-is-happening-in-the-corn-plant-during-the-month-of-august/> (2016).
176. Muhammad, S., Alkali, M., Abdullahi, U. & Haruna, S. Exploring the effect of climate variability on the outputs of some selected crop in Gombe, Nigeria: A bound test approach. *Int. J. Intellect. Discourse* 5(2), 141–157 (2022).

## Acknowledgements

Authors acknowledge Dr. Yen-Heng Lin at Mississippi State University's Northern Gulf Institute for helping with the relative humidity data collection.

## Author contributions

R.S.: Conceptualization; Data curation; Visualization; Writing – original draft, J.D.: Conceptualization; Funding acquisition; Supervision; Project administration; Writing – review & editing, P.K.: Formal analysis; Methodology; Writing – review & editing, RB: Writing – review & editing, X.L.: Writing – review & editing, M.C.: Writing – review & editing, and K.R.: Writing – review & editing.

## Funding

This publication is a contribution of the Mississippi Agricultural and Forestry Experiment Station.

## Competing interests

The authors declare no competing interests.

## Additional information

**Correspondence** and requests for materials should be addressed to J.D.

**Reprints and permissions information** is available at [www.nature.com/reprints](http://www.nature.com/reprints).

**Publisher's note** Springer Nature remains neutral with regard to jurisdictional claims in published maps and institutional affiliations.



**Open Access** This article is licensed under a Creative Commons Attribution 4.0 International License, which permits use, sharing, adaptation, distribution and reproduction in any medium or format, as long as you give appropriate credit to the original author(s) and the source, provide a link to the Creative Commons licence, and indicate if changes were made. The images or other third party material in this article are included in the article's Creative Commons licence, unless indicated otherwise in a credit line to the material. If material is not included in the article's Creative Commons licence and your intended use is not permitted by statutory regulation or exceeds the permitted use, you will need to obtain permission directly from the copyright holder. To view a copy of this licence, visit <http://creativecommons.org/licenses/by/4.0/>.

© The Author(s) 2023



Article

# Molecular Structure-Based Prediction of Absorption Maxima of Dyes Using ANN Model

Neeraj Tomar <sup>1</sup>, Geeta Rani <sup>2,\*</sup>, Vijaypal Singh Dhaka <sup>2</sup>, Praveen K. Surolia <sup>1,\*</sup>, Kalpit Gupta <sup>2</sup>, Eugenio Vocaturo <sup>3,4</sup> and Ester Zumpano <sup>3,4</sup>

- <sup>1</sup> Department of Chemistry, Manipal University Jaipur, Jaipur 303007, India; neerajtomar225@gmail.com  
<sup>2</sup> Department of Computer and Communication Engineering, Manipal University Jaipur, Jaipur 303007, India; vijaypalsingh.dhaka@jaipur.manipal.edu (V.S.D.); kalpitgupta369@gmail.com (K.G.)  
<sup>3</sup> Department of Computer Engineering, Modeling, Electronics and Systems, University of Calabria, 87036 Rende, Italy; e.vocaturo@dimes.unical.it or eugenio.vocaturo@cnr.it (E.V.); e.zumpano@dimes.unical.it (E.Z.)  
<sup>4</sup> CNR NANOTEC, Via Pietro Bucci 33C, 87036 Arcavacata, Italy  
\* Correspondence: geetachhikara@gmail.com (G.R.); praveenkumar.surolia@jaipur.manipal.edu (P.K.S.)

**Abstract:** The exponentially growing energy requirements and, in turn, extensive depletion of non-restorable sources of energy are a major cause of concern. Restorable energy sources such as solar cells can be used as an alternative. However, their low efficiency is a barrier to their practical use. This provokes the research community to design efficient solar cells. Based on the study of efficacy, design feasibility, and cost of fabrication, DSSC shows supremacy over other photovoltaic solar cells. However, fabricating DSSC in a laboratory and then assessing their characteristics is a costly affair. The researchers applied techniques of computational chemistry such as Time-Dependent Density Functional Theory, and an ab initio method for defining the structure and electronic properties of dyes without synthesizing them. However, the inability of descriptors to provide an intuitive physical depiction of the effect of all parameters is a limitation of the proposed approaches. The proven potential of neural network models in data analysis, pattern recognition, and object detection motivated researchers to extend their applicability for predicting the absorption maxima ( $\lambda_{\max}$ ) of dye. The objective of this research is to develop an ANN-based QSPR model for correctly predicting the value of  $\lambda_{\max}$  for inorganic ruthenium complex dyes used in DSSC. Furthermore, it demonstrates the impact of different activation functions, optimizers, and loss functions on the prediction accuracy of  $\lambda_{\max}$ . Moreover, this research showcases the impact of atomic weight, types of bonds between constituents of the dye molecule, and the molecular weight of the dye molecule on the value of  $\lambda_{\max}$ . The experimental results proved that the value of  $\lambda_{\max}$  varies with changes in constituent atoms and types of bonds in a dye molecule. In addition, the model minimizes the difference in the experimental and calculated values of absorption maxima. The comparison with the existing models proved the dominance of the proposed model.

**Keywords:** solar; DSSC; artificial neural network; energy;  $\lambda_{\max}$



**Citation:** Tomar, N.; Rani, G.; Dhaka, V.S.; Surolia, P.K.; Gupta, K.; Vocaturo, E.; Zumpano, E. Molecular Structure-Based Prediction of Absorption Maxima of Dyes Using ANN Model. *Big Data Cogn. Comput.* **2023**, *7*, 115. <https://doi.org/10.3390/bdcc7020115>

Academic Editors: Domenico Ursino, Miguel-Angel Sicilia, Nik Bessis and Marcello Trovati

Received: 4 April 2023

Revised: 13 May 2023

Accepted: 26 May 2023

Published: 8 June 2023



**Copyright:** © 2023 by the authors. Licensee MDPI, Basel, Switzerland. This article is an open access article distributed under the terms and conditions of the Creative Commons Attribution (CC BY) license (<https://creativecommons.org/licenses/by/4.0/>).

## 1. Introduction

Electricity consumption is increasing proportionally with an increase in population. Mankind mainly depends on non-restorable energy sources such as coal and fossil fuels for electricity production [1]. These non-restorable sources will be exhausted in the future if depletion continues at the same rate. Furthermore, these sources cause environmental pollution. Therefore, researchers emphasize designing the devices to harness the energy from renewable sources such as biomass, wind, hydroelectric, geothermal, and solar energy [2]. Electricity production utilizing solar energy is cleaner and safer than conventional sources. In the recent era, Photovoltaics (PV) technology is considered the most encouraging technology due to its potential to convert solar energy into electrical energy [3]. The PV cells

developed so far have been categorized into three generations. The cells designed in the first generation consist of monocrystalline and polycrystalline silicon. The PV cells of the second generation consist of silicon of non-crystalline form, cadmium telluride, and copper gallium indium diselenide. Along with the advantages of the first and second generation of solar cells in their better performance, there are certain limitations. The materials used in the development of the first and second generation of solar cells are hazardous and expensive. To conquer these issues, scientists have developed third-generation solar cells, such as Dye-Sensitized Solar Cells (DSSC), quantum Dot (QDs) organic, and Perovskite Solar Cells (PSC) [4–7]. Based on the study of efficacy, design feasibility, and cost of fabrication, DSSC shows supremacy over other PV cells developed in the first and second-generation [8–10]. Furthermore, DSSC is attractive to industry and users due to its high molar absorption coefficient, and potential to perform under diffused light conditions. Moreover, DSSC has low fabrication cost, is processable at ambient temperature, easy to manufacture, and suitable for roll-to-roll production. Further, the material's ecofriendly nature, printability on a flexible substrate, and availability in a variety of colors increase the importance of DSSC in real-life [11,12].

DSSC is an integration of components viz. photoanode, with a semiconductor layer, dye sensitizer, electrolyte and counter electrode with a thin layer of catalyst [13]. Along with all components, the dye plays an important role in deciding the efficiency of a DSSC because it is responsible for the absorption of photons from the incident sunlight [14,15]. It is covalently bonded to semiconductor oxide. These dyes have been extensively tested in the fabrication of DSSC and are classified into three groups based on their source or components used for manufacturing. For example, dyes extracted from plant parts such as fruits, flowers, and leaves are considered natural dyes [16]. Dyes fabricated by using metal complexes such as ruthenium [8,17], osmium [18], platinum [19], copper [20], iridium [21], etc. are classified as metal complex dyes. Metal-based dyes are preferred in DSSC due to their advanced photo-conversion efficiency. In contrast, the metal-free organic dyes were introduced at a later stage due to their low cost, high molar extinction coefficient, and simple fabrication technique [22,23]. However, metal-free dyes still show less photovoltaic efficiency compared to metal-complex dyes. Among natural, organic and inorganic dyes, the inorganic dyes' mainly polypyridyl complex of ruthenium metal has been widely used and investigated [24]. Inorganic dyes are selected for their high stability and excellent redox properties [25]. Further, an efficient sensitizer satisfies the following five conditions.

- (i) The bond between the semiconductor oxide surface and dye must be strong enough to move the electron injection in the Conduction Band (CB) of the semiconductor oxide.
- (ii) The LUMO of the sensitizer should be greater than  $\text{TiO}_2$  CB. It empowers the charge injection.
- (iii) The molecule of dye must be small because the bulky molecule can lead to a lower optical cross-section.
- (iv) The dye must be thermally, photochemically, and electrochemically vigorous. If the oxidation-back reduction turnover number exceeds 106, then the stability of DSSC can reach up to approximately 20 years.
- (v) The sensitizer should be effective in absorbing all light below the 920 nm wavelength strike to the surface of the semiconductor oxide [2].

The above-discussed conditions are indicative of the challenging synthesis of such an efficient and novel dye sensitizer that includes all the above-mentioned characteristics. The hit and trial experiments in the laboratory incur a high cost, require expertise in the synthesis of DSSC, and consume a lot of time. Thus, fabricating DSSC in the laboratory and then assessing their characteristics is a costly affair. Therefore, there is a strong need to find an alternative that minimizes the cost and time for trial experiments.

The researchers apply computational chemistry in defining the structure and electronic properties of dyes without actually synthesizing them. For example, the Time-Dependent Density Functional Theory (TD-DFT) [26] and an ab initio method [27] have been employed for identifying new organic dyes for synthesizing DSSC. TD-DFT is preferred for investi-

gating the properties of organic dyes in their excited state due to its higher accuracy and lower computational time than the ab initio method [28,29].

To further improve the prediction accuracy, Xu et. al. employed the QSPR model using Polak–Ribiere algorithm in HYPERCHEM for the prediction of absorption maxima ( $\lambda_{\max}$ ) of organic dyes [30]. They employed DRAGON software to calculate three-dimensional (3-D) descriptors from the optimized molecular geometries. In the subsequent research work, Xu et.al. designed a QSPR between descriptors [31]. They represented that the molecular structures and the  $\lambda_{\max}$  of organic dyes used in DSSC follow the same protocols as applied by Colombo et al. in [20]. The disadvantage of the QSPR approach is that the descriptors do not always provide an intuitive physical depiction of the effect of all parameters [32].

Further, to develop a nonlinear model, researchers applied a quasi-Newton Broyden–Fletcher–Goldfarb–Shanno (BFGS) algorithm [31,33]. They applied the algorithm on the same dataset as used in the research works discussed in [30,31,34]. The details of the dataset are shown in Table S1.

In the BFGS algorithm, there is no need to specify the rate or momentum. Furthermore, it undergoes fast training. However, it is unable to determine small and medium scale minimizing functions. It requires a large amount of memory, and therefore, it involves a huge extent of numerical operations [35].

These challenges can be resolved by employing the Artificial Neural Networks (ANN) models [36,37]. Although the potential of neural network models in data analysis [38], pattern recognition [39], and object detection [40] is proven in various application areas such as healthcare [41–43], agriculture [44], and material science [45], only a few researchers employed the ANN-based models for predicting the absorption maxima ( $\lambda_{\max}$ ) of dye [30,31]. Thus, there is a huge scope to extend their applicability. In this research, we propose an ANN-based QSPR model for correctly predicting the value of  $\lambda_{\max}$  for inorganic ruthenium complex dyes used in DSSC.

The major objectives of this research are as follows.

- (i) To develop an ANN-based model for predicting the absorption maxima of the dye sensitizer used in DSSC.
- (ii) To minimize the difference in the experimental and calculated values of absorption maxima.
- (iii) To showcase the impacts of the atomic weight of each atom and molecular weight on the value of  $\lambda_{\max}$ .
- (iv) To demonstrate the impact of different types of bonds on the value of  $\lambda_{\max}$ .
- (v) To justify the impact of different activation functions, optimizers, and loss functions on the prediction accuracy of  $\lambda_{\max}$  using the ANN model.

The structure of the article is as follows: Section 1 provides the introduction. It gives an overview of the research topic, introduces the research problem, highlights the gaps in existing knowledge, and presents the objectives of the study. Section 2 describes the data collection and methodology of the research work. Section 3 illustrates the results. It presents the findings of the study. It includes tables, figures, and statistical analyses to support the findings. Section 4 presents the discussion of the research work. It interprets and analyzes the results, relates them to the objectives, and compares them with previous research. Section 5 presents the conclusion of the work. It summarizes the main findings and their implications. It also offers insights for future investigations.

## 2. Materials and Methods

### 2.1. Data Set

To prepare the dataset, the molecular structures of 81 ruthenium dye complexes were taken from the literature. From these structures of ruthenium dye complexes, molecular weight, atomic weight, number of all types of bonds such as C-C, C=C, C-N, Ru-N, C=O, Ru-NCS, C-O, and other bonds were calculated for each dye. The prepared dataset comprises 81 rows and 15 columns. The sample dataset is shown in Table 1 and the complete dataset is shown in Table S1. As reported in the earlier works [46,47], the experimental

values of  $\lambda_{\max}$  are also dependent on the solvent. Therefore, to ignore the impact of solvent, the dataset is collected for a single solvent viz. Dimethylformamide (DMF). It is obvious from the sample dataset shown in Table 1 that the values of  $\lambda_{\max}$  lie in the range from 473 to 631 nm in the collected dataset. This large variation in the range of values is important for improving the robustness of the ANN model. It means that the performance of the model does not degrade with any change in the value of  $\lambda_{\max}$ . So, the model works efficiently for a wide range of dyes to correctly predict the value of  $\lambda_{\max}$ .

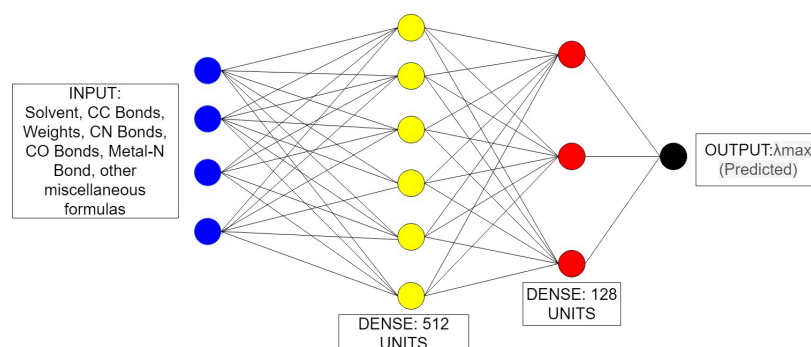
Further, the number of each type of bond was inferred from the structure of dyes. These are shown as  $N^+Bu_4 = 2$ , O-H=1, O-Na=1, O-H=2, C-S=4, C-S=8, C-Se=4, C-S=12,  $N^+(C_4H_9)_4=1$ , C-S=2, O-H=3, C-F=3,  $N \equiv N=1$ , C-F=6, O-H=7,  $N \equiv N=2$ ,  $TBA^+=1$ , N-H=2, N-H=4, O-H=4, and  $TBA^+=1$ . Here, the symbol shows the type of bond, and the digit denotes the number of bonds or functional groups present in a dye molecule. For example,  $N^+Bu_4 = 2$  means that the dye contains two  $N^+Bu_4$  groups, and O-H=1 means that the dye contains one O-H bond. The other groups can be interpreted in the same way.

## 2.2. Experiments

### 2.2.1. Architecture of Model

An Artificial Neural Network (ANN) is a machine learning model that is inspired by the structure and function of biological neurons in the brain. An ANN consists of multiple interconnected nodes i.e., neurons, organized into layers. Each neuron in the network has a set of weights associated with it, which determine the strength of its connections to other neurons in the network. The input layer of an ANN receives input data, which is then passed through one or more hidden layers. Each hidden layer applies a non-linear transformation to the input. During the training phase, its neurons adjust the weights to minimize the difference (value of loss function) between the predicted output and the actual output. Finally, the output layer of the network provides the prediction.

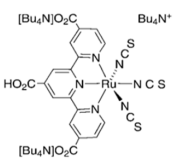
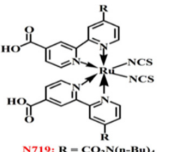
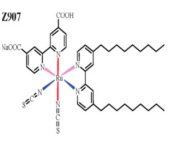
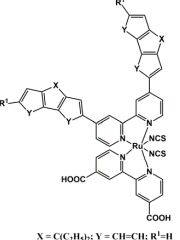
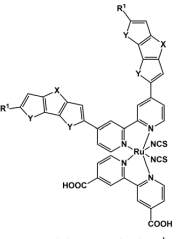
Rather than using the ANN models available in the literature [30,31], a customized ANN-based shallow network has been designed in this research. Its architecture is shown in Figure 1.



**Figure 1.** Sequential ANN Model.

The designed model can deal with observable outliers available in the data. Furthermore, the model requires a smaller dataset for training. Before, the final selection of the architecture, the ANN-based architectures with dense layers comprising 16, 32, 64, and 1024 Units were implemented on a trial-and-error basis. Furthermore, the experiments by employing different activation functions viz. Leaky ReLu, ReLu, Softmax, and Sigmoid; optimizers viz. Adam, AdaGrad, SGD, and RMSProp; and loss functions viz. Mean Absolute Error, Mean Square Error, Mean Squared Logarithmic Error, Binary Cross-Entropy, and Kullback Leibler Divergence Error were employed for experiments. The experimental results obtained by employing the above-mentioned parameters are shown in the subsequent Section 2.2. The impacts of these parameters on the prediction accuracy justify the selection of the 'Relu' activation function, Mean Absolute Error (MSE) loss function, and 'Adam' optimizer in the proposed ANN architecture.

Table 1. Collected and calculated data of Ruthenium dyes.

Dye	Structure	Formula	Mol. Weight	Atomic Weight	$\lambda_{\max}$ (MLCT)	Solvent	C-C Bond	C=C Bond	C-N Bond	Metal-N Bond	C=O Bond	Metal-NCS Bond	C-O Bond	Other Bonds/Groups	Ref.
N749		C <sub>69</sub> H <sub>116</sub> N <sub>9</sub> O <sub>6</sub> RuS <sub>3</sub>	1364.98	C-828.74 H-116.92 N-126.06 O-96 Ru-101.07 S-96.19	600	DMF	11	6	6	3	3	3	3	N <sup>+</sup> Bu <sub>4</sub> =2	[48]
N719		C <sub>58</sub> H <sub>86</sub> N <sub>8</sub> O <sub>8</sub> RuS <sub>2</sub>	1188.55	C-696.62 H-86.68 N-112.05 O-128.00 Ru-101.07 S-64.13	525	DMF	13	8	8	4	4	2	4	N+Bu4 =2	[49,50]
Z907		C <sub>42</sub> H <sub>52</sub> N <sub>6</sub> O <sub>4</sub> RuS <sub>2</sub>	870.10	C-504.45 H-52.41 N-84.04 O-64 Ru-101.07 S-64.13	520	DMF	30	8	8	4	2	2	2	O-H=1 O-Na=1	[51]
YS-1		C <sub>58</sub> H <sub>48</sub> N <sub>6</sub> O <sub>4</sub> RuS <sub>2</sub>	1058.24	C-696.62 H-48.38 N-84.04 O-64 Ru-101.07 S-64.13	536	DMF	40	16	8	4	2	2	2	O-H=2	[51]
YS-2		C <sub>74</sub> H <sub>80</sub> N <sub>6</sub> O <sub>4</sub> RuS <sub>2</sub>	1282.66	C-888.79 H-80.63 N-84.04 O-64 Ru-101.07 S-64.13	536	DMF	56	16	8	4	2	2	2	O-H=2	[51]

The proposed ANN model comprises one input layer, two dense layers, and one output layer. The first and second dense layers comprise 512 and 128 units, respectively. Further, the model contains 20,480; 65,664 parameters at the first and second dense layers, respectively. The number of trainable parameters was reduced to 129 at the output layer. This shows that the employed ANN model involves 86,273 trainable parameters. It does not involve any non-trainable parameter in its architecture. The model is trained with a batch size of 40 for 1000 epochs. Its efficacy is evaluated by using the evaluation metrics defined below.

- i **Difference  $\lambda_{\max}$ :** This is the difference in the predicted and experimental value of absorption maxima, as defined in Equation (1):

$$\text{Difference } \lambda_{\max} = \text{Predicted } \lambda_{\max} - \text{Experimental } \lambda_{\max} \quad (1)$$

- ii **Percentage error (Error%):** This is the percentage of difference in the predicted and experimental value of absorption maxima, as defined in Equation (2).

$$\text{Error \%} = \frac{\text{Difference } \lambda_{\max}}{\text{Experimental } \lambda_{\max}} \times 100 \quad (2)$$

- iii **Correlation matrix:** This matrix shows the correlation between (i)  $\lambda_{\max}$  and all bonds in dye molecule (ii)  $\lambda_{\max}$  and other additional groups present in a dye structure (iii)  $\lambda_{\max}$  and atomic and molecular weight. The matrix represents the direct as well as inverse correlation. The value '0' denotes no correlation, '1' indicates complete and direct correlation. Whereas '-1' shows that the given parameters have a complete and inverse correlation. The values increasing from 0 to 1 show an increasing degree of direct correlation. On the other hand, values approaching from 0 to -1 indicate the increasing degree of negative correlation between the parameters.

### 2.2.2. Selection of Hyperparameters

In this sub-section, the experiments conducted to select the optimum parameters are demonstrated.

#### Selection of Activation Function

Activation functions are employed in the neural networks to introduce non-linearity and enabling them to learn complex patterns in the input data. In this research, we employed the ReLU (Rectified Linear Unit) activation function. It is a simple and computationally efficient function that sets all negative values in the input to zero and leaves positive values unchanged as defined in Equation (3).

$$f(x) = \max(0, x) \quad (3)$$

Here,  $x$  is the input to the function, and  $f(x)$  is the output. The ReLU function returns the input  $x$ , if it is positive, and returns 0 otherwise. This makes the ReLU function a simple yet powerful way to introduce non-linearity into neural networks.

The selection of ReLU activation function is based on the set of experiments conducted. The performance of ANN by employing different activation functions viz. Leaky ReLU, ReLU, Sigmoid, and Softmax are demonstrated in Figure 2. The difference in the predicted and experimental values of absorption maxima was observed. Further, the percentage error was calculated by employing the above-mentioned activation functions. It is evident from the results demonstrated in Figure 2 that employing the ReLU activation function in the proposed ANN model reports the minimum, whereas the softmax activation function results in the maximum percentage error in predicting of  $\lambda_{\max}$ . Therefore, the ReLU activation function was employed in this research.

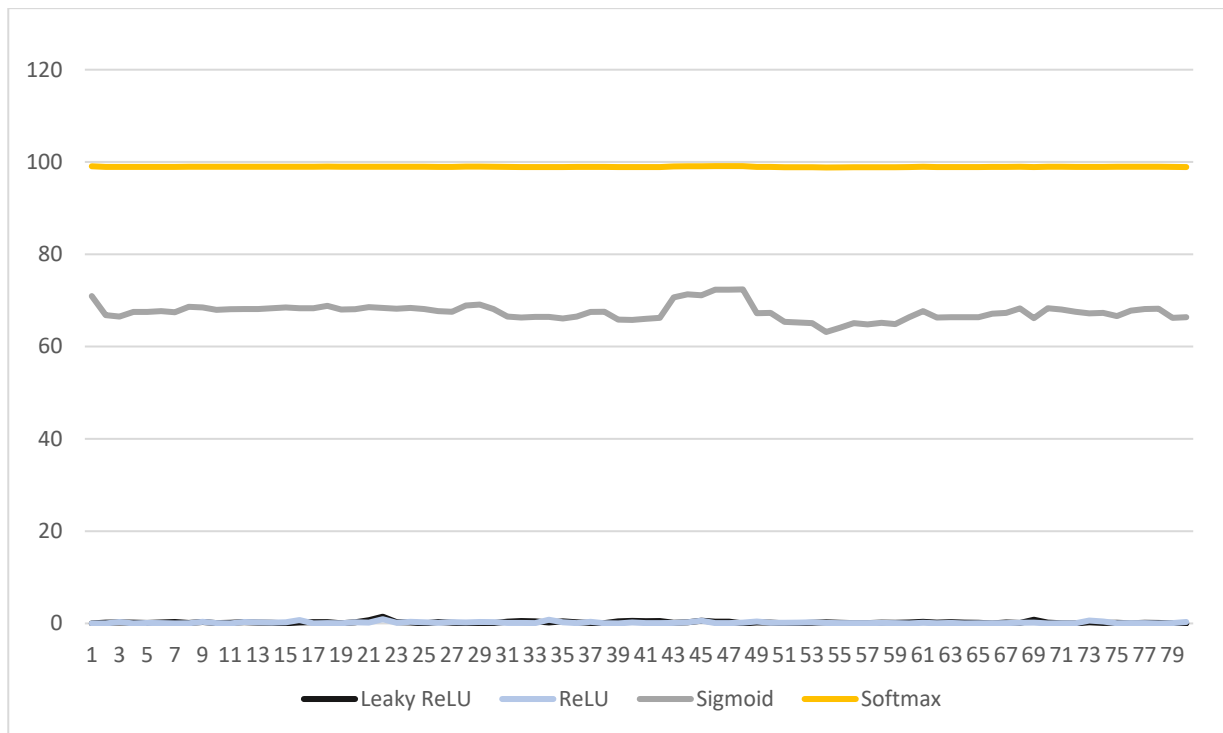


Figure 2. Comparison in percentage error reported by activation functions.

#### Selection of Loss Function

In this work, the selection of loss functions is accomplished strategically. Initially, the loss functions viz. mean absolute error, mean squared error, mean squared logarithmic error, categorical cross entropy and Kullback–Leibler divergence error were employed individually for predicting the value of  $\lambda_{max}$ . The values of percentage error in the  $\lambda_{max}$  obtained for each loss function were evaluated. It is evident from the results demonstrated in Figure 3 that the mean absolute error reports the minimum value of percentage error. Thus, this loss function is employed in the architecture of the proposed ANN model.

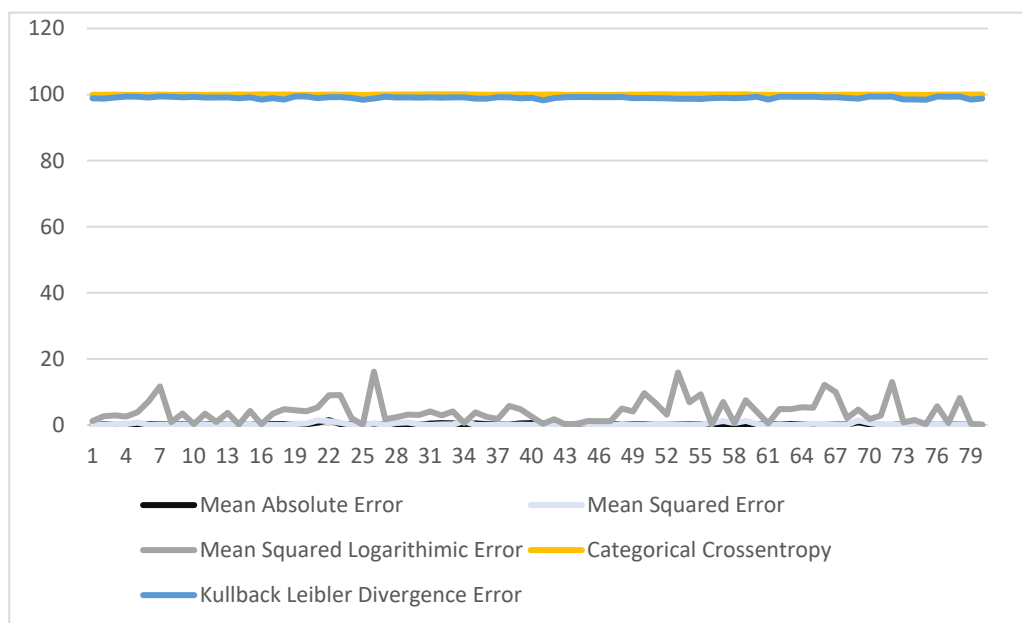


Figure 3. Percentage error comparison for loss functions.



### Selection of Optimizer

Selecting the most suitable optimizer plays an important role in improving the prediction accuracy and minimizing the percentage error. For selecting the appropriate optimizer for the proposed model, a series of experiments were conducted. The optimizers, namely Adam, SGD, RMSProp, AdaGrad, were employed individually and the values of percentage error in the  $\lambda_{\max}$  were recorded. It is clear from the results shown in Figure 4 that the Adam optimizer results in the minimum value of percentage error. Therefore, the Adam optimizer was employed with the proposed ANN model.

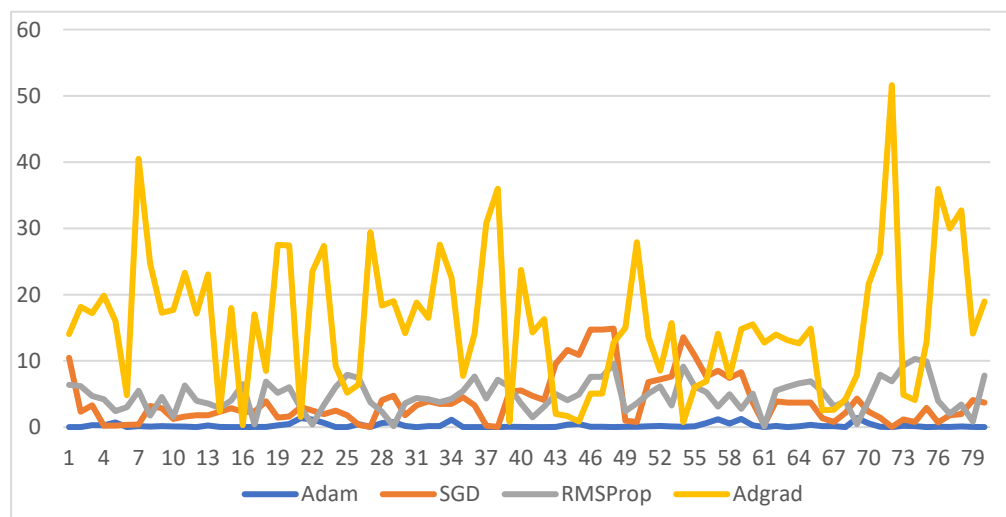


Figure 4. Percentage error comparison for optimizer functions.

### 3. Results

The proposed ANN model is trained for 1000 epochs. The results of the trained model were recorded on the validation and testing datasets. The predicted values of absorption maxima based on the structure of the dye molecule, numbers of bonds, molecular weight, and atomic weight are demonstrated in the correlation matrices shown in Figures 5–9. The details of the correlation obtained are discussed below. Two more machine learning algorithms ‘XGBoost’, and random forest were applied, and their performance is compared with the ANN model. The comparative analysis is demonstrated in Figures 10 and 11.

$\lambda_{\max}$ (MLCT)	1	-0.01	-0.049	-0.48	-0.123	0.770	0.230	-0.743	-0.019	0.019
C-C Single Bond	-0.009	1	0.542	0.376	0.254	0.178	0.110	-0.141	-0.049	0.049
C=C double bond	-0.049	0.542	1	0.470	-0.237	0.052	-0.065	-0.017	-0.023	0.023
C-N bond	-0.484	0.376	0.470	1	0.260	-0.470	0.190	0.493	0.077	-0.077
C=O bond	-0.123	0.254	-0.237	0.260	1	-0.063	0.130	0.072	0.045	-0.045
Metal-NCS bond	0.770	0.178	0.052	-0.47	-0.063	1	0.160	-0.985	-0.048	0.048
C-O bond	0.230	0.115	-0.065	-0.19	0.130	0.160	1	-0.152	0.059	-0.059
Metal-N bond	-0.743	-0.14	-0.017	0.493	0.072	-0.985	-0.150	1	0.044	-0.044
DMF	-0.019	-0.05	-0.023	0.077	0.045	-0.048	0.059	0.044	1	-1
Ethanol	0.019	0.049	0.023	-0.077	-0.045	0.048	-0.059	-0.044	-1	1
	$\lambda_{\max}$ (MLCT)	C-C Single Bond	C=C double bond	C-N bond	C=O bond	Metal-NCS bond	C-O bond	Metal-N bond	DMF	Ethanol

Figure 5. Correlation matrix for  $\lambda_{\max}$  and C-C, C=C, C-N, C=O, Metal-NCS, C-O, Metal-N bonds.

$\lambda_{max}$ (MLCT)	1	0.1304	0.1	0.152	0.192	-0.0068	-0.065	0.05
N+Bu4 =2	0.13	1	-0.07	-0.06	-0.19	-0.0727	-0.053	-0.02
O-H=1	0.10	-0.073	1	0.867	-0.54	0.13646	0.068	0.24
O-Na=1	0.15	-0.063	0.87	1	-0.47	0.1	0.11	0.28
O-H=2	0.19	-0.19	-0.54	-0.47	1	0.058	0.11	-0.13
C-S=4	-0.0068	-0.073	0.14	0.105	0.058	1	-0.15	-0.05
C-S=8	-0.0651	-0.053	0.07	0.11	0.114	-0.15	1	-0.04
C-Se=4	0.045	-0.018	0.24	0.28	-0.13	-0.051	-0.037	1
$\lambda_{max}$ (MLCT)		N+Bu4 =2	O-H=1	O-Na=1	O-H=2	C-S=4	C-S=8	C-Se=4

Figure 6. Correlation matrix for  $\lambda_{max}$  and N<sup>+</sup>Bu<sub>4</sub>=2, O-H=1, O-Na=1, O-H=2 C-S=4, C-S=8, and C-Se=4.

$\lambda_{max}$ (MLCT)	1	-0.017	0.034	0.37	-0.26	-0.17	-0.11	-0.52
C-S=12	-0.017	1	-0.0178	-0.063	-0.056	-0.0527	-0.03	-0.073
N+(C4H9)4=1	0.034	-0.018	1	-0.044	-0.04	-0.037	-0.02	-0.051
C-S=2	0.37	-0.063	-0.0443	1	0.204	0.11035	0.17	0.0094
O-H=3	-0.26	-0.056	-0.0395	0.20	1	0.67	0.45	0.046
C-F=3	-0.17	-0.053	-0.037	0.11	0.67	1	0.48	-0.15
N-N=1	-0.11	-0.025	-0.0178	0.17	0.45	0.48	1	-0.073
C-F=6	-0.52	-0.073	-0.0511	0.0094	0.046	-0.15	-0.073	1
$\lambda_{max}$ (MLCT)		C-S=12	N+(C4H9)4=1	C-S=2	O-H=3	C-F=3	N-N=1	C-F=6

Figure 7. Correlation matrix for  $\lambda_{max}$  and C-S, N<sup>+</sup>(C<sub>4</sub>H<sub>9</sub>), O-H, C-F, N≡N bonds.

$\lambda_{max}$ (MLCT)	1	-0.092	-0.36	0.66	0.00444	-0.031	-0.059	-0.081
O-H=7	-0.092	1	-0.037	-0.0344	-0.0125	-0.018	-0.013	-0.013
N-N=2	-0.36	-0.037	1	-0.1	-0.037	-0.053	-0.037	-0.037
TBA+=1	0.66	-0.034	-0.1	1	-0.0344	-0.049	-0.034	-0.034
N-H=2	0.004	-0.012	-0.037	-0.0344	1	-0.018	-0.012	-0.013
N-H=4	-0.031	-0.018	-0.0527	-0.0489	-0.0178	1	-0.018	-0.018
O-H=4	-0.059	-0.013	-0.037	-0.0344	-0.0125	-0.018	1	-0.013
TBA=1	-0.081	-0.013	-0.037	-0.0344	-0.0125	-0.018	-0.013	1
$\lambda_{max}$ (MLCT)		O-H=7	N-N=2	TBA+=1	N-H=2	N-H=4	O-H=4	TBA=1

Figure 8. Correlation matrix for  $\lambda_{max}$  and O-H, N≡N, TBA<sup>+</sup>, N-H bonds.

$\lambda_{\max}$ (MLCT)	1	0.16	0.36	-0.32	0.098	0.44	0.16	0.045	-0.58	0.17	
C_Weight	0.16	1	0.75	0.37	0.14	0.26	0.03	-0.07	-0.34	0.95	
H_Weight	0.36	0.75	1	0.21	0.317	0.23	-0.04	-0.05	-0.42	0.78	
N_Weight	-0.32	0.37	0.21	1	0.094	-0.36	-0.01	-0.1	0.39	0.42	
O_Weight	0.098	0.14	0.32	0.09	1	-0.02	0.24	-0.07	-0.03	0.27	
Ru_Weight						1	0.07	-0.04	-0.53	0.33	
S_Weight	0.44	0.26	0.23	-0.36	-0.02	0.07	1	-0.03	-0.15	0.05	
Na_Weight	0.16	0.03	-0	-0.01	0.242	-0.04	-0.03	1	-0.06	-0	
Se_Weight	0.045	-0.07	-0	-0.1	-0.07	-0.04	-0.03	-0.06	1	-0.25	
F_Weight	-0.58	-0.34	-0.4	0.39	-0.03	-0.53	-0.15	-0.06	-0.25	1	
Molecular Weight	0.17	0.95	0.78	0.42	0.266	0.33	0.05	-0.02	-0.25	1	
	$\lambda_{\max}$ (MLCT)	C_Weight	H_Weight	N_Weight	O_Weight	Ru_Weight	S_Weight	Na_Weight	Se_Weight	F_Weight	Molecular Weight

Figure 9. Correlation matrix for  $\lambda_{\max}$  based on atomic and molecular weight.

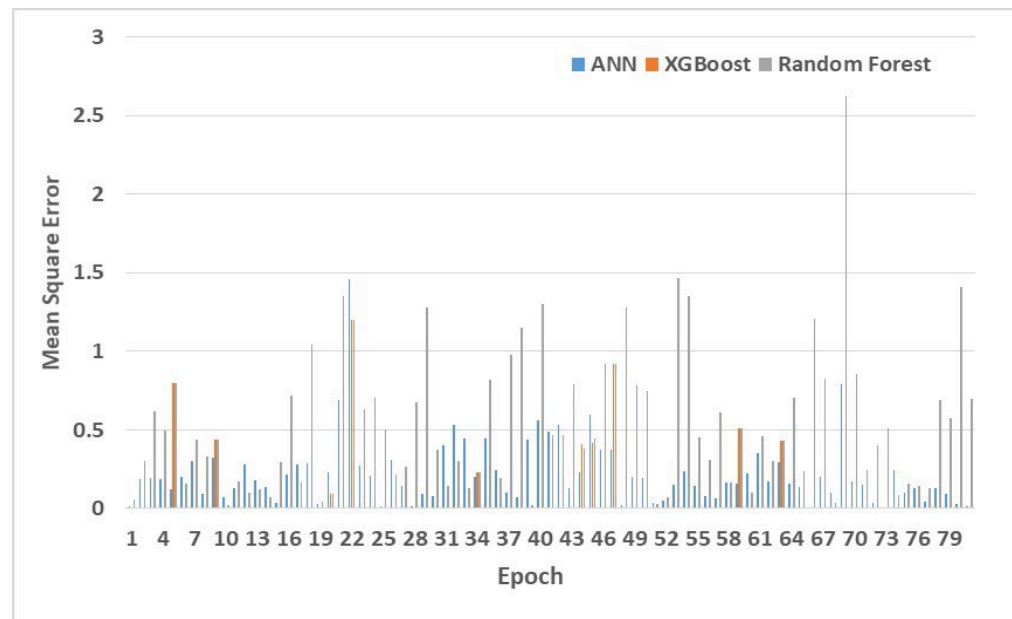
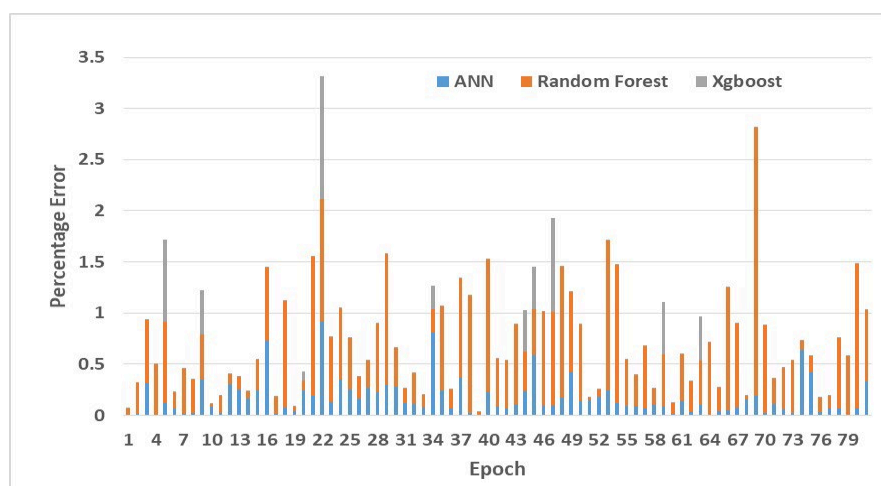


Figure 10. Comparison in MSE of ANN, XGBoost, and Random Forest Models.

### 3.1. Prediction of $\lambda_{\max}$ Based on the C-C, C=C, C-N, C=O, Metal-NCS, C-O, Metal-N Bonds

The correlation between  $\lambda_{\max}$  and different types of bonds is demonstrated in Figure 5. The correlation studied from the correlation matrix is observed as linear. The range of  $\lambda_{\max}$  varies from 1 to  $-1$ . Values of 1 or close to 1 indicate a higher positive correlation, whereas the value  $-1$  or close to  $-1$  denote a negative correlation between the considered parameters. For example, it is evident from the sixth row and first column of the correlation chart shown in Figure 5 that the metal-NCS bond reports the value 0.77 which is close to 1. It shows the highest correlation between the metal-NCS bond and the value of  $\lambda_{\max}$ . Furthermore, it is evident from its positive value that the increase in the metal-NCS bond leads to an increase in the value of  $\lambda_{\max}$  proportionally.



**Figure 11.** Comparison in percentage error reported by ANN, Xgboost, and Random Forest.

Further, the value ‘ $-0.74$ ’ shown in the eighth row, the first column of the correlation matrix indicates the high inverse correlation of metal-N bond with the value of  $\lambda_{\max}$ . This means that the increase in the number of metal-N bonds in a dye leads to a decrease in the value of  $\lambda_{\max}$ . Similarly, the value ‘ $-0.48$ ’ in the fourth row and first column shows that  $\lambda_{\max}$  and C–N bond are inversely correlated but the degree of correlation is lower than a metal-N bond. Next, the observation from column one of the second and ninth row shows that the C–C bond and DMF have a negligible correlation with the value of  $\lambda_{\max}$ .

Additionally, the correlation matrix also shows the correlation between different bonds and functional groups present in a dye. For example, the value ‘ $0.54$ ’ recorded in the third column, the second row indicates that the number of C=C increases with an increase in the number of C–C single in the molecular structure of a dye. In contrast, the correlation of C–C with C–N is  $0.38$ , C=O is  $0.25$ , the metal-NCS bond is  $0.18$  and C–O is  $0.11$ . These values are too small to have an impact on each other.

Similarly, the inter-correlation of C–N with C–C bond is  $0.38$ , C=C bond is  $0.47$ , C=O is  $0.26$ , metal-NCS is  $-0.47$ , C–O is  $-0.19$ , and with the metal-N bond is  $0.49$ . It reflects that the C–N bond has the highest correlation with the metal-N bond among all the above-stated bonds.

Next, the C=O bond is correlated to C–C, C=C, C–N, metal-NCS, C–O, and metal-N bonds with the values  $0.25$ ,  $-0.24$ ,  $0.26$ ,  $-0.063$ ,  $0.13$ , and  $0.072$  respectively. The highest value of the Metal-N bond indicates that it has the maximum and direct correlation with C=O. In contrast, the smaller values for the other bonds mentioned above show their trivial impact on C=O.

Moreover, metal-NCS bond shows  $0.18$ ,  $0.052$ ,  $-0.47$ ,  $-0.063$ ,  $0.16$ , with C–C bond, C=C bond, C–N bond, C=O bond, C–O bond, respectively. All the positive values are too small to impact each other. However, the value  $-0.99$  reported in the sixth row and eighth column of fig 5 indicates the highest inverse correlation of the metal-NCS bond with the Metal-N bond. The presence of one such bond is a strong hindrance for another bond in the same dye.

Next, the C–O bond shows  $0.11$ ,  $-0.065$ ,  $-0.19$ ,  $0.13$ ,  $0.16$ ,  $-0.15$  with C–C bond, C=C bond, C–N, C=O, metal-NCS bond, and metal-N bond respectively. This indicates the minimum impact of these bonds on the presence of a C–O bond in a dye.

Further, the Metal-N bond shows  $-0.14$ ,  $-0.017$ ,  $0.49$ ,  $0.072$ ,  $-0.99$ ,  $-0.15$  with C–C bond, C=C bond, C–N, C=O, metal-NCS bond, C–O bond respectively. It is clear from these values that the Metal-N bond has the maximum direct correlation with the C=O bond, and the highest inverse correlation with the metal-NCS bond.

Based on the above interpretation, it is obvious that the highest direct correction value of  $\lambda_{\max}$  is  $0.77$ , observed with metal-NCS bonds. Whereas the maximum inverse correlation

is  $-0.74$ , observed with metal-N bonds. Therefore, if we want to fabricate a dye with a higher value of  $\lambda_{\max}$ , the dye with a greater number of metal-NCS bonds should be fabricated and vice versa.

### 3.2. Prediction of $\lambda_{\max}$ Based on $N^+Bu_4$ , O-H, O-Na, C-S, and C-Se Bonds

The correlation between  $\lambda_{\max}$  and other bonds viz.  $N^+Bu_4=2$ , O-H=1, O-Na=1, O-H=2, C-S=4, C-S=8, and C-Se=4 present in a dye molecule was also studied. The correlation of these bonds with the value of  $\lambda_{\max}$  as well as a favor for co-existence of these bonds are shown in Figure 6. The highest correlation of  $\lambda_{\max}$  is 0.19 is observed in the first row and fifth column when two O-H groups are present in a dye. The positive correlation of 0.13, 0.1, 0.15, 0.19, 0.045 is observed between  $\lambda_{\max}$  and other bonds  $N^+Bu_4=2$ , O-H=1, O-Na=1, O-H=2 and C-Se=4 respectively. In contrast, a negative correlation of  $-0.0068$ ,  $-0.065$  exists with bond C-S=4, C-S=8 respectively. So, it is evident from the results reported in Figure 6 that the above-stated bonds have a negligible impact on the value of  $\lambda_{\max}$ . Therefore, the study of a number of these bonds can be ignored while fabricating a dye with the desired value of  $\lambda_{\max}$ .

More analysis of the results given in Figure 6 shows that the maximum correlation of 0.87 is observed in the number of O-H and O-Na groups. However, these also have a negligible impact on the value of  $\lambda_{\max}$ .

### 3.3. Prediction of $\lambda_{\max}$ Based on C-S, $N^+(C_4H_9)$ , O-H, C-F, $N\equiv N$ Bonds

Now, the correlation of absorption maxima with the bonds such as twelve C-S groups, one  $N^+(C_4H_9)$ , two C-S, three O-H, three C-F, one  $N\equiv N$ , six C-F was also studied as shown in Figure 7. The analysis of results given in Figure 7 shows that the  $\lambda_{\max}$  is negatively correlated with C-S, O-H, C-F,  $N\equiv N$  with a negligible impact. On the other hand, the  $\lambda_{\max}$  is positively correlated with  $N^+(C_4H_9)$  and C-S groups with values of 0.034 and 0.37. These values indicate that the C-S group has the highest impact on the value of  $\lambda_{\max}$ . However, the degree of correlation is not very significant. The remaining groups have a negligible impact on the value of  $\lambda_{\max}$ .

Further, it is clear from the results shown in Figure 7 that C-F, O-H, and  $N\equiv N$  bonds favor their coexistence in a dye. Therefore, while fabricating a dye with the desired value of  $\lambda_{\max}$ , the number of C-S groups should be considered. Furthermore, the number of C-F, O-H, and  $N\equiv N$  bonds can be increased or decreased in proportion to each other.

### 3.4. Prediction of $\lambda_{\max}$ Based on O-H, $N\equiv N$ , $TBA^+$ , N-H Bond

Now, the correlation of  $\lambda_{\max}$  with different bonds such as O-H=7,  $N\equiv N=2$ ,  $TBA^+=1$ , N-H=2, N-H=4, O-H=4, and  $TBA^+=1$  was also studied. It has been observed that only the presence of one  $TBA^+$  group in a dye have a significant and direct correlation with the value of  $\lambda_{\max}$ . Increasing the number of  $TBA^+$  groups can result in the dye with a higher value of  $\lambda_{\max}$ . However, there is a negligible direct impact of the N-H group on the value of  $\lambda_{\max}$ .

Similarly, there is an insignificant inverse impact of O-H=7,  $N\equiv N=2$ , O-H=4 groups on the value of  $\lambda_{\max}$ . Furthermore, it is clear from the values reported in Figure 8 that the aforementioned bonds do not favor or hinder their co-existence.

### 3.5. Prediction of $\lambda_{\max}$ Based on Atomic and Molecular Weight

The value of  $\lambda_{\max}$  is also dependent on the atomic mass of an atom present in a dye molecule. Furthermore, it is dependent on the molecular mass of a molecule present in a dye and the complete molecule of a dye. The inter-correlation of  $\lambda_{\max}$  with the individual atomic masses of Carbon (C), Hydrogen (H), Nitrogen (N), Oxygen (O), Ruthenium (Ru), Sulfur (S), Sodium (Na), Selenium (Se), Fluorine (F) is demonstrated in Figure 9. Furthermore, the directly or inversely correlated atoms or groups of a dye are presented in Figure 9.

The absorption maxima show a negative correlation with an atomic weight of N and F in proportion to values  $-0.32$  and  $-0.58$  respectively. However, it shows a positive

correlation with C, H, O, S, Na and molecular weight of the dye in proportion to the values 0.16, 0.36, 0.098, 0.44, 0.16, and 0.17 respectively. It is obvious from these values that increasing the mass of Sulfur in a dye leads to a significant increase in the value of  $\lambda_{\max}$ .

Increasing the mass of Fluorine may lead to a decrease in the value of  $\lambda_{\max}$ . Thus, it is apparent that if we want to fabricate the dye with a higher value of  $\lambda_{\max}$  then the number of Sulfur atoms in a dye molecule must be increased. On the other hand, if we want to fabricate a dye with a lower value of  $\lambda_{\max}$ , then the number of F atoms in a dye molecule must be increased. The other atoms, viz. C, H, N, O, Ru, Na, and Se, have a negligible impact on the value of  $\lambda_{\max}$ . Furthermore, the molecular weight of a dye has an insignificant impact on the value of  $\lambda_{\max}$ . The impact is in proportion to the value of 0.17 only.

Further, it is evident from the results reported in Figure 8 that the atomic weight of C shows a correlation to H, N, O, S, Na, F with values 0.75, 0.37, 0.14, 0.26, 0.26, and 0.34, respectively. The C atom is in a strong correlation of 0.95 with the molecular weight of a dye. This shows that a greater number of C atoms are present in a dye with high molecular weight and vice versa.

Similarly, the atomic weight of the H atom shows a correlation with C, N, O, S, Na, and F in proportion to values 0.75, 0.21, 0.32, 0.23,  $-0.043$ , and  $-0.42$  respectively. These values indicate that C and H atoms significantly favor their co-existence in a dye molecule. Whereas H and F atoms hinder the co-existence of each other. Other atoms, viz. N, O, S, and Na, have a negligible impact on the presence of H atoms in a dye molecule. Further, the H atom shows a correlation of 0.78 with the molecular weight of a dye. The higher molecular weight of a dye favors the presence of a greater number of H atoms in it.

Next, it is evident from Figure 8 that the atomic weight of N is correlated to atomic weights of C, H, O, S, Na, and F, with values 0.37, 0.21, 0.094, 0.36,  $-0.0066$ , and 0.39, respectively. These values are too small to have any significant effect on each other. Further, it is correlated to the molecular weight of dye in proportion to the value 0.42.

Similarly, the molecular weight of the O atom is also correlated with the molecular weight of C, H, N, S, Na, Se, F in proportion to values 0.14, 0.32, 0.094,  $-0.021$ , 0.24,  $-0.074$ , and  $-0.028$ , respectively. These values indicate that the O atom has minimum interference with the presence of the other atoms in a dye molecule. Moreover, the molecular weight of a dye also has a minimum correlation of 0.098 with the presence of an O atom in a dye molecule.

Further, the atomic weight of the S atom shows values 0.26, 0.23,  $-0.36$ ,  $-0.021$ , 0.073,  $-0.036$ ,  $-0.53$ , for the atomic weight of C, H, N, O, Na, Se, and F, respectively. Its correlation with the molecular weight of a dye is observed as 0.33. These values show that the atomic weight of S is inversely correlated with the atomic weight of N, O, Se, and F atoms but the degree of correlation is not significant. It is, however, directly correlated to atomic weights of C, H, and Na. Furthermore, the degree of direct correlation is insignificant.

The atomic weight of Na also shows a correlation with the atomic weight of C, H, N, O, Ru, Se, S, and F with values 0.16, 0.026,  $-0.043$ ,  $-0.0066$ , 0.24, 0.073,  $-0.032$ ,  $-0.15$ , respectively. It is apparent from these values that the direct, as well as inverse correlation of atomic weight of Na with above-stated atoms, is negligible.

Now, it has been observed from Figure 9 that the atomic weight of Se is correlated with C, H, N, O, S, Na, and F with values  $-0.066$ ,  $-0.046$ ,  $-0.1$ ,  $-0.074$ ,  $-0.036$ ,  $-0.032$ ,  $-0.061$ , respectively. The low positive, as well as negative values, clearly show that the presence of the Se atom in a dye molecule is not determined by the presence of other atoms.

Similarly, the atomic weight of F is correlated with the atomic weights of C, H, N, O, S, Na, and Se with the values of  $-0.34$ ,  $-0.42$ , 0.39,  $-0.028$ ,  $-0.53$ ,  $-0.15$ ,  $-0.061$ , respectively. These values indicate that the presence of F is inversely related to all the above-mentioned atoms except N. However, the degree of correlation is not very high.

Further, the molecular weight of the dye is also correlated with absorption maxima and atomic weights of C, H, N, O, S, Na, Se, and F in proportion to the values 0.95, 0.78,

0.42, 0.27, 0.33, 0.054,  $-0.023$ ,  $-0.25$ , respectively. It indicates that the molecular weight is highly dependent on the atomic weight of carbon and H.

### 3.6. Difference and Percentage Error

To validate the reliability and accuracy of the proposed model, we calculated the difference in the experimental values of  $\lambda_{\max}$  reported in the literature and the predicted values [30,31]. Furthermore, we calculated the percentage error in the experimental and predicted values of  $\lambda_{\max}$ . The values of difference and percentage error of individual dyes are demonstrated in Table 2. Its first column shows the name of the dye, the second column shows the experimental value of  $\lambda_{\max}$ , the third column includes the predicted value of  $\lambda_{\max}$ , the fourth column shows the difference in  $\lambda_{\max}$  values, and the last column contains the values of percentage error.

**Table 2.** Comparison of experimental and predicted values of absorption maxima.

Dye	$\lambda_{\max}$ (Experimental)	$\lambda_{\max}$ (Predicted)	Difference	Percentage Error	t-Score	Ref.
N749	600	599.9605103	$-0.039489746$	0.006581625	2.962804	[48]
N719	525	525.081115723	0.081115723	0.015450614	2.573224	[52]
Z907	520	518.3882446	$-1.611755371$	0.309952945	2.554664	[51]
YS-1	536	535.9921265	$-0.007873535$	0.001468943	2.633939	[51]
YS-2	536	536.6464233	0.64642334	0.120601371	2.637666	[51]
YS-3	539	538.6637573	$-0.336242676$	0.062382687	2.65839	[51]
YS-4	535	534.9170532	$-0.082946777$	0.015504071	2.642976	[51]
YS-5	555	554.8757324	$-0.124267578$	0.022390554	2.746662	[51]
CYC-B1	553	554.9368896	1.936889648	0.350251287	2.737349	[53]
CYC-B3	544	543.5513306	$-0.448669434$	0.082475998	2.699216	[54]
SJW-E1	546	545.9083252	$-0.091674805$	0.016790258	2.713337	[54]
C101	547	545.3406372	$-1.659362793$	0.303357005	2.72482	[55]
C102	547	545.6287842	$-1.37121582$	0.250679314	2.728966	[55]
C103	550	549.0956421	$-0.90435791$	0.164428711	2.74789	[56]
C104	553	554.3543701	1.354370117	0.24491322	2.764281	[57]
C105	550	546.0117188	$-3.98828125$	0.725142062	2.759501	[58]
C106	550	549.9251099	$-0.074890137$	0.013616389	2.759075	[55]
C107	559	558.5645142	$-0.43548584$	0.07790444	2.808949	[56]
K19	545	545.203064	0.203063965	0.037259445	2.740354	[59]
K77	546	544.6682739	$-1.331726074$	0.243905872	2.752063	[60]
CYC-B11	554	552.9317627	$-1.068237305$	0.19282262	2.796931	[61]
CYC-B6L	551	545.9569702	$-5.043029785$	0.915250421	2.790254	[62]
CYC-B6S	548	547.302124	$-0.697875977$	0.12734963	2.774375	[62]
CYC-B7	551	552.8936157	1.893615723	0.343668908	2.791177	[63]
CYC-B13	547	548.375	1.375	0.251371115	2.775524	[64]
JK-55	539	538.1456909	$-0.854309082$	0.158498898	2.74214	[65]
JK-56	537	538.4175415	1.417541504	0.26397422	2.734822	[65]
RC-31	560	558.7681274	$-1.231872559$	0.219977245	2.860881	[66]
RC-32	564	562.3169556	$-1.683044434$	0.298412144	2.884413	[66]
RC-36	547	545.4786377	$-1.521362305$	0.278128386	2.798735	[66]
PRT1	520	520.6152954	0.61529541	0.118326038	2.663049	[67]
PRT2	517	517.5576172	0.557617188	0.107856326	2.652854	[67]
PRT3	519	519.3753052	0.375305176	0.072313137	2.668113	[67]
PRT4	519	514.8287964	$-4.171203613$	0.803700089	2.678184	[67]
PRT21	514	515.2487793	1.248779297	0.242953166	2.651222	[68]
PRT22	520	519.6818237	$-0.31817627$	0.061187744	2.688368	[68]
PRT23	536	537.9351196	1.935119629	0.361029774	2.774103	[68]
PRT24	537	537.1176147	0.117614746	0.021902187	2.787605	[68]
TF1	510	509.9632568	$-0.036743164$	0.007204542	2.653727	[69]
TF2	509	510.1255798	1.125579834	0.221135527	2.651082	[69]
TF3	513	513.4284058	0.428405762	0.083509892	2.676337	[69]
TF4	516	516.3215942	0.321594238	0.062324464	2.69655	[69]

Table 2. Cont.

Dye	$\lambda_{\max}$ (Experimental)	$\lambda_{\max}$ (Predicted)	Difference	Percentage Error	<i>t</i> -Score	Ref.
MJ-4	594	594.5967407	0.596740723	0.100461401	3.109695	[70]
MJ-6	608	606.5596313	−1.440368652	0.236902744	3.174494	[70]
MJ-7	603	606.5596313	3.559631348	0.590320289	3.119411	[70]
MJ-10	630	630.5605469	0.560546875	0.088975698	3.233595	[70]
MJ-11	630	630.5605469	0.560546875	0.088975698	3.149689	[70]
MJ-12	631	632.057312	1.057312012	0.167561337	3.010226	[70]
TFRS-1	532	534.241333	2.241333008	0.421303183	2.251667	[71]
TFRS-2	533	533.7162476	0.716247559	0.1343804	2.269726	[71]
TFRS-3	503	503.7233887	0.723388672	0.143814847	2.151846	[71]
TFRS-4	501	501.8835449	0.883544922	0.176356271	2.146519	[71]
TFRS-21	499	500.2005005	1.200500488	0.240581259	2.137079	[72]
TFRS-22	473	473.5461426	0.546142578	0.115463547	2.022101	[72]
TFRS-24	485	485.4335938	0.43359375	0.089400776	1.963301	[72]
TFRS-51	499	499.3976135	0.397613525	0.079682067	1.925546	[73]
TFRS-52	495	495.3208618	0.320861816	0.064820565	1.866991	[73]
TFRS-53	500	500.4888611	0.488861084	0.097772218	1.795062	[73]
TFRS-54	496	496.4121094	0.412109375	0.083086565	1.695218	[73]
CS9	518	518.0759277	0.075927734	0.014657863	1.573186	[74]
A597	539	538.2700806	−0.729919434	0.135421053	1.632301	[75]
CS27	517	517.1707764	0.170776367	0.033032179	1.590288	[76]
CS28	518	517.486084	−0.513916016	0.099211589	1.579045	[76]
CS32	518	518.0393066	0.039306641	0.007588155	1.557655	[76]
CS43	518	518.1796875	0.1796875	0.034688707	1.529054	[76]
CS17	530	529.7614136	−0.238586426	0.045016307	1.521574	[76]
CS22	533	532.6157837	−0.384216309	0.072085612	1.578218	[76]
LXJ-1	549	548.1496582	−0.850341797	0.154889211	1.686294	[56]
KW-1#	515	514.050293	−0.949707031	0.184409127	1.566551	[77]
KW-2#	550	549.9004517	−0.09954834	0.018099697	1.529517	[77]
HRD-1	543	542.3900757	−0.609924316	0.112324923	1.449902	[78]
K-73	545	545.2966309	0.296630859	0.05442768	1.48967	[79]
KC-5#	537	537.1211548	0.121154785	0.022561412	1.454641	[80]
KC-6#	531	527.5883179	−3.411682129	0.642501354	1.539624	[80]
KC-7#	533	530.7481079	−2.25189209	0.422493815	1.649544	[80]
KC-8	522	522.1340332	0.134033203	0.02567686	1.730241	[80]
MH06	541	540.6497192	−0.350280762	0.064746909	1.841917	[81]
MH11	547	546.6559448	−0.344055176	0.062898569	1.987435	[81]
MC119	548	548.0170898	0.017089844	0.003118585	1.976855	[82]
S3	516	515.6741333	−0.325866699	0.063152462	1.256043	[83]
S4	518	519.6868286	1.686828613	0.325642586	1.462133	[83]

# These compounds were named after the initials of the first author of the reference cited.

It is evident from the results shown in Table 2 that the predicted values of  $\lambda_{\max}$  are closer to the experimental values of  $\lambda_{\max}$  collected from the literature. The range of difference in predicted and experimental values is  $-5.04$  to  $3.559$ , which is very low. Furthermore, the percentage error observed in the experimental and predicted values lie in the range of  $0.00145$  to  $0.915$ . The low values prove the reliability of the model.

Statistical Analysis: For statistical analysis of the results shown in Table 2, we applied the *t*-test as defined in Equation (4). The value of *t* as shown in column 6 of Table 2 lies in the range of  $1.25$  to  $3.25$ . A positive absolute value of *t* indicates a moderate difference between the means of the two sets of values. It also suggests that the difference between the means is statistically significant, implying that the predicted values significantly deviate from the experimental values.

$$t - score = \frac{\text{Difference between experimental and predicted value}}{\text{standard error}} \quad (4)$$



#### 4. Discussion

The research work proposed in this work meets the objectives of accurately predicting the absorption maxima. The ANN model designed in this research correctly predicts the value of absorption maxima of the dye sensitizer based on the structure of the dye molecule, numbers of bonds, molecular weight, and atomic weight. The model, trained with different sets of values of these parameters and their corresponding value of the compound, learns to predict the correct value of the absorption maxima. It magnificently reduced the difference and percentage error in the experimental and predicted values of  $\lambda_{\max}$  of a dye, reported in the literature [30,31]. Furthermore, it predicted the impact of collective atomic weights of each atom type and molecular weight of the dye molecule on the value of  $\lambda_{\max}$  of a dye. Moreover, the proposed research work successfully showed the impact of different bonds between constituent atoms of a dye on its absorption maxima.

To achieve the first objective ANN model is trained to predict the absorption maxima of inorganic dye mainly ruthenium complexes used in DSSC. Further, the calculated values of absorption maxima are very close to the experimental values collected from the literature as shown in Table S1. Moreover, it reported the lesser difference in experimental and calculated values of absorption maxima reported by Xu et.al. [30,31]. They reported the difference in range of  $-27.3$  to  $27.1$  [30] and  $-16.6$  to  $16.2$  [31]. In contrast, the difference reported in the work proposed in this manuscript lies in the range of  $-5.043029785$  to  $3.559631348$ . This shows that the proposed model more accurately predicts the value of  $\lambda_{\max}$ . Moreover, the statistical analysis of the difference in the experimental and predicted values in terms of the  $t$ -test validates the obtained result. The  $t$ -score obtained in the range of  $1.25$  to  $3.23$  signifies the importance of the  $t$ -test.

In addition, the percentage error observed from the experimental results lies in the range of  $0.01468943$  to  $0.915250421$ , which are  $96.63$  and  $94.35\%$  less than the percentage error calculated in the works reported in [30,31].

To demonstrate the impacts of the atomic weight of each atom and molecular weight on the value of  $\lambda_{\max}$ , a correlation matrix was studied as shown in Figure 9. The atomic weight of sulfur and fluorine shows a considerable impact on  $\lambda_{\max}$  value. The  $\lambda_{\max}$  value is directly proportional to the sulfur atoms, whereas it is indirectly proportional to the fluorine atoms.

Further, the correlation matrix of  $\lambda_{\max}$  with different bonds was studied as shown in Figures 5–8. Initially, the correlation matrix of  $\lambda_{\max}$  with C-C, C=C, C-N, C=O, Metal-NCS, C-O, Metal-N bonds as demonstrated in Figure 5 shows that the  $\lambda_{\max}$  directly depends only on the Metal-NCS bond and inversely depends on Metal-N bonds. The next correlation matrix as shown in Figure 6 indicates the relation of  $\lambda_{\max}$  and N+Bu4=2, O-H=1, O-Na=1, O-H=2 C-S=4, C-S=8, and C-Se=4. It is concluded that the  $\lambda_{\max}$  directly depends on the bond O-H=2, whereas it inversely depends on the C-S=8 bond. Likewise, the correlation of  $\lambda_{\max}$  based on C-S, N<sup>+</sup>(C4H9), O-H, C-F, N $\equiv$ N bonds were studied. It is observed that  $\lambda_{\max}$  directly depends on the C-S bonds and is inversely dependent on the C-F bond. Furthermore, the correlation of  $\lambda_{\max}$  based on O-H, N-N, TBA<sup>+</sup>, N-H bonds were studied. It is concluded that the impact on the  $\lambda_{\max}$  is observed at its maximum with the increase in the TBA<sup>+</sup> group in dye structure, whereas the  $\lambda_{\max}$  value decreases with an increase in N $\equiv$ N bonds.

The impacts of activation function 'ReLU', loss function Mean Absolute Error (MSE), and optimizer 'Adam' on the prediction accuracy of  $\lambda_{\max}$  using the ANN model were observed. It is concluded that the proposed model is more efficient than the methods available in the literature [30,31]. It accounts for the diminishing difference in predicted and experimental values of  $\lambda_{\max}$ . Furthermore, justify the relation of  $\lambda_{\max}$  with other bonds of dye molecule as well as the impact of atomic and molecular weight on it.

Further, the superiority of the customized ANN model over the traditional machine learning models is proved by conducting the experiments. The values of Mean Square Error (MSE), and Percentage Error reported by ANN, Xgboost, and Random Forest models were recorded for each epoch. These values are illustrated in Figures 10 and 11, respectively.

This is evident from Figure 10, that the ANN model reports the lowest value of MSE among all the three models. This proves that ANN model outperforms the Xgboost and Random Forest in predicting the value of absorption maxima.

Similarly, the results demonstrated in Figure 11 prove that the ANN model reports the lowest value of percentage error among all the above-stated three models. This justifies the efficacy of ANN model in correctly predicting the value of absorption maxima.

## 5. Conclusions

In this manuscript, a customized ANN model is developed for automating the prediction of the value of absorption maxima of dye without actually fabricating the dye. Further, the ANN model is fine-tuned to minimize the difference in the experimental and predicted values. The model precisely predicted values of absorption maxima. The difference reported in the proposed work is  $-22.3$  to  $23.6$  values lower than the range of difference reported in [30,31]. Similarly, the difference is lower by values from 11.56 to 12.7. This proves the supremacy of the proposed work over the reported methods in the literature.

Furthermore, the research work available so far does not focus on showing the impact of the atomic weight of atoms in a dye molecule, the number, and types of bonds available in a dye molecule. The research works presented in this manuscript showcase the role of atomic weights and different types of bonds present in dye molecules on the value of their absorption maxima. Furthermore, they show the direct and inverse correlation of individual atoms present in a dye molecule on the value of absorption maxima. Moreover, they predict the inter-correlation among different atoms present in a dye molecule. The experimental results prove the efficacy of the proposed work, minimizing the requirements for hit and trial experiments. Therefore, it is a cost-saving approach for fabricating the dye of desired characteristics.

The model is purely dependent on the descriptors originated from the chemical structure of the dye molecule and valid for regular dyes of whichever chemical structure. Therefore, this model would be beneficial for the synthesis of new sensitizers with preferred absorption maxima values for DSSC.

**Supplementary Materials:** The following are available online at <https://www.mdpi.com/article/10.3390/bdcc7020115/s1>, Table S1: Dataset.

**Author Contributions:** All authors of this manuscript have equal contribution in conceptualization, methodology, software, validation, formal analysis, investigation, data curation, writing—original draft preparation, writing—review and editing, and visualization. N.T. and K.G. are involved in implementation and conducting experiments, G.R., V.S.D. and P.K.S. are also involved in supervision. E.Z. and E.V. are also involved in project administration, and funding acquisition. All authors have read and agreed to the published version of the manuscript.

**Funding:** This research is funded by DIMES (Department of Informatics, Modeling, Electronics and Systems)—University of Calabria with Grant/Award Number: SIMPATICO\_ZUMPARNO.

**Data Availability Statement:** The sample dataset used in this research is submitted as Supplementary Material. The code is available with authors. They will provide the code on request.

**Acknowledgments:** The authors would like to acknowledge the financial support by the Science and Engineering Research Board (SERB) under Grant No. [EMR/2016/006259].

**Conflicts of Interest:** The authors declare no conflict of interest.

## References

1. Käberger, T. Progress of renewable electricity replacing fossil fuels. *Glob. Energy Interconnect.* **2018**, *1*, 48–52.
2. Tomar, N.; Dhaka, V.S.; Suroolia, P.K. A brief review on carbon nanomaterial counter electrodes for N719 based dye-sensitized solar cells. *Mater. Today Proc.* **2021**, *43*, 2975–2978. [[CrossRef](#)]
3. Gangopadhyay, U.; Jana, S.; Das, S. State of Art of Solar Photovoltaic Technology. In *Conference Papers in Science*; Hindawi: London, UK, 2013.
4. Giribabu, L.; Sudhakar, K.; Velkannan, V. Phthalocyanines: Potential alternative sensitizers to Ru (II) polypyridyl complexes for dye-sensitized solar cells. *Curr. Sci.* **2012**, *102*, 991–1000.

5. Glunz, S.W.; Feldmann, F. SiO<sub>2</sub> surface passivation layers—A key technology for silicon solar cells. *Sol. Energy Mater. Sol. Cells* **2018**, *185*, 260–269. [[CrossRef](#)]
6. Lyons, C.; Dev, P.; Maji, P.; Rathi, N.; Surolia, P.K.; Byrne, O.; Xiao, X.; English, N.J.; Magner, E.; MacElroy, J.M.D.; et al. Silicon-bridged triphenylamine-based organic dyes for efficient dye-sensitized solar cells. *Sol. Energy* **2018**, *160*, 64–75. [[CrossRef](#)]
7. Meng, K.; Surolia, P.K.; Byrne, O.; Thampi, K.R. Quantum dot and quantum dot-dye co-sensitized solar cells containing organic thiolate—Disulfide redox electrolyte. *J. Power Sources* **2015**, *275*, 681–687. [[CrossRef](#)]
8. Tomar, N.; Agrawal, A.; Dhaka, V.S.; Surolia, P.K. Ruthenium complexes based dye sensitized solar cells: Fundamentals and research trends. *Sol. Energy* **2020**, *207*, 59–76. [[CrossRef](#)]
9. Brennan, L.J.; Surolia, P.K.; Rovelli, L.; Loudon, A.; Torsney, S.P.; Roche, S.; Thampi, K.R.; Gun'ko, Y.K. Electrophoretic separation and deposition of metal–graphene nanocomposites and their application as electrodes in solar cells. *RSC Adv.* **2016**, *6*, 64097–64109. [[CrossRef](#)]
10. Byrne, O.; Coughlan, A.; Surolia, P.K.; Thampi, K.R. Succinonitrile-based solid-state electrolytes for dye-sensitized solar cells. *Prog. Photovolt. Res. Appl.* **2015**, *23*, 417–427. [[CrossRef](#)]
11. Calogero, G.; Sinopoli, A.; Citro, I.; Di Marco, G.; Petrov, V.; Diniz, A.M.; Parola, A.J.; Pina, F. Synthetic analogues of anthocyanins as sensitizers for dye-sensitized solar cells. *Photochem. Photobiol. Sci.* **2013**, *12*, 883–894. [[CrossRef](#)]
12. Sheehan, S.; Surolia, P.; Byrne, O.; Garner, S.; Cimo, P.; Li, X.; Dowling, D.; Thampi, K. Flexible glass substrate based dye sensitized solar cells. *Sol. Energy Mater. Sol. Cells* **2015**, *132*, 237–244. [[CrossRef](#)]
13. Sugathan, V.; John, E.; Sudhakar, K. Recent improvements in dye sensitized solar cells: A review. *Renew. Sustain. Energy Rev.* **2015**, *52*, 54–64. [[CrossRef](#)]
14. Meyer, G.J. *Efficient Light-to-Electrical Energy Conversion: Nanocrystalline TiO<sub>2</sub> Films Modified with Inorganic Sensitizers*; ACS Publications: Washington, DC, USA, 1997.
15. Selvaraj, P.; Baig, H.; Mallick, T.K.; Siviter, J.; Montecucco, A.; Li, W.; Paul, M.; Sweet, T.; Gao, M.; Knox, A.R.; et al. Enhancing the efficiency of transparent dye-sensitized solar cells using concentrated light. *Sol. Energy Mater. Sol. Cells* **2018**, *175*, 29–34. [[CrossRef](#)]
16. Richhariya, G.; Kumar, A.; Tekasakul, P.; Gupta, B. Natural dyes for dye sensitized solar cell: A review. *Renew. Sustain. Energy Rev.* **2017**, *69*, 705–718. [[CrossRef](#)]
17. Jin, L.; Shi, S.; Zhao, C.; Yu, X.; Lu, J.; Wang, Q.; Wei, Y. Y-shaped organic dyes with D2–π–A configuration as efficient co-sensitizers for ruthenium-based dye sensitized solar cells. *J. Power Sources* **2021**, *481*, 228952. [[CrossRef](#)]
18. Juwita, R.; Lin, J.-Y.; Lin, S.-J.; Liu, Y.-C.; Wu, T.-Y.; Feng, Y.-M.; Chen, C.-Y.; Tsai, H.-H.G.; Wu, C.-G. Osmium sensitizer with enhanced spin–orbit coupling for panchromatic dye-sensitized solar cells. *J. Mater. Chem. A* **2020**, *8*, 12361–12369. [[CrossRef](#)]
19. Semalti, P.; Sharma, S.N. Dye sensitized solar cells (DSSCs) electrolytes and natural photo-sensitizers: A review. *J. Nanosci. Nanotechnol.* **2020**, *20*, 3647–3658. [[CrossRef](#)]
20. Colombo, A.; Dragonetti, C.; Roberto, D.; Fagnani, F. Copper Complexes as Alternative Redox Mediators in Dye-Sensitized Solar Cells. *Molecules* **2021**, *26*, 194. [[CrossRef](#)]
21. Bobo, M.V.; Paul, A.; Robb, A.J.; Arcidiacono, A.M.; Smith, M.D.; Hanson, K.; Vannucci, A.K. Bis-Cyclometalated Iridium Complexes Containing 4, 4'-Bis (phosphonomethyl)-2, 2'-bipyridine Ligands: Photophysics, Electrochemistry, and High-Voltage Dye-Sensitized Solar Cells. *Inorg. Chem.* **2020**, *59*, 6351–6358. [[CrossRef](#)]
22. Alhorani, S.; Kumar, S.; Genwa, M.; Meena, P. Review of latest efficient sensitizer in dye-sensitized solar cells. In Proceedings of the AIP Conference Proceedings, Coimbatore, India, 17–18 July 2020; AIP Publishing LLC: College Park, MD, USA, 2020; p. 030632.
23. Lyons, C.; Rathi, N.; Dev, P.; Byrne, O.; Surolia, P.K.; Maji, P.; MacElroy, J.; Yella, A.; Grätzel, M.; Magner, E. Organic dyes containing coplanar dihexyl-substituted dithienosilole groups for efficient dye-sensitized solar cells. *Int. J. Photoenergy* **2017**, *2017*, 7594869. [[CrossRef](#)]
24. Ghavre, M.; Byrne, O.; Altes, L.; Surolia, P.K.; Spulak, M.; Quilty, B.; Thampi, K.R.; Gathergood, N. Low toxicity functionalised imidazolium salts for task specific ionic liquid electrolytes in dye-sensitized solar cells: A step towards less hazardous energy production. *Green Chem.* **2014**, *16*, 2252–2265. [[CrossRef](#)]
25. Sekar, N.; Gehlot, V.Y. Metal complex dyes for dye-sensitized solar cells: Recent developments. *Resonance* **2010**, *15*, 819–831. [[CrossRef](#)]
26. Cai-Rong, Z.; Zi-Jiang, L.; Yu-Hong, C.; Hong-Shan, C.; You-Zhi, W.; Li-Hua, Y. DFT and TDDFT study on organic dye sensitizers D5, DST and DSS for solar cells. *J. Mol. Struct. THEOCHEM* **2009**, *899*, 86–93. [[CrossRef](#)]
27. Jamshidvand, A.; Keshavarzi, R.; Mirkhani, V.; Moghadam, M.; Tangestaninejad, S.; Mohammadpoor-Baltork, I.; Afzali, N.; Nematollahi, J.; Amini, M. A novel Ru (II) complex with high absorbance coefficient: Efficient sensitizer for dye-sensitized solar cells. *J. Mater. Sci. Mater. Electron.* **2021**, *32*, 9345–9356. [[CrossRef](#)]
28. El alamy, A.; Bourass, M.; Amine, A.; Hamidi, M.; Bouachrine, M. New organic dyes based on phenylenevinylene for solar cells: DFT and TD-DFT investigation. *Karbala Int. J. Mod. Sci.* **2017**, *3*, 75–82. [[CrossRef](#)]
29. Nashed, R.; Ismail, Y.; Allam, N.K. Recent advances in the use of density functional theory to design efficient solar energy-based renewable systems. *J. Renew. Sustain. Energy* **2013**, *5*, 022701. [[CrossRef](#)]
30. Xu, J.; Zhang, H.; Wang, L.; Liang, G.; Wang, L.; Shen, X.; Xu, W. QSPR study of absorption maxima of organic dyes for dye-sensitized solar cells based on 3D descriptors. *Spectrochim. Acta Part A Mol. Biomol. Spectrosc.* **2010**, *76*, 239–247. [[CrossRef](#)]

31. Xu, J.; Zhang, H.; Wang, L.; Liang, G.; Wang, L.; Shen, X. Artificial neural network-based QSPR study on absorption maxima of organic dyes for dye-sensitized solar cells. *Mol. Simul.* **2011**, *37*, 1–10. [[CrossRef](#)]
32. Schweitzer, R.C.; Morris, J.B. The development of a quantitative structure property relationship (QSPR) for the prediction of dielectric constants using neural networks. *Anal. Chim. Acta* **1999**, *384*, 285–303. [[CrossRef](#)]
33. Wessel, M.D.; Jurs, P.C. Prediction of reduced ion mobility constants from structural information using multiple linear regression analysis and computational neural networks. *Anal. Chem.* **1994**, *66*, 2480–2487. [[CrossRef](#)]
34. Asadollahi-Baboli, M.; Mani-Varnosfaderani, A. Application of computational methods to predict absorption maxima of organic dyes used in solar cells. *J. Theor. Comput. Chem.* **2013**, *12*, 1250114. [[CrossRef](#)]
35. Andrei, N. A note on memory-less SR1 and memory-less BFGS methods for large-scale unconstrained optimization. *Numer. Algorithms* **2022**, *90*, 223–240. [[CrossRef](#)]
36. Zupan, J.; Novič, M.; Ruisánchez, I. Kohonen and counterpropagation artificial neural networks in analytical chemistry. *Chemom. Intell. Lab. Syst.* **1997**, *38*, 1–23. [[CrossRef](#)]
37. Heidari, E.; Sobati, M.A.; Movahedirad, S. Accurate prediction of nanofluid viscosity using a multilayer perceptron artificial neural network (MLP-ANN). *Chemom. Intell. Lab. Syst.* **2016**, *155*, 73–85. [[CrossRef](#)]
38. Taghavi, M.; Ghareghani, A.; Nejad, F.B.; Mirsalim, M. Developing a model to predict the start of combustion in HCCI engine using ANN-GA approach. *Energy Convers. Manag.* **2019**, *195*, 57–69. [[CrossRef](#)]
39. Pradhan, N.; Singh Dhaka, V.; Rani, G.; Chaudhary, H. Machine Learning Model for Multi-View Visualization of Medical Images. *Comput. J.* **2022**, *65*, 805–817. [[CrossRef](#)]
40. Pradhan, N.; Dhaka, V.S.; Rani, G.; Chaudhary, H. Transforming view of medical images using deep learning. *Neural Comput. Appl.* **2020**, *32*, 15043–15054. [[CrossRef](#)]
41. Chaves, L.; Marques, G. Data Mining Techniques for Early Diagnosis of Diabetes: A Comparative Study. *Appl. Sci.* **2021**, *11*, 2218. [[CrossRef](#)]
42. Dhaka, V.S.; Rani, G.; Oza, M.G.; Sharma, T.; Misra, A. A deep learning model for mass screening of COVID-19. *Int. J. Imaging Syst. Technol.* **2021**, *31*, 483–498. [[CrossRef](#)]
43. Rani, G.; Oza, M.G.; Dhaka, V.S.; Pradhan, N.; Verma, S.; Rodrigues, J.J. Applying deep learning-based multi-modal for detection of coronavirus. *Multimed. Syst.* **2022**, *28*, 1251–1262. [[CrossRef](#)]
44. Sinwar, D.; Dhaka, V.S.; Sharma, M.K.; Rani, G. AI-Based Yield Prediction and Smart Irrigation. In *Internet of Things and Analytics for Agriculture*; Springer: Berlin/Heidelberg, Germany, 2020; Volume 2, pp. 155–180.
45. Dhaka, V.S.; Meena, S.V.; Rani, G.; Sinwar, D.; Ijaz, M.F.; Woźniak, M. A survey of deep convolutional neural networks applied for prediction of plant leaf diseases. *Sensors* **2021**, *21*, 4749. [[CrossRef](#)] [[PubMed](#)]
46. Ozawa, H.; Awa, M.; Ono, T.; Arakawa, H. Effects of Dye-Adsorption Solvent on the Performances of the Dye-Sensitized Solar Cells Based on Black Dye. *Chem. Asian J.* **2012**, *7*, 156–162. [[CrossRef](#)] [[PubMed](#)]
47. Gibson, E.A.; Le Pleux, L.; Fortage, J.; Pellegrin, Y.; Blart, E.; Odobel, F.; Hagfeldt, A.; Boschloo, G. Role of the Triiodide/Iodide Redox Couple in Dye Regeneration in p-Type Dye-Sensitized Solar Cells. *Langmuir* **2012**, *28*, 6485–6493. [[CrossRef](#)] [[PubMed](#)]
48. Nazeeruddin, M.K.; Pechy, P.; Renouard, T.; Zakeeruddin, S.M.; Humphry-Baker, R.; Comte, P.; Liska, P.; Cevey, L.; Costa, E.; Shklover, V. Engineering of efficient panchromatic sensitizers for nanocrystalline TiO<sub>2</sub>-based solar cells. *J. Am. Chem. Soc.* **2001**, *123*, 1613–1624. [[CrossRef](#)] [[PubMed](#)]
49. Nazeeruddin, M.K.; De Angelis, F.; Fantacci, S.; Selloni, A.; Viscardi, G.; Liska, P.; Ito, S.; Takeru, B.; Grätzel, M. Combined experimental and DFT-TDDFT computational study of photoelectrochemical cell ruthenium sensitizers. *J. Am. Chem. Soc.* **2005**, *127*, 16835–16847. [[CrossRef](#)]
50. Wen, P.; Han, Y.; Zhao, W. Influence of TiO<sub>2</sub> nanocrystals fabricating dye-sensitized solar cell on the absorption spectra of N719 sensitizer. *Int. J. Photoenergy* **2012**, *2012*, 906198. [[CrossRef](#)]
51. Yen, Y.S.; Chen, Y.C.; Hsu, Y.C.; Chou, H.H.; Lin, J.T.; Yin, D.J. Heteroleptic Ruthenium Sensitizers That Contain an Ancillary Bipyridine Ligand Tethered with Hydrocarbon Chains for Efficient Dye-Sensitized Solar Cells. *Chem. A Eur. J.* **2011**, *17*, 6781–6788. [[CrossRef](#)]
52. Nazeeruddin, M.K.; Baranoff, E.; Grätzel, M. Dye-sensitized solar cells: A brief overview. *Sol. Energy* **2011**, *85*, 1172–1178. [[CrossRef](#)]
53. Chen, C.Y.; Wu, S.J.; Wu, C.G.; Chen, J.G.; Ho, K.C. A Ruthenium complex with superhigh light-harvesting capacity for dye-sensitized solar cells. *Angew. Chem.* **2006**, *118*, 5954–5957. [[CrossRef](#)]
54. Chen, C.Y.; Wu, S.J.; Li, J.Y.; Wu, C.G.; Chen, J.G.; Ho, K.C. A new route to enhance the light-harvesting capability of ruthenium complexes for dye-sensitized solar cells. *Adv. Mater.* **2007**, *19*, 3888–3891. [[CrossRef](#)]
55. Gao, F.; Wang, Y.; Shi, D.; Zhang, J.; Wang, M.; Jing, X.; Humphry-Baker, R.; Wang, P.; Zakeeruddin, S.M.; Grätzel, M. Enhance the optical absorptivity of nanocrystalline TiO<sub>2</sub> film with high molar extinction coefficient ruthenium sensitizers for high performance dye-sensitized solar cells. *J. Am. Chem. Soc.* **2008**, *130*, 10720–10728. [[CrossRef](#)]
56. Yu, Q.; Liu, S.; Zhang, M.; Cai, N.; Wang, Y.; Wang, P. An extremely high molar extinction coefficient ruthenium sensitizer in dye-sensitized solar cells: The effects of  $\pi$ -conjugation extension. *J. Phys. Chem. C* **2009**, *113*, 14559–14566. [[CrossRef](#)]
57. Gao, F.; Wang, Y.; Zhang, J.; Shi, D.; Wang, M.; Humphry-Baker, R.; Wang, P.; Zakeeruddin, S.M.; Grätzel, M. A new heteroleptic ruthenium sensitizer enhances the absorptivity of mesoporous titania film for a high efficiency dye-sensitized solar cell. *Chem. Commun.* **2008**, *59*, 2635–2637. [[CrossRef](#)]

58. Gao, F.; Cheng, Y.; Yu, Q.; Liu, S.; Shi, D.; Li, Y.; Wang, P. Conjugation of selenophene with bipyridine for a high molar extinction coefficient sensitizer in dye-sensitized solar cells. *Inorg. Chem.* **2009**, *48*, 2664–2669. [CrossRef]
59. Wang, P.; Klein, C.; Humphry-Baker, R.; Zakeeruddin, S.M.; Grätzel, M. A high molar extinction coefficient sensitizer for stable dye-sensitized solar cells. *J. Am. Chem. Soc.* **2005**, *127*, 808–809. [CrossRef]
60. Kuang, D.; Klein, C.; Ito, S.; Moser, J.E.; Humphry-Baker, R.; Evans, N.; Duriaux, F.; Graetzel, C.; Zakeeruddin, S.M.; Grätzel, M. High-efficiency and stable mesoscopic dye-sensitized solar cells based on a high molar extinction coefficient ruthenium sensitizer and nonvolatile electrolyte. *Adv. Mater.* **2007**, *19*, 1133–1137. [CrossRef]
61. Chen, C.-Y.; Wang, M.; Li, J.-Y.; Pootrakulchote, N.; Alibabaei, L.; Ngoc-le, C.-h.; Decoppet, J.-D.; Tsai, J.-H.; Grätzel, C.; Wu, C.-G. Highly efficient light-harvesting ruthenium sensitizer for thin-film dye-sensitized solar cells. *ACS Nano* **2009**, *3*, 3103–3109. [CrossRef]
62. Chen, C.Y.; Chen, J.G.; Wu, S.J.; Li, J.Y.; Wu, C.G.; Ho, K.C. Multifunctionalized ruthenium-based supersensitizers for highly efficient dye-sensitized solar cells. *Angew. Chem.* **2008**, *120*, 7452–7455. [CrossRef]
63. Li, J.-Y.; Chen, C.-Y.; Chen, J.-G.; Tan, C.-J.; Lee, K.-M.; Wu, S.-J.; Tung, Y.-L.; Tsai, H.-H.; Ho, K.-C.; Wu, C.-G. Heteroleptic ruthenium antenna-dye for high-voltage dye-sensitized solar cells. *J. Mater. Chem.* **2010**, *20*, 7158–7164. [CrossRef]
64. Chen, C.-Y.; Pootrakulchote, N.; Wu, S.-J.; Wang, M.; Li, J.-Y.; Tsai, J.-H.; Wu, C.-G.; Zakeeruddin, S.M.; Grätzel, M. New ruthenium sensitizer with carbazole antennas for efficient and stable thin-film dye-sensitized solar cells. *J. Phys. Chem. C* **2009**, *113*, 20752–20757. [CrossRef]
65. Choi, H.; Baik, C.; Kim, S.; Kang, M.-S.; Xu, X.; Kang, H.S.; Kang, S.O.; Ko, J.; Nazeeruddin, M.K.; Grätzel, M. Molecular engineering of hybrid sensitizers incorporating an organic antenna into ruthenium complex and their application in solar cells. *N. J. Chem.* **2008**, *32*, 2233–2237. [CrossRef]
66. Chen, W.-C.; Kong, F.-T.; Ghadari, R.; Li, Z.-Q.; Guo, F.-L.; Liu, X.-P.; Huang, Y.; Yu, T.; Hayat, T.; Dai, S.-Y. Unravelling the structural-electronic impact of arylamine electron-donating antennas on the performances of efficient ruthenium sensitizers for dye-sensitized solar cells. *J. Power Sources* **2017**, *346*, 71–79. [CrossRef]
67. Chen, B.-S.; Chen, K.; Hong, Y.-H.; Liu, W.-H.; Li, T.-H.; Lai, C.-H.; Chou, P.-T.; Chi, Y.; Lee, G.-H. Neutral, panchromatic Ru (II) terpyridine sensitizers bearing pyridine pyrazolate chelates with superior DSSC performance. *Chem. Commun.* **2009**, *39*, 5844–5846. [CrossRef] [PubMed]
68. Wang, S.-W.; Chou, C.-C.; Hu, F.-C.; Wu, K.-L.; Chi, Y.; Clifford, J.N.; Palomares, E.; Liu, S.-H.; Chou, P.-T.; Wei, T.-C. Panchromatic Ru (II) sensitizers bearing single thiocyanate for high efficiency dye sensitized solar cells. *J. Mater. Chem. A* **2014**, *2*, 17618–17627. [CrossRef]
69. Chou, C.C.; Wu, K.L.; Chi, Y.; Hu, W.P.; Yu, S.J.; Lee, G.H.; Lin, C.L.; Chou, P.T. Ruthenium (II) Sensitizers with Heteroleptic Tridentate Chelates for Dye-Sensitized Solar Cells. *Angew. Chem.* **2011**, *123*, 2102–2106. [CrossRef]
70. Kimura, M.; Masuo, J.; Tohata, Y.; Obuchi, K.; Masaki, N.; Murakami, T.N.; Koumura, N.; Hara, K.; Fukui, A.; Yamanaka, R. Improvement of TiO<sub>2</sub>/dye/electrolyte interface conditions by positional change of alkyl chains in modified panchromatic Ru complex dyes. *Chem.—A Eur. J.* **2013**, *19*, 1028–1034. [CrossRef]
71. Wu, K.-L.; Hsu, H.-C.; Chen, K.; Chi, Y.; Chung, M.-W.; Liu, W.-H.; Chou, P.-T. Development of thiocyanate-free, charge-neutral Ru (II) sensitizers for dye-sensitized solar cells. *Chem. Commun.* **2010**, *46*, 5124–5126. [CrossRef]
72. Wang, S.-W.; Wu, K.-L.; Ghadiri, E.; Lobello, M.G.; Ho, S.-T.; Chi, Y.; Moser, J.-E.; De Angelis, F.; Grätzel, M.; Nazeeruddin, M.K. Engineering of thiocyanate-free Ru (II) sensitizers for high efficiency dye-sensitized solar cells. *Chem. Sci.* **2013**, *4*, 2423–2433. [CrossRef]
73. Wu, K.-L.; Ku, W.-P.; Clifford, J.N.; Palomares, E.; Ho, S.-T.; Chi, Y.; Liu, S.-H.; Chou, P.-T.; Nazeeruddin, M.K.; Grätzel, M. Harnessing the open-circuit voltage via a new series of Ru (II) sensitizers bearing (iso-) quinolinyl pyrazolate ancillaries. *Energy Environ. Sci.* **2013**, *6*, 859–870. [CrossRef]
74. Sahin, C.; Tozlu, C.; Ocakoglu, K.; Zafer, C.; Varlikli, C.; Icli, S. Synthesis of an amphiphilic ruthenium complex with swallow-tail bipyridyl ligand and its application in nc-DSSC. *Inorg. Chim. Acta* **2008**, *361*, 671–676. [CrossRef]
75. Qin, Y.; Peng, Q. Ruthenium sensitizers and their applications in dye-sensitized solar cells. *Int. J. Photoenergy* **2012**, *2012*, 291579. [CrossRef]
76. Sahin, C.; Dittrich, T.; Varlikli, C.; Icli, S.; Lux-Steiner, M.C. Role of side groups in pyridine and bipyridine ruthenium dye complexes for modulated surface photovoltage in nanoporous TiO<sub>2</sub>. *Sol. Energy Mater. Sol. Cells* **2010**, *94*, 686–690. [CrossRef]
77. Willinger, K.; Fischer, K.; Kisselev, R.; Thelakkat, M. Synthesis, spectral, electrochemical and photovoltaic properties of novel heteroleptic polypyridyl ruthenium (II) donor-antenna dyes. *J. Mater. Chem.* **2009**, *19*, 5364–5376. [CrossRef]
78. Giribabu, L.; Kumar, C.V.; Rao, C.S.; Reddy, V.G.; Reddy, P.Y.; Chandrasekharam, M.; Soujanya, Y. High molar extinction coefficient amphiphilic ruthenium sensitizers for efficient and stable mesoscopic dye-sensitized solar cells. *Energy Environ. Sci.* **2009**, *2*, 770–773. [CrossRef]
79. Kuang, D.; Ito, S.; Wenger, B.; Klein, C.; Moser, J.-E.; Humphry-Baker, R.; Zakeeruddin, S.M.; Grätzel, M. High molar extinction coefficient heteroleptic ruthenium complexes for thin film dye-sensitized solar cells. *J. Am. Chem. Soc.* **2006**, *128*, 4146–4154. [CrossRef]
80. Klein, C.; Nazeeruddin, M.K.; Di Censo, D.; Liska, P.; Grätzel, M. Amphiphilic ruthenium sensitizers and their applications in dye-sensitized solar cells. *Inorg. Chem.* **2004**, *43*, 4216–4226. [CrossRef]

81. Hussain, M.; El-Shafei, A.; Islam, A.; Han, L. Structure–property relationship of extended  $\pi$ -conjugation of ancillary ligands with and without an electron donor of heteroleptic Ru (II) bipyridyl complexes for high efficiency dye-sensitized solar cells. *Phys. Chem. Chem. Phys.* **2013**, *15*, 8401–8408. [[CrossRef](#)]
82. Chandrasekharam, M.; Suresh, T.; Singh, S.P.; Priyanka, B.; Bhanuprakash, K.; Islam, A.; Han, L.; Kantam, M.L. Functionalized styryl bipyridine as a superior chelate for a ruthenium sensitizer in dye sensitized solar cells. *Dalton Trans.* **2012**, *41*, 8770–8772. [[CrossRef](#)]
83. Sivakumar, R.; Recabarren, R.; Ramkumar, S.; Manivel, A.; Alzate-Morales, J.; Contreras, D.; Manidurai, P. Ruthenium (ii) complexes incorporating carbazole–diazfluorene based bipolar ligands for dye sensitized solar cell applications. *N. J. Chem.* **2017**, *41*, 5605–5612. [[CrossRef](#)]

**Disclaimer/Publisher’s Note:** The statements, opinions and data contained in all publications are solely those of the individual author(s) and contributor(s) and not of MDPI and/or the editor(s). MDPI and/or the editor(s) disclaim responsibility for any injury to people or property resulting from any ideas, methods, instructions or products referred to in the content.




**MANIPAL UNIVERSITY  
JAIPUR**

**FACULTY OF DESIGN**

**International Conference on Sustainable Development for  
Heritage and Built Environment**

**22/06/2023 – 23/06/2023**

  
Head, Department of Interior Design  
SD&A, Faculty of Design  
Manipal University Jaipur



## Content of Report

1. Introduction of the Event
2. Objective of the Event
3. Beneficiaries of the Event
4. Brief Description of the event
5. Photographs
6. Poster of an Event
7. Schedule of the Event
8. Attendance of the Event



## 1. Introduction of the Event

The conference is inspired from the critical challenge of human, environmental, heritage and built sustainability concerning the present and future generations in a global-scale context. This theme emphasizes the strong foundation that is provided by using research to inform our everyday practices, policies, and analytical approaches. This interdisciplinary forum is for scholars, teachers, and practitioners from the built environment professional discipline who share an interest in—and concern for— sustainability in an holistic perspective, where environmental, cultural, economic and social concerns intersect. It will provide a platform for various individuals to connect the past and present and develop solutions to a more universal and environmentally friendly approach towards built environment.

The conference will include topics such as

- (i) Sustainable approach to design in built environment,
- (ii) Sustainability & built Heritage,
- (iii) Conserving Built Heritage,
- (iv) Sustainable Policies for Environmental and Infrastructure Planning,
- (v) Earth and Environmental Planning & Design

## 2. Objective of the Event

This conference was a gathering of minds dedicated to addressing the pressing challenges of sustainability that affect our world today and tomorrow. It recognized that sustainability is a multifaceted concept that requires interdisciplinary collaboration and rigorous research. By bringing together scholars, educators, and practitioners, the conference facilitated the exchange of ideas and the development of solutions that promote a more sustainable, resilient, and environmentally friendly built environment.

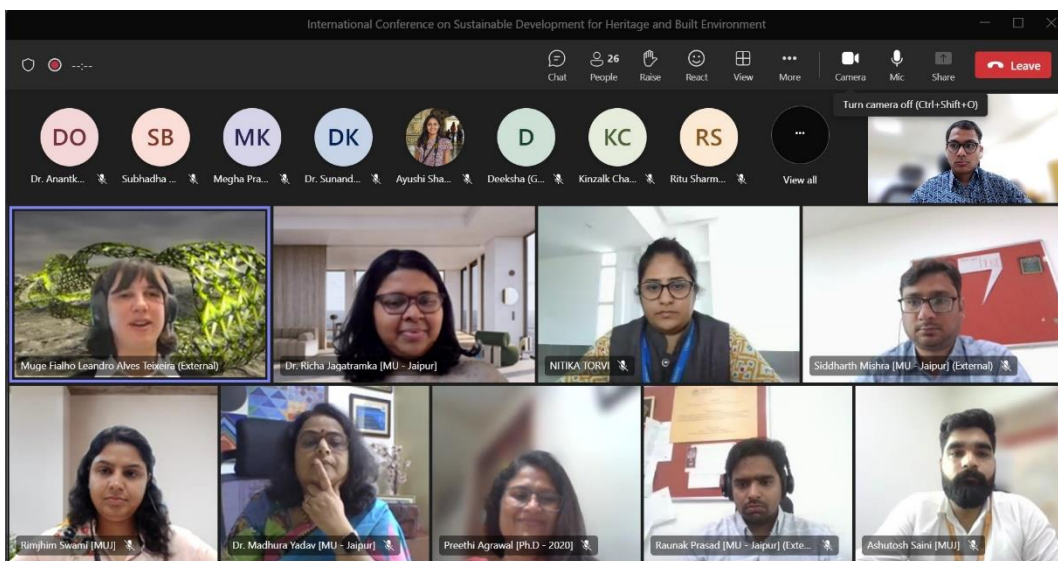
## 3. Beneficiary of the event

This interdisciplinary forum is for scholars, teachers, and practitioners from the built environment professional discipline who share an interest in—and concern for— sustainability in an holistic perspective, where environmental, cultural, economic and social concerns intersect.

## 4. Brief Description of the event

The conference was hosted by Department of Interior Design and School of Architecture and Design, Faculty of Design at Manipal University Jaipur. This interactive and engaging event is tailored exclusively for our researchers, as part of our commitment to foster continuous learning, future research opportunities. The presentations focused on sustainability as the prime agenda and paved way for the researchers to present their work at an international level.

## 5. Photographs of the Event



Snippets of the Conference

## 6. Poster of the event



**MANIPAL UNIVERSITY  
JAIPUR**  
(University under Section 2(f) of the UGC Act)

School of Architecture and  
Design and Department of  
Interior Design

International Conference  
on  
**“Sustainable  
Development for  
Heritage and Built  
Environment”**

**22<sup>nd</sup> June – 23<sup>rd</sup> June 2023**

Venue:  
Manipal University Jaipur/ Hybrid  
Mode

**About the University**  
The Manipal Education Group, with its heritage of excellence in higher education for over 60 years, launched Manipal University Jaipur (MUJ) in 2011. MUJ is affiliated by University Grants Commission, Association of Indian Universities, Council of Architecture, Bar Council of India and All India Council of Technical Education. MUJ is the first university in the state of Rajasthan, accredited as A+ (3.28) grade by NAAC. The university offers courses in different disciplines like Architecture, Interior Design, Fashion Design, Applied arts, Engineering, Management, Hospitality, Humanities & Social Sciences, Journalism and Mass communication, Basic Sciences, Law, Business & Commerce.

**Organizing Committee**  
**Patron**  
Dr. G. K. Prabhu (President, MUJ)  
**Co - Patrons**  
Dr. Thammaiah Chekkera (Pro-President, MUJ)  
Dr. Nitu Bhatnagar (Registrar, MUJ)  
**Chair:**  
Dr. Madhura Yadav (Dean, FoD, MUJ)  
Dr. J.P. Sampath Kumar (Director, SD&A, MUJ)  
**Convenors:**  
Dr. Richa Jagatramka (Assist. Prof., ID-SD&A)  
Ar. Raunak Prasad (Assist. Prof., SA&D)  
**Coordinators:**  
Ar. Megha Prabhu (Assist. Prof., ID-SD&A)  
Ar. Himangshu Kedia (Assist. Prof., ID-SD&A)  
Ar. Akshay Gupta (Assist. Prof., SA&D)  
Ar. Ashutosh Saini (Assist. Prof., SA&D)

**About the Conference**  
The conference will include topics such as

- (i) Sustainable approach to design in built environment,
- (ii) Sustainability & built Heritage,
- (iii) Conserving Built Heritage,
- (iv) Sustainable Policies for Environmental and Infrastructure Planning,
- (v) Earth and Environmental Planning & Design.

Participants will gain exposure and insight To various sustainable approaches to sustain the heritage as well as define the built environment. It will provide a platform for various individuals to connect the past and present and develop solutions to a more universal and environmentally friendly approach towards built environment.

**Submission Deadline:**  
**Call for Papers – 23<sup>rd</sup> Feb 2023**  
**Abstract Submission – 30<sup>th</sup> March 2023**  
**Acceptance Notification – 7<sup>th</sup> April 2023**  
**Full paper Submission – 23<sup>rd</sup> April 2023**

**Publication –**  
**Conference proceedings with IOP**  
**Conference Series: Earth and Environmental Science (SCOPUS Indexed)**

**Notable Speakers**

1. Dr Ranjith Dayaranthe , Associate Professor, Asian School of Architecture, Australia
2. Dr Muge Belek Fialho Teixeira, Queensland University of Technology.
3. Dr. Shikha Jain, Director, DRONAH
4. Dr Rajat Gupta, Oxford Brookes, Director, Dept. of sustainable development
5. Ar. Chitra Vishwanath, Biome Bangalore.

**Conference Fees :**  
Students 9500 INR  
Academics & professional 10500 INR

For International Participants  
Students - 150 USD  
Academics & professional – 180 USD

For additional information contact –  
[richa.jagatramka@jaipur.manipal.edu](mailto:richa.jagatramka@jaipur.manipal.edu)  
[raunak.prasad@jaipur.manipal.edu](mailto:raunak.prasad@jaipur.manipal.edu)

## 7. Schedule of the event

Time	Event	Speaker
11:00 – 11:30 AM	Opening speech	Dr Richa Jagatramka
11: 30 – 11:35 AM	Welcome address	Dr Madhura Yadav
11: 35 – 11:45 AM	Introduction of international speaker	Ar Himangshu Kedia
11: 45 AM – 12:45 PM	Presentation by Dr Muge	Dr Muge
12: 45 – 01:00 PM	Q & A session	
01:00 – 01:05PM	Vote of Thanks	Ar. Himangshu Kedia

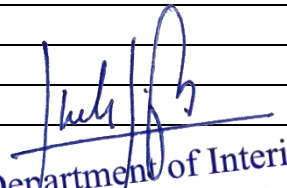
## Meeting Link :

[https://teams.microsoft.com/l/meetup-join/19%3ameeting\\_MmRjNjZiN2ltMTc1NS00YmJlLTkwMTItMzBiYTVjNTIOYTRh%40thread.v2/0?context=%7b%22Tid%22%3a%227d0726e8-bf4b-4ac1-99f1-010fb11f1d3f%22%2c%22Oid%22%3a%2216be8839-914f-456c-9836-e6b3ba8fa2f9%22%7d](https://teams.microsoft.com/l/meetup-join/19%3ameeting_MmRjNjZiN2ltMTc1NS00YmJlLTkwMTItMzBiYTVjNTIOYTRh%40thread.v2/0?context=%7b%22Tid%22%3a%227d0726e8-bf4b-4ac1-99f1-010fb11f1d3f%22%2c%22Oid%22%3a%2216be8839-914f-456c-9836-e6b3ba8fa2f9%22%7d)

## 8. Attendance of the Event

Total attendees – 28 participants from MUJ and outside

Sl.no	Name	Organisation
1	Dr. Richa Jagatramka	FOD
2	Megha Prabhu K	FOD
3	Dr. Sampath Kumar Padmanabha Jinka	FOD
4	Dr. Madhura Yadav	FOD
5	Dr. Anantkumar Dada Ozarkar	FOD
6	Dr. Subhash Chandra Devrath	FOD
7	Nisha Nelson	FOD
8	Preethi Agrawal	Practicing Architect and PhD scholar
9	NITIKA TORVI	Christ University
10	Subhadha B	Christ University
11	Himangshu Kedia	FOD
12	Rushikesh Kolte	MNIT
13	Dr. Sunanda Kapoor	FOD
14	Ananya Tripathi	AKTU - GCA
15	Kinzalk Chauhan	FOD
16	Ritu Sharma	FOS – Phd Scholar
17	Rimjhim Swami	FOD
18	Ayushi Sharma	FOD
19	Apoorva Agarwal	FOD
20	Muge Fialho Leandro Alves Teixeira	QUT Australia
21	Deeksha	MNIT
22	Siddharth Mishra	FOD
23	Akshay Gupta	FOD
24	Ritu Sharma	FOD
25	Neha Saxena	FOD
26	Antima Kuda	MAHE Dubai
27	Raunak Prasad	FOD
28	Ashutosh Saini	FOD

  
Head, Department of Interior Design  
SD&A, Faculty of Design  
Manipal University Jaipur



## Bioprospecting of novel ligninolytic bacteria for effective bioremediation of agricultural by-product and synthetic pollutant dyes

Devendra Jain<sup>a,\*</sup>, Jitendra Kumar Navariya<sup>a</sup>, Ali Asger Bhojiya<sup>a,b</sup>, Abhijeet Singh<sup>c</sup>, Santosh Ranjan Mohanty<sup>d</sup>, Sudhir K. Upadhyay<sup>e,\*</sup>

<sup>a</sup> All India Network Project on Soil Biodiversity and Biofertilizers, Department of Molecular Biology and Biotechnology, Rajasthan College of Agriculture, Maharana Pratap University of Agriculture and Technology, Udaipur 313001, India

<sup>b</sup> Faculty of Science, US Ostwal Science, Arts and Commerce College, Mangalwad, Chittorgarh, Rajasthan 302024, India

<sup>c</sup> Department of Biosciences, Manipal University Jaipur, Jaipur 303007, India

<sup>d</sup> All India Network Project on Soil Biodiversity-Biofertilizers, ICAR-Indian Institute of Soil Science, Bhopal 462038, India

<sup>e</sup> Department of Environmental Science, V.B.S. Purvanchal University, Jaunpur 222003, India

### ARTICLE INFO

#### Keywords:

Lignin  
Methylene blue  
Lignin degradation bacteria  
Ligninolytic enzymes  
16 S rRNA gene sequencing  
Biodegradation

### ABSTRACT

Lignin is a significant renewable carbon source that needs to be exploited to manufacture bio-ethanol and chemical feedstocks. Lignin mimicking methylene blue (MB) dye is widely used in industries and causes water pollution. Using kraft lignin, methylene blue, and guaiacol as a full carbon source, 27 lignin-degrading bacteria (LDB) were isolated from 12 distinct traditional organic manures for the current investigation. The ligninolytic potential of 27 lignin-degrading bacteria was assessed by qualitative and quantitative assay. In a qualitative plate assay, the LDB-25 strain produced the largest zone, measuring  $6.32 \pm 0.297$ , on MSM-L-kraft lignin plates, while the LDB-23 strain produced the largest zone, measuring  $3.44 \pm 0.413$ , on MSM-L-Guaiacol plates. The LDB-9 strain in MSM-L-kraft lignin broth was able to decolorize lignin to a maximum of  $38.327 \pm 0.011\%$  in a quantitative lignin degradation assay, which was later verified by FTIR assay. In contrast, LDB-20 produced the highest decolorization ( $49.633 \pm 0.017\%$ ) in the MSM-L-Methylene blue broth. The highest manganese peroxidase enzyme activity, measuring  $6322.314 \pm 0.034 \text{ U L}^{-1}$ , was found in the LDB-25 strain, while the highest laccase enzyme activity, measuring  $1.5105 \pm 0.017 \text{ U L}^{-1}$ , was found in the LDB-23 strain. A preliminary examination into the biodegradation of rice straw using effective LDB was carried out, and efficient lignin-degrading bacteria were identified using 16SrDNA sequencing. SEM investigations also supported lignin degradation. LDB-8 strain had the highest percentage of lignin degradation (52.86%), followed by LDB-25, LDB-20, and LDB-9. These lignin-degrading bacteria have the ability to significantly reduce lignin and lignin-analog environmental contaminants, therefore they can be further researched for effective bio-waste management mediated breakdown.

### 1. Introduction

Plant biomass naturally decomposes over time and is mostly triggered by enzymatic activity of neighboring bacterial and fungal species (Janusz et al., 2017; da Costa et al., 2018; Jimenez et al., 2018; Lee et al., 2019; Riyadi et al., 2020). Numerous microorganisms, such as bacteria and fungi, have been the focus of the most thorough investigations on lignin alteration and breakdown (Lee et al., 2019; Atiwesh et al., 2022). When lignocellulosic organic wastes are processed for use in the

production of bioethanol and the paper industry, respectively, powerful lignin-degrading microorganisms or their ligninolytic enzymes can be used successfully (Fang et al., 2018; Brink et al., 2019; Li et al., 2022). Plants' rigidity and tensile strength come from lignin, a complex, chemically heterogeneous polymer made up of 4-hydroxyl phenylpropanoid units (Hasanin et al., 2018). Biomass is essentially resistant because lignin acts as a physical barrier to stop cellulose from being hydrolyzed by biological or chemical processes (Wu et al., 2022).

For the production of biofuels, lignocellulosic biomass is highly

\* Corresponding authors.

E-mail addresses: [devendrajain@mpuat.ac.in](mailto:devendrajain@mpuat.ac.in), [devroshan@gmail.com](mailto:devroshan@gmail.com) (D. Jain), [sku.env.lko@gmail.com](mailto:sku.env.lko@gmail.com) (S.K. Upadhyay).

<sup>1</sup> ORCID: <https://orcid.org/0000-0002-4345-1536>

<sup>2</sup> ORCID: <https://orcid.org/0000-0002-2228-8063>

desirable as a raw component (Malode et al., 2021). Lignin and cellulose make up the majority of 80% of crop residue/biomass (Chen et al., 2018). Large volumes of lignocellulosic waste are produced by forestry and agricultural activities, paper-pulp companies, wood industries etc. and burning is a common method of decreasing this waste, which otherwise may contribute to pollution (Haile et al., 2021). Therefore, enhancing lignin breakdown has enormous promise to save the environment and build new beneficial products (Gupta et al., 2022). Chemical contaminants like synthetic dyes are significant contributors to water pollution. Methylene blue (MB) dye is one of these and is frequently used in various industries such as dyeing, textile, tannery, and paper, etc. (Bhat et al., 2022; Pham et al., 2022). Using promising microbial isolates, a biological strategy giving a more affordable and sustainable alternative method has been used to remove MB. Microorganisms, which can degrade MB, come from a wide range of taxa, including *Acinetobacter*, *Aspergillus*, *Bacillus*, *Pseudomonas*, *Staphylococcus* etc. (Eslami et al., 2017; Karim et al., 2018; Bharti et al., 2019; Ogunlaja et al., 2020; Kishor et al., 2021b; Haque et al., 2021). To participate in central carbon metabolism, bacteria that degrade lignin and lignin-imitating dyes secrete extracellular enzymes that break down lignin into smaller components (Beckham et al., 2016). A range of extracellular oxidative enzymes, such as laccases, lignin peroxidases (LiPs), manganese peroxidases (MnPs), and multifunctional peroxidases, are released by the lignin-degrading organisms (Kumar and Chandra, 2020).

Several bacteria, in addition to wood-rot fungus, can degrade lignin (Haq et al., 2022). Pretreatments may become economically viable if lignin is removed selectively using lignin-degrading enzymes (Lee et al., 2019; Wu et al., 2022). A biological (or primarily biological) approach to removing lignin could overcome these limitations, enabling the generation of bio-fuel at a cheaper cost and with less impact on the environment. Microorganisms can produce metabolites and enzymes that hasten the breakdown of organic waste and raise the caliber of soil humus (Singh et al., 2017).

The breakdown of rice straw into smaller products so they can be digested by microorganisms occurs through a microbial process (Goodman, 2020). In the past, the majority of these lignin-degrading bacteria were found in soil and the intestines of insects that fed wood (Zhang et al., 2021). This research was focused on identifying and characterizing the microbial inoculants that causes rice straw to break down so quickly. In this study, we identify new lignin-degrading bacteria from a variety of organic sources, characterize them, and assess their potential for lignin degradation.

## 2. Material and methods

### 2.1. Isolation and screening of lignin-degrading bacteria

The isolation of LDB was carried out using the method reported by Rahman et al. (2013). The minimal salt media-Luria agar (MSM-L agar) medium supplemented with 1% Kraft lignin (KL) as the primary carbon and energy source was used for the isolation of ligninolytic bacteria from freshly prepared organic manures (Jain et al., 2021) (Table 1). The bacterial strains that showed proper growth were purified on fresh MSM-L agar plates and stored at 4 °C. Screening of LDB was carried out on MSM-L agar plate containing Kraft lignin (0.5%) (Chen et al., 2012b) and guaiacol (10%) (Atalla et al., 2010) and methylene blue indicator dye (50 mg/L) (Bandounas et al., 2011) and incubated at 30 ± 2<sup>o</sup> C for 4–5 days for the development of the de-colorization zone. After growth, the plates were taken out and flooded with 10 ml of a ferric chloride/potassium ferricyanide solution [1% (w/v)]. After 10 min, the solution was drained off, leaving the agar where the aromatic compounds were present stained blue or green. It was assumed that a yellowish zone where growth had been eradicated was proof of lignin breakdown (McCarthy and Broda, 1984). The degrading of indicator dye is considered a positive test for lignin degradation (Bandounas et al.,

**Table 1**

Determination of lignolytic activities of lignin degrading bacteria isolated from traditional organic manures.

S. N.	Source	Strain Name	Growth and de-colorization of ligninolytic substrates		
			Kraft Lignin	Guaiacol	Methylene blue
1	JeevaAmrat	SBD-LDB-1	+	+	-
2	BhabhutAmritPani	SBD-LDB-2	+	+	+
3	PanchGavya	SBD-LDB-3	+	+	+
4	MatkaKhad	SBD-LDB-4	+	+	+
5	Vermiwash (Silica enriched)	SBD-LDB-5	+	+	-
6	BeejaAmrat	SBD-LDB-6	+	-	+
7	Vermi Wash	SBD-LDB-7	+	+	+
8	Silica enriched Compost tea	SBD-LDB-8	+	+	+
9	Compost Tea	SBD-LDB-9	+	+	+
10	BD500	SBD-LDB-10	+	+	-
11	BD500	SBD-LDB-11	+	+	+
12	JeevaAmrat	SBD-LDB-12	+	+	-
13	BhabhutAmritPani	SBD-LDB-14	+	+	+
14	PanchGavya	SBD-LDB-15	+	+	-
15	MatkaKhad	SBD-LDB-16	+	+	-
16	Silica enriched vermi wash	SBD-LDB-17	+	+	-
17	BeejaAmrat	SBD-LDB-18	+	-	-
18	Vermi Wash	SBD-LDB-19	+	+	+
19	Compost tea (Silica enriched)	SBD-LDB-20	+	+	+
20	Compost Tea	SBD-LDB-21	+	-	-
21	BD 501	SBD-LDB-22	+	+	+
22	BD 501	SBD-LDB-23	+	+	+
23	PanchGavya	SBD-LDB-24	+	+	+
24	MatkaKhad	SBD-LDB-25	+	+	+
25	Silica enriched vermi wash	SBD-LDB-26	+	+	+
26	BeejaAmrat	SBD-LDB-28	+	+	-
27	Vermi Wash	SBD-LDB-29	+	+	+

2011).

### 3. Ligninolytic enzyme activity assay

A 50 ml conical flask filled with MSM-L medium was used to inoculate the chosen positive isolates for screening assays. These inoculated flasks were incubated for 6 days per the procedures outlined by Rahman et al. (2013), during which time culture samples were collected for manganese peroxidase (MnP) and laccase activity were assessed using the oxidation of Guaiacol (2-methoxyphenol) and ABTS (2, 2'-azinobis-(3-ethylbenzothiazoline-6-sulphonate) method respectively (Rahman et al., 2013; Bourbonnais et al., 1995).

### 3.1. Decolorization activity of bacteria on liquid MSM containing MB dye and Kraft lignin

Decolorization of lignin-mimicking dyes i.e. Methylene Blue (MB) was assessed in test tubes as liquid-phase assays. For broth assays, the individual bacterial strains were grown in MSM containing methylene blue indicator dye (50 mg/L) at 30 °C with shaking at 200 rpm. Control without inoculation was also maintained. The samples were centrifuged and dye de-colorization was absorbance was measured at  $\lambda_{663}$  (Saratale et al., 2009).

All the test bacterial cultures were inoculated in 10 ml of MSM-L agar medium containing 0.5% lignin in 25 ml capacity screwed cap tubes with the maintenance of un-inoculated control for comparison. All the tubes were incubated at  $30 \pm 2^{\circ}$  C at 120 rpm for 5 days in a shaker incubator and color change was measured by spectrophotometer on the 5th day at 465 nm. The decolorization percentage of 0.5% lignin by respective bacteria was calculated using the formula given by (Sani and Banerjee, 1999).

$$\% \text{ decolorization} = \frac{\text{Initial absorbance} - \text{observed absorbance}}{\text{Initial absorbance}} \times 100$$

Additionally, Fourier transform infrared (FTIR) spectroscopy study was done to verify that the isolates had degraded and depolymerized kraft lignin (Khan et al., 2022).

### 3.2. In vitro efficacy of ligninolytic bacteria for degradation of agro-waste residues

After being treated with 1% NaOH for 24 h at room temperature, deionized water was used to adjust the pH to 7, and then the rice straw was dried at 80 °C (Yu et al., 2009). The 3 g quantity of pretreated rice straw was immersed in 100 ml flasks in triplicate and steam sterilized and then 5 ml of selected lignin-degrading bacteria were inoculated in each flask incubated for 21 days at ambient temperature (room temperature) and assayed for lignin degradation and the observations of weight reduction and consistency were also monitored (Bakar et al., 2018). After the end of the incubation period, the acid detergent fiber (ADF) and acid detergent lignin (ADL) methods (Thimmaiah, 2009) were used to determine the amount of lignin in rice straw.

### 4. Effects of bio-pretreatment on the structure of the rice straw

Using a freeze drier, untreated and bio-pretreated rice straw was dehydrated. Using a scanning electron microscope (SEM), the various surface morphologies of the untreated and bio-pretreated rice stover were observed (Dong et al., 2019).

### 5. Sequencing and Phylogenetic Analysis of 16 S rDNA of Potent LDB Isolates

The five most effective LDB isolates' PCR-amplified 16 S rDNA region was sequenced using an automated DNA sequencer (ABI model 377, Applied Biosystems, USA) in accordance with the normal technique utilizing universal 16 S rDNA primers (27 F and 1492 R; amplicons size  $\approx$  1465 bp). Prior to BLAST, the 16 S rDNA sequences were modified using the Bio Edit software. Utilizing the nucleotide BLASTn programme, the sequences collected during the investigation were compared to previously submitted sequences in the nucleotide database GenBank at the National Center for Biotechnology (NCBI) (Altschul et al., 1990). The online programme CLUSTAL-W was used to align the 16 S rDNA consensus sequences (Thompson et al., 1994). Phylogenetic trees were constructed using this alignment and the greatest likelihood technique using MEGA 6.06 software (Tamura et al., 2013).

### 6. Statistical analyses

Using SPSS-20, the statistical analysis known as the standard

deviation (SD) was performed on all the observed data. Additionally, correlation functional interaction between all chosen bacterial isolates' production of the enzymes that break down Kraft lignin and Methylene Blue was performed using Past3 software, and correlation heat maps were created using TB tools.

## 7. Result and discussion

### 7.1. Isolation and screening of lignin degrading bacteria

The isolation and screening of lignin-degrading bacteria were carried out on the MSM-L agar medium supplemented with Kraft lignin (0.5%), Guaiacol (10%), and Methylene blue (50 mg/L). In the present study, 27 lignin-degrading bacteria were isolated and purified from 12 different organic produces and are summarized in Table 1. All the strains were able to grow on MSM-L containing Kraft lignin (0.5%), whereas 24 strains and 18 strains were able to grow and utilize Guaiacol (10%) and Methylene blue (50 mg/L) respectively. The 16 strains along with the positive culture showed positive growth and de-colorization on all three different ligninolytic substrates. The decolorization zone was measured to determine the lignin degradation index (LDI), and the findings are shown in Table 2. This is the first report that we are aware of lignin-degrading microbial strains being isolated from conventional liquid organic manures.

The various lignin-degrading bacteria were identified in rotting oil palm, empty fruit bunches, rotten wood, textile effluent, and sludge etc. (Faisal et al., 2021; Kishor et al., 2021a). While Harith et al. (2014) isolated 8 strains with lignin degradation ability from agro-industrial waste, Sharifi-Yazdi et al. (2001) isolated 22 LDB strains from decayed plants, Falade et al. (2017) isolated 30 potential strains of ligninolytic bacteria from water and sediment samples, and Couger et al. (2020) isolated lignin-degrading bacteria from the termite gut. Nahrowi et al. (2018) previously reported a correlation between ligninolytic activities of bacterial isolates and the lignin degradation index (LDI), and they

**Table 2**

Determination of lignolytic activities of lignin degrading bacteria using plate assay by measuring decolourisation zone.

S.NO	Strain Name	Lignin degradation index by measuring decolourisation zone after 72 h	
		Kraft Lignin (0.5%)	Guaiacol (10%)
1	SBD-LDB-1	3.24 ± 0.035	2.86 ± 0.125
2	SBD-LDB-2	2.1 ± 0.10	2.21 ± 0.257
3	SBD-LDB-3	3.6 ± 0.200	2.28 ± 0.145
4	SBD-LDB-4	3.46 ± 0.351	1.31 ± 0.162
5	SBD-LDB-5	1.01 ± 0.11	1.83 ± 0.175
6	SBD-LDB-6	1.04 ± 0.12	ND
7	SBD-LDB-7	3.38 ± 0.325	1.63 ± 0.126
8	SBD-LDB-8	5.23 ± 0.321	3.01 ± 0.225
9	SBD-LDB-9	5.47 ± 0.240	3.21 ± 0.256
10	SBD-LDB-10	3.48 ± 0.141	1.65 ± 0.200
11	SBD-LDB-11	4.53 ± 0.251	3.02 ± 0.087
12	SBD-LDB-12	5.15 ± 0.160	2.21 ± 0.256
13	SBD-LDB-14	2.35 ± 0.100	2.01 ± 0.225
14	SBD-LDB-15	0.94 ± 0.18	1.78 ± 0.257
15	SBD-LDB-16	4.32 ± 0.192	2.26 ± 0.205
16	SBD-LDB-17	5.57 ± 0.222	2.41 ± 0.272
17	SBD-LDB-18	0.98 ± 0.08	ND
18	SBD-LDB-19	1.24 ± 0.250	1.52 ± 0.087
19	SBD-LDB-20	5.17 ± 0.210	3.30 ± 0.174
20	SBD-LDB-21	0.84 ± 0.14	ND
21	SBD-LDB-22	3.34 ± 0.262	2.36 ± 0.127
22	SBD-LDB-23	6.14 ± 0.161	3.44 ± 0.413
23	SBD-LDB-24	6.31 ± 0.298	2.88 ± 0.247
24	SBD-LDB-25	6.32 ± 0.297	3.29 ± 0.187
25	SBD-LDB-26	3.61 ± 0.135	2.09 ± 0.085
26	SBD-LDB-28	1.04 ± 0.13	1.93 ± 0.081
27	SBD-LDB-29	3.42 ± 0.186	2.84 ± 0.177

\*ND: Not Detected; Data (Mean of triplicate value ± SD)

demonstrated that lignin-degrading bacterial isolates had LDI values ranging from 2.6 to 1.22, validating the results of the Lignin degradation index by lignin-degrading bacterial strains. Falade et al. (2017) assessed the lignin-degrading activity of bacterial strains using guaiacol decolorization and found that only 5 strains out of 30 displayed decolorization zone, which validates our current findings.

### 8. Ligninolytic enzyme activity assay

The quantification of ligninolytic enzymes viz. Manganese peroxidase enzyme and Laccase enzyme in the lignin-degrading bacteria were conducted further to understand the mechanism of their ligninolytic activities. The results of the Manganese peroxidase enzyme and Laccase enzyme were summarized in Fig. 1.

Fig. 1 shows the correlation between the percentage of KL and MB elimination and the bacterial enzymes (MnP and laccase). The lines in the graph below indicate the ligninolytic bacteria, while the columns stand in for the enzymes. The level of enzymatic activity was indicated by the colour of the tiles. The bacterial strains SBD-LDB-9, SBD-LDB-8, SBD-LDB-20, SBD-LDB-23, and SBD-LDB-25 that significantly reduce KL and MB were determined to have the highest enzymatic activity, as depicted in Fig. 1.

The highest Manganese peroxidase enzyme activity of  $6322.314 \pm 0.034 \text{ U L}^{-1}$  was observed in the strain SBD-LDB-25 whereas the minimum activity of  $2630.854 \pm 0.031 \text{ U L}^{-1}$  was observed in SBD-LDB-3 strain. In the case of Laccase enzyme, the maximum degradation activity was observed in SBD-LDB-23 strain of  $1.510 \pm 0.017 \text{ U ml}^{-1}$  whereas minimum activity was reported in SBD-LDB-18

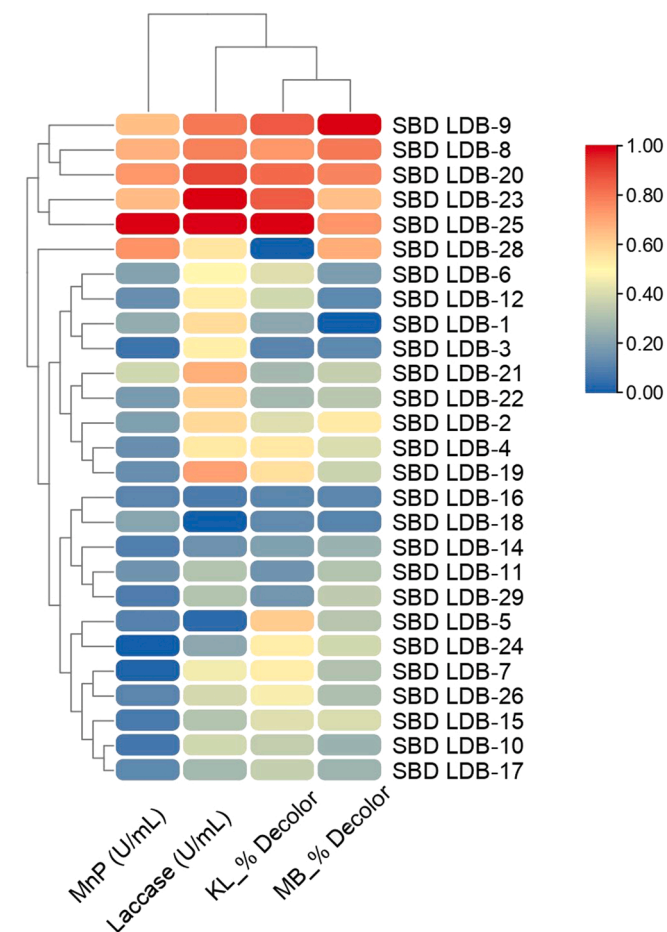


Fig. 1. Heatmap correlation analysis of the percentage of KL (Kraft Lignin) and MB (Methylene Blue) removed by several bacterial isolates producing the enzymes MnP and laccase.

strain of  $0.825 \pm 0.026 \text{ U ml}^{-1}$ . Shamseldin and Abdelkhalek (2015) studied Manganese peroxidase enzyme activities and reported that MnP activity was found as  $1720 \text{ U L}^{-1}$  and  $1750 \text{ U L}^{-1}$  after the third day whereas the Laccase enzymes were found as  $810 \text{ U L}^{-1}$  and  $915 \text{ U L}^{-1}$  after six days in two examined LDB strains. The enzyme activities reported by Shamseldin, Abdelkhalek (2015) were lower compared to the results obtained in the present studies. The results observed by Chen et al. (2012a) and Yang et al. (2017) were in close agreement with the result obtained in the present study. Chen et al. (2012b) revealed the maximum Manganese peroxidase activity was  $3229.8 \text{ U L}^{-1}$  on the 4th day and the highest Laccase activity of  $1275 \text{ U L}^{-1}$  was recorded at the 5th day of the growth of the bacteria. Yang et al. (2017) reported that the Laccase activity of most LDB increased significantly from 24 to 48 h, with a maximum of  $2250 \text{ U L}^{-1}$  in the bacterial strain H2 at 60 h incubation. In the case of the Manganese peroxidase enzyme, the highest activity of  $1119 \text{ U L}^{-1}$  was observed in strain J12 at 24 h.

#### 8.1. Decolorization activity of bacteria on liquid MSM containing MB dye and Kraft lignin

The quantitative determination of the ligninolytic activities of the LDB was identified by measuring of percent decolorization of MSM-L broth medium supplemented with kraft lignin (0.5%) and Methylene blue indicator dye (50 mg/L) after 72hrs of incubation. All the strains showed significant activity and the results of the % degradation of Kraft lignin and methylene blue indicator dye were summarized in Table 3.

The data of the % decolorization is displayed in heat map graph format in Fig. 1. It is a method of condensing information, with the lines denoting the investigated ligninolytic bacteria and the columns denoting Kraft Lignin and Methylene Blue decolorization. The degree of the % decolorization is shown by the colored tiles. Fig. 1 demonstrates that the bacterial strains SBD-LDB-9, SBD-LDB-8, SBD-LDB-20, SBD-LDB-23, and SBD-LDB-25 achieved the highest % decolorization.

The maximum percent decolorization of  $38.327 \pm 0.011\%$  was observed by the SBD-LDB-9 strain in MSM-L broth containing Kraft

Table 3  
Quantitative determination of Ligninolytic activity of bacteria.

S.N.	Percent decolourisation		
	Strain Name	Kraft lignin (0.25%)	Methylene blue (50 mg/L)
1	SBD-LDB-1	19.566 ± 0.010	17.866 ± 0.013
2	SBD-LDB-2	21.025 ± 0.005	30.250 ± 0.016
3	SBD-LDB-3	23.587 ± 0.025	23.495 ± 0.018
4	SBD-LDB-4	19.771 ± 0.027	21.684 ± 0.012
5	SBD-LDB-5	19.809 ± 0.012	22.222 ± 0.017
6	SBD-LDB-6	24.429 ± 0.021	26.383 ± 0.015
7	SBD-LDB-7	23.419 ± 0.020	28.732 ± 0.012
8	SBD-LDB-8	37.298 ± 0.013	46.256 ± 0.020
9	SBD-LDB-9	38.327 ± 0.011	48.458 ± 0.015
10	SBD-LDB-10	24.317 ± 0.021	29.613 ± 0.007
11	SBD-LDB-11	20.819 ± 0.014	30.886 ± 0.016
12	SBD-LDB-12	30.134 ± 0.028	38.228 ± 0.017
13	SBD-LDB-14	22.409 ± 0.031	29.662 ± 0.019
14	SBD-LDB-15	19.0422 ± 0.012	21.390 ± 0.013
15	SBD-LDB-16	22.858 ± 0.011	23.201 ± 0.014
16	SBD-LDB-17	29.985 ± 0.012	44.542 ± 0.019
17	SBD-LDB-18	17.385 ± 0.015	22.663 ± 0.014
18	SBD-LDB-19	18.387 ± 0.011	30.299 ± 0.012
19	SBD-LDB-20	35.185 ± 0.030	49.633 ± 0.017
20	SBD-LDB-21	23.943 ± 0.016	29.075 ± 0.012
21	SBD-LDB-22	23.228 ± 0.007	32.795 ± 0.006
22	SBD-LDB-23	35.652 ± 0.005	46.941 ± 0.022
23	SBD-LDB-24	22.521 ± 0.019	31.082 ± 0.012
24	SBD-LDB-25	33.558 ± 0.017	47.969 ± 0.007
25	SBD-LDB-26	25.065 ± 0.009	39.452 ± 0.020
26	SBD-LDB-28	16.666 ± 0.009	26.258 ± 0.017
27	SBD-LDB-29	23.251 ± 0.014	30.299 ± 0.010

Data (Mean of triplicate value ± SD)



lignin whereas the minimum activity was observed in the SBD-LDB-28 strain with  $16.666 \pm 0.009\%$  decolorization. A similar percent decolorization was observed in MSM-L broth containing Methylene blue dye and after 72 hrs incubation, the maximum percent decolorization ( $49.633 \pm 0.017\%$ ) was observed in the SBD-LDB-20 strain whereas the minimum percent decolorization ( $17.866 \pm 0.013\%$ ) was observed in SBD-LDB-1 strain. It has been speculated that the depolymerization of lignin polymers by bacterial ligninolytic systems, which consists of several enzymes secreted by these bacteria, is what causes the reduction in a color that results from lignin biodegradation. *Bacillus amyloliquefaciens* (SL-7) bacteria produced manganese peroxidase, lignin peroxidase, Laccase activity, and degraded 28.55% of tobacco straw lignin (Mei et al., 2020). Xiong et al. (2013) reported that *Panteoa* spp. strain Sd-1 effectively reduced lignin color (52.4%) after 4 days of incubation. The ligninolytic bacterial strain, *Bacillus velezensis*, was used by Verma et al. (2020) and found that under ideal conditions, this strain had a maximum capacity for KL decolorization and degradation of 56.16% and 40.39%, respectively. These findings were in close agreement with those of the current study.

## 9. FTIR analysis

The lignin-degrading bacterial isolates were evaluated using FT-IR to determine how they had altered the structural and chemical properties of kraft lignin (Fig. 2). Lignin degradation was evident from the FTIR spectra of untreated and treated kraft lignin using lignin degrading bacteria depicted discrete changes, especially in the FTIR absorbance range from  $1350$  to  $1715$   $\text{cm}^{-1}$  correlated to the stretching of C=C bonds in the aromatic skeleton of lignin when incubated in the broth for 5 days (Wang et al., 2021). The C=C bonds in the aromatic skeleton of lignin are the primary targets of the ligninolytic enzymes, resulting in lignin structural depolymerization (Zeng et al., 2014). Further, the decrease in absorbance around wave number  $3500$ – $3000$   $\text{cm}^{-1}$  corresponds to –OH bonds in alcohol and phenol in lignin in treated samples also indicating lignin degradation (Khan et al., 2022). Kraft lignin's FTIR spectrum underwent significant changes at  $3210$   $\text{cm}^{-1}$  (OH stretching

vibration),  $2927$   $\text{cm}^{-1}$  (stretching vibration of C–H band in  $\text{CH}_2$ ,  $\text{CH}_3$ , and  $\text{CH}_3\text{O}$  groups of the lignin structure),  $2860$   $\text{cm}^{-1}$  (C–H stretching in aromatic methoxyl groups),  $1715$   $\text{cm}^{-1}$  (C=O stretching),  $1650$   $\text{cm}^{-1}$  (Absorbed O–H and conjugated C–O),  $1635$   $\text{cm}^{-1}$  (C=C stretching vibration in benzene ring),  $1580$   $\text{cm}^{-1}$ ,  $1511$   $\text{cm}^{-1}$  (attributed to the stretching vibration of aromatic rings),  $1420$   $\text{cm}^{-1}$  (O– $\text{CH}_3$  stretching vibration),  $1330$   $\text{cm}^{-1}$  (–CH stretching vibration),  $1042$   $\text{cm}^{-1}$  (C–O vibrations) and  $618$   $\text{cm}^{-1}$  (stretching vibrations of the C–S bond linked to the aromatic ring) (Kumar et al., 2015; Xu et al., 2018; Ma et al., 2021). The absorbance at  $1335$   $\text{cm}^{-1}$  (S) significantly decreased during biodegradation, but the absorbance at  $1275$   $\text{cm}^{-1}$  (G) barely changed. Significant differences between the FTIR spectra of the treated samples and the control samples showed that the lignin structure was largely destroyed by the different enzymes secreted by LDB used in the present study.

### 9.1. In vitro screening of lignin-degrading bacteria using rice straw bio-waste as substrate

Furthermore, research was conducted to determine the optimal strain for in vitro degradation of agricultural waste. The consistency of rice straw altered when the lignin content in the straw was broken down by lignin-degrading bacteria, as shown in Fig. 3. The results of the decomposition of rice straw by using lignin degrading bacteria were summarized in Table 4. In rice straw that had been exposed to lignin-degrading bacteria, the amount of lignin was substantially reduced after 20 days after inoculation compared to the control rice straw. Among all LDB strains, the maximum percent lignin degradation were obtained in the SBD-LDB-8 strain (52.86%) followed by SBD-LDB-25 (52.69%), and SBD-LDB-20 (48.01%) and SBD-LDB-9 (45.99%) whereas the minimum percent lignin degradation was observed in SBD-LDB-17 strain (17.98%).

In a comparison of three bacterial isolates for lignin degradation on rice straw, Bakar et al. (2018) found that the rice straw treated with the AMB1 bacterial strain had significantly less lignin, at 4.97% compared to the lignin content of the control which was  $8.89 \pm 1.0$ . Similarly,

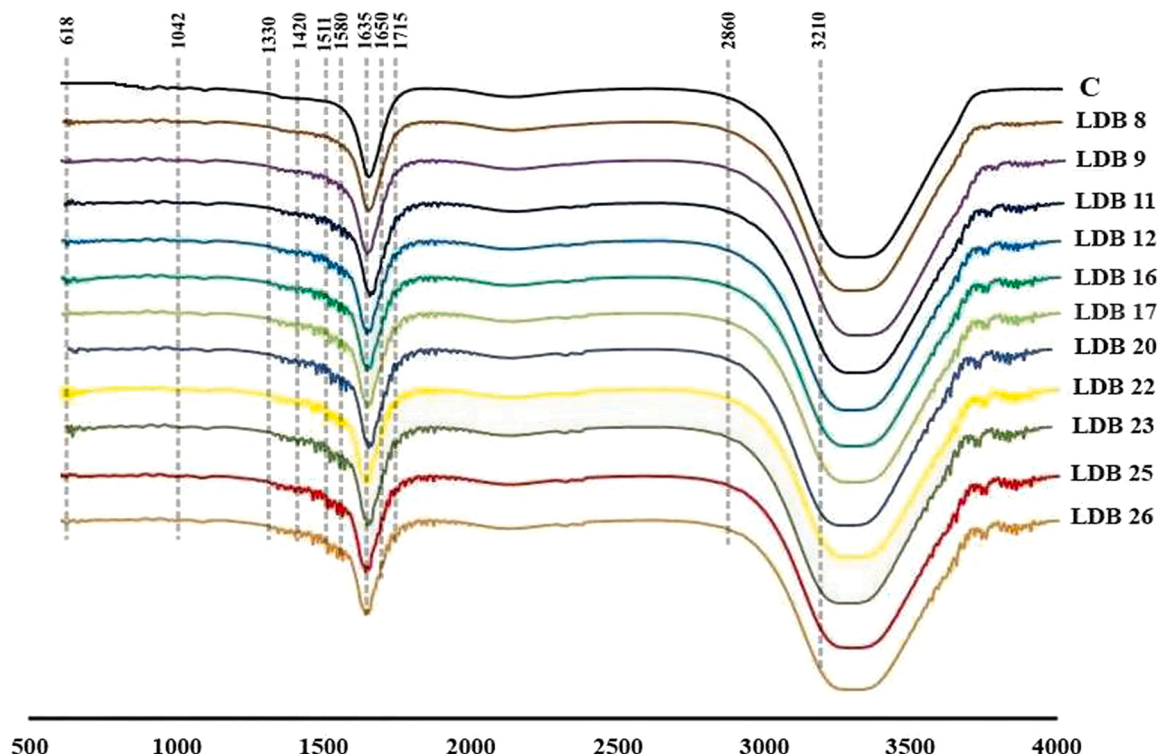


Fig. 2. FTIR spectrum of LDB treated and untreated kraft lignin.



Fig. 3. *In vitro* efficacy evaluation of lignin degrading bacteria for rice-straw degradation.

Table 4

Effect of effective lignin degrading bacteria pretreatment on the composition of rice straw.

Strain Name	ADF %*	ADL %* *	ASH %	Lignin%	% Lignin degradation
CONTROL	88.04	25.35	7	18.35 ± 0.014	100
SBD-LDB-8	68.43	13.98	5.3	8.65 ± 0.018	52.86
SBD-LDB-9	69.55	13.91	4	9.91 ± 0.016	45.99
SBD-LDB-11	76.03	18.73	4.6	14.06 ± 0.044	23.37
SBD-LDB-12	74.06	15.03	4	11.03 ± 0.027	39.89
SBD-LDB-16	75.44	16.55	4.6	11.08 ± 0.045	39.61
SBD-LDB-17	78.14	18.72	3.6	15.05 ± 0.023	17.98
SBD-LDB-20	72.46	13.87	4.3	9.54 ± 0.023	48.01
SBD-LDB-22	77.72	17.73	4.6	13.06 ± 0.015	28.82
SBD-LDB-23	69.42	13.57	3.6	9.91 ± 0.008	45.99
SBD-LDB-25	66.53	12.02	3.3	8.68 ± 0.038	52.69
SBD-LDB-26	76.16	16.78	4	12.78 ± 0.016	30.35

\* Acid Detergent Lignin: Lignin+Ash (Data recorded after 21 days pretreatment)

\* Acid Detergent Fiber (Cellulose+Hemi-cellulose+Lignin+Mineral);

*Ochrobactrum oryzae* BMP03 strain-treated rice straw's chemical makeup was investigated by Tsegaye et al. (2018) and reported that the BMP03 treatment degraded and mineralized 53.74% lignin after 14 days of pretreatment. According to Chandra et al. (2007), *Novosphingobium* sp. B-7 bacteria were responsible for 37% of the breakdown of Kraft lignin. Shi et al. (2017) found that after 7 days of pretreatment with the *Cupriavidus basilensis* B-8 bacterial strain, 41.5% of kraft lignin was eliminated, which was quite similar to the findings of the current study.

### 9.2. Effects of bio-pretreatment on the structure of the rice straw using SEM

The morphological modification of the rice straw that was treated by lignin-degrading bacterial isolates was analysed by scanning electron microscopy. The original rice straw displayed smooth, well-organized, and complete frameworks (Fig. 4). It was noticed that the surface was fairly smooth. It became fragmented and porous after being treated with lignin-degrading bacterial isolates. The rice straw developed some holes. After bacterial treatment, the rice straw's morphology showed that its linkages had been broken, and its lignin contents had been noticeably reduced. Various researchers observed the change in morphology of lignin using SEM which confirm the degradation of lignin visually (Xu et al., 2018; Ma et al., 2021). Dong et al. (2019) analyzes the lignin degradation by SEM technique and they observed that the microbial treated lignin sample became cracked and porous as compared to

ordered and intact structures of untreated lignin samples which further supports the observation in the present study.

### 9.3. Sequencing and phylogenetic analysis of 16 S rDNA of potent LDB isolates

Based on *in vitro* rice straw degradation efficacy, the comprehensive sequences of the 16 S rDNA genes of the most effective lignin-degrading bacterial strains were sequenced and examined using the nucleotide BLASTn programme. These strains were identified as LDB-8: *Enterobacter ludwigii* (MW264070), LDB-25: *Klebsiella variicola* (MW265009), LDB-20: *Rahnella aquatilis* (MW264333), LDB-9: *Bacillus paramycoides* (MW264994), and LDB-23: *Bacillus paramycoides* (MW423733) as shown in Fig. 5. Table 5 lists the molecular details and NCBI GeneBank accession number associated with these strains. Similar approach was adopted by Upadhyay et al. (2009, 2011) for identification of salt tolerant rhizobacterial isolates. Rahman et al. (2013) characterized lignin-degrading bacteria using 16 SrRNA gene sequencing analysis and identified the bacterial strains as *Bacillus* sp., *Ochrobactrum* sp., and *Leucobactersp.*, with 99% sequence similarity to the strains from NCBI-Gene bank databases. El-Hanafy et al. (2008) isolated two lignin-degrading bacterial strains from Egyptian soils and identified them as *Bacillus* sp. (EU344809) and *Bacillus subtilis* based on the partial 16 S rRNA sequencing (EU344808). From a decomposing empty fruit bunch of an oil palm, Riyadi et al. (2020) isolated and described a lignin-degrading bacterial strain. Based on 16S rDNA sequencing, the isolated strain was identified as *Streptomyces* sp. S6.

## 10. Conclusion

The current investigation was based on the isolation of 27 lignin-degrading bacteria from 12 conventional manures. These strains were strong in ligninolytic enzymes such laccase and MnP, which can degrade KL and MB. SBD-LDB-8, SBD-LDB-25, SBD-LDB-20, SBD-LDB-9, and SBD-LDB-23 were shown to be the best LDB isolates based on their *in vitro* lignin degradation capacity using rice straw as the substrate. SEM images indicating changes in surface morphological properties linked with lignin breakdown backed up this claim. Despite tremendous progress in the isolation and characterization of lignin-degrading microbes to date, appropriate and effective formulations for waste breakdown and biodegradation of synthetic dyes like MB must be developed. According to these results, the isolated LDB strains from the current study would make a good choice for lignin valorization. Therefore, more thorough research is needed to establish their capacity to degrade waste biomass on the ground and in certain environmental conditions.

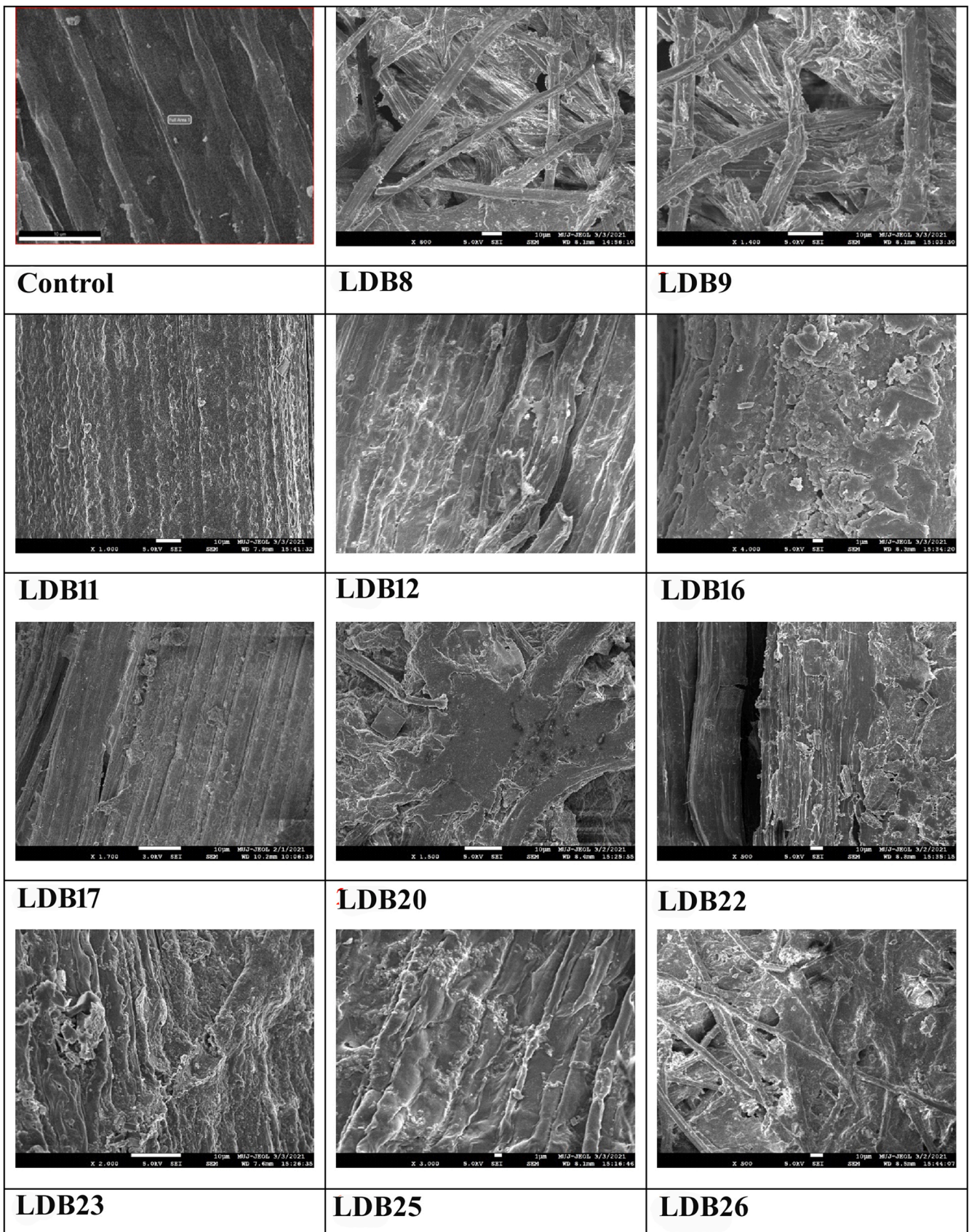


Fig. 4. Scanning electron micrographs of the control and LDB treated rice straw for 21 days.

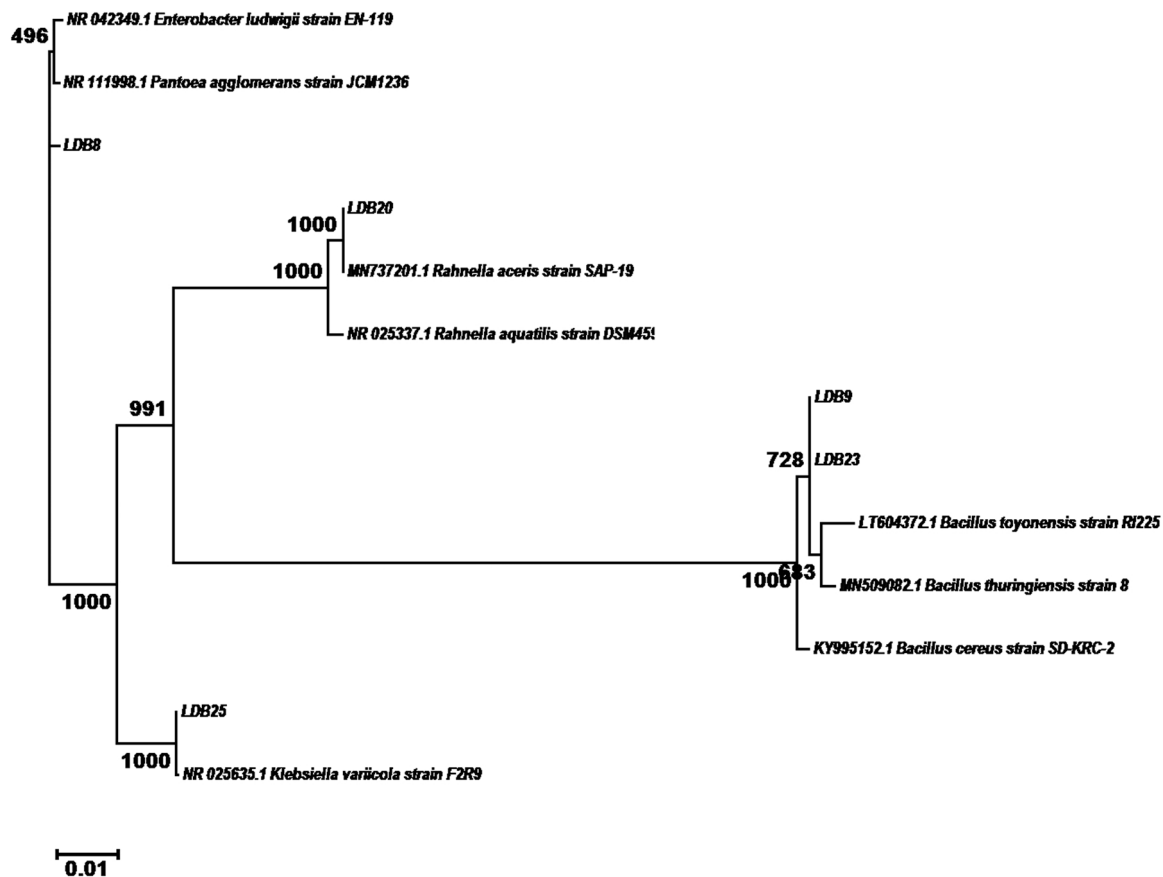


Fig. 5. Phylogenetic analysis of potent lignin degrading bacteria.

**Table 5**  
Molecular identification of potent Lignin Degrading Bacteria.

Strains	Identification/ Accession number	Closest type strain			
		Molecular identity	Strain	Accession number	% Similarity/ Query Coverage
LBD-8	<i>Enterobacter ludwigii</i> / MW264070	<i>Enterobacter ludwigii</i>	EN-119	NR_042349.1	99.71/100
LDB-9	<i>Bacillus paramycooides</i> / MW264994	<i>Bacillus paramycooides</i>	MCCC 1A04098	NR_157734.1	99.00/99.09
LBD-20	<i>Rahnella aquatilis</i> / MW264333	<i>Rahnella aquatilis</i>	DSM 4594	NR_025337.1	99.57/100
LDB-23	<i>Bacillus paramycooides</i> / MW423733	<i>Bacillus paramycooides</i>	MCCC 1A04098	NR_157734.1	99.00/99.09
LBD-25	<i>Klebsiella variicola</i> / MW265009	<i>Klebsiella variicola</i>	F2R9	NR_025635.1	99/100

#### CRediT authorship contribution statement

DJ conceived and designed the experiments; JKN, AAB performed laboratory experiments; AS performed FTIR and SEM analysis; DJ, AAB, SKU, and SRM wrote the manuscript. All authors read and approved the final manuscript.

#### Declaration of Competing Interest

The authors declare that they have no known competing financial interests or personal relationships that could have appeared to influence the work reported in this paper.

#### Data Availability

Data will be made available on request.

#### Acknowledgments

The financial assistance from the All India Network Project on soil biodiversity and biofertilizers is highly acknowledged.

#### Disclosure statement

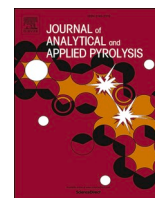
No potential conflict of interest was reported by the authors.

#### References

- Altschul, S.F., Gish, W., Miller, W., Myers, E.W., Lipman, D.J., 1990. Basic local alignment search tool. *J. Mol. Biol.* 215 (3), 403–410.
- Atalla, M.M., Zeinab, H.K., Eman, R.H., Amani, A.Y., Abeer, A.A.E.A., 2010. Screening of some marine-derived fungal isolates for lignin degrading enzymes (LDEs) production. *Agric. Biol. J. North Am.* 1 (4), 591–599.
- Atiweh, G., Parrish, C.C., Banoub, J., Le, T.T., 2022. Lignin degradation by microorganisms: a review. *Biotechnol. Prog.* 38 (2), e3226 <https://doi.org/10.1002/btpr.3226>.

- Bakar, N.A.A., Rahman, M.H.A., Shakri, N.A., Bakar, S.A., Hamid, A.A., 2018. Preliminary study on rice straw degradation using microbial inoculant under shake flask condition. *Afr. J. Biotechnol.* 17 (49), 1377–1382.
- Bandounas, L., Wierckx, N.J., de Winde, J.H., Ruijsenaars, H.J., 2011. Isolation and characterization of novel bacterial strains exhibiting ligninolytic potential. *BMC Biotechnol.* 11 (1), 94.
- Beckham, G.T., Johnson, C.W., Karp, E.M., Salvachua, D., Vardon, D.R., 2016. Opportunities and challenges in biological lignin valorization. *Curr. Opin. Biotechnol.* 42, 40–53.
- Bharti, V., Vikrant, K., Goswami, M., Tiwari, H., Sonwani, R.K., Lee, J., Tsang, D.C.W., Kim, K.H., Saeed, M., Kumar, S., et al., 2019. Biodegradation of methylene blue dye in a batch and continuous mode using biochar as packing media. *Environ. Res.* 1, 356–364.
- Bourbonnais, R., Paice, M.G., Reid, I.D., Lanthier, P., Yaguchi, M., 1995. Lignin oxidation by laccase isozymes from *Trametes versicolor* and role of the mediator 2,2-azino-bis(3-ethylbenzothiazoline-6-sulfonate) in kraft lignin depolymerization. *Appl. Environ. Microbiol.* 61, 1876–1880.
- Brink, D.P., Ravi, K., Lidén, G., et al., 2019. Mapping the diversity of microbial lignin catabolism: experiences from the eLignin database. *Appl. Microbiol. Biotechnol.* 103, 3979–4002. <https://doi.org/10.1007/s00253-019-09692-4>.
- Chandra, R., Raj, A., Purohit, H.J., Kapley, A., 2007. Characterisation and optimisation of three potential aerobic bacterial strains for kraft lignin degradation from pulp paper waste. *Chemosphere* 67 (4), 839–846.
- Chen, X., Hu, Y., Feng, S., et al., 2018. Lignin and cellulose dynamics with straw incorporation in two contrasting cropping soils. *Sci. Rep.* 8, 1633. <https://doi.org/10.1038/s41598-018-20134-5>.
- Chen, Y.H., Chai, L.Y., Zhu, Y.H., Yang, Z.H., Zheng, Y., Zhang, H., 2012a. Biodegradation of Kraft lignin by a bacterial strain *Comamonas* sp. B-9 isolated from eroded bamboo slips. *J. Appl. Microbiol.* 112 (5), 900–906.
- Chen, Y.H., Chai, L.Y., Tang, C., Yang, Z.H., Zheng, Y., Shi, Y., Zhang, H., 2012b. Kraft lignin biodegradation by *Novosphingobium* sp. B-7 and analysis of the degradation process. *Bioresour. Technol.* 123, 682–685.
- da Costa, R.R., Hu, H., Pilgaard, B., Vreeburg, S.M.E., Schückel, J., Pedersen, K.S.K., Kracun, S.K., Busk, P.K., Harholt, J., Sapoutziz, P., Lange, L., Aanen, D.K., Poulsen, M., 2018. Enzyme activities at different stages of plant biomass decomposition in three species of fungus-growing termites. *Appl. Environ. Microbiol.* 84 (5), e01815–e01817. <https://doi.org/10.1128/AEM.01815-17>.
- Couger, M.B., Graham, C., Fathepure, B.Z., 2020. Genome sequence of lignin-degrading *Arthrobacter* sp. Strain RT-1, isolated from termite gut and rumen fluid. *Microbiol. Resour. Announc.* 9, 3.
- Dong, S.-J., Zhang, B.-X., Wang, F.-L., Xin, L., Gao, Y.-F., Ding, W., He, X.-M., Liu, D., Hu, X.-M., 2019. Efficient lignin degradation of corn stalk by *Trametes* with high Laccase activity and Enzymatic stability in salt and ionic liquid. *BioResources* 14 (3), 5339–5354.
- El-Hanafy, A.A., Abd-Elsalam, H.E., Hafez, E.E., 2008. Molecular characterization of two native Egyptian ligninolytic bacterial strains. *J. Appl. Sci. Res.* 4 (10), 1291–1296.
- Eslami, H., Khavidak, S.S., Salehi, F., Khosravi, R., Ali Fallahzadeh, R., Peirovi, R., Sadeghi, S., 2017. Biodegradation of methylene blue from aqueous solution by bacteria isolated from contaminated soil. *J. Adv. Environ. Health Res.* 5, 10–15.
- Faisal, U.H., Sabri, N.S.A., Yusoff, N., Tahir, A.A., Said, N.N.M., Riyadi, F.A., Akhir, F.N.M., Othman, N., Hara, H., 2021. Draft genome sequence of lignin-degrading *Agrobacterium* sp. strain S2, isolated from a decaying oil palm empty fruit bunch. *Microbiol. Resour. Announc.* 10, e00259–21. <https://doi.org/10.1128/MRA.00259-21>.
- Falade, A.O., Eyisi, O.A., Mabinya, L.V., Nwodo, U.U., Okoh, A.I., 2017. Peroxidase production and ligninolytic potentials of fresh water bacteria *Raoultella ornithinolytica* and *Ensifer adhaerens*. *Biotechnol. Rep.* 16, 12–17.
- Fang, X., Li, Q., Lin, Y., Lin, X., Dai, Y., Guo, Z., Pan, D., 2018. Screening of a microbial consortium for selective degradation of lignin from tree trimmings. *Bioresour. Technol.* 254, 247–255.
- Goodman, B.A., 2020. Utilization of waste straw and husks from rice production: a review. *J. Bioresour. Bioprod.* 5 (3), 143–162. <https://doi.org/10.1016/j.jobab.2020.07.001>.
- Gupta, J., Kumari, M., Mishra, A., Swati, Akram, M., Thakur, I.S., 2022. Agro-forestry waste management-A review. *Chemosphere* 287 (3), 132321. <https://doi.org/10.1016/j.chemosphere.2021.132321>.
- Haile, A., Gelebo, G.G., Tesfaye, T., Mengie, W., Mebrate, M.A., Abuhay, A., Limeneh, D. Y., 2021. Pulp and paper mill wastes: utilizations and prospects for high value-added biomaterials. *Bioresour. Bioprocess.* 8, 35. <https://doi.org/10.1186/s40643-021-00385-3>.
- Haq, I.U., Hillmann, B., Moran, M., et al., 2022. Bacterial communities associated with wood rot fungi that use distinct decomposition mechanisms. *ISME COMMUN* 2, 26. <https://doi.org/10.1038/s43705-022-00108-5>.
- Haque, M.M., Haque, M.A., Mosharaf, M.K., Marcus, P.K., 2021. Decolorization, degradation and detoxification of carcinogenic sulfonated azo dye methyl orange by newly developed biofilm consortia. *Saudi J. Biol. Sci.* 28, 793–804.
- Harith, Z.T., Ibrahim, N.A., Yusoff, N., 2014. Isolation and identification of locally isolated lignin degrading bacteria. *J. Sustain. Sci. Manag.* 9 (2), 114–118.
- Hasanin, M.S., Mostafa, A.M., Mwafy, E.A., Darwesh, O.M., 2018. Eco-friendly cellulose nano fibers via first reported Egyptian *Humicola fuscoatra* X4: Isolation and characterization. *Environ. Nanotechnol. Monit. Manag.* 10, 409–418.
- Jain, D., Ravina, Bhojija, A.A., Chauhan, S., Rajpurohit, D., Mohanty, S.R., 2021. Polyphasic characterization of plant growth promoting cellulose degrading bacteria isolated from organic manures. *Curr. Microbiol.* 78, 739–748. <https://doi.org/10.1007/s00284-020-02342-3>.
- Janusz, G., Pawlik, A., Sulej, J., Swiderska-Burek, U., Jarosz-Wilkolazka, A., Paszczynski, A., 2017. Lignin degradation: microorganisms, enzymes involved, genomes analysis and evolution. *FEMS Microbiol. Rev.* 41 (6), 941–962.
- Jimenez, D.J., Chaib, De Mares, M., Salles, J.F., 2018. Temporal expression dynamics of plant biomass-degrading enzymes by a synthetic bacterial consortium growing on sugarcane bagasse. *Front Microbiol.* 9, 299. <https://doi.org/10.3389/fmicb.2018.00299>.
- Karim, M.E., Dhar, K., Hossain, M.T., 2018. Decolorization of textile reactive dyes by bacterial monoculture and consortium screened from textile dyeing effluent. *J. Genet. Eng. Biotechnol.* 16, 375–380.
- Khan, S.I., Zarin, A., Ahmed, S., Hasan, F., Belduz, A.O., Çanakçı, S., Khan, S., Badshah, M., Farman, M., Shah, A.A., 2022. Degradation of lignin by *Bacillus altitudinis* SL7 isolated from pulp and paper mill effluent. *Water Sci. Technol.* 8 (1), 420. <https://doi.org/10.2166/wst.2021.610>.
- Kishor, R., Purchase, D., Saratale, G.D., Saratale, R.G., Ferreira, L.F.R., Bilal, M., Chandra, R., Bharagava, R.N., 2021a. Ecotoxicological and health concerns of persistent coloring pollutants of textile industry wastewater and treatment approaches for environmental safety. *J. Environ. Chem. Eng.* 9, 105012.
- Kishor, R., Saratale, G.D., Saratale, R.G., Ferreira, L.F.R., Bilal, M., Iqbal, H.M.N., Bharagava, R.N., 2021b. Efficient degradation and detoxification of methylene blue dye by a newly isolated ligninolytic enzyme producing bacterium *Bacillus Albus* MW47057. *Coll. Surf. B Biointerfaces*, 111947. <https://doi.org/10.1016/j.colsurfb.2021.111947>.
- Kumar, A., Chandra, R., 2020. Ligninolytic enzymes and its mechanisms for degradation of lignocellulosic waste in environment. *Heliyon* 6 (2), e03170. <https://doi.org/10.1016/j.heliyon.2020.e03170>.
- Kumar, M., Singh, J., Singh, M.K., Singhal, A., Thakur, I.S., 2015. Investigating the degradation process of kraft lignin by  $\beta$ -proteobacterium, *Pandoraea* sp. ISTRKB. *Environ. Sci. Pollut. Res.* 22, 15690–15702. <https://doi.org/10.1007/s11356-015-4771-5>.
- Lee, S., Kang, M., Bae, J.-H., Sohn, J.-H., Sung, B.H., 2019. Bacterial valorization of lignin: strains, enzymes, conversion pathways, biosensors, and perspectives. *Front. Bioeng. Biotechnol.* 7, 209. <https://doi.org/10.3389/fbioe.2019.00209>.
- Li, X., Shi, Y., Kong, W., Wei, J., Song, W., Wang, S., 2022. Improving enzymatic hydrolysis of lignocellulosic biomass by bio-coordinated physicochemical pretreatment—A review. *Energy Rep.* 8, 696–709. <https://doi.org/10.1016/j.egyrb.2021.12.015>.
- Ma, J., Li, Q., Wu, Y., Yue, H., Zhang, Y., Zhang, J., Shi, M., Wang, S., Liu, G.-Q., 2021. Elucidation of ligninolysis mechanism of a newly isolated white-rot basidiomycete *Trametes hirsute* X-13. *Biotechnol. Biofuels.* 14, 189. <https://doi.org/10.1186/s13068-021-02040-7>.
- Malode, S.J., Prabhu, K.K., Mascarenhas, R.J., Shetti, N.P., Aminabhavi, T.M., 2021. Recent advances and viability in biofuel production. *Energy Convers. Manag.* X 10, 100070. <https://doi.org/10.1016/j.ecmc.2020.100070>.
- McCarthy, A.J., Broda, P., 1984. Screening for lignin-degrading actinomycetes and characterization of their activity against [<sup>14</sup>C] lignin-labelled wheat lignocellulose. *Microbiology* 130 (11), 2905–2913.
- Mei, J., Shen, X., Gang, L., Xu, H., Wu, F., Sheng, L., 2020. A novel lignin degradation bacteria-Bacillus amyloliquefaciens SL-7 used to degrade straw lignin efficiently. *Bioresour. Technol.* 310, 123445. <https://doi.org/10.1016/j.biortech.2020.123445>.
- Nahrowi, B., Susilowati, A., Setyaningsih, R., 2018. Screening and identification of lignolytic bacteria from the forest at eastern slope of Lawu Mountain. *AIP Conf. Proc.* 2002 (1), 020–042. <https://doi.org/10.1063/1.5050138>.
- Ogunlaja, A., Nwankwo, I.N., Omaliko, M.E., Oluakanni, O.D., 2020. Biodegradation of Methylene Blue as an evidence of synthetic dyes mineralization during textile effluent biotreatment by *Acinetobacter pittii*. *Environ. Process.* 7, 931–947.
- Pham, V.H.T., Kim, J., Chang, S., Chung, W., 2022. Biodegradation of methylene blue using a novel lignin peroxidase enzyme producing bacteria, named *Bacillus* sp. React3, as a promising candidate for dye-contaminated wastewater treatment. *Fermentation* 8, 190. <https://doi.org/10.3390/fermentation8050190>.
- Rahman, N.H.A., Abd Aziz, S., Hassan, M.A., 2013. Production of ligninolytic enzymes by newly isolated bacteria from palm oil plantation soils. *Bio Resour.* 8 (4), 6136–6150.
- Riyadi, F.A., Tahir, A.A., Yusoff, N., Sabri, N.S.A., Noor, M.J.M.M., Akhir, F.N.M., Zakaria, Z., Hara, H., 2020. Enzymatic and genetic characterization of lignin depolymerization by *Streptomyces* sp. S6 isolated from a tropical environment. *Sci. Rep.* 10, 7813. <https://doi.org/10.1038/s41598-020-64817-4>.
- Sani, R.K., Banerjee, U.C., 1999. Decolorization of triphenylmethane dyes and textile and dye-stuff effluent by *Kurtzia* sp. *Enzym. Microb. Technol.* 24 (7), 433–437.
- Saratale, R.G., Saratale, G.D., Kalyani, D.C., Chang, J.S., Govindwar, S.P., 2009. Enhanced decolorization and biodegradation of textile azo dye Scarlet R by using developed microbial consortium-GR. *Bioresour. Technol.* 100 (9), 2493–2500.
- Shamseldin, A., Abdelkhalak, A.A., 2015. Isolation and identification of newly effective bacterial strains exhibiting great ability of lignin and Rice straw biodegradation. *Int. J. Curr. Microbiol. Appl. Sci.* 4 (6), 1039–1049.
- Sharif-Yazdi, M.K., Azimi, C., Khalili, M.B., 2001. Isolation and identification of bacteria present in the activated sludge unit, in the treatment of industrial waste water. *Iran J. Public Health* 91–94.
- Shi, Y., Yan, X., Li, Q., Wang, X., Xie, S., Chai, L., Yuan, J., 2017. Directed bioconversion of Kraft lignin to polyhydroxy alkanolate by *Cupriavidus basilensis* B-8 without any pretreatment. *Process Biochem.* 52, 238–242.
- Singh, R., Kumar, M., Mittal, A., Mehta, P.K., 2017. Microbial metabolites in nutrition, healthcare and agriculture. *3 Biotech* 7 (1), 15. <https://doi.org/10.1007/s13205-016-0586-4>.
- Tamura, K., Stecher, G., Peterson, D., Filipiak, A., Kumar, S., 2013. MEGA6: molecular evolutionary genetics analysis version 6.0. *Mol. Biol. Evol.* 30 (12), 2725–2729.
- Thimmaiah, S.K., 2009. Standard Methods Of Biochemical Analysis. Kalyani Publishers.

- Thompson, J.D., Higgins, D.G., Gibson, J., 1994. CLUSTAL W: improving the sensitivity of progressive multiple sequence alignment through sequence weighting, position-specific gap penalties and weight matrix choice. *Nucleic Acid. Res* 22 (22), 4673–4680.
- Tsegaye, B., Balomajumder, C., Roy, P., 2018. Biodegradation of wheat straw by *Ochrobactrumoryzae* BMP03 and *Bacillus* sp. BMP01 bacteria to enhance biofuel production by increasing total reducing sugars yield. *Environ. Sci. Pollut. Res.* 25 (30), 30585–30596.
- Upadhyay, S.K., Singh, D.P., Saikia, R., 2009. Genetic diversity of plant growth promoting rhizobacteria isolated from rhizospheric soil of wheat under saline condition. *Curr. Micro* 59, 489–496. <https://doi.org/10.1007/s00284-009-9464-1>.
- Upadhyay, S.K., Singh, J.S., Singh, D.P., 2011. Exopolysaccharide-producing plant growth-promoting rhizobacteria under salinity condition. *Pedosphere* 21, 214–222. [https://doi.org/10.1016/S1002-0160\(11\)60120-3](https://doi.org/10.1016/S1002-0160(11)60120-3).
- Verma, M., Ekka, A., Mohapatra, T., Ghosh, P., 2020. Optimization of kraft lignin decolorization and degradation by bacterial strain *Bacillus velezensis* using response surface methodology. *J. Environ. Chem. Eng.* 8 (5), 104–270.
- Wang, M., Dessie, W., Li, H., 2021. Chemically modified lignin: correlation between structure and biodegradability. *J. Renew. Mater.* 9, 2119.
- Wu, Z., Peng, K., Zhang, Y., Wang, M., Yong, C., Chen, L., Qu, P., Huang, H., Sun, E., Pan, M., 2022. Lignocellulose dissociation with biological pretreatment towards the biochemical platform: a review. *Mater. Today Bio* 16, 100445. <https://doi.org/10.1016/j.mtbio.2022.100445>.
- Xiong, X.Q., Liao, H.D., Ma, J.S., Liu, X.M., Zhang, L.Y., Shi, X.W., Yang, X.L., Lu, X.N., Zhu, Y.H., 2013. Isolation of a rice endophytic bacterium, *Pantoea* sp. S d-1, with ligninolytic activity and characterization of its rice straw degradation ability. *Lett. Appl. Microbiol.* 58 (2), 123–129.
- Xu, Z., Qin, L., Cai, M., Hua, W., Jin, M., 2018. Biodegradation of kraft lignin by newly isolated *Klebsiella pneumoniae*, *Pseudomonas putida*, and *Ochrobactrum tritici* strains. *Environ. Sci. Pollut. Res.* 25, 14171–14181. <https://doi.org/10.1007/s11356-018-1633-y>.
- Yang, C.X., Wang, T., Gao, L.N., Yin, H.J., Lu, X., 2017. Isolation, identification and characterization of lignin-degrading bacteria from Qinling, China. *J. Appl. Microbiol.* 123 (6), 1447–1460.
- Yu, G., Wen, X., Li, R., Qian, Y., 2009. In vitro degradation of a reactive azo dye by crude ligninolytic enzymes from non immersed liquid culture of *Phanerochaete chrysosporium*. *Process Biochem.* 41 (9), 1987–1993.
- Zeng, Y., Zhao, S., Yang, S., Ding, S.Y., 2014. Lignin plays a negative role in the biochemical process for producing lignocellulosic biofuels. *Curr. Opin. Biotechnol.* 27, 98–45.
- Zhang, W., Ren, X., Lei, Q., Wang, L., 2021. Screening and comparison of lignin degradation microbial consortia from wooden antiques. *Molecules* 26, 2862 <https://doi.org/10.3390/molecules26102862>.



## Enhancing the pyrolytic conversion of biosolids to value-added products via mild acid pre-treatment

Ibrahim Gbolahan Hakeem<sup>a,b</sup>, Pobitra Halder<sup>b,c</sup>, Savankumar Patel<sup>a,b</sup>, Abhishek Sharma<sup>b,d</sup>, Rajender Gupta<sup>e</sup>, Aravind Surapaneni<sup>b,f</sup>, Jorge Paz-Ferreiro<sup>a</sup>, Kalpit Shah<sup>a,b,\*</sup>

<sup>a</sup> Chemical and Environmental Engineering, School of Engineering, RMIT University, Melbourne, VIC 3000, Australia

<sup>b</sup> ARC Training Centre for the Transformation of Australia's Biosolids Resources, RMIT University, Bundoora, VIC 3058, Australia

<sup>c</sup> School of Engineering, Deakin University, VIC 3216, Australia

<sup>d</sup> Department of Chemical Engineering, Manipal University Jaipur, Rajasthan 303007, India

<sup>e</sup> Department of Chemical & Materials Engineering, University of Alberta, Edmonton, Canada

<sup>f</sup> South East Water Corporation, Frankston, VIC 3199, Australia

### ARTICLE INFO

#### Keywords:

Demineralisation  
Metal passivation  
Sewage sludge  
Pyrolysis  
Heavy metals

### ABSTRACT

High concentrations of inorganic matter such as silicates, alkali and alkaline earth metals (AAEMs), and heavy metals (HMs) in biosolids limit their pyrolysis conversion to high-value products. Therefore, the reduction or passivation of the deleterious pyrolytic activities of these native inorganics in biosolids can enhance the yield and quality of products obtained during pyrolysis. The pyrolysis of raw and 3% sulfuric acid pre-treated biosolids was carried out in a fluidised bed reactor at 300–700 °C, and the influence of pre-treatment was examined on biochar properties, gas production, and bio-oil composition. At all temperatures, the selective removal of ash-forming elements (demineralisation) in biosolids by pre-treatment improved organic matter devolatilisation yielding higher bio-oil and lower biochar than untreated biosolids. Demineralisation weakened gas production, particularly at higher pyrolysis temperatures. At 700 °C, the in-situ formation of acidic metal sulfate salts in sulfuric acid-infused biosolids facilitated H<sup>+</sup> release, thereby increasing H<sub>2</sub> yield to a maximum of 15 mol% compared to 8 mol% from untreated biosolids and 4 mol% from demineralised biosolids. Biochar produced from treated biosolids had considerably lower HMs concentration and higher organic matter retention compared to raw biosolids biochar. The effect of pre-treatment on biochar properties was profound at 700 °C pyrolysis temperature. Pre-treatment increased biochar fixed carbon by 57%, calorific value by 37%, fuel ratio by 44%, doubled the specific surface area from 55 to 107 m<sup>2</sup>/g, and enhanced porous structure formation. At 300 °C, the major chemical compounds in the bio-oil were amides (20%), N-heterocyclics (25%), and ketones (30%), and higher temperatures favoured phenols and aromatic hydrocarbon production. Pre-treatment enhanced the selectivity of furans by 10-fold, anhydrosugars by 2-fold, and aromatic hydrocarbons by 1.5-fold relative to the raw biosolids bio-oil. Acid pre-treatment is a promising strategy for improving biosolids quality as feedstock for pyrolysis to generate high-value products.

### 1. Introduction

Biosolids (stabilised sewage sludge) are solid residues of the wastewater treatment process. Biosolids are enriched with plant nutrients (N, P, K), facilitating their widespread application on agricultural land. However, the presence of microbial, organic, and inorganic contaminants is reducing the attractiveness of biosolids for direct land application [1]. Therefore, a substantial volume of biosolids may not be safely applied on land due to increasingly stringent regulations on biosolids

management. Non-combustive thermal techniques such as pyrolysis, gasification, and hydrothermal carbonisation/liquefaction have been widely demonstrated for treating biosolids with the potential for contaminant destruction and resource recovery [2,3]. Pyrolysis is the most promising thermal treatment technique for biosolids processing and has been extensively studied under different conditions. At typical pyrolysis conditions (usually 400–700 °C under an inert atmosphere), pathogens and organic contaminants can be effectively degraded, and the waste volume can be reduced by at least 30% while generating solid

\* Corresponding author at: Chemical and Environmental Engineering, School of Engineering, RMIT University, Melbourne, VIC 3000, Australia.

E-mail addresses: [ibrahim.hakeem@rmit.edu.au](mailto:ibrahim.hakeem@rmit.edu.au) (I.G. Hakeem), [kalpit.shah@rmit.edu.au](mailto:kalpit.shah@rmit.edu.au) (K. Shah).

<https://doi.org/10.1016/j.jaap.2023.106087>

Received 17 May 2023; Received in revised form 13 July 2023; Accepted 15 July 2023

Available online 18 July 2023

0165-2370/© 2023 Elsevier B.V. All rights reserved.

(biochar), liquid (bio-oil), and gaseous (syngas) products [4]. However, despite these promising outcomes, biosolids pyrolysis can be limited by low conversion, poor selectivity, and product contamination [5]. Unlike lignocellulosic biomass, biosolids can have high amounts of inorganic matter (up to 50 wt%), depending on the source and stabilisation method [6]. The high ash content (and low volatile solids) may limit the suitability of biosolids as a pyrolysis feedstock. The inorganic content such as silicates, aluminates, alkali and alkaline earth minerals (AAEMs), and heavy metals (HMs) can inhibit the conversion of organic matter and interferes with the formation pathway of valuable chemical compounds during pyrolysis [7]. After pyrolysis, the inorganic minerals are largely retained in the biosolids-derived biochar at a higher concentration with deleterious influence on the biochar physicochemical properties and application potential [8]. For example, biosolids biochar with higher HMs concentration may not be attractive for land application. Excessively high amounts of ash content and inorganic minerals in biochar can reduce the oxidation resistance of the biochar carbon, lower the ash fusion temperature, and induce slagging and fouling during combustion for energy recovery [9]. Also, higher concentrations of minerals can lower chars' activation potential, reduce microporous structure development, and decrease the specific surface areas [10].

Three improvement strategies, such as i) feed pre-treatment, ii) use of catalysts, and iii) feed co-processing, have been demonstrated to enhance the pyrolytic conversion of biosolids to high-value products [11]. The extensively studied approaches are co-pyrolysis and in-situ catalytic pyrolysis, which involves the wet or dry mixing of biosolids with other biomass feedstock or catalyst additives [12–14]. Besides the opportunity to manage more than one waste stream, the potential advantages of co-processing biosolids with other feedstock in the presence or absence of catalysts include improved process selectivity, faster conversion kinetics, suppression of pollutant release, and enhanced product properties [15,16]. Co-pyrolysis, catalytic pyrolysis, and their combinations have been demonstrated to improve the pyrolytic conversion of biosolids through beneficial synergistic interactions of co-feedstock and catalysts additive. However, there are still some technical issues that require further attention, such as (i) deconvolution of the complex conversion kinetics and synergistic interactions, (ii) poor product homogeneity arising from feedstock variability and feed particle segregation, and (iii) difficulty in catalyst separation and recovery during in-situ operations.

The chemical pre-treatment of biosolids as an initial process step before pyrolysis has not been fully explored. Previous works suggested that mild acid pre-treatment of biosolids can selectively remove inorganic elements and partially hydrolyse recalcitrant organics to produce organic-rich residue suitable for pyrolysis conversion to bio-oil [8, 17–19]. During acid pre-treatment, protons ( $H^+$ ) from the acid solution replaced free or loosely bound metal ions in biosolids via an ion exchange mechanism, causing the removal of ash-forming elements [11]. Also, deprotonation of carboxylic O–H and hydroxylic O–H functional groups can produce many  $H^+$  and negatively charged polyions that promote the desorption of metal ions in biosolids [20]. Depending on the severity of the acid pre-treatment conditions, disintegration (hydrolysis) of organic matter in biosolids can occur attributed to the disruption of hydroxyl bonds and cleavage of carbonyl groups, as well as the transformation of crystalline compounds to amorphous form, thereby reducing the structural and thermal recalcitrance of the treated residue [21,22]. For example, mild acid (<5%  $H_2SO_4$  at 25 °C and 1 h) pre-treatment of biosolids was reported to remove about 75–95% of inherent HMs and 80–95% AAEMs, which reduced the ash content by 50% without degradation of organic constituents [17]. Then, the pyrolysis of acid-pre-treated biosolids had higher rates of devolatilisation occurring at lower temperatures to produce lower char residues than untreated biosolids [8,17]. Similarly, Liu et al. [18] reported that acid washing using 0.1 M  $H_2SO_4$  at ambient conditions for 12 h reduced biosolids ash content from 32 wt% to 20 wt% and increased carbon content by 26%. Therefore, acid pre-treatment of biosolids before

pyrolysis may be desired for many reasons, such as (i) reduction of HMs concentration and bioavailability in the resultant biochar, (ii) reduction of ash content and increased organic matter retention in biochar, (iii) enhancement of char textural properties and specific surface area, and (iv) improvement of both energy and chemical value of bio-oil through reduction of water and oxygenates content ordinarily catalysed by native AAEMs. Furthermore, there is an extensive demonstration of acid pre-treatment of biosolids for removing HMs and other limiting contaminants, thereby improving the grade of biosolids for unrestricted beneficial land reuse [20,23,24]. Therefore, biosolids pre-treatment may have a two-fold benefit for improving biosolids quality for land application as well as for pyrolysis upcycling.

Existing studies on integrated acid pre-treatment and pyrolysis were centred on understanding the role of inherent metals on biosolids' thermal decomposition behaviour and pyrolysis kinetics [19,25,26]. The analytical pyrolysis of acid-demineralised biosolids or demineralised biosolids spiked with specific metal additive have been used to elucidate the catalytic role of internal or added metals in fostering or inhibiting the release of gaseous nitrogen and sulfur compounds, degradation characteristics of organic matter, volatiles evolution, and pyrolysis activation energy [19,25–27]. There are limited studies on the bench-scale pyrolysis of acid-treated biosolids [18,28]. The role of acid pre-treatment on the distribution of pyrolysis product fractions (oil, char, and gas) and their properties have not been fully documented in the literature. Also, the observed effect of pre-treatment of biosolids in analytical pyrolysis setup may differ in practical reactor systems such as the fluidised bed reactor where gas-solid interactions are faster due to improved mass and heat transfer. Hence, biosolids pre-treatment before pyrolysis demands an extensive investigation in a typical fluid bed reactor under wide conditions of pre-treatment and pyrolysis.

This work studied the pyrolysis of raw and acid-treated biosolids in a fluidised bed reactor at 300–700 °C to understand the role of pre-treatment on biosolids pyrolysis. It was hypothesised that the removal or passivation of inherent metals in biosolids through acid pre-treatment could enhance the biochar quality, influence the formation path of chemical components in the bio-oil, and affect gas production during pyrolysis. Two pre-treatment scenarios were selected to include (i) biosolids acid treatment followed by water washing as a neutralisation step for selective demineralisation and (ii) biosolids acid treatment having residual acid unwashed for metal passivation. The specific objectives of this work were to study the effect of mild acid pre-treatment on (i) biosolids' physicochemical properties and thermal decomposition behaviour, (ii) pyrolysis product distributions, (iii) biochar quality with respect to carbon retention, calorific value, HMs concentration and bioavailability, and surface morphology, (iv) compositions of chemical compounds in the pyrolysis liquid to assess the chemical value of the bio-oil, and (v) compositions and evolution profile of non-condensable pyrolysis gases.

## 2. Materials and methods

### 2.1. Biosolids collection and sample preparation

Biosolids used in this study were collected from Mount Martha Water Recycling Plant, South East Water Corporation, Melbourne, Australia. The plant uses a dissolved air flotation process for sludge activation, then anaerobic followed by aerobic digestion for sludge treatment. The digested sludge is then dosed with polymer additives to coalesce the flocs, followed by mechanical dewatering in a centrifuge and drying in solar dryer shed. The biosolids employed in this study are the final solids from the dryer. The as-obtained biosolids were dried in an oven at 105 °C, ground, and sieved to 100–300  $\mu m$  particle size before further use.



## 2.2. Biosolids pre-treatment

The pre-treatment procedure was as described in our previous work [17]. The biosolids were pre-treated using a 3% (v/v) sulfuric solution at a solid-to-liquid ratio of 1:10 (g/mL) at 25 °C under continuous stirring at 600 rpm for 1 h. These conditions were obtained from an earlier optimisation study [17]. At the end of the pre-treatment experiment, the slurry was vacuum filtered to separate into aqueous phase (filtrate) and solid residue (treated biosolids). The residue was divided into two portions. The first portion was washed many times with deionised water until the filtrate pH was near neutral to remove residual acid and other water-soluble inorganics. The second portion was used as obtained with no further water washing to study the effects of residual acid on biosolids pyrolysis performance. The raw (untreated) biosolids were denoted as RB, treated biosolids with water washing were denoted as TB, while treated biosolids with no water washing were denoted as TB<sub>nw</sub>. The generation of large volumes of aqueous waste is a typical limitation of acid pre-treatment; however, our recent work has developed a closed-loop hydrometallurgical process for managing the generated aqueous acidic leachate stream via recycling and metal recovery [23]. The effect of pre-treatment on the pyrolysis behaviour of biosolids was assessed through Thermogravimetry analysis using a high-temperature TG/DSC Discovery series SDT650 equipment (TA instrument).

## 2.3. Pyrolysis experiments and products yield

Pyrolysis experiments were carried out in a quartz tubular fluidized bed reactor under atmospheric conditions. The details of the pyrolysis rig and reactor specifications can be found in our previous works [15, 29]. The pyrolysis procedure involves weighing 40 g of dry biosolids feed (RB or TB or TB<sub>nw</sub>) into a clean, dry pre-weighed reactor. The reactor and its content were inserted vertically into a three-zone electrically controlled furnace with an average heating rate of 35 °C/min. The reactor and its content were continuously flushed with a stream of pure nitrogen to create an inert atmosphere before heating the reactor. The experimental setup is shown in Fig S1. Biosolids pyrolysis was conducted at three temperatures: 300, 500, and 700 °C, which were selected to study the effect of pre-treatment on the product distribution and properties over a wide temperature range. During pyrolysis, a continuous stream of nitrogen flow required to achieve a gas velocity equivalent to 2.5 times the minimum fluidisation velocity was maintained using the Ergun correlation described in our previous work [30]. After reaching the desired temperature, the experiment was continued for 60 min, sufficient to complete the pyrolysis process. At the end of each experiment, biochar was collected from the reactor after cooling down to ambient temperature, and bio-oil was collected from the condensers. Non-condensable pyrolysis gas was continuously analysed on-line using micro-GC equipment connected to the pyrolysis gas cleaning units. Nine primary experiments were conducted, 3 samples by 3 temperatures. The pyrolysis product notations are distinguished by sample name-pyrolysis temperature, e.g., RB300 denoted Raw biosolids pyrolysed at 300 °C. At least a single repeat experiment was conducted for all samples, and average data has been reported with error bars representing the standard deviation. Product yields were calculated using Eqs. (1)–(3).

$$\text{Biochar}(\text{wt}\%) = \frac{\text{Weight of biochar}}{\text{Weight of biosolids feed}} \times 100\% \quad (1)$$

$$\text{Bio-oil}(\text{wt}\%) = \frac{W_{CT, \text{after}} - W_{CT, \text{before}}}{\text{Weight of biosolids feed}} \times 100\% \quad (2)$$

$$\text{Gas}(\text{wt}\%) = 100\% - \text{Biochar}(\text{wt}\%) - \text{Biooil}(\text{wt}\%) \quad (3)$$

Where  $W_{CT}$  refers to the weight of the condensers and oil collecting tubes.

## 2.4. Products characterisation

### 2.4.1. Biochar

Proximate analysis of biosolids and their biochar were carried out using a TGA 8000 Perkin Elmer equipment, and the ultimate analysis was performed in a CHNS 2400 Series II Perkin Elmer equipment coupled to a thermal conductivity detector. Physicochemical properties such as pH and electrical conductivity (EC) were determined using a pre-calibrated platinum electrode probe. Higher heating value (HHV) was estimated using the correlation of Channiwala and Parikh [31] shown in Eq. (4). Bulk density of the biosolids and biochar samples was determined using the standard measuring cylinder method [30]. FTIR Spectra were captured in absorbance mode over a scanning wavelength of 4000–650  $\text{cm}^{-1}$  at 32 scanning times and 4  $\text{cm}^{-1}$  resolutions using Frontier FTIR Spectroscopy (Spectrum 100, Perkin Elmer). Scanning electron microscope (SEM) FEI Quanta 200, USA, was used to analyse the surface morphologies of biochar samples after coating with iridium using Leica EM ACE 600 sputter coating instrument. The SEM instrument was operated at 30 kV, and SEM images were captured at the same spot size (5.0) and magnification ( $\times 3000$ ) to compare all samples' surface morphology. Brunauer–Emmett–Teller (BET) Surface Area Analysis was employed to estimate the surface area of the samples using Micromeritics TriStar II instrument.

The concentration of major elements in biosolids and biochar samples was measured using XRF analysis (S4 Pioneer Bruker AXS). Trace elements were measured using ICP-MS analysis following the acid digestion of the biosolids samples in aqua regia following the procedure described in Hakeem et al. [17]. Lastly, the potential soil bioavailable HMs concentration in biochar samples was measured using the diethylenetriamine pentaacetate (DTPA) acid extractable metal procedure [32]. Briefly, the extractant was prepared by weighing 1.97 g of DTPA, 1.47 g of  $\text{CaCl}_2 \cdot 2 \text{H}_2\text{O}$ , and 14.92 g of triethanolamine and dissolved in deionised water to make up 1 L solution. The pH of the solution was adjusted to 7.3 using concentrated HCl. Then 1 g of biochar sample was added to 10 mL of the pH-adjusted extractant solution, and the mixture was agitated at 250 rpm overnight at room conditions. The metal enrichment factor (MEF<sub>i</sub>) and metal retention/recovery (R<sub>i</sub>) in the biochar was estimated using Eqs. (5) and (6), respectively [17].

$$\text{HHV} \left( \frac{\text{MJ}}{\text{kg}} \right) = 0.3491C + 1.1783H + 0.1005S - 0.1034O - 0.0151N - 0.0211Ash \quad (4)$$

$$\text{MEF}_i = \frac{\text{Metal}_i \text{ concentration} \left( \frac{\text{mg}}{\text{kg}} \right) \text{ in biochar}}{\text{Metal}_i \text{ concentration} \left( \frac{\text{mg}}{\text{kg}} \right) \text{ in biosolids}} \quad (5)$$

$$R_i(\%) = \text{MEF}_i \times \text{biochar yield (wt}\%) \quad (6)$$

### 2.4.2. Bio-oil compositions

Pure bio-oil oil samples collected from the condenser during pyrolysis were used for the analysis. Bio-oil samples were dissolved in DCM before analysis in a Gas Chromatography-Mass Spectrometry (GC/MS Agilent Technologies, GC/MSD 5977B, 8860 GC system) instrument. HP-5MS (19091S-433UI) capillary column (30 m length, 0.25 mm I.D. and 0.25  $\mu\text{m}$  film thickness) was used in the GC/MS equipment, and the temperature program of the oven was as follows: isothermal hold at 45 °C for 3 min, ramp to 300 °C at 7 °C/min and isothermal hold at 300 °C for 5 min. Other conditions were 300 °C - injection temperature; 280 °C - MS transfer line; 230 °C - MS ion source; 1  $\mu\text{L}$  - splitless injection volume; 23.0 mL/min - total inlet flow, and helium was used as the carrier gas. The relative composition of chemical compounds in each bio-oil sample was determined by peak area normalisation, denoted as peak area percentage [15]. For further analysis, the identified compounds in each bio-oil sample were categorised into different chemical groups such as oxygenated, nitrogenated, hydrocarbons, phenolics,

anhydrosugars, and sulfur-containing compounds. Acids, alcohols, aldehydes, esters, ethers, furans, and ketones were categorised into oxygenated, while pyrazine, pyridine, pyrrole, azole, amines, amides, and nitriles were categorised into nitrogenated. Phenols and their derivatives are phenolics, while saccharides and sugar alcohols are classified as anhydrosugars. Finally, olefin, paraffin, BTXS (benzene, toluene, xylene, and styrene), and PAHs were classified as hydrocarbons. This classification was used to provide insight into the chemical value of the bio-oil based on dominant platform chemical species and study the effect of pre-treatment on the distribution of the chemical compounds.

#### 2.4.3. Pyrolysis gas compositions

The components and relative compositions (mol%) of the gas stream from each pyrolysis experiment were analysed online using a Micro-GC 490 (Agilent Technologies) instrument connected to the gas scrubbing unit from the pyrolysis reactor. The microGC has been calibrated with standard gases such as CO<sub>2</sub>, CO, H<sub>2</sub>, N<sub>2</sub>, O<sub>2</sub> and C1-C4 hydrocarbon. Pyrolysis gasses were sampled every 4 min until the end of the experiment to identify and quantify the gas components. The gas evolution profile during the pyrolysis was obtained by plotting the relative gas compositions as a function of pyrolysis time.

### 3. Results and discussions

#### 3.1. Effect of pre-treatment on biosolids physicochemical properties

The effect of H<sub>2</sub>SO<sub>4</sub> pre-treatment on the physicochemical properties of biosolids is summarised in Table 1. The mild acid pre-treatment (3% H<sub>2</sub>SO<sub>4</sub> at 25 °C for 60 min) of biosolids impacted the proximate compositions of the biosolids without substantial change in the ultimate compositions. Hence demineralisation mechanism dominated the pre-treatment process, which selectively removed inorganic matter. The percentage change in carbon contents was far lower than the percentage change in ash content of biosolids after pre-treatment. Specifically, there was a 40% and 20% decrease in ash content for TB and TB<sub>nw</sub>, respectively and a 10% increase in the volatile matter for the treated samples. In contrast, the carbon, hydrogen, and nitrogen contents of the treated samples differ by less than 10% relative to the raw biosolids, attributed to the loss of acid-soluble light volatiles. The ash content decreased due to the substantial removal (>60%) of ash-forming elements (such as AAEMs, Fe, Al, and HMs) from the biosolids. Devolatilisation was slightly enhanced by pre-treatment due to the hydrolysis of recalcitrant organics, thereby increasing volatile matter from 57% in raw biosolids to over 63% in treated feeds.

There was also a considerable reduction in HMs concentration, particularly Cu and Zn, which are the major limiting HMs in biosolids for land application. Overall, there was about a 75% reduction in HMs concentration in the TB relative to RB. The intensity of demineralisation and HMs reduction, as well as other physicochemical changes, were lesser in TB<sub>nw</sub> than in TB due to the subsequent water-washing step performed in the latter, which aided the removal of water-soluble inorganics and organic components. The HMs concentration (except Cu) in TB is within the concentration limit prescribed by Victoria EPA for C1-grade (least contaminant grade) biosolids for unrestricted land application [33]. The bioavailability of the residual HMs in TB is considerably low and can be an attractive material for direct land use in its current form [17]. However, other rapidly emerging contaminants in biosolids, such as per- and polyfluoroalkyl substances (PFAS) and microplastics, might still be present in TB. Our earlier work observed that sulfuric acid pre-treatment could not extract PFAS from biosolids; rather, the process concentrated PFAS in the treated solids due to volume reduction [23]. Therefore, the thermal treatment of TB via pyrolysis might be necessary to completely degrade all potential organic and microbial contaminants and produce quality biochar for land beneficiation and other high-value applications.

**Table 1**  
Effect of pre-treatment on biosolids physicochemical properties.

Properties	Compositions/ Elements	Biosolids samples			C1-grade biosolids*
		RB	TB	TB <sub>nw</sub>	
Proximate analysis (wt% dry basis)	Moisture	1.9	1.8	0.8	
	Volatile matter	57.5	63.4	63.6	
	Fixed carbon	10.6	16.4	11.3	
	Ash	30.0	18.5	24.3	
Ultimate analysis (wt% dry basis) <sup>a</sup>	Carbon	35.4	36.4	32.9	
	Hydrogen	4.4	5.1	4.5	
	Nitrogen	5.6	5.6	5.5	
	Sulfur	0.9	2.3	7.4	
	Oxygen	23.8	32.1	25.5	
pH		6.8	6.0	2.0	
EC (μS/cm)		1885	2400	9385	
HHV (MJ/kg) <sup>b</sup>		14.4	15.1	14.2	
Bulk density (g/cm <sup>3</sup> )		0.78	0.73	0.77	
Solids recovery (%)		-	80	95	
Carbon retention (%) <sup>c</sup>		-	82.3	88.3	
Major elements in ash (wt%)	Al	0.74	0.54	0.56	
	Ca	10.18	5.35	8.54	
	Cl	0.35	0.08	0.08	
	Fe	4.23	4.07	2.25	
	Na	0.12	BDL	BDL <sup>d</sup>	
	K	1.07	0.18	0.35	
	Mg	0.53	0.12	0.12	
	P	1.32	0.54	0.51	
	Si	2.69	3.29	2.91	
	Demineralisation efficiency (%) <sup>e</sup>		-	38.6	19.0
AAEMs removal efficiency (%) <sup>f</sup>		-	77.0	65.2	
Heavy metals (mg/kg)	As	2.5	1.3	1.9	20
	Cd	1.3	0.3	0.5	1
	Co	1.3	0.5	0.9	-
	Cu	690	220	500	100
	Cr	20	13	16	400
	Ni	18	7	12	60
	Mn	210	10	53	-
	Pb	20	18	17	300
Zn	850	160	560	200	
HMs removal efficiency (%)		-	76	35	

<sup>a</sup> Obtained by difference Oxygen = (100-C-H-N-S-Ash);

<sup>b</sup> Estimated using the correlation of Channiwala and Parikh (Eq. 4)

<sup>c</sup>  $(\text{Carbon content (wt\% in treated feeds)} / (\text{Carbon content (wt\%) in raw biosolids}) \times \text{Solids recovery}(\%))$

<sup>d</sup> BDL – Below Detection Limit;

<sup>e</sup> Based on ash content reduction;

<sup>f</sup> Based on average Na, K, Mg, and Ca content reduction

\* Biosolids grade for land application as prescribed by EPA Victoria [33].

Notably, there was an increase in sulfur content in TB<sub>nw</sub> compared to the other two samples indicating the presence of high residual sulfur from H<sub>2</sub>SO<sub>4</sub> pre-treatment without any post-treatment water washing. The sulfur from H<sub>2</sub>SO<sub>4</sub> could react with organic matter in biosolids to form organosulfur compounds, which might initiate the release of sulfur-containing volatiles during pyrolysis. The FTIR spectra (Fig S2) of the treated biosolids confirmed the formation of organosulfur compounds such as C-S, C=S, S=O, and SO<sub>2</sub>NH<sub>2</sub> groups. The water-washing neutralisation steps neutralised residual sulfuric acid and removed the precipitated metal sulfate salts, raising the treated solids' pH to 6.5 (Table 1). However, the water-washing process caused a loss of total solids with a solids recovery of 85% and carbon retention of 82% in TB compared to 95% solids recovery and 88% carbon retention in TB<sub>nw</sub>. Pre-treatment had a negligible change on the calorific value of the feed materials due to the contrasting effect of ash and oxygen concentration on the HHV correlation (Eq. (4)); however, pre-treatment reduced the bulk density of the biosolids, which was more profound in TB due to the extra water washing step. The overall observation of the acid pre-

treatment process on the changes in the physicochemical properties of biosolids is comparable with the literature [8,18,19]. For instance, in the study of Liu et al. [18], 0.1 M H<sub>2</sub>SO<sub>4</sub> pre-treatment of biosolids at ambient temperature for 12 h reduced the ash content by 12 wt% and increased volatile matter and carbon contents by ~10 wt% relative to the untreated biosolids. Tang et al. [19] using 5% HCl, 25 °C and 6 h for biosolids pre-treatment yielded 8 wt% decrease in ash content and ~5 wt% increase in volatile matter and carbon contents while nitrogen and hydrogen contents remained relatively unchanged compared to the raw biosolids. The current work used 3% H<sub>2</sub>SO<sub>4</sub>, 25 °C and 1 h to achieve 12 wt% reductions in ash content and 6 wt% increments in volatile matter while ultimate compositions were least impacted.

### 3.2. Effect of pre-treatment on biosolids thermal decomposition behaviour

The influence of pre-treatment on the pyrolysis behaviour of biosolids is illustrated by the various thermographs shown in Fig. 1. The DTG profile (Fig. 1(A)) occurs in three distinct degradation stages, which are: (I) dehydration (50–165 °C), (II) devolatilisation of organic components (150–600 °C), and (III) decomposition of recalcitrant carbonaceous materials and residual char organics (>600 °C). In stage I, the dehydration peak attributed to the loss of moisture and light volatiles occurred at 100 °C with < 4% mass loss. The major mass loss

(>50%) occurred in stage II over three degradation peaks at 250, 350, and 400 °C, corresponding to the thermal decomposition of carbohydrates, lipids and proteins/biopolymers, respectively [34,35]. The last degradation stage III, with < 10% mass loss, peaked at 750 °C and was attributed to the degradation of recalcitrant organics, such as lignin, and a fraction of inorganics, usually carbonates. There were clear differences in the DTG thermograph of RB, TB, and TB\_nw with respect to changes in maximum degradation temperatures and rate of weight loss. The maximum degradation temperature shifted to lower values in treated samples compared to the raw sample. In contrast, the raw sample's degradation rate was higher than the treated biosolids. For example, the maximum degradation temperature was 285 °C for RB, and it shifted to 245 °C for TB\_nw and 260 °C for TB, and while the rate of weight loss was 5.5%/°C for RB and it slightly decreased to 5.3%/°C for TB and 4.3%/°C for TB\_nw. These differences can be attributed to the partial hydrolysis of organic matter and the removal of inorganics by the pre-treatment step, facilitating the thermal devolatilisation reactions at lower degradation temperatures. However, the pre-treatment process also resulted in the slight dissolution of organic matter, which decreased the overall quantity of volatile matter in the treated samples relative to RB, thereby reducing the rate of volatile degradation. The lower rate of TB\_nw degradation compared to the other samples confirmed the formation of thermally stable metal sulfate salts, which inhibited organic

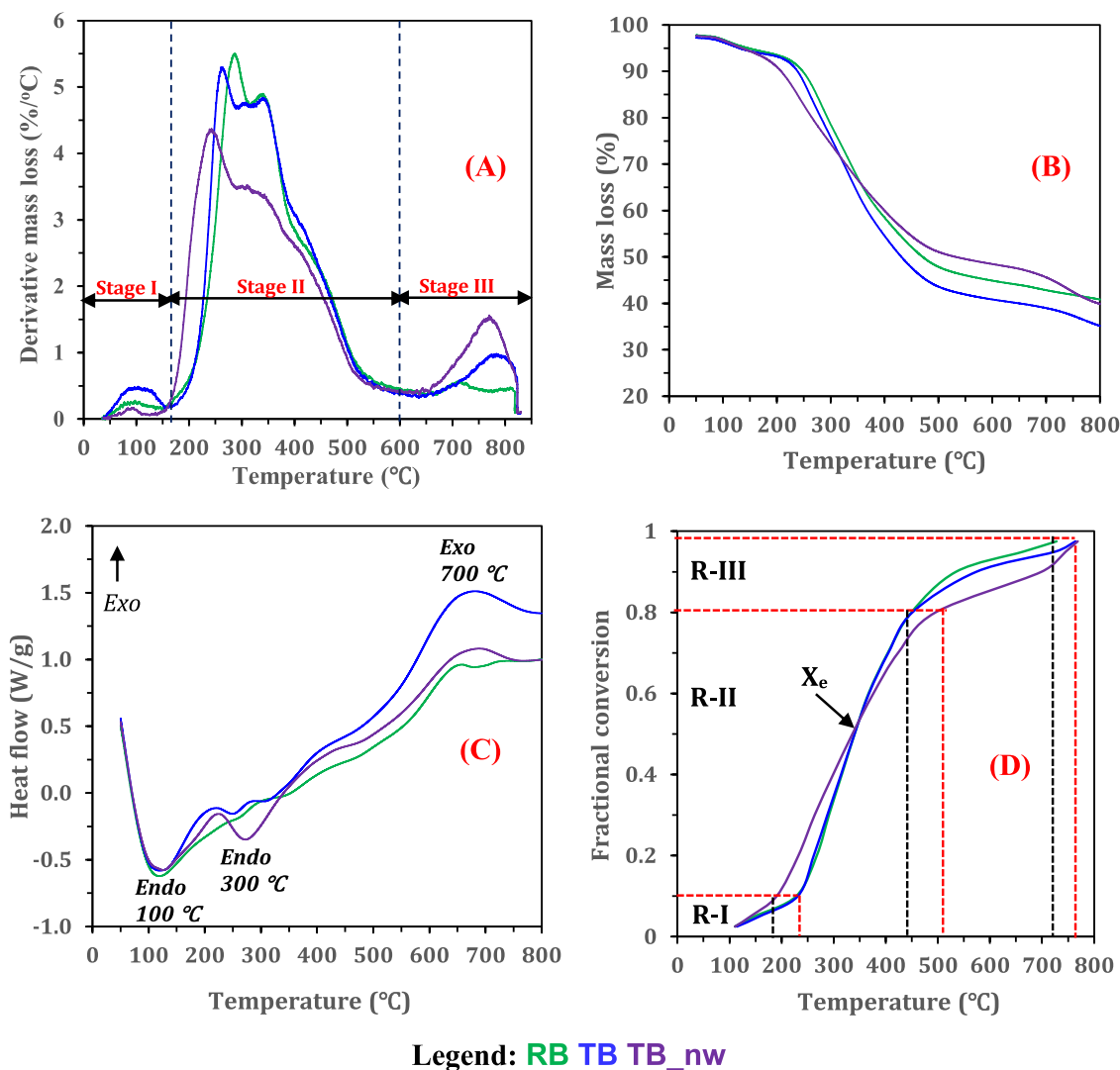


Fig. 1. Effect of pre-treatment on the thermal decomposition behaviour of biosolids (A) DTG thermograph showing decomposition peaks (B) TG mass degradation curve (C) DSC profile showing heat flow (D) plot of fractional conversion as a function of pyrolysis temperature.

matter conversion [36]. The TG curve (Fig. 1(B)) shows that the decomposition profile of TB and RB was closely similar with no overlapping, and at all temperatures, the degradation of TB was always higher than RB. This indicated that both samples have a similar organic matrix, and the lower ash content in TB was largely responsible for the higher mass loss at all temperatures. In contrast, TB<sub>nw</sub> had a different degradation profile whose mass loss was faster than the other materials up to 320 °C. Beyond this temperature, the mass loss was slower than in the other samples. The residual mass of RB and TB<sub>nw</sub> was similar (40%), while that of TB was the lowest (35%).

Fig. 1(C) illustrates the DSC curve of the biosolids samples showing the thermal energy flow as a function of pyrolysis temperature. Pyrolysis is an endothermic process where external energy is needed to break chemical bonds and decompose major biochemical components into primary decomposition products. From Fig. 1(C), two distinct endothermic peaks occurred at 100 °C and 300 °C, corresponding to loss of moisture and organic devolatilisation, respectively. After the initial transformation up to 350 °C, the energy needed to heat the feed materials began to decline, and the decrease of heat flow with increasing pyrolysis temperature from 350 to 600 °C was almost linear. During this stage, there are traces of broad endotherms indicating that the decomposition of organic matter at 300–600 °C required minimal thermal energy. However, the non-distinct endotherms made attributing the degradation behaviour to specific organic components difficult. Beyond 600 °C, a small exothermic spike was observed occurring at 650–750 °C attributed to the decomposition of carbon refractories such as aromatic ring, N-alkyl long chain structures, and carbonates with the release of CO<sub>2</sub> [37,38]. The intensity of the endothermic peak at 300 °C in TB<sub>nw</sub> suggests that the thermal energy required to decompose its organic structure is higher. The infusion of sulfuric acid might have changed the organic structure of TB<sub>nw</sub> to a thermally recalcitrant matrix through the formation of stable metal sulfate salts, consistent with observations reported in other works [18,39].

The iso-conversional temperature required for the pyrolysis of the three biosolids samples at the same heating rate (20 °C/min) is shown in Fig. 1(D). The figure indicates that the pyrolysis conversion of biosolids occurred over at least three kinetic regimes: i)  $\leq 10\%$  conversion occurring at 100–240 °C (R-I), ii) 10–80% conversion occurring at 240–500 °C (R-II), and iii)  $\geq 80\%$  conversion at 500–800 °C (R-III). These three kinetic regimes denoted dehydration, primary devolatilisation, and secondary devolatilisation and char cracking stages. However, the temperature required for each conversion stage differs for individual samples. For example, 10% conversion of TB<sub>nw</sub> occurred at 190 °C and about 230 °C for both RB and TB, suggesting that the dehydration stage occurred faster in TB<sub>nw</sub> compared to the other two samples. The faster conversion kinetics of TB<sub>nw</sub> continued into the primary devolatilisation stage up to 50% conversion, after which the rate was slower than RB and TB. Meanwhile, both RB and TB showed similar kinetics, up to 80% conversion, suggesting that the organic structure of both samples is identical. The slightly higher conversion rate of RB beyond 80% can be attributed to the role of native inorganic minerals, which promoted the cracking of recalcitrant organic matter. Notably, the pyrolysis temperature required to achieve 50% conversion was largely similar for all samples (340 °C), as the conversion rate of all samples overlapped at that temperature (indicated by X<sub>c</sub> in Fig. 1(D)). Overall, the required pyrolysis temperature was lowest for TB<sub>nw</sub> at any given conversion  $< 50\%$  and was highest at any given conversion  $> 50\%$ .

### 3.3. Pyrolysis products distribution: effect of pre-treatment and temperature

The product distribution of raw and treated biosolids at 300–700 °C is shown in Fig. 2. The product yields are expressed in dry feed weight to compare the influence of the temperature and pre-treatment on pyrolysis product distributions (Fig. 2(A)). According to Fig. 2, with

increasing pyrolysis temperature (from 300 to 700 °C), biochar yields decreased while bio-oil and gas products yield increased irrespective of feed material. This trend in product distribution as a function of pyrolysis temperature is consistent with extant literature [29,30,40]. With increasing pyrolysis temperature, mass and heat transfer rates are faster, and several thermolysis decomposition reactions are enhanced with the rapid cleavage of chemical bonds. For all samples, the effect of pyrolysis temperature on biosolids devolatilisation was profound between 300 and 500 °C compared to that between 500 and 700 °C. Nevertheless, bio-oil and gas products yield monotonically increased with temperatures up to 700 °C, indicating that biosolids contain recalcitrant organic fraction requiring higher temperatures to devolatilise. For example, during RB pyrolysis, the conversion was 28.8% at 300 °C; it increased to 49.7% at 500 °C and 58.6% at 700 °C. A similar trend can be observed for TB and TB<sub>nw</sub>. The DTG profile in Fig. 1(A) showed that most of the organic components in biosolids volatilised at temperatures between 200 and 500 °C. There were only slight improvements in bio-oil and gas yield by raising the temperature to 700 °C.

Pre-treatment had a clear effect on pyrolysis product distribution. From Fig. 2(A), pyrolysis of TB produced lower biochar yield (38.2–65.6 wt%) than that from RB (41.4–71.2 wt%), and the biochar yield from TB<sub>nw</sub> (43.0–68.7 wt%) was found to be between the yields from RB and TB. In contrast, bio-oil yield from TB (24.7–42.6 wt%) was higher than that from RB (20.6–37.0 wt%) and TB<sub>nw</sub> (19.6–36.8 wt%). Removal of ash-forming elements from biosolids and partial hydrolysis of the organic matter by H<sub>2</sub>SO<sub>4</sub> pre-treatment improved the devolatilisation of TB to produce more bio-oil and less char residues compared to other biosolids samples. It has been indicated that trace levels ( $< 1$  wt%) of certain ash components in biomass have significant catalytic effect during pyrolysis, which can decrease bio-oil yield considerably [41]. From Fig. 1(A), TB<sub>nw</sub> had the least conversion of all biosolids samples producing the highest biochar yield at 500 and 700 °C. The residual sulfuric acid in TB<sub>nw</sub> can catalyse crosslinking and polycondensation reactions at higher temperatures to form extra char, thereby increasing biochar yield [42]. The effect of pre-treatment was prominent on the distribution of biochar and bio-oil fractions, suggesting that the removal of inorganics had a remarkable influence on the thermal devolatilisation of organic matter in biosolids. Depending on the metal species and chemical form, mineral components have been shown to play various catalytic roles in releasing pyrolytic volatiles from organic matter [26, 43]. The extent of the interaction of mineral matter on organic matter conversion during biosolids pyrolysis has been elucidated in another work [8]. The gas product yield increased with increasing pyrolysis temperature and was higher for RB and TB<sub>nw</sub> than for TB. The catalytic effect of the inherent inorganics in RB and residual acid in TB<sub>nw</sub> facilitated gas production through secondary cracking and dehydration reactions, respectively.

Fig. 2(B) shows the pyrolysis product yield expressed on volatile solids (VS) or dry-ash-free basis to discount the effect of ash matter on product distribution as well as understand the real impact of pre-treatment on the downstream pyrolysis conversion of VS. At all pyrolysis temperatures, RB and TB had a similar yield of bio-oil in the range of 30–53 wt%, and biochar yield (30–59 wt%) was only similar for both samples at 300–500 °C. However, gas and biochar yield varies substantially for RB and TB at 700 °C. This indicates that VS conversion to bio-oil was not negatively impacted by demineralisation as in the case of TB. In contrast, biosolids pre-treatment without the water neutralisation step, as in TB<sub>nw</sub>, negatively impacted VS conversion to bio-oil during pyrolysis at all temperatures. The higher biochar yield at 500 and 700 °C for treated biosolids compared to the RB clearly indicates the char cracking role of native mineral matter during biosolids pyrolysis. The presence of mineral matter in RB caused a substantial cracking of recalcitrant volatiles at 700 °C to decrease biochar yield and increase gas yield. Consequently, RB conversion was 84% against 75% for treated biosolids. The elevated VS conversion attributed to the internal minerals in RB caused a decrease in fixed carbon and organic matter retention of

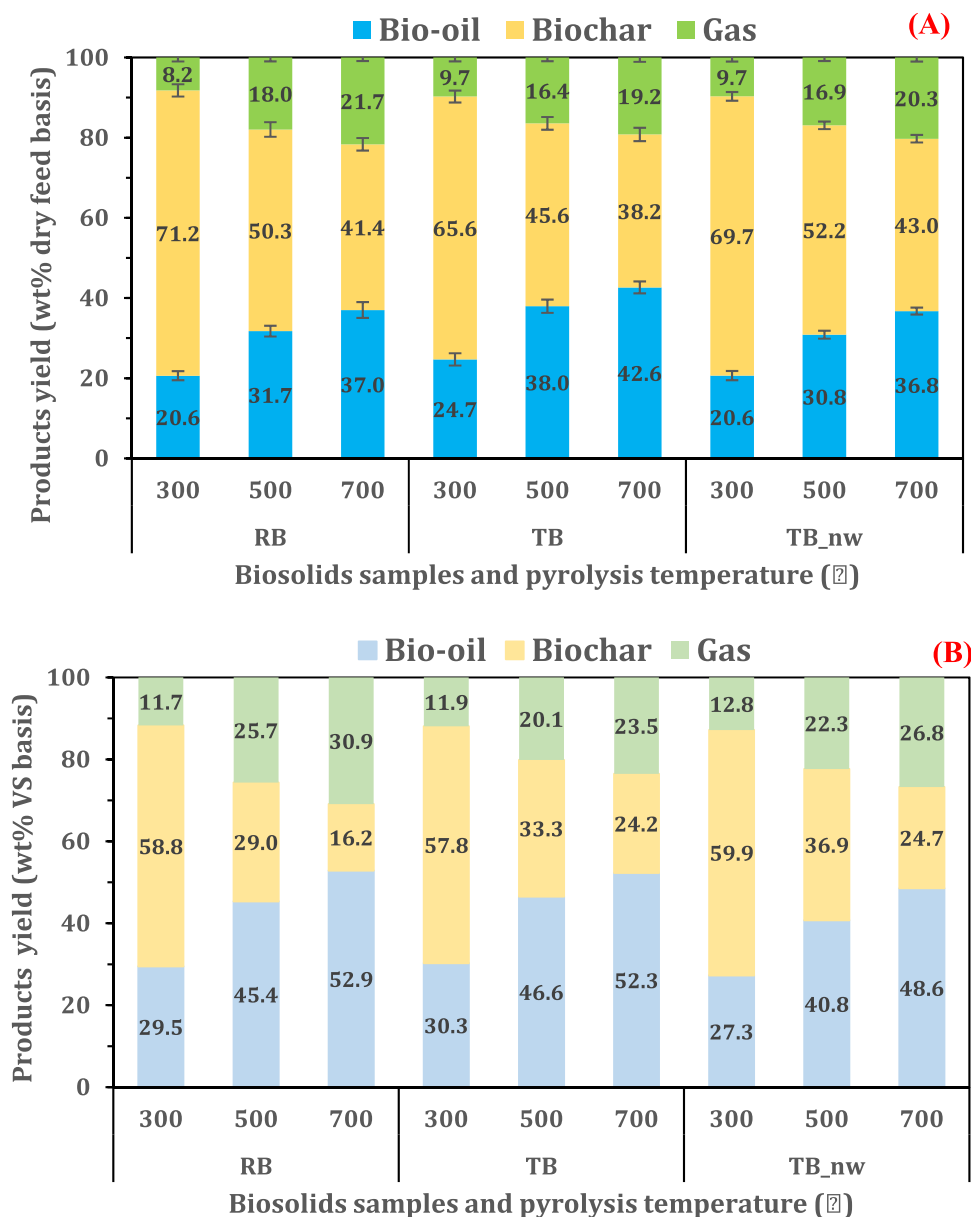


Fig. 2. Effect of pre-treatment and temperature on biosolids pyrolysis product distribution (A) expressed on a dry feed weight basis (B) expressed on volatile solids (dry-ash-free) basis.

the resulting biochar. In contrast, the lower conversion of VS in treated biosolids increased fixed carbon content and organic matter retention in the biochar. The higher biochar yield from the treated samples suggests that the pre-treatment process caused a reduction of thermally labile VS through the dissolution of acid-soluble organics and the loss of total solids during the process. This observation was confirmed by the 80–95% solids recovery and 82–88% carbon retention in treated biosolids relative to RB (Table 1). Besides the loss of total solids and light volatiles during pre-treatment, the residual organic structure might also be impacted by pre-treatment, increasing the stable VS fraction as indicated by the higher fixed carbon contents in treated biosolids. In sum, pre-treatment weakened the pyrolysis conversion of biosolids VS to gas product only at 700 °C.

Under the conditions of this work, there could be more than one mechanism through which acid pre-treatment influenced biosolids organic matter devolatilisation to produce higher bio-oil and lower biochar compared to RB. Perspectives on how biosolids' devolatilisation could be enhanced by acid pre-treatment with water washing step (as in

TB) have been provided.

- The substantial reduction of ash content by pre-treatment increased volatile matter concentration in TB. Since the volatile matter content per solid mass is higher in TB than RB, the pyrolysis of equal amounts of TB and RB implies more volatiles per unit TB mass is available for thermal conversion to bio-oil. The lower biochar yield in TB is due to reduced ash content since ash components are largely retained in the biochar. The proximate compositions of the biosolids changed substantially after pre-treatment, with a major opposite shift in the volatile matter and ash matter contents (Table 1).
- During pre-treatment, complex organic components in biosolids can be hydrolysed into simpler components through the disruption of O-H bonds by  $H^+$  from acid solution and surface deprotonation reaction causing the cleavage of carbonyl groups in protein and carbohydrate structures [20,22]. The partially hydrolysed organic macromolecules in TB are thermally less stable, and their characteristics decomposition temperature occurs in a lower region than untreated biosolids

**Table 2**  
Effect of pre-treatment on biochar physicochemical properties.

Pyrolysis temperature (°C)	300			500			700		
	RB	TB	TB_nw	RB	TB	TB_nw	RB	TB	TB_nw
Proximate analysis (wt% dry basis)									
Moisture	0.37	0.47	0.45	0.80	0.65	0.84	0.84	0.91	0.89
Volatile matter	46.16	52.11	50.69	29.28	30.67	35.67	20.07	21.70	16.71
Fixed carbon	14.66	18.45	13.28	17.62	27.66	17.15	19.99	31.32	27.26
Ash	38.82	28.97	35.57	52.31	41.02	46.35	59.10	46.06	55.15
Ultimate analysis (wt% dry basis)									
Carbon	39.35	45.08	40.07	32.82	41.67	35.34	30.41	37.27	30.21
Hydrogen	3.18	3.57	2.80	1.01	1.50	1.08	0.29	0.83	0.48
Nitrogen	6.55	7.35	6.39	5.47	5.63	5.21	3.25	4.83	4.01
Sulfur	0.89	2.58	6.13	0.58	3.12	6.06	0.65	3.14	7.32
Oxygen <sup>a</sup>	11.22	12.45	9.04	7.81	7.07	5.97	6.30	7.87	2.84
Other properties									
O/C	0.21	0.21	0.17	0.18	0.13	0.13	0.16	0.16	0.07
H/C	0.97	0.95	0.84	0.37	0.43	0.37	0.11	0.27	0.19
pH	5.8	5.5	4.1	7.8	6.8	6.3	9.8	9.4	9.6
EC ( $\mu\text{S}/\text{cm}$ )	722	1042	2614	305	1500	1868	2160	3218	2902
Bulk density ( $\text{g}/\text{cm}^3$ )	0.79	0.74	0.69	0.80	0.78	0.67	0.83	0.70	0.65
HHV ( $\text{MJ}/\text{kg}$ ) <sup>b</sup>	15.49	18.19	16.13	10.71	14.95	12.54	9.07	12.44	10.33
Fuel ratio (FC/VM) <sup>c</sup>	0.32	0.35	0.26	0.60	0.90	0.48	1.00	1.44	1.63
Organic matter retention (%VS) <sup>d</sup>	58.8	57.8	58.6	29.0	33.3	36.8	16.3	24.2	24.7

<sup>a</sup> Obtained by difference, i.e.  $O = 100 - (C + H + N + S + \text{Ash})$ ;

<sup>b</sup> Estimated by the correlation of Channiwala and Parikh [31] (Eq. 4);

<sup>c</sup> Fuel ratio was estimated by dividing the fixed carbon content (wt%) by the volatile matter content (wt%) in each sample;

<sup>d</sup> Calculated by dividing the volatile solids (VS) in biochar (Biochar yield (wt%)–ash content (wt%)) by the corresponding VS in the respective feedstock (100 (wt%)–ash content (wt%)).

(The TGA/DTG curve confirmed the shift to lower degradation temperature) (Fig. 1(A)).

The results of this work provide insight into the impact of acid pre-treatment on biosolids pyrolysis product distribution under a wide range of temperatures. However, the findings cannot sufficiently identify the specific organic chemical bonds and components being transformed during pyrolysis, aided or inhibited by pre-treatment. Further studies are needed to comprehensively understand the pre-treatment process and the exact mechanisms through which organic matter devolatilisation occurs to increase bio-oil yield.

### 3.4. Effect of pre-treatment on biochar quality

#### 3.4.1. Physicochemical properties

The physicochemical properties such as proximate and ultimate analyses, caloric value, pH, carbon retention and bulk densities of the resultant biochar obtained from the three biosolids feed samples at 300–700 °C are summarised in Table 2. Generally, volatile matter (VM) decreased, while fixed carbon (FC) and ash content increased in all biochar samples with increasing pyrolysis temperature. However, the increase in FC was negatively influenced by higher ash contents in biochar as the metal oxides in the ash can further oxidise FC, particularly at higher temperatures. During pyrolysis, thermally labile organic matter in the biosolids is removed, leading to substantial volume reduction. As a result, recalcitrant organic matter and inorganic matter are concentrated in the biochar. Increasing pyrolysis temperature increased the intensity of organic matter degradation and inorganic matter retention. The reduction of VM with increasing temperature had a consequential decrease in the ultimate compositions (C, H, N, O) of the biochar through dehydration, deoxygenation, decarboxylation, and denitrogenation reactions. Pre-treatment had clear effects on the proximate and ultimate compositions of the biochar samples. At all pyrolysis temperatures, biochar obtained from treated feeds had lower ash contents and higher FC than RB-biochar due to the prior removal of the ash-forming elements via the pre-treatment demineralisation process. TB-derived biochar had the highest VM and FC increase, and the lowest ash contents decrease compared to corresponding biochar obtained from

other biosolids feeds, albeit at the cost of biochar yield. Pre-treatment with water neutralisation steps retained higher organic matter in the biochar (24–58%), supported by the higher carbon contents and calorific value in the TB-derived biochar relative to RB and TB\_nw biochar (Table 2). Also, the fuel ratio of TB biochar was higher than RB-biochar, particularly at 700 °C; the fuel ratio of treated biosolids biochar was higher by 44–63% than RB-biochar. It is then suggested that removing minerals before pyrolysis can be a promising approach for strengthening biochar carbon-sequestration and energy-recovery potential. Also, the lower ash contents in the TB-derived biochar can enhance the biochar-carbon resistance to thermal and chemical oxidation, thereby increasing the carbon stability, as demonstrated in previous work [8]. However, the increase in sulfur contents in the biochar may be an undesired outcome of the pre-treatment process, particularly when the sulfuric acid pre-treatment is not followed by the water-washing neutralisation step, as in TB\_nw. Nevertheless, sulfur is an essential plant micronutrient in biochar for land application, and the pre-treatment can enrich the derived biochar of sulfur contents compared to RB-biochar.

The elemental H/C and O/C ratio is typically used to measure biochar aromaticity and biochemical stability and can be correlated to pyrolysis temperature [44]. The decrease in the H/C ratio indicated higher biochar aromaticity due to the strong degree of carbonisation with increasing pyrolysis temperature [40]. Biochar produced at higher temperatures and from pre-treated biosolids had aromatic and hydrophobic structures through the loss of oxygen-containing functional groups (such as hydroxyl and carboxyl). Nan et al. [8] also observed that removing inherent minerals from sewage sludge via acid pre-treatment facilitated the disappearance of oxygen-containing functional groups such as C=O, O=C–O, and C–O, while promoting C–C/C=C bonds, indicating higher aromatisation of biochar. Pyrolysis temperature plays an important role in shaping biochar's surface chemistry and organic structure. At lower temperatures (<500 °C), the hydrogen-bonding network in the organic compounds is eliminated, and hydroxyl groups are oxidised to carboxyls. At higher temperatures, methylene groups are heavily dehydrogenated to aromatic structures [45]. The bulk (or apparent) densities of the biochar obtained at 300–700 °C from the three biosolids feed samples were found to vary substantially. Generally, there was a monotonic increase in bulk density with increasing pyrolysis

**Table 3**  
Effect of pre-treatment and pyrolysis temperature on metal concentration in biochar.

Temp. (°C)	300			500			700		
	RB	TB	TB_nw	RB	TB	TB_nw	RB	TB	TB_nw
Major metal oxides (wt%)									
Al <sub>2</sub> O <sub>3</sub>	2.1	1.7	1.7	3.0	2.5	2.0	3.4	2.8	2.7
CaO	14.3	8.7	12.9	17.3	10.8	14.2	18.8	11.7	15.9
Fe <sub>2</sub> O <sub>3</sub>	6.6	4.6	4.0	8.0	6.0	4.7	8.2	6.4	5.0
K <sub>2</sub> O	1.5	0.3	0.5	1.8	0.4	0.6	1.9	0.4	0.6
MgO	1.1	0.3	0.3	1.6	0.5	0.4	1.8	0.5	0.5
Na <sub>2</sub> O	0.5	BDL <sup>a</sup>	BDL	0.7	BDL	BDL	0.7	BDL	BDL
P <sub>2</sub> O <sub>5</sub>	3.4	1.5	1.3	4.4	1.9	1.4	4.8	2.1	1.7
SiO <sub>2</sub>	7.7	10.6	8.6	10.6	14.9	8.9	11.9	16.0	11.4
Heavy metals (mg/kg)									
As	3.0	2.0	2.5	3.5	2.4	3.0	2.1	1.7	1.9
Cd	1.8	0.5	0.7	2.5	0.7	1	1.8	0.8	0.8
Cr	30	15	23	47	28	32	35	30	22
Cu	890	1100	1600	950	1200	1800	1200	1400	1900
Ni	26	10	17	38	13	24	29	16	16
Pb	29	25	21	37	40	34	40	40	36
Zn	1300	400	770	1500	580	970	1600	530	930

<sup>a</sup> BDL – Below detection limit

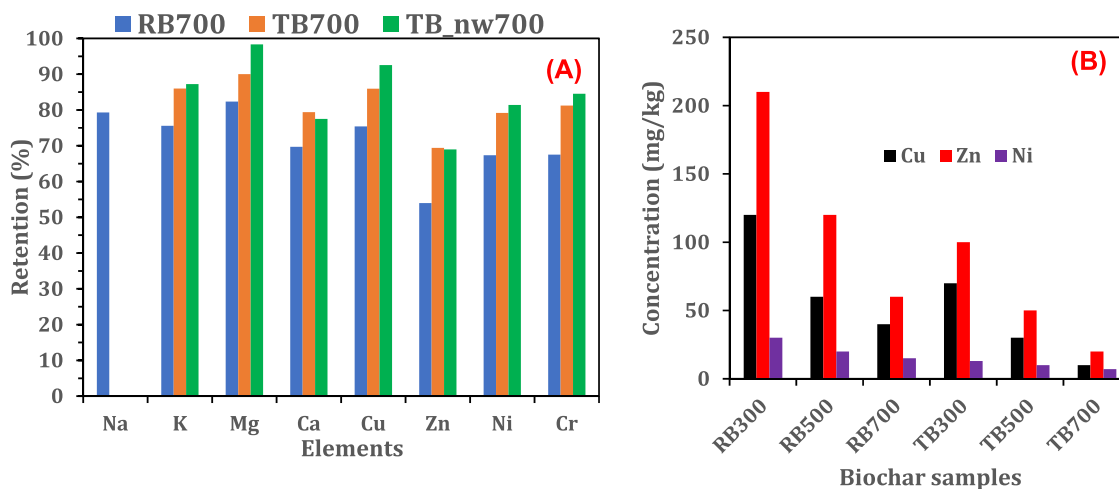


**Fig. 3.** Effect of pre-treatment on (A) metal retention in biosolids biochar at 700 °C (B) bioavailable HMs concentration in biosolids biochar.

temperature reflected by the extent of volume reduction caused by pyrolysis. The bulk density of the RB-biochar was the highest, followed by TB\_nw and TB-biochar, which is reflective of the lower ash content in treated biosolids relative to raw biosolids at a given pyrolysis temperature. Lastly, the pH of the biochar was observed to generally increase with increasing temperature largely due to the destruction of acidic functional groups and the increase in the concentration of basic functional groups such as char-N as well as metal oxides in the ash contents. Biochar produced from TB\_nw at 300 °C was more acidic (pH 4) than biochar from other biosolids samples (pH 5.5–5.8) due to residual sulfuric acid in TB\_nw. However, the pH of all biochar samples was similar at 700 °C suggesting the inherent acid in TB\_nw has no influence on the resultant biochar pH, possibly because acidic metal sulfate salts have been cracked into normal metal sulfate or oxides form.

#### 3.4.2. Metals concentration, retention, and bioavailability

The effect of pre-treatment on the concentration of inorganic elements in biochar was assessed. The compositions and concentration of metal oxides and HMs in the raw and treated biosolids-derived biochar produced at 300–700 °C are summarised in Table 3. The major ash-forming elements enriched in the biochar are oxides of Ca, Si, Fe, P, Al, K, Mg, and Na in decreasing order. Expectedly, the metal concentration increased with increasing pyrolysis temperature (decreasing biochar yield). The metal concentrations were highest for the RB biochar

samples containing the full spectrum of metal components. The prior removal of inorganic elements during pre-treatment substantially reduced the final concentration in the treated biosolids biochar. Notably, Na removal in biosolids via pre-treatment was almost 100%; consequently, Na<sub>2</sub>O was only detected in RB biochar and was below the detection limit in all treated biosolids biochar samples. According to Fig. 3(A), the metal contents in the respective biosolids feed were largely retained in their derived biochar with a retention rate of > 90%, confirming the thermal stability of the metal species at the pyrolysis conditions. However, at the highest pyrolysis temperature (700 °C), there appears to be some volatilisation of AAEMs, particularly Ca and K, attributed to the decomposition of Ca-containing minerals such as CaCO<sub>3</sub> in the case of RB and CaSO<sub>4</sub> hydrates in the case of treated biosolids. In addition, the sublimation of KCl at high temperatures may cause K loss from the biochar [29]. Moreover, recalcitrant organics bonded to mineral matter may decompose at high temperatures leading to the release of metal species to the gas phase, lowering their recovery in the biochar [46].

Heavy metals are limiting contaminants in biosolids and their derived char, particularly for land application purposes. The HMs concentration in the biochar obtained from the three biosolids samples at 300–700 °C is shown in Table 3. The concentration generally increases with temperature with an enrichment factor of at least 1.2 times the concentration in the parent biosolids at 300 °C and up to 2.5 times at

700 °C. Up to 500 °C, there was an upward trend in the increase in the HMs concentration. However, at 700 °C, there was a decline in the concentration of the metals attributed to the rise in the thermal volatilities of certain elements. Specifically, at 700 °C, less than 50% of As and Cd were retained in the biochar, and Zn retention was less than 70%. Zhang et al. [47] reported similar observations during sewage sludge pyrolysis, with Hg being completely partitioned in the oil and gas product fractions as low as 300 °C while Cd and As had less than 10% recovery in the biochar at 650 °C. At 700 °C, the thermal volatilities of HMs can be ranked as Cu < Cr < Ni < Pb < Zn < As = Cd, suggesting that Cu, Cr, and Ni were least involved in migration during biosolids pyrolysis. This observation was similar to that reported in previous works [29,47]. Cu had the highest retention in biochar due to the high affinity of Cu to organic matter [17]. The higher organic matter retention in TB/TB\_nw biochar also explains the higher Cu concentration in treated biosolids biochar compared to RB biochar. The poor removal of Pb with sulfuric acid resulted in the inconsequential effect of pre-treatment on Pb concentration in the biochar obtained from all samples. The concentration of all other HMs was lower in treated

biosolids biochar compared to RB biochar, with the lowest for TB biochar. However, the enrichment factor for a given HM was higher in TB biochar than in RB biochar. The low ash content in TB weakens the dilution effect resulting in higher MEF. For instance, in biochar obtained at 500 °C, Cd concentration increases by 1.9 times for RB and 2.3 times for TB; similarly, Zn enrichment was 1.8 for TB and 3.6 for TB. Besides the reduction of metal concentration by pre-treatment, there was an increase in the stability of the metal as their recovery in the biochar was higher for treated samples than the RB (Fig. 3(A)). The removal of acid-exchangeable (ionisable) and reducible metal (bound to carbonates and Fe-Mn oxides) fractions during pre-treatment facilitated the transformation and stabilisation of the remaining HMs in the treated samples to oxidisable (bound to organic matter) and residual fractions (bound to silicates) [48]. Therefore, stabilising HMs in the TB and TB\_nw biochar compared to RB biochar can reduce the undesired migration of HMs into oil and gas product fraction during biosolids pyrolysis.

The reduction of HMs concentration and the increased metal stability in the biochar facilitated by pre-treatment may not be enough indication of the potential toxicity of the residual HMs. Therefore, DTPA-plant

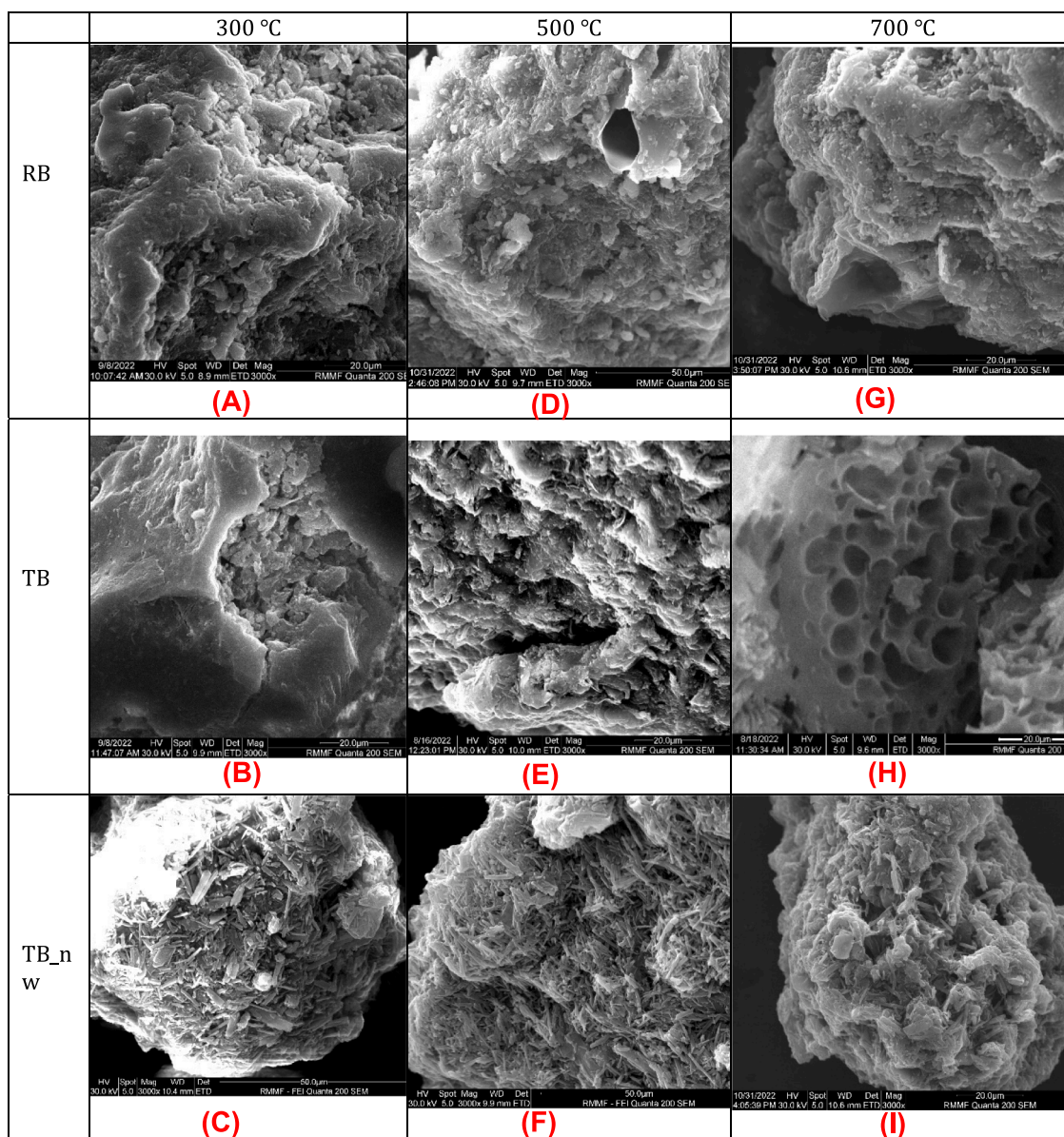


Fig. 4. Effect of pre-treatment and temperature on the surface morphology of biosolids biochar (A) RB300 (B) TB300 (C)TB\_nw300 (D) RB500 (E) TB500 (F) TB\_nw500 (G) RB700 (H) TB700 (I) TB\_nw700.



available HMs concentration was assessed, and the result showed that pre-treatment drastically reduces the bioavailable metal concentration in the biochar (Fig. 3(B)). Specifically, at 500 °C, the DTPA-extractable Cu concentration from RB biochar was 60 mg/kg, while it was 20 mg/kg for TB biochar. Similarly, Zn bioavailable concentration in TB biochar was reduced by at least 50% compared to RB biochar at the same pyrolysis temperature. The effect of pre-treatment follows a similar trend for Ni bioavailable concentration reaching about 7 mg/kg in TB700 compared to 15 mg/kg in RB700. The higher organic matter retention and surface functional groups in TB biochar could promote organometallic complexation reaction, thereby enhancing HMs immobilisation in the char matrix and decreasing the extractable metal concentrations [49].

### 3.4.3. Morphological properties

The SEM imaging of the biochar obtained from raw and treated biosolids samples at 300–700 °C is shown in Fig. 4. There was a clear distinction in the image of the samples, highlighting the effect of pre-treatment and pyrolysis temperatures on biochar surface morphology. The image of the biochar obtained at 300 °C (Fig. 4(A-C)) showed a bulky structure with particle shrinkage resulting from the dehydration and decarboxylation of organic matter. The char sample from RB and TB appeared similar (Fig. 4(A&B)), and the biochar sample from TB\_nw (Fig. 4(C)) had a flaky structure with a surface covering arising from the acidic metal sulfate salts. At 500 °C, the image of the char samples (Fig. 4(D-F)) showed a matured organic conversion with the compact structure becoming disintegrated into small fragments; however, the pore structure is not well developed with traces of pore openings. The char from TB\_nw still showed the thermally stable metal sulfate salts coverings, limiting the full development of the pores (Fig. 4(F)). At 700 °C (Fig. 4(G-I)), organic compounds have been completely degraded, and the char cracking reaction removed residual volatiles, opening up pores within the char matrix and exposing the char surface. TB biochar has a strong pore development (Fig. 4(H)) due to enhanced devolatilisation and lower ash residues. The RB700 (Fig. 4(G)), due to its high ash content, had poor pore structure development attributed to the creation of stable organometallic compounds within the aromatic structures, which are recalcitrant to thermal volatilisation at 700 °C [29]. It has been suggested that high levels of ash-forming minerals in biosolids would require higher pyrolysis temperatures for their biochar pore structure to be fully developed compared to low-ash-containing biomass biochar [6]. Hence, reducing the ash minerals in biosolids by mild sulfuric acid pre-treatment was beneficial in producing biochar with a porous structure, albeit the effect was profound only at 700 °C. However, the presence of residual acid and acidic metal sulfate salts inhibited volatile removal and caused pore blockage, as observed in the SEM images of TB\_nw.

The BET-specific surface areas and average pore volume of the biochar samples are summarised in Table 4. At 300 °C, the surface area (15–25 m<sup>2</sup>/g) of the biochar from all feed samples was largely similar;

however, the pore volume of TB (0.024 cm<sup>3</sup>/g) was almost double of the RB (0.012 cm<sup>3</sup>/g) supporting the elevated rate of inorganic removal by pre-treatment and organic matter removal from the bulk of TB sample during pyrolysis. Increasing the pyrolysis temperature to 500 °C increased the biochar surface area by at least 40%, reaching 27 m<sup>2</sup>/g for RB and 40 m<sup>2</sup>/g for TB, and a further increase in temperature to 700 °C increased the surface area to 55 m<sup>2</sup>/g for RB and 107 m<sup>2</sup>/g to TB. The 2-fold higher surface area of TB-biochar compared to RB-biochar was supported by the improved pore structure development of TB biochar, as shown in Fig. 4(H). Higher surface area and pore volume are indicative of the stability of the char structure, which can enhance their application in catalysis and adsorption [6]. The pore size distribution indicates that the biochar materials are largely mesoporous with pore width in the 2–50 nm range. However, the relatively lowest pore width in the case of TB\_nw indicates possible pore blockage by the poorly soluble metal sulfate salt, particularly CaSO<sub>4</sub> hydrates that covers the surface as observed under the SEM imaging.

### 3.5. Effect of pre-treatment on bio-oil compositions

The chemical compositions identified through the GC/MS analysis of the bio-oil obtained from the pyrolysis of raw and treated biosolids are summarised in Table 5. The results showed that the bio-oil is a complex mixture of various chemical compounds grouped into oxygenates, nitrogenated compounds, sulfur-containing, and hydrocarbons. Temperature and pre-treatment considerably affect the evolution of volatile organic compounds in the bio-oil. Generally, for all biosolids samples, the yield of nitrogenated and oxygenated compounds decreased with increasing pyrolysis temperature, while hydrocarbons and phenol yield increased with temperature. The effects of pre-treatment on the distribution of chemical components in the bio-oil varied with pyrolysis temperature. For instance, pre-treatment enhanced hydrocarbon production from 20% in RB to 30–35% in treated biosolids at ≥ 500 °C, whereas anhydrosugars yield was increased from 2.1% in RB to 4.5% in TB only at 300 °C, while phenolics yield was similar for all bio-oils at all temperatures.

The bio-oil obtained at 300 °C consists mainly of high molecular weight nitrogenated and oxygenated compounds, with major chemical species being *N*-heterocyclics and ketones. Nitrogenated compounds in bio-oil originated from the thermal devolatilisation of proteins, while ketonic compounds are from the primary decomposition of carbohydrates. *N*-heterocyclics could be formed by dehydrogenation of the amino group present in proteins and nucleic acids in biosolids and through the addition of HCN and/or NH<sub>3</sub> to benzene/toluene aromatic ring during pyrolysis [50]. Dehydration and decarboxylation of organic matter are prominent thermolysis reactions at lower temperatures resulting in the formation of high-molecular-weight reactive oxygenate fragments such as R-CHO, R-C-O-R, R-CO-OH, and R-O-R [51]. Pyrolysis at 300 °C was selective for producing a few kinds of *N*-heterocyclics, amides/amines, and ketones, irrespective of the biosolids feed

**Table 4**  
Surface properties of biochar samples.

Pyrolysis temperature (°C)	Feed samples	Surface properties		
		BET specific surface area (m <sup>2</sup> /g)	BJH average pore volume (cm <sup>3</sup> /g)	BJH average pore width (nm)
300	RB	15.2	0.012	7.94
	TB	25.2	0.024	8.00
	TB_nw	20.5	0.015	7.84
500	RB	26.9	0.021	8.67
	TB	43.7	0.030	8.81
	TB_nw	32.9	0.017	8.22
700	RB	55.3	0.039	7.65
	TB	106.9	0.061	8.54
	TB_nw	72.5	0.043	7.03

**Table 5**  
GC/MS analysis showing the chemical composition of the bio-oil samples.

Bio-oil compositions									
Pyrolysis temperature (°C)	300			500			700		
Biosolids samples	RB	TB	TB_nw	RB	TB	TB_nw	RB	TB	TB_nw
Compounds	Peak Area (%)								
Pyrazine	14.1	2.9	16.3	-	-	2.3	4.5	-	-
Pyridine	8.3	6.4	8.5	3.0	1.5	2.3	1.7	1.0	8.5
Pyrrrole	3.4	0.4	-	8.2	1.4	0.4	1.6	5.7	0.5
Azole	0.3	0.2	-	0.9	6.3	0.9	9.0	8.0	0.5
Amines	5.3	5.8	16.9	3.4	2.0	0.6	1.3	0.4	4.6
Amides	19.3	17.6	8.5	7.4	4.8	2.1	4.2	2.3	1.6
Nitriles	1.8	1.1	3.2	4.5	7.1	7.2	3.8	5.9	6.5
Total Nitrogenated	<b>52.5</b>	<b>34.4</b>	<b>53.4</b>	<b>27.3</b>	<b>23.0</b>	<b>15.8</b>	<b>26.2</b>	<b>23.7</b>	<b>22.2</b>
Esters	1.2	2.9	3.5	8.3	15.0	18.8	14.4	10.9	13.0
Ethers	-	-	-	2.5	-	-	2.5	-	-
Ketones	30.5	37.7	16.7	20.9	11.5	8.8	10.6	8.6	6.1
Aldehydes	-	1.0	-	-	0.8	-	-	0.9	1.0
Acids	2.1	4.5	7.8	4.4	0.9	3.8	3.6	3.3	6.9
Alcohols	2.1	0.5	-	0.8	1.5	9.3	1.5	3.0	6.6
Furans	1.0	10.6	10.4	-	-	-	-	-	0.5
Total Oxygenated	<b>37.0</b>	<b>57.2</b>	<b>38.4</b>	<b>36.9</b>	<b>29.7</b>	<b>40.6</b>	<b>32.6</b>	<b>26.7</b>	<b>34.0</b>
1,4:3,6-Dianhydro- $\alpha$ -D-glucopyranose	1.2	1.9	-	-	-	-	-	-	-
2,3,4-Trimethyllevoglucosan	0.5	0.4	-	-	-	-	-	-	-
Maltol	-	0.7	0.7	-	-	-	-	-	-
Others	0.4	1.5	-	-	-	-	-	-	-
Total Anhydrosugars	<b>2.1</b>	<b>4.5</b>	<b>0.7</b>	-	-	-	-	-	-
Phenols	8.6	1.0	2.7	11.3	9.3	4.7	8.9	10.2	6.0
<i>p</i> -Cresol	-	-	-	4.1	5.3	1.4	4.8	6.2	4.2
Total Phenolics	<b>8.6</b>	<b>1.0</b>	<b>2.7</b>	<b>15.4</b>	<b>14.6</b>	<b>6.1</b>	<b>13.7</b>	<b>16.4</b>	<b>10.2</b>
Olefin	-	0.3	1.0	1.9	2.1	2.1	2.9	2.3	1.8
Paraffin	-	1.2	0.8	6.2	7.7	8.1	11.6	10.4	5.2
BTXS <sup>a</sup>	-	0.6	1.2	12.4	20.6	25.0	13.1	18.6	20.9
Polyaromatic	-	-	-	-	0.4	0.3	-	0.8	2.8
Total Hydrocarbons	-	<b>2.1</b>	<b>3.0</b>	<b>20.5</b>	<b>30.8</b>	<b>35.5</b>	<b>27.6</b>	<b>32.1</b>	<b>30.7</b>
Total S-containing compounds	-	<b>1.0</b>	<b>1.5</b>	-	<b>2.0</b>	<b>2.7</b>	-	<b>0.9</b>	<b>3.0</b>

<sup>a</sup> BTXS- Benzene, Toluene, Xylene, and Styrene

samples. However, inherent minerals in RB and residual acid in TB\_nw facilitated denitrogenation reactions to generate more volatile-N compounds than TB. For instance, at 300 °C, total N-compounds were 53% for RB and TB\_nw and 34% for TB. Significant thermal cracking of heavy N-heterocyclic compounds to simple aromatic/aliphatic N-compounds occurred at higher pyrolysis temperatures (500–700 °C), reducing total nitrogenated compounds in the bio-oil to  $\approx$  23% for all samples. The effect of pre-treatment on the evolution of N-compounds was less intense at 500 and 700 °C. It has been observed that the interaction between mineral matter and N-containing compounds in biosolids was strongly limited by pyrolysis temperature [52].

Notably, anhydrosugars (including sugar alcohols) production was sensitive to pyrolysis temperatures. It was detected only at 300 °C, and the yield was improved by more than 50% following the removal of AAEMs in TB. At 500–700 °C, pre-treatment had no impact on the production of anhydrosugars as they are highly susceptible to secondary degradation facilitated by metal and acid catalysts as well as higher pyrolysis temperatures [53]. However, biosolids pre-treatment favoured the production of sugar dehydration products such as maltol and furans (10%), mainly comprising 3-HMF, furfural, and 5-methyl furfural. The acid catalysis of sugars is a popular route to enhance the formation of furfural compounds [54]. The passivation of AAEMs by acid infusion selectively enhanced sugar dehydration products, such as levoglucosone and furfural, whose yield was observed to be related to the quantity of acid added [55]. Phenols and their derivatives may originate from biosolids pyrolysis through the secondary decomposition of polysaccharides and proteins and are generally enhanced at higher temperatures from aromatisation reactions [56]. At 300 °C, the total phenolics yield was less than 10%, mostly detected in RB bio-oil. At higher temperatures, phenolics yield increased to  $\approx$  15% for both RB and TB, whereas it was no more than 10% for TB\_nw. Mineral removal by pre-treatment had no significant effect on phenol production; however,

residual acid in TB\_nw suppressed phenol formation relative to RB. Other works [36,57] have also suggested that phenol precursor such as lignin is relatively inert to AAEMs. While AAEMs are largely inert in catalysing the cleavage of the ester group in lignin to produce guaiacols (vinyl-phenols), it has been found effective in promoting the cleavage of  $\beta$ -O-4 aryl ether bonds to produce simple phenolic monomers such as cresols [55]. This could explain the higher yield of *p*-cresol with acid-pre-treated biosolids compared to RB.

Hydrocarbon production increased monotonically with temperature, and it grew from 0% to 3% at 300 °C to 20–35% at 500 °C for all samples, with RB having the lowest yield. Raising the temperature to 700 °C increased hydrocarbon yield to 28% for RB, slightly decreasing the yield to about 32% for treated biosolids. Monoaromatic hydrocarbons, mainly benzene, toluene, xylene, and styrene (BTXS), are the major compounds in the bio-oil at higher temperatures  $\geq$  500 °C. In contrast, aliphatic hydrocarbons, mainly paraffin and olefin, were detected in bio-oil from untreated biosolids at  $<$  500 °C. Acid pre-treatment enhanced aromatisation reactions, which increased the yields of monoaromatic hydrocarbons due to the suppression of AAEMs-catalysed ring opening and fragmentation reactions that would otherwise convert -CH to light oxygenates, COx gases, and char [36,58]. In a previous study [36], acid washing and infusion enhanced the formation of aromatic hydrocarbons by  $\sim$ 30%; however, both pre-treatment did not significantly change the yield of olefins, similar to the observation in the current work. The weaker effect of inherent AAEMs caused by acid pre-treatment increased the formation of undesired stable polycyclic aromatic hydrocarbons (PAHs) in bio-oil from TB and TB\_nw; however, PAHs were not detected in RB bio-oil at all temperatures. AAEMs and their minerals can enhance the cracking of heavy PAHs into monoaromatics, particularly at higher temperatures [59]. Lastly, aromatic sulfur compounds such as benzisothiazole, thiazolidine, thiophene, and aliphatic S-compounds, mainly methyl sulfides, were detected in the bio-oil obtained from treated

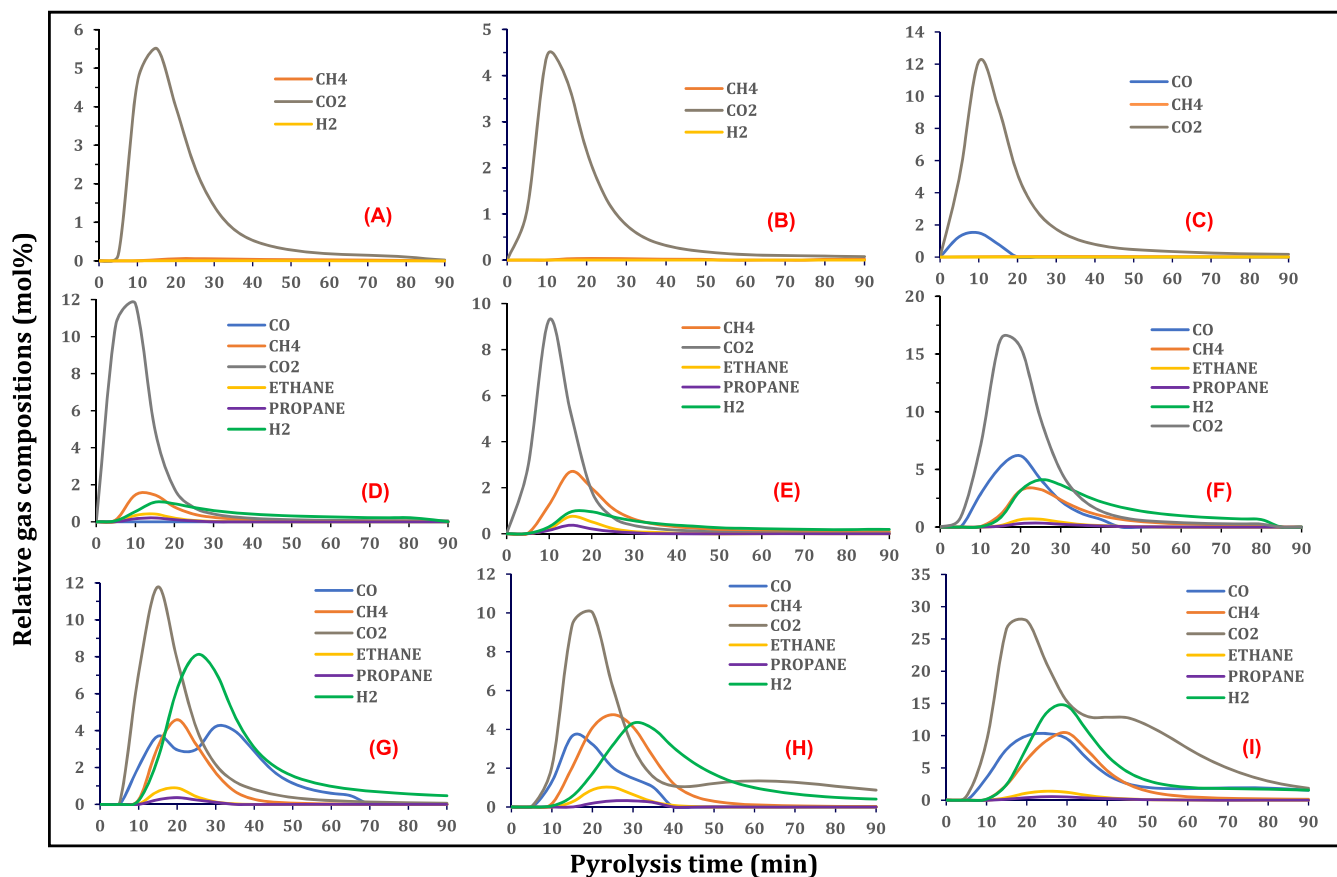


Fig. 5. Effect of pre-treatment and temperature on pyrolysis gas compositions (A) RB300 (B) TB300 (C)TB\_nw300 (D) RB500 (E) TB500 (F) TB\_nw500 (G) RB700 (H) TB700 (I) TB\_nw700.

biosolids. The evolution of these S-compounds was stronger at  $\geq 500$  °C and for TB\_nw (up to 3%). Therefore, the acid treatment should be accompanied by a neutralisation step, as in TB, to mitigate the release of volatile S-compounds.

Due to the generally high nitrogen and oxygen contents, the bio-oil may not be suitable as fuel for energy recovery. However, the chemical value of the bio-oil obtained at 300 °C can be explored for the selective recovery of N-containing compounds, and the ketone-rich fraction can be subjected to catalytic hydrodeoxygenation to produce olefins [60]. Therefore, biosolids pyrolysis at 300 °C may be considered a thermal pre-treatment step for the reduction of nitrogen and oxygen contents and improve hydrocarbon yield during subsequent pyrolysis at higher temperatures [61]. The addition of acid pre-treatment can further enhance the chemical value of the bio-oil by increasing sugars, furans, and aromatic hydrocarbon, as observed in the current work. Fonts et al. [62] reported that ammonia,  $\alpha$ -olefins, n-paraffins, aromatic hydrocarbons, nitriles, phenols, fatty acids, short carboxylic acids and indole were the most attractive chemical compounds in biosolids bio-oil.

### 3.6. Effect of pre-treatment on pyrolysis gas compositions

The evolution profile of non-condensable gases from the pyrolysis of raw and treated biosolids at 300–700 °C is shown in Fig. 5. The identified gas components are carbon oxides (CO and CO<sub>2</sub>), H<sub>2</sub>, and C<sub>1</sub>–C<sub>3</sub> saturated hydrocarbon gases (methane, ethane, and propane). The concentration of the gases was low at the start of pyrolysis as the feed was gradually heated to the desired temperature. The gas concentration steadily increased between 10 and 30 min; after that, the concentration gradually decreased, reaching zero at 60–90 min. The most abundant

gas components were H<sub>2</sub>, CO, CO<sub>2</sub> and CH<sub>4</sub>, while only traces of ethane and propane were detected at higher pyrolysis temperatures > 500 °C. Generally, gas production increased with increasing pyrolysis temperature due to the profound thermal cracking of primary decomposition products and secondary reactions. At 300 °C (Fig. 5(A–C)), CO<sub>2</sub> was the dominant gas component, with traces of CH<sub>4</sub> and H<sub>2</sub> in the pyrolysis gas stream largely from the decarboxylation of organic matter. At higher pyrolysis temperatures, gasification reactions matured, and more gas components were formed at higher concentrations stemming from the thermal cracking of heavy molecular weight volatiles to lighter ones accompanied by the release of C<sub>1</sub>–C<sub>3</sub> hydrocarbons (Fig. 5(D–I)). At 700 °C (Fig. 5(G–I)), the gas evolution was stronger, and the concentrations were highest attributed to the profound secondary cracking reactions heightened by char-volatile interactions [63].

The removal or passivation of inherent metals in biosolids via pre-treatment affected the gas evolution and concentration during pyrolysis, especially at higher pyrolysis temperatures. The pyrolysis of TB produced less CO<sub>2</sub>, CO, and H<sub>2</sub> but slightly more C<sub>1</sub>–C<sub>3</sub> hydrocarbons than RB, suggesting that pre-treatment inhibited gas production due to the inferior catalytic cracking effect of ash elements. For example, at 700 °C, the highest CO and H<sub>2</sub> concentration was 4.2 mol% and 8 mol%, respectively, for RB (Fig. 5(G)), and it was 3.6 mol% and 4.3 mol%, respectively, for TB (Fig. 5(H)). Secondary cracking was prominent and catalysed by the native metal in RB, leading to higher concentrations of CO and H<sub>2</sub>. The second CO peak in RB at 700 °C (Fig. 5(G)) after 30 min pyrolysis time can be attributed to Boudouard char gasification reactions where CO<sub>2</sub> is reacted with carbon to give CO [30]. Notably, the highest gas concentrations were observed during the pyrolysis of TB\_nw at all temperatures. The XRD pattern of TB\_nw identified Ca(HSO<sub>4</sub>)<sub>2</sub> and

Fe(HSO<sub>4</sub>)<sub>3</sub> as the major acidic sulfate salts, which facilitated H<sub>2</sub> production via the release of H<sup>+</sup> through thermal hydrolysis reactions to form normal sulfate salts (CaSO<sub>4</sub> and Fe<sub>2</sub>(SO<sub>4</sub>)<sub>3</sub>) [64]. The presence of residual acid in TB<sub>nw</sub> had a remarkable catalytic effect on gas production, with CO<sub>2</sub>, CO, CH<sub>4</sub>, and H<sub>2</sub> yield reaching a maximum concentration of 28 mol%, 10 mol%, 10.5 mol%, and 15 mol%, respectively (Fig. 5(I)). Whereas, with the full spectrum of metals in RB, the maximum gas concentration at 700 °C was 12 mol% CO<sub>2</sub>, 4 mol% CO, 4.5 mol% CH<sub>4</sub>, and 8 mol% H<sub>2</sub> (Fig. 5(G)). The improved gas production in TB<sub>nw</sub> despite lean mineral matter compared to RB was attributed to the dehydration reactions catalysed by residual H<sub>2</sub>SO<sub>4</sub>, favouring water-gas reactions [42]. Biosolids acid pre-treatment for demineralisation (as in TB) can be helpful to weaken gas production and CO<sub>2</sub> release, while pre-treatment as in TB<sub>nw</sub> strengthened gas production, and CO<sub>2</sub> yield was more than 2-fold higher than that from RB.

#### 4. Conclusions

The quality of biosolids as feedstock for pyrolysis can be improved by acid pre-treatment to selectively remove the ash-forming elements and HMs without degrading the organic matter. Mild acid pre-treatment process (using 3% v/v H<sub>2</sub>SO<sub>4</sub> at 25 °C for 60 min) followed by a water washing step achieved about 40% reduction of ash content and a 10% increase in volatile matter with carbon retention of 80%. In contrast, the acid treatment without the water washing step achieved lower demineralisation efficiency (28%) with higher carbon retention (88%). At all operating temperatures, the pyrolysis of neutralised acid-treated biosolids produced higher bio-oil and lower biochar yield due to improved organic matter devolatilisation and inorganic content reduction. The presence of residual acid in treated biosolids inhibited organic matter conversion to bio-oil; however, it enhanced gas production attributed to dehydration reactions and hydrolysis of acidic metal sulfate salts to normal metal sulfate salts. Biochar obtained from treated biosolids had higher organic matter retention, calorific value, fuel ratio, and fixed carbon due to the weakened catalytic cracking of organics, particularly at higher pyrolysis temperatures. Biosolids pre-treatment increased the stability and reduced the concentration and bioavailability of HMs in the derived biochar. The bio-oil composition was impacted by pre-treatment, and at 300 °C, anhydrosugars yield doubled in treated biosolids' bio-oil compared to raw biosolids' bio-oil. While pre-treatment did not have much effect on phenol production, monoaromatic hydrocarbon yield was remarkably improved. However, the evolution of PAHs and sulfur-containing compounds was stronger during the pyrolysis of treated biosolids than raw biosolids. Biosolids acid pre-treatment with the water washing step is preferred to increase bio-oil yield and enhance biochar quality.

#### CRedit authorship contribution statement

**Ibrahim Gbolahan Hakeem:** Conceptualization, Methodology, Formal analysis, Investigation, Writing - original draft, Writing - review & editing. **Pobitra Halder:** Validation, Writing - review & editing. **Savankumar Patel:** Writing - review & editing. **Abhishek Sharma:** Writing - review & editing. **Rajender Gupta:** Writing - review & editing. **Aravind Surapaneni:** Resources, Supervision. **Jorge Paz-Ferreiro:** Supervision, Writing - review & editing. **Kalpita Shah:** Conceptualization, Methodology, Validation, Supervision, Project administration.

#### Declaration of Competing Interest

The authors declare that they have no known competing financial interests or personal relationships that could have appeared to influence the work reported in this paper.

#### Data availability

Data will be made available on request.

#### Acknowledgements

This work is supported through Top-Up Scholarships provided by the School of Engineering, RMIT University and the ARC Training Centre for the Transformation of Australia's Biosolids Resource at RMIT University, Australia. The use of the Scanning Electron Microscope instrument in the RMIT Microanalysis and Microscopy Facility is acknowledged. The BET equipment in the Advanced Porous Materials Lab at RMIT University was used in this study. Finally, the first author acknowledged the PhD research stipend scholarship received from RMIT University, Australia.

#### Appendix A. Supporting information

Supplementary data associated with this article can be found in the online version at [doi:10.1016/j.jaap.2023.106087](https://doi.org/10.1016/j.jaap.2023.106087).

#### References

- [1] A. Gianico, C.M. Braguglia, A. Gallipoli, D. Montecchio, G. Mininni, Land application of biosolids in Europe: possibilities, con-strains and future perspectives, *Water* 13 (2021) 103, <https://doi.org/10.3390/W13010103>.
- [2] N. Gao, K. Kamran, C. Quan, P.T. Williams, Thermochemical conversion of sewage sludge: A critical review, *Prog. Energy Combust. Sci.* 79 (2020), 100843, <https://doi.org/10.1016/j.pecs.2020.100843>.
- [3] W. Zhang, Y. Liang, Effects of hydrothermal treatments on destruction of per- and polyfluoroalkyl substances in sewage sludge, *Environ. Pollut.* 285 (2021), 117276, <https://doi.org/10.1016/j.envpol.2021.117276>.
- [4] J.J. Ross, D.H. Zitomer, T.R. Miller, C.A. Weirich, P.J. Mcnamara, Emerging investigators series: pyrolysis removes common microconstituents triclocarban, triclosan, and nonylphenol from biosolids, *Environ. Sci. Water Res. Technol.* 2 (2016) 282–289, <https://doi.org/10.1039/C5EW00229J>.
- [5] O.S. Djandja, Z.C. Wang, F. Wang, Y.P. Xu, P.G. Duan, Pyrolysis of municipal sewage sludge for biofuel production: A review, *Ind. Eng. Chem. Res.* 59 (2020) 16939–16956, <https://doi.org/10.1021/acs.iecr.0c01546>.
- [6] S. Patel, S. Kundu, P. Halder, N. Ratnmayake, M.H. Marzbali, S. Aktar, E. Selezneva, J. Paz-Ferreiro, A. Surapaneni, C.C. de Figueiredo, A. Sharma, M. Megharaj, K. Shah, A critical literature review on biosolids to biochar: an alternative biosolids management option, *Rev. Environ. Sci. Biotechnol.* 19 (2020) 807–841, <https://doi.org/10.1007/s11157-020-09553-x>.
- [7] P. Giudicianni, V. Gargiulo, C.M. Grottola, M. Alfè, A.I. Ferreiro, M.A.A. Mendes, M. Fagnano, R. Ragucci, Inherent metal elements in biomass pyrolysis: a review, *Energy Fuels* 35 (2021) 5407–5478, <https://doi.org/10.1021/ACS.ENERGYFUELS.0C04046>.
- [8] H. Nan, F. Yang, L. Zhao, O. Mašek, X. Cao, Z. Xiao, Interaction of inherent minerals with carbon during biomass pyrolysis weakens biochar carbon sequestration potential, *ACS Sustain. Chem. Eng.* 7 (2018) 1591–1599, <https://doi.org/10.1021/ACSSUSCHEMENG.8B05364>.
- [9] Y. Niu, H. Tan, S. Hui, Ash-related issues during biomass combustion: Alkali-induced slagging, silicate melt-induced slagging (ash fusion), agglomeration, corrosion, ash utilization, and related countermeasures, *Prog. Energy Combust. Sci.* 52 (2016) 1–61, <https://doi.org/10.1016/j.pecs.2015.09.003>.
- [10] M.J. Bentley, J.P. Kearns, B.M. Murphy, R.S. Summers, Pre-pyrolysis metal and base addition catalyzes pore development and improves organic micropollutant adsorption to pine biochar, *Chemosphere* 286 (2022), 131949, <https://doi.org/10.1016/j.chemosphere.2021.131949>.
- [11] I.G. Hakeem, P. Halder, C.C. Dike, K. Chiang, A. Sharma, J. Paz-Ferreiro, K. Shah, Advances in biosolids pyrolysis: Roles of pre-treatments, catalysts, and co-feeding on products distribution and high-value chemical production, *J. Anal. Appl. Pyrolysis* 166 (2022), 105608, <https://doi.org/10.1016/J.JAAP.2022.105608>.
- [12] R. Patel, P. Zaveri, N.S. Munshi, Microbial fuel cell, the Indian scenario: developments and scopes, *Biofuels* 10 (2019) 101–108, <https://doi.org/10.1080/17597269.2017.1398953>.
- [13] N.A. Haji Morni, C.M. Yeung, H. Tian, Y. Yang, N. Phusunti, M.S. Abu Bakar, A. K. Azad, Catalytic fast Co-Pyrolysis of sewage sludge—sawdust using mixed metal oxides modified with ZSM-5 catalysts on dual-catalysts for product upgrading, *J. Energy Inst.* 94 (2021) 387–397, <https://doi.org/10.1016/J.JOIEI.2020.10.005>.
- [14] Z. Qiu, Y. Zhai, S. Li, X. Liu, X. Liu, B. Wang, Y. Liu, C. Li, Y. Hu, Catalytic co-pyrolysis of sewage sludge and rice husk over biochar catalyst: Bio-oil upgrading and catalytic mechanism, *Waste Manag* 114 (2020) 225–233, <https://doi.org/10.1016/J.WASMAN.2020.07.013>.
- [15] N. Rathnayake, S. Patel, I.G. Hakeem, J. Pazferreiro, A. Sharma, R. Gupta, C. Rees, D. Bergmann, J. Blackbeard, A. Surapaneni, K. Shah, Co-pyrolysis of biosolids with lignocellulosic biomass: Effect of feedstock on product yield and composition, *Process Saf. Environ. Prot.* (2023), <https://doi.org/10.1016/J.PSEP.2023.02.087>.

- [16] X. Wang, S. Deng, H. Tan, A. Adeosun, M. Vujanović, F. Yang, N. Duić, Synergetic effect of sewage sludge and biomass co-pyrolysis: A combined study in thermogravimetric analyzer and a fixed bed reactor, *Energy Convers. Manag* 118 (2016) 399–405, <https://doi.org/10.1016/j.enconman.2016.04.014>.
- [17] I.G. Hakeem, P. Halder, M.H. Marzbali, S. Patel, N. Rathnayake, A. Surapaneni, G. Short, J. Paz-Ferreiro, K. Shah, Mild sulphuric acid pre-treatment for metals removal from biosolids and the fate of metals in the treated biosolids derived biochar, *J. Environ. Chem. Eng.* 10 (2022), 107378, <https://doi.org/10.1016/J.JECE.2022.107378>.
- [18] G. Liu, M.M. Wright, Q. Zhao, R.C. Brown, Hydrocarbon and ammonia production from catalytic pyrolysis of sewage sludge with acid pretreatment, *ACS Sustain. Chem. Eng.* 4 (2016) 1819–1826, <https://doi.org/10.1021/acssuschemeng.6b00016>.
- [19] S. Tang, C. Zheng, Z. Zhang, Effect of inherent minerals on sewage sludge pyrolysis: Product characteristics, kinetics and thermodynamics, *Waste Manag* 80 (2018) 175–185, <https://doi.org/10.1016/j.wasman.2018.09.012>.
- [20] Z. Yang, D. Wang, G. Wang, S. Zhang, Z. Cheng, J. Xian, Y. Pu, T. Li, Y. Jia, Y. Li, W. Zhou, X. Xu, Removal of Pb, Zn, Ni and Cr from industrial sludge by biodegradable washing agents: Caboxyethylthiosuccinic acid and itaconic-acrylic acid, *J. Environ. Chem. Eng.* 9 (2021), 105846, <https://doi.org/10.1016/J.JECE.2021.105846>.
- [21] R. Kumar, V. Strezov, H. Weldekidan, J. He, S. Singh, T. Kan, B. Dastjerdi, Lignocellulose biomass pyrolysis for bio-oil production: A review of biomass pre-treatment methods for production of drop-in fuels, *Renew. Sustain. Energy Rev.* 123 (2020), 109763, <https://doi.org/10.1016/J.RSER.2020.109763>.
- [22] V.T. Pham, C.Y. Guan, P.C. Han, B.M. Matsagar, K.C.W. Wu, T. Ahamad, C. Y. Chang, C.P. Yu, Acid-catalyzed hydrothermal treatment of sewage sludge: effects of reaction temperature and acid concentration on the production of hydrolysis by-products, *Biomass - Convers. Biorefinery.* 13 (2021) 7533–7546, <https://doi.org/10.1007/S13399-021-01495-W/FIGURES/5>.
- [23] I.G. Hakeem, P. Halder, S. Aktar, M.H. Marzbali, A. Sharma, A. Surapaneni, G. Short, J. Paz-Ferreiro, K. Shah, Investigations into the closed-loop hydrometallurgical process for heavy metals removal and recovery from biosolids via mild acid pre-treatment, *Hydrometallurgy* 218 (2023), 106044, <https://doi.org/10.1016/J.HYDROMET.2023.106044>.
- [24] I. Beauchesne, R. Ben Cheikh, G. Mercier, J.F. Blais, T. Ourada, Chemical treatment of sludge: In-depth study on toxic metal removal efficiency, dewatering ability and fertilizing property preservation, *Water Res* 41 (2007) 2028–2038, <https://doi.org/10.1016/J.WATRES.2007.01.051>.
- [25] J. Shao, R. Yan, H. Chen, H. Yang, D.H. Lee, Catalytic effect of metal oxides on pyrolysis of sewage sludge, *Fuel Process. Technol.* 91 (2010) 1113–1118, <https://doi.org/10.1016/j.fuproc.2010.03.023>.
- [26] S. Tang, C. Zheng, F. Yan, N. Shao, Y. Tang, Z. Zhang, Product characteristics and kinetics of sewage sludge pyrolysis driven by alkaline earth metals, *energy* 153 (2018) 921–932, <https://doi.org/10.1016/j.energy.2018.04.108>.
- [27] S. Tang, S. Tian, C. Zheng, Z. Zhang, Effect of Calcium Hydroxide on the Pyrolysis Behavior of Sewage Sludge: Reaction Characteristics and Kinetics, *Energy Fuels* 31 (2017) 5079–5087, <https://doi.org/10.1021/acs.energyfuels.6b03256>.
- [28] Y. Kim, W. Parker, A technical and economic evaluation of the pyrolysis of sewage sludge for the production of bio-oil, *Bioresour. Technol.* 99 (2008) 1409–1416, <https://doi.org/10.1016/j.biortech.2007.01.056>.
- [29] N. Rathnayake, S. Patel, P. Halder, S. Aktar, J. Pazferreiro, A. Sharma, A. Surapaneni, K. Shah, Co-pyrolysis of biosolids with alum sludge: Effect of temperature and mixing ratio on product properties, *J. Anal. Appl. Pyrolysis* 163 (2022), 105488, <https://doi.org/10.1016/J.JAAP.2022.105488>.
- [30] S. Patel, S. Kundu, P. Halder, G. Velusamy, B. Pramanik, Slow pyrolysis of biosolids in a bubbling fluidised bed reactor using biochar, activated char and lime, *J. Anal. Appl. Pyrolysis* 144 (2019) 1–11, <https://doi.org/10.1016/j.jaap.2019.104697>.
- [31] S.A. Channiwala, P.P. Parikh, A unified correlation for estimating HHV of solid, liquid and gaseous fuels, *Fuel* 81 (2002) 1051–1063, [https://doi.org/10.1016/S0016-2361\(01\)00131-4](https://doi.org/10.1016/S0016-2361(01)00131-4).
- [32] W.L. Lindsay, W.A. Norvell, Development of a DTPA Soil Test for Zinc, Iron, Manganese, and Copper, *Soil Sci. Soc. Am. J.* 42 (1978) 421–428, <https://doi.org/10.2136/SSSAJ1978.03615995004200030009X>.
- [33] E.P.A. Victoria, Guidelines for Environmental Management: Biosolids Land Application, Southbank, Victoria 3006, Australia, 2004.
- [34] X. Wang, L. Sheng, X. Yang, Pyrolysis characteristics and pathways of protein, lipid and carbohydrate isolated from microalgae *Nannochloropsis* sp, *Bioresour. Technol.* 229 (2017) 119–125, <https://doi.org/10.1016/J.BIORTECH.2017.01.018>.
- [35] S.R. Patel, S.K. Kundu, P.K. Halder, A. Setiawan, J. Paz-Ferreiro, A. Surapaneni, K. V. Shah, A Hybrid Kinetic Analysis of the Biosolids Pyrolysis using Thermogravimetric Analyser, *ChemistrySelect* 3 (2018) 13400–13407, <https://doi.org/10.1002/slct.201802957>.
- [36] K. Wang, J. Zhang, B.H. Shanks, R.C. Brown, The deleterious effect of inorganic salts on hydrocarbon yields from catalytic pyrolysis of lignocellulosic biomass and its mitigation, *Appl. Energy* 148 (2015) 115–120, <https://doi.org/10.1016/j.apenergy.2015.03.034>.
- [37] X. Zhu, L. Zhao, F. Fu, Z. Yang, F. Li, W. Yuan, M. Zhou, W. Fang, G. Zhen, X. Lu, X. Zhang, Pyrolysis of pre-dried dewatered sewage sludge under different heating rates: Characteristics and kinetics study, *Fuel* 255 (2019), 115591, <https://doi.org/10.1016/J.FUEL.2019.05.174>.
- [38] N. Gao, J. Li, B. Qi, A. Li, Y. Duan, Z. Wang, Thermal analysis and products distribution of dried sewage sludge pyrolysis, *J. Anal. Appl. Pyrolysis* 105 (2014) 43–48, <https://doi.org/10.1016/J.JAAP.2013.10.002>.
- [39] S. Zhou, Z. Wang, S. Liaw, C. Li, M. Garcia-perez, Effect of sulfuric acid on the pyrolysis of Douglas fir and hybrid poplar wood: Py-GC / MS and TG studies, *J. Anal. Appl. Pyrolysis* 104 (2013) 117–130, <https://doi.org/10.1016/j.jaap.2013.08.013>.
- [40] S. Aktar, M.A. Hossain, N. Rathnayake, S. Patel, G. Gasco, A. Mendez, C. de Figueiredo, A. Surapaneni, K. Shah, J. Paz-Ferreiro, Effects of temperature and carrier gas on physico-chemical properties of biochar derived from biosolids, *J. Anal. Appl. Pyrolysis* 164 (2022), 105542, <https://doi.org/10.1016/J.JAAP.2022.105542>.
- [41] D. Carpenter, T.L. Westover, S. Czernik, W. Jablonski, Biomass feedstocks for renewable fuel production: a review of the impacts of feedstock and pretreatment on the yield and product distribution of fast pyrolysis bio-oils and vapors, *Green. Chem.* 16 (2014) 384–406, <https://doi.org/10.1039/C3GC41631C>.
- [42] S. Zhou, D. Mourant, C. Lievens, Y. Wang, C. Li, M. Garcia-perez, Effect of sulfuric acid concentration on the yield and properties of the bio-oils obtained from the auger and fast pyrolysis of Douglas Fir, *Fuel* 104 (2013) 536–546, <https://doi.org/10.1016/j.fuel.2012.06.010>.
- [43] Y. Zhang, P. Lv, J. Wang, J. Wei, P. Cao, N. Bie, Y. Bai, G. Yu, Product characteristics of rice straw pyrolysis at different temperatures: Role of inherent alkali and alkaline earth metals with different occurrence forms, *J. Energy Inst.* 101 (2022) 201–208, <https://doi.org/10.1016/J.JOEI.2022.01.016>.
- [44] X. Sun, R. Shan, X. Li, J. Pan, X. Liu, R. Deng, J. Song, Characterization of 60 types of Chinese biomass waste and resultant biochars in terms of their candidacy for soil application, *GCB Bioenergy* 9 (2017) 1423–1435, <https://doi.org/10.1111/GCBB.12435>.
- [45] X. Xiao, Z. Chen, B. Chen, H/C atomic ratio as a smart linkage between pyrolytic temperatures, aromatic clusters and sorption properties of biochars derived from diverse precursory materials, *Sci. Rep.* 6 (2016), <https://doi.org/10.1038/srep22644>.
- [46] M. Praspaliauskas, N. Pedišius, N. Striugas, Elemental Migration and Transformation from Sewage Sludge to Residual Products during the Pyrolysis Process, *Energy Fuels* 32 (2018) 5199–5208, [https://doi.org/10.1021/ACS.ENERGYFUELS.8B00196/ASSET/IMAGES/LARGE/EF-2018-001968\\_0006.JPEG](https://doi.org/10.1021/ACS.ENERGYFUELS.8B00196/ASSET/IMAGES/LARGE/EF-2018-001968_0006.JPEG).
- [47] Z. Zhang, R. Ju, H. Zhou, H. Chen, Migration characteristics of heavy metals during sludge pyrolysis, *Waste Manag* 120 (2021) 25–32, <https://doi.org/10.1016/j.wasman.2020.11.018>.
- [48] D. del Mundo Dacera, S. Babel, Use of citric acid for heavy metals extraction from contaminated sewage sludge for land application, *Water Sci. Technol.* 54 (2006) 129–135, <https://doi.org/10.2166/wst.2006.764>.
- [49] Z. Cui, G. Xu, B. Ormeci, H. Liu, Z. Zhang, Transformation and stabilization of heavy metals during pyrolysis of organic and inorganic-dominated sewage sludges and their mechanisms, *Waste Manag* 150 (2022) 57–65, <https://doi.org/10.1016/J.WASMAN.2022.06.023>.
- [50] A. Fullana, J.A. Conesa, R. Font, I. Martin-Gullon, Pyrolysis of sewage sludge: nitrogenated compounds and pretreatment effects, *J. Anal. Appl. Pyrolysis* 69 (2003) 561–575, [https://doi.org/10.1016/S0165-2370\(03\)00052-4](https://doi.org/10.1016/S0165-2370(03)00052-4).
- [51] X. Yang, B. Wang, Y. Guo, F. Yang, F. Cheng, Co-hydrothermal carbonization of sewage sludge and coal slime for clean solid fuel production: a comprehensive assessment of hydrochar fuel characteristics and combustion behavior, *Biomass - Convers. Biorefinery* (2022), <https://doi.org/10.1007/s13399-022-03601-y>.
- [52] L.H. Wei, L.N. Wen, M.J. Liu, T.H. Yang, Interaction Characteristics of Mineral Matter and Nitrogen during Sewage Sludge Pyrolysis, *Energy Fuels* 30 (2016) 10505–10510, <https://doi.org/10.1021/acs.energyfuels.6b02146>.
- [53] I.G. Hakeem, P. Halder, M.H. Marzbali, S. Patel, S. Kundu, J. Paz-Ferreiro, A. Surapaneni, K. Shah, Research progress on levoglucosan production via pyrolysis of lignocellulosic biomass and its effective recovery from bio-oil, *J. Environ. Chem. Eng.* 9 (2021), 105614, <https://doi.org/10.1016/j.jece.2021.105614>.
- [54] S.R.G. Oudenhoven, R.J.M. Westerhof, N. Aldenkamp, D.W.F. Brilman, S.R.A. Kersten, Demineralization of wood using wood-derived acid: Towards a selective pyrolysis process for fuel and chemicals production, *J. Anal. Appl. Pyrolysis* 103 (2013) 112–118, <https://doi.org/10.1016/j.jaap.2012.10.002>.
- [55] S. Zhou, Y. Xue, J. Cai, C. Cui, Z. Ni, Z. Zhou, An understanding for improved biomass pyrolysis: Toward a systematic comparison of different acid pretreatments, *Chem. Eng. J.* 411 (2021), 128513, <https://doi.org/10.1016/J.CEJ.2021.128513>.
- [56] X. Huang, J.P. Cao, P. Shi, X.Y. Zhao, X.B. Feng, Y.P. Zhao, X. Fan, X.Y. Wei, T. Takarada, Influences of pyrolysis conditions in the production and chemical composition of the bio-oils from fast pyrolysis of sewage sludge, *J. Anal. Appl. Pyrolysis* 110 (2014) 353–362, <https://doi.org/10.1016/J.JAAP.2014.10.003>.
- [57] P.R. Patwardhan, R.C. Brown, B.H. Shanks, Understanding the Fast Pyrolysis of Lignin, *ChemSusChem* 4 (2011) 1629–1636, <https://doi.org/10.1002/CSSC.201100133>.
- [58] D.L. Dalluge, T. Daugaard, P. Johnston, N. Kuzhiyil, M.M. Wright, R.C. Brown, Continuous production of sugars from pyrolysis of acid-infused lignocellulosic biomass, *Green. Chem.* 16 (2014) 4144–4155, <https://doi.org/10.1039/c4gc00602j>.
- [59] S. Hu, L. Jiang, Y. Wang, S. Su, L. Sun, B. Xu, L. He, J. Xiang, Effects of inherent alkali and alkaline earth metallic species on biomass pyrolysis at different temperatures, *Bioresour. Technol.* 192 (2015) 23–30, <https://doi.org/10.1016/j.biortech.2015.05.042>.
- [60] A. Witsuthammakul, T. Sooknoi, Selective hydrodeoxygenation of bio-oil derived products: ketones to olefins, *Catal. Sci. Technol.* 5 (2015) 3639–3648, <https://doi.org/10.1039/C5CY00367A>.
- [61] Y. Liu, Y. Zhai, S. Li, X. Liu, X. Liu, B. Wang, Z. Qiu, C. Li, Production of bio-oil with low oxygen and nitrogen contents by combined hydrothermal pretreatment and

- pyrolysis of sewage sludge, *energy* 203 (2020), 117829, <https://doi.org/10.1016/J.ENERGY.2020.117829>.
- [62] I. Fonts, A. Navarro-Puyuelo, N. Ruiz-Gómez, M. Atienza-Martínez, A. Wisniewski, G. Gea, Assessment of the production of value-added chemical compounds from sewage sludge pyrolysis liquids, *Energy Technol.* 5 (2017) 151–171, <https://doi.org/10.1002/ente.201600183>.
- [63] Q. Guo, Z. Cheng, G. Chen, B. Yan, J. Li, L. Hou, F. Ronsse, Assessment of biomass demineralization on gasification: From experimental investigation, mechanism to potential application, *Sci. Total Environ.* 726 (2020), 138634, <https://doi.org/10.1016/J.SCITOTENV.2020.138634>.
- [64] N. Kuzhiyil, D. Dalluge, X. Bai, H. Kim, Pyrolytic sugars from cellulosic biomass, *ChemSusChem* 0 (2012) 1–10, <https://doi.org/10.1002/cssc.201200341>.

# Induced Toxicity and Bioaccumulation of Chromium (VI) in Cluster Bean: Oxidative Stress, Antioxidative Protection Strategy, Accumulation and Translocation of Certain Nutrient

Kamlesh Kumar Tiwari<sup>1,\*</sup>, Manoj Kumar Bidhar<sup>1</sup>, Naveen Kumar Singh<sup>2</sup>

<sup>1</sup>Sophisticated Instrumentation Centre for Applied Research and Testing (SICART), Sardar Patel Centre for Science and Technology,

Vallabh Vidyanagar, Anand- 388120 (Gujarat), India; <sup>2</sup>Department of Chemistry, Environmental Science Discipline

Manipal University Jaipur- 303007 (Rajasthan), India

Received: September 14, 2022; Revised: November 3, 2022; Accepted: December 2, 2022

## Abstract

(Language note by the journal's language editor: the whole manuscript should be checked for accurate use of active and passive sentence structures!!!!)

The present investigation was carried out to examine the noticeable phytotoxicity symptoms, growth behavior, metabolic changes, sulfur, phosphorus, iron, chromium translocation and accumulation in the cluster bean (*Cyamopsis tetragonoloba* L) plants under different concentration of Cr (VI) treatment. Initially plants were grown after sowing of seeds for 90 d with supplying essential nutrients solution. On the day 91 after plant growth, Cr treatment was given as potassium dichromate at 0.05 mM, 0.25 mM and 0.50 mM concentration along with a set of control (0.00 mM Cr). At 0.5 mM of Cr (VI), visual toxicity symptoms were noticed 8-9 days after exposure expressed as loss of turgor, old as well as central leaves became chlorotic, wilted and reductions in leaf dimension. Later phases of toxicity symptoms appear on newly young upper leaves followed by chlorosis and necrosis in patches at subsequent stages. After 15 days of Cr exposure, toxicity symptoms showed at lower levels (0.25 mM) with decreased leaf area, RWC, biomass, yield, concentration of chlorophyll, non-reducing sugar, protein nitrogen, total nitrogen, starch, protein, hill activity, glutathione reductase and non-protein thiol; however, the concentration of reducing sugar, total sugar, non-protein nitrogen, catalase activity, peroxidase, ribonuclease, acid phosphatase, proline and lipid peroxidation increased in the Cr treated plants. Excess levels of Cr concentration resulted in reduction of iron (Fe) accumulation in the leaves from 497 to 176  $\mu\text{g/g}^1\text{dw}$  along with sulfur (S) and phosphorus (P) translocation significantly at 0.50 mM Cr concentration. Maximum Cr accumulation recorded in the roots ( $197\mu\text{g g}^{-1}\text{dw}$ ) and leaves ( $142\mu\text{g g}^{-1}\text{dw}$ ) and minimum in the shoots ( $69\mu\text{g g}^{-1}\text{dw}$ ) at higher concentration of Cr (0.50 mM) and 30 days of treatment duration. The present study concludes that uptake and accumulation of Cr at higher concentration affect the plant growth, metabolic processes, translocation of essential nutrients, crop yield and may lead to health hazards.

**Keywords :** Chromium; Phytotoxicity; RWC; Glutathione reductase; Non protein thiol

## 1. Introduction

The chromium (Cr) is a metal known for its toxic effects due to its detrimental effects on living organisms including human beings and persistent nature in the soil and water for a long time once contaminated (Kapoor et al., 2022). Cr (VI) and Cr (III) are more stable among several chromium oxidation state (Shanker et al., 2005), and hexavalent chromium causes more toxicity in the living being as compared to trivalent chromium due to its more reactivity and mobility (Cervantes et al., 2001; Von Handorf et al., 2021). Cr has been listed as one of the 14 most dangerous substances due to its toxic and detrimental effects on plants and other organisms (EPA 2000).

Chromium (Cr) in trace amount required in animals including human beings for certain metabolism (Mertz 1969), however, no known biological role reported in the plant metabolism (Reale et al., 2016). Presence of chromium in water bodies is largely due to discharge of industrial effluent particularly from tanneries (Nriagu, 1988) and electroplating industries. On average, 2000–3200 tons of Cr beings discharged in the aquatic environment by tanneries effluent annually in India (Chandra et al., 1997). Discharge of more Cr in the water and soil leads to serious health concern through environmental and food chain contamination (Dube et al., 2003; Ahmed et al., 2016; Singh et al., 2021).

Effects of chromium in relation to phytotoxicity have been investigated by Tiwari et al., (2008; 2009; 2013) on

\* Corresponding author. e-mail: drkktiware14@rediffmail.com; kkt@sicart.res.in.

The author K.K. Tiwari and N.K. Singh contributed equally to the paper.

\***Abbreviations :** Cr Chromium, Cr (VI) Hexavalent chromium, RWC Relative Water Content, d Days

important crop plants due to its uptake from soil, water and subsequent accumulation in the plant tissues. Cr has detrimental impacts on the plant's growth due to imbalances in nutrients uptake and metabolic processes due to its competing uptake with other essential elements having similar structure and absorption pathway. Also, Cr uptake in plants leads to formation of more reactive oxygen species (ROS) due to oxidative damage of plant tissues, ultrastructural changes in the chloroplast, cell membrane and subsequent phytotoxicity (Sharma et al., 2020a). Phytotoxicity leads to retarded growth of plants, seed germination inhibition, degradation of photosynthetic pigments, nutrient imbalances, and oxidative injuries (Panda et al., 2003; Tiwari et al., 2009; Tiwari et al., 2013). Trivalent chromium (Cr III) treatment induces stunted growth and phytotoxicity with smaller leaves, wilting and chlorosis (Chatterjee and Chatterjee 2000). Similarly, Cr induced biochemical changes and enzyme activities in the crop plant under different concentrations leads to chlorosis and necrosis of leaves (Dube et al., 2003).

Cr effects nutrients and water uptake in plants leads to reduction in cell division, reduced translocation of essential elements, decrease uptake of selective inorganic nutrients, increase in generation of reactive radicals and oxidative stress, essential nutrients substitution with ligands and other key molecules, damage to plant tissues and organelles including chloroplasts, mitochondria and nucleic acids (Cervantes et al., 2001; Shanker et al., 2005; Tiwari et al., 2013). Although Cr induced stress may be alleviated by activities of antioxidants, it is more susceptible to Cr toxicity in plants at higher concentration (Dong et al., 2007). Toxicity of Cr basically depends on the oxidation state, mobility in rhizosphere, uptake, translocation, and accumulation in the plant tissues. Cr (VI) follows the same pathway of active transport for plant uptake as other anions like sulphate (Cervantes et al., 2001). Iron (Fe), Sulfur (S) and phosphorus (P) compete with chromium for binding sites of carriers (Wallace et al., 1976). Micronutrient deficiencies in different crops were reported from agricultural fields irrigated with tannery effluent (Sujatha and Gupta 1996; Broadway et al., 2010). Present study was undertaken to evaluate tolerance level of Cr (VI), visual toxicity symptoms, physiological and metabolic changes, nutrient uptake and translocation in the plant, cluster bean at different concentration of Cr (VI) exposures under sand pot culture growth condition.

## 2. Materials and Methods

### 2.1. Sand pot culture experimental setup

The plant Cluster bean (*Cyamopsis tetragonoloba* L) cv. Agaita Guara-112 grown in pre-washed sand as per procedure of Hewitt (1966) with slight modification (Agarwala and Chatterjee 1996) to maintain ambient temperature optimum (25<sup>0</sup>-30<sup>0</sup>C) under glasshouse-controlled condition for Indian climatic condition. Polyethylene made containers with 10 L size having a hole at center used to grow plants having roofed with a reversed watch glass and glass wool. Nutrient solution was prepared (control) with a composition of 4m MKNO<sub>3</sub> (Potassium nitrate), 4 mM Ca (NO<sub>3</sub>)<sub>2</sub> (Calcium nitrate), 2 mM MgSO<sub>4</sub> (Magnesium sulfate), 1.33 mM NaH<sub>2</sub>PO<sub>4</sub> (Sodium

dihydrogen phosphate), 100 μM Fe EDTA (Ferric Ethylene Diamine Tetra Acetic Acid), 10 μM MnSO<sub>4</sub> (Manganese sulfate), 30 μM H<sub>3</sub>BO<sub>3</sub> (Boric Acid), 1 μM CuSO<sub>4</sub> (Copper sulphate), 1 μM ZnSO<sub>4</sub> (Zinc sulphate), 0.2 MNa<sub>2</sub>MoO<sub>4</sub> (Sodium molybdate), 0.1 μM CaSO<sub>4</sub> (Calcium sulfate), 0.1 μM NiSO<sub>4</sub> (Nickel sulphate) and 0.1 Mm NaCl (Sodium chloride). Concentration of iron in the nutrient solution is maintained with Fe EDTA (Ferric ethylene diamine tetra acetic acid) chelate as per the recommendation of Jacobson (1951) and pH maintained to 6.8±0.2 in the prepared nutrient solution during the entire treatment duration.

### 2.2. Plant growth and chromium treatment

Based on the growth condition, life cycle of test plant and assessed phytotoxic parameters under treatment of Cr (VI), plants were initially grown for 90 d along with complete nutrient solution after sowing of planting seeds in the pots to acclimatize and achieve uniform growth under sand culture experimental condition. Prepared nutrient solution was supplied on regular basis during the experiment duration except in case flushing of pots with deionized water removing the roots exudates and settled salts. After acclimatization under normal growth sand culture conditions, on the day 91, pots were kept in a group of three pots and three lots along with one lot to serve as the control, in which no Cr was added. In the remaining lots, Cr (VI) was supplied at 0.05, 0.25, 0.50 mM concentration superimposed along with base nutrient solutions. Nutrient solution was supplied to plant pots every day on a regular basis except during the removal of salts and other substances from the sand culture medium by flushing with deionized water. Visible phytotoxic symptoms and other phytotoxic parameters of Cr treatment were observed continuously for 30 d after Cr exposures with short treatment duration to complete the study before the achieving maturity stage of the test plant. Plant pots were regularly monitored and maintained under sand culture growth condition for 120 days throughout during the Cr treatment experiment.

### 2.3. Measurement of growth parameters and biochemical analysis

Cr induced effects on growth behavior, metabolic changes, imbalances in uptake and translocation of sulphur, phosphorus, iron and chromium were studied in detail in the present investigation. On 106 d (16 d of chromium treatment), the Relative Water Content (RWC) was analyzed in the analogous middle leaves as per procedure of Barrs and Weatherley (1962) during between 9.00 and 11.00 AM under waterlogged sand with nutrient solution in the pots. Temperature (Ambient) was recorded between 25-30°C along with atmospheric humidity at the range of 65-75%. As an index of plant growth, leaf area (cm<sup>2</sup>) deliberated by Delta-T leaf area dimension system was measured at d 16 after Cr treatment. At d 107 (17 d after Cr treatment), mature young leaves were harvested from the plants and processed with crude leaf extract for determination of chlorophyll (a, b and total) and Hill activity, sugars and starch content, nitrogen and phenol concentration, and enzyme activities (peroxidase, catalase, ribonuclease, and acid phosphatase), lipid peroxidation, proline, non-protein thiol and soluble protein by following the prescribed standard procedures. Chlorophyll a, b and



total content were determined in the leaves extracted from harvested fresh leaves by crushing in 80% acetone by following the procedure of Arnon (1949). Similarly, Hill activity was determined at 620 nm by using calorimeter with reaction of 2,4,6-Dichlorophenol Indo Phenol (DCPIP) and determined changes in optical density (O.D./10 min/100mg fw) by following the method of Brewer and Jogendorf 1965. Reducing, non-reducing and total sugar concentration in tested plants was determined by the method of Nelson (1944). Starch concentration was measured as per the method prescribed by Montgomery (1957). Nitrogen fraction was analyzed as per the method given by Chibnall et al. (1943). Phenols content is analyzed by using the method of Swain and Hillis (1959). *Enzymatic activities* of peroxidase, catalase, ribonuclease, and *acid phosphatase* were determined in the harvested fresh leaves extract after homogenizing leaf sample in the ice-cold glass distilled water (1:10) and grinding with help of pestle and mortar at 4°C. Peroxidase and catalase activity was assayed by the method of Luck (1963) and Bisht et al. (1989), respectively. Similarly, ribonuclease was assayed by the method of Tuve and Anfinson (1960) and acid phosphatase by method of Schmidt (1955). Lipid peroxidation is determined in terms of malondialdehyde (MDA) content in the leaves by the reaction of Thiobarbituric Acid (TBA) as described by Heath and Packer, 1968. Proline content was determined by following the method of Bates *et al.*, 1973. Glutathione reductase was determined in the leaves extract by following the procedure of Smith *et al.*, 1988. Non protein thiol (NP-SH) and soluble protein were determined in leaf homogenate precipitated in TCA following the method of Boyer (1954) and Bradford (1976) using bovine serum albumin (BSA) as standard, respectively.

#### 2.4. Estimation of iron and chromium

At 120 d of growth (30 d after Cr treatment), Cluster Bean plants are harvested for analysis of tissue. Harvested treated plant samples, washed with tap water, were wiped with 0.01 N HCl and rinsed with deionized water then roots, shoots and leaves were separated, chopped, and kept in a forced-draught oven at 70°C for complete dryness. *For analysis of Fe and Cr, harvested dried plant sample was digested in a mixture of HClO<sub>4</sub>: HNO<sub>3</sub> (1:4v/v), up to dryness (Piper, 1942) to get clear digests samples and then diluted with distilled water (milli-Q grade) for estimation of iron and chromium using ICP-OES (Optima 3300 RL).*

#### 2.5. Quality control and assurance

For quality control and quality assurance, the instrumental techniques and standard calibration reference materials of Cr (EPA, quality control samples from E-Merck, Germany) used, and for Iron (BND, 1101.02) from National Physical Laboratory (NPL), India used. Analytical data quality of the tested element was ensured by multiple analysis (n=5) of standard reference samples and data established about ±2.01% of certified value. Blanks were taken in triplicate for all sets of samples to ensure accuracy of the method with the detection limit of chromium (0.5 ppb) and iron (0.3 ppb). Mean resurgence was observed around 98 and 96 for chromium and iron, respectively.

## 2.6. Analysis of data

Experiment conducted in a randomized block design and all measurements were conducted in triplicate and twice. *All data was analyzed for two-way analysis of variance (ANOVA) to measure significance between treatments and to ensure variability and validity of results.* Standard deviation of the means was calculated and given along with the mean according to the method of Panse and Sukhatme (1954).

## 3. Results

### 3.1. Periodic observation of phytotoxic symptoms

To investigate Cr induced phytotoxicity, the plants of cluster bean grown under refined sand pot culture condition with Cr (VI) treatment at different concentration (0.05, 0.25, 0.50 mM) along with a set of control. The sand culture technique was very useful for specific symptoms-based study, plant nutrition, plant-metal interaction, plant physiology and plant biochemistry study of a single or mixed metal treatment under controlled conditions as it provides better growth conditions as soil without any interference of other elements. Phytotoxic effects of chromium treatment in the treated plants were observed in terms of grain yield production up to the maturity stage. After d 8 of Cr treatment, toxicity symptoms were observed as chlorosis on the middle leaves followed by wilting at 0.25 mM and 0.50 mM Cr of treatment. On 10<sup>th</sup> d of Cr treatment, older leaves changed into golden yellow color with reduced number and small size followed by chlorosis intensification and severe necrosis in subsequent days and formed large necrotic areas. Further after a few days, chlorotic leaves observed were permanently dried and wilted leading to leaf fall. Similarly, the next upper young leaf showed the same pattern of toxicity spread over a large area. After 15-16 d of Cr treatment, chlorosis symptoms are relatively delayed in the leaves of plants grown at low concentration of Cr.

### 3.2. Growth Responses of cluster bean under Cr treatment

Growth responses of cluster bean plant under chromium treatment in terms of biomass production, leaf area index and relative water content (RWC), grain yield are given in the Table 1. In the present study, dry biomass of cluster bean is recorded to decrease with increased chromium in the growth medium (Nutrient solution) from 0.05 mM to 0.50 mM. At 0.5 mM Cr (VI) concentration, and after 120 days of maturity, significant reduction (76.9%) in biomass was observed as comparison to the control plants. In term of grain yield, pods produced only in the pots treated with 0.05 mM and 0.25 mM Cr (VI), pods were not produced at higher level (0.50 mM). Similarly, grain weight decreased considerably from 0.05 mM and 0.25 mM of Cr treatment which was more pronounced at 0.25 mM Cr (VI) in comparison to control plant. Seed size and shape were found abnormal with more deformed and shriveled seed in plants treated with higher Cr concentration with reduction grain yield (85.94%) at 0.25 mM of Cr (VI) concentration. At d 118 (28 d after metal exposure), leaf area of cluster beans observed decrease with increasing Cr (VI) concentration in the solution in comparison to control plants and recorded a

depression of 55.58% in the plants treated with 0.50 mM of Cr (VI). Similarly, relative water content (RWC) was observed to decrease gradually in leaves with increasing Cr concentration as compared to control plants which showed a decrease of 4.26%, 42.9% and 60.3% at

0.05mM, 0.1 mM and 0.25mM Cr concentration, respectively. Biomass reduction in Cr treated cluster beans may be due to profound loss of moisture content and tissue damage.

**Table 1.** Effect of variable chromium exposure on biomass, grain yield, leaf area and relative water content of cluster bean plants.

Days of growth	Days after metal supply		mM chromium treatment				LSD (P=0.05)
			Control	0.05	0.25	0.50	
120	30	Biomass: g plant <sup>-1</sup>	28.52 ±1.80	21.75 ±1.03	10.46 ±0.48	6.58 ±0.21	0.81
120	30	Grains: g plant <sup>-1</sup>	9.75 ±0.14	5.21 ±0.11	1.37 ±0.01	-	0.27
118	28	Leaf area: cm <sup>2</sup>	93.15 ±4.72	77.24 ±3.84	58.12 ±2.93	41.37 ±1.89	2.75
106	16	RWC: %	96.28 ±5.63	92.17 ±4.05	54.96 ±2.42	38.18 ±0.94	3.51

Values are means ± SE (n=5).

### 3.3. Chlorophyll content and biochemical changes in cluster bean

Effects of Cr treatment on the photosynthetic pigment and biochemical changes in the cluster bean under different concentrations of Cr (VI) are shown in Table 2. In the present study, concentration of chlorophyll total, a and b decreased variably and manifestly with increase of Cr (VI) concentration in the solution supplied to the treated plant. However, decrease in content of photosynthetic pigment in leaves of the cluster bean observed more at 0.25 mM and 0.50 mM of Cr treatment with 53.09 % reduction in total chlorophyll in comparison

to control plant. Decrease in chlorophyll content might be due to inhibition of chlorophyll biosynthesis enzymes or lipid peroxidation of chloroplast membrane by ROS exposed with high concentration of Cr (VI) treatment. Carotene content in fresh leaves of cluster bean plant recorded decreased with increasing concentration of Cr (VI) in the solution. Highest decline was observed at 0.50 mM treatment by 82.09%. Similarly, reducing sugars content was recorded appreciably in higher order. Compared to control leaves, Cr treated plants showed higher reducing sugars with increasing Cr (VI) concentration.

**Table 2.** Variable chromium exposure on concentration of chlorophyll, carbohydrate fraction, starch, nitrogen and phenol in leaves of cluster bean leaves (at d 107; 17 d after metal exposure).

Parameters	mM chromium treatment				LSD (P=0.05)
	Control	0.05	0.25	0.5	
Chlorophyll: mg g <sup>-1</sup> fresh wt					
A	0.985 ±0.06	0.639 ±0.04	0.418 ±0.42	0.356 ±0.02	0.07
B	0.518 ±0.05	0.347 ±0.03	0.287 ±0.03	0.175 ±0.02	0.03
Total	1.503 ±0.13	0.986 ±0.11	0.705 ±0.09	0.531 ±0.03	0.09
Carotene (mg g <sup>-1</sup> fw)					
	4.86±0.23	4.12±0.27	2.27±0.15	0.87±0.08	0.03
Sugars: % fresh weight					
Reducing	0.27 ±0.02	0.34 ±0.02	0.41 ±0.03	0.49 ±0.04	0.04
Non reducing	0.08 ±0.01	0.07 ±0.01	0.05 ±0.01	0.03 ±0.01	0.01
Total sugars	0.31± 0.02	0.45 ±0.03	0.49 ±0.05	0.49 ±0.04	0.03
Nitrogen: % fresh weight					
protein nitrogen	1.131 ±0.13	0.927± 0.12	0.655± 0.10	0.572± 0.06	0.08
non protein nitrogen	0.253± 0.01	0.288 ±0.02	0.396 ±0.04	0.465 ±0.03	0.04
total nitrogen	1.384 ±0.15	1.215 ±0.12	1.051 ±0.11	1.037 ±0.07	0.07
Starch: % fresh weight	1.175 ±0.13	0.962 ±0.11	0.537 ±0.07	0.381 ±0.02	0.06
Phenols: % fresh weight	0.002± 0.001	0.004± 0.001	0.005±0.001	0.007± 0.001	0.001

Values are mean ±SE (n=5).

In the same trend, total sugars content also increased gradually with increasing chromium in the treatment solution. In contrast, Cr treated plants showed a declining trend of non-reducing sugars with increasing concentration of Cr in the medium. Concentration of protein N decreased with an increasing Cr (VI) level in the nutrient medium, however, the value of non- protein N was recorded with increasing order as compared to non- treated plant. In case of total nitrogen content, a decreasing trend is observed

with increasing Cr concentration in comparison to control plant. The starch content decreased in the Cr (VI) treated plants and a maximum 67.57% reduction was recorded in the plant grown at 0.50 mM of chromium treatment. In the present study phenols level was found to increase with Cr (VI) concentration in the medium in cluster bean plants in comparison to non-treated plants and observed increase by 47% at higher Cr (VI) concentration (0.50 mM).

### 3.4. Protein content and antioxidant enzyme activities in cluster bean

In the present study, data of protein contents and antioxidant enzyme activities in the plant cluster bean under Cr (VI) treatment in the sand culture condition were quite evident (Fig.1). Results indicate that Cr (VI) treatment affects protein content which was observed to decrease gradually with increasing Cr (VI) concentration in the growth medium and maximum 32.2% and 47.9% reduction observed in the plants grown at 0.25mM and 0.50 mM of Cr (VI) treatment. At d 107 (17 d of treatment), catalase activity was found to decrease with

differential Cr (VI) concentration in treated plants. In contrast, peroxidase activity at the same treatment duration and concentration of Cr (VI) is recorded to increase in treated plants as compared to control plants. Excess treatment of Cr at 0.25 mM resulted in slight decrease of ribonuclease activity; however, the activity further increased gradually up to 0.50 mM. The present study showed an increasing trend of activity of acid phosphatase at 0.05mM to 0.50 mM of Cr treatment. Hill activity in fresh leaves of cluster beans was observed to decrease with increased Cr (VI) concentrations.

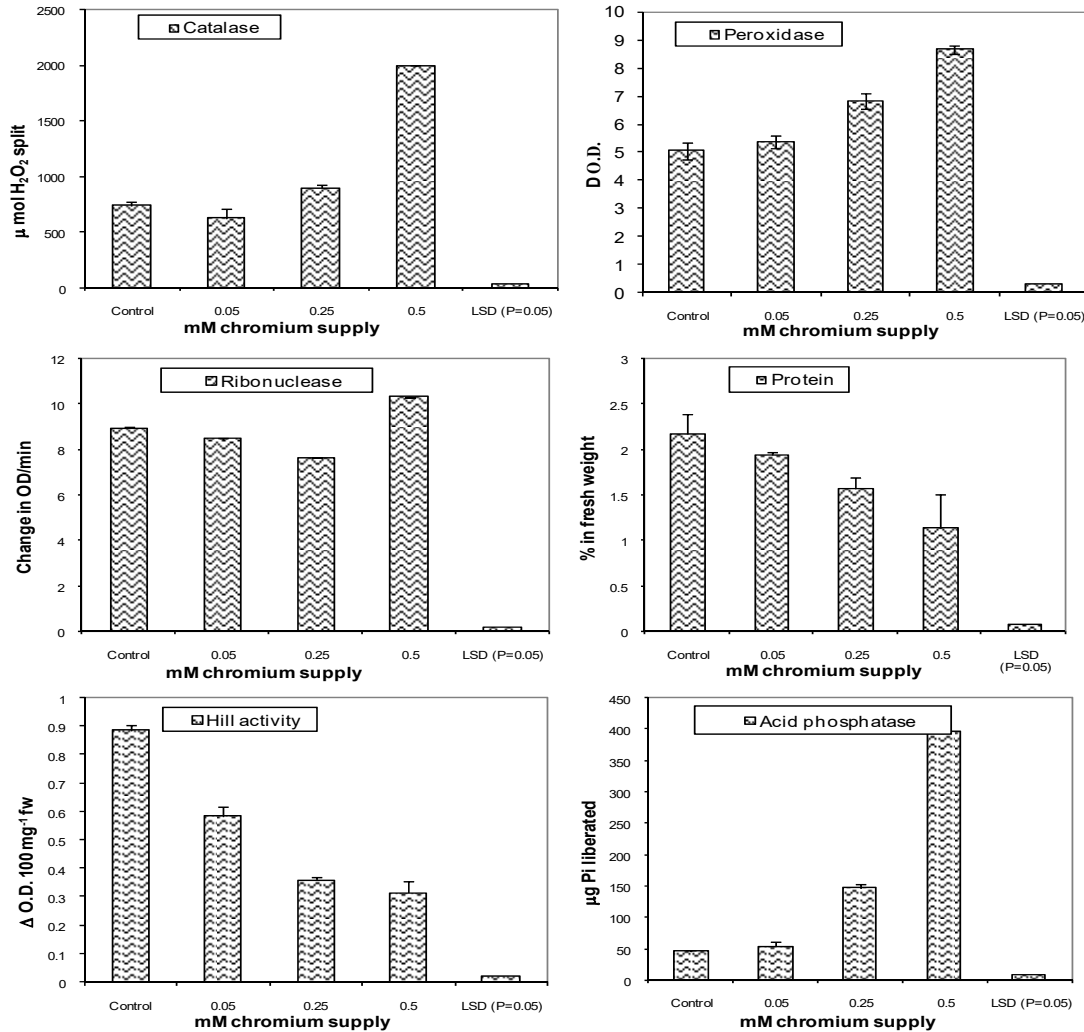


**Figure 1.** Variable chromium treatment and activities of enzymes, catalase, peroxidase, ribonuclease; hill reaction, acid phosphatase and protein concentration in leaves of cluster beans at 107 d (after 17 days of metal treatment). Values are means  $\pm$  SE (n=5)

### 3.5. Proline, glutathione reductase, non-protein thiol and lipid peroxidation

Proline content, activities of glutathione reductase, lipid peroxidation and non-protein thiol (NP-SH) in the leaves of cluster beans under different chromium treatment are depicted in Table 3. The present investigation data showed changes in proline content at higher concentration of chromium and increasing trend observed with Cr (VI)

concentration in the nutrient solution. However, activity of glutathione reductase in the Cr treated cluster bean is observed to decrease with increasing Cr concentration. At d 107 (17 days of metal supply), the activity of lipid peroxidation increased with increasing level of Cr (VI) from 0.05mM to 0.50 mM, as Cr generates induced phytotoxic results in the plant of cluster beans. The activity of non-protein thiol (NPSH) was found to decrease with excess of Cr (VI) supply in the growth medium.

**Table 3.** Variable chromium exposure on proline, glutathione reductase and lipid peroxidation and Non protein thiol in the Cluster Bean plant leaves (at d 107; 17 d after metal exposure).

Parameters	mM chromium treatment				LSD (P=0.05)
	Control	0.05	0.25	0.5	
Proline ( $\mu\text{g g}^{-1}\text{fw}$ )	0.79 $\pm$ 0.06	1.32 $\pm$ 0.09	2.05 $\pm$ 0.11	3.14 $\pm$ 0.15	0.05
Glutathione reductase (GR) (unit/ min/ mg/ protein)	1.29 $\pm$ 0.08	1.17 $\pm$ 0.06	1.12 $\pm$ 0.07	0.92 $\pm$ 0.04	0.03
Lipid Peroxidation ( $\mu\text{g g}^{-1}\text{fw}$ )	26.74 $\pm$ 2.75	33.62 $\pm$ 3.18	39.54 $\pm$ 2.54	51.21 $\pm$ 4.71	0.09
Non protein thiol (NPSH) ( $\mu\text{g g}^{-1}\text{fw}$ )	98.61 $\pm$ 4.82	91.53 $\pm$ 3.86	72.19 $\pm$ 4.19	57.42 $\pm$ 3.07	0.07

Values are mean  $\pm$  SE (n=5).

### 3.6. Phosphorus, sulfur, iron and chromium concentration in cluster bean

Translocation of phosphorus (P) and sulfur(S) from roots to other parts of the cluster beans is affected by higher concentration of Cr (VI) treatment. At higher

concentration of Cr, the plant cluster bean showed higher concentration of P and S in different plant parts as compared to the control plant; however, analytical results showed more accumulation of P and S considerably in the roots (Fig 2).

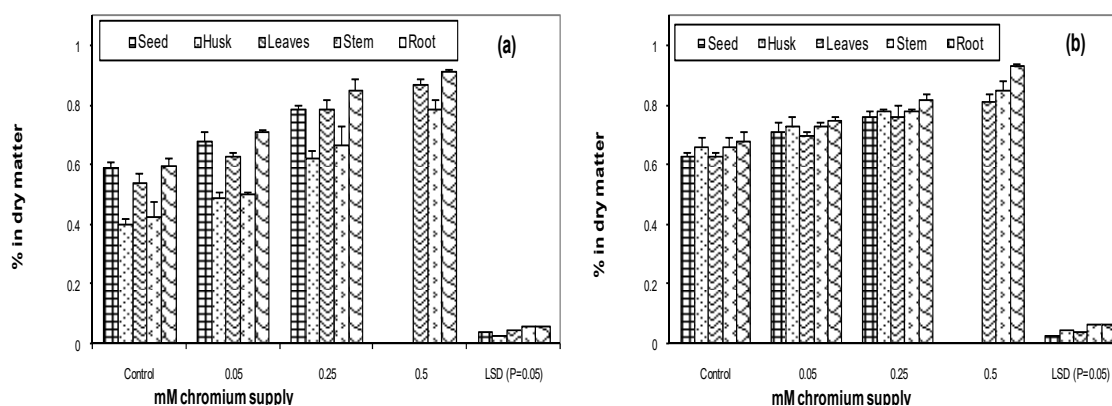


**Figure 2.** Variable chromium treatment and S (a) and P (b) uptake and accumulation in different parts of the plant of cluster beans at 120 d growth (after 30 days of chromium exposure). Values are means  $\pm$  SE (n=5)

Higher concentration of Cr (VI) treatment resulted in less accumulation of iron in the upper portion of the plant including stem, leaves, husk and seed and more accumulation in the roots (Fig 3). Chromium accumulation in different parts of cluster bean plants varied with response to Cr (VI) concentration in the medium (Fig 3) and roots, shoots, leaves and other parts of the tested plants. Maximum Cr accumulation observed in the roots,

followed by leaves at higher concentration of Cr treatment (0.50 mM). Cr induced toxicity as resulted in reduction of economic yields in terms of seed quality and quantity observed in the present study. High concentration of Cr ranged from 44 to 197  $\mu\text{g/g}$  dw recorded in the roots, however, least accumulation of Cr in the shoots observed with a range from 49 to 69  $\mu\text{g/g}$  dw at different concentration of Cr(VI) treatment.

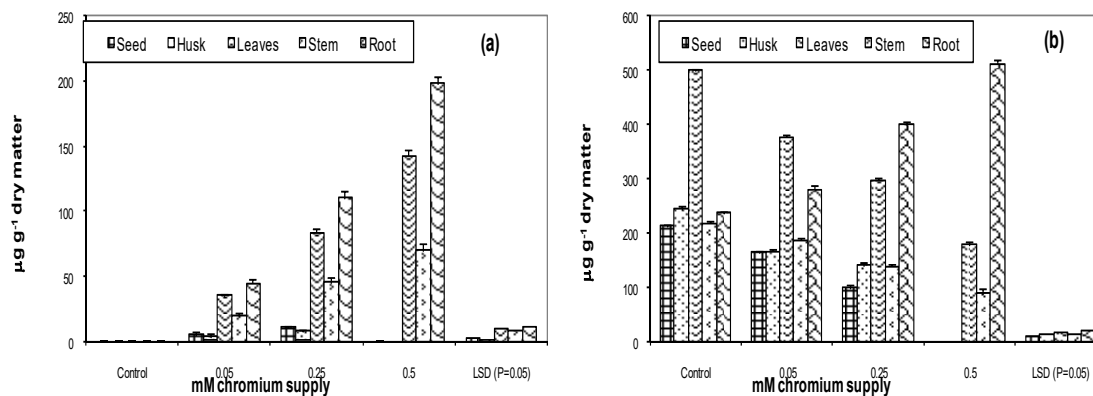


**Figure 3:** Variable chromium supply and accumulation of chromium (a) and iron (b) in different parts of the plant of cluster beans at 120 d growth (after 30 days of chromium exposure). Values are means  $\pm$  SE (n=5)

#### 4. Discussion

Various symptoms of phytotoxicity were observed in the plant cluster beans grown under different concentrations of Cr (VI) initially as chlorosis on middle leaves and subsequently, wilting of affected leaves appeared and finally leaf fall at higher concentration (0.25mM and 0.50 mM). The color of middle leaves of tested plants started to change from green to golden yellow in the Cr treated plant. Smaller size and lower number of leaves were observed in the Cr treated plants with severe chlorosis and necrosis in successive days of the treatment. Later, necrotic patches were spread with large areas over the entire leaves followed by wilted dry permanently and premature leaf fall. However, chlorosis observed delayed in the plants grown comparatively at low concentration of Cr treatment even after 15 d. The symptoms of high concentration Cr in cluster bean plants are new insight in ecotoxicological studies and more resemble as reported by Dube et al. (2003). Tiwari et al. (2013) reported on radish plants and recommend that the Cr may generate induced phytotoxic symptoms, reduction in leaf development, growth depression and changes in several biochemical activities as common characteristics under Cr stress. Cr treated plants showed reduced growth with gradual decrease of biomass of cluster bean at 0.05 mM to 0.50 mM concentration. Similar observation reported by many investigators with conclusion that Cr (VI) induces toxicity in the plants by effecting physiological and biochemical processes leading to reduced crop yield (Tiwari et al., 2009; Tiwari et al., 2013; Eleftheriou et al., 2015). In our finding, the crop yields produced only at 0.05 mM and 0.25 mM Cr (VI) treatment level; however, abnormal and deformed size and shape of seed observed with a noticeable reduction in grain yield in cluster beans under Cr treatment. Plant yield is reliant on leaf growth and leaf area; in our present observation the depression in leaf area is observed in treated plants at 0.50 mM as compared to control plants. Many studies examined the Cr and its interaction with plant growth and reported that Cr impedes plant growth, leaf development and yield production while going beyond the threshold levels (Arun et al., 2005; Tiwari et al., 2009). Reduced RWC observed at higher concentration of Cr (VI) treatment with respect to control plants. Reduction in the fresh biomass of cluster bean recorded due to loss of water as apparent from the low RWC of the leaves of plants resulted in wilting. Higher concentration of Cr (VI) exhibited lower water potential and relative water content which in agreement with the observation of Rauser and Dumbroff (1981). The extensively high levels of Cr (VI) exposures cause moribund the stomatal conductance might be owing to the higher oxidative ability of Cr (VI) in the nutrient medium, which in turn might be active in hurtful of the cells and membrane of stomatal protector cells.

Decreasing trends of concentration of chlorophyll content a, b and total in the leaves of cluster bean under Cr (VI) treatment observed, which indicates reduction in the photosynthetic synthesis under Cr treatment as compared to non-treated control plants. Reduction of chlorophyll content may be due to interference of chlorophyll biosynthesis (Lushchak, 2011; Sharma et al., 2020b; Guanet al., 2021), changes in the chloroplastic structure or

due to Cr (VI) competes with Mg at functional site of the porphyrin ring (Mengel and Kirkby, 2001). Similarly, carotene content was also found to decrease as compared with control plants which support comparable observations reported previously (Mondal et al., 2013; Mondal et al., 2015). Concentration of reducing sugars and total sugars in cluster bean plant leaves was appreciably recorded in higher order with increasing Cr (VI) supply; however, non-reducing sugars concentration recorded declining. Similarly, no significant effects of Cr on non-reducing sugars were reported (Agarwala et al., 1977); however, reducing sugars content was found to increase with Cr(VI) concentration in the growth solution. Increase in reducing sugars due to reduction in the vein and inhibition of photoassimilate export with more sugar accumulation (Rauser and Samarkoon, 1980). Reduction in protein nitrogen, total N and increase in non-protein N concentration in cluster bean leaves recorded in the Cr treated plant in comparison to the control plant. Sharma et al. (1995) reported that Cr affects nitrogen accumulation and absorption which is apparent in decline in protein N content in leaves of wheat plant as N is constituent element of protein as well as core element in the different biomolecules. In cluster bean leaves starch content is also found to decrease under different concentrations of Cr (VI) treatment. Similar observation of reduction in biosynthesis of starch was reported in citrullus plant (Tiwari et al., 2008). The concentration of phenols increased in cluster bean plant at 0.50 mM of Cr treatment as compared to control plants which related to previous study reported by Tewari et al. (2001) and reported same trend of increasing phenols level could be due to fast diffusion of H<sub>2</sub>O<sub>2</sub> in the cytosol or due to accretion of high phenols and lower protein formation under Cr stress. The content of protein gradually decreased with increasing Cr (VI) concentration in the growth medium. Chatterjee and Chatterjee (2000) reported the reduced plant biomass in cauliflower might be due to low protein synthesis under stress of Cr, Co and Cu. Degradation of protein can also result in the inhibition of activity of nitrate reductase (Solomonson and Barber, 1990; Nazet al., 2021). In cluster bean leaves, the catalase activity was found to significantly decrease in Cr (VI) treated plants, and the observation agreed with the conclusion of Adrees et al. (2015). Catalase might be more susceptible to excess levels of Cr (VI) since it binds willingly to thiol groups and thereby inactivates the thiol-containing enzyme. The efficiency of catalase as an H<sub>2</sub>O<sub>2</sub> scavenger is lowered; therefore, it would not play a significant role as an antioxidant (Luna et al., 1994). In cluster bean plant leaves, the activity of peroxidase is observed to increase with an increase in concentration of Cr (VI) in the growth medium. Peroxidase is an enzyme which catalyzes reduction of H<sub>2</sub>O<sub>2</sub> into H<sub>2</sub>O; however, ascorbate restricts the reduction of H<sub>2</sub>O<sub>2</sub> (Luna et al., 1994; Tiwari et al., 2008; Shahid et al., 2016). In cluster bean plant leaves, treatment of Cr up to 0.25 mM reduced ribonuclease activity; however, further increased activity expressed at 0.50 mM of Cr treatment. Enhancement of ribonuclease activity contradicts with the earlier finding (Strakhov and Chazova, 1981) in the plant grapevines. However, some other findings by Tiwari et al. (2013) reported the enhanced ribonuclease activity and acid phosphatase activity seems similar as per our observation. This may be owing to reduced protein synthesis or uptake

of inorganic phosphorus (Marschner, 1995). In our present observation, the Hill activity in cluster bean plant was found to decrease with increasing Cr concentration in the medium. Reduced chlorophyll content owing to chromium stress has an impact on the Hill activity in the tested plant. Krupa and Baszynski (1995) investigated that the Cr can also inhibit the Hill reaction disturbing together light and dark reaction. Proline content showed an increasing trend with increase of Cr (VI) concentration in the nutrient solution. Similarly, high levels of amino acids such as cysteine and enhanced synthesis of proline have been observed at high concentration of chromium (Vajpayee et al., 2001) and support other studies suggesting only proline accumulates in the plants grown under metal stress among other amino acids (Zdunek-Zastocka et al., 2021). In comparison to the non-treated plant, glutathione activity of reductase is recorded to decrease in the cluster bean due under higher concentration of Cr (VI). Cr (VI) treatment also affected antioxidant enzymes and inhibited activities of glutathione reductase (GR), catalase and peroxidase (Adrees et al., 2015; Ali et al., 2015). In cluster bean leaves, the activity of lipid peroxidation increased from 0.05 mM to 0.50 mM of Cr (VI). Various studies reported increased ROS generation in plants under Cr stress resulted in damage of DNA, pigments, proteins, lipids and initiate the process peroxidation of lipid leads to oxidative burst (Choudhury et al., 2005; Ullah et al., 2009). Similarly, lipid peroxidation and enhanced proline were reported in radish plants under Cr (VI) treatment (Azmat and Akhter 2010). Non-protein thiol (NPSH) activity decreased due to excess amount of Cr in nutrient solution. Cysteine, proline, nonprotein thiol acts as non-enzymatic antioxidants and assist in modulating tolerance under Cr toxicity to protect biomolecules from the free radicals generated during the oxidative stress (Hayat et al., 2012).

In plants, Cr (VI) treatment affects nutrient uptake by interfering uptake of essential nutrients. In excess Cr treatment resulted in increased phosphorus (P) and Sulphur (S) content in various plant parts of cluster bean. However, nutrients element accumulated more significantly in the roots and translocation of P and S from roots to shoot and leaves of plants affected by chromium treatment. Findings of Dube et al. (2003) indicated that high concentration of Cr affects translocation of P, S and other essential nutrients in the Citrullus plants. It is observed that high concentration of Cr (VI) treatment resulted in a decrease accumulation of iron in shoots and increase in the roots. Chlorosis due to Cr treatment has been normally associated with lower plant Fe mobilization and uptake from root to leaves via stems. In iron deficient conditions, leguminous plants enhance root Fe (III) reductase activity to increase the efficiency to reduce Fe (III) to Fe (II), which is more bioavailable and accumulates in the roots (Alcantara et al., 1994). It is also suggested that the excess levels Cr disturbs the nutrient uptake stability from the nutrient sources (Tiwari et al., 2009). This might specify poor utilization of vital nutrients due to Cr toxicity. Translocation and accumulation of Cr in different parts of cluster bean plant from the nutrient solution indicate tolerance responses, which somewhat coincides with an earlier study (Dube et al., 2003; Aoet al., 2022) and showed variable uptake and accumulation of Cr roots, shoot and leaves of plant. Our findings are in consonance

with the other studied conducted by Huffman and Allaway (1973) who recommended that the mobilization of chromium from roots to shoot and leaves is poor as Cr remains restricted in root.

## 5. Conclusion

In the present investigation chromium (VI) induced phytotoxicity emphasized in cluster beans with visible symptoms, inhibition of plant growth, reduction of biomass and yield quality. Cr (VI) stress involves particularly with plant metabolism through uptake, translocation, interference in enzymatic activities, and competing essential nutrients on binding sites. It is also concluded that the tolerance limit of Cr (VI) for cluster bean plant was monitored by 0.25 mM level of treatment along with essential nutrient solutions, above which the behind limit plant does not sustain the induced toxicity generated by Cr. Consequently, it is vital to understand the potential strategies to restrict Cr uptake and accumulation in edible parts of crop plants from contaminated sites and to minimize related detrimental effects in the other living beings due to Cr contamination. Further, physiological and biochemical aspects of Cr (VI) toxicity have not been as much considered for study on intact plants in detail. This might lead us to conclude that uptake of Cr from the contaminated agriculture field-grown crop plants may lead to serious health hazards and risk to environmental safety. Importance of present studies could be a new insight in ecotoxicological studies in assessing possible environmental concerns of chromium contamination and ensuring safe and sustainable agriculture.

## Acknowledgements

Authors greatly acknowledge Sophisticated Instrumentation Centre for Applied Research & Testing, Vallabh Vidyanagar for utilization of sophisticated analytical instrumentation facility used for the present investigation. The author NKS is thankful to the Manipal University Jaipur for essential support and continuous encouragement.

## Conflicts of interest

The authors declares no conflict of interests in this manuscript.

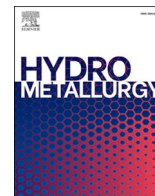
## References

- Adrees M, Ali S, Iqbal M, Bharwana SA, Siddiqi Z, Farid M, Ali Q, Saeed R and Rizwan M. 2015. Mannitol alleviates chromium toxicity in wheat plants in relation to growth, yield, stimulation of anti-oxidative enzymes, oxidative stress and Cr uptake in sand and soil media. *Ecotoxicol Environ Saf.*, **122**: 1-8.
- Agarwala SC and Chatterjee C. 1996. Techniques in micronutrient research. In: Hemantranjan E (Ed), **Advancements in Micronutrients Research**. Scientific Publishers, Jodhpur, India, pp. 401-453.
- Agarwala SC, Bisht SS and Sharma CP. 1977. Relative effectiveness of certain heavy metals in producing toxicity and symptoms of iron deficiency in barley. *Can J Bot.*, **55**: 1299-1307.

- Ahmed F, Hossain M, Abdulla, AT, Akbor M and Ahsan M. 2016. Public health risk assessment of chromium intake from vegetable grown in the wastewater irrigated site in Bangladesh. *Pollution2*: 425-432.
- Alcantara E, Romera FJ, Canete M and De la Guardia MD. 1994. Effects of heavy metals on both induction and function of root Fe (III) reductase in Fe-deficient cucumber (*Cucumis sativus* L.) plants. *J Exp Bot.*, **45**: 1983-1998.
- Ali S, Chaudhary A, Rizwan M, Anwar HT, Adrees M, Farid M, Irshad MK, Hayat T and Anjum SA. 2015. Alleviation of chromium toxicity by glycinebetaine related to elevated antioxidant enzymes and suppressed chromium uptake and oxidative stress in wheat (*Triticum aestivum* L.). *Environ Sci Pollut Res.*, **22**:10669-10678.
- Ao M, Chen X, Deng T, Sun S, Tang Y, Morel JL, Qiu R and Wang S. 2022. Chromium biogeochemical behavior in soil-plant systems and remediation strategies: A critical review. *J Hazard Mater.*, **424**:127233.
- Arnon DI. 1949. Copper enzyme in isolated chloroplasts. Polyphenol oxidase in *Beta vulgaris*. *Plant Physiol* 24:1-15.
- Arun KS, Cervantes C, Herminia LT and Avudainayagam D. 2005. Chromium toxicity in plants. *Environ Int.*, **31**: 739-753.
- Azmat R and Akhter H. 2010. Changes in some biophysical and biochemical parameters of mung bean (*Vigna radiata* L) Wilczek grown on chromium-contaminated soil treated with solid tea wastage. *Pak J Bot.*, **42**: 3065-3071.
- Barrs HD and Weatherley PE. 1962. A reexamination of the relative turgidity technique for estimating water deficits in leaves. *Aust J Biol Sci.*, **15**: 413-428.
- Bates LS, Waldren RP and Thomas CE. 1973. Rapid determination of free proline for water stress studies. *Plant Soil.*, **39**: 205-207.
- Bisht SS, Sharma D and Chaturvedi K. 1989. Certain metabolic lesions of chromium toxicity in radish. *Indian J Agri Biochem.*, **2**:109-115.
- Boyer PD. 1954. Spectrophotometric Study of the Reaction of Protein Sulfhydryl Groups with Organic Mercurials. *J Amer Chem Soc.*, **76**: 4331.
- Bradford MN. 1976. A rapid and sensitive method for the quantitation of microgram quantities of protein utilizing the principle of protein-dye binding. *Anal Biochem.*, **72**:248-254.
- Brewer J and Jogendorf AT. 1965. Damage to spinach chloroplast induced by dark preincubation with ferricyanide. *Plant Physiol.*, **40**: 303-311.
- Broadway A, Cave MR, Wragg J, Fordyce FM, Bewley RJ, Graham MC, Ngwenya BT and Farmer JG. 2010. Determination of the bioaccessibility of chromium in Glasgow soil and the implications for human health risk assessment. *Sci Total Environ.*, **409**: 267-277.
- Cervantes C, Garcia JC, Devars S, Corona FG, Tavera HL and Torres-Guzman JC. 2001. Interactions of chromium with microorganisms and plants. *FEMS Microbiol Rev.*, **25**: 335-347.
- Chandra P, Sinha S and Rai UN. 1997. Bioremediation of Cr from water and soil by vascular aquatic plants. In: Kruger EL, Anderson TA, Coats JR (Eds), **Phytoremediation of soil and water contaminants**. ACS Symposium Series 664. American Chemical Society, Washington, DC, pp. 274-282.
- Chatterjee J and Chatterjee C. 2000. Phytotoxicity of cobalt, chromium and copper in cauliflower. *Environ Pollut.*, **109**: 69-74.
- Chibnall AC, Rees MW and Williams EF. 1943. The total nitrogen content of egg albumin and other proteins. *Biochem J.*, **37**:354-359.
- Choudhury S and Panda SK. 2005. Toxic effects, oxidative stress and ultrastructural changes in moss *Taxithelium nepalense* (Schwaegr.) Broth. under chromium and lead phytotoxicity. *Water Air Soil Pollut.*, **167**: 73-90.
- Dong J, Wu F, Huang R and Zang G. 2007. A Chromium tolerant plant growing in Cr-contaminated land. *Int J. of Phytoremedia.*, **9**:167-179.
- Dube BK, Tewari K., Chatterjee J and Chatterjee C. 2003. Excess chromium alters uptake and translocation of certain nutrients in *citrus*. *Chemosphere.*, **53**: 1147-1153.
- Eleftheriou EP, Adamakis IDS, Panteris E and Fatsiou M. 2015. Chromium-induced ultrastructural changes and oxidative stress in roots of *Arabidopsis thaliana*. *Int J Mol Sci.*, **16**: 15852-15871.
- EPA (Environmental Protection Agency). 2000. Effluent Limitations Guidelines, Pretreatment Standards, and New Source Performance Standards for the Commercial Hazardous Waste Combustor Subcategory of the Waste Combustors Point Source Category. *Fed Regist* 4360-4385.
- Guan X, Li Q, Maimaiti T, Lan S, Ouyang P, Ouyang B, Wu X and Yang ST. 2021. Toxicity and photosynthetic inhibition of metal-organic framework MOF-199 to pea seedlings. *J Hazard Mater.*, **409**: 124521.
- Hayat S, Khalique G, Irfan M, Wani AS, Tripathi BN and Ahmad A. 2012. Physiological changes induced by chromium stress in plants: An overview. *Protoplasma.*, **249**: 599-611.
- Heath RL and Packer L. 1968. Photoperoxidation in isolated chloroplasts. I. Kinetics and stoichiometry of fatty acid peroxidation. *Arch Biochem Biophys.*, **125**: 189-198.
- Hewitt EJ. 1966. Sand and water culture methods used in the Study of Plant Nutrition, Technical Communication 22. Commonwealth Agricultural Bureau, London.
- Huffman EWD and Allaway WH. 1973. Chromium in plants: distribution in tissues, organelles and extracts and availability of bean leaf chromium to animals. *J Agric Chem.*, **21**: 982-986.
- Jacobson L. 1951. Maintenance of iron supply in nutrient solutions by a single addition of ferric potassium ethylenediamine tetra acetate. *Plant Physiol.*, **26**: 411-413.
- Kapoor RT, Bani Mfarrej MF, Alam P, Rinklebe J and Ahmad P. 2022. Accumulation of chromium in plants and its repercussion in animals and humans. *Environ Pollut.*, **301**: 119044.
- Krupa Z. and Baszynski T. 1995. Some aspects of heavy metals toxicity towards photosynthetic apparatus-direct and indirect effects on light and dark reactions. *Acta Physiol Plant.*, **17**: 177-190.
- Luck H. 1963. Peroxidase. In: Hill B (Ed), **Methods in enzymatic analysis**. Academic, New York, pp. 895-897.
- Luna CM, Gonzalez CA and Trippi VS. 1994. Oxidative damage caused by an excess of copper in oat leaves. *Plant Cell Physiol.*, **35**: 11-15.
- Lushchak VI. 2011. Adaptive response to oxidative stress: Bacteria, fungi, plants and animals. *Comp Biochem Physiol C ToxicolPharmacol.*, **153**: 175-90.
- Marschner H. 1995. **Mineral nutrition of higher plants**. Academic Press, New York.
- Mengel K and Kirkby EA. 2001. Elements with more toxic effects. In: Mengel, K., Kirkby, E.A., Kosegarten, H., Appel, T. (Eds), **Principles of plant nutrition**, Kluwer Academic Publishers, London, pp. 656-670.
- Mertz W. 1969. Chromium occurrence and functions in biological systems. *Physiol Rev.*, **49**: 163-239.

- Mondal NK, Das C and Datta JK. 2015. Effect of mercury on seedling growth, nodulation and ultrastructural deformation of *Vigna radiata* (L) Wilczek. *Environ Monit Assess.*, **187**: 1-14.
- Mondal NK, Das C, Roy S, Datta JK and Banerjee A. 2013. Effect of varying cadmium stress on chickpea (*Cicer Arietinum* L) seedlings: an Ultrastructural study. *Ann Environ Sci.*, **7**: 59-70.
- Montgomery R. 1957. Determination of glycogen. *Arch BiochemBiophys.*, **67**: 378-386.
- Naz R, Sarfraz A, Anwar Z, Yasmin H, Nosheen A, Keyani R, Roberts TH. 2021. Combined ability of salicylic acid and spermidine to mitigate the individual and interactive effects of drought and chromium stress in maize (*Zea mays* L.). *Plant PhysiolBiochem.*, **159**: 285-300.
- Nelson N. 1944. Photometric adaptation of Somogyi method for determination of glucose. *J Biol Chem.*, **153**: 375-380.
- Nriagu JO. 1988. Production and uses of chromium. In: Nriagu JO, Nieboer E. (Eds), **Chromium in natural and human environment**. John Wiley and Sons, pp. 81-105.
- Panda SK, Chaudhury I and Khan MH. 2003. Heavy metals induce lipid peroxidation and affects antioxidants in wheat leaves. *Biol Plant.*, **46**: 289-294.
- Panse VG and Sukhatme PV. 1954. **Statistical Methods for Agriculture Workers**. ICAR, New Delhi.
- Piper CS. 1942. **Soil and plant analysis**. Monograph. Waite Agricultural Research Institute, The University, Adelaide, Australia.
- Rauser WE and Dumbroff EB. 1981. Effect of excess cobalt, nickel and zinc on the water relations of *Phaseolus vulgaris*. *Environ Expt Bot.*, **21**: 249-255.
- Rauser WE and Samarukoon AB. 1980. Vein loading in seedlings of *Phaseolus vulgaris* exposed to excess cobalt, nickel and zinc. *Plant Physiol.*, **65**: 578-583.
- Reale L, Ferranti F, Mantilacci S, Corboli M, Aversa S, Landucci F, Baldisserotto C, Ferroni L, Pancaldi S and Venanzoni R., 2016. Cyto-histological and morpho-physiological responses of common duckweed (*Lemna minor* L.) to chromium. *Chemosphere.*, **145**: 98-105.
- Schmidt, G. 1955. Acid prostatic phosphatase, In: Colowick N. and Kaplan O. (Eds.), **Methods in enzymology**, Academic Press, New York, 2: pp. 523-530.
- Shahid M, Dumat C, Khalid S, Niazi NK and Antunes PMC. 2016. Cadmium Bioavailability, Uptake, Toxicity and Detoxification in Soil-plant System. *Rev Environ Contam Toxicol.*, **239**:1-65.
- Shanker AK, Cervantes C and Loza-Tavera H. 2005. Chromium toxicity in plants. *Environ Inter* **31**: 739-753.
- Sharma A, Wang J, Xu D, Tao S, Chong S, Yan D, Li Z, Yuan H and Zheng B. 2020b. Melatonin regulates the functional components of photosynthesis, antioxidant system, gene expression, and metabolic pathways to induce drought resistance in grafted *Carya cathayensis* plants. *Sci Total Environ.*, **713**: 136675.
- Sharma A, Kapoor D, Wang J, Shahzad B, Kumar V, Bali AS, Jasrotia S, Zheng B, Yuan H and Yan D. 2020a. Chromium bioaccumulation and Its Impacts on Plants: An Overview. *Plants.*, **9**: 1-17.
- Sharma DC, Chaterjee C and Sharma CP. 1995. Chromium accumulation and its effect on wheat (*Triticum aestivum* L. cv. HD 2004) metabolism. *Plant Science.*, **111**: 145-151.
- Singh P, Itankar N and Patil Y. 2021. Biomangement of hexavalent chromium: Current trends and promising perspectives. *J Environ Manage.*, **279**: 111547.
- Smith IK, Vierhellaer TL and Thorne CA. 1988. Assay of glutathione reductase in crude tissue homogenates using 5,5-dithiobis (2-nitrobenzoic acid). *Anal Biochem.*, **175**: 408-413.
- Solomonson LP and Barbar MJ. 1990. Assimilatory nitrate reductase: functional properties and regulation. *Ann Rev Plant Mol Biol.*, **41**: 225-253.
- Strakhov VG and Chazova TP. 1981. Effect of chromium, molybdenum and tungsten on grapevine quality. *Sodovod Vinograd. Vinodel Mold.*, **36**: 58-60.
- Sujatha P and Gupta A. 1996. Tannery effluent characteristics and its effects on agriculture. *J Ecotoxicol Environ Monit.*, **6**: 45-48.
- Swain T and Hillis WE. 1959. The phenolic constituent of *Prunus domestica*. The qualitative analysis of phenolic constituents. *J Sci Food Agri.*, **10**: 63-68.
- Tewari RK, Kumar P, Sharma PN and Bisht SS. 2002. Modulation of oxidative stress responsive enzymes by excess cobalt. *Plant Science.*, **162**: 381-388.
- Tiwari KK, Dube BK, Sinha P and Chatterjee C. 2008. Phytotoxic effects of high chromium on oxidative stress and metabolic changes in *Citrullus*. *Ind J Horticult.*, **65**: 171-175
- Tiwari KK, Dwivedi S, Singh NK, Rai UN and Tripathi RD. 2009. Chromium (VI) induced phytotoxicity and oxidative stress in pea (*Pisum sativum* L.): Biochemical changes and translocation of essential nutrients. *J Environ Biol.*, **30**: 389-394.
- Tiwari KK, Singh NK and Rai UN. 2013. Chromium Phytotoxicity in Radish (*Raphanus sativus*): Effects on Metabolism and Nutrient Uptake. *Bull Environ Contam Toxicol.*, **91**: 339-344.
- Tuve TV and Anfinsen CB. 1960. Preparation and properties of spinach ribonuclease. *J Biol Chem.*, **235**: 3437-3441.
- Ullah A, Shahzad B, Tanveer M, Nadeem F, Sharma A, Lee DJ and Rehman A. 2019. Abiotic Stress Tolerance in Plants Through Pre-sowing Seed Treatments with Mineral Elements and Growth Regulators. In: Hasanuzzaman M, Fotopoulos V (Eds), **Priming and Pretreatment of Seeds and Seedlings: Implication in Plant Stress Tolerance and Enhancing Productivity in Crop Plants**; Springer, Singapore pp. 427-445.
- Vajpayee P, Rai UN, Ali M, Tripathi RD, Yadav V, Sinha S and Singh SN. 2001. Chromium-Induced Physiologic Changes in *Vallisneria spiralis* L. and Its Role in Phytoremediation of Tannery Effluent. *Bull Environ Contam Toxicol.*, **67**: 246-256.
- VonHandorf A, Zablouk HA and Puga A. 2021. Hexavalent chromium disrupts chromatin architecture. *Semin Cancer Biol.*, **76**: 54-60.
- Wallace A, Soufi SM, Cha JW and Romney EM. 1976. Some effects of chromium toxicity on bush bean plants grown in soil. *Plant Soil.*, **44**: 471-473.
- Zdunek-Zastocka E, Grabowska A, Michniewska B and Orzechowski S. 2021. Proline Concentration and Its Metabolism Are Regulated in a Leaf Age Dependent Manner But Not by Abscisic Acid in Pea Plants Exposed to Cadmium Stress. *Cells.* **10**: 946.





# Investigations into the closed-loop hydrometallurgical process for heavy metals removal and recovery from biosolids via mild acid pre-treatment

Ibrahim Gbolahan Hakeem<sup>a,b</sup>, Pobitra Halder<sup>b,c</sup>, Shefali Aktar<sup>a</sup>, Mojtaba Hedayati Marzbali<sup>a,b</sup>, Abhishek Sharma<sup>b,d</sup>, Aravind Surapaneni<sup>b,e</sup>, Graeme Short<sup>e</sup>, Jorge Paz-Ferreiro<sup>a</sup>, Kalpit Shah<sup>a,b,\*</sup>

<sup>a</sup> Chemical and Environmental Engineering, School of Engineering, RMIT University, Melbourne, VIC 3000, Australia

<sup>b</sup> ARC Training Centre for the Transformation of Australia's Biosolids Resource, RMIT University, Bundoora, VIC 3082, Australia

<sup>c</sup> School of Engineering, Deakin University, VIC 3216, Australia

<sup>d</sup> Department of Chemical Engineering, Manipal University, Jaipur, Rajasthan 303007, India

<sup>e</sup> South East Water Corporation, Frankston, VIC 3199, Australia

## ARTICLE INFO

### Keywords:

Leachate recycling  
Biosolids treatment  
Heavy metals  
Metal recovery  
Metal extraction

## ABSTRACT

Biosolids contain heavy metals (HMs), restricting their beneficial reuse in agricultural land. However, these metals can be a valuable resource in many applications if recovered efficiently. Therefore, the removal and recovery of HMs and other limiting contaminants in biosolids without degrading the organic nutrients of the resulting treated biosolids demands holistic investigations. A closed-loop hydrometallurgical treatment process for metal removal and recovery from biosolids was developed in this study. Firstly, mild acid treatment using 3% v/v H<sub>2</sub>SO<sub>4</sub> at 25 °C, 600 rpm for 30 min was performed in a 1 L continuous stirred tank reactor to extract common HMs (such as As, Cd, Co, Cr, Cu, Ni, Pb, and Zn) from biosolids into the aqueous phase. The effects of solids concentration and acid types on the HMs extraction efficiency were studied. Then, the primary acid leachate stream was continuously recycled for metal extraction from biosolids until the dissolved metals in the solution reached saturation concentration. After that, the dissolved metals were recovered in staged NaOH precipitation and adsorption. Low solids contents (<5% w/v) using mineral acids having pH <2 and oxidation-reduction potential (ORP) ~500 mV (versus SHE) favoured HMs solubilisation from biosolids with an average extraction efficiency of 70%. The dissolution of ferric iron (Fe<sup>3+</sup>) by H<sub>2</sub>SO<sub>4</sub> and subsequent in-situ formation of ferric sulfate enhanced the metal extraction strength of the spent leachate stream during recycling. However, the solids loading in each leaching process must be kept low to prevent ferric concentration build-up and precipitation as the leachate pH steadily increases above 2 during recycling. Amongst the metal recovery methods investigated, H<sub>2</sub>O<sub>2</sub> oxidation prior to 2-stage NaOH precipitation had the highest efficiency with 75–95% HMs recovery. The clarified stream was used to neutralise the acidic treated biosolids to close the process loop. The complete process flowsheet was developed with mass balances, and the fate of nutrients (mainly C, N, and P) and major *per-* and polyfluoro alkyl substances (PFAS) were overviewed.

## 1. Introduction

Biosolids, also known as stabilised sewage sludge, are the by-product of the wastewater treatment process. Biosolids contain valuable organic and inorganic components (mainly N, P, and K) that constitute important plant nutrients. These nutrients facilitate the application of a substantial volume of biosolids in agricultural soils in many countries, including Australia (Paz-ferreiro et al., 2018). However, heavy metals

(HMs) and other contaminants such as pesticides, microbial pathogens, microplastics, and surfactants are limiting the attractiveness of biosolids for direct land application with increasingly stringent regulations (EPA Victoria, 2004; LeBlanc et al., 2009). Thermochemical treatment of sub-grade biosolids via pyrolysis, gasification, hydrothermal carbonisation/liquefaction or incineration process can effectively degrade the organic and microbial contaminants (Kundu et al., 2021; Ross et al., 2016). However, HMs remain a persistent pollutant in biosolids and their

\* Corresponding author at: Chemical and Environmental Engineering, School of Engineering, RMIT University, Melbourne, VIC 3000, Australia.  
E-mail address: [kalpit.shah@rmit.edu.au](mailto:kalpit.shah@rmit.edu.au) (K. Shah).

thermally-derived products due to the low thermal degradation as well as the formidable bioaccumulation and high environmental toxicity of HMs (Feng et al., 2018).

The pre-treatment of biosolids is considered an effective process for removing the HMs before land application or thermal processing. Several pre-treatment methods, including chemical leaching with acids (Gaber et al., 2011; Stylianou et al., 2007), chelating agents (Gheju et al., 2011; Leštan et al., 2008), ferric salts (Bayat and Sari, 2010; Ito et al., 2000), ionic liquids (Abouelela et al., 2022; Yao et al., 2021), surfactants (Guan et al., 2017; Tang et al., 2017), and microbial agents (Pathak et al., 2009; Xiang et al., 2000) have been investigated for this purpose. Amongst all, leaching with acids is the most common, efficient with short operation times, and cost-effective with high industrial maturity (Babel and del Mundo Dacera, 2006; Gunarathne et al., 2020; Hakeem et al., 2022a). The high oxidising potential, as well as the low pH of acids, are favourable for metal dissolution (Ma et al., 2020). In addition, most metal cations are basic and readily ion-exchangeable with protons from acids (Persson et al., 2017). Therefore, acid leaching plays a leading role in hydrometallurgical processes for metals recovery from different materials, including biosolids (Gunarathne et al., 2020; Montenegro et al., 2016). In a typical acid leaching process, a high liquid-to-solid ratio is desired to achieve high HMs dissolution by overcoming thermodynamic equilibrium, which occurs when the solid dissociates to such an extent that the metal species are fully saturated in the solution (Lee et al., 2006). Hence, acid leaching is usually accompanied by a large volume of aqueous waste stream with dilute metal concentrations. Metal recovery from this dilute stream is unattractive and improper disposal poses environmental threats.

One of the potential ways to manage the resulting leachate stream from biosolids pre-treatment is to reuse and recycle the stream for another leaching process until the leachate stream gets saturated with HMs. The heavily concentrated leachate stream can be a precursor for recovering valuable metals. Recycling the aqueous acidic leachate stream can be attractive for metal extraction due to its low pH, high oxidation-reduction potential (ORP), and presence of surrogate leaching components such as dissolved ferric sulfates or chlorides (Beauchesne et al., 2007; Ito et al., 2000; Strasser et al., 1995). In addition, recycling the acidic waste stream can reduce the overall acid solution requirements during the metal extraction process, with the potential to favour the techno-economics of the process. The effect of process variables such as temperature, acid concentration, solids contents, agitation speeds, and contact time on HMs removal efficiency has been elucidated in previous studies (del Mundo Dacera and Babel, 2006; Gaber et al., 2011; Hakeem et al., 2022b; Yang et al., 2021). However, there is a limited investigation on the recyclability of the acidic leachate stream as a solvent for metal extraction from raw biosolids (Shim, 2023). Particularly, the effects of solids loading on the recycling performance of the leachate stream have not been reported in extant literature.

The overall hydrometallurgical process can be grouped into three sequential stages: metal extraction, leachate concentration and purification, and metal recovery (Gunarathne et al., 2020). The growing interest in resource recovery has increased the prospect of critical element extraction and recovery from biosolids via hydrometallurgical operations (Tyagi and Lo, 2013). However, metal recovery from biosolids has not been fully explored in the literature beyond the acid leaching stage, which removes the metals from biosolids to the liquid phase, as described earlier. Therefore, developing a comprehensive hydrometallurgical process chain to understand the feasibility of metal recovery from biosolids through the production of less contaminated biosolids is desired. While the metal extraction stage is the most critical in the overall hydrometallurgical process, leachate purification and metal recovery are the most challenging because acidic solvents have poor selectivity during metal solubilisation. Moreover, biosolids have many metal and non-metal components that elute simultaneously into solution during acid leaching. For example, the co-solubilisation of iron, aluminium, and alkali and alkaline earth metals (AAEMs) alongside HMs

usually complicates the selective recovery of valuable metals from the leachate stream (Lee et al., 2002). In some cases, elements such as carbon (C), nitrogen (N), and phosphorous (P) are dissolved in the acidic stream, interfering with the purification and recovery of desired metals.

The main techniques for metal recovery from aqueous streams are chemical precipitation (Liang et al., 2019; Marchioretto et al., 2005), electrodeposition (Yao et al., 2021), adsorption (Singh et al., 2020), ion exchange (Yoshizaki and Tomida, 2000), and solvent extraction (Montenegro et al., 2016). Chemical precipitation using caustic soda (NaOH) or slaked lime (Ca(OH)<sub>2</sub>) and adsorption are the most common, less laborious, and suitable for multi-components metal streams typical of biosolids leachate (Li et al., 2021; Marchioretto et al., 2005). However, the efficacy of alkali precipitation of HMs is challenged by the amphoteric nature of some metal ions having different optimum hydroxides solubility as well as interferences from other metal species, particularly iron (de Fátima da Silva et al., 2020). Given the number of metal in a biosolids leachate stream, identifying suitable metal recovery methods will depend on the final composition, metal concentration, and pH (Sethurajan et al., 2017). Studies involving the chemical precipitation of multiple metal from real biosolids leach solutions are limited in the literature (Marchioretto et al., 2005). Chemical precipitation and adsorption have only been extensively applied on metal ores leachate or simulated wastewater containing single or dual metal components (Ait Ahsaine et al., 2017; Ni et al., 2019; Xu et al., 2009).

In summary, the full spectrum of chemical treatment of biosolids for HMs removal involving metal extraction, separation of solids from the leach liquor, leachate concentration and purification, and metal recovery is missing in the literature. Hence, this study explored a comprehensive mild acid treatment of biosolids for HMs extraction and the subsequent recovery of the metal from the concentrated leachate stream. The specific objectives of the work were to (i) study the effect of acid solution and solids concentration on the extraction efficiency of metals from biosolids, (ii) investigate the reusability and extraction performance of the primary leachate stream through partial and complete recycling at optimum solids concentrations, (iii) examine the efficacy of staged NaOH co-precipitation, H<sub>2</sub>O<sub>2</sub> oxidation followed by NaOH co-precipitation, and biochar adsorption for the purification and recovery of HMs from the concentrated leachate stream, (iv) understand the fate of dissolved nutrients (mainly C, N, K, and P) and *per*- and poly-fluoro alkyl substance (PFAS) compounds in the process streams, and (v) develop and propose optimum process flow diagrams with mass balances for biosolids metal removal and recovery. This detailed investigation will help to understand the feasibility of developing an in-situ or ex-situ hydrometallurgical process for biosolids HMs decontamination with potential for nutrient and critical metal recovery within the existing wastewater treatment facilities.

## 2. Materials and methods

### 2.1. Biosolids preparation and analyses

Biosolids used in this study were obtained from Mount Martha Water Recycling Plant, South East Water Corporation, Victoria, Australia. The biosolids production process was described in our previous study (Hakeem et al., 2022b). Before use in the pre-treatment experiments, biosolids were dried overnight in an oven at 105 °C and sieved to 100–300 µm particle size. The elemental composition was determined by X-ray Fluorescence (XRF, S4 AXS Bruker), ultimate analysis was performed using a CHNS Series II Perkin Elmer instrument, and the metal concentration was measured using Inductive Coupled Plasma-Mass Spectrometry (ICP-MS 2200 series, Agilent Technologies). The chemicals used in this work were of analytical grades. They include 98% H<sub>2</sub>SO<sub>4</sub> (Chem-Supply Pty Ltd), 65% HNO<sub>3</sub> (Univar Pty Ltd), 35% HCl (Emplura Pty Ltd), 99% glacial acetic acid (Sigma Aldrich), 99.5% citric acid (Sigma Aldrich), 21–23% ferric sulfate pentahydrate (Chem-Supply) and 30% hydrogen peroxide (Rowe Scientific Pty Ltd). Milli-Q

water with a resistivity of 18.2 M $\Omega$  cm was used throughout this study. Table 1 shows the composition of the biosolids. The concentration of some of the HMs, such as Cu, Zn, and Cd, is higher than that prescribed for the least contaminant grade (C1) for unrestricted beneficial reuse of biosolids according to Victoria EPA biosolids guidelines (EPA Victoria, 2004).

## 2.2. Heavy metals fractionation in the biosolids

The efficacy of acid leaching for metal extraction depends on the chemical fractionation of the metal in the biosolids matrix (Geng et al., 2020). Therefore, according to previous literature, a modified three-step Community Bureau of Reference (BCR) sequential extraction technique was used to determine the distribution of metal in the biosolids (Liu et al., 2021, 2018; Wang et al., 2019). This method allows the chemical classification of HMs species in biosolids, soils, and sediments into four major fractions: exchangeable (F-1), reducible (F-2), oxidisable (F-3), and residual (F-4) based on the ease of extraction with standard reagents (Zhao et al., 2018). The F-1 refers to acid-ionisable metals, F-2 are metals bound to carbonates and Fe–Mn oxides, F-3 are metals bound to organic matter and sulfides, and F-4 are bound to silicates and recalcitrant organics. Depending on the severity of the acid leaching conditions, such as acid concentration (or pH), temperature, and time, F-1, F-2, and F-3 metals can be removed at various rates in decreasing order, while F-4 metals are hardly removed via chemical leaching. The result of this analysis is presented in Fig. S1. From Fig. S1, the potential mobility of the metals in the biosolids can be estimated by adding F-1 and F-2 metal percentages (Geng et al., 2020), and this can be ranked as Mn > Zn > Cd  $\approx$  Ni  $\approx$  Co > Cr > As > Pb > Cu  $\approx$  Fe. Copper has the highest F-3 percentage due to the higher affinity of Cu to organic matter (Beauchesne et al., 2007), while Fe and Pb have the highest F-4 percentages. Copper is the most challenging HM to remove in biosolids via acid leaching; this observation has been widely reported in other works (Beauchesne et al., 2007; Blais et al., 2005; Mercier et al., 2002). Therefore, the extraction of Cu under mild acid leaching conditions may be limited.

## 2.3. Biosolids metals extraction

The batch pre-treatment procedure was as described previously (Hakeem et al., 2022b). All leaching experiments were conducted at room temperature (25  $\pm$  2  $^{\circ}$ C) using 3% (v/v) acid concentration under continuous stirring at 600 rpm for 30  $\pm$  2 min in a 1 L continuous stirred tank reactor. These are the optimised conditions from our previous investigation (Hakeem et al., 2022b). The effect of acid types was studied by using three mineral acids (H<sub>2</sub>SO<sub>4</sub>, HCl, HNO<sub>3</sub>) and two organic acids (acetic and citric) to extract HMs (such as As, Cd, Co, Cr, Cu, Ni, Pb, and Zn) from biosolids at 5% (w/v) solids loading using 3% (v/v) acid solution. Similarly, the effect of solids concentration was studied by leaching biosolids at 1, 3, 5, 10, 15 and 20% (w/v) solids using 3% (v/v) H<sub>2</sub>SO<sub>4</sub> solution. At the end of each metal extraction experiment, the slurry was transferred into Eppendorf tubes and centrifuged at 4000 rpm for 30 min. The leachate stream was carefully decanted into sample vials, and the residue (treated biosolids) was dried and stored for further analysis. The pH and ORP of the leachate stream

were measured, and 1 mL aliquot of the well-mixed leachate was filtered, diluted, and quantified for metals by ICP-MS. All leaching experiments were performed in triplicates, and average results were reported with errors expressed as the standard deviation of the measurements. A schematic illustration of the metal extraction process including the downstream separation and metal recovery processes is shown in Fig. 1.

## 2.4. Concentration of the leachate stream

### 2.4.1. Total recycling of the leachate

The recovered aqueous stream from the parent (primary) pre-treatment was reused fully for another extraction process at 5% and 10% (w/v) fresh biosolids loading; all other conditions remain unchanged. The process was repeated for five leaching cycles (after the parent leaching) using 100% spent leachate stream and fresh biosolids in each cycle. The volume of the leachate stream and mass of the fresh biosolids were adjusted to achieve 5% or 10% solids loading in each cycle. It is assumed that the metals dissolved in the leachate will remain in the solution all the time unless the pH  $\geq$  2.5, where ferric precipitation will be initiated. During the recycling, precipitate from poorly soluble metals such as Ca and Pb is partitioned in the treated solids. The parent (primary) leachate stream and leachate stream after each successive recycle are denoted by R0 and Rn, where n = 1, 2, 3 etc., denotes the number of cycles.

### 2.4.2. Partial recycling of the leachate

A constant volume pre-treatment experiment was performed with biosolids to liquid (g/mL) ratio of 1:10 (10% solids) and 1:20 (5% solids) using the recovered leachate. A fixed mass of biosolids (10 g or 5 g) and a solution volume of 100 mL were maintained for this experiment. The recycled stream was topped with fresh 3% (v/v) H<sub>2</sub>SO<sub>4</sub> to maintain the solution volume at 100 mL for each leaching experiment. The added fresh lixiviant (FL) volume replaced the lost solution volume during each leaching cycle, including aliquots taken for analysis. Thus, the make-up ratio (volume of FL to volume of spent leachate) was  $\sim$ 15 vol% and  $\sim$ 20 vol% at 5% and 10% solids, respectively. The number of effective leaching cycles (n) was determined by continuously reusing the spent stream with make-up solution until the solution became saturated with dissolved metals. At the end of each leaching cycle, the recovered leachate stream was filtered to reduce suspended solids carryover before reusing it in another leaching cycle. All pre-treatment experiment with leachate recycling was repeated at least two times, and average data was reported.

## 2.5. Metals recovery

Most HMs precipitate out of solution at a pH range of 7–12 (Fu and Wang, 2011); however, the concentrated leachate stream obtained from the partial leachate recycling experiment was in the acidic pH (2.45). Therefore, an alkaline solution is required to adjust the solution pH to the metal precipitation region. Since each metal has different optimal precipitation pH depending on the metal ion concentration in the solution (Sethurajan et al., 2017), a typical pH of 9 was chosen for the precipitation experiment. A concentrated NaOH (6 M, pH 14) solution

**Table 1**  
Metals composition of biosolids.

Metal type	Source	Metals composition (mg/kg)								
		Ca	Mg	Na	K	Al	Fe	Mn	Mo	Ba
Major and trace metals	This study	35,600	3630	2790	3530	5180	13,440	210	6	185
		Cr	Ni	Pb	Cd	As	Co	Cu	Zn	
Heavy metals	This study	22	14	17	1.3	2	3	825	815	
	C1 grade*	400	60	300	1	20	–	100	200	
	C2 grade*	3000	270	500	10	60	–	2000	2500	

\* Biosolids contaminant grade as prescribed by Victoria EPA biosolids guidelines (EPA Victoria, 2004).

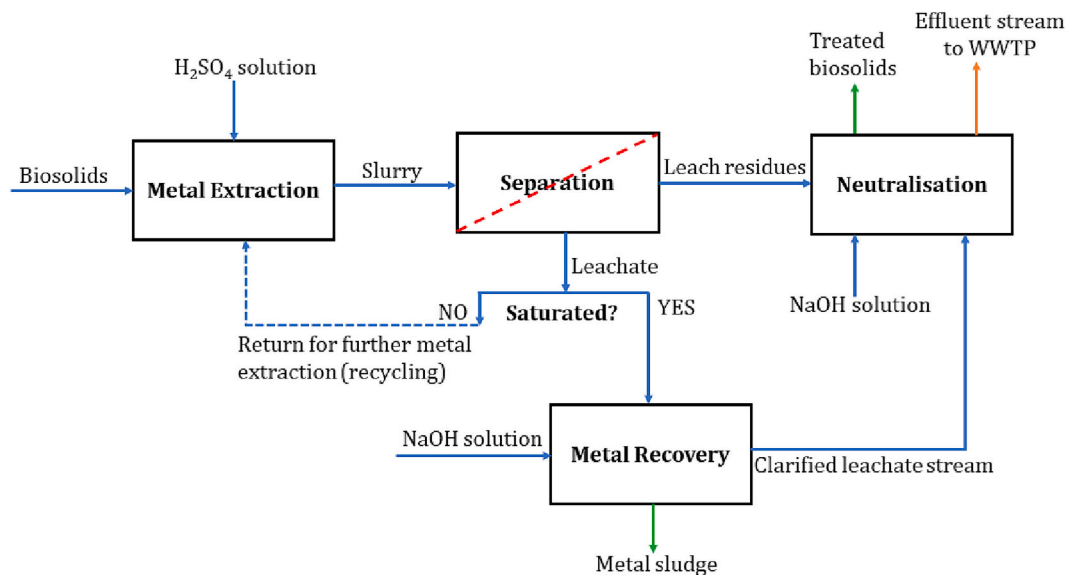


Fig. 1. Schematic of biosolids hydrometallurgical process for metal removal and recovery.

was used for the precipitation of metal ions to reduce the dilution effect on the concentration of the metals. The metal ion precipitation experiment was designed in the following ways to maximise the recovery of the HMs from other metal and non-metal contaminants.

- 1) Two-step NaOH precipitation when Fe/Al precipitation was considered: 20 mL of well-mixed and filtered leachate stream was measured in a conical flask, and 6 M NaOH was added in drops under continuous stirring until the solution pH was  $4.5 \pm 0.2$ . The pH of the solution was monitored via a well-calibrated pH meter, and the amount of NaOH added was noted. The sample was left to stay still for 2 h and centrifuged at 4000 rpm for 30 min to recover the precipitates. Then, 5 mL of the clarified stream was treated in the second step with NaOH in drops until the solution pH was  $9.0 \pm 0.5$ ; the solution was left to settle for 2 h and centrifuged to recover the precipitates. The concentration of metal in the treated liquid after each step was measured by ICP-MS.
- 2) Single-step NaOH precipitation when Fe/Al precipitation was not considered: 10 mL of the leachate stream was treated with NaOH until the final pH was  $9.0 \pm 0.5$ . The presence of Fe and Al in the stream may help in the co-precipitation reaction with HMs since  $\text{Fe}^{3+}$  and  $\text{Al}^{3+}$  salts are common coagulants used in the wastewater treatment process.
- 3) Fenton reaction by adding  $\text{H}_2\text{O}_2$  when oxidation of Fe and dissolved organics were considered: Ferric iron is known to precipitate at low pH  $<4$ , whereas ferrous has a high precipitation pH  $>8.5$ , so  $\text{H}_2\text{O}_2$  can oxidise ferrous to ferric for recovery at stage 1 (pH 4.5). Moreover, dissolved organics in the form of COD (chemical oxygen demand) can limit HMs recovery, so the oxidation of dissolved organic by  $\text{H}_2\text{O}_2$  was considered before NaOH precipitation. Briefly, a few drops of 30% v/v  $\text{H}_2\text{O}_2$  ( $<0.5$  mL) were added to 10 mL of well-filtered leachate stream. Then, the pH of the stream was adjusted to 4.5 with the addition of NaOH in drops to recover Fe/Al. The clarified stream was treated in a second stage to co-precipitate all other metals at pH 9.0 by adding NaOH.
- 4) Adsorption: An attempt to use biochar for adsorption when the leachate stream was at acidic pH (2.45) caused the leaching of metals from the biochar to the liquid, so adjustment of the leachate pH is necessary. Ten mL of clarified leachate (pH 4.5) obtained after the first step of Fe/Al precipitation was used for the adsorption experiment. Biochar produced from raw biosolids at 500 °C for 3 h residence time in a muffle furnace was used as the adsorbent and

charged at a dose of 0.05 g per mL leachate (0.048 g/g leachate). The adsorption was carried out at room temperature overnight under a constant agitation speed of 250 rpm. The mixture was filtered to separate the biochar and the aqueous stream, which was analysed for metal contents by ICP-MS. It should be noted that the presence of HMs in biosolids-biochar is a major concern only for land application of biochar. Metal-loaded biochar can have many valuable applications in catalysis and energy storage (Shen and Chen, 2022; Wang et al., 2017). Besides, biochar adsorption could be an effective and cheaper alternative than alkali precipitation for recovering dissolved metals from the acidic leachate stream.

## 2.6. Process configurations and the fate of nutrients and PFAS

The process flow diagram was developed to capture the entire hydrometallurgical treatment chain from metal extraction via acid leaching to metal recovery via alkali precipitation and, finally, the neutralisation of treated solids. Material balances were performed assuming a steady-state operation. The flow of C, N, and P in the process streams from the biosolids feed to the leachate stream and treated biosolids was overviewed. Similarly, twenty-eight compounds of PFAS (per- and polyfluoroalkyl substances) were measured in the raw biosolids, neutralised treated biosolids, the acidic leachate, and the final liquid effluent. The change in pH of both solid and liquid streams along the treatment chain might influence the leachability and the final fate of PFAS compounds (Kabiri et al., 2022). The C and N content in the raw and treated biosolids was determined using a CHN Series II Perkin Elmer instrument, while P content was measured by XRF analysis. Total organic carbon dissolved in the leachate stream was measured using TOC-L (Shimadzu Corporation). Total N representing the sum of total Kjeldahl nitrogen (TKN) and  $\text{NO}_x$  and total P analysis, as well as PFAS analysis, were performed externally at ALS Water Resource Group, Melbourne, Australia.

## 3. Results and discussions

### 3.1. Effect of acid types

The efficiency of three mineral acids (sulfuric, nitric and hydrochloric) and two organic (acetic and citric) acids at the same volume concentration of 3% (v/v) and 5% (w/v) solids were studied on HMs extraction (Fig. 2). Mineral acids outperformed organic acids, and

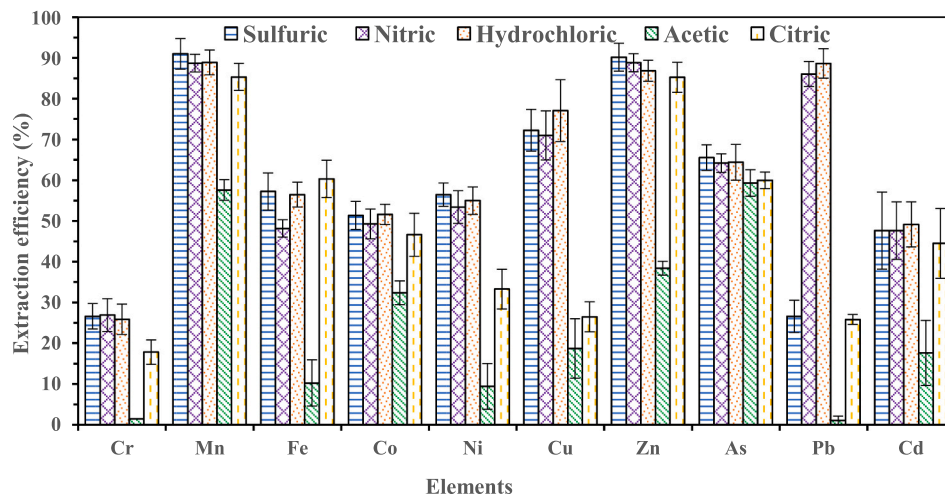


Fig. 2. Effect of mineral and organic acid solutions on the metal extraction efficiency from biosolids (conditions: 5% (w/v) solids, 3% (v/v) acid concentration, 25 °C, 30 min, and 600 rpm).

except for Pb, all mineral acids perform similarly in the metal extraction process. The high ionising power and extremely low pH of the mineral acids (~1.7) compared to the organic acids (~2.7) favoured the solubilisation of HMs (Gaber et al., 2011). Most sulfate, nitrate, and chloride salts are highly soluble in water and dilute acids, which may explain the similar metal extraction efficiencies of the three mineral acids. Sulfuric acid performed poorly in removing Pb owing to the low solubility (0.038 g/L) of  $\text{PbSO}_4$  in water ( $K_{sp@298\text{ K}} 1.6 \times 10^{-8}$ ). Generally, organic acids are considered weak acids ( $\text{pK}_a > 1$ ) as the ionised hydrogen concentration is typically lower than strong acids ( $\text{pK}_a < 0$ ) at the same molar concentration. For instance, the ionised hydrogen concentration of nitric acid is 100% of the acid concentration, whereas the ionised hydrogen concentration of citric acid is equivalent to 1.3–2.1% of nitric acid concentration (Lee et al., 2005). Therefore, it is expected that both organic acids have weaker ionic strength to desorb HMs ions in the biosolids, especially at low acid concentrations. However, of the two organic acids, citric acid was competitive with mineral acids despite having a similar pH to acetic acid in the metal extraction process. Citric acid is a natural chelating agent, and citrate ions form soluble complexes with cations of metals (Ma et al., 2020). Moreover, acetic acid is dicarboxylic while citric acid is tricarboxylic; the presence of an extra carboxylic group in citric acid also favours the number of available chelating sites for metal extraction (Gheju et al., 2011). Therefore, the chelating mechanism of citric acid was responsible for the high metal extraction rather than the acidolysis (reaction with  $\text{H}^+$ ) mechanism for the mineral acid-based leaching. Studies have demonstrated that the oxidation-reduction potential (ORP) of the leaching solvents can affect their metal extraction ability since metal solubilisation usually involves an ion-exchange reaction with protons from acid (Babel and del Mundo Dacera, 2006; Bayat and Sari, 2010; Blais et al., 2005; Pathak et al., 2009). In this work, 3% nitric acid had the highest ORP of 611 mV, followed by sulfuric acid (590 mV) and hydrochloric acid (473 mV). This ORP value can be related to the amount of dissolved oxygen each solvent can donate to participate in redox reactions involving metal ions and  $\text{H}^+$ . However, there is no obvious difference in the removal efficiency of the three mineral acids for all metal ions (except Pb), irrespective of the ORP of the slurry/solution. Hence, the metal leaching process observed in this study can be stated to be largely controlled by the solution pH. This observation is contrary to a few studies reporting that both the leaching solution pH and ORP influence HMs solubilisation in biosolids (Beauchesne et al., 2007; Blais et al., 2005; Mercier et al., 2002). In particular, Cu dissolution was found to be driven by the redoxolysis mechanism rather than acidolysis due to the higher affinity of Cu to organic matter in sludge (Blais et al., 2005; Strasser et al., 1995). Based on this, the

leaching of biosolids was further tested with strong oxidising solutions such as 3% acidified ferric sulfate (670 mV) and ferric sulfate added hydrogen peroxide (603 mV). However, no significant improvement in metal extraction was observed, particularly for Cu and Cr, compared to mineral acids (data not shown). A previous study has reported that there was an optimum pH at which ORP of slurry becomes influential on HMs extraction efficiency (Beauchesne et al., 2007). Also, different washing agents may have various degrees of affinity and selectivity for different HMs. The removal efficiencies of multiple HMs in biosolids can be greatly improved by composite or sequential treatment (Shi et al., 2020). From these results, sulfuric acid was selected for subsequent experiments due to the relatively low cost of  $\text{H}_2\text{SO}_4$ , industrial maturity, and lesser toxicity of sulfates of HMs than their corresponding nitrates or chlorides salts at the same molar concentration (Erichsen Jones, 1934; Nie et al., 2015).

### 3.2. Effect of solids concentration

The effect of solids concentration on the metal extraction from biosolids using 3% v/v  $\text{H}_2\text{SO}_4$  at 25 °C, 600 rpm for 30 min was investigated, and the results are presented in Fig. 3. The solids concentration significantly influenced the extraction of the metals ( $p < 0.05$ ). The extraction of all metals (except Pb and Cr) at lower solids contents (1–3%) achieved ~60–95% removal compared to 30–80% removal at higher solids content (5–15%). This behaviour is expected from the stoichiometry of the leaching/desorption reaction. Notably, Mn and Zn had the least variation in extraction efficiency with the change in solids concentration because they have the highest proportion (75–90%) of acid-leachable metal fractions (F-1 + F-2) in the biosolids used in this study (Fig. S1). The change in solids concentration was largely inconsequential on Cr and Pb extraction. The consistent low solubilisation of Cr in biosolids can be attributed to the poor mobility of Cr; the trivalent metal ions such as Fe and Cr are more difficult to extract than the divalent ions such as Zn, Ni, and Cd due to the competitive uptake of protons by the more reactive species. Lead has the highest residual (inert) fraction (F-4) of all metals in the biosolids (Fig. S1); therefore, its extraction is usually limited by common acids (Gheju et al., 2011; Xiao et al., 2015). Moreover,  $\text{H}_2\text{SO}_4$  is not a suitable lixiviant for Pb extraction due to the low solubility of  $\text{PbSO}_4$  in water (see Fig. 2). The removal efficiencies of all other metals increased with decreasing solid/liquid ratio, and the maximum extraction efficiency for all metals was observed at the lowest solids content (1%). The result agrees with previous literature on the effect of solids concentration on metal extraction (Bayat and Sari, 2010; Kuan et al., 2010; Wu et al., 2009). Low solids content is

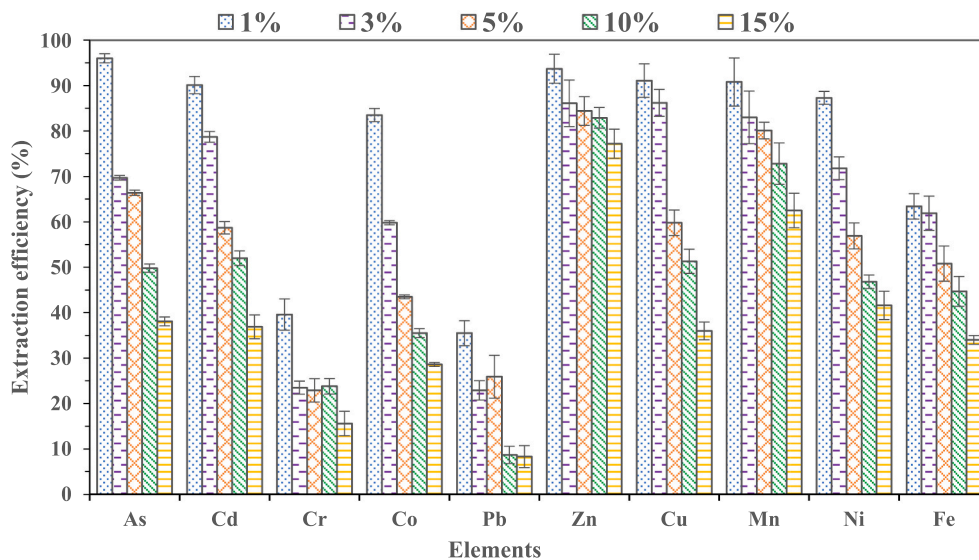


Fig. 3. Effect of solids concentration (w/v) on metal extraction efficiency from biosolids (conditions: 3% (v/v) H<sub>2</sub>SO<sub>4</sub>, 25 °C, 30 min, and 600 rpm).

associated with a higher volume of lixiviant and higher proton (H<sup>+</sup>) concentration, benefiting the dissolution of acid-exchangeable HMs fraction (F-1) in the biosolids. Since there are more H<sup>+</sup> than available surface chelating sites on the biosolids, the excess H<sub>2</sub>SO<sub>4</sub> can penetrate the biosolids pores and react with more metal ions, particularly the reducible (F-2) and oxidisable (F-3) HMs fractions, leading to overall higher extraction efficiency (Yang et al., 2021).

Table S1 shows the dissolved metal ion concentration in the leachate at different solids loading. The dissolved metal ion concentration in mg/

L liquid increased with increasing solids contents, while the metal ion concentration in mg/kg solids decreased with increasing solids contents (Table S1). Treatment using 1% (w/v) solids concentration produced cleaner biosolids, while the 15% (w/v) solids produced a highly concentrated metal-laden leachate stream which can make the recovery of metals more attractive. On the other hand, lower solid loading produced a dilute liquor stream. Moreover, 1% solids concentration appears unrealistic in practical scenarios in wastewater treatment plants (WWTPs). Besides, lower solids concentration is associated with higher

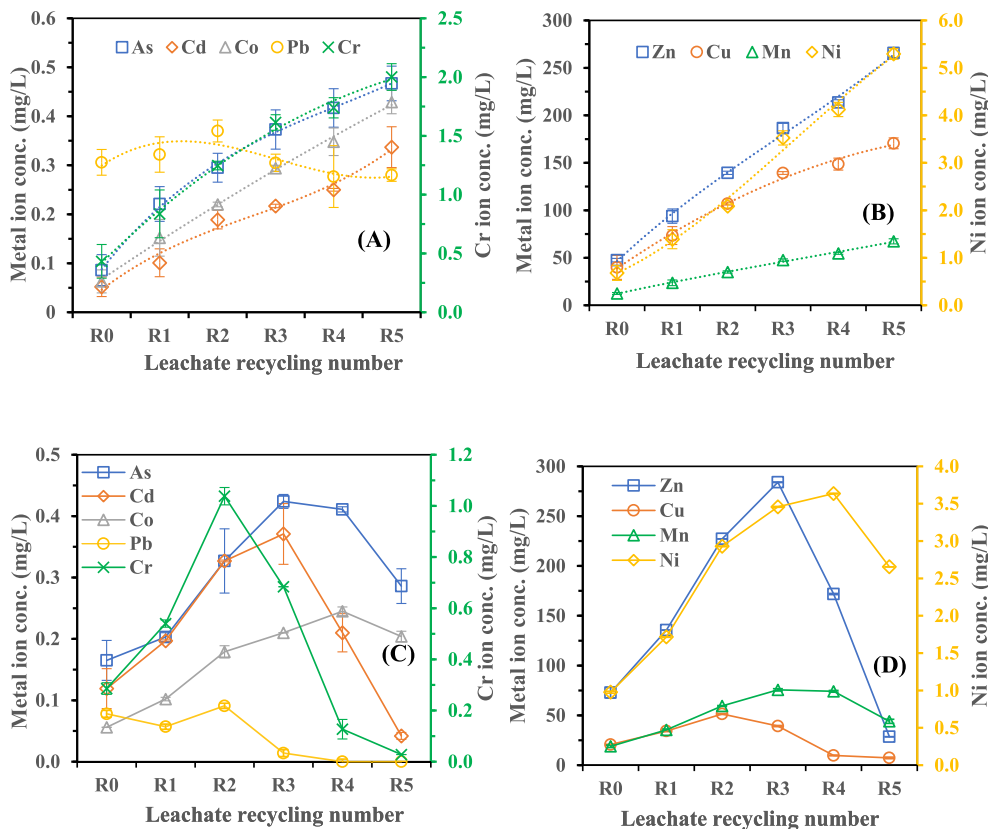


Fig. 4. Effect of fresh biosolids concentration on 100% recycling of the leachate stream (A) & (B) 5% solids (C) & (D) 10% solids (conditions: 3% (v/v) H<sub>2</sub>SO<sub>4</sub>, 25 °C, 30 min, and 600 rpm).

lixiviant consumption, and dewaterability can be challenging (Vesilind and Hsu, 1997). Similarly, at 15% solids, the mass transfer limitation was significant, negatively impacting mixing and liquid recovery, and the overall metal ion removal efficiency was the lowest. In fact, at 20% solids, mixing and separation became difficult, and the leaching process was not successful (data not reported). Hence, a moderate 5–10% solids loading may be a good balance and are the typical value in most biosolids leaching operations (Gheju et al., 2011; Wang et al., 2015; Wu et al., 2009).

### 3.3. Recyclability of the leachate stream

#### 3.3.1. Metal saturation concentration and the leachate recycling efficiency

The cumulative metal concentration in the leachate stream after five successive leaching cycles at 5% and 10% solids using 3% v/v H<sub>2</sub>SO<sub>4</sub> solution, 25 °C, 30 min, and 600 rpm is presented in Fig. 4(A–D). It is obvious that the primary leachate stream (R0) from the parent leaching experiment has not reached its maximum extraction capacity as more metals were extracted from fresh biosolids using the R0 stream five times. At 5% solids, the R0 stream had higher extraction strength than that at 10% because of the higher liquid-to-solid ratio and the dilute concentration of the dissolved metal. A higher liquid-to-solid ratio slowed the attainment of thermodynamic equilibrium between the dissolved metal species and the acidic solution (Lee et al., 2006). The leachate streams obtained at 10% solids were saturated faster compared to 5% solids. The primary leachate at 5% solids was recycled up to five times without reaching saturation point (Fig. 4(A&B)), while the leachate at 10% solids can only be reused up to three times, beyond which a rapid decline in cumulative concentration was observed (Fig. 4(C&D)). There was at least a 3-fold increase in the concentration of all metals (except Pb) by completely reusing the primary leachate stream from R0 to R5 (Fig. 4(A&B)). At 5% solids, the percentage increase in metal ion concentration in the leachate from R0 to R3 can be ranked as Cu(II) (249) < Cr(III) (273) < Mn(II) (284) < Zn(II) (293) < Cd(II) (317) < As(III) (334) < Co(II) (367) < Ni(II) (419). However, at 10% solids (Fig. 4(C&D)), there was a lesser increase in the cumulative concentration from R0 to R3, and the percentage increase was Cu(II) (90) < Cr(III) (139) < As(III) (157) < Cd(II) (212) < Ni(II) (254) < Co(II) (275) < Zn(II) (290) < Mn(II) (300). The percentage increase in cumulative concentration for Mn and Zn was similar at 5% and 10% solids, whereas there was a substantial decrease in the accumulation of other metals at 10% solids compared to 5% solids. Expectedly, higher solids loading limited the efficiency of metal accumulation during leachate recycling at the same extraction cycle with 5% solids. In particular, the cumulative Cu loading during recycling was severely impacted at 10% solids, possibly due to the dominant redox reaction between soluble Cu(II) and iron(II) sulfate, the mechanism which has been elucidated in previous literature (Matocha et al., 2005). The 100% recycling of the leachate stream at 10% solids performed competitively with 5% solids only in removing easily leachable metal fractions (F-1 and F-2) such as Zn and Mn, while the removal of other metal species dominant in F-3 was largely difficult. The removal of metal ions in F-3 fractions will require abundant protons from fresh H<sub>2</sub>SO<sub>4</sub> solution as well as harsh oxidising conditions to break the organometallic bond (Beauchesne et al., 2007). The monotonic decline in the extraction efficiency after the third recycling at 10% solids (Fig. 4(C&D)) was due to Al/Fe-induced co-precipitation of metal from the leachate to the solid phase as the solution pH approaches 3, which is conducive for ferric precipitation (Marchiorretto et al., 2005). The pH of the R5 stream at 10% solids was 4.5, while it was 2.4 at 5% solids.

Furthermore, it was observed that all metal extraction profiles followed closely that of Fe, and the improved extraction of HMs using the spent leachate stream can be attributed to the role of ferric sulfate hydrates in the metal desorption process. The iron source in the biosolids is the ferric salt coagulant used during the wastewater treatment process. Sulfuric acid solution can partly dissolve ferric-containing salts (such as

FeCl<sub>3</sub> or FeOOH), and then dissolved ferric ion can form ferric sulfate through ion exchange reaction with SO<sub>4</sub><sup>2-</sup> or HSO<sub>4</sub><sup>-</sup> from H<sub>2</sub>SO<sub>4</sub> (Demol et al., 2022). Ferric sulfate is a well-known leaching agent which acidifies by hydrolysis (Fe<sup>3+</sup> + H<sub>2</sub>O = FeOH<sup>2+</sup> + H<sup>+</sup>) and increases the elution efficiency of HMs from soils and biosolids (Bayat and Sari, 2010; Ito et al., 2000; Shi et al., 2020; Strasser et al., 1995). X-ray photoelectron spectra of the metal precipitates confirmed the presence of ferric sulfate (Fig. S2). The effective extraction of HMs by dissolved Fe<sup>3+</sup> is due to its ability to oxidise metal sulfides to soluble metallic ions and the release of more protons through the hydrolysis of ferric hydrates (Pathak et al., 2009). The dissolution of inherent ferric-containing components in biosolids and the subsequent formation of ferric sulfates extended the overall extraction strength of the leachate stream during recycling. The presence of native ferric salts was beneficial for the reuse of the leachate stream; however, there is a critical Fe<sup>3+</sup> concentration beyond which it counteracts the HMs extraction as Fe<sup>3+</sup> precipitates at a low pH value (<4). It was observed that the higher the concentration of Fe in the stream, the better the extraction efficiency of other metals up to a certain Fe concentration (~1400 mg/L). This is consistent with the study of Ito et al. (2000), who observed that the higher the amount of ferric iron added, the lower the pH of the lixiviant and the higher the extraction efficiency of HMs (~80%) from digested biosolids at low solids concentration (2% w/w). In other studies, leaching at pH 2 with acidified ferric iron outperformed H<sub>2</sub>SO<sub>4</sub> in extracting common HMs from biosolids (Bayat and Sari, 2010; Ito et al., 2000). The combination of ferric sulfate and acid solutions at different dosage had positive synergistic interactions for the solubilisation of multiple HMs from biosolids and soils (Beauchesne et al., 2007; Shi et al., 2020).

#### 3.3.2. Effect of make-up solution on the leachate recyclability

The cumulative metal ion concentration in the leachate stream after ten successive cycles with the addition of make-up lixiviant between each cycle is shown in Fig. 5. A constant feed rate of 5 g or 10 g of dry biosolids per 100 mL liquid for a 30 min leaching cycle was maintained. Contrary to the observation at 100% leachate recycling, without adding make up lixiviant (Fig. 4), the continuous addition of 3% H<sub>2</sub>SO<sub>4</sub> as FL prolonged the extraction strength of the spent leachate until R8 stage (Fig. 5). At 5% solids (Fig. 5), there was a substantial increase (at least 250%) in the cumulative metal ion concentration (except for Pb) from R0 to R10. For instance, Ni(II) was concentrated from 0.5 to 3.5 mg/L, Zn(II) from 38.9 to 277 mg/L, Cu(II) from 11.5 to 100 mg/L, As(III) from 0.14 to 0.51 mg/L, Cd(II) from 0.04 to 0.34 mg/L, Cr(III) from 0.12 to 1.2 mg/L, Co(II) from 0.04 to 0.22 mg/L, and Mn(II) from 10.3 to 71.5 mg/L. There was a steady increase in the cumulative metal ion concentration from R0 to R4 due to the low make-up ratio of the FL in the total leachate stream (<25%). The addition of FL to the leachate stream possibly aided the dilution of the metal ion concentration and hence enhanced the extraction strength (and capacity) of the stream. Up to R7, the increase in the metal ion concentration far outweighed the dilution effect of the added fresh solution. Nevertheless, adding FL was not beneficial beyond R6 as the leachate had been fully saturated with the metal ions. This observation was due to the similar extent of metal ions dilution and extraction efficiency in the stream by the added FL beyond R6. At R6, increasing the make-up ratio above 15 vol% would likely enhance the metal extraction strength of the stream further. The overall extraction trend of the HMs was largely governed by Fe, which reached saturation at R6. Contrary to the observation for 100% leachate recycling without adding make up lixiviant (Fig. 4), the continuous addition of the FL and the acidifying effect of Fe<sup>3+</sup> kept the pH of the leachate stream at <2 throughout the process, limiting ferric precipitation.

The addition of make-up acid lixiviant was less beneficial in enhancing the recyclability of the leachate stream at 10% solids compared to 5% solids (Fig. S3). There was no monotonic increase in the concentration of metal ions, and the irregular increase and decrease in the cumulative concentration across the ten leaching cycles can be

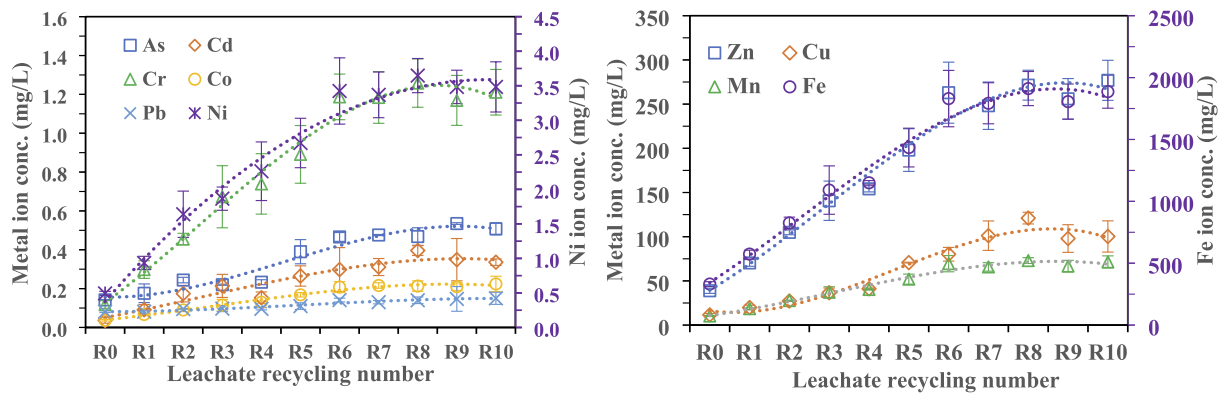


Fig. 5. Effect of make-up lixiviant on the recyclability strength of the leachate stream at 5% fresh biosolids concentration (conditions: 3% (v/v) H<sub>2</sub>SO<sub>4</sub>, 25 °C, 30 min, and 600 rpm).

attributed to Fe(III) precipitation. The leachate at 10% solids saturated faster than at 5% solids, and pH increased rapidly, thus facilitating Fe (III) precipitation much earlier. Iron(III) co-precipitated other metals in the stream. Contrary to the observation at 5% solids, adding FL between successive leaching could not suppress Fe precipitation (Fig. S3) at 10% solids. The dilution and acidifying effect of the FL on the metal ion concentration in the leachate stream were minimal at higher solids loading. The sharp rise in solution pH rather than the increase in Fe concentration stimulated Fe co-precipitation reaction at 10% solids. For instance, at 10% solids, Fe precipitation began at a maximum concentration of ~1400 mg/L (pH 2.45), whereas, at 5%, no Fe precipitation occurred even at the maximum concentration of 1830 mg/L (pH 1.85). At low pulp density (5% solids), the overall extraction efficiency of the spent stream was competitive with the FL, and the performance improved with increasing Fe concentration in the stream. Acidified ferric salt leaching is optimally performed at low solids concentration (<5% w/v) to avoid a rapid increase in pH and minimise ferric precipitation, which is counterproductive for HMs solubilisation (Bayat and Sari, 2010; Ito et al., 2000).

Leachate recycling could bring significant cost savings for H<sub>2</sub>SO<sub>4</sub> lixiviant besides environmental benefits. The 100% recycling of the spent leachate at 5% solids loading for five leaching cycles (Fig. 4) could save 4.5 times the required H<sub>2</sub>SO<sub>4</sub> volume at 90% liquid recovery per leaching cycle. Similarly, for the partial recycling of the leachate with 15% make-up lixiviant at 5% solids for six leaching cycles (Fig. 5), there

could be ~5 times reduction in the volume of H<sub>2</sub>SO<sub>4</sub>. Assuming a linear relationship between H<sub>2</sub>SO<sub>4</sub> volume and cost, around 400% cost savings can be achieved with leachate recycling with make-up lixiviant, which may substantially lower the cost of acid leaching.

### 3.4. Metal recovery from the concentrated leachate stream

A single-step or two-step NaOH co-precipitation and biochar adsorption were investigated for recovering HMs from the saturated leachate stream. Metals like Cr, Cu, Pb, and Zn do not form hydroxide precipitates at pH <6, allowing the separation from ferric iron and aluminium, which precipitate at pH <5 (Marchioretto et al., 2005). Table S2 shows the metal ion composition of the leachate stream used for the metal recovery experiments. It was observed that the concentration of Zn, Mn, and Cu in the leachate was up to 100 mg/L. Concentrations of all other HMs were < 5 mg/L, while Fe, Al, and alkali and alkaline earth metals (AAEMs: Na, K, Mg, and Ca) were highly concentrated in the stream (>500 mg/L). The metal recovery at each precipitation stage is shown in Table 2, while the overall metal recovery from the different methods is shown in Fig. 6.

The single-stage NaOH precipitation at pH 9 recovered about 9–99% of the HMs. The recovery efficiency of the metals can be ranked as Zn (99%) ≈ Cd (99%) > Cr (97%) > Pb (79%) > Co (33%) > Ni (31%) > As (11%) > Cu (9%). The precipitation of these HMs was accompanied by the precipitation of >90% for Fe, Al, Ca, Mg, and Mn. The precipitation

Table 2  
Metals recovery from the leachate stream under different methods.

Description	Metals	NaOH consumption, pH, and metal removal efficiency in different methods					
		Single-stage co-precipitation	2-stage co-precipitation		H <sub>2</sub> O <sub>2</sub> pre-2-stage co-precipitation	Biochar sorption	
Stages	–	One stage	1st	2nd	1st	2nd	One stage
NaOH (g/mL) <sup>a</sup>	–	0.11	0.04	0.08	0.05	0.06	0.04
pH range	–	2.5–9.0	2.5–4.5	4.5–9.0	2.5–4.5	4.5–9.0	2.5–4.5
Heavy metals (%) <sup>b</sup>	As	11.4	20.4	8.4	13.0	60.6	19.0
	Cd	98.9	32.7	94.3	35.5	97.2	46.8
	Co	32.9	3.2	32.3	13.4	51.5	32.1
	Cr	97.4	72.7	85.5	82.6	57.3	47.1
	Cu	9.30	15.1	31.3	24.5	49.0	56.0
	Ni	30.7	3.50	33.2	33.2	73.8	70.5
	Pb	78.7	34.0	78.7	80.9	26.6	3.80
	Zn	99.3	35.5	96.3	50.0	99.0	56.8
Other metals (%) <sup>b</sup>	Al	97.4	91.4	77.9	95.4	96.6	95.8
	Ca	91.0	2.30	88.9	23.8	76.9	20.9
	Fe	98.5	99.0	59.5	99.1	96.1	46.6
	K	18.7	16.8	22.3	24.7	46.2	22.6
	Mg	98.0	3.40	99.0	13.3	92.2	29.6
	Mn	99.3	11.4	99.2	22.1	94.4	35.6

<sup>a</sup> 6 M NaOH consumed (g/mL leachate).

<sup>b</sup> The metal removal efficiency in the second stage refers to the percentage removal of the remaining metal in solution after the first stage.



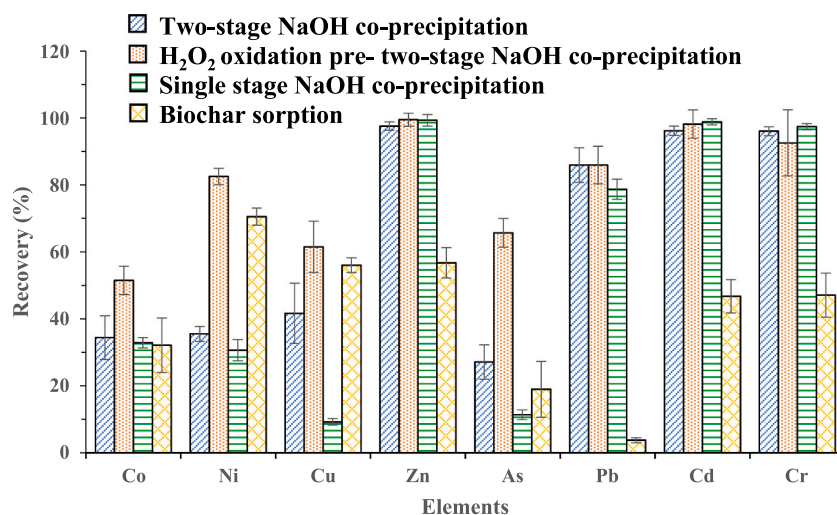


Fig. 6. Overall removal efficiency of HMs under different recovery techniques.

of Co, Ni, As, and Cu was low under this condition due to the high solubility of their respective metal hydroxide at pH 9 (see Fig. S4). It was hypothesised that the presence of Fe and Al would facilitate the precipitation of HMs in the stream. However, the presence of both metal salts did not improve HMs recovery at the basic pH 9 relative to the observation at acidic pH 4.5. The co-precipitating effect of Fe and Al on the other metals cannot be observed under the single-stage recovery, and only the solubility of the various metal hydroxides at pH 9 can be assessed. The single-stage precipitation resulted in a low recovery efficiency of some HMs and, at the same time, produced a highly contaminated HMs sludge stream. This may reduce the attractiveness of the recovered metal sludge for downstream separation and subsequent applications in catalysis or smelting.

The staged recovery of the metals at pH 4.5 (stage 1) and pH 9.0 (stage 2) effectively precipitated Fe and Al from the leachate stream in the first stage, while most of the HMs were recovered in the second stage (Table 2). About 99% Fe and 91% Al were recovered in the first stage (pH 4.5); however, 3–73% of some HMs were co-precipitated. For example, 73% Cr, 36% Zn, 34% Pb, 33% Cd, 20% As, 15% Cu, 4% Ni and 3% Co were co-precipitated with Fe/Al at pH 4.5. The removal of these HMs at pH 4.5 was due to the sorption capacity and co-precipitating ability of Fe and Al hydroxides (Lee et al., 2002). No precipitation of these metals was observed at pH 4.5 in the absence of Fe and Al when the solution of their pure salts was treated with NaOH (data not shown). Only Cd and Zn had the highest removal efficiency of >94% in the second stage. In comparison, other HMs' removal efficiency was 8–79%, similar to the single-stage precipitation from solutions of same pH value of 9 (Table 2). The recovery of As was minimal in the staged NaOH co-precipitation; the highest recovery of 20% occurred at pH 4.5, which could be attributed to the formation of ferric arsenate (Hao et al., 2018). The major benefit of the dual-stage precipitation, aside from the selective recovery of Al, Fe and Cr, was the improvement in Cu recovery from 9% in the single-stage to 31% in the two-stage at pH 9. The mechanism involving the precipitation of ferric iron and the associated Cu loss from solution has been elucidated elsewhere (Javed and Asselin, 2020). The chosen pH 9 is a compromise for the recovery of all the HMs; further optimisation studies are required to identify the optimum recovery pH for each metal species in the solution. From the theoretical solubility curve for metal hydroxides (Fig. S4), Cu has the lowest solubility (<0.1 mg/L) at pH 9 relative to other HMs. However, this theoretical solubility behaviour contradicts the low recovery of Cu (<50%) at pH 9 with a solubility concentration of 36 mg/L. Probable explanations for this include the affinity of Cu(II) to dissolved organic ligands making complexes and the crystal growth vs (super)saturation level of the various metals in the solution (Weng et al., 2002). Moreover, the leachate

stream contains many metal and non-metal species, which may cause significant deviation from the theoretical solubility behaviour of pure metal in aqueous systems.

Adding H<sub>2</sub>O<sub>2</sub> prior to NaOH precipitation improved the recovery of some HMs from the leachate. For example, without adding H<sub>2</sub>O<sub>2</sub>, the overall recovery of As was 27%; however, it increased to 66% when H<sub>2</sub>O<sub>2</sub> was added. Similarly, Cu recovery increased by 47%, Co recovery improved by 53%, and Ni recovery increased by 130%. In fact, increasing the amount of H<sub>2</sub>O<sub>2</sub> added by a unit volume before the staged NaOH precipitation further increased the recovery of As, Co, Cu, and Ni by 48%, 22%, 18%, and 68%, respectively (Fig. S5). The addition of H<sub>2</sub>O<sub>2</sub> had no improvement on the recovery of Zn, Pb, Cd, and Cr compared to the sole 2-stage NaOH co-precipitation. The oxidation of dissolved organics by H<sub>2</sub>O<sub>2</sub> enhanced the desorption of metal species. The biosolids used in this study contain organically bonded HMs (F-3 fraction; Fig. S1), where the bonding strength can be ranked as Cu > As > Co > Ni. The complexation of HMs with dissolved organic matter in aqueous solutions has been reported to influence the solubility and mobility of metals (Weng et al., 2002).

The removal efficiency of the HMs via biochar adsorption was poor compared to the alkali precipitation and did not follow any specific trend. Only a modest 3–70% uptake was achieved, with the highest for Ni and the lowest for Pb. The performance of biochar adsorption for HMs uptake from aqueous solutions is influenced by many factors, including the adsorbent properties, pH, adsorbate concentration, temperature, and solution chemistry of the metal species (Ni et al., 2019). Most of these factors have not been optimised in this study and may contribute to the relatively poor removal efficiency of the biochar sorption process. The FTIR spectra of the biochar before and after the sorption (Fig. S6) confirmed the non-depletion of the surface functional group of the biochar, suggesting the dominance of physisorption. Chemisorption usually involves the chemical reaction between the charged surface functional group of the biochar adsorbent and the metal ions via electrostatic precipitation, organo-metallic complexation, and deprotonation phenomena (Yang et al., 2021).

### 3.5. Process configurations and mass balances

The various unit operations were put together in a process flow diagram (Fig. 7) to provide an insight into the materials requirement of the treatment process demonstrated in this work. Based on our findings, leachate recycling is only attractive at 5% solids which can considerably lower acid and alkali consumption. However, processing 10% solids with no leachate recycling may be favourable commercially. Fig. 7(A) shows the mass balance for processing 10% solids with no leachate

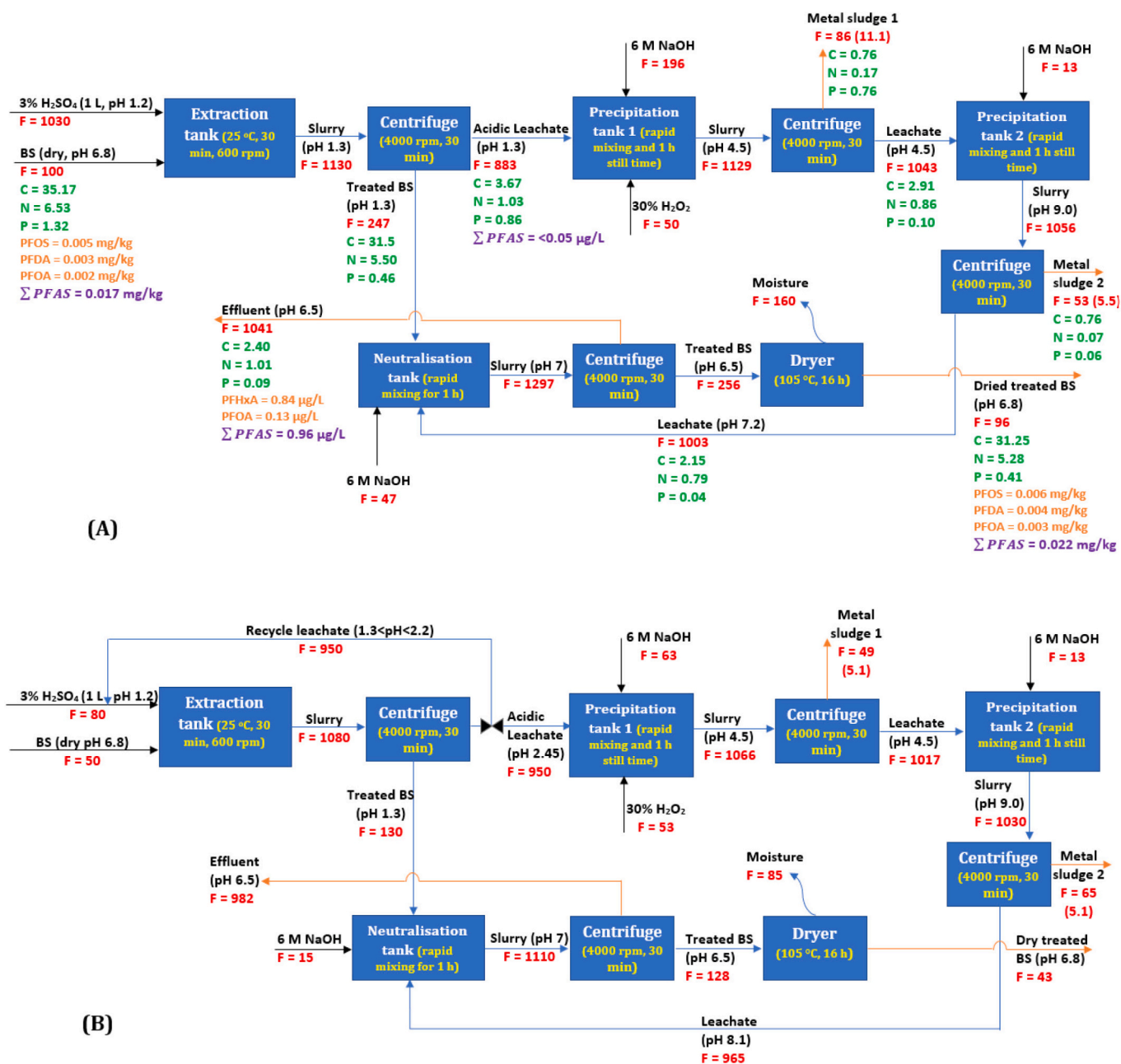


Fig. 7. Process block flow diagram for HMs removal and recovery from biosolids. (A) for processing 10% solids with no leachate recycling (B) for processing 5% solids with leachate recycling (with top-up lixiviant). Red font (F) denotes mass flow in grams; the flowrate in parenthesis corresponds to the dry weight of the metal sludge; green font (C, N, and P) denotes carbon, nitrogen, and phosphorous mass flows in grams, while the purple font denotes total PFAS concentration in the major streams. (For interpretation of the references to colour in this figure legend, the reader is referred to the web version of this article).

recycling, while Fig. 7(B) shows the balance for processing 5% solids with leachate recycling with make-up lixiviant. The separation of solids from the leachate produced acidic treated biosolids (pH 1.3), which cannot be used directly for land application or thermal processing without prior neutralisation or conditioning. A considerable volume of water is required to wash off residual acid in the treated biosolids and raise the pH to near neutral values. It is proposed that the clarified alkali stream be used to neutralise the acidic treated biosolids in an attempt to close the process loop and reduce the volume of aqueous waste generated. In Fig. 7, the total mass flow of streams (grams) in and out of each unit operation is denoted as F, and carbon, nitrogen and phosphorous mass flows (in grams) are denoted as C, N, and P, respectively. For a 1:10 w/v (biosolids to H<sub>2</sub>SO<sub>4</sub> solution ratio) feed rate (Fig. 7(A)), the

overall liquid recovery was 77%, while overall solids recovery was 96% (dry biosolids basis). When the feed ratio was changed to 1:20 w/v (5% solids) with leachate recycling, the mass balance is shown in Fig. 7(B). Overall liquid and solids recovery was 84% and 86%, respectively. Notably, the leachate recycling yielded about a 92% and 43% decrease in H<sub>2</sub>SO<sub>4</sub> and NaOH consumption, respectively. The lixiviant consumption changes remarkably when processing 5% solids with no leachate recycling (Fig. S7). The total H<sub>2</sub>SO<sub>4</sub> consumption (g/g biosolids) doubled, and total NaOH consumption increased by 25% relative to processing 10% solids. The overall results with respect to solids and liquid recovery, metal sludge recovery as well as H<sub>2</sub>SO<sub>4</sub> and NaOH consumption at different process configurations are summarised in Table 3. At 10% solids processing, the major composition (wt%) of

**Table 3**  
Summary of process performance at different configurations.

Indicators	Unit	Process configurations		
		10% solids with no leachate recycling	5% solids with no leachate recycling	5% solids with leachate recycling with make-up lixiviant
Overall solids recovery	wt% dry basis	96	87.6	85.8
Overall liquid recovery	wt%	76.7	80.3	82.4
Total metal sludge recovery	g/g dry biosolids	0.17	0.19	0.21
H <sub>2</sub> SO <sub>4</sub> consumption <sup>a</sup>	g/g dry biosolids	0.57	1.14	0.09
NaOH consumption <sup>b</sup>	g/g dry biosolids	0.50	0.63	0.36

<sup>a</sup> H<sub>2</sub>SO<sub>4</sub> stock solution (98% Assay, SG = 1.84).

<sup>b</sup> NaOH (Analytical reagent grade pellets, SG = 2.13).

recovered metal sludge 1 is 10.7% Fe, 8.8% Na, 8.2% S, 7.9% P, and 5.5% Al while that of metal sludge 2 is 13.1% Na, 12.5% S, 12.4% Ca, 6.0% P, and 3.3% Mg. The detailed composition is provided in Table S3, and the thermal stability profile of the recovered metal sludge is shown in Fig. S8. The recovered metal can be employed in a number of potential applications in catalysis, smelting, and materials production, such as metal-based adsorbents/nanomaterials depending on the required purity and properties (Tawalbeh et al., 2021; Yu et al., 2022).

### 3.6. Fate of nutrients and PFAS

Considering the processing of 10% solids with no leachate recycling, the balance around organic nutrients (C, N, and P) is presented in Fig. 7 (A). The overall process modestly preserved the organic matter in the biosolids as the reduction in C, N, and P contents from raw biosolids to treated biosolids was 11%, 19%, and 65% (w/w), respectively. This observation on nutrient dissolution is comparable to other studies. For example, Mercier et al. (2002) reported about 19% decrease in dissolved organic carbon in treated sludge compared to raw sludge. Similarly, Beauchesne et al. (2007) and Shiba and Ntuli (2017) observed about 77% P and 82% P solubilisation, respectively, from biosolids treatment using H<sub>2</sub>SO<sub>4</sub> (pH <2). The excessive dissolution of P in biosolids is a typical limitation of mineral acid leaching. The joint use of ferric salts and/or H<sub>2</sub>O<sub>2</sub> with H<sub>2</sub>SO<sub>4</sub> has been reported to enhance P retention in biosolids as ferric phosphate (Beauchesne et al., 2007). However, unlike C and N, which largely remain in the dissolved form in the liquid streams, >90% of the total dissolved P was recovered at the metal precipitation stages. Phosphorous has a high affinity for metal ions (particularly Fe) in aqueous media which can be recovered as metal phosphate precipitates (Vardanyan et al., 2018). The dissolution and recovery of P is more sensitive to pH compared to C and N. In the neutralisation stage, where the acid-leached biosolids are treated with NaOH, about 1% C, 4% N and 11% P were further lost from the solids to the liquid phase. The final effluent stream contains about 0.23% C, 0.10% N and 0.009% P (w/w). The guideline for the disposal of this effluent stream as trade wastewater was assessed with respect to the organic and metal concentration load (Table S4). All the metals and organic nutrient concentrations (except for N) are within the acceptable criteria set by South East Water Recycling Corporation, Melbourne, Australia. The excess nitrogen can be removed from the effluent stream by adsorption, and the final liquid can be safely discharged.

Per- and poly-fluoroalkyl substances (PFAS) are rapidly becoming a limiting contaminant for biosolids reuse in agricultural land. Therefore, there is interest in understanding the fate of the plethora of PFAS compounds during the hydrometallurgical treatment process. Twenty-eight common PFAS compounds, the major ones being PFOA (C<sub>8</sub>HF<sub>15</sub>O<sub>2</sub>), PFOS (C<sub>8</sub>HF<sub>17</sub>O<sub>3</sub>S), PFDA (C<sub>10</sub>HF<sub>19</sub>O<sub>2</sub>), PFBS (C<sub>4</sub>HF<sub>9</sub>O<sub>3</sub>S), and PFHxA (C<sub>6</sub>HF<sub>11</sub>O<sub>2</sub>), were measured in the raw biosolids, treated biosolids (with leachate neutralisation), acidic leachate, and the final effluent stream. The representative PFAS compounds detected in the

selected process streams and the total sum of PFAS are shown in Fig. 7 (A). The overall PFAS result is presented in Table S5. The acid extraction (at pH <2) did not leach out the PFAS compounds in the raw biosolids (0.0165 mg/kg), as the concentration of the PFAS in the acidic leachate stream was <0.05 µg/L. However, there appears to be an increase in the leachability of PFAS compounds with a carboxylic head group (particularly PFHxA and PFOA) at the neutralisation stage at pH > 7. The leaching of these PFAS compounds from the acidic treated biosolids (pH 1.3) slightly increased the concentration of the PFAS compounds in the final effluent to 0.96 µg/L. Nevertheless, the PFAS compounds reaching the liquid stream are substantially negligible (<1 µg/L), and the PFAS are largely retained in the treated biosolids (0.0221 mg/kg). Further investigations into the mechanisms controlling the mobility and the final fate of the diverse PFAS compounds during biosolids acid pre-treatment are needed.

Lastly, the viability of the developed closed-loop process with respect to residual nutrients and HMs concentration in the treated biosolids was briefly assessed. The concentration of nutrients and HMs in the treated biosolids with leachate neutralisation was compared with treated biosolids obtained under two different neutralisation washing scenarios at the same pre-treatment conditions. The neutralisation washing scenarios were (i) treated biosolids with leachate neutralisation, (ii) treated biosolids with no neutralisation, and (iii) treated biosolids with deionised water neutralisation. The concentration of the residual nutrients, HMs, and PFAS in the three treated biosolids streams are presented in Table 4. The concentrations are further benchmarked with EPA Victoria prescribed concentration for contaminant-grade biosolids (C1-grade and C2-grade) (EPA Victoria, 2004). The C1-grade refers to the least contaminant grade biosolids with respect to HMs concentration which can be applied to land unrestrictedly. Except for Cu in all scenarios, all other HMs concentrations met the requirements of C1-grade biosolids, with the lowest concentration obtained in treated biosolids with water neutralisation step. Most metal sulfates are soluble in water; therefore, water neutralisation washing helped in the dissolution of metal sulfate salts as well as the removal of H<sub>2</sub>SO<sub>4</sub>-insoluble metal species. Hence it is proposed that the treated biosolids obtained with the leachate neutralisation step be neutralised in a second step with deionised water to reduce the residual metal concentration load further, particularly for Cu. There is largely an inconsequential difference in residual nutrient concentration in the treated biosolids with respect to neutralisation washing scenarios.

## 4. Conclusions

This work provided a detailed investigation into the hydrometallurgical process for extracting and recovering HMs from biosolids. The extraction performance of mineral acids (H<sub>2</sub>SO<sub>4</sub>, HNO<sub>3</sub> and HCl) was similar and only citric acid performed competitively with mineral acids in achieving ~70% extraction of HMs at 5% solids loading. Low solids content (1–5% w/v) favoured HMs extraction and produced a leachate

**Table 4**

Concentration of residual nutrients, metals, and PFAS in biosolids streams obtained under different neutralisation washing scenarios by processing 10% solids.

Content	Elements/ abbreviations	Streams, pH, and concentration					
		Raw biosolids	Treated biosolids (no washing) <sup>a</sup>	Treated biosolids (leachate washing) <sup>b</sup>	Treated biosolids (water washing) <sup>c</sup>	C1-grade biosolids <sup>d</sup>	C2-grade biosolids <sup>d</sup>
	pH	6.8	2.0	6.5	7.0	7.0	7.0
Nutrients (% w/w dry feed basis)	C	35.4	32.9	35.2	36.4	–	–
	N	5.6	5.5	6.2	5.6	–	–
	K	1.1	0.4	0.3	0.2	–	–
	P	1.3	0.5	0.4	0.5	–	–
Major metals (% w/w dry feed basis)	Na	0.1	BDL <sup>e</sup>	1.5	BDL	–	–
	Mg	0.5	0.1	0.1	0.1	–	–
	Al	0.7	0.6	0.4	0.5	–	–
	Ca	10.2	8.5	6.8	5.4	–	–
	Fe	4.2	2.3	2.9	4.1	–	–
Trace metals (mg/kg dry feed basis)	As	<5	<5	<5	<5	20	60
	Cd	1.3	0.5	0.4	0.3	1	10
	Co	<5	<5	<5	<5	–	–
	Cu	690	380	420	220	100	2000
	Cr	20	16	14	14	400	3000
	Hg	0.7	0.9	0.9	0.9	1	5
	Mn	210	53	39	17	–	–
	Mo	8	8	8	9	–	–
	Ni	18	12	14	8	60	270
	Pb	20	17	18	18	300	500
	Se	5	4	4	3	3	50
Zn	850	160	160	48	200	2500	
Major PFAS <sup>f</sup> (mg/kg dry feed basis)	PFBS	0.0005	–	0.0003	–	–	–
	PFDA	0.0028	–	0.0040	–	–	–
	PFHxA	0.0014	–	0.0014	–	–	–
	PFOS	0.0048	–	0.0060	–	–	–
	PFOA	0.0019	–	0.0029	–	–	–
	∑PFAS	0.0165	–	0.0221	–	–	–

<sup>a</sup> Refers to the as-obtained acidic treated biosolids.<sup>b</sup> Refers to the treated biosolids obtained from the closed-loop process developed in this study (see Fig. 7(A)).<sup>c</sup> Refers to treated biosolids obtained from deionised water washing post the acid treatment step until neutral pH.<sup>d</sup> Refers to contaminant-grade biosolids as prescribed in Victoria EPA biosolids management guidelines (EPA Victoria, 2004).<sup>e</sup> BDL- Below detection limit.<sup>f</sup> Abbreviations and chemical formulae–PFBS: Perfluorobutanesulfonic acid, C<sub>4</sub>HF<sub>9</sub>O<sub>3</sub>S.PFDA: Perfluorodecanoic acid, C<sub>10</sub>HF<sub>19</sub>O<sub>2</sub>.PFHxA: Perfluorohexanoic acid, C<sub>6</sub>HF<sub>11</sub>O<sub>2</sub>.PFOS: Perfluorooctanesulfonic acid, C<sub>8</sub>HF<sub>17</sub>O<sub>3</sub>S.PFOA: Perfluorooctanoic acid, C<sub>8</sub>HF<sub>15</sub>O<sub>2</sub>.

stream with dilute metal concentration suitable for recycling, whereas high solids content >5% w/v produced a highly concentrated leachate stream attractive for metal recovery. The leachate stream produced at 5 and 10% solids can be completely recycled at least two times to reach saturation levels of metal ion concentration. However, the recycling of the leachate stream was only attractive at 5% solids; the rapid build-up of ferric iron concentration and increase in solution pH limit the recycling performance of the leachate stream at 10% solids loading. The continuous addition of fresh H<sub>2</sub>SO<sub>4</sub> solution as a make-up lixiviant during the partial recycling (85%) of the spent leachate stream enhanced the dilution of the metal ion concentration and suppressed the precipitation of ferric from the solution at 5% solids. The oxidation of dissolved organics by H<sub>2</sub>O<sub>2</sub> before the 2-stage NaOH precipitation achieved the optimum metal recovery of ~75% from the concentrated leachate stream. The developed process modestly preserved the organic nutrient to a larger extent in the treated biosolids with about 11% loss of carbon and 19% loss of nitrogen. The leaching of PFAS from biosolids into the aqueous phase was limited under the investigated conditions. The findings of this work provide a framework for developing a hydrometallurgical process for biosolids treatment which may be implemented within the existing wastewater treatment facilities.

#### CRediT authorship contribution statement

**Ibrahim Gbolahan Hakeem:** Conceptualization, Methodology,

Formal analysis, Investigation, Software, Writing – original draft. **Pobitra Halder:** Validation, Visualization, Data curation, Writing – review & editing. **Shefali Aktar:** Formal analysis. **Mojtaba Hedayati Marzbali:** Validation, Writing – review & editing. **Abhishek Sharma:** Writing – review & editing. **Aravind Surapaneni:** Resources, Supervision, Writing – review & editing. **Graeme Short:** Methodology, Supervision. **Jorge Paz-Ferreiro:** Supervision, Writing – review & editing. **Kalpiti Shah:** Conceptualization, Validation, Supervision, Project administration.

#### Declaration of Competing Interest

The authors declare that they have no known competing financial interests or personal relationships that could have appeared to influence the work reported in this paper.

#### Acknowledgements

This work is supported through Top-up scholarships from the School of Engineering, RMIT University and the ARC Training Centre for the Transformation of Australia's Biosolids Resources at RMIT University, Australia. The first author acknowledges the postgraduate scholarship received from RMIT University, Australia.

## Appendix A. Supplementary data

Supplementary data to this article can be found online at <https://doi.org/10.1016/j.hydromet.2023.106044>.

## References

- Abouelela, A.R., Mussa, A.A., Talhami, M., Das, P., Hawari, A.H., 2022. Industrial sludge valorization and decontamination via lipid extraction and heavy metals removal using low-cost protic ionic liquid. *Sci. Total Environ.* 835, 155451 <https://doi.org/10.1016/j.scitotenv.2022.155451>.
- Ait Ahsaine, H., Zbair, M., El Haouti, R., 2017. Mesoporous treated sewage sludge as outstanding low-cost adsorbent for cadmium removal. *Desalin. Water Treat.* 85, 330–338. <https://doi.org/10.5004/dwt.2017.21310>.
- Babel, S., del Mundo Dacera, D., 2006. Heavy metal removal from contaminated sludge for land application: a review. *Waste Manag.* 26, 988–1004. <https://doi.org/10.1016/j.wasman.2005.09.017>.
- Bayat, B., Sari, B., 2010. Comparative evaluation of microbial and chemical leaching processes for heavy metal removal from dewatered metal plating sludge. *J. Hazard. Mater.* 174, 763–769. <https://doi.org/10.1016/j.jhazmat.2009.09.117>.
- Beauchesne, I., Cheikh, R. Ben, Mercier, G., Blais, J.F., Ouarda, T., 2007. Chemical treatment of sludge: in-depth study on toxic metal removal efficiency, dewatering ability and fertilizing property preservation. *Water Res.* 41, 2028–2038. <https://doi.org/10.1016/j.watres.2007.01.051>.
- Blais, J.-F., Meunier, N., Sasseville, J.-L., Tyagi, R.D., Mercier, G., Hammy, F., 2005. Hybrid chemical and biological process for decontaminating sludge from municipal sewage. *US 6,855,256 B2*.
- de Fátima da Silva, M., de Sousa Oliveira, M.R., dos Santos, I.D., Radino-Rouse, P., Mansur, M.B., 2020. Iron precipitation strategies from nickel laterite ore sulfuric acid leach liquor. *Miner. Process. Extr. Metall. Rev.* 1–12 <https://doi.org/10.1080/08827508.2020.1809392>.
- del Mundo Dacera, D., Babel, S., 2006. Use of citric acid for heavy metals extraction from contaminated sewage sludge for land application. *Water Sci. Technol.* 54, 129–135. <https://doi.org/10.2166/wst.2006.764>.
- Demol, J., Ho, E., Soldenhoff, K., Karatchevseva, I., Senanayake, G., 2022. Beneficial effect of iron oxide/hydroxide minerals on sulfuric acid baking and leaching of monazite. *Hydrometallurgy* 211, 105864. <https://doi.org/10.1016/j.hydromet.2022.105864>.
- EPA Victoria, 2004. Guidelines for Environmental Management: Biosolids Land Application. Southbank, Victoria 3006, Australia.
- Ericksen Jones, J., 1934. *The Toxic Action of Heavy Metal Salts on the Three-Spined Stickleback (Gasterosteus Aculeatus)*. Aberystwyth, Wales.
- Feng, J.J., Jia, L., Liu, Q.Z., Chen, X.L., Cheng, J.P., 2018. Source identification of heavy metals in sewage sludge and the effect of influent characteristics: a case study from China. *Urban Water J.* 15, 381–387. [https://doi.org/10.1080/1573062X.2018.1483525/SUPPL\\_FILE/NURW\\_A\\_1483525\\_SM7700.PDF](https://doi.org/10.1080/1573062X.2018.1483525/SUPPL_FILE/NURW_A_1483525_SM7700.PDF).
- Fu, F., Wang, Q., 2011. Removal of heavy metal ions from wastewaters: a review. *J. Environ. Manag.* 92, 407–418. <https://doi.org/10.1016/j.jenvman.2010.11.011>.
- Gaber, S., Rizk, M., Yehia, M., 2011. Extraction of certain heavy metals from sewage sludge using different types of acids. *Biokemistri* 23, 41–48. <https://doi.org/10.4314/biokem.v23i1>.
- Geng, H., Xu, Y., Zheng, L., Gong, H., Dai, L., Dai, X., 2020. An overview of removing heavy metals from sewage sludge: achievements and perspectives. *Environ. Pollut.* 266, 115375 <https://doi.org/10.1016/j.envpol.2020.115375>.
- Gheju, M., Pode, R., Manea, F., 2011. Comparative heavy metal chemical extraction from anaerobically digested biosolids. *Hydrometallurgy* 108, 115–121. <https://doi.org/10.1016/j.hydromet.2011.03.006>.
- Guan, R., Yuan, X., Wu, Z., Wang, H., Jiang, L., Li, Y., Zeng, G., 2017. Functionality of surfactants in waste-activated sludge treatment: a review. *Sci. Total Environ.* 609, 1433–1442. <https://doi.org/10.1016/j.scitotenv.2017.07.189>.
- Gunarathne, V., Rajapaksha, A.U., Vithanage, M., Alessi, D.S., Selvasembian, R., Naushad, M., You, S., Oleszczuk, P., Ok, Y.S., 2020. Hydrometallurgical processes for heavy metals recovery from industrial sludges. *Crit. Rev. Environ. Sci. Technol.* 1–42 <https://doi.org/10.1080/10643389.2020.1847949>.
- Hakeem, I.G., Halder, P., Dike, C.C., Chiang, K., Sharma, A., Paz-Ferreiro, J., Shah, K., 2022a. Advances in biosolids pyrolysis: roles of pre-treatments, catalysts, and co-feeding on products distribution and high-value chemical production. *J. Anal. Appl. Pyrolysis* 166, 105608. <https://doi.org/10.1016/j.jaap.2022.105608>.
- Hakeem, I.G., Halder, P., Marzbali, M.H., Patel, S., Rathnayake, N., Surapaneni, A., Short, G., Paz-Ferreiro, J., Shah, K., 2022b. Mild sulphuric acid pre-treatment for metals removal from biosolids and the fate of metals in the treated biosolids derived biochar. *J. Environ. Chem. Eng.* 10, 107378 <https://doi.org/10.1016/j.jece.2022.107378>.
- Hao, L., Liu, M., Wang, N., Li, G., 2018. A critical review on arsenic removal from water using iron-based adsorbents. *RSC Adv.* 8, 39545–39560. <https://doi.org/10.1039/C8RA08512A>.
- Ito, A., Umata, T., Aizawa, J., Takachi, T., Morinaga, K., 2000. Removal of heavy metals from anaerobically digested sewage sludge by a new chemical method using ferric sulfate. *Water Res.* 34, 751–758. [https://doi.org/10.1016/S0043-1354\(99\)00215-8](https://doi.org/10.1016/S0043-1354(99)00215-8).
- Javed, T., Asselin, E., 2020. Fe(III) precipitation and copper loss from sulphate-chloride solutions at 150 °C: a statistical approach. *Metals (Basel)* 10, 669. <https://doi.org/10.3390/MET10050669>.
- Kabiri, S., Tucker, W., Navarro, D.A., Bräunig, J., Thompson, K., Knight, E.R., Nguyen, T. M.H., Grimison, C., Barnes, C.M., Higgins, C.P., Mueller, J.F., Kookana, R.S., McLaughlin, M.J., 2022. Comparing the leaching behavior of per- and polyfluoroalkyl substances from contaminated soils using static and column leaching tests. *Environ. Sci. Technol.* 56, 368–378. [https://doi.org/10.1021/ACS.EST.1C06604/ASSET/IMAGES/LARGE/ESI06604\\_0005.JPEG](https://doi.org/10.1021/ACS.EST.1C06604/ASSET/IMAGES/LARGE/ESI06604_0005.JPEG).
- Kuan, Y.C., Lee, I.H., Chern, J.M., 2010. Heavy metal extraction from PCB wastewater treatment sludge by sulfuric acid. *J. Hazard. Mater.* 177, 881–886. <https://doi.org/10.1016/j.jhazmat.2009.12.115>.
- Kundu, S., Patel, S., Halder, P., Patel, T., Hedayati Marzbali, M., Pramanik, B.K., Paz-Ferreiro, J., De Figueiredo, C.C., Bergmann, D., Surapaneni, A., Megharaj, M., Shah, K., 2021. Removal of PFASs from biosolids using a semi-pilot scale pyrolysis reactor and the application of biosolids derived biochar for the removal of PFASs from contaminated water. *Environ. Sci. Water Res. Technol.* 7, 638–649. <https://doi.org/10.1039/d0ew00763c>.
- LeBlanc, R.J., Matthews, P., Richard, R.P., 2009. Global atlas of excreta, wastewater sludge, and biosolids management: Moving forward the sustainable and welcome uses of a global resource. United Nations Human Settlements Programme, UN-HABITAT, P.O. Box 30030, Nairobi 00100, Kenya.
- Lee, G., Bigham, J.M., Faure, G., 2002. Removal of trace metals by coprecipitation with Fe, Al and Mn from natural waters contaminated with acid mine drainage in the Ducktown Mining District, Tennessee. *Appl. Geochem.* 17, 569–581. [https://doi.org/10.1016/S0883-2927\(01\)00125-1](https://doi.org/10.1016/S0883-2927(01)00125-1).
- Lee, I.H., Wang, Y.J., Chern, J.M., 2005. Extraction kinetics of heavy metal-containing sludge. *J. Hazard. Mater.* 123, 112–119. <https://doi.org/10.1016/J.JHAZMAT.2005.03.035>.
- Lee, I.H., Kuan, Y.C., Chern, J.M., 2006. Factorial experimental design for recovering heavy metals from sludge with ion-exchange resin. *J. Hazard. Mater.* 138, 549–559. <https://doi.org/10.1016/J.JHAZMAT.2006.05.090>.
- Leštan, D., Luo, C., Ling, Li, X., Dong, 2008. The use of chelating agents in the remediation of metal-contaminated soils: a review. *Environ. Pollut.* 153, 3–13. <https://doi.org/10.1016/j.envpol.2007.11.015>.
- Li, Y., Yu, Han, Liu, L., Yu, Hongbing, 2021. Application of co-pyrolysis biochar for the adsorption and immobilization of heavy metals in contaminated environmental substrates. *J. Hazard. Mater.* 420, 126655 <https://doi.org/10.1016/J.JHAZMAT.2021.126655>.
- Liang, S., Chen, H., Zeng, X., Li, Z., Yu, W., Xiao, K., Hu, J., Hou, H., Liu, B., Tao, S., Yang, J., 2019. A comparison between sulfuric acid and oxalic acid leaching with subsequent purification and precipitation for phosphorus recovery from sewage sludge incineration ash. *Water Res.* 159, 242–251. <https://doi.org/10.1016/J.WATRES.2019.05.022>.
- Liu, T., Liu, Z., Zheng, Q., Lang, Q., Xia, Y., Peng, N., Gai, C., 2018. Effect of hydrothermal carbonization on migration and environmental risk of heavy metals in sewage sludge during pyrolysis. *Bioresour. Technol.* 247, 282–290. <https://doi.org/10.1016/J.BIORTECH.2017.09.090>.
- Liu, L., Huang, L., Huang, R., Lin, H., Wang, D., 2021. Immobilization of heavy metals in biochar derived from co-pyrolysis of sewage sludge and calcium sulfate. *J. Hazard. Mater.* 403, 123648 <https://doi.org/10.1016/J.JHAZMAT.2020.123648>.
- Ma, D., Su, M., Qian, J., Wang, Q., Meng, F., Ge, X., Ye, Y., Song, C., 2020. Heavy metal removal from sewage sludge under citric acid and electroosmotic leaching processes. *Sep. Purif. Technol.* 242, 116822 <https://doi.org/10.1016/j.seppur.2020.116822>.
- Marchioretto, M.M., Bruning, H., Rulkens, W., 2005. Heavy metals precipitation in sewage sludge. *Sep. Sci. Technol.* 40, 3393–3405. <https://doi.org/10.1080/01496390500423748>.
- Matocha, C.J., Karathanasis, A.D., Rakshit, S., Wagner, K.M., 2005. Reduction of copper (II) by iron(II). *J. Environ. Qual.* 34, 1539–1546. <https://doi.org/10.2134/jeq2005.0002>.
- Mercier, G., Blais, J.F., Hammy, F., Lounès, M., Sasseville, J.L., 2002. A decontamination process to remove metals and stabilise Montreal sewage sludge. *Sci. World J.* 2, 1121–1126. <https://doi.org/10.1100/tsw.2002.201>.
- Montenegro, V., Agatzini-Leonardou, S., Oustadakis, P., Tsakiridis, P., 2016. Hydrometallurgical treatment of EAF dust by direct sulphuric acid leaching at atmospheric pressure. *Waste Biomass Valorization* 76 (7), 1531–1548. <https://doi.org/10.1007/S12649-016-9543-Z>.
- Ni, B.J., Huang, Q.S., Wang, C., Ni, T.Y., Sun, J., Wei, W., 2019. Competitive adsorption of heavy metals in aqueous solution onto biochar derived from anaerobically digested sludge. *Chemosphere* 219, 351–357. <https://doi.org/10.1016/J.CHEMOSPHERE.2018.12.053>.
- Nie, J., Pan, Y., Shi, J., Guo, Y., Yan, Z., Duan, X., Xu, M., 2015. A comparative study on the uptake and toxicity of nickel added in the form of different salts to maize seedlings. *Int. J. Environ. Res. Public Health* 12, 15075–15087. <https://doi.org/10.3390/IJERPH121214972>.
- Pathak, A., Dastidar, M.G., Sreekrishnan, T.R., 2009. Bioleaching of heavy metals from sewage sludge: a review. *J. Environ. Manag.* <https://doi.org/10.1016/j.jenvman.2008.11.005>.
- Paz-ferreiro, J., Nieto, A., Méndez, A., Askeland, M.P.J., Gasco, G., 2018. Biochar from biosolids pyrolysis: a review. *Int. J. Environ. Res. Public Health* 15, 1–16. <https://doi.org/10.3390/ijerph15050956>.
- Persson, H., Kantarelis, E., Evangelopoulos, P., Yang, W., 2017. Wood-derived acid leaching of biomass for enhanced production of sugars and sugar derivatives during pyrolysis: in fl uence of acidity and treatment time. *J. Anal. Appl. Pyrolysis* 127, 329–334. <https://doi.org/10.1016/j.jaap.2017.07.018>.
- Ross, J.J., Zitomer, D.H., Miller, T.R., Weirich, C.A., Mcnamara, P.J., 2016. Emerging investigators series: pyrolysis removes common microconstituents trichloroan, triclosan, and nonylphenol from biosolids. *Environ. Sci. Water Res. Technol.* 2, 282–289. <https://doi.org/10.1039/C5EW00229J>.

- Sethurajan, M., Lens, P.N.L., Horn, H.A., Figueiredo, L.H.A., van Hullebusch, E.D., 2017. Leaching and recovery of metals. In: Rene, E.R. (Ed.), *Sustainable Heavy Metal Remediation*. Springer International Publishing AG, pp. 161–206. [https://doi.org/10.1007/978-3-319-61146-4\\_6](https://doi.org/10.1007/978-3-319-61146-4_6).
- Shen, Y., Chen, L., 2022. Catalytic pyrolysis of cellulose with biochar modified by Ni–Co–Mn cathode material recovered from spent lithium-ion battery. *Chemosphere* 305, 135430. <https://doi.org/10.1016/J.CHEMOSPHERE.2022.135430>.
- Shi, J., Pang, J., Liu, Q., Luo, Y., Ye, J., Xu, Q., Long, B., Ye, B., Yuan, X., 2020. Simultaneous removal of multiple heavy metals from soil by washing with citric acid and ferric chloride. *RSC Adv.* 10, 7432–7442. <https://doi.org/10.1039/C9RA09999A>.
- Shiba, N.C., Ntuli, F., 2017. Extraction and precipitation of phosphorus from sewage sludge. *Waste Manag.* 60, 191–200. <https://doi.org/10.1016/J.WASMAN.2016.07.031>.
- Shim, M.J., 2023. Recycling of washing agents for heavy metal removal from digested sewage sludge. *Int. J. Environ. Sci. Technol.* 1–12 <https://doi.org/10.1007/S13762-023-04757-4/FIGURES/9>.
- Singh, S., Kumar, V., Dhanjal, D.S., Datta, S., Bhatia, D., Dhiman, J., Samuel, J., Prasad, R., Singh, J., 2020. A sustainable paradigm of sewage sludge biochar: valorization, opportunities, challenges and future prospects. *J. Clean. Prod.* 269, 122259 <https://doi.org/10.1016/J.JCLEPRO.2020.122259>.
- Strasser, H., Brunner, H., Schinner, F., 1995. Leaching of iron and toxic heavy metals from anaerobically-digested sewage sludge. *J. Ind. Microbiol.* 14, 281–287. <https://doi.org/10.1007/BF01569940>.
- Stylianou, M.A., Kollia, D., Haralambous, K.J., Inglezakis, V.J., Moustakas, K.G., Loizidou, M.D., 2007. Effect of acid treatment on the removal of heavy metals from sewage sludge. *Desalination* 215, 73–81. <https://doi.org/10.1016/j.desal.2006.11.015>.
- Tang, J., He, J., Liu, T., Xin, X., 2017. Removal of heavy metals with sequential sludge washing techniques using saponin: optimization conditions, kinetics, removal effectiveness, binding intensity, mobility and mechanism. *RSC Adv.* 7, 33385–33401. <https://doi.org/10.1039/C7RA04284A>.
- Tawalbeh, M., Al-Othman, A., Salamah, T., Alkasrawi, M., Martis, R., El-Rub, Z.A., 2021. A critical review on metal-based catalysts used in the pyrolysis of lignocellulosic biomass materials. *J. Environ. Manag.* 299, 113597 <https://doi.org/10.1016/J.JENVMAN.2021.113597>.
- Tyagi, V.K., Lo, S.L., 2013. Sludge: a waste or renewable source for energy and resources recovery? *Renew. Sust. Energ. Rev.* <https://doi.org/10.1016/j.rser.2013.05.029>.
- Vardanyan, A., Kafa, N., Konstantinidis, V., Shin, S.G., Vyrides, I., 2018. Phosphorus dissolution from dewatered anaerobic sludge: effect of pHs, microorganisms, and sequential extraction. *Bioresour. Technol.* 249, 464–472. <https://doi.org/10.1016/J.BIORTECH.2017.09.188>.
- Vesilind, P.A., Hsu, C.C., 1997. Limits of sludge dewaterability. *Water Sci. Technol.* 36, 87–91. [https://doi.org/10.1016/S0273-1223\(97\)00673-2](https://doi.org/10.1016/S0273-1223(97)00673-2).
- Wang, Xuejiang, Chen, J., Yan, X., Wang, Xin, Zhang, J., Huang, J., Zhao, J., 2015. Heavy metal chemical extraction from industrial and municipal mixed sludge by ultrasound-assisted citric acid. *J. Ind. Eng. Chem.* 27, 368–372. <https://doi.org/10.1016/J.JIEC.2015.01.016>.
- Wang, Y., Zhang, Y., Pei, L., Ying, D., Xu, X., Zhao, L., Jia, J., Cao, X., 2017. Converting Ni-loaded biochars into supercapacitors: implication on the reuse of exhausted carbonaceous sorbents. *Sci. Report.* 71 (7), 1–8. <https://doi.org/10.1038/srep41523>.
- Wang, X., Chi, Q., Liu, X., Wang, Y., 2019. Influence of pyrolysis temperature on characteristics and environmental risk of heavy metals in pyrolyzed biochar made from hydrothermally treated sewage sludge. *Chemosphere* 216, 698–706. <https://doi.org/10.1016/J.CHEMOSPHERE.2018.10.189>.
- Weng, L., Temminghoff, E.J.M., Lofts, S., Tipping, E., Van Riemsdijk, W.H., 2002. Complexation with dissolved organic matter and solubility control of heavy metals in a sandy soil. *Environ. Sci. Technol.* 36, 4804–4810. [https://doi.org/10.1021/ES0200084/SUPPL\\_FILE/ES0200084\\_S.PDF](https://doi.org/10.1021/ES0200084/SUPPL_FILE/ES0200084_S.PDF).
- Wu, C.H., Kuo, C.Y., Lo, S.L., 2009. Recovery of heavy metals from industrial sludge using various acid extraction approaches. *Water Sci. Technol.* 59, 289–293. <https://doi.org/10.2166/wst.2009.859>.
- Xiang, L., Chan, L.C., Wong, J.W.C., 2000. Removal of heavy metals from anaerobically digested sewage sludge by isolated indigenous iron-oxidizing bacteria. *Chemosphere* 41, 283–287. [https://doi.org/10.1016/S0045-6535\(99\)00422-1](https://doi.org/10.1016/S0045-6535(99)00422-1).
- Xiao, Z., Yuan, X., Li, H., Jiang, L., Leng, L., Chen, X., Zeng, G., Li, F., Cao, L., 2015. Chemical speciation, mobility and phyto-accessibility of heavy metals in fly ash and slag from combustion of pelletized municipal sewage sludge. *Sci. Total Environ.* 536, 774–783. <https://doi.org/10.1016/J.SCITOTENV.2015.07.126>.
- Xu, Y., Xie, Y., Liu, J., Yan, L., Yang, R., 2009. Enrichment of valuable metals from the sulfuric acid leach liquors of nickeliferous oxide ores. *Hydrometallurgy* 95, 28–32. <https://doi.org/10.1016/J.HYDROMET.2008.04.003>.
- Yang, Z., Wang, D., Wang, G., Zhang, S., Cheng, Z., Xian, J., Pu, Y., Li, T., Jia, Y., Li, Y., Zhou, W., Xu, X., 2021. Removal of Pb, Zn, Ni and Cr from industrial sludge by biodegradable washing agents: Caboxyethylthiosuccinic acid and itaconic-acrylic acid. *J. Environ. Chem. Eng.* 9, 105846 <https://doi.org/10.1016/J.JECE.2021.105846>.
- Yao, J.G., Tan, S.Y., Metcalfe, P.I., Fennell, P.S., Kelsall, G.H., Hallett, J.P., 2021. Demetallization of sewage sludge using low-cost ionic liquids. *Environ. Sci. Technol.* 55, 5291–5300. <https://doi.org/10.1021/acs.est.0c03724>.
- Yoshizaki, S., Tomida, T., 2000. Principle and process of heavy metal removal from sewage sludge. *Environ. Sci. Technol.* 34, 1572–1575. <https://doi.org/10.1021/es990979s>.
- Yu, H., Naidu, G., Zhang, C., Wang, C., Razmjou, A., Han, D.S., He, T., Shon, H., 2022. Metal-based adsorbents for lithium recovery from aqueous resources. *Desalination* 539, 115951. <https://doi.org/10.1016/J.DESAL.2022.115951>.
- Zhao, B., Xu, X., Zeng, F., Li, H., Chen, X., 2018. The hierarchical porous structure biochar assessments produced by co-pyrolysis of municipal sewage sludge and hazelnut shell and Cu(II) adsorption kinetics. *Environ. Sci. Pollut. Res.* 25, 19423–19435. <https://doi.org/10.1007/S11356-018-2079-Y>.



# Geophysical and geostatistical assessment of groundwater and soil quality using GIS, VES, and PCA techniques in the Jaipur region of Western India

Jabbar Khan<sup>1</sup> · Govind Gupta<sup>1</sup> · Naveen Kumar Singh<sup>1</sup> · Vivek Narayan Bhawe<sup>2</sup> · Vinay Bhardwaj<sup>2</sup> · Pallavi Upreti<sup>3</sup> · Rani Singh<sup>4</sup> · Amarendra Kumar Sinha<sup>5</sup>

Received: 15 February 2023 / Accepted: 25 May 2023 / Published online: 1 June 2023  
© The Author(s), under exclusive licence to Springer-Verlag GmbH Germany, part of Springer Nature 2023

## Abstract

In present study, geophysical and geostatistical variability of ground water and agricultural soil investigated in the Jaipur region of Rajasthan (Western India) by applying the geographic information system (GIS), vertical electrical sounding (VES), and statistical analysis. Ground water and soil samples collected from different sites from the selected study area and variation pattern of quality parameters were assessed. A contour map analysis of distribution of metals and other contaminants in the samples was conducted using GIS. Maximum concentration of metals recorded in the soil samples in order of Fe, 11.25 mg kg<sup>-1</sup> > Mn, 8.6 mg kg<sup>-1</sup> > Zn, 7.2 mg kg<sup>-1</sup> > Cu, 0.455 mg kg<sup>-1</sup>; however, maximum concentration of metals in the ground water samples was found as Zn, 2.64 mg L<sup>-1</sup> > Cu, 0.86 mg L<sup>-1</sup> > Fe, 0.39 mg L<sup>-1</sup> > Mn, 0.18 mg L<sup>-1</sup> > Pb, 0.065 mg L<sup>-1</sup> > Ni, 0.016 mg L<sup>-1</sup>. Observed data emphasis variability in groundwater and soil quality parameter by PCA technique indicated 84.60% and 66.98% of variance, respectively. Soil quality index (SQI) value was observed as 0.482 indicating that 46% of soil sampling sites deteriorated and shown poor quality. Similarly, water quality index (WQI) value indicates good water quality at the sampling sites TW1, TW8, TW10, and TW12; however, TW3, TW4, TW6, TW19, TW20, and TW22 sites showed very poor water quality. The present study concludes that overexploitation of groundwater and unregulated discharge of wastewater leads to depletion of water and soil quality. Further, applying geographical and geostatistical techniques in assessing water and soil quality could be more effective tools in environmental monitoring and management for environmental and health safety.

**Keywords** Bioaccumulation · Bioavailability · Biotransformation · Contamination · Groundwater · Metals · Principal component analysis (PCA) · Water quality

Responsible Editor: Wei Liu

✉ Naveen Kumar Singh  
naveenenviro04@gmail.com

<sup>1</sup> Department of Chemistry, Environmental Science discipline, School of Basic Sciences, Manipal University Jaipur, Dehmi Kalan, Jaipur, Rajasthan 303007, India

<sup>2</sup> Ground Water Department, Jaipur, Rajasthan, India

<sup>3</sup> Department of Geography, Dr. Nityanand Himalayan Research and Study Centre (DNHRSC), Dehradun, Uttarakhand, India

<sup>4</sup> Subodh P.G. (Autonomous) College, Rambagh, Jaipur, Rajasthan, India

<sup>5</sup> Chhatrapati Shivaji Maharaj University, (Panvel) Navi Mumbai, Maharashtra 410206, India

## Introduction

Rapid urbanization leads to several environmental issues, including poor living conditions, changes in land use pattern, overexploitation of water and soil, transportation congestion, resettlement, disasters, and environmental pollution (Kalayci Onac et al. 2021; Aksoy et al. 2022; Tay and Ocansey 2022; Dogan et al. 2023). Fresh water including ground water is one of the most important components of the environment and essential for human survival and wellbeing (Gavrilescu 2021). However, extensive exploitation of water by human being leads to substantial environmental cost due to contamination, scarcity, and depletion of water resources affecting water supply and health safety (Tzanakakis et al. 2020; Singh et al. 2022). Scarcity of safe drinking water is now becoming a problem due to

extensive urbanisation, industrialization, agriculture, and climate change affecting about 40% of human population globally (Calzadilla et al. 2011; Bilge Ozturk et al. 2022). Groundwater found underground in cracks and crannies in rock, sand, and soil is the main source of drinking water supply. Exploitation of groundwater may result in dissolution of numerous contaminants as it passes through the rocks and soil during leaching and percolation (Saleem et al. 2018). Trace metals emanating from different industrial, transportation, construction, and agricultural activities affect soil and water quality as recalcitrant and toxic contaminants (Romic and Romic 2003; Cetin et al. 2022a; Sahin et al., 2022). Link between soil quality and socioeconomic well-being of humans, particularly, global food security and human health have been reported (Yu et al. 2018; Kopittke et al. 2019). Soil and water contamination occurs due to various anthropogenic activities and geological processes releasing metals and other elements; therefore, assessment of soil and water quality is becoming more crucial in adapting appropriate strategies to prevent and preserve the land and water resources for human wellbeing (Ahmet et al. 2006; Cesur et al. 2021). More common metal contaminants in soil and water are Pb, Cr, As, Zn, V, Cd, Cu, and Sn reported with high levels of toxicity for biota (Yang et al. 2016; Hanfi et al. 2020; Cetin et al. 2022b).

India is one of the emerging nations with more industrial and other developmental activities having wastewater generation and discharge on the land and in the aquatic ecosystems leads to soil and water contamination (Tiwari et al. 2011). Metals persist in the soil and water, accumulates in the plants by roots uptake, and biomagnifies in the animals through food chain, which causes detrimental impact to the biota (Luo et al. 2012; Ali et al. 2019; Cetin and Abo Aisha 2023). Certain metals easily enter the food chain due to their bioavailability in the rhizosphere, uptake, and accumulation in the plants and can reach to other animals and humans through food (Gu et al. 2016; Rajendran et al. 2022). It has been reported that excessive accumulation of trace elements like cadmium, lead, and nickel in the plants causes toxicity and slows down the growth and productivity (Pandey and Sharma 2002; Zouboulis et al. 2004). A substantial threat to aquatic and terrestrial biodiversity as well as health hazards for humans posed by contaminated water and soil (Olayinka-Olagunju et al. 2021). Types of rock, physicochemical characteristics of soil, atmospheric precipitation, and surface geochemical processes affect the groundwater quality parameters and contamination (Garg and Hassan 2007; Cesur et al. 2021). Groundwater is most reliable source even in India because it provides a significant proportion of the country's drinking and agricultural water requirements (Mahmood and Kundu 2005).

Physico-chemical characteristics of soil also affects the water quality of groundwater at a given regions (Griffiths

et al. 2010; Hermans et al. 2020). Different physio-chemical and biological indicators have been used in various studies to evaluate the soil quality (Filip 2002; Schloter et al. 2003). GIS has evolved into a trustworthy instrument for absorbing, analyzing, and displaying spatial data that can be utilized for environmental monitoring, planning, and resource management applications (Cetin 2015; Singha et al. 2015). The geographical information system (GIS) has become an important tool in research for resource management as it allows users to use geographical data in a variety of context and way in an integrated approach. Remote sensing (RS) and GIS studies in integration make it easier to work in relatively broad areas, particularly in environmental impact assessment for sustainable urban planning and resource utilization (Cetin 2019; Pekkan et al. 2021; Cetin et al. 2022c). Convergence of data concerning environmental assessment-related issues as well as the manipulation of spatial data into various forms in response to geosocial requirements may be accomplished using GIS (Cetin et al. 2022d). The principal component analysis (PCA) is a prominent statistical analysis tool for investigating data patterns thorough factor analysis approach. Basic purpose of PCA is to create new variables as principal components, from a set of existing original variables (Wu et al. 2020). Potential of geophysical information system-based geostatistical methodologies in assessing the region's groundwater and soil quality as well as its susceptibility to water-borne diseases reported (Ali and Ahmad 2020).

The Sanganer, Jaipur region of Rajasthan, Western India, having more industrial activities specially printing and dyeing operations leads to huge amount of wastewater generation and discharge in water and agricultural soil through unregulated disposal and irrigation practices. Very limited data are available related to using geographical information system and geostatistical techniques in the ground water and soil quality assessment. Therefore, the present study was conducted to assess ground water and soil quality at different sites based on a minimal set of interconnected geophysical and chemical criteria at Sanganer, Jaipur region of Rajasthan, Western India, and apply geophysical and geostatistical including GIS, VES, and PCA techniques to emphasize the water and soil quality parameters for environmental monitoring and assessment.

## Materials and methods

### Study area

The whole study conducted in the industrial and agricultural tracts in the north of Jaipur–Sanganer regions at different selected sampling sites, situated between 26° 49' and 26° 51' N and 75° 46' and 75° 51' E in the Jaipur district,



Rajasthan, Western India (Fig. 1). One selected study site, the Sanganer, is famous for its hand-printed textiles have land size of 78.24 square kilometres, situated on NH-12, 10 kilometres to the southwest of Jaipur City. The Sanganer is well-known for its distinctive type of printing “Sanganer Printing” basically in the small-scale industries of the

Chippas community, involving dyeing and printing of textiles (Dadhich et al. 2016). Dyeing and printing processes release wastewater during water-based color fixing procedure and discharged in the surrounding areas which pollutes water and soil. The chippas community either transport the textiles to a well dug on the bank of the Dravyawati River or

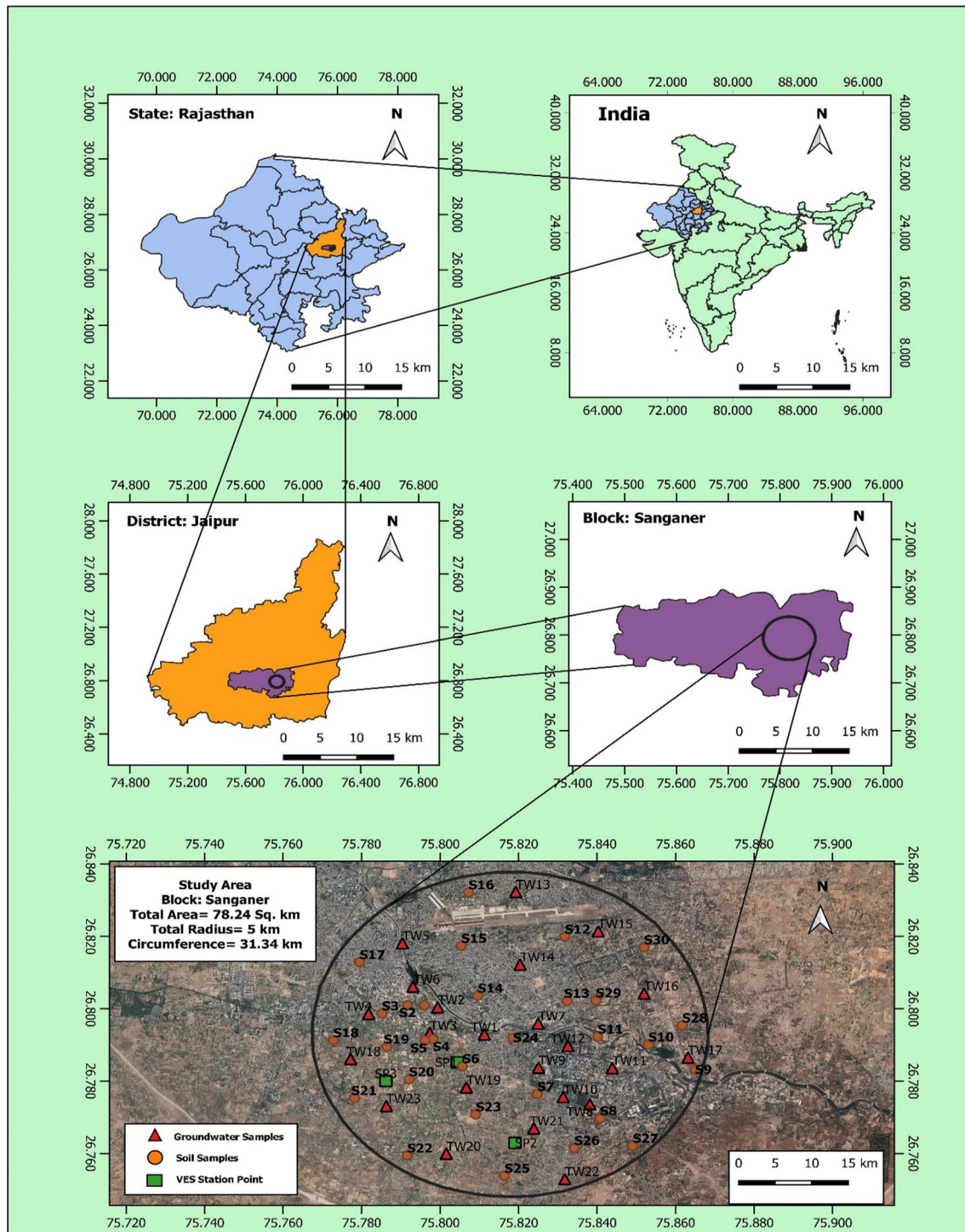


Fig. 1 Sampling sites of soil and ground water selected in the study area, Sanganer, Jaipur, Rajasthan, India

wash it at their wells in the city at various places randomly. Textile wastewater along with sewage from across the of Jaipur city discharged directly into the Dravyawati river in the selected study area is being polluted. Historically, Sanganer was primarily an agricultural region; however, during the last decade, the textile and dyeing industries have dramatically risen in the area and encroached the previously untapped agricultural land. With more than 250 separate printing units connected, it has emerged as one of the major centers of the printing and dyeing industries nowadays today in India. Growing demand and low production costs leads to the introduction of synthetic and chemical dyes, which have several environmental impacts. The regions of Jaipur–Sanganer with a high number of dyeing and printing industrial units releasing tonnes of waste into the aquatic environment, agricultural fields, and on open spaces nearby, polluting the water and soil (Sharma et al. 2014). Contamination of water and soil have negative impact on nutrition and human health due to deterioration of drinking water quality and food quality; however, at severe stage, poor quality may prevent soil from performing its natural physio-chemical and biological functions and deteriorate region's overall productivity of the terrestrial ecosystem.

### Sampling sites and sampling

One-liter capacity plastic bottle rinsed with distilled water used to collect the groundwater samples. Grab sampling conducted for groundwater water sampling and samples preserved in the bottles with adjusted pH 2 and stored in refrigerator at 4 °C with slightly acidified with nitric acid (HNO<sub>3</sub>) for analysis of water quality parameters including metals (Mn, Cu, Ni, Zn, Pb, and Cu). In Sanganer industrial region, having a new industrial area (RICCO) and an industrial zone (RSMDC), a quantitative soil and water sampling conducted to evaluate the water and soil quality parameters of the agricultural land as well as the degree of contamination in water due to industrial activities. Soil samples (250 g) taken from 30 randomly selected sites with a depth of 45 to 60 cm within a 5-kilometer radius of the Sanganer industrial zone and packed in fresh plastic zip-lock bag separately to determine the soil quality parameters (Fig. 2). All the sampling sites were precisely geotagged and labeled from S1 to S30 using a Garmin GPS device (model 68 s), allowing for the retrieval of a variety of location-specific data (Luo et al. 2011). Description of location and sampling sites are shown in the Table 1. The geoelectrical resistivity approach used to conduct field surveys in the study region which requires injecting a man-made current through several electrodes (AB) into the subsurface medium and observing the voltage changes at the potential electrodes (MN) to assess the variation in the ground's resistivity (Binley et al. 2015).

### Analysis of soil and water quality parameters

Collected soil samples analyzed for 10 functional indicators parameters (i.e., pH, EC, OC, P, S, K, Zn, Fe, Cu, and Mn) for soil quality (YanBing et al. 2009). Similarly, collected water samples from different selected sites analyzed for water quality parameters in the laboratory. Average of all sets of triplicates calculated and values recorded into the data system (Juhos et al. 2019). All the analysis conducted following the procedure established by the American Public Health Association (Baird and Bridgewater 2017). A typical laboratory digital micro-processor pH meter used to estimate hydrogen ion concentration (pH) in the water samples (Salem et al. 2020). Similarly, electrical conductivity (EC) determined using an electrical conductivity meter (an EC probe and equipment that had been calibrated) by following the procedure of McNeill 1992. A digital water quality test kit used to evaluate total dissolved solids (TDS); however, EDTA titration method was used to calculate total hardness in the water samples. An argentometric titration used to quantify the amount of chloride in a water sample followed by alkalinity determined using the titrimetric method. UV-visible spectrophotometer used to determine the amount of fluoride in the collected water samples. Titration method used to estimate soil organic carbon (SOC) in the soil samples (Walkley and Black 1934) which involves oxidizing organic material in sulfuric acid with a predetermined quantity of chromate (Sato et al. 2014; Gelman et al. 2012). The Johnson–Nishita procedure used to measure sulfur content in the soil samples (Dean 1966). Sulfur and other minerals present in soil solution specially SO<sub>4</sub> ions adsorbed are the principal source of sulfur in soil. The replacement of SO<sub>4</sub> ions is of the utmost importance, and phosphate ions substituted wherever possible for adsorption and monocalcium phosphate, or phosphate ions, are present in the soil. The SO<sub>4</sub> ions are replaced with CaCl<sub>2</sub> ions in a more effective way throughout the extraction process and SO<sub>4</sub> extract turbulence determined by using a spectrophotometer. Potash content in soil samples estimated using a flame photometer following the procedure of Brondi et al. (2016).

### Metal estimation

The concentration of Fe, Cu, Zn, Ni, Mn, and Pb in groundwater samples, whereas the metal Fe, Zn, Cu, and Mn analyzed in the soil samples estimated after complete digestion in HClO<sub>4</sub> and HNO<sub>3</sub> (3 : 1), using hollow cathode lamp at a certain wavelength into an atomic absorption spectrophotometer (AAS, Shimadzu) in comparison to standard metal solutions.

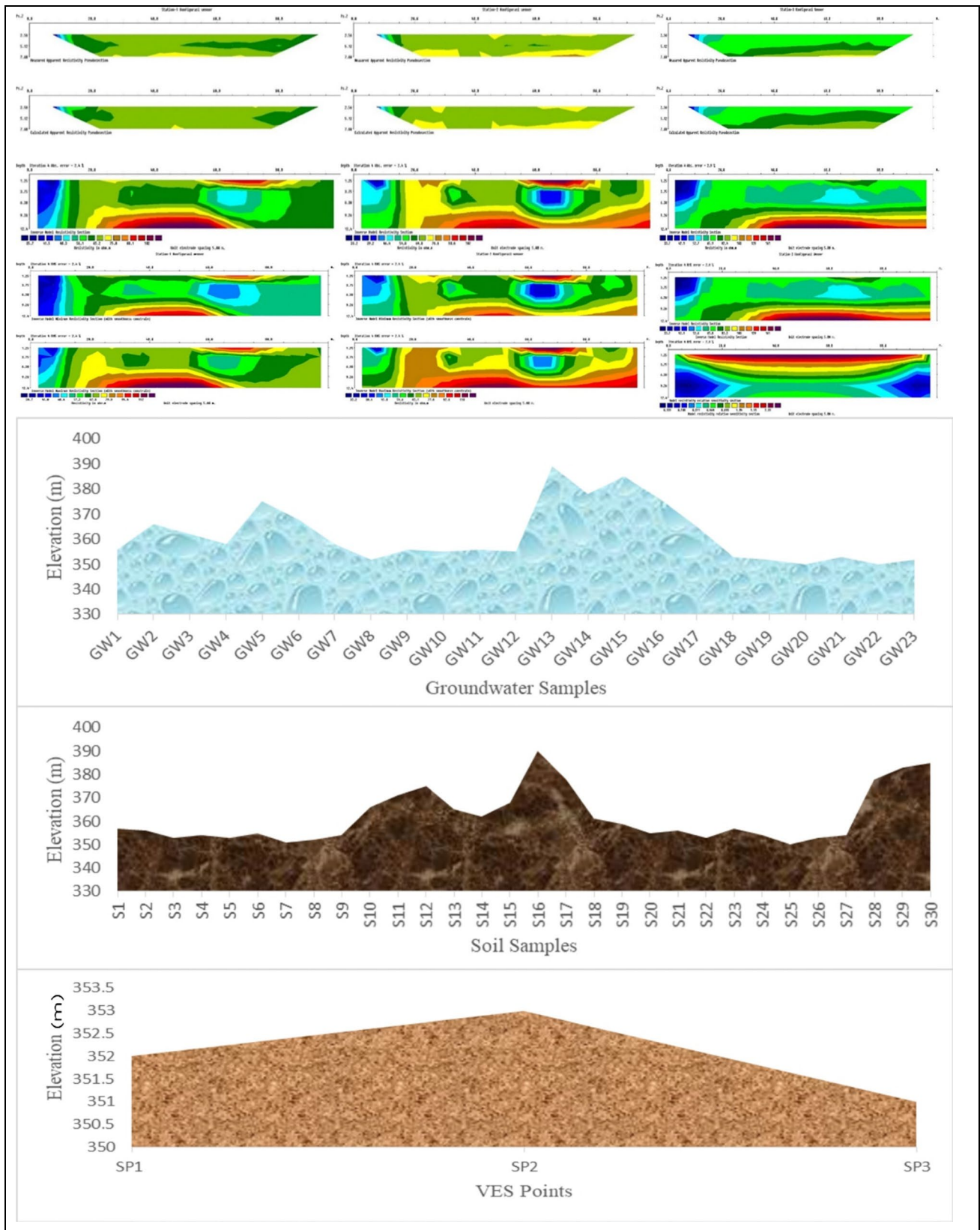


Fig. 2 Geoelectrical layers and elevation point of different sampling sites at the study area, Sanganer, Jaipur, Rajasthan, India

**Table 1.** Description of sampling sites of ground water samples, soil samples and VES station selected at Sanganer study area, Jaipur (Rajasthan), India

Ground water sample			Soil samples		
Sampling site	Latitudinal and longitudinal position	Elevation (m)	Sampling site	Latitudinal and longitudinal position	Elevation (m)
GW1	26.7929 N, 75.8113 E	357	S1	26.8010 N, 75.7960 E	354
GW2	26.8004 N, 75.7994 E	356	S2	26.8010 N, 75.7917 E	350
GW3	26.7933 N, 75.7974 E	353	S3	26.7987 N, 75.7852 E	353
GW4	26.7986 N, 75.7818 E	354	S4	26.7916 N, 75.7982 E	354
GW5	26.8181 N, 75.7904 E	353	S5	26.7912 N, 75.7962 E	378
GW6	26.8061 N, 75.7931 E	355	S6	26.7841 N, 75.8057 E	383
GW7	26.7959 N, 75.8250 E	351	S7	26.7764 N, 75.8248 E	385
GW8	26.7736 N, 75.8382 E	352	S8	26.7697 N, 75.8408 E	356
GW9	26.7837 N, 75.8251 E	354	S9	26.7832 N, 75.8650 E	366
GW10	26.7756 N, 75.8314 E	366	S10	26.7901 N, 75.8531 E	362
GW11	26.7836 N, 75.8439 E	371	S11	26.7923 N, 75.8402 E	358
GW12	26.7897 N, 75.8326 E	375	S12	26.8199 N, 75.8318 E	375
GW13	26.8323 N, 75.8193 E	365	S13	26.8022 N, 75.8324 E	368
GW14	26.8122 N, 75.8204 E	362	S14	26.8036 N, 75.8096 E	358
GW15	26.8214 N, 75.8403 E	368	S15	26.8174 N, 75.8054 E	352
GW16	26.8042 N, 75.8520 E	390	S16	26.8322 N, 75.8073 E	356
GW17	26.7865 N, 75.8632 E	378	S17	26.8129 N, 75.7795 E	355
GW18	26.7861 N, 75.7772 E	361	S18	26.7913 N, 75.7728 E	356
GW19	26.7782 N, 75.8067 E	359	S19	26.7895 N, 75.7865 E	355
GW20	26.7599 N, 75.8016 E	355	S20	26.7805 N, 75.7921 E	389
GW21	26.7669 N, 75.8239 E	356	S21	26.7753 N, 75.7782 E	378
GW22	26.7529 N, 75.8318 E	353	S22	26.7594 N, 75.7916 E	385
GW23	26.7731 N, 75.7863 E	357	S23	26.7708 N, 75.8091 E	376
	VES		S24	26.7920 N, 75.8186 E	365
SP1 (VES)	26.7852 N, 75.8044 E	352	S25	26.7538 N, 75.8164 E	353
SP2 (VES)	26.7629 N, 75.8191 E	353	S26	26.7615 N, 75.8342 E	352
SP3 (VES)	26.7800 N, 75.7862 E	351	S27	26.7621 N, 75.8491 E	350
			S28	26.7954 N, 75.8617 E	353
			S29	26.8023 N, 75.8397 E	350
			S30	26.8170 N, 75.8520 E	352

## Geostatistical analysis

To assess overall quality of water and soil samples collected from the different sites in the study area, data of soil and water quality parameters analysed thoroughly by applying geostatistical tools. Quantitative evaluation's framework combines geotechnical and physicochemical analysis of water and soil samples with descriptive statistics and statistical modelling. Outcome data is gathered after the laboratory chemical analysis of selected soil and water samples, followed by review with analysis of data on SPSS software (version 22 for Windows). Discriminating analysis (correlation) of data performed using Statistical Package for the Social Sciences (SPSS) for Windows, version 23.0. (Ukah et al. 2019, 2020). Several statistical methods used in data

analysis and models including MV, SD, and CV (Li et al. 2016; Zhu et al. 2019). Further, water quality index (WQI) and soil quality index (SQI) evaluated to assess the region's overall variations and patterns of water and soil quality parameters using site-specific indicator evaluation outputs. Weighted arithmetic mean technique for WQI was used in this investigation (Tyagi et al. 2013).

$$WQI_A = \sum_{i=1}^n qi X Wi,$$

$$\sum_{i=1}^n Wi = 1,$$

where  $Wi$  is the unit weight of each parameter,  $qi$  is the 0–100 subindex rating for each variable, and  $n$  is the number


of subindices aggregated. Multivariate statistical technique, the principal component analysis (PCA), was used to reduce the dataset into new variables, create a minimum data set (MDS), and analyze relationships between different metal contents in the water and soil samples and other quality parameters including pH, TOC, and EC along with factor analysis (FA) to identify specific factor weight of a particular metal (Weissmannová and Pavlovský 2017). The SAS Systems for Windows 10 platform and Statistica 12.5® software used to perform principal component analysis (PCA), followed by a Varimax rotation used to rotate each PCA component. The Varimax rotation method of factor analysis and the principal component primary result analysis performed by following the procedure of Kaiser 1958 and Maiz et al. 2000. For the GIS-based evaluation, SQI and WQI maps, spatial distribution maps, area maps, and thematic maps for the region produced by using Sentinel 2 Satellite data (March 2021) in bands: 3, 4, 8 developed on ArcGIS software 10.8 (2020).

## Results

Groundwater samples (23) and soil samples (30) collected from selected sampling sites of the study area, Jaipur regions of Rajasthan, Western India, analyzed for quality parameters. Based on the sounding data, the present study inferred with three geoelectrical layers comprising topsoil, unsaturated, and saturated zones (Fig. 2). For all the sections topmost layer assumed to be topsoil, above the water table and substantially drier more often reflects greater resistivity. Peat investigated in the topsoil layer by resistance correlation with soil lithology from neighboring boreholes. Regional lithology of Sanganer shown in the Table 2 which indicates formation depth range as alluvium, 0.0–95 m; weathered, 0.69–128 m; and hard rock, 9.2 m. In present study, the

third layer of all the sections represent highest concentration of geoelectrical sections with low resistivities (less than 10 m). Values and their variation pattern of water quality parameters in 23 groundwater samples at different sites of the study area depicted in Fig. 3. Maximum values of different parameters of groundwater samples recorded as pH, 8.0; electrical conductivity (EC), 3.01 S/m, TDS, 1501 mg/l; fluoride, 1.9 mg/l; total hardness, 273 mg/l; Ca, 88.1 mg/l; Mg, 12.67 mg/l; chloride, 227.42 mg/l; HCO<sub>3</sub>, 61.87 mg/l; and CO<sub>3</sub>, 58.29 mg/l. However, maximum metal concentration in groundwater samples recorded as Zn, 2.64 mg/l; Cu, 0.862 mg/l; Fe, 0.392 mg/l; Mn, 0.181 mg/l, Pb, 0.065 mg/l; and Ni, 0.016 mg/l. pH and TDS level in the ground water samples found in the range of 7.0 to 8.0 and 559 to 1501 mg/l, indicate that values are within the range of 6.5 to 8.5 and 500 to 1500 mg/l, respectively, as per WHO standard of water quality. Similarly, for 30 soil samples, maximum values of soil quality parameters recorded as pH, 8.4; electrical conductivity (EC), 0.27 μS/m; organic carbon, 0.23 %; phosphorous, 50.23 mg/kg; potash, 786 mg/kg; sulfur, 29.68 mg/kg. However, maximum metal concentration in the soil samples recorded as Fe, 11.25 mg/kg; Mn, 8.65 mg/kg; Zn, 7.26 mg/kg; and Cu, 0.45 mg/kg as shown in Fig. 4. Result shows that none of the parameters including pH have a strong correlation. Samples' scores and loadings plots together showed physio-chemical characteristics of soil that affect each order on the score plots. Retained variables divided into groups using the factor analysis technique in accordance with statistical factors and correlation matrix (Table 3). As depicted in the Table 4, maximum WQI found in groundwater sample collected at sampling site TW22 and minimum in the sample collected from TW12. Results of PCA and FA analysis for groundwater revealed that the first component (PC1), which accounted for 39.12% of the total variance, included Mn, pH, and EC; however, S, OC, and P made the second component (PC2) with a total variance of 12.54%. Similarly, pH, Mn,

**Table 2.** Regional lithology of the study area, Sanganer, Jaipur (Rajasthan), India

Aquifers depth (m)	Aquifers	Geological formation	Depth (m)	Laboratory experiment model
0–95	Alluvium	Surface soil, sandy clay	0–4	
		Clayey sand	4–13	
		Clayey kankar	13–19	
0.6–128	Weathered	Sandy clay with kankar	19–29	
		Kankar and clay	29–38	
		Kankar and sand	38–47	
9.2	Hardrock	Weathered schist	47–73	
		Schist	73–150	

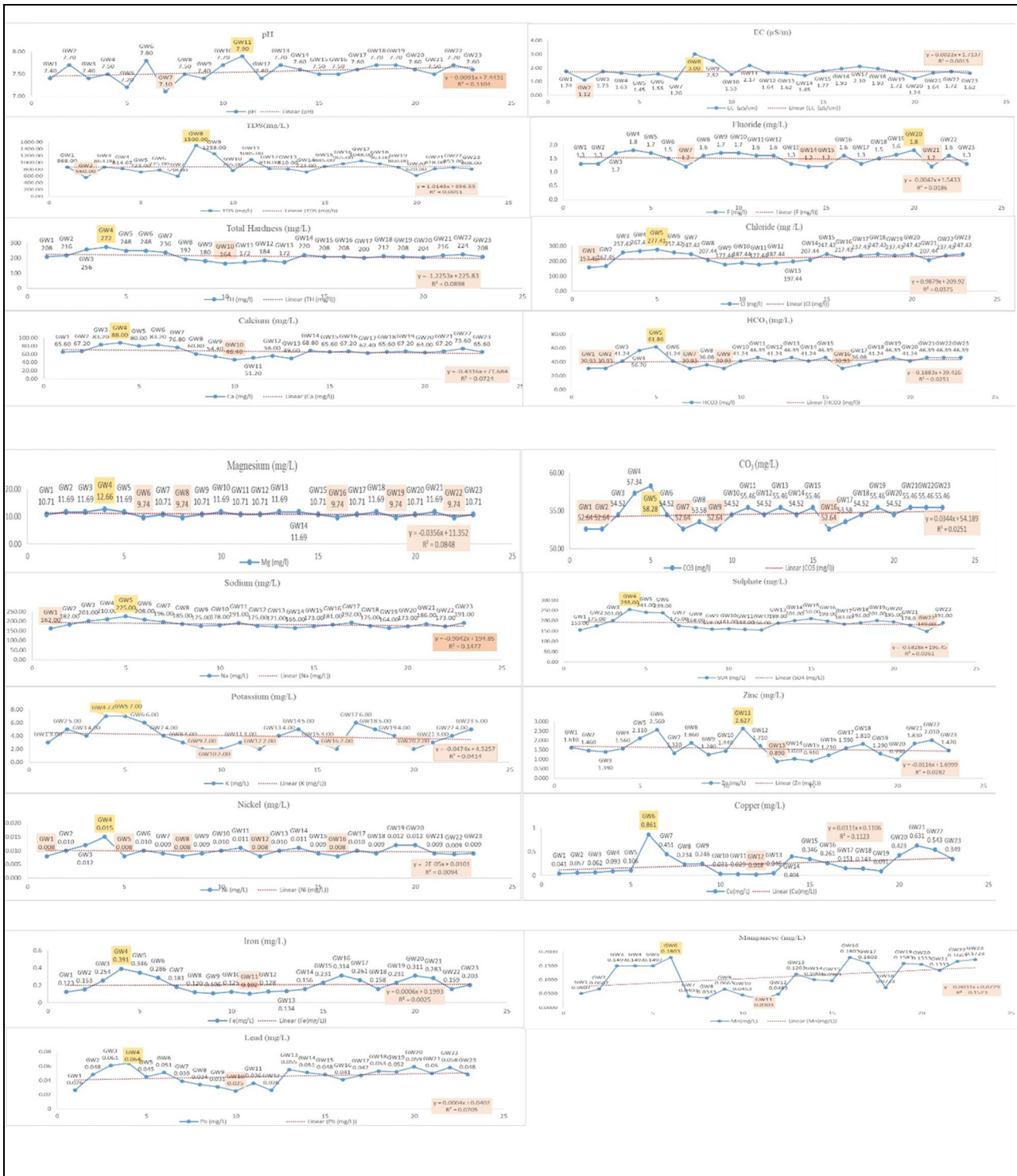


**Fig. 3** Variations in water quality parameters of ground water samples collected from in different sites at the study area, Sanganer, Jaipur, Rajasthan, India

and Cu made PC3 with a total variance of 11.42% followed by phosphorous made PC4 a total variance of 9.06%, while all four extraction factors accounted for 72.15% of the overall variation. However, in case for soil samples Mn, pH, and

EC produced the first component (PC1) with 24.26% of the variance followed by the second component (PC2) produced included S, OC, and P with a total variation of 17.48%, while PC3 made up of pH, Cu, and Mn with a total variance of

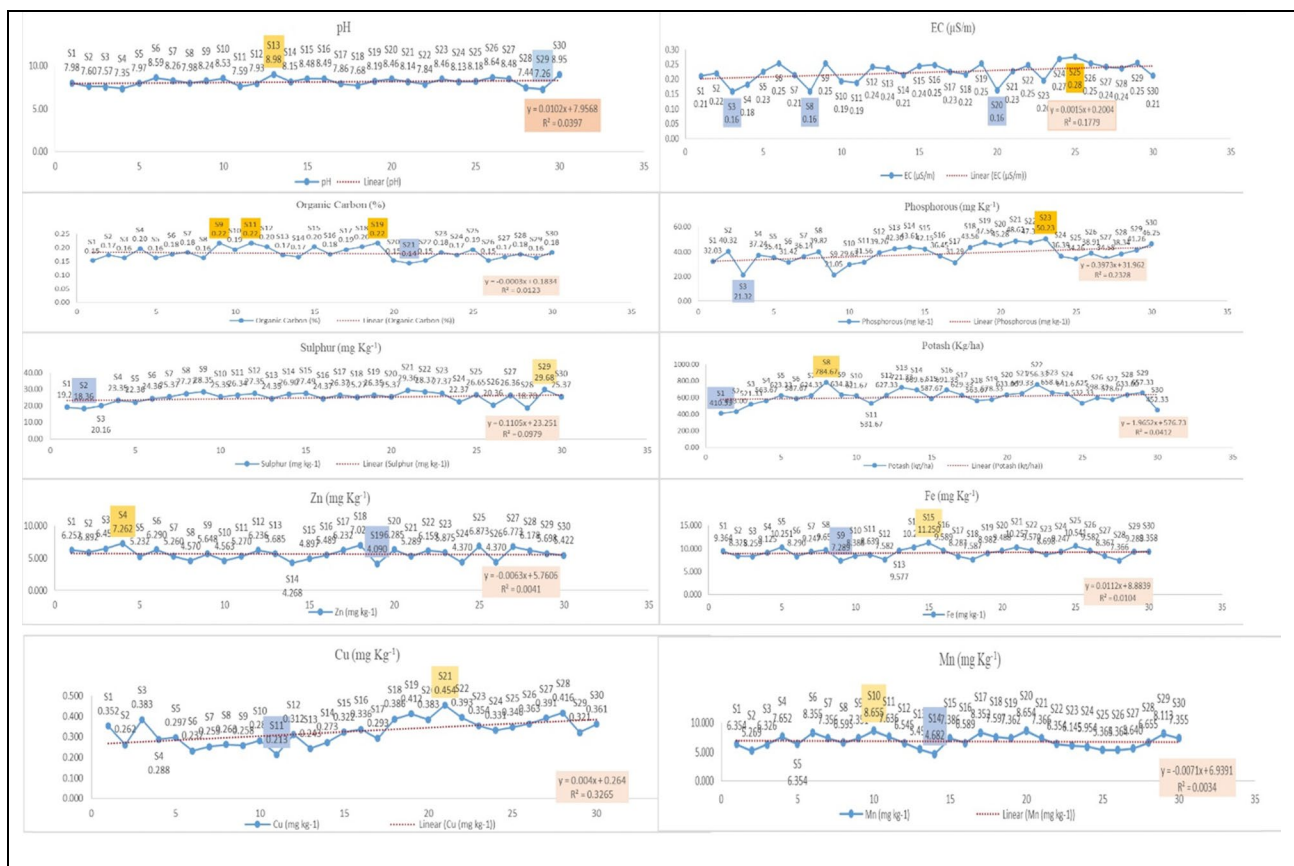


**Fig. 4** Variations in soil quality parameters of soil samples collected from different sites at the study area, Sanganer, Jaipur, Rajasthan, India

13.65% and PC4 contained phosphorus with a total variance of 11.58% (Fig. 5A). Result shows that water quality of groundwater samples collected at TW1, TW8, TW10, and TW12 sampling sites in the Sanganer area are in very good quality category; however, groundwater samples from TW3, TW4, TW6, TW19, and TW22 sites recorded under very poor water quality category with high level of contaminants (Fig. 5B). Similarly, total 9 soil quality parameters including pH, EC, OC, P, S, K, Zn, Fe, and Mn used to evaluate the soil quality index (SQI), and an average soil quality index (SQI) value 0.517 recorded for the selected study area based on MDS, with a range of 0.341 to 0.635 (Fig. 5B). According to the suggested framework, the SQI values for the entire selected region divided into three categories viz; category 1 (C1), SQI value less than 0.4 (degraded); category 2 (C2), SQI value between 0.41 and 0.5 (moderately degraded); and category 3 (C3), SQI value greater than 0.51 (least degraded). SQI revealed that soil samples at S19 site showed highest SQI score, 0.636, followed by S6, S7, S12, S13, S15, S16, S17, S18, S20, S21, S22, S23, S25, S27, S29, and S30 more than average as shown in Fig. 5B. Data shows that 13.3% of the soil samples from the study area have low soil pollution with good soil health; however,

40% of the soil samples have moderate contamination with SQI values in the range of 0.41 to 0.5 and 46.6% of soil samples shown as degraded soil under the poor-quality category with SQI values more than 0.51. At 5 kilometers away from the Sanganer industrial regions, high-intensity farming techniques, and conventional farming practices, excessive fertilizer use may be responsible for the soil degradation in the selected sites. Based on SQI score, the S19 site showed highly contaminated soil in the study area; however, it is crucial to note that the high score may be due to increased chemical build-up and other components like sulfur rather than trace metals having low concentration; however, it may be useful in environmental health assessment. Results of the factor analysis (FA) recorded insufficient if the Kaiser–Meyer–Olkin (KMO) test result value found to be less than 0.5; however, KMO found less FA findings in the test’s outcome than the chemical examination of soil samples. FA did not alter KMO testing significantly because there is no related cut-off point, and the results for the sample given a less clear indication of the applicability of the FA as KMO values estimated 0.487 and 0.466 (less than 0.5) for the groundwater and soil samples, respectively. Percentage (%) of variance evaluated by placing three components out of

**Table 3.** Correlation matrix<sup>a</sup> of ground water and soil samples collected from different sites at Sanganer study area, Jaipur, Rajasthan, India

Groundwater quality parameters		pH	EC	TDS	F	TH	Ca	Mg	Cl	HCO <sub>3</sub>	CO <sub>3</sub>	Na	K	SO <sub>4</sub>	Zn	Mn	Cu	Fe	Pb
Correlation	pH	1.000	.080	.082	.047	-.348	-.338	-.1	-.207	.078	.078	-.284	.008	-.087	.250	.121	.047	-.213	.219
	EC	.080	1.000	1.000	.217	-.366	-.327	-.371	-.211	-.185	-.185	-.088	-.251	-.282	.214	-.241	-.147	-.309	-.326
	TDS	.082	1.000	1.000	.217	-.367	-.328	-.370	-.212	-.185	-.185	-.088	-.252	-.279	.212	-.239	-.149	-.308	-.326
	F	.047	.217	.217	1.000	.068	.074	-.040	.194	.267	.267	.257	-.111	.155	.213	.337	-.259	.240	.036
	TH	-.348	-.366	-.367	.068	1.000	.993	.217	.695	.320	.320	.605	.671	.698	.153	.491	.322	.693	.599
	Ca	-.338	-.327	-.328	.074	.993	1.000	.096	.705	.282	.281	.586	.641	.676	.180	.517	.374	.687	.580
	Mg	-.132	-.371	-.370	-.040	.217	.096	1.000	.028	.361	.361	.241	.346	.280	-.190	.399	-.366	.156	.244
	Cl	-.207	-.211	-.212	.194	.695	.705	.028	1.000	.538	.538	.572	.569	.734	.044	.295	.345	.735	.659
	HCO <sub>3</sub>	.078	-.185	-.185	.267	.320	.282	.361	.538	1.000	1.000	.441	.480	.560	.242	.343	-.032	.462	.449
	CO <sub>3</sub>	.078	-.185	-.185	.267	.320	.281	.361	.538	1.000	1.000	.441	.480	.560	.242	.343	-.032	.462	.449
	Na	-.284	-.088	-.088	.257	.605	.586	.241	.572	.441	.441	1.000	.615	.590	.498	.154	.115	.582	.215
	K	.008	-.251	-.252	-.111	.671	.641	.346	.569	.480	.480	.615	1.000	.672	.284	.314	.074	.459	.529
	SO <sub>4</sub>	-.087	-.282	-.279	.155	.698	.676	.280	.734	.560	.560	.590	.672	1.000	-.010	.589	.185	.811	.590
	Zn	.250	.214	.212	.213	.153	.180	-.190	.044	.242	.242	.498	.284	-.010	1.000	-.145	-.117	.388	.604
	Ni	.300	-.241	-.239	.337	.351	.307	.399	.295	.343	.343	.154	.314	.451	1.000	.281	.393	.750	.695
	Mn	.121	-.241	-.242	.131	.491	.517	-.131	.645	.381	.381	.288	.411	.589	-.054	1.000	.270	.288	.288
	Cu	.047	-.147	-.149	-.259	.322	.374	-.366	.345	-.032	-.032	.115	.074	.185	.175	-.117	1.000	.270	.288
	Fe	-.213	-.309	-.308	.240	.693	.687	.156	.735	.462	.462	.582	.459	.811	-.008	.388	.750	1.000	.582
	Pb	.219	-.326	-.326	.036	.599	.580	.244	.659	.449	.449	.215	.529	.590	-.143	.604	.288	.582	1.000
	Soil quality parameter																		
	pH	1.000	.163	-.071	.166	.148	.111	-.324	.291	-.039	-.089								
Correlation	EC	.163	1.000	.125	.059	.113	.075	-.064	.079	.131	-.264								
	OC	-.071	.125	1.000	-.237	.226	-.174	.023	-.382	-.331	.288								
	Phosphorus	.166	.059	-.237	1.000	.290	.250	-.178	.385	.400	-.109								
	Sulfur	.148	.113	.226	.290	1.000	.493	-.101	.202	-.026	.314								
	Potash	.111	.075	-.174	.250	.493	1.000	-.291	.160	-.064	-.012								
	Zn	-.324	-.064	.023	-.178	-.101	-.291	1.000	-.362	.149	.110								
	Fe	.291	.079	-.382	.385	.202	.160	-.362	1.000	.054	-.234								
	Cu	-.039	.131	-.331	.400	-.026	-.064	.149	.054	1.000	-.059								
	Mn	-.089	-.264	.288	-.109	.314	-.012	.110	-.234	-.059	1.000								



**Table 4.** Water quality and soil quality Index

Groundwater quality index						
Parameters	Quantity of sample	WQI (mean)	Std. deviation	Std. error	Maximum	Minimum
pH	23	7.5522	.0035	.0020	8.0000	7.0000
EC ( $\mu\text{S/m}$ )	23	1.7400	.0027	.0015	3.0100	1.1100
TDS (mg/l)	23	868.7246	.7633	.4407	1501.0000	559.0000
Fluoride (mg/l)	23	1.4928	.0054	.0031	1.9000	1.1000
TH (mg/l)	23	211.1304	.5325	.3074	273.0000	163.0000
Ca (mg/l)	23	66.5043	.0035	.0020	88.1000	46.3000
Mg (mg/l)	23	10.9249	.0009	.0005	12.6700	9.7300
Cl (mg/l)	23	221.7787	.0025	.0014	277.4200	157.4400
HCO <sub>3</sub> (mg/l)	23	41.6862	.0041	.0024	61.8700	30.9200
CO <sub>3</sub> (mg/l)	23	54.6017	.0082	.0047	58.2900	52.6300
Na (mg/l)	23	184.0000	.6035	.3484	226.0000	161.0000
K (mg/l)	23	3.9565	.6745	.3894	8.0000	1.0000
SO <sub>4</sub> (mg/l)	23	188.2609	.8165	.4714	256.0000	148.0000
Zn (mg/l)	23	1.5612	.0083	.0048	2.6400	1.6000
Ni (mg/l)	23	0.0098	.0010	.0006	.0160	.0011
Mn (mg/l)	23	0.1099	.0004	.0002	.1810	.0300
Cu (mg/l)	23	0.2442	.0008	.0005	.8620	.0170
Fe (mg/l)	23	0.2068	.0008	.0005	.3920	.1010
Pb (mg/l)	23	0.0456	.0008	.0004	.0650	.0240
Soil quality index						
Parameters	Quantity of sample	SQI (mean)	Std. deviation	Std. error	Maximum	Minimum
pH	30	8.11	.0064	.0037	8.40	7.98
EC ( $\mu\text{S/m}$ )	30	.2240	.0008	.0005	.2760	.1580
Organic carbon (%)	30	.1793	.0061	.0035	.2300	.1400
Phosphorous (mg kg <sup>-1</sup> )	30	38.1197	.0009	.0005	50.2310	21.0500
Sulfur (mg kg <sup>-1</sup> )	30	24.9634	.0006	.0004	29.6810	18.3620
Potash (kg/ha)	30	607.1889	.7385	.4264	786.00	410.00
Zn (mg kg <sup>-1</sup> )	30	5.6635	.0010	.0006	7.2630	4.0890
Fe (mg kg <sup>-1</sup> )	30	9.0579	.0006	.0003	11.2510	7.2890
Cu (mg kg <sup>-1</sup> )	30	.3261	.0005	.0003	.4550	.2130
Mn (mg kg <sup>-1</sup> )	30	6.8290	.0007	.0004	8.6560	4.6810

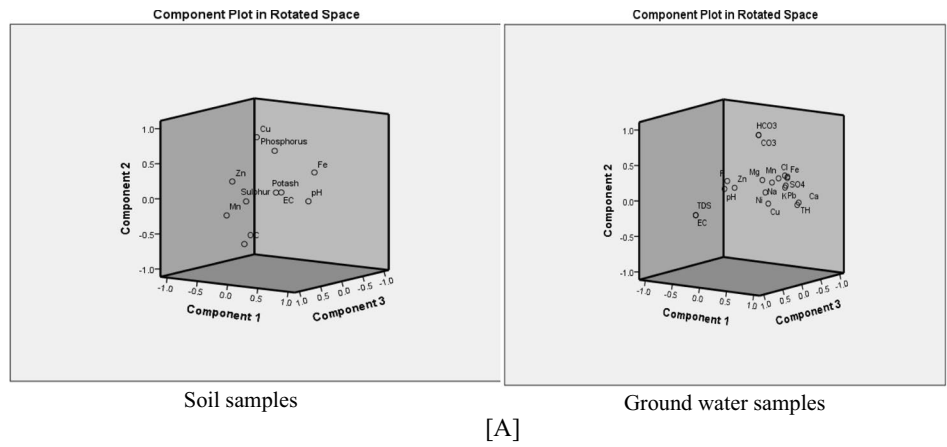
the four PC ranges (component based on Jolliffe's criterion) and recorded 84.60% and 66.98% for groundwater and soil samples, respectively (supplementary data).

## Discussion

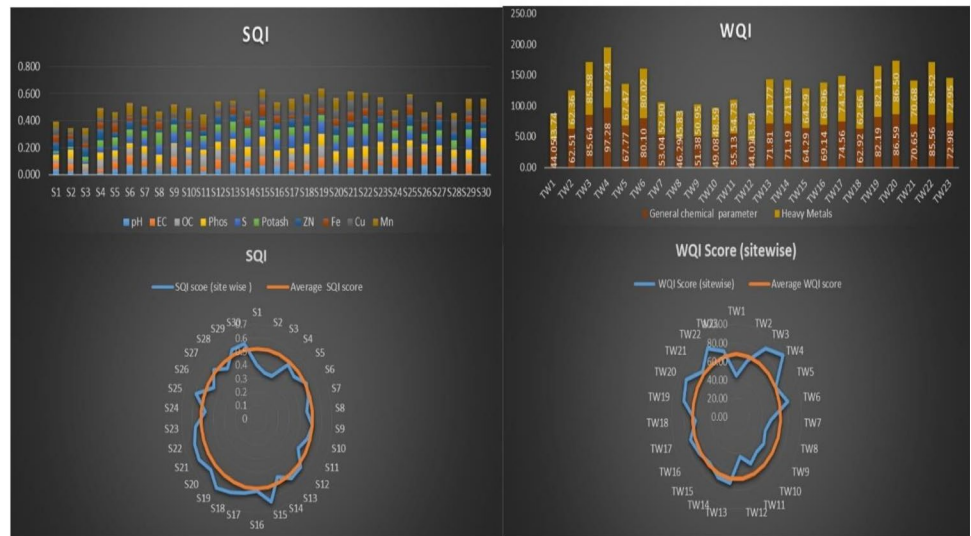
Collected samples from the selected study area, Jaipur regions of Rajasthan, Western India, evaluated for water and soil quality parameters which indicate slightly basic in nature as pH varied within the ranged of 7.0 to 8.0 in the samples. pH is one of the essentially functional parameters for evaluating the quality of soil and water (Filip 2002). Depending on the underlying geological units' actual resistivity, the geoelectrical characteristics utilized to create earth models which displayed as subsurface stratigraphy

and from which possible aquifer zones mapped for sampling and assessing the groundwater quality parameters at different sites in the selected region (Mogaji and Omobude 2017). Higher value of EC in groundwater samples indicates impurity as compared to pure water which is not an excellent conductor of electricity having a lower EC than the groundwater. According to previous studies, groundwater exhibits low resistivities between 10 and 100  $\Omega\text{m}$  in the context of sedimentary (Adagunodo et al. 2018). Kaiser's criterion replaced with Jolliffe's criterion since it is too high and allows for a graphic representation of the factor loading through a dipole using the first three components (Jolliffe 1972). However, soil solution's EC indicates total amount of salts and ions present in the soil (Bronson et al. 2005; Peralta and Costa 2013). A significant indicator of the soil quality is electrical conductivity, which reflects the salinity of the soil

**Fig. 5** Component plot of ground water and soil samples (A). Soil quality index (SQI) and water quality index (WQI) of collected samples (B)



[A]



Category-A	0-25	Excellent
Category-B	26-50	Good
Category-C	51-75	Poor
Category-D	76-100	Very Poor

[B]

(Hardie and Doyle 2012). Studies revealed that low resistivity values inside the underlying strata likely caused by high ion concentrations and fine-grained sediments like silt and clay (Amaya et al. 2018). Another soil quality parameter of soil is known as soil organic carbon (SOC) contains organic remains of dead animals and plants at various stages of decomposition which affects physicochemical characteristics of the soil (Campbell 1978). Concentration of SOC in the soil samples is one of the fundamental criteria for soil quality (Unger 1997). Agricultural production, plant development, and soil fertility also depend on phosphorus content, which is the second-most important macronutrient

in soil after nitrogen (Malhotra et al. 2018). Similarly, soil fertility, pH levels, plant development, and efficient nitrogen fixation processes dependent on its existence in the soil (Jordan and Ensminger 1959). Potash content is another essential macronutrient for preserving soil fertility and pH homeostasis. Fertilizer used usually to supplement K into the soil in case of its deficiency because plants require K for their growth and development during the life cycle (Morgan and Connolly 2013). However, high concentration of potash in soil also effects soil quality and causes soil degradation (Sillanpaa 1982). Water and soil quality assessment studies have sparked interest on a global scale due to growing

attention on the depletion of water and soil quality to assess the environmental impact of anthropogenic activities for environmental sustainability (Raiesi and Kabiri 2016). Various attempts have been made to measure the quality of the soil and water using different indicators (Armenise et al. 2013; Seybold et al. 2018). Water quality index makes it possible to examine water quality in a variety of ways that affect a stream's ability to sustain by its processes and to ensure sustainable use of water resources to minimize risks and preserve aquatic ecosystems (Akkaraboyina and Raju 2012). WQI is an important distinctive grade which summarizes overall quality of water and helps in selecting the most effective treatment strategy for wastewater before its final discharge and disposal to prevent water contamination (Tyagi et al. 2013). Status and level of contamination of water has been evaluated by using water quality parameters and quality index (Shah and Joshi 2017). The WQI and SQI approach is one of the best and most widely used techniques for assessing the quality of soil and water for adapting treatment and conservation strategies (Arshad and Martin 2002; YanBing et al. 2009). Physio-chemical and biological characteristics of soil indicated by the soil quality which is crucial to its long-term functionality and productivity and sustainability. An encompassing view of the region's overall soil quality evaluated assessing the soil quality index (Bhattacharyya 2017). Similarly, minimum data set (MDS) for the data reflecting the soil's functional capacity used in evaluating the soil quality index (Klimkowitz-Pawlas et al. 2019). By using multivariate geostatistical techniques, contemporary data analysis and metal content estimation of four metals (Zn, Cu, Mn, and Fe) in the soil and six metals (Zn, Cu, Mn, Fe, Pb, and Ni) in groundwater emphasis water and soil quality (Lu et al., 2010). Metals Zn, Ni, Mn, Cu, Fe, and Pb chosen based on PCA, FA, and CA investigations as reference elements for soil and groundwater contamination. Several studies evaluated metal contamination of soil and water in the different urban and industrial regions using principal component analysis (Manta et al. 2002; Skrbic and Djurisc-Mladenovic, 2007, Guo et al., 2013). PCA technique used to show the relationship among metals concentration and other parameters (pH, EC, TOC) in the soil and water (Weissmannová and Pavlovský 2017). FA produced using a constant value for all the soil and water quality parameters with a correlation matrix to minimize the effect of varying units on the variables (Lin et al. 2002). Kaiser–Meyer–Olkin (KMO) test used to evaluate whether the sample is large enough to use factor analysis (Kaiser 1974). In principal component analysis (PCA), variables referred to as principal components (PC) used to illustrate the relation between two elements (Esbensen and Geladi 2010). In similar study, Tripathi and Singal (2019) evaluated water quality of the Ganga River using PCA technique. In contrast, Praus (2019) used primary component weighted

index (PCWI) for assessing the quality of both untreated and treated wastewater to evaluate WQI. Data indicate that unregulated discharge of wastewater including urban sewage contaminate water and soil by the process of seepage and leaching or irrigation with wastewater leads to depletion of groundwater and soil quality. High concentration of metals and other contaminants in the soil and groundwater may be due to continuous and long-term disposal of wastewater containing metals from industrial units leading to health hazards (Wuana and Okieimen 2011). Therefore, applying geographical and geostatistical techniques with an integrated approach could be more effective ways in environmental monitoring and assessment of soil and water contamination to ensure environmental and health safety.

## Conclusion

Groundwater and soil quality parameters of water and soil samples varied with different sites of the selected study area, indicate about 13.3% of the sites found to have good soil health with minimum contamination level followed by 40% of sites with moderate contamination; however, 46.6% of sites shown high level of contamination of soil. Evaluating WQI and SQI values in the present study offers insightful information about site-wise variation pattern of quality parameters including metals identifying the sites with high level of contamination to opt appropriate strategies and mitigation measures to ensure preserving groundwater and soil quality. Further, a study concludes that contamination of water and soil with metals and other contaminants leads to depletion of quality parameters which affects nutrients cycling in the aquatic and terrestrial ecosystem with more imbalances in availability of NPK. GIS-based WQI maps provide more description of sites in categorizing contaminated regions to ensure safe water supply and developing wastewater treatment facilities for sustainable urban planning. Besides, water and soil quality assessment using GIS and geostatistical technique provide regional and spatial variability of contaminants with their correlation to establish standards of soil health and drinking for effective natural resource management in a particular region. Therefore, the present study could be a new insight in environmental monitoring involving quantitative and qualitative assessment of water and soil quality for sustainable resource utilization and conservation applying geographical and geostatistical techniques.

**Supplementary Information** The online version contains supplementary material available at <https://doi.org/10.1007/s11356-023-28004-y>.

**Acknowledgments** The authors are thankful to Manipal University Jaipur, India, for providing facilities and continuous encouragements and Ground Water Department, Jaipur, Rajasthan, India for support.

**Author contribution** All authors contributed to the study conception and design. Sampling of water and soil samples, analysis, and drafting of manuscript were performed by J. Khan and G. Gupta. All authors commented on previous versions of the manuscript. Hypothesis and designing of the experiment were done by N. K. Singh; data analysis and improving the manuscript were done by V.N. Bhave and V. Bhardwaj; map designing and statistical analysis were done by P. Upreti and R. Singh; and geophysical analysis and editing were done by A. K. Sinha. All authors read and approved the final manuscript.

**Data availability** This is not applicable.

## Declarations

**Ethical approval** This is not applicable.

**Consent to participate** The authors mutually agreed to submit the manuscript in the esteemed journal ESPR.

**Consent to publish** All authors are mutually agreed to publish the manuscript in the journal ESPR.

**Competing interests** The authors declare no competing interests.

## References

- Adagunodo TA, Akinloye MK, Sunmonu LA, Aizebeokhai AP, Oyeyemi KD, Abodunrin FO (2018) Groundwater exploration in Aaba residential area of Akure, Nigeria. *Front Earth Sci* 6
- Ahmet D, Fevzi Y, Tuna AL, Nedim O (2006) Heavy metals in water, sediment and tissues of *Leuciscus cephalus* from a stream in southwestern Turkey. *Chemosphere* 63:1451–1458
- Akkaraboyina MK, Raju PS (2012) A comparative study of water quality indices of River Godavari. *UJERT* 2:161–167
- Aksoy T, Dabanli A, Cetin M, Senyel Kurkcuoglu MA, Cengiz AE, Cabuk SN, Agacsapan B, Cabuk A (2022) Evaluation of comparing urban area land use change with Urban Atlas and CORINE data. *Environ Sci Pollut Res Int* 29:28995–29015
- Ali H, Khan E, Ilahi I (2019) Environmental chemistry and ecotoxicology of hazardous heavy metals: Environmental persistence, toxicity, and bioaccumulation. *J Chem* 6730305
- Ali SA, Ahmad A (2020) Analysing water-borne diseases susceptibility in Kolkata Municipal Corporation using WQI and GIS based Kriging interpolation. *Geo Journal* 85:1151–1174
- Amaya GA, Mårdh J, Dahlin T (2018) Delimiting a saline water zone in Quaternary fluvial–alluvial deposits using transient electromagnetic: a case study in Punata, Bolivia. *Environ Earth Sci* 77:46
- Armenise E, Redmile-Gordon MA, Stellacci AM, Ciccicarese A, Rubino P (2013) Developing a soil quality index to compare soil fitness for agricultural use under different managements in the Mediterranean environment. *Soil Tillage Res* 130:91–98
- Arshad MA, Martin S (2002) Identifying critical limits for soil quality indicators in agro-ecosystems. *Agric Eco Environ* 88:153–160
- Baird R, Bridgewater L (2017) Standard methods for the examination of water and wastewater. APHA, Washington, DC
- Bhattacharyya P (2017) Soil quality index under organic farming. *Organic farming in tropical islands of india*, 260–267
- Bilge Ozturk G, Ozenen Kavlak M, Cabuk SN, Cabuk A, Cetin M (2022) Estimation of the water footprint of kiwifruit: in the areas transferred from hazelnut to kiwi. *Environ Sci Pollut Res Int* 29:73171–73180
- Binley A, Hubbard SS, Huisman JA, Revil A, Robinson DA, Singha K, Slater LD (2015) The emergence of hydrogeophysics for improved understanding of subsurface processes over multiple scales. *Water Resour Res* 51:3837–3866
- Brondi AM, Daniel JSP, de Castro VXM, Bertoli AC, Garcia JS, Trevisan MG (2016) Quantification of humic and fulvic acids, macro- and micronutrients and C/N ratio in organic fertilizers. *Commun Soil Sci Plant Anal* 47:2506–2513
- Bronson KF, Booker JD, Officer SJ, Lascano RJ, Maas SJ, Searcy SW, Booker J (2005) Apparent electrical conductivity, soil properties and spatial covariance in the US Southern High Plains. *Precision Agriculture* 6:297–311
- Calzadilla A, Rehdanz K, Tol RSJ (2011) Trade liberalization and climate change: a computable general equilibrium analysis of the impacts on global agriculture. *Water* 3:526–550
- Campbell CA (1978) Soil organic carbon, nitrogen and fertility. In: Schnitzer M, Khan S.U. (Eds.). *Developments in soil science* 8:173–271
- Cesur A, Zeren Cetin I, Abo Aisha AES, Alrabiti OBM, Aljama AMO, Jawed AA, Cetin M, Sevik H, Ozel HB (2021) The usability of *Cupressus arizonica* annual rings in monitoring the changes in heavy metal concentration in air. *Environ Sci Pollut Res Int* 28:35642–35648
- Cetin M (2019) The effect of urban planning on urban formations determining bioclimatic comfort area's effect using satellitia imagines on air quality: a case study of Bursa city. *Air Qual Atmos Health* 12:1237–1249
- Cetin M, Abo Aisha AES (2023) Variation of AI concentrations depending on the growing environment in some indoor plants that used in architectural designs. *Environ Sci Pollut Res Int* 30:18748–18754
- Cetin M, Aksoy T, Bilge Ozturk G, Cabuk A (2022d) Developing a model for the relationship between vegetation and wind power using remote sensing and geographic information systems technology. *Water Air Soil Pollut* 233:450
- Cetin M, Aljama AMO, Alrabiti OBM, Adiguzel F, Sevik H, Cetin IZ (2022a) Determination and mapping of regional change of Pb and Cr pollution in Ankara City Center. *Water Air Soil Pollut* 233:163
- Cetin M, Aljama AMO, Alrabiti OBM, Adiguzel F, Sevik H, Cetin IZ (2022b) Using topsoil analysis to determine and map changes in Ni Co pollution. *Water Air Soil Pollut* 233:293
- Cetin M, Isik Pekkan O, Bilge Ozturk G, Anil Senyel Kurkcuoglu M, Kucukpehlivan T, Cabuk A (2022c) Examination of the change in the vegetation around the Kirka Boron Mine Site by using remote sensing techniques. *Water Air Soil Pollut* 233:254
- Cetin M (2015) Using GIS analysis to assess urban green space in terms of accessibility: case study in Kutahya. *Int J Sust Devel W Ecol* 22:420–424
- Dadhich PN, Jain H, Meena J, Meena H, Meena CS (2016) Water resource management based on GIS- a case study of municipality of Sanganer, Jaipur. *IJERT, NCACE* 4:23
- Dean GA (1966) A simple colorimetric finish for the Johnson-Nishita microdistillation of sulphur. *Analyst* 91:530
- Dogan S, Kilicoglu C, Akinci H, Sevik H, Cetin M (2023) Determining the suitable settlement areas in Alanya with GIS-based site selection analyses. *Environ Sci Pollut Res Int* 30:29180–29189
- Esbensen KH, Geladi P (2010) Principles of proper validation: use and abuse of re-sampling for validation. *J Chemom* 24:168–187
- Filip Z (2002) International approach to assessing soil quality by ecologically related biological parameters. *Agric Ecosys Environ* 88:169–174
- Garg NK, Hassan Q (2007) Alarming scarcity of water in India. *Curr Sci* 93:932–941
- Gąsiorek M, Kowalska J, Mazurek R, Pająk M (2017) Comprehensive assessment of heavy metal pollution in topsoil of historical urban park on an example of the Planty Park in Krakow (Poland). *Chemosphere* 179:148–158

- Gavrilescu M (2021) Water, Soil, and Plants Interactions in a Threatened Environment. *Water* 13:2746
- Gelman F, Binstock R, Halicz L (2012) Application of the Walkley–Black titration for the organic carbon quantification in organic rich sedimentary rocks. *Fuel* 96:608–610
- Griffiths BS, Ball BC, Daniell TJ, Hallett PD, Neilson R, Wheatley RE, Osler G, Bohanec M (2010) Integrating soil quality changes to arable agricultural systems following organic matter addition, or adoption of a ley-arable rotation. *Appl Soil Ecol* 46:43–53
- Gu YG, Gao Y, Lin Q (2016) Contamination, bioaccessibility and human health risk of heavy metals in exposed-lawn soils from 28 urban parks in southern China's largest city, Guangzhou. *Appl Geochem* 67:52–58
- Guo X, Yuan D, Jiang J, Zhang H, Deng Y (2013) Detection of dissolved organic matter in saline-alkali soils using synchronous fluorescence spectroscopy and principal component analysis. *Spectrochim Acta A* 104:280–286
- Hanfi MY, Mostafa MY, Zhukovsky MV (2020) Heavy metal contamination in urban surface sediments: sources, distribution, contamination control, and remediation. *Environ Monitor Assess* 192:1–21
- Hardie M, Doyle R (2012) Measuring soil salinity. In: *Methods in molecular biology (Clifton, N.J.)*, 913:415–425
- Hermans SM, Buckley HL, Case BS, Curran-Cournane F, Taylor M, Lear G (2020) Using soil bacterial communities to predict physico-chemical variables and soil quality. *Microbiome* 8:79
- Jolliffe IT (1972) Discarding variables in a principal component analysis. I: artificial data. *J R Stat Soc Ser C Appl Stat* 160–173
- Jordan HV, Ensminger LE (1959) The role of sulfur in soil fertility. In: Normax AG (ed) *Advances in agronomy*, vol 10. Academic Press, pp 407–434
- Juhos K, Czigány S, Madarász B, Ladányi M (2019) Interpretation of soil quality indicators for land suitability assessment—a multivariate approach for Central European arable soils. *Ecol Indic* 99:261–272
- Kaiser HF (1958) The varimax criterion for analytic rotation in factor analysis. *Psychometrika* 23:187–200
- Kaiser HF (1974) An index of factorial simplicity. *Psychometrika* 39:31–36
- Kalayci Onac A, Cetin M, Sevik H, Orman P, Karci A, Gonullu Sutcuoglu G (2021) Rethinking the campus transportation network in the scope of ecological design principles: case study of Izmir Katip Çelebi University Çiğli Campus. *Environ Sci Pollut Res* 28:50847–50866
- Klimkowicz-Pawlas A, Ukalska-Jaruga A, Smreczak B (2019) Soil quality index for agricultural areas under different levels of anthropopressure. *Inter Agrophys* 33:455–462
- Kopittke PM, Menzies NW, Wang P, McKenna BA, Lombi E (2019) Soil and the intensification of agriculture for global food security. *Environ Int* 132:105078
- Li D, Gao G, Shao M, Fu B (2016) Predicting available water of soil from particle-size distribution and bulk density in an oasis–desert transect in northwestern China. *J Hydrol* 538:539–550
- Lin YP, Teng TP, Chang TK (2002) Multivariate analysis of soil heavy metal pollution and landscape pattern in Changhua country in Taiwan. *Landsc Urban Plan* 62:19–35
- Lu X, Wang L, Li LY, Lei K, Huang L, Kang D (2010) Multivariate statistical analysis of heavy metals in street dust of Baoji, NW China. *J Hazard Mater* 173:744–749
- Luo XS, Ding J, Xu B, Wang YJ, Li HB, Yu S (2012) Incorporating bioaccessibility into human health risk assessments of heavy metals in urban park soils. *Sci Total Environ* 424:88–96
- Luo Y, Su B, Yuan J, Li H, Zhang Q (2011) GIS techniques for watershed delineation of SWAT Model in Plain Polders. *Procedia Environ Sci* 10:2050–2057
- Mahmood A, Kundu (2005) “Status of water supply, sanitation and solid waste management in urban areas” New Delhi, National Institute of Urban Affairs (NIUA)
- Maiz I, Arambarri I, Garcia R, Millán E (2000) Evaluation of heavy metal availability in polluted soils by two sequential extraction procedures using factor analysis. *Environ Pollut* 110:3–9
- Malhotra H, Vandana Sharma S, Pandey R (2018) Phosphorus nutrition: plant growth in response to deficiency and excess. In: Hasanuzzaman M, Fujita M, Oku H, Nahar K, Hawrylak-Nowak B (eds) *Plant Nutrients and Abiotic Stress Tolerance*. Springer, pp 171–190
- Manta DS, Angelone M, Bellanca A, Neri R, Sprovieri M (2002) Heavy metals in urban soils: a case study from the city of Palermo (Sicily), Italy. *Sci Total Environ* 300:229–243
- McNeill JD (1992) Rapid, accurate mapping of soil salinity by electromagnetic ground conductivity meters. In: *Advances in measurement of soil physical properties: bringing theory into practice*. John Wiley & Sons, Ltd, pp. 209–229
- Mogaji KA, Omobude OB (2017) Modeling of geoelectric parameters for assessing groundwater potentiality in a multifaceted geologic terrain, Ipinsa Southwest, Nigeria – a GIS-based GODT approach. *NRIAG J Astron Geophys* 6:434–451
- Morgan JB, Connolly EL (2013) Plant-soil interactions: Nutrient uptake learn science at scitable. *National J Edu* 4:2
- Olayinka-Olagunju JO, Dosumu AA, Olatunji-Ojo AM (2021) Bioaccumulation of heavy metals in pelagic and benthic fishes of Ogbese River, Ondo State, South-Western Nigeria. *Water Air & Soil Pollut* 232:44
- Pandey N, Sharma CP (2002) Effect of heavy metals  $\text{Co}^{2+}$ ,  $\text{Ni}^{2+}$  and  $\text{Cd}^{2+}$  on growth and metabolism of cabbage. *Plant Sci* 163:753–758
- Pekkan OI, Senyel Kurkcuoglu MA, Cabuk SN, Aksoy T, Yilmazel B, Kucukpehlivan T, Dabanli A, Cabuk A, Cetin M (2021) Assessing the effects of wind farms on soil organic carbon. *Environ Sci Pollut Res Int* 28:18216–18233
- Peralta NR, Costa JL (2013) Delineation of management zones with soil apparent electrical conductivity to improve nutrient management. *Comp Electron Agricul* 99:218–226
- Praus P (2019) Principal component weighted index for wastewater Quality Monitoring. *Water* 11:2376
- Raiesi F, Kabiri V (2016) Identification of soil quality indicators for assessing the effect of different tillage practices through a soil quality index in a semi-arid environment. *Ecol Indic* 71:198–207
- Rajendran S, Priya TAK, Khoo KS, Hoang TK, Ng HS, Munawaroh HSH, Show PL (2022) A critical review on various remediation approaches for heavy metal contaminants removal from contaminated soils. *Chemosphere* 287:132369
- Romic M, Romic D (2003) Heavy metals distribution in agricultural topsoils in urban area. *Environ Geol* 43:795–805
- Sahin G, Cabuk SN, Cetin M (2022) The change detection in coastal settlements using image processing techniques: a case study of Korfez. *Environ Sci Pollut Res Int* 29:15172–15187
- Saleem M, Hussain A, Mahmood G, Waseem M (2018) Hydrogeochemical assessment of groundwater in shallow aquifer of greater Noida region, Uttar Pradesh (U.P), India. *Appl Water Sci* 8:186
- Salem A, Dezső J, El-Rawy M, Lóczy D (2020) Hydrological modeling to assess the efficiency of groundwater replenishment through natural reservoirs in the Hungarian Drava River Floodplain. *Water* 12:250
- Sato JH, de Figueiredo CC, Marchão RL, Madari BE, Benedito LEC, Busato JG, de Souza DM (2014) Methods of soil organic carbon determination in Brazilian savannah soils. *J Agric Sci* 71:302–308
- Schlöter M, Dilly O, Munch JC (2003) Indicators for evaluating soil quality. *Agric Ecosys Environ* 98:255–262

- Seybold CA, Mansbach MJ, Karlen DL, Rogers HH (2018) Quantification of soil quality. In: Soil processes and the carbon cycle. CRC Press, pp 387–404
- Shah KA, Joshi GS (2017) Evaluation of water quality index for River Sabarmati, Gujarat, India. *Appl Water Sci* 7:1349–1358
- Sharma N, Sharma S, Gehlot A (2014) Influence of dyeing and printing industrial effluent on physicochemical characteristics of water – case study on the printing cluster of Bagru, Jaipur (Rajasthan), India. *IOSR J Appl Chem* 7:61–64
- Sillanpää M (1982) Micronutrients and the nutrient status of soils: a global study. *FAO Soil Bulletin No. 48*, Food and Agriculture Organization, Rome
- Singh R, Upreti P, Allemailam KS, Almatroudi A, Rahmani AH, Albalawi GM (2022) Geospatial assessment of ground water quality and associated health problems in the Western Region of India. *Water*. 14:296
- Singha SS, Devatha CP, Singha S, Verma MK (2015) Assessing ground water quality using GIS. *International J Eng Res Technol* 4:11
- Skrbic B, Djuricic-Mladenovic N (2007) Principal component analysis for soil contamination with organochlorine compounds. *Chemosphere* 68:2144–2152
- Tay DA, Ocansey RTA (2022) Impact of urbanization on health and well-being in Ghana. Status of research, intervention strategies and future directions: a rapid review. *Front Pub health* 10:877920
- Tiwari KK, Singh NK, Patel MP, Tiwari MR, Rai UN (2011) Metal contamination of soil and translocation in vegetables growing under industrial wastewater irrigated agricultural field of Vadodara, Gujarat, India. *Ecotoxicol Environ Saf* 74:1670–1677
- Tripathi M, Singal SK (2019) Allocation of weights using factor analysis for development of a novel water quality index. *Ecotoxicol Environ Saf* 183:109510
- Tyagi S, Sharma B, Singh P, Dobhal R (2013) Water quality assessment in terms of water quality index. *Am J Water Resour* 1:34–38
- Tzanakakis VA, Paranychanakis NV, Angelakis AN (2020) Water supply and water scarcity. *Water* 12:2347
- Ukah BU, Ameh PD, Egbueri JC, Unigwe CO, Ubido OE (2020) Impact of effluent-derived heavy metals on the groundwater quality in Ajao industrial area, Nigeria: an assessment using entropy water quality index (EWQI). *IJWREE* 4:231–244
- Ukah BU, Egbueri JC, Unigwe CO, Ubido OE (2019) Extent of heavy metals pollution and health risk assessment of groundwater in a densely populated industrial area, Lagos, Nigeria. *IJWREE* 3:291–303
- Unger PW (1997) Aggregate and organic carbon concentration inter-relationships of a Torricite Paleustoll. *Soil and Tillage Res* 42:95–113
- Walkley A, Black IA (1934) An examination of the degtjareff method for determining soil organic matter, and a proposed modification of the chromic acid titration method. *Soil Sci* 37:29–38
- Weissmannová HD, Pavlovský J (2017) Indices of soil contamination by heavy metals—methodology of calculation for pollution assessment (minireview). *Environ Monit Assess* 189:616
- Wu J, Li P, Wang D, Ren X, Wei M (2020) Statistical and multivariate statistical techniques to trace the sources and affecting factors of groundwater pollution in a rapidly growing city on the Chinese Loess Plateau. *Hum Ecol Risk Assess* 26:1603–1621
- Wuana RA, Okieimen FE (2011) Heavy metals in contaminated soils: a review of sources, chemistry, risks and best available strategies for remediation. *ISRN Ecol* 402647
- Yanbing Q, Darilek JL, Huang B, Yongcun Z, Weixia S, Zhiquan G (2009) Evaluating soil quality indices in an agricultural region of Jiangsu Province, China. *Geoderma* 149:325–334
- Yang K, Nam T, Nam K, Kim YJ (2016) Characteristics of heavy metal contamination by anthropogenic sources in artificial lakes of urban environment. *KSCE J Civ Eng* 20:121–128
- Yu P, Han D, Liu S, Wen X, Huang Y, Jia H (2018) Soil quality assessment under different land uses in an alpine grassland. *CATENA* 171:280–287
- Zhu Y, Chen L, Wang K, Wang W, Wang C, Shen Z (2019) Evaluating the spatial scaling effect of baseflow and baseflow nonpoint source pollution in a nested watershed. *J Hydrol* 579:124221
- Zouboulis AI, Loukidou MX, Matis KA (2004) Biosorption of toxic metals from aqueous solutions by bacteria strains isolated from metal-polluted soils. *Process Biochem* 39:909–916

**Publisher's note** Springer Nature remains neutral with regard to jurisdictional claims in published maps and institutional affiliations.

Springer Nature or its licensor (e.g. a society or other partner) holds exclusive rights to this article under a publishing agreement with the author(s) or other rightsholder(s); author self-archiving of the accepted manuscript version of this article is solely governed by the terms of such publishing agreement and applicable law.



Alexandria University  
Alexandria Engineering Journal

[www.elsevier.com/locate/aej](http://www.elsevier.com/locate/aej)  
[www.sciencedirect.com](http://www.sciencedirect.com)



# Removal of congo red from water by adsorption onto activated carbon derived from waste black cardamom peels and machine learning modeling



Rameez Ahmad Aftab<sup>a</sup>, Sadaf Zaidi<sup>b,\*</sup>, Aftab Aslam Parwaz Khan<sup>c,\*</sup>,  
Mohd Arish Usman<sup>d</sup>, Anees Y. Khan<sup>d</sup>, Muhammad Tariq Saeed Chani<sup>c</sup>,  
Abdullah M. Asiri<sup>c</sup>

<sup>a</sup> Department of Chemical Engineering, Zakir Husain College of Engineering and Technology, Aligarh Muslim University, Aligarh 202002, Uttar Pradesh, India

<sup>b</sup> Department of Post Harvest Engineering and Technology, Faculty of Agricultural Sciences, Aligarh Muslim University, Aligarh 202002, Uttar Pradesh, India

<sup>c</sup> Center of Excellence for Advanced Materials Research, King Abdulaziz University, Jeddah 21589, Saudi Arabia

<sup>d</sup> Department of Chemical Engineering, Manipal University Jaipur, Dehmi Kalan, Off. Jaipur-Ajmer Expressway, Jaipur 303007, Rajasthan, India

Received 19 October 2022; revised 12 January 2023; accepted 12 March 2023

## KEYWORDS

Black cardamom;  
Activated carbon;  
Machine learning modeling;  
Support vector regression;  
Langmuir isotherm

**Abstract** The present work utilizes waste black cardamom (BC) as an inexpensive and environmentally friendly adsorbent for sequestering the Congo Red (CR) dye from aqueous media for the first time. Following a carbonization process at 600 °C, chemical activation with KOH was carried out for waste BC and subsequent black cardamom activated carbon (BCAC) was employed as an adsorbent for CR eradication. The effect of experimental factors, including pH, adsorption time, dose and CR initial concentration, was investigated. 96.21 % of CR dye removal was achieved at pH 6 for 100 mg/L of CR concentration having 0.1 g dose at 30 °C. Maximum Langmuir adsorption capacity of BCAC was found to be 69.93 mg/g at 30 °C. The kinetic analyses showed that the CR adsorption over BCAC behaved in accordance with a pseudo-second order kinetic model as high  $R^2$  values (0.997–1) were obtained. Thermodynamic parameters ( $\Delta H^\circ$ ,  $\Delta S^\circ$ , and  $\Delta G^\circ$ ) demonstrated that the CR adsorption over BCAC was feasible, spontaneous and exothermic in nature. In addition, the state-of-the-art machine learning (ML) approaches namely, support vector regression (SVR) and artificial neural network (ANN) were employed for modeling the BCAC adsorbent for CR removal. The statistical analysis revealed high prediction performance of SVR model with AARE value of 0.0491 and RMSE value of 0.4635 while the corresponding values for the ANN model were 0.0781 and 0.5395,

*Abbreviations:* BC, Black Cardamom; BCAC, Black cardamom activated carbon; CR, Congo Red; ML, Machine Learning; ANN, Artificial neural networks; SVR, Support vector regression; AARE, Average absolute relative error;  $R^2$ , Coefficient of determination; RMSE, Root mean square error; SEM, Scanning Electron Microscopy; FTIR, Fourier Transform Infra-Red

\* Corresponding authors.

E-mail addresses: [sadaf63in@yahoo.com](mailto:sadaf63in@yahoo.com) (S. Zaidi), [draapk@gmail.com](mailto:draapk@gmail.com) (A. Aslam Parwaz Khan).

Peer review under responsibility of Faculty of Engineering, Alexandria University.

<https://doi.org/10.1016/j.aej.2023.03.055>

1110-0168 © 2023 The Authors. Published by Elsevier B.V. on behalf of Faculty of Engineering, Alexandria University  
This is an open access article under the CC BY-NC-ND license (<http://creativecommons.org/licenses/by-nc-nd/4.0/>).

**Nomenclature**

$C_o$	Initial dye concentration ( $\text{mg L}^{-1}$ )	$K_L$	Langmuir constant ( $\text{L mg}^{-1}$ )
$C_e$	Dye concentration at equilibrium ( $\text{mg L}^{-1}$ )	qm	Maximum adsorption capacity ( $\text{mg g}^{-1}$ )
$q_e$	Adsorption capacity at equilibrium ( $\text{mg g}^{-1}$ )	$R_L$	Separation factor
m	Mass of Adsorbent (g)	$K_F$	Freundlich adsorption constant ( $\text{mg g}^{-1}$ ) ( $\text{L mg}^{-1}$ ) <sup>1/n</sup>
V	Volume (L)	n	Freundlich exponent ( $\text{g L}^{-1}$ )
$\varepsilon$	Loss function	A	Temkin constant for binding energy ( $\text{L/g}^{-1}$ )
w	Weight vector	B	Temkin constant for heat of adsorption ( $\text{J mol}^{-1}$ )
$\lambda(c_i)$	High dimensional feature function for input vector c	$\chi^2$	Chi-squared error
$\alpha$ and $\alpha^*$	Lagrange multipliers	$K_1$	Pseudo-first-order rate constant ( $\text{min}^{-1}$ )
f(c)	Regression function	$K_2$	Pseudo-second-order rate constant ( $\text{g mg}^{-1} \text{min}^{-1}$ )
b	Bias term	$K_{id}$	Intra particle diffusion constant ( $\text{mg g}^{-1} \text{min}^{-1}$ )
$K(c_i, c_j)$	Kernel function	I	Intra particle constant
L	Dual form of the Lagrangian function	$K_C$	Equilibrium constant
$c_i$	Input vector	$\Delta G^\circ$	Standard Free energy change ( $\text{kJ mol}^{-1}$ )
$d_i$	Output vector	$\Delta H^\circ$	Standard Enthalpy change ( $\text{kJ mol}^{-1}$ )
$P_i$	Predicted value	$\Delta S^\circ$	Standard Entropy change ( $\text{kJ mol}^{-1} \text{K}^{-1}$ )
$E_i$	Experimental value	T	Absolute temperature (K)
N	Total data points	t	Time (min)
$R^2$	Coefficient of determination		

respectively. Furthermore, the plots between experimental CR data and ML forecasted data were closely matched ( $R^2 > 0.99$ ). Thus, it can be concluded that BC, an agro waste could be utilized for CR removal and that the adoption of ML approaches can benefit users by providing them with a tool to enhance the design and performance of wastewater treatment operations.

© 2023 The Authors. Published by Elsevier B.V. on behalf of Faculty of Engineering, Alexandria University This is an open access article under the CC BY-NC-ND license (<http://creativecommons.org/licenses/by-nc-nd/4.0/>).

**1. Introduction**

Water contamination is one of the main issues of our time as a result of the uncontrolled urbanization, population expansion, and industry that has occurred rapidly [1]. Although strict laws and regulations have been promulgated but proper wastewater treatment and its disposal has not been applied [2]. Particularly, a significant volume of polluted water has been released into the environment directly, harming the water resources. An important class of pollutants is synthetic dyes, which are utilized in a variety of sectors including the textile, dyeing, paper, leather tanning, cosmetics, and others [3,4].  $> 7 \times 10^5$  tons of dyes are generated yearly of which about 10% are released into the environment by the textile and associated sectors [5]. Dyes are categorised according to their chemical structures, which influence their characteristics and are divided as cationic or anionic dyes [6]. It is highly challenging to handle wastewater from the dyeing industry because dyes contain complicated molecular structures that prevent biodegradation and make them resilient to light, heat, and oxidising agents [7]. Colored dyes are aesthetically pleasing, cancer-causing, and block light from entering aquatic systems. Additionally, the hazardous and cancer-causing nature of dyeing wastewaters has an impact on both the aquatic ecology and human health [8]. Therefore, it is crucial to remove dye from wastewater or effluents before releasing them into the environment. In this study, the removal of Congo Red (CR) is considered.

Anionic CR dye is very soluble in water which causes disagreeable color changes that endanger water species [9]. CR is an azo dye that metabolizes to benzidine which poses grave risk to human health, including skin, ocular, and gastrointestinal irritation [10]. The removal of CR dye from wastewater has been accomplished using a variety of methods, including coagulation, membrane separation, adsorption, reverse osmosis and ion exchange [11]. Adsorption is rapidly rising to the forefront of treatment technologies as a means of handling dye contaminated aqueous effluent due to its affordability, procedural simplicity, efficacy, and practicality [12]. Due to its porous nature and thermal durability, activated carbon is most frequently utilized as an adsorbent on a large scale [13]. Because it is more expensive and difficult to produce, activated carbon made from non-renewable sources has fewer uses overall [14]. However, various agricultural based materials have been looked at as advantageous raw materials for the production of activated carbon, due to their abundance and non-toxic makeup [15]. Several adsorbents namely, coconut fibre [16], celery residue [7], cabbage waste [12], *Cornulaca monacantha* stem [17], Antigonon leptopus leaf [18] kenaf fibre [19], Casuarina empty fruit [20], *Teucrium polium* L.[10], Eucalyptus leaf powder [21] walnut shell [22], *Eichhornia* shoots [23], pine bark [24], Arjuna seed [25], mango leaves [26], jujube shell [27] *Phoenix dactylifera* seeds [8], apricot stone [28], powder *Bombax Buonopozense* bark [29], teak leaf [30], pineapple stem [31], litchi seed [32] have been utilized for CR removal. Thus, it is observed that efficient adsorbents have been



obtained from agricultural sources. In view of the encouraging development, an effort was made to identify some locally available, cost-effective, and novel bio-waste for scavenging of CR dye from water. It was discovered that black cardamom waste, which is usually discarded in the open or dumped in landfills, aggravates pollution and impinges upon the availability of arable land. It is estimated that nearly 400 kg of black cardamom waste is generated annually in the small Indian town of Aligarh alone. Hence, it was planned to carry out the present study by converting the BC into BCAC and estimate its performance as an adsorbent in the removal of CR dye from water by adsorption.

Modeling of any system or a process is a significant and challenging task in engineering. The challenge may be due to the physical complexity of the natural phenomenon or our limited knowledge of mathematics. Recently, ML has been found to be a very powerful tool in helping to overcome those challenges, by building basic models from the observed patterns as well as assisting decision makers in facing real world problems. Since ML is able to map causal factors and consequent outcomes from the observed patterns (experimental data), without deep knowledge of the complex physical process, these modeling techniques are becoming popular among engineers. Recently, a wide range of applications have benefited greatly from the extensive use of ML techniques for the predictive modeling of the many engineering problems in areas such as air pollution monitoring [33], heat exchanger performance analysis [34], breakthrough mechanism [35], circulation rate in thermosiphon reboiler [36], energy resources forecasting [37] and reservoir properties [38], to name a few. These computational methods accurately forecast complicated processes and quickly give an understanding of how these systems work [39]. The model eliminates the requirement for completing a pilot experiment and aids in developing adsorption apparatus [40].

The main goals of the current study were two-fold. The first was dedicated to the investigation of the efficacy of waste black cardamom based activated carbon (BCAC) to remove CR from aqueous solutions, and generate experimental data. The second was to use this data to develop ML models namely, support vector regression (SVR) and artificial neural network (ANN) for the first time to forecast the uptake capacity of the BCAC adsorbent. Study was done on the variables that affected the CR removal, including temperature, starting dye concentration and pH of the dye water. To verify the performance of the developed ML models, statistical parameters namely, coefficient of determination ( $R^2$ ), average absolute relative error (AARE), root mean squared error (RMSE), and chi-square ( $\chi^2$ ) were employed. It was observed that the BCAC adsorbent was a promising adsorbent for CR removal from aqueous media and the novel application of ML techniques to model the dye removal efficiency of BCAC may be widely employed as a practical tool to enhance treatment procedures for the removal dyes from aqueous solutions.

## 2. Materials and methods

### 2.1. Black cardamom and reagents

Black cardamom waste was collected from local herbal medicine manufacturing plant in Aligarh. Congo Red dye was purchased from Sigma Aldrich. Salts namely, potassium

hydroxide (KOH), hydrochloric acid (HCl) and sodium hydroxide (NaOH) used in the experiments were of analytical grade. Deionized water was utilized in carrying out all the studies. One gram of CR was dissolved in one litre of deionized water to create a stock solution (1000 PPM), which was then diluted with deionized water to the precise concentrations needed.

### 2.2. Preparation of BCAC

The waste black cardamom pods were washed with water to eliminate dust particles and then dried in the sun for two days. Furthermore, all of these BC pods were oven dried for 24 h at 70 °C. Now the dried BC was pre-carbonised at 300 °C for 1.5 h. The pre-carbonized BC samples were then weighed and blended with a KOH solution (impregnation ratio of 1.5). The impregnated sample were dried in oven and further activated in furnace for 2 hrs at 600 °C. The obtained material was repeatedly refluxed with water. The sample material was then dried and kept before being used.

### 2.3. Characterization of BCAC

Scanning electron microscope (SEM) was employed for structural pattern and surface morphology of BCAC. SEM (JEOL JSM-7610 FPLUS model) was used to acquire the electron micrographs of gold-coated BCAC prior and post CR dye adsorption. The Fourier transform infra-Red (FTIR) analysis was performed using Bruker ALPHA FTIR Spectrophotometer in KBr pellets (spectroscopic grade) in the wavelength range of 500–4000  $\text{cm}^{-1}$ . This approach could be useful in describing potential surface functional differences between feedstock and BCAC. The concentrations of CR dye were analysed by visible – spectrophotometer (Electronics India). The solid addition technique was used to determine the pH values of the adsorbent at the (pH<sub>pzc</sub>). The pH of solutions was ascertained by Labman pH meter (India).

### 2.4. Adsorption experiments

The effect on the CR adsorption mechanism was studied by adjusting operational conditions such dose, pH (6–10), beginning CR dye concentration (50–200 mg/L), and temperature (30 °C – 50 °C) and interaction time (0–120 min) of CR dye and BCAC. The CR batch adsorption investigations were conducted using the temperature-controlled water bath shaker (REMI CIS 24). In a 250-ml conical flask, an aliquot of 0.2 g of BCAC was assorted with 20 ml of CR required concentration solution and flask was put at 150 rpm agitation speed of water bath until equilibrium was attained. The spectrophotometer (Electronics India) was used to determine the final concentration of the filtered sample. The pollutant removal percentage (% R) of CR dye and quantity of adsorption at equilibrium  $Q_e$  (mg/g), was determined at time (t) using equation (1) and (2) respectively.

$$\%R = \left( \frac{C_o - C_e}{C_o} \right) \times 100 \quad (1)$$

$$q_e = \left( \frac{C_o - C_e}{m} \right) \times V \quad (2)$$

Where, Co and Ce are the CR concentrations at the start and end of the experiment, respectively. The number V represents the volume of CR aqueous solution (in litres), whereas m symbolizes the BCAC adsorbent mass (in grams).

The effect of solution pH on the removal effectiveness of CR using BCAC was explored by regulating pH in the range of 6–10 for CR and utilising 0.01 M HCl and 0.01 M NaOH solution as adjusting medium. The point-of-zero charges ( $pH_{PZC}$ ) is a property that establishes the pH level at which the adsorbent surface achieves net electrical neutrality and offers important details on the electrostatic interactions between the adsorbent and adsorbate. The  $pH_{PZC}$  is determined by solid addition method. At a constant temperature of 30 °C, adsorption isotherm studies were carried out with starting CR concentrations ranging from 50 to 200 mg/L. The kinetic tests were performed, with residual dye concentrations measured at specified time intervals at five different starting CR concentrations of 50, 70, 100, 150 and 200 mg/L, respectively.

### 2.5. Desorption studies

To conduct the reusability test, 0.1 g of CR loaded BCAC adsorbent was placed into 10 ml of 0.05 M NaOH for 24 hrs. The regenerated adsorbent was then removed and properly cleaned with deionized water before being dried at 55 °C for the subsequent cycle.

### 2.6. Machine learning modelling

#### 2.6.1. Artificial neural network

The building of ANN intelligent models is based on a variety of straightforward simulations of the biological processes in the human brain that enable learning, remembering, and problem-solving [41]. The neurons of ANN are core processing units, capable of acquiring complex relationship between input and output variables [42]. The mathematical neuron's output is often represented as:

$$Y_n = F(I) = F\left(b + \sum_{n=1}^N w_n X_n\right) \quad (3)$$

In the multi layered (input, hidden and output layers) network fit the data during training, these algorithms modify the weights of the neurons based on the discrepancy between the actual output values and the desired output [43]. The best ANN architecture and training method for a particular job are discovered through a process of trial and error [44]. One of the popular ANN architecture is a first order gradient descent approach called back-propagation which is used to train an algorithm to minimise error [38]. The nodes modified their weights, and the process iterates until error is reduced to a low-est value.

#### 2.6.2. Support vector regression (SVR)

Many literatures provides a detailed explanation of SVMs [45]. The support vector regression makes use of data sets  $P = \{(c_1, d_1), (c_2, d_2), \dots, (c_n, d_n)\}$ , such that each input  $c_i$  has its output  $d_i$ . The goal of epsilon SVR model is to adjust the function,  $d = f(c)$ , so that when it is evaluated with unknown input data  $\{c_i\}$ , it can predict the output values  $\{d_i\}$ . The regression function can be expressed as:

$$f(c, w) = (w \cdot \lambda(c) + b) \quad (4)$$

Where  $\lambda(c)$  is the high dimensional input function and the dot product ( $w \cdot \lambda(c)$ ).

The regression function represented in equation (4) can be minimized as follows:

$$\text{Minimize : } Q(f) = C \frac{1}{N} L_\epsilon(d, f(c, w)) + \frac{1}{2} \|w^2\| \quad (5)$$

The aforementioned equation has two components. The first is the empirical error, which may be assessed using the following insensitive loss function:

$$L_\epsilon(d, f(c, w)) = \begin{cases} 0 & \text{if } |d - f(c, w)| \leq \epsilon \\ |d - f(c, w)| - \epsilon & \text{otherwise} \end{cases} \quad (6)$$

The second term in the equation stands in for the function flatness. The trade-off between training error and model function flatness is provided by parameter C. With the addition of slack variables ( $\xi_i, \xi_i^*$ ), the SVR problem is transformed into a dual optimization problem as follows:

$$\text{Minimize : } \frac{1}{2} \|w^2\| + C \sum_{i=1}^N \xi_i + \xi_i^* \quad (7)$$

Subjected to

$$(d_i - w \cdot \lambda(c) - b) \leq \epsilon + \xi_i$$

$$(w \cdot \lambda(c) + b - d_i) \leq \epsilon + \xi_i^*, \quad \xi_i \text{ and } \xi_i^* \geq 0 \quad (8)$$

The introduction of Lagrangian multiplier  $\alpha_i$  and  $\alpha_i^*$  in the above convex optimization equation transforms it into dual form expressed as:

$$f(c, \alpha_i, \alpha_i^*) = \sum_{i=1}^{N_{SV}} (\alpha_i - \alpha_i^*) (\lambda(c_i) \cdot \lambda(c_j)) + b \quad (9)$$

The non-zero values of coefficients ( $\alpha_i - \alpha_i^*$ ) and their input vectors  $c_i$  create the support vectors (SVs). The basic expression for SVR is finally got after applying the kernel function as follows:

$$f(c, \alpha_i, \alpha_i^*) = \sum_{i=1}^{N_{SV}} (\alpha_i - \alpha_i^*) k(c_i, c_j) + b \quad (10)$$

The Karush-Kuhn Tucker (KKT) conditions are used to evaluate the constant b.

#### 2.6.3. ML Models' formulation

The computational ML models (ANN and SVR) were created with five inputs, namely starting CR concentration (50–200 mg/L), dosage (0.04–0.12 g), pH of solution (6–10), Temperature (30 °C –50 °C) and time (2–120 mins), and adsorption capacity of CR as an output, in order to forecast the performance of BCAC for CR batch adsorption. Following the identification of independent – dependent variables, random normalised data was separated into train and test sets. In this study, the ANN toolbox component of the software package MATLAB (2019b) software was adopted. Three layers in feed forward sequence make up the ANN design, with the hidden layer and output layer each having a different transfer function of tansig and purelin respectively. For little to medium-sized data, one of the most effective back propagation methods is Levenberg-Marquardt optimization. Twelve neu-

rons at hidden layer resulted in lowest prediction error of the formulated ANN model.

The SVR model to predict CR removal over BCAC was programmed by implementing `fitsvm` in MATLAB (2019b). Since just a few settings needed to be changed and the RBF kernel has a high general efficiency, it was chosen for this study out of all the available kernels [46]. To Reduce the five-fold cross-validation loss, the optimal hyperparameter combination was determined via Bayesian optimization [47]. It is possible to compare the performance of these developed models equitably since all models are trained and evaluated using the same data sets. Statistical assessment metrics such as  $R^2$ , AARE, RMSE and Chi-square value were used to verify the performance standard of the developed models as follows:

$$AARE = \frac{1}{N} \sum_{i=1}^N \left| \frac{p_i - E_i}{E_i} \right| \quad (11)$$

$$RMSE = \sqrt{\frac{\sum_{i=1}^N \left( \frac{E_i - p_i}{p_i} \right)^2}{N}} \quad (12)$$

$$\text{Chi-square value, } \chi^2 = \sum \frac{(E_i - p_i)^2}{p_i} \quad (13)$$

Where,  $E_i$  and  $p_i$  represent experimental and predicted data points respectively. Whereas,  $N$  denotes total data points. The  $R^2$  values were obtained using its command in M. S. Excel (2010).

### 3. Results and discussion

#### 3.1. BCAC characterization

The SEM micrographs of BCAC and CR laden BCAC at 1  $\mu\text{m}$  are depicted in Fig. 1 (a)-(b). By the pictures from the SEM examination, the structural characteristic of the BCAC adsorbent demonstrates a interconnected porous structure that provides effective CR dye adsorption. Before adsorption, empty spherical holes indicated that there was a substantial surface area available for dye uptake [48]. As from Fig. 1(b) after CR interacted with BCAC, the surface shape changes to become smoother and acquire flaky patches. These modifications show that the CR dye has effectively been loaded onto the adsorbent surface.

The FTIR spectra of BCAC can be seen in Fig. 2 indicating the existence of functional groups and bonds on the BCAC adsorbent. The band at 3438 ( $\text{cm}^{-1}$ ) was shifted after CR accumulation over BCAC to 3425 ( $\text{cm}^{-1}$ ) due to stretching vibrations of -OH group. The peak appear at 2886 ( $\text{cm}^{-1}$ ) may be attributed to -CH stretching [49]. The alkyne group located band at 2310 ( $\text{cm}^{-1}$ ) was moved to 2311 ( $\text{cm}^{-1}$ ) on CR adsorption [50]. The pronounced peak at 1428 ( $\text{cm}^{-1}$ ) changes to 1437 ( $\text{cm}^{-1}$ ) suggest bending  $\text{CH}_2$  and  $\text{CH}_3$  deformation vibrations [51]. The presence of the C-N length of the aliphatic amines was confirmed by the peak at 1034  $\text{cm}^{-1}$  which shifted to 1032 after CR treatment [26]. Following the application of

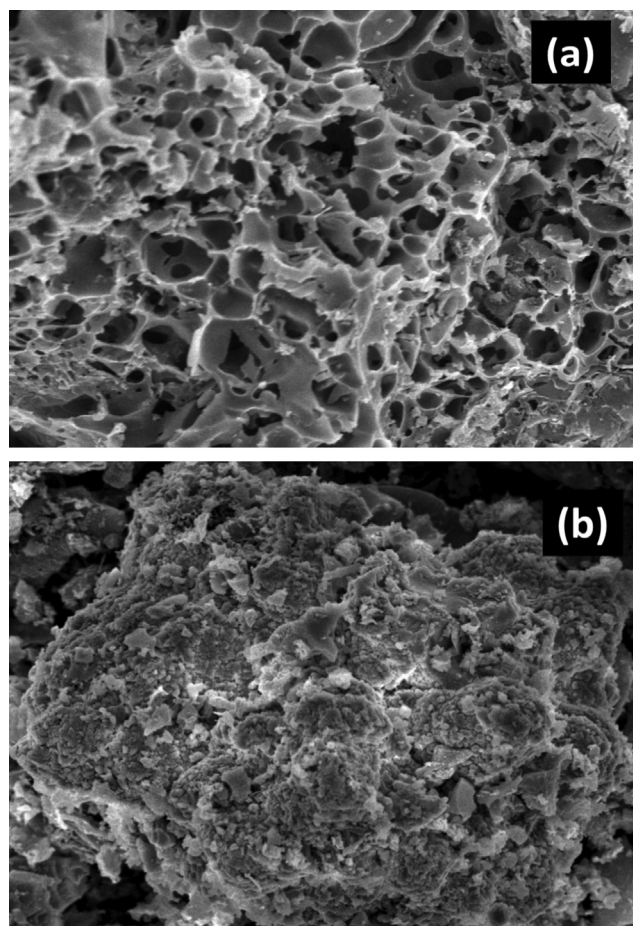


Fig. 1 SEM images of BCAC (a) Prior to CR adsorption and (b) after adsorption of CR at (Magnification: 6000 X; scale: 1  $\mu\text{m}$ ).

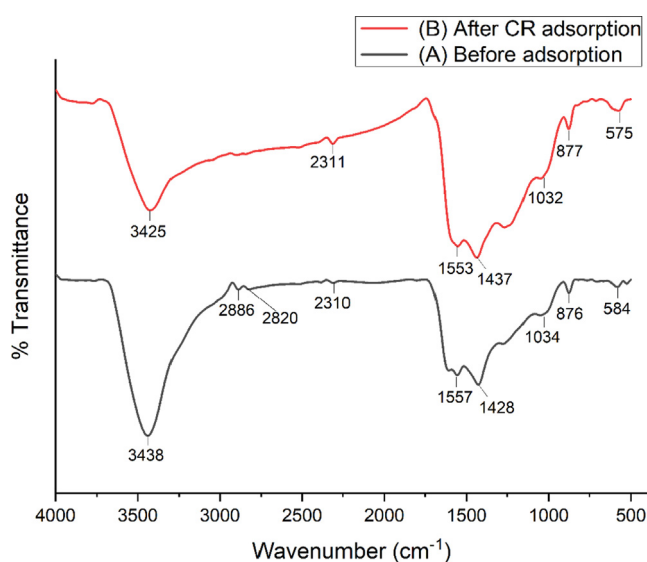


Fig. 2 FTIR spectra of BCAC.

CR dye, there were changes in peak positions, indicating that the CR dye had been successfully adhered onto the BCAC surface. The bands between 400 cm and 800 cm were due to presence of stretch vibrations of C-O and C-H.

### 3.2. Influence of pH

The pH exhibits a key characteristic throughout the adsorption process by regulating the adsorbent charge and ionisation level of the adsorbate in the solution. It is recognised that pH has an impact on CR's structural stability, which in turn affects the intensity of its hue. When the pH is acidic (pH 3.0–5.0), CR turns blue, whereas between pH 10.0 and 12.0, it turns to different shade of red color compared to original of CR dye [52]. It is stable in the pH range of 6 to 10. Fig. 3 illustrates the outcomes of altering the pH from 6 to 10 in order to investigate the impact of initial pH on CR adsorption. The 96.21 percent of CR dye removal was achieved at

pH 6 for 100 mg/L of CR concentration at 30 °C. Fig. 3A demonstrates that when the solution pH rose to 10, the adsorption effectiveness of BCAC for CR fell to 39.44 percent. This impact of pH change can be explained based on obtained PZC value of 7.54 (Fig. 3B). The  $pH_{PZC}$  was determined by salt addition method. The surface of the BCAC is negatively charged below this value [53]. Since CR is an azo anionic dye, removing it was facilitated by a pH value lower than  $pH_{PZC}$  because of the stronger electrostatic attraction between the anionic dye molecules and the positive adsorbent surface [40]. Thus, optimum CR uptake on BCAC was obtained at pH 6. In line with our findings, maximum adsorption of CR by bio magnetic composite was occurRed at pH 6.95 [52]; nevertheless, another published study also shows that at pH 6 maximum CR was adsorbed over coffee husk [54].

A detailed description of possible adsorption mechanisms between CR onto BCAC is proposed and described schemati-

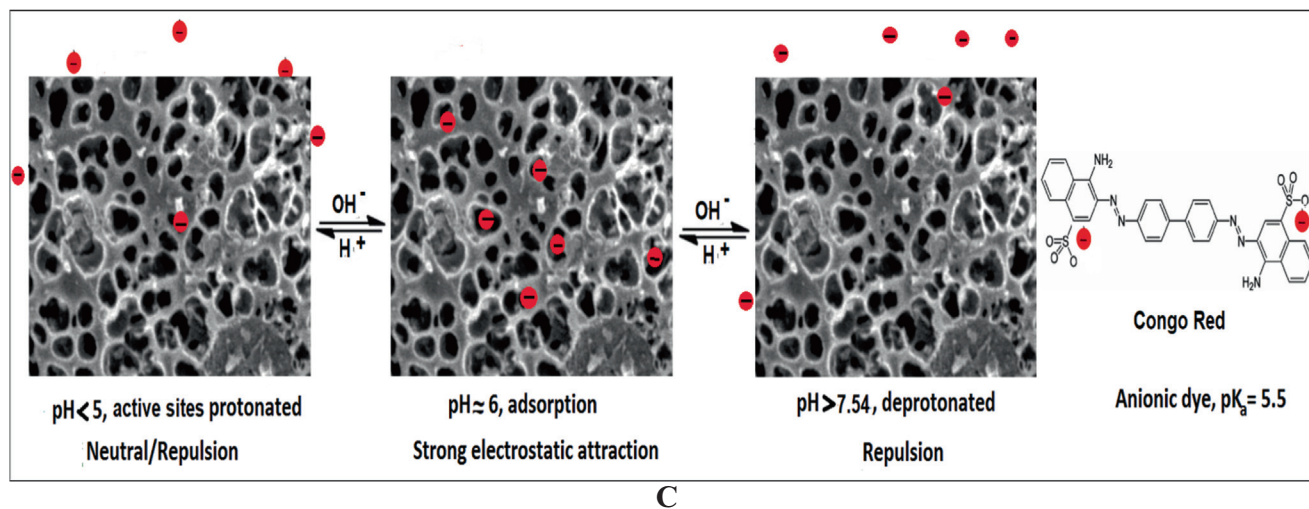
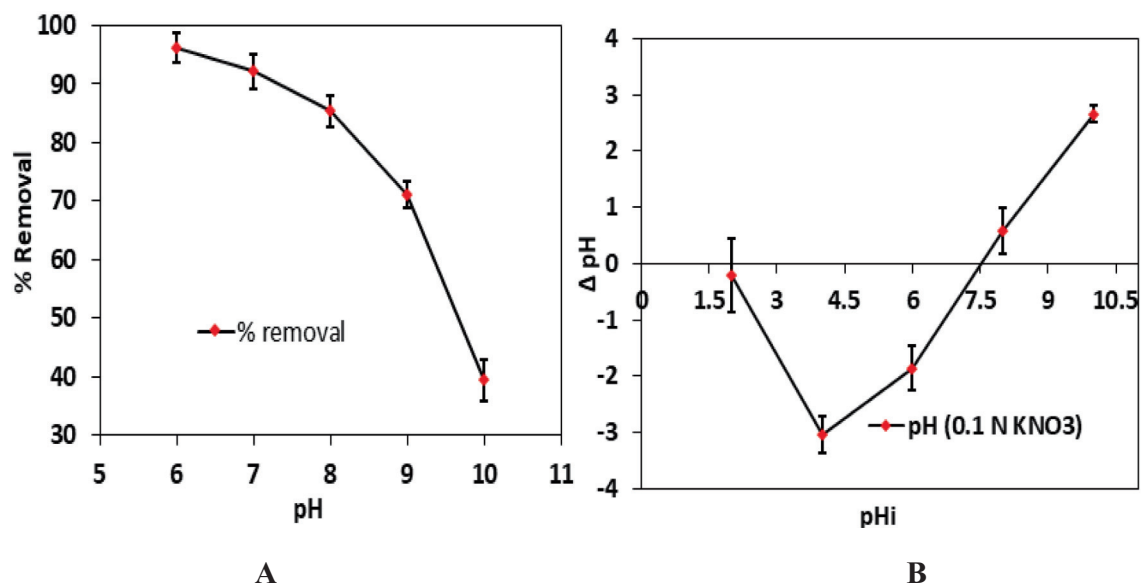


**Fig. 3** (A) Outcome of pH change on CR adsorption on BCAC (B) Point of zero charge of BCAC. (C) Possible adsorption mechanism for the adsorption of CR onto BCAC.

cally in Fig. 3(C). The effect of pH on the adsorption of CR on BCAC can be explained based on the surface charges of both the sorbent and the dye in the aqueous medium and also on the basis of  $pK_a$  values of major constituents [55]. At high solution  $pH > 7.54$ , active sites of BCAC are completely deprotonated; at neutral  $pH (\sim 7)$  active sites are primarily protonated; while at low  $pH < 4$ , most of the active sites are protonated [55]. Typically, CR is negatively charged when  $pH > 5.5$  ( $pK_a = 5.5$ ) [55] as can be seen in Fig. 3 (C). When the solution  $pH$  is 6 (above  $pK_a$  values of CR), dye molecules are negatively charged, while adsorbent sites of BCAC are relatively highly protonated (because of  $pH$  is much lower than 7.54). This leads to a strong electrostatic attraction between  $SO_3^-$  groups of CR and positively charged BCAC (as shown in Fig. 3(C)), thus resulting in a higher adsorption capacity for CR. However, when  $pH$  increases, the  $OH^-$  ions increase gradually, which compete with anionic dye molecules for penetrating the positively charged adsorbent. Hence adsorption capacity decreases for CR at higher  $pH$ . Therefore, based on the above-mentioned results, it is evident that the surface charge of the adsorbent surface and dye governs the adsorption behavior towards anionic dye CR.

### 3.3. Variation of concentration with time

Fig. 4 displays the relationship between the contact time (0–120 mins) and the CR adsorption capability of BCAC at  $pH$  6 for initial CR concentration range (50–200 mg/L). The CR adsorption capacity increased quickly for brief time periods before settling towards equilibrium although the quantity varied for each concentration. This can be explained as at early stage of experiment many vacant spots were present and due to passage of time these active pores were get saturated [56]. The shorter equilibrium period (10, 15 and 30 mins) were attained for lower (50, 70 and 100 mg/L) initial concentration of CR. Similarly, for raised initial CR concentrations of 150 mg/L and 200 mg/L, the equilibrium times were found to be 60 and 90 mins. A similar pattern was observed in literature where equilibrium was attained within 100 mins for CR dye over pine powder adsorbent [57].

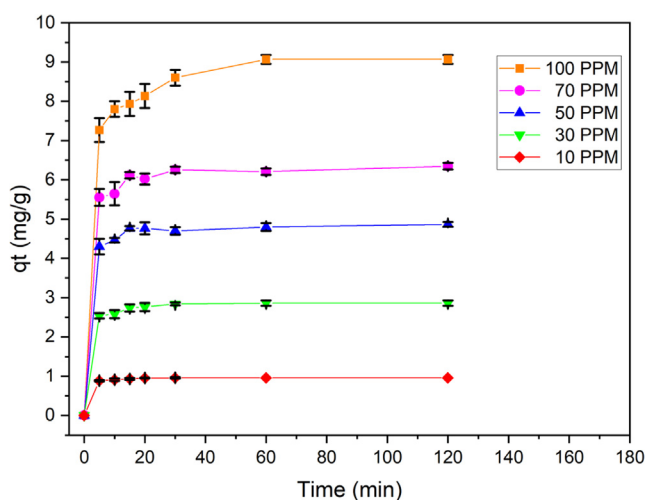


Fig. 4 The concentration vs. time graph for CR adsorption on BCAC.

### 3.4. Variation of dose

Fig. 5 shows how adsorbent dosage affects the amount of CR that can be adsorbed onto BCAC. Increases in BCAC dosage of 0.04, 0.06, 0.08, 0.1 and 0.12 g, respectively, resulted in increases in CR removal percentage of 84.3, 88.65, 91.33, 95.89 and 96.35 % as depicted in Fig. 5. This might be attributed to the rise in the total aggregate surface area of the BCAC particles and the number of accessible active adsorption sites [7]. At 0.1 g and 0.12 g loading of dose, there was no discernible difference in elimination of CR that may be due aggregation of adsorbent particles [8]. Thus for all experiments, BCAC of 0.1 g was discovered to be the best dosage when taking CR removal percentage values into account.

### 3.5. Adsorption isotherms

Adsorption isotherm investigations are crucial because they describe the distribution of the adsorbed molecules between the adsorbent and the liquid solutions at equilibrium. As it serves a useful purpose in the analysis and design of adsorption systems, it is vital to establish the most suitable correlation for equilibrium data and empirical equations. The Langmuir, Freundlich, and Temkin models were utilised to evaluate the data in order to determine which isothermal model is most appropriate for delivering the CR adsorption over BCAC. The linear forms of aforementioned isotherm models are presented in Table 1 and values of corresponding parameters were analysed from Fig. 6.

#### 3.5.1. Langmuir isotherm

The Langmuir isotherm model, state that adsorption happens at specified homogenous sites on the adsorbent through monolayer adsorption [58]. It is also hypothesised that once a sorbate molecule fills a space, no further sorption may occur there. The adsorbate draws to all of the active vacant sites of the adsorbent using the same amount of energy [59]. In Table 1,  $q_e$  is the dye amount per unit weight of BCAC (mg/g) and  $C_e$  is remaining CR concentration at equilibrium (mg/L). The con-

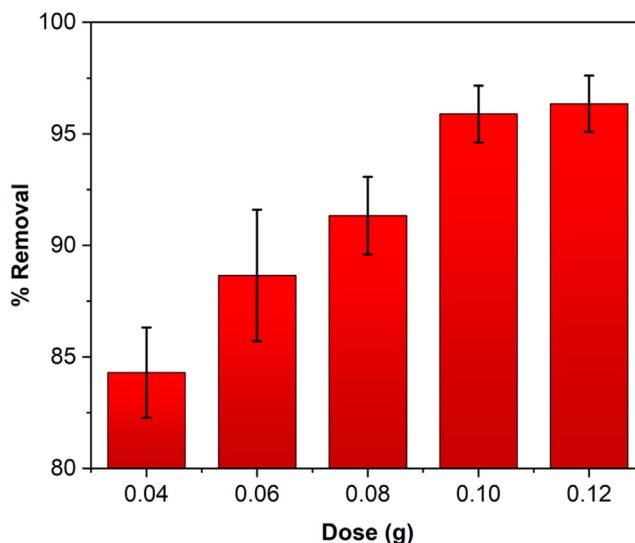
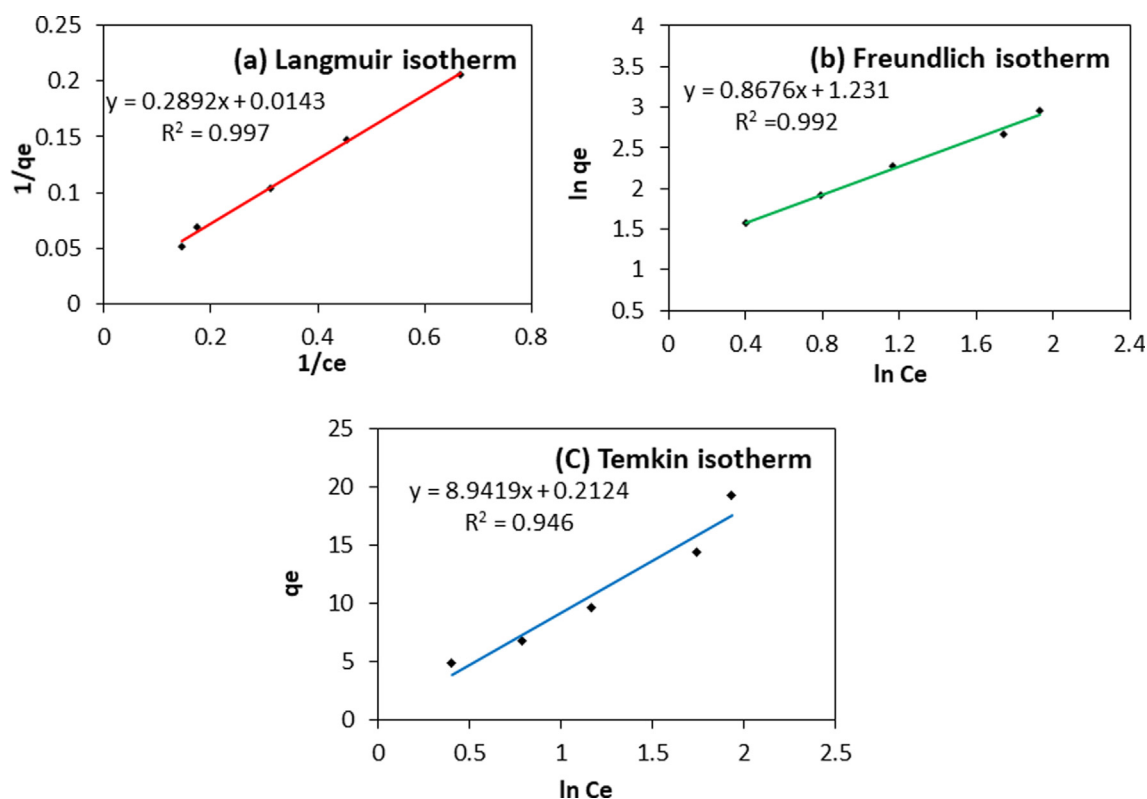


Fig. 5 Impact of changing the BCAC dose on CR adsorption.

**Table 1** Isotherm's equations and constants for CR adsorption on BCAC.

Isotherms	Equations	Parameters	Values
Langmuir	$\frac{1}{q_e} = \left( \frac{1}{q_m} \times \frac{1}{b} \times \frac{1}{C_e} \right) + \frac{1}{q_m}$	$q_m$ (mg g <sup>-1</sup> )	69.93
		$b$ (L mg <sup>-1</sup> )	0.049
		$R_L$	0.091–0.287
		$R^2$	0.997
Freundlich	$\ln q_e = \ln K_F + \frac{1}{n} \ln C_e$	$K_F$ (mg g <sup>-1</sup> ) (L mg <sup>-1</sup> ) <sup>1/n</sup>	3.424
		$n$	1.152
		$R^2$	0.992
Temkin	$q_e = B \ln A + B \ln C_e$	$A$ (L g <sup>-1</sup> )	1.024
		$B$ (J mol <sup>-1</sup> )	8.941
		$R^2$	0.946

**Fig. 6** Adsorption isotherm for CR uptake on BCAC (Temp = 30 °C, pH = 6 and contact time 120 min).

stant  $q_{\max}$  is related to the sites filled by a dye monolayer and reflects the adsorption capacity (mg/g).  $K_L$  is a constant related to adsorption energy (L/mg). Plotting the adsorption curve;  $1/q_e$  vs  $1/C_e$  gives the value of  $q_{\max}$  and  $K_L$ . The graph showed that the Langmuir adsorption capacity was 69.93 mg/g, and an excellent  $R^2$  of 0.997 was observed suggesting monolayer coverage of sites by CR dye molecules (Fig. 6). Separation factor ( $R_L$ ), is another dimensionless measure which provides information on how favourable is the adsorption process. The adsorption is indicated by  $R_L$ , which can be either unfavourable ( $R_L > 1$ ), favourable ( $0 < R_L < 1$ ), irreversible ( $R_L = 0$ ), or linear ( $R_L = 1$ ) [60]. The separation factor values for the present study lie in order (0.091–0.287), which ranges

from 0 to 1, indicates favourable adsorption [60]. In conformity to our results, several investigations have demonstrated that the Langmuir model best describes the sorption of CR onto agro-based adsorbent [17,32].

### 3.5.2. Freundlich isotherm

The Freundlich model, which is frequently used in heterogeneous systems and denotes multilayer adsorption with unstable distribution of enthalpies and affinities between adsorbent and adsorbate [61]. Freundlich sorption equilibrium constant  $K_F$  is expressed in (mg/g). (L/mg)<sup>1/n</sup>, and  $n$  stands for distinctive surface heterogeneity. The linear graph  $\log q_e$  vs  $\log C_e$  is used to estimate the model parameters. The result of correlation

coefficient of this model is represented in Table 1. Due to lower  $R^2$  value than Langmuir model indicate that this model does not adequately account for the variation in the experimental data.

### 3.5.3. Temkin isotherm

According to the above isotherm, all molecules' adsorption heat decreases in a linear manner, proving that the binding energy is homogeneous [62,63]. The constants  $A$  (g/L) and  $B$  (J/mol) corresponding to the maximal equilibrium binding energy and heat of adsorption respectively, were calculated

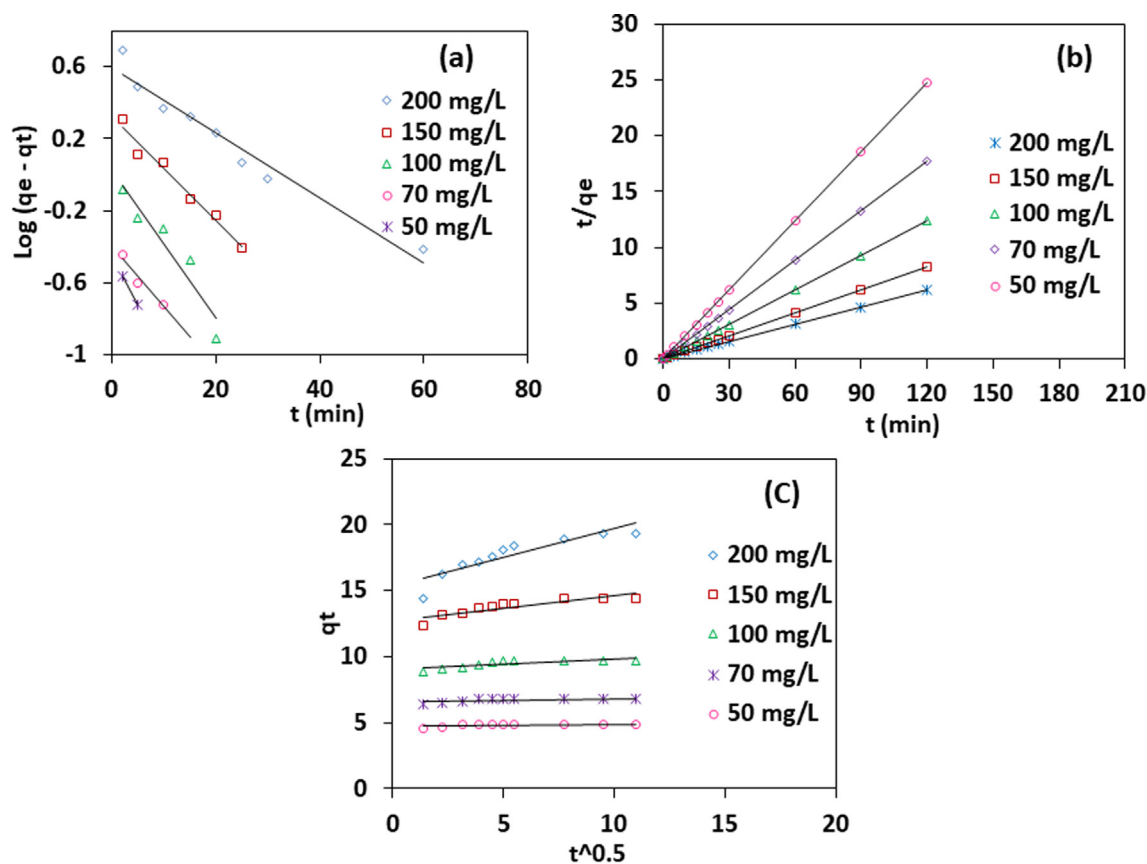
using the linearized Temkin equation. The obtained values of  $A$  and  $B$  are given in the following Table 1. The computed  $R^2$  value (0.94) for Temkin isotherm in the case of CR adsorption is less than those for the Langmuir and Freundlich isotherms. This finding suggests that the Temkin model does not provided an adequate fit for the experimental data.

### 3.6. Adsorption kinetics

The process by which a solute bind to a sorbent can be expressed using a variety of models. Studies on adsorption rate

**Table 2** Kinetic parameters for CR removal on BCAC at different initial concentration.

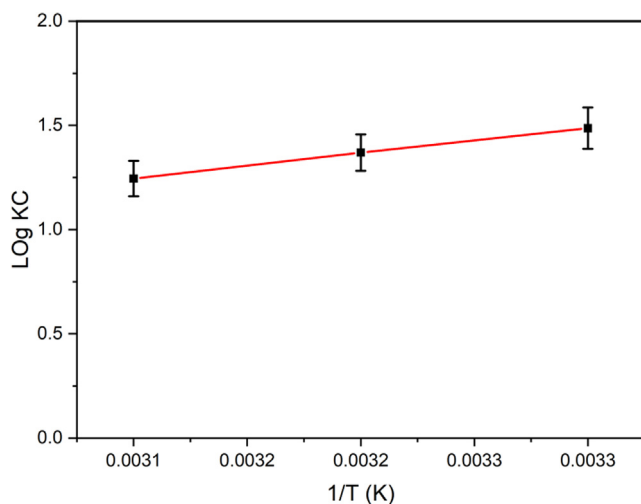
Kinetic models & Equations	Parameters	Concentrations (mg L <sup>-1</sup> )				
		50	70	100	150	200
Pseudo-first order $\log(q_e - q_t) = \log q_e - \left(\frac{K_1}{2.303}\right) \times t$	$q_e$ (exp)	4.849	6.777	9.678	14.428	19.308
	$q_e$ (calc)	0.346	0.401	1.058	2.102	3.908
	$K_1$	0.120	0.0778	0.094	0.066	0.041
	$R^2$	1	0.952	0.903	0.974	0.953
Pseudo-second order kinetics $\frac{t}{q_t} = \left(\frac{1}{K_2 q_e^2}\right) + \left(\frac{1}{q_e}\right) \times t$	$q_e$ (exp)	4.849	6.777	9.678	14.428	19.308
	$q_e$ (calc)	4.852	6.784	9.708	14.513	19.493
	$K_2$	4.045	1.633	0.392	0.108	0.038
	$R^2$	1	1	0.999	0.999	0.997
Intra-particle diffusion model $q_e = k_{id} \times t^{1/2} + I$	$K_{id}$	0.019	0.030	0.077	0.188	0.441
	$I$	4.699	6.534	9.025	12.753	15.271
	$R^2$	0.362	0.484	0.639	0.779	0.806



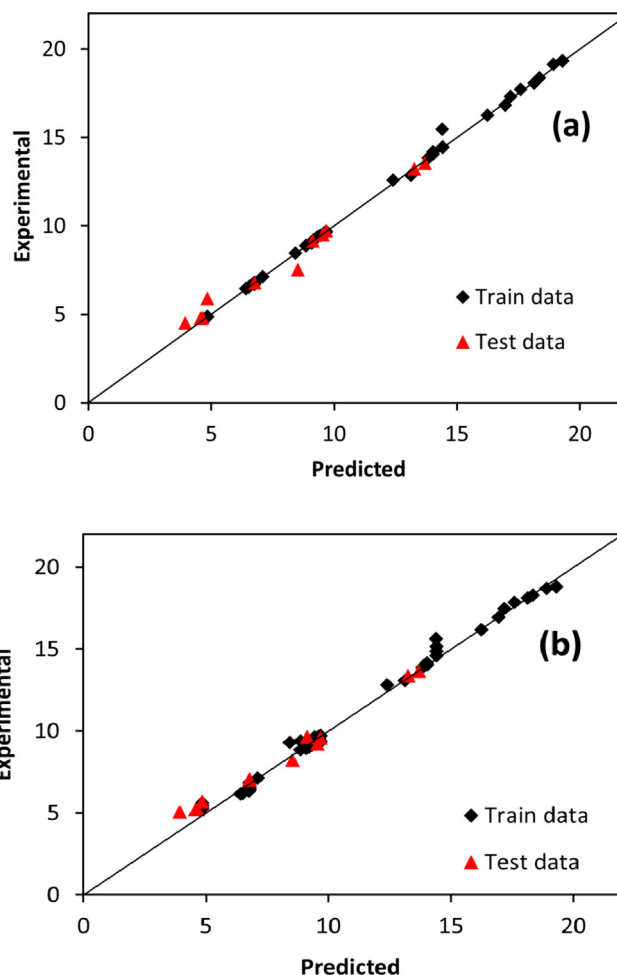
**Fig. 7** Adsorption Kinetics for CR dye onto BCAC (a) pseudo-first order, (b) pseudo-second order and (c) Intra-particle diffusion (at pH = 6, temp = 30 °C and dose = 0.1 g).

**Table 3** Thermodynamic variables for CR adsorptions on BCAC.

Temperature (K)	$\Delta G^\circ$ (kJ mol <sup>-1</sup> )	$\Delta H^\circ$ (kJ mol <sup>-1</sup> )	$\Delta S^\circ$ (kJ mol <sup>-1</sup> K <sup>-1</sup> )
303	-8.621	-22.697	-0.046
313	-8.202		
323	-7.696		

**Fig. 8** A graph of  $\log K_c$  plotted against  $1/T$  for CR adsorption on BCAC.

were conducted in order to quickly and effectively construct a model. Adsorption kinetics demonstrates how the rate of dye uptake is time-dependent and aids in calculating the residence time for the purpose of optimising the size of the adsorption device [64]. The uptake of CR over BCAC was established by fitting data into kinetic models namely, pseudo-first order, pseudo-second order and intra-particle diffusion kinetics. The linear expressions and coefficients of these kinetic models are described in Table 2. According to Fig. 7 (a-c) for adsorption of CR dye by BCAC, pseudo-second order rate kinetics had an  $R^2$  value of 0.998, which was higher than first order rate kinetics. Additionally, the  $q_e$  values for the pseudo-first-order equation varied considerably with the experimental ones. As opposed to that,  $q_e$  values estimated by pseudo-second order rate kinetics were closely matched with experimental data. According to the intraparticle diffusion model, the value of constant (I) provides information about the boundary layer impact [3]. As  $qt$  vs  $t^{1/2}$  plot show divergence from the origin pointed that the CR adsorption over BCAC comprise intra particle diffusion, in addition to the rate control step and other ways such film diffusion, surface adsorption, and pore diffusion [65]. Similar findings for the kinetics of CR uptake over kenaf activated carbon [19] and litchi seed powder [32]

**Fig. 9** ML-modelling of CR adsorption on BCAC for (a) SVR model and (b) ANN model.

that follows pseudo-second order kinetics were reported recently.

### 3.7. Adsorption thermodynamics

An investigation of the thermodynamics was done at three different temperatures (30 °C, 40 °C and 50 °C) for CR uptake on BCAC. The following equations (14–16) were used to compute the thermodynamic characteristics of the process, including the change in Gibbs free energy ( $\Delta G^\circ$ ), change in enthalpy ( $\Delta H^\circ$ ), and change in entropy ( $\Delta S^\circ$ ).

$$K_c = \frac{C_{AC}}{C_e} \quad (14)$$

$$\Delta G = -RT \ln K_c \quad (15)$$

**Table 4** Optimized hyperparameters for the SVR Model.

Model	Box constraint	Kernel Scale	Epsilon	Type of Kernel	Loss Function
CR-SVR Model	927.902	2.7123	0.0126	RBF	$\epsilon$ -insensitive



$$\log K_c = \frac{\Delta S^\circ}{2.303 \times R} - \frac{\Delta H^\circ}{2.303 \times R \times T} \quad (16)$$

Here,  $R$  stands for the universal gas constant ( $8.314 \text{ J K}^{-1} \text{ mol}^{-1}$ ), and  $T$  stands for the temperature on the Kelvin scale.  $C_a$  and  $C_e$  represent the equilibrium concentrations of CR on the BCAC and in the solution, respectively. Table 3 lists the computed thermodynamic parameters obtained from Fig. 8. The process is more impulsive as  $\Delta G^\circ$  becomes more negative [66]. The CR adsorption process is spontaneous, as evidenced by the negative values of total free energy changes during the process. In light of the computed  $\Delta G^\circ$  values, which ranged between  $-7.696$  and  $-8.621 \text{ kJ mol}^{-1}$ , the thermodynamic investigation came to the conclusion that the adsorption happened by a physical sorption process as  $\Delta G^\circ < 20 \text{ kJ mol}^{-1}$  [67]. Since, the negative values  $\Delta H^\circ$  and  $\Delta G^\circ$  represents exothermic and spontaneous process [68]. Thus, the findings demonstrated that the negative values of  $\Delta H^\circ$  and  $\Delta S^\circ$  establish the exothermic nature of CR dye adsorption onto BCAC and Reduction in randomness. Several investigations that have been conducted for the elimination of CR reported similar thermodynamic results [23,32].

### 3.8. Desorption and regeneration

Regeneration of the adsorbent is a crucial consideration when evaluating the process's viability in terms of both practical use

and economics. During desorption process dye molecules are liberated from the carbon surface. Experiments with Congo Red-loaded BCAC for desorption study have been carried out by using NaOH solution. The interaction bonds between the surface sites of BCAC and adsorbed CR become weaker in an alkaline NaOH solution, making regeneration simple. According to the regeneration data, the CR percentage adsorption by BCAC was decreased in the third cycle to 84.77 % from 96.81 %. Moreover, desorption percentage was seen to diminish with an increase in the number of regeneration cycles, remaining at 88.31 % of its initial level after the first cycle and falling to 72.58% after the third. As a result, the adsorbent can be successfully employed for up to three cycles. Similar desorption studies were performed utilizing NaOH to recover Congo Red dye from jujube shell [27] and methyl orange from pumpkin seed powder adsorbent [69].

### 4. Simulation of machine leaning models

In order for the ML-based SVR model to function properly, the model parameters must be chosen correctly. The optimised hyperparameters are listed in Table 4. The results showed that the optimal ANN design was created using the tansig-purelin transfer functions, trainlm as the back-propagation technique, and 10 neurons in a single hidden layer. The models' output was employed, in order to create parity graphs between the

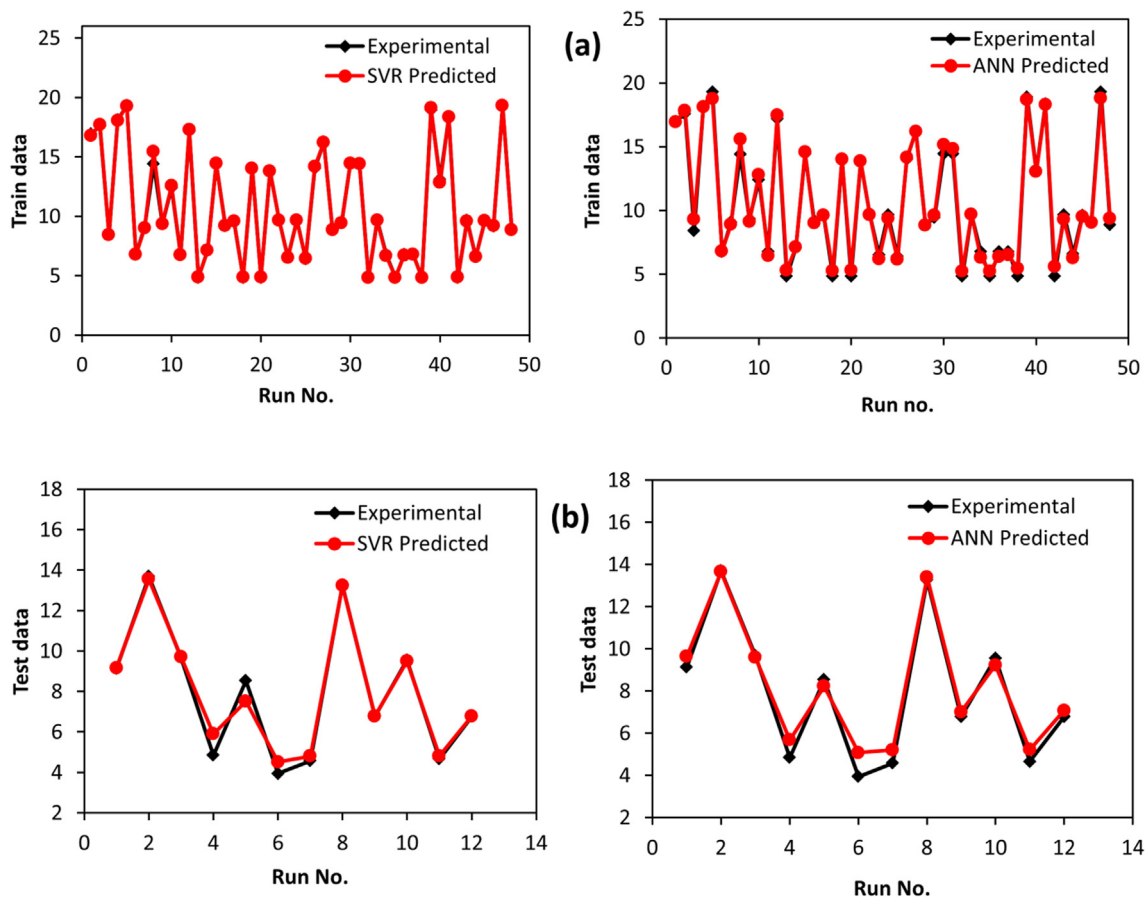


**Fig. 10** Plots of Congo Red ML models during (a) training course and (b) testing course. (For interpretation of the references to color in this figure legend, the reader is referred to the web version of this article.)

**Table 5** SVR model performance evaluation.

Parameter	Train data	Test data
R <sup>2</sup>	0.9987	0.9816
AARE	0.0053	0.0491
RMSE	0.1686	0.4635
Chi-squared	0.0913	0.4165

**Table 6** ANN model performance evaluation.

Parameter	Train data	Test data
R <sup>2</sup>	0.9931	0.9884
AARE	0.0365	0.0781
RMSE	0.3855	0.5395
Chi-squared	0.8131	0.5797

actual adsorption capacity of CR over BCAC and those predicted by the ML-based models as represented in Fig. 9 (a-b). It is obvious that the anticipated train and test data both fall very near the optimum fit line, signifying that the two ML-based models performed effectively. Fig. 10 (a) - (b) demonstrates the training process and testing phase for ML-SVR and ML-ANN models respectively. It is noted that the forecasted results closely match the experimentally determined values of adsorption capacity for almost all sample runs. The two constructed ML-models produce good results, with high R<sup>2</sup> values of 0.9978 for SVR and 0.9931 for the ANN model obtained during training. These ML models were generalised since, during testing, they functioned effectively for even anonymous data, with R<sup>2</sup> for the SVR and ANN models being equivalent to 0.9816 and 0.9884, respectively. Furthermore, as depicted in Tables 5 and 6, low AARE values in ranges (0.0053–0.0491) for SVR and (0.0365–0.0781) for ANN, whereas evaluated RMSE values were found to be in ranges (0.1686–0.4635) for SVR and (0.3855 – 0.5395) for ANN were close to ideal error value of zero, confirms ML models' capacity for prediction CR removal onto BCAC. The results of the ML approach for present adsorption study were found to be consistent with previously reported literature where prediction of Chromium adsorption over Medlar seed by SVR and ANN models have R<sup>2</sup> of 0.981 and 0.958 respectively [70]. Similar

trend was also noted in ANN modelling of Basic Red 46 dye and Cu (II) with R<sup>2</sup> in between 0.98 and 0.99 [71].

## 5. Comparison with other adsorbents

Table 7 shows that the BCAC has a notable capacity for CR adsorption when compared to the other adsorbents that are being used. It has been determined how well various adsorbents can remove the CR dye when compared to the maximal adsorption capacity of BCAC for CR.

## 6. Conclusion

The herbal waste derived BCAC was discovered through this investigation to be a potential material for the elimination of harmful CR dye in water systems. Increases in initial dye concentration (50–200 mg/L), contact time (0–120 mins), and dose (0.04–0.12) were shown to enhance the amount of Congo Red dye uptake on BCAC, whereas increases in solution pH (6–10) and temperature (30–50 °C) were found to decrease it. The reported negative values for  $\Delta H^\circ$  (–22.697 kJ mol<sup>–1</sup>) and  $\Delta G^\circ$  (–8.621 kJ mol<sup>–1</sup>), respectively, show that adsorption is exothermic and spontaneous in nature. The provided results (R<sup>2</sup> > 0.9) demonstrate that ML models are potential forecasting techniques that can be applied successfully and have adequate accuracy for the prediction of the CR dye removal. Thus, ML prediction can help in the planning and development of a more efficient treatment for removing dye from waste effluent.

## Declaration of Competing Interest

The authors declare that they have no known competing financial interests or personal relationships that could have appeared to influence the work reported in this paper.

## Acknowledgements

This research work was funded by Institutional Fund Projects under grant no. (IFPIP: 1820-961-1443). The authors gratefully acknowledge technical and financial support provided by the Ministry of Education and King Abdulaziz University, DSR, Jeddah, Saudi Arabia.

**Table 7** Comparison of CR adsorption over various adsorbents.

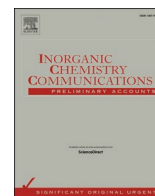
Adsorbent	Adsorption Isotherm	Adsorption Kinetic	Optimum pH	Max Adsorption (mg/g)	Reference
Mango Leaves	Freundlich	Pseudo-second order	7	21.28	[26]
Dactylifera seeds	Langmuir	Pseudo-second order	2	61.72	[8]
Kenaf-based activated carbon	Freundlich	Pseudo-second order	4	14.20	[19]
	Langmuir				
Coconut fiber based activated carbon	–	Pseudo-second order	3	22.10	[16]
Litchi seed	Freundlich	Pseudo-second order	2	20.49	[32]
	Langmuir				
<i>Acacia auriculiformis</i> biochar	Freundlich	Pseudo-second order	2	130.0	[72]
Apricote stone	Langmuir	Pseudo-second order	13	32.68	[28]
	Dubinini-Radushkevich				
Black Cardamom activated carbon	Langmuir	Pseudo-second order	6	69.93	Present study

## References

- [1] M. Danish, K.B. Ansari, M. Danish, A. Khatoon, R. Ali Khan Rao, S. Zaidi, R. Ahmad Aftab, A comprehensive investigation of external mass transfer and intraparticle diffusion for batch and continuous adsorption of heavy metals using pore volume and surface diffusion model, *Sep. Purif. Technol.* 292 (2022), <https://doi.org/10.1016/j.seppur.2022.120996> 120996.
- [2] M.A. Usman, A.Y. Khan, Selective adsorption of anionic dye from wastewater using polyethyleneimine based macroporous sponge: Batch and continuous studies, *J. Hazard. Mater.* 428 (2022), <https://doi.org/10.1016/j.jhazmat.2022.128238> 128238.
- [3] M.A. Fawzy, M. Gomaa, Use of algal biorefinery waste and waste office paper in the development of xerogels: A low cost and eco-friendly biosorbent for the effective removal of congo red and Fe (II) from aqueous solutions, *J. Environ. Manage.* 262 (2020), <https://doi.org/10.1016/j.jenvman.2020.110380> 110380.
- [4] M.T. Yagub, T.K. Sen, S. Afroze, H.M. Ang, Dye and its removal from aqueous solution by adsorption: A review, *Adv. Colloid Interface Sci.* 209 (2014) 172–184, <https://doi.org/10.1016/j.cis.2014.04.002>.
- [5] S. Parvin, B.K. Biswas, A. Rahman, Chemosphere Study on adsorption of Congo red onto chemically modified egg shell membrane 236 (2019), <https://doi.org/10.1016/j.chemosphere.2019.07.057>.
- [6] Y.H. Chiu, T.F.M. Chang, C.Y. Chen, M. Sone, Y.J. Hsu, Mechanistic insights into photodegradation of organic dyes using heterostructure photocatalysts, *Catalysts*. 9 (2019), <https://doi.org/10.3390/catal9050430>.
- [7] S. Mohebbi, D. Bastani, H. Shayesteh, Equilibrium, kinetic and thermodynamic studies of a low-cost biosorbent for the removal of Congo red dye: acid and CTAB-acid modified celery (*Apium graveolens*), *J. Mol. Struct.* 1176 (2018) 181–193, <https://doi.org/10.1016/j.molstruc.2018.08.068>.
- [8] D. Pathania, A. Sharma, Z. Siddiqi, Removal of congo red dye from aqueous system using Phoenix dactylifera seeds, *J. Mol. Liq.* 219 (2016) 359–367, <https://doi.org/10.1016/j.molliq.2016.03.020>.
- [9] M.A. Adebayo, J.M. Jabar, J.S. Amoko, E.O. Openiyi, O.O. Shodiya, Coconut husk-raw clay-Fe composite: preparation, characteristics and mechanisms of Congo red adsorption, *Sci. Rep.* 12 (2022) 1–12, <https://doi.org/10.1038/s41598-022-18763-y>.
- [10] N.A. Alamrani, Elimination of Congo Red Dye from Industrial Wastewater Using *Teucrium polium L.* as a Low-Cost Local Adsorbent, *Adsorpt. Sci. Technol.* (2021) 12.
- [11] S. Mishra, L. Cheng, A. Maiti, The utilization of agro-biomass/byproducts for effective bio-removal of dyes from dyeing wastewater: A comprehensive review, *J. Environ. Chem. Eng.* 9 (2021), <https://doi.org/10.1016/j.jece.2020.104901> 104901.
- [12] J.N. Wekoye, W.C. Wanyonyi, P.T. Wangila, M.K. Tonui, Kinetic and equilibrium studies of Congo red dye adsorption on cabbage waste powder, *Environ. Chem. Ecotoxicol.* 2 (2020) 24–31, <https://doi.org/10.1016/j.enceco.2020.01.004>.
- [13] A. Kumar, H.M. Jena, Removal of methylene blue and phenol onto prepared activated carbon from Fox nutshell by chemical activation in batch and fixed-bed column, *J. Clean. Prod.* 137 (2016) 1246–1259, <https://doi.org/10.1016/j.jclepro.2016.07.177>.
- [14] A. Sharma, G. Sharma, M. Naushad, A.A. Ghfar, D. Pathania, Remediation of anionic dye from aqueous system using bio-adsorbent prepared by microwave activation, *Environ. Technol. (United Kingdom)* 39 (2018) 917–930, <https://doi.org/10.1080/09593330.2017.1317293>.
- [15] R.A.K. Rao, U. Khan, Adsorption of Ni(II) on alkali treated pineapple residue (*Ananas comosus L.*): Batch and column studies, *Groundw. Sustain. Dev.* 5 (2017) 244–252, <https://doi.org/10.1016/j.gsd.2017.08.002>.
- [16] L. Zhang, L.Y. Tu, Y. Liang, Q. Chen, Z.S. Li, C.H. Li, Z.H. Wang, W. Li, Coconut-based activated carbon fibers for efficient adsorption of various organic dyes, *RSC Adv.* 8 (2018) 42280–42291, <https://doi.org/10.1039/c8ra08990f>.
- [17] A. Sharma, Z.M. Siddiqui, S. Dhar, P. Mehta, D. Pathania, Adsorptive removal of congo red dye (CR) from aqueous solution by *Cornulaca monacantha* stem and biomass-based activated carbon: isotherm, kinetics and thermodynamics, *Sep. Sci. Technol.* 54 (2019) 916–929, <https://doi.org/10.1080/01496395.2018.1524908>.
- [18] V.S. Devi, B. Sudhakar, K. Prasad, P. Jeremiah Sunadh, M. Krishna, Adsorption of Congo red from aqueous solution onto *Antigonon leptopus* leaf powder: Equilibrium and kinetic modeling, *Mater. Today Proc.* 26 (2019) 3197–3206, <https://doi.org/10.1016/j.matpr.2020.02.715>.
- [19] S. Mandal, J. Calderon, S.B. Marpu, M.A. Omary, S.Q. Shi, Mesoporous activated carbon as a green adsorbent for the removal of heavy metals and Congo red: Characterization, adsorption kinetics, and isotherm studies, *J. Contam. Hydrol.* 243 (2021), <https://doi.org/10.1016/j.jconhyd.2021.103869> 103869.
- [20] F. Amran, M.A.A. Zaini, Sodium hydroxide-activated Casuarina empty fruit: Isotherm, kinetics and thermodynamics of methylene blue and congo red adsorption, *Environ. Technol. Innov.* 23 (2021), <https://doi.org/10.1016/j.eti.2021.101727> 101727.
- [21] R. Kumari, J. Mohanta, B. Dey, S. Dey, Eucalyptus leaf powder as an efficient scavenger for Congo red from water: Comprehensive batch and column investigation, *Sep. Sci. Technol.* 55 (2020) 3047–3059, <https://doi.org/10.1080/01496395.2019.1670208>.
- [22] Z. Li, H. Hanafy, L. Zhang, L. Sellaoui, M. Schadeck Netto, M. L.S. Oliveira, M.K. Seliem, G. Luiz Dotto, A. Bonilla-Petriciolet, Q. Li, Adsorption of congo red and methylene blue dyes on an ashitaba waste and a walnut shell-based activated carbon from aqueous solutions: Experiments, characterization and physical interpretations, *Chem. Eng. J.* 388 (2020), <https://doi.org/10.1016/j.cej.2020.124263> 124263.
- [23] T.K. Roy, N.K. Mondal, Potentiality of *Eichhornia* shoots ash towards removal of Congo red from aqueous solution: Isotherms, kinetics, thermodynamics and optimization studies, *Groundw. Sustain. Dev.* 9 (2019), <https://doi.org/10.1016/j.gsd.2019.100269> 100269.
- [24] K. Litefti, M.S. Freire, M. Stitou, J. González-Álvarez, Adsorption of an anionic dye (Congo red) from aqueous solutions by pine bark, *Sci. Rep.* 9 (2019) 1–11, <https://doi.org/10.1038/s41598-019-53046-z>.
- [25] M. Goswami, P. Chaturvedi, R. Kumar Sonwani, A. Dutta Gupta, R. Rani Singhania, B. Shekher Giri, B. Nath Rai, H. Singh, S. Yadav, R. Sharan Singh, Application of *Arjuna* (*Terminalia arjuna*) seed biochar in hybrid treatment system for the bioremediation of Congo red dye, *Bioresour. Technol.* 307 (2020), <https://doi.org/10.1016/j.biortech.2020.123203> 123203.
- [26] O.A. Adelaja, A.C. Bankole, M.E. Oladipo, D.B. Lene, Biosorption of Hg(II) ions, Congo red and their binary mixture using raw and chemically activated mango leaves, *Int. J. Energy Water Resour.* 3 (2019) 1–12, <https://doi.org/10.1007/s42108-019-00012-0>.
- [27] N. El messaoudi, M. Elkhomri, A. Dbik, S. Bentahar, A. Lacherai, B. Bakiz, Biosorption of Congo red in a fixed-bed column from aqueous solution using jujube shell: Experimental and mathematical modeling, *J. Environ. Chem. Eng.* 4 (2016) 3848–3855, <https://doi.org/10.1016/j.jece.2016.08.027>.
- [28] M. Abbas, M. Trari, Kinetic, equilibrium and thermodynamic study on the removal of Congo Red from aqueous solutions by adsorption onto apricot stone, *Process Saf. Environ. Prot.* 98 (2015) 424–436, <https://doi.org/10.1016/j.psep.2015.09.015>.

- [29] Y. Achour, L. Bahsis, E.H. Ablouh, H. Yazid, M.R. Laamari, M. El Haddad, Insight into adsorption mechanism of Congo red dye onto Bombax Buonopozense bark Activated-carbon using Central composite design and DFT studies, *Surfaces and Interfaces*. 23 (2021), <https://doi.org/10.1016/j.surfin.2021.100977>.
- [30] V.V. Gedam, P. Raut, A. Chahande, P. Pathak, Kinetic, thermodynamics and equilibrium studies on the removal of Congo red dye using activated teak leaf powder, *Appl. Water Sci.* 9 (2019) 1–13, <https://doi.org/10.1007/s13201-019-0933-9>.
- [31] S.L. Chan, Y.P. Tan, A.H. Abdullah, S.T. Ong, Equilibrium, kinetic and thermodynamic studies of a new potential biosorbent for the removal of Basic Blue 3 and Congo Red dyes: Pineapple (*Ananas comosus*) plant stem, *J. Taiwan Inst. Chem. Eng.* 61 (2016) 306–315, <https://doi.org/10.1016/j.jtice.2016.01.010>.
- [32] J.N. Edokpayi, E. Makete, Removal of Congo red dye from aqueous media using Litchi seeds powder: Equilibrium, kinetics and thermodynamics, *Phys. Chem. Earth*. 123 (2021), <https://doi.org/10.1016/j.pce.2021.103007>.
- [33] W.C. Leong, R.O. Kelani, Z. Ahmad, Prediction of air pollution index (API) using support vector machine (SVM), *J. Environ. Chem. Eng.* 8 (2020), <https://doi.org/10.1016/j.jece.2019.103208>.
- [34] J. Huang, T. Jin, M. Liang, H. Chen, Prediction of heat exchanger performance in cryogenic oscillating flow conditions by support vector machine, *Appl. Therm. Eng.* 182 (2021), <https://doi.org/10.1016/j.applthermaleng.2020.116053>.
- [35] R.A. Aftab, S. Zaidi, M. Danish, K.B. Ansari, M. Danish, Novel Machine Learning (ML) Models for Predicting the Performance of Multi-Metal Binding Green Adsorbent for the Removal of Cd (II), Cu (II), Pb (II) and Zn (II) ions, *Environ. Adv.* 9 (2022), <https://doi.org/10.1016/j.envadv.2022.100256>.
- [36] S. Zaidi, Development of support vector regression (SVR)-based model for prediction of circulation rate in a vertical tube thermosiphon reboiler, *Chem. Eng. Sci.* 69 (2012) 514–521, <https://doi.org/10.1016/j.ces.2011.11.005>.
- [37] A. Zendejboudi, M.A. Baseer, R. Saidur, Application of support vector machine models for forecasting solar and wind energy resources: A review, *J. Clean. Prod.* 199 (2018) 272–285, <https://doi.org/10.1016/j.jclepro.2018.07.164>.
- [38] D.A. Otchere, T.O.A. Ganat, R. Gholami, S. Ridha, Application of supervised machine learning paradigms in the prediction of petroleum reservoir properties: Comparative analysis of ANN and SVM models, *J. Pet. Sci. Eng.* 200 (2020), <https://doi.org/10.1016/j.petrol.2020.108182>.
- [39] M. Danish, K.B. Ansari, R.A. Aftab, M. Danish, S. Zaidi, Q.T. Trinh, gPROMS-driven modeling and simulation of fixed bed adsorption of heavy metals on a biosorbent: benchmarking and case study, *Environ. Sci. Pollut. Res.* (2021), <https://doi.org/10.1007/s11356-021-13207-y>.
- [40] M.A. Usman, R.A. Aftab, S. Zaidi, S.M. Adnan, R.A.K. Rao, Adsorption of aniline blue dye on activated pomegranate peel: equilibrium, kinetics, thermodynamics and support vector regression modelling, *Int. J. Environ. Sci. Technol.* (2021), <https://doi.org/10.1007/s13762-021-03571-0>.
- [41] A.M. Ghaedi, A. Vafaei, Applications of artificial neural networks for adsorption removal of dyes from aqueous solution: A review, *Adv. Colloid Interface Sci.* 245 (2017) 20–39, <https://doi.org/10.1016/j.cis.2017.04.015>.
- [42] R.A. Aftab, S. Zaidi, M. Danish, S.M. Adnan, K.B. Ansari, M. Danish, Support vector regression-based model for phenol adsorption in rotating packed bed adsorber, *Environ. Sci. Pollut. Res.* (2021), <https://doi.org/10.1007/s11356-021-14953-9>.
- [43] P.R. Souza, G.L. Dotto, N.P.G. Salau, Artificial neural network (ANN) and adaptive neuro-fuzzy interference system (ANFIS) modelling for nickel adsorption onto agro-wastes and commercial activated carbon, *J. Environ. Chem. Eng.* 6 (2018) 7152–7160, <https://doi.org/10.1016/j.jece.2018.11.013>.
- [44] S. Ullah, M.A. Assiri, A.G. Al-Sehemi, M.A. Bustam, M. Sagir, F.A. Abdulkareem, M.R. Raza, M. Ayoub, A. Irfan, Characteristically Insights, Artificial Neural Network (ANN), Equilibrium, and Kinetic Studies of Pb(II) Ion Adsorption on Rice Husks Treated with Nitric Acid, *Int. J. Environ. Res.* 14 (2020) 43–60, <https://doi.org/10.1007/s41742-019-00235-3>.
- [45] A.J. Smola, B. Scholkopf, A tutorial on support vector regression, *Stat. Comput.* 14 (2004) 199–222, <https://doi.org/10.1023/B:STCO.0000035301.49549.88>.
- [46] H. Peng, X. Ling, Predicting thermal – hydraulic performances in compact heat exchangers by support vector regression, *Int. J. Heat Mass Transf.* 84 (2015) 203–213, <https://doi.org/10.1016/j.ijheatmasstransfer.2015.01.017>.
- [47] I. Olanrewaju, M. Amiruddin, A. Rahman, T.A. Saleh, An approach to predict the isobaric specific heat capacity of nitrides / ethylene glycol-based nanofluids using support vector regression, *J. Energy Storage*. 29 (2020) 1–10.
- [48] M.K. Uddin, A. Nasar, Walnut shell powder as a low-cost adsorbent for methylene blue dye: isotherm, kinetics, thermodynamic, desorption and response surface methodology examinations, *Sci. Rep.* 10 (2020) 1–13, <https://doi.org/10.1038/s41598-020-64745-3>.
- [49] R. Ahmad, R. Kumar, Adsorptive removal of congo red dye from aqueous solution using bael shell carbon, *Appl. Surf. Sci.* 257 (2010) 1628–1633, <https://doi.org/10.1016/j.apsusc.2010.08.111>.
- [50] N. Hoc Thang, D. Sy Khang, T. Duy Hai, D. Thi Nga, P. Dinh Tuan, Methylene blue adsorption mechanism of activated carbon synthesised from cashew nut shells, *RSC Adv.* 11 (2021) 26563–26570, <https://doi.org/10.1039/d1ra04672a>.
- [51] Q. Du, J. Sun, Y. Li, X. Yang, X. Wang, Z. Wang, L. Xia, Highly enhanced adsorption of congo red onto graphene oxide/chitosan fibers by wet-chemical etching off silica nanoparticles, *Chem. Eng. J.* 245 (2014) 99–106, <https://doi.org/10.1016/j.ccej.2014.02.006>.
- [52] G. Akkaya Saygılı, Synthesis, characterization and adsorption properties of a novel biomagnetic composite for the removal of Congo red from aqueous medium, *J. Mol. Liq.* 211 (2015) 515–526, <https://doi.org/10.1016/j.molliq.2015.07.048>.
- [53] F. Gündüz, B. Bayrak, Biosorption of malachite green from an aqueous solution using pomegranate peel: Equilibrium modelling, kinetic and thermodynamic studies, *J. Mol. Liq.* 243 (2017) 790–798, <https://doi.org/10.1016/j.molliq.2017.08.095>.
- [54] P. Vairavel, N. Rampal, G. Jeppu, Adsorption of toxic Congo red dye from aqueous solution using untreated coffee husks: kinetics, equilibrium, thermodynamics and desorption study, *Int. J. Environ. Anal. Chem.* 00 (2021) 1–20, <https://doi.org/10.1080/03067319.2021.1897982>.
- [55] B. Huang, Y. Liu, B. Li, H. Wang, G. Zeng, Adsorption mechanism of polyethyleneimine modified magnetic core-shell Fe<sub>3</sub>O<sub>4</sub>@SiO<sub>2</sub> nanoparticles for anionic dye removal, *RSC Adv.* 9 (2019) 32462–32471, <https://doi.org/10.1039/c9ra06299h>.
- [56] O. Paşka, R. Ianoş, C. Păcurariu, A. Brădeanu, Magnetic nanopowder as effective adsorbent for the removal of Congo Red from aqueous solution, *Water Sci. Technol.* 69 (2014) 1234–1240, <https://doi.org/10.2166/wst.2013.827>.
- [57] S. Dawood, T.K. Sen, Removal of anionic dye Congo red from aqueous solution by raw pine and acid-treated pine cone powder as adsorbent: Equilibrium, thermodynamic, kinetics, mechanism and process design, *Water Res.* 46 (2012) 1933–1946, <https://doi.org/10.1016/j.watres.2012.01.009>.
- [58] P.C. Bhomick, A. Supong, M. Baruah, C. Pongener, D. Sinha, Pine Cone biomass as an efficient precursor for the synthesis of activated biocarbon for adsorption of anionic dye from aqueous solution: Isotherm, kinetic, thermodynamic and regeneration

- studies, *Sustain. Chem. Pharm.* 10 (2018) 41–49, <https://doi.org/10.1016/j.scp.2018.09.001>.
- [59] I. Langmuir, The adsorption of gases on plane surfaces of glass, mica and platinum, *J. Am. Chem. Soc.* 40 (1918) 1361–1403, <https://doi.org/10.1021/ja02242a004>.
- [60] M. Dirbaz, A. Roosta, Adsorption, kinetic and thermodynamic studies for the biosorption of cadmium onto microalgae *Parachlorella sp.*, *J. Environ. Chem. Eng.* 6 (2018) 2302–2309, <https://doi.org/10.1016/j.jece.2018.03.039>.
- [61] H.M.F. Freundlich, Over the adsorption in solution, *J. Phys. Chem.* 57 (1906) 385–471, <https://doi.org/10.4161/epi.6.7.16250>.
- [62] S.J. Allen, G. Mckay, J.F. Porter, Adsorption isotherm models for basic dye adsorption by peat in single and binary component systems, *J. Colloid Interface Sci.* 280 (2004) 322–333, <https://doi.org/10.1016/j.jcis.2004.08.078>.
- [63] H. Shayesteh, A. Rahbar-kelishami, R. Norouzbeigi, Treatment Adsorption of malachite green and crystal violet cationic dyes from aqueous solution using pumice stone as a low-cost adsorbent : kinetic, equilibrium, and thermodynamic studies, *Desalin. Water Treat.* (2015) 12822–12831, <https://doi.org/10.1080/19443994.2015.1054315>.
- [64] A. Dutta, Y. Diao, R. Jain, E.R. Rene, S. Dutta, Adsorption of Cadmium from Aqueous Solutions onto Coffee Grounds and Wheat Straw : Equilibrium and Kinetic Study, *J. Environ. Eng.* 142 (2016) 1–6, [https://doi.org/10.1061/\(ASCE\)EE.1943-7870.0001015](https://doi.org/10.1061/(ASCE)EE.1943-7870.0001015).
- [65] F. Zhang, B. Ma, X. Jiang, Y. Ji, Dual function magnetic hydroxyapatite nanopowder for removal of malachite green and Congo red from aqueous solution, *Powder Technol.* 302 (2016) 207–214, <https://doi.org/10.1016/j.powtec.2016.08.044>.
- [66] H.S. AL-Shehri, E. Almudaifer, A.Q. Alorabi, H.S. Alanazi, A. S. Alkorbi, F.A. Alharthi, Effective adsorption of crystal violet from aqueous solutions with effective adsorbent: equilibrium, mechanism studies and modeling analysis, *Environ. Pollut.* Bioavailab. 33 (2021) 214–226, <https://doi.org/10.1080/26395940.2021.1960199>.
- [67] M.A. Ahmad, N.A. Ahmad Puad, O.S. Bello, Kinetic, equilibrium and thermodynamic studies of synthetic dye removal using pomegranate peel activated carbon prepared by microwave-induced KOH activation, *Water Resour. Ind.* 6 (2014) 18–35, <https://doi.org/10.1016/j.wri.2014.06.002>.
- [68] A.T. Ojedokun, O.S. Bello, Kinetic modeling of liquid-phase adsorption of Congo red dye using guava leaf-based activated carbon, *Appl. Water Sci.* 7 (2017) 1965–1977, <https://doi.org/10.1007/s13201-015-0375-y>.
- [69] M.V. Subbaiah, D.S. Kim, Adsorption of methyl orange from aqueous solution by aminated pumpkin seed powder: Kinetics, isotherms, and thermodynamic studies, *Ecotoxicol. Environ. Saf.* 128 (2016) 109–117, <https://doi.org/10.1016/j.ecoenv.2016.02.016>.
- [70] M. Solgi, T. Najib, S. Ahmadnejad, B. Nasernejad, Synthesis and characterization of novel activated carbon from Medlar seed for chromium removal: Experimental analysis and modeling with artificial neural network and support vector regression, *Resour. Technol.* 3 (2017) 236–248, <https://doi.org/10.1016/j.refit.2017.08.003>.
- [71] M. Dolatabadi, M. Mehrabpour, M. Esfandyari, H. Alidadi, M. Davoudi, Modeling of simultaneous adsorption of dye and metal ion by sawdust from aqueous solution using of ANN and ANFIS, *Chemom. Intell. Lab. Syst.* 181 (2018) 72–78, <https://doi.org/10.1016/j.chemolab.2018.07.012>.
- [72] D.L.T. Nguyen, Q.A. Binh, X.C. Nguyen, T.T. Huyen Nguyen, Q.N. Vo, T.D. Nguyen, T.C. Phuong Tran, T.A. Hang Nguyen, S.Y. Kim, T.P. Nguyen, J. Bae, I.T. Kim, Q. Van Le, Metal salt-modified biochars derived from agro-waste for effective congo red dye removal, *Environ. Res.* 200 (2021), <https://doi.org/10.1016/j.envres.2021.111492> 111492.



Short communication

## Role of Ag and g-C<sub>3</sub>N<sub>4</sub> over CaTiO<sub>3</sub> for effective photocatalytic degradation of nitrobenzene

Akshima Soni<sup>a</sup>, Saurav Mishra<sup>b</sup>, Dipti Vaya<sup>a,\*</sup>, Praveen K. Surolia<sup>b,\*</sup><sup>a</sup> Department of Chemistry, Amity School of Applied Sciences, Gurugram, Haryana, India<sup>b</sup> Solar Energy Conversion and Nanomaterials Laboratory, Department of Chemistry, Manipal University Jaipur, Jaipur 303007, Rajasthan, India

## ARTICLE INFO

## Keywords:

Photocatalysis  
Degradation  
Ag/g-C<sub>3</sub>N<sub>4</sub>/CaTiO<sub>3</sub>  
CaTiO<sub>3</sub>, g-C<sub>3</sub>N<sub>4</sub>  
Nitrobenzene

## ABSTRACT

In the present study, g-C<sub>3</sub>N<sub>4</sub>/CaTiO<sub>3</sub> (GCT) heterostructure with various Ag contents have been synthesized via simple hydrothermal method and characterized using various instrumental techniques. Stability of synthesized samples was measured by thermogravimetric analysis (TGA) and zeta potential measurement. The photocatalytic activity of all the synthesized was evaluated by the degradation of nitrobenzene (NB) in aqueous media. The photocatalytic activity of heterostructure AGCT was observed enhanced under the light irradiation. This would be attributed to the suitable band structure, resulting in the efficient charge separation and transfer of photo-generated charge carriers. The final percentage of degradation was observed 70% with AGCT5 and 64% with AGCT1 which were highest among other catalysts applied after 2 h. The Ag doping in CT catalyst led to antagonist performance, and to better degradation of NB. The multivalency of Ag leads to prevent agglomeration and recombination of electrons and holes and transferring them from Ag to Ca. The reaction rate ( $2.36 \times 10^{-3} \text{ molL}^{-1} \text{ min}^{-1}$  at 20 °C) and percentage degradation (~70%) were observed to get increased with the increase in the temperature with the apparent activation energy of 40.3 kJ/mol. The enhanced performance at increased temperature was attributed to overcome the energy of activation and high mobility of charge carriers.

### 1. Introduction

Exponential increase in water pollution has attracted the attention all over the world. For the sack of development, ample quantity of wastewater is released from industries without proper pre-treatment. Thus, a balance in clean water supply and management is a must requirement in current scenario. Various inorganic and organic materials are released from industries such as dyes, pesticides, antibiotics, phenol, nitrobenzene etc. The regular exposure to nitrobenzene can reduce the oxygen carrying capacity of blood to body organs and tissues. This can cause many serious health problems, from dizziness to respiratory distress, called methemoglobinemia. The change in skin colour to blue is a key indicator of this disease [1–5]. Many water treatment technologies have been adopted to treat the wastewater and photocatalysis is one of the prominent fields to handle this situation [6,7].

CaTiO<sub>3</sub> (CT) is a member of perovskite material and one of the conventional photocatalyst. It offers combinations of high ionic conductivity, good ferroelectric, excellent photoluminescent, and unique dielectric polarization [8]. CT belong to metal titanate compounds with a perovskite structure that has attracted attention in fundamental and

applied research fields [9]. The novel structure of these functional materials makes them a suitable candidate for a wide range of optical and electrical applications [10]. Similarly, graphitic carbon nitride (g-C<sub>3</sub>N<sub>4</sub>) is also utilized not only as photocatalyst but also as supporting material [11]. It is a two-dimensional polymeric semiconductor with a bandgap of around 2.7 eV, which is considered as a prominent photocatalyst for the degradation of organic pollutant. g-C<sub>3</sub>N<sub>4</sub> exhibit good chemical stability and unique optical and electronic properties. In addition, it can be prepared from the low-cost nitrogen-rich compound by simple heat treatment process [12]. It was observed that conventional photocatalysts such as TiO<sub>2</sub>, ZnO, Fe<sub>2</sub>O<sub>3</sub>, SnO<sub>2</sub> CaTiO<sub>3</sub> etc. were modified and make heterostructure with another semiconductor to enhance their photocatalytic performance [13–16]. Further, it was found that CT and g-C<sub>3</sub>N<sub>4</sub> have well-matched overlapping band structures, suitable for the construction of heterostructures which favour high photocatalytic performance [17]. Owing to the polymeric nature of g-C<sub>3</sub>N<sub>4</sub>, its surface chemistry can be modified by surface engineering without obviously altering the theoretical composition [18]. The composite of the g-C<sub>3</sub>N<sub>4</sub> with a semiconductor such as CaTiO<sub>3</sub> could reduce the bandgap of the semiconductor which may shift the activity of the photocatalyst in

\* Corresponding authors.

E-mail addresses: [diptivaya08@gmail.com](mailto:diptivaya08@gmail.com) (D. Vaya), [praveenkumar.surolia@jaipur.manipal.edu](mailto:praveenkumar.surolia@jaipur.manipal.edu) (P.K. Surolia).<https://doi.org/10.1016/j.inoche.2023.111862>

Received 11 October 2023; Received in revised form 28 November 2023; Accepted 8 December 2023

Available online 12 December 2023

1387-7003/© 2023 Elsevier B.V. All rights reserved.

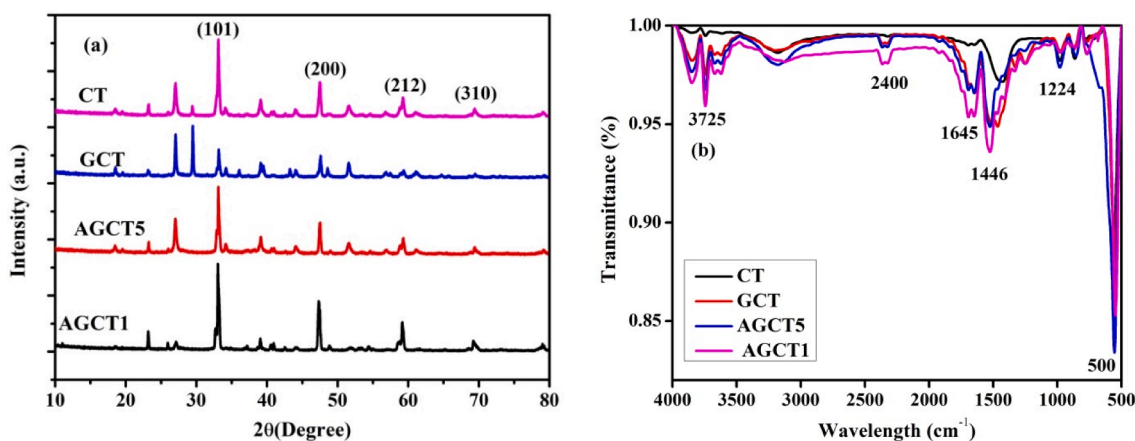


Fig. 1. (a) P-XRD and (b) FTIR spectra of the synthesized photocatalysts.

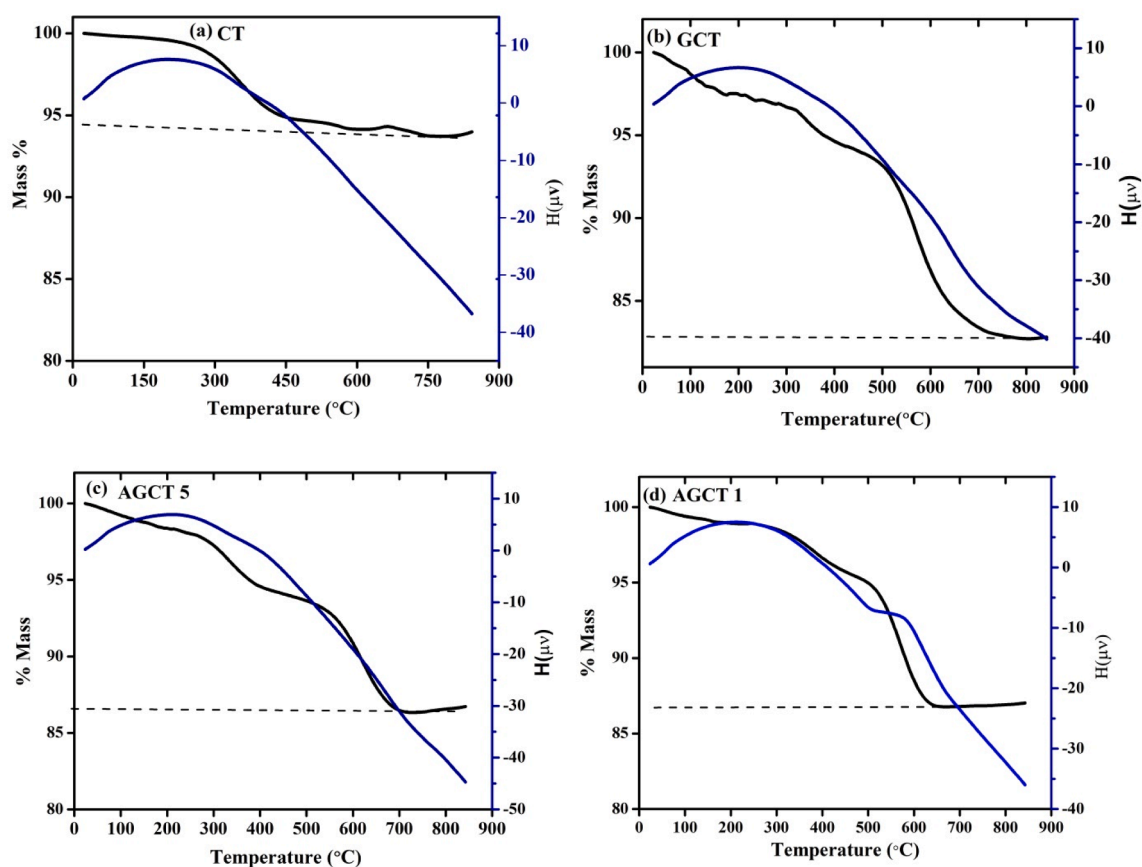


Fig. 2. TGA and DTA spectra of the synthesized photocatalysts.

visible region [11]. Different studies conducted with the combination of  $g\text{-C}_3\text{N}_4/\text{CT}$  (GCT) revealed that nanocomposite exhibit superior activity as compared to its counterpart [19,20]. To increase further performance of these nanocomposites, metal and non-metal doping were reported in literature [8,21,22]. Several authors have reported that introduction of  $\text{Ag}^+$  ions in semiconductor can generate the intrinsic defects in the host that usefully modify the photocatalytic properties of semiconductor [13,23,24]. Ag leads to a red-shift and increases its photocatalytic efficiency in the visible-light region. Since Ag metal is a good conductor, it can act as a sink for free electrons and increases the separation rates of photo-induced electron-hole pairs.

In this work, we have synthesized ternary  $\text{Ag}/g\text{C}_3\text{N}_4/\text{CaTiO}_3$

nanocomposites and their photocatalytic activity was studied for the degradation of model organic pollutant nitrobenzene (NB). A kinetic study was applied to all the reaction performed and results were analysed in terms of final degradation, initial rate of reaction and rate constant. The results demonstrated that the photocatalytic activity of ternary composite was superior to the other combination tried. Further, thermodynamic study was also conducted with the best performing ternary nanocomposite. As per our best knowledge, Ag incorporated  $\text{Ag}/g\text{C}_3\text{N}_4/\text{CaTiO}_3$  nanocomposites has not been reported so far for the photocatalytic degradation to remove organic pollutants in water.

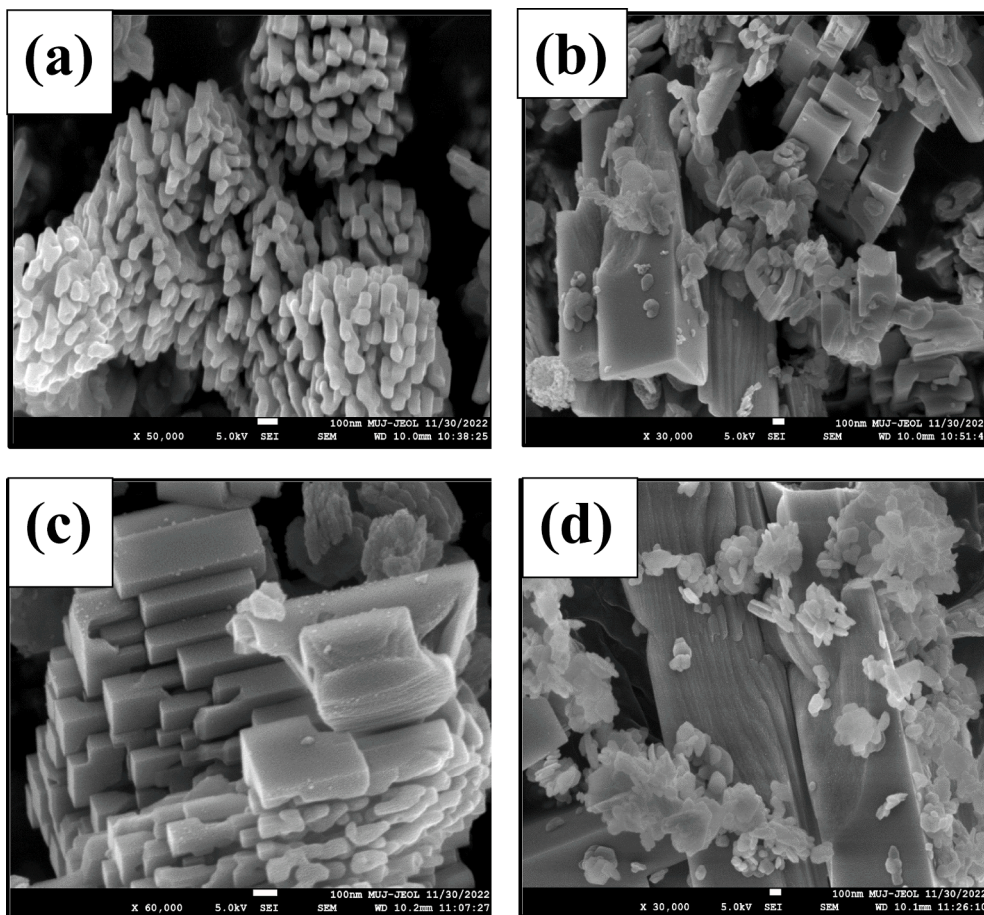


Fig. 3. SEM Images of (a) CT, (b) GCT, (c) AGCT5, (d) AGCT1 samples.

## 2. Experimental

### 2.1. Materials and synthesis of the catalysts

CaTiO<sub>3</sub> (CT), g-C<sub>3</sub>N<sub>4</sub>/CaTiO<sub>3</sub> (GCT) heterostructure and Ag/g-C<sub>3</sub>N<sub>4</sub>/CaTiO<sub>3</sub> (AGCT) nanocomposite were synthesized and applied as photocatalysts. The detailed synthesis method and materials used are reported in the [supporting information S.1–S.4](#).

### 2.2. Catalyst characterization

The prepared catalysts were characterized using different analysis techniques such as XRD, FESEM, DRS, FT-IR, TGA, and UV-Visible analysis was done to measure the progress of degradation reaction. The details are provided in [supporting information \(Section S.5\)](#).

### 2.3. Photocatalytic activity set-up

The photocatalytic reactor equipped with 500 mL reaction vessel and a 450-Watt power mercury lamp manufactured and supplied by the 'Lelesil Innovation Systems, India' was used to investigate photocatalytic properties of all synthesized samples. The reactor was consisting of two parts. The inner part was made of double-wall jacket quartz with the facility to place the lamp at the centre of it and a water inlet–outlet facility to maintain the temperature throughout the reaction progress [25]. The outer part was made of 500 mL capacity borosilicate glass. The 50 mg photocatalyst was spread in 500 mL of 25 ppm NB solution. Afterwards, the samples were magnetically stirred for 30 min in the dark condition to determine the adsorption–desorption equilibrium. After that 5 mL of sample was taken at every 10 min for first hour,

and finally one sample at 90 min. All the reactions were performed with similar conditions.

## 3. Results and discussion

### 3.1. X-ray diffraction analysis

Fig. 1 depicts powder X-ray diffraction (PXRD) patterns for all prepared samples. The PXRD pattern showed a single-phase orthorhombic structure of CT. The corresponding planes were (101), (200), (212) and (310), confirmed with JCPDS card No. 78-2480 with having unit cell parameters as  $a = 5.377$ ,  $b = 5.358$  and  $c = 7.586$  Å and that were calculated using the formula  $d = a/(h^2 + k^2 + l^2)$  [26].

Addition of g-C<sub>3</sub>N<sub>4</sub> caused in the shift in the composite peaks. Diffraction peak was not seen due to the low amount of g-C<sub>3</sub>N<sub>4</sub>. After silver doping no additional plane could be seen that might be due to its low concentration. The crystallite size of nanoparticles was calculated using Debye Scherrer Equation (1).

$$D = k\lambda/\beta\cos\theta \quad (1)$$

where  $D$  = crystalline size (nm),  $K = 0.9$  (Scherrer constant),  $\lambda = 0.15406$  nm (wavelength of the X-ray source),  $\beta$  = FWHM (radians),  $\theta$  = Peak position (radian).

The crystalline size of CT, GCT, AGCT5 and AGCT1 was calculated as 26.31, 47.03, 23.63, 24.87 nm, respectively. It was observed that the particle size decreased with increase in the dopant concentration [27].



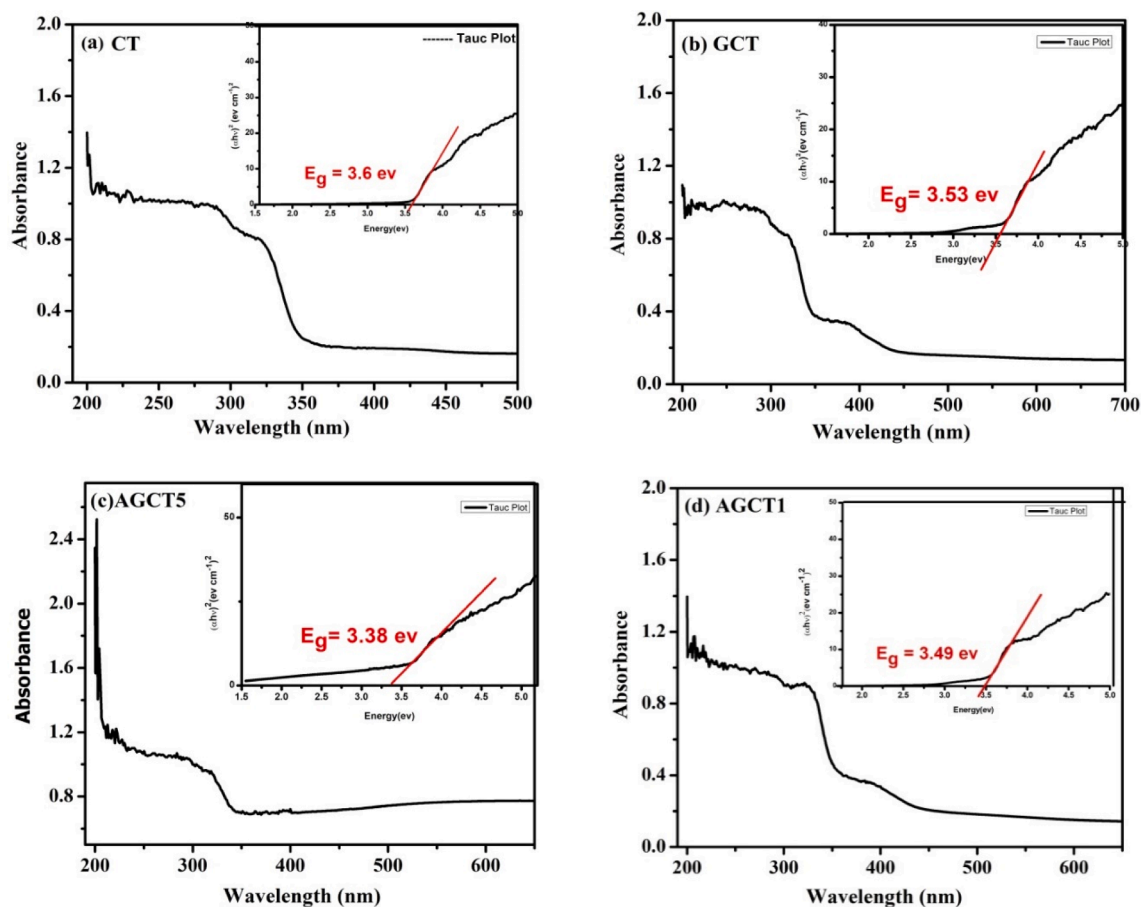


Fig. 4. Tauc plot and bandgap energy of (a) CT, (b) GCT, (c) AGCT5 (d) AGCT1.

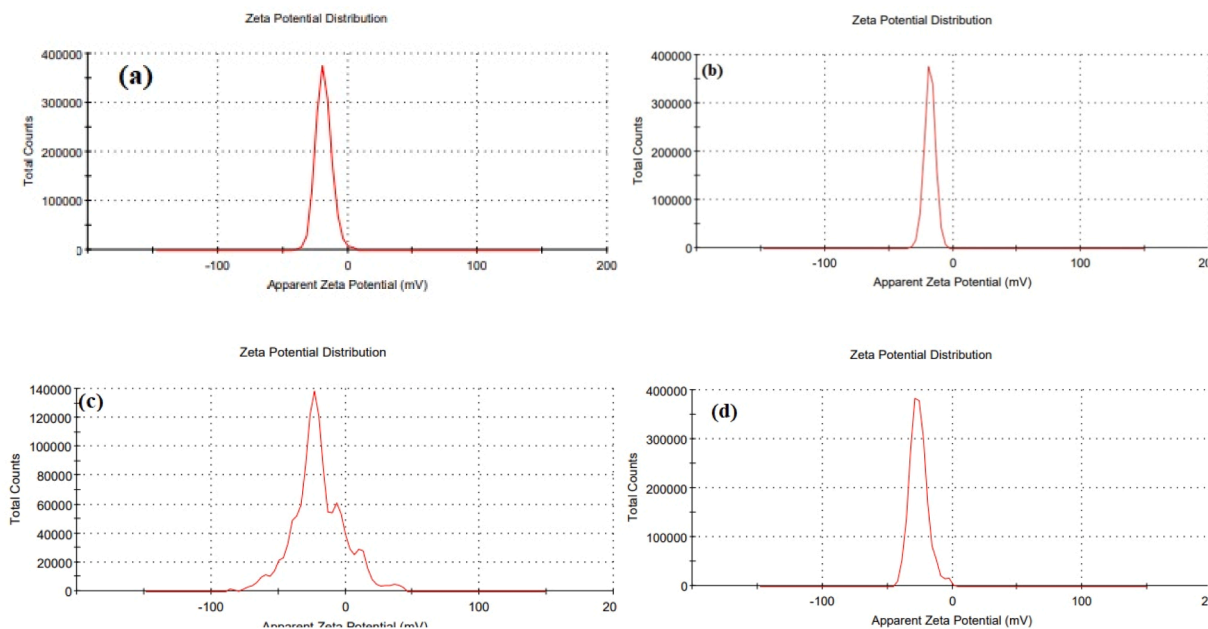


Fig. 5. Zeta potential of (a) CT, (b) GCT, (c) AGCT5 and (d) AGCT1 photocatalysts.

### 3.2. Fourier transform infrared spectra (FTIR) analysis

Fig. 1 (b) displays the FTIR spectra of CT, GCT, and AGCT heterostructures. The characteristic bands of  $g\text{-C}_3\text{N}_4$  and CT were found in the

FTIR spectra of GCT [28]. The strong peak at  $1446\text{ cm}^{-1}$  is assigned to the bending vibration of the O–H bond (OH), due to the formation of the Ca–Ti–O–H layer. The peak at  $3725\text{ cm}^{-1}$  is ascribed in GCT and AGCT whereas it is not observed in CT due to N–H or  $\text{NH}_2$  stretching. The peak

**Table 1**

Electronic and kinetic properties of all the photocatalytic materials for NB degradation.

Catalyst	Bandgap (eV)	% degradation	Initial rate $\times 10^{-3}$ [mol/L min <sup>-1</sup> ]	Rate constant $\times 10^{-3}$ [min <sup>-1</sup> ]	R <sup>2</sup>
Blank	–	38.8	1.10	2.6	0.97
CT	3.6	60.9	2.62	5.0	0.95
GCT	3.53	55.7	2.56	4.4	0.95
AGCT5	3.38	70.0	2.36	5.6	0.99
AGCT1	3.49	64.3	2.36	5.3	0.98

at 1224 cm<sup>-1</sup> is ascribed in CT, GCT and AGCT due to C–OH stretching. The peak at 1645 cm<sup>-1</sup> is not observed in CT while GCT shows a bit broader peak as compared to silver doped sample due to C=N stretching [29]. The prominent peak at 500 cm<sup>-1</sup> is present in all samples due to Ti–O stretching vibration.

### 3.3. Thermogravimetric analysis (TGA) and differential thermal analysis (DTA)

The spectra of all samples CT, GCT, AGCT5 and AGCT1 are displayed in Fig. 2. Three steps of weight loss in TGA were observed in all samples except CT. First weight loss from 50 to 350 °C was due to the moisture loss and removal of water content, second weight loss from 350 to 600 °C was due to the degradation of functional groups such as hydroxyl, nitride etc and then finally in third stage weight loss represent degradation of carbon chain in smaller fragments from 600 to 850 °C [26]. Two steps degradation was observed with CT. First step is removal of moisture, and second stage is removal of functional groups. However, total weight loss % in CT was 6%, GCT 18% while AGCT 5 and AGCT1 13%. This data favour that thermal stability increases by addition of silver doping in GCT. Different concentration of silver doping show nearly same thermal stability.

### 3.4. Scanning electron microscopy (SEM) analysis

The particle size and surface morphology of all the synthesized samples were studied using SEM as shown in Fig. 3 (a–d). The agglomeration was seen due to the smaller particle size of CT in Fig. 3 (a). With addition of g-C<sub>3</sub>N<sub>4</sub>, rod like morphology was seen, which is clearly visible in 4 (b) and in this case CT is scattered over surface. In Fig. 3 (c) and 3 (d), there is no visible difference in the images. Silver nanoparticles have spherical morphology and distribute over the complete surface. AGCT1 and AGCT5 nanoparticles were agglomerated and

there was high interconnectivity among grains [30].

### 3.5. UV – Vis spectroscopy (DRS) analysis

The Optical properties of the samples were analysed using UV–Vis diffuse reflectance spectroscopy, and the bandgap of the samples were determined from the Tauc plots (Fig. 4) [31]. The DRS of CT showed an absorption edge at around 300–330 nm and second absorption edge at around 330–350 nm respectively and the band gap (E<sub>g</sub>) calculated of CT was 3.6 eV. The absorption edge of GCT heterostructures was observed to be in between 330–350 nm and the bandgap calculated was 3.53 eV, g-C<sub>3</sub>N<sub>4</sub> might be act as a sensitizer, thus the CT heterostructures showed absorption ability towards red end of spectrum. Similarly, bandgaps of AGCT5, AGCT1 calculated were 3.38, 3.49 eV respectively (see Fig. 4).

### 3.6. Zeta potential study

Zeta potential was measured to check stability of nanomaterials in dispersion (see Fig. 5). In this work, water was used as dispersing solvent. The values of zeta potential measured were –18.4, –18, –19.2, –25.8 mV for CT, GCT, AGCT5 and AGCT1 respectively. The zeta potential from +30 to –30 mV showed stability in the dispersed systems [32]. It can be clearly seen that silver doped samples AGCT5 and AGCT1 showed higher dispersion stability in water and that can be seen in their effective photocatalytic performance as well.

## 4. Photocatalytic activity and kinetics of nitrobenzene degradation

The photocatalytic degradation study of the synthesized catalysts was conducted for the degradation of NB solution and results are provided in Table 1. A 500 mL 25 ppm solution of NB was taken in the photochemical reactor and a catalyst dose of 50 mg was used in all the performed experiments. The initial rate of degradation was calculated at a time 10 min of the reaction and the final degradation was reported at

**Table 2**

Electronic and kinetic properties of Ag/g-C<sub>3</sub>N<sub>4</sub>/CaTiO<sub>3</sub> for NB degradation at different temperature.

Temperature	% Degradation	Initial rate $\times 10^{-3}$ [molL <sup>-1</sup> min <sup>-1</sup> ]	Rate constant $\times 10^{-3}$ [min <sup>-1</sup> ]	R <sup>2</sup>
5 °C	39.4	0.85	2.3	0.99
10 °C	51.1	1.25	3.6	0.99
15 °C	63.9	2.21	5.2	0.97
20 °C	70.4	2.36	5.6	0.98

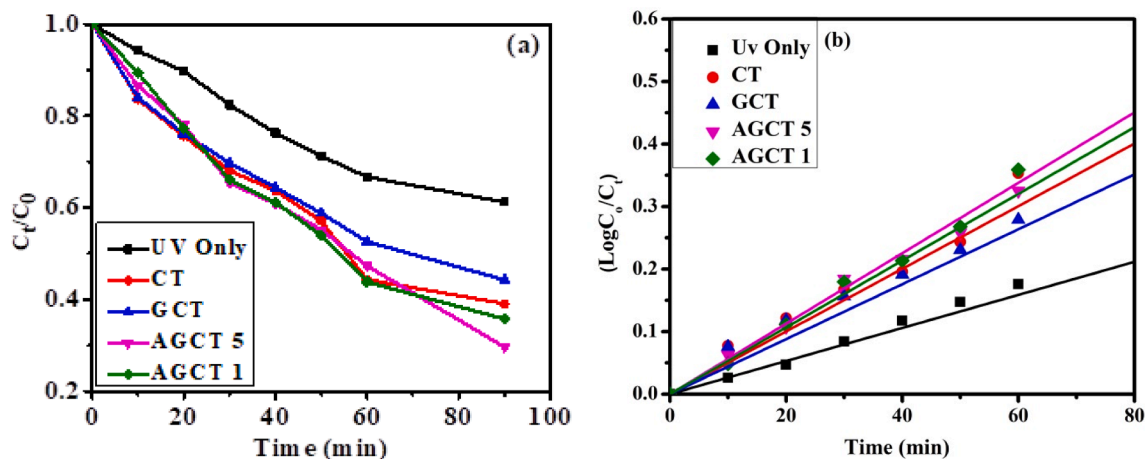


**Fig. 6.** (a) Increase in % degradation of nitrobenzene as a function of irradiation time, and (b) kinetics of nitrobenzene degradation [NB = 500 mL, 25 ppm; Catalyst: 50 mg; Reaction time: 90 min].

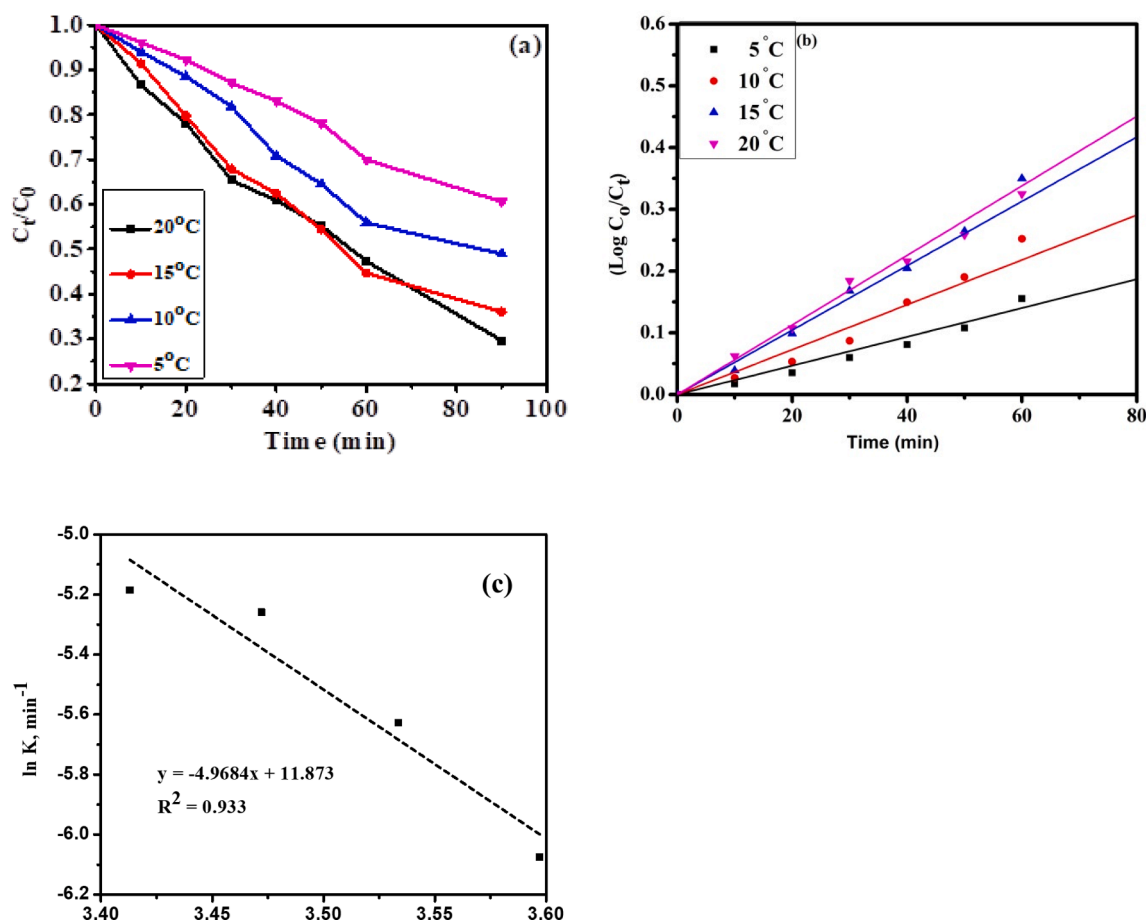


Fig. 7. Kinetics of nitrobenzene degradation with AGCT5 (a) Increase in % degradation of as a function of irradiation time at different temperature, (b) kinetics of Nitrobenzene degradation at different temperature (c) the plot of natural logarithm of rate constant,  $\ln(k)$  as a function of reciprocal temperature ( $1/T$ ).

Table 3

Comparison of synthesized Ag/g- $C_3N_4$ /CaTiO<sub>3</sub> nanocomposite catalyst with other similar kind of photocatalysts.

S. No	Photocatalyst	Application	Efficiency	Ref.
1.	Silver decorated ZnO nanocomposite with sulfurized graphitic carbon nitride	Photodegradation of MB	98%	[35]
2.	$C_3N_4$ @porphyrin nanorods hybrid material	Photodegradation of MB	100%	[36]
3.	g- $C_3N_4$ /SrTiO <sub>3</sub>	Photocatalytic degradation of reactive blue 198 (RB 198), reactive black 5 (RB 5) and reactive yellow 145 (RY 145)	50%	[12]
4.	CaTiO <sub>3</sub> /g- $C_3N_4$ /AgBr	Degradation of RhB	99.6%	[20]
5.	TiO <sub>2</sub> /ZrO <sub>2</sub> /g- $C_3N_4$	Degradation of berberine hydrochloride	86%	[37]
6.	Ag/g- $C_3N_4$ /NaTaO <sub>3</sub>	Degradation of tetracycline	95.47%	[38]
7.	Ag/g- $C_3N_4$ /CaTiO <sub>3</sub> nanocomposite	Photodegradation of nitrobenzene	70%	This Work

90 min. The final percentage of degradation was observed 70% with AGCT5 and 64.2% with AGCT1 which were highest among other catalyst applied after 90 min. Pristine CT showed 60.9% and GCT 55.7% degradation in the similar time. For a comparison, a blank study was also conducted without any catalyst and 34.7% degradation was observed

after 90 min. This clearly shows the role of catalyst in the photocatalytic degradation process. The final percentage degradation was observed in the range of 34 to 70% for all the reaction performed. The initial rate of reactions was almost in similar range of  $2.36 \times 10^{-3}$  to  $2.62 \times 10^{-3} \text{ molL}^{-1}\text{min}^{-1}$ . These values were very high compared to blank reaction without any catalyst ( $1.10 \times 10^{-3} \text{ molL}^{-1}\text{min}^{-1}$ ). Comparison of photocatalytic performance of CT, GCT, AGCT5, AGCT1 validates that the AGCT5 expressed the higher extent of photocatalytic performance compared to other applied photocatalysts. Further, it could be seen that the addition of Ag content increased the photocatalytic performance. The Ag dopant possesses the multivalency which leads to prevent agglomeration and recombination of electrons and holes and transferring them from Ag to Ca. Thus, we may conclude that the Ag doping in CT catalyst leads to antagonist performance, and to better degradation of NB (Table 1). Kinetics in Fig. 6 (a) shows that the degradation pattern of NB follow pseudo-first order kinetics, where the rate of degradation reaction “r” is proportional to the concentration  $C_t$  at time “t” (Eq. (2)) [33].

$$r = kK C_t \div 1 + K C_t \quad (2)$$

where  $k$  is the reaction rate constant, and  $K$  is the reactant adsorption constant. The apparent first order linear expression is expressed in Fig. 6. The calculated apparent  $R^2$  values of linearity are specified in Table 1. Further, the best performing catalyst AGCT5 was tested at four different reaction temperatures viz. 5, 10, 15 and 20 °C. The results are shown in Table 2. The reaction rate and percentage degradation were observed to get increased with the increase in the temperature. The minimum degradation was just 39.4% at 5 °C and highest 70.4% at 20 °C. The initial rate of reaction and rate constant values also followed the similar

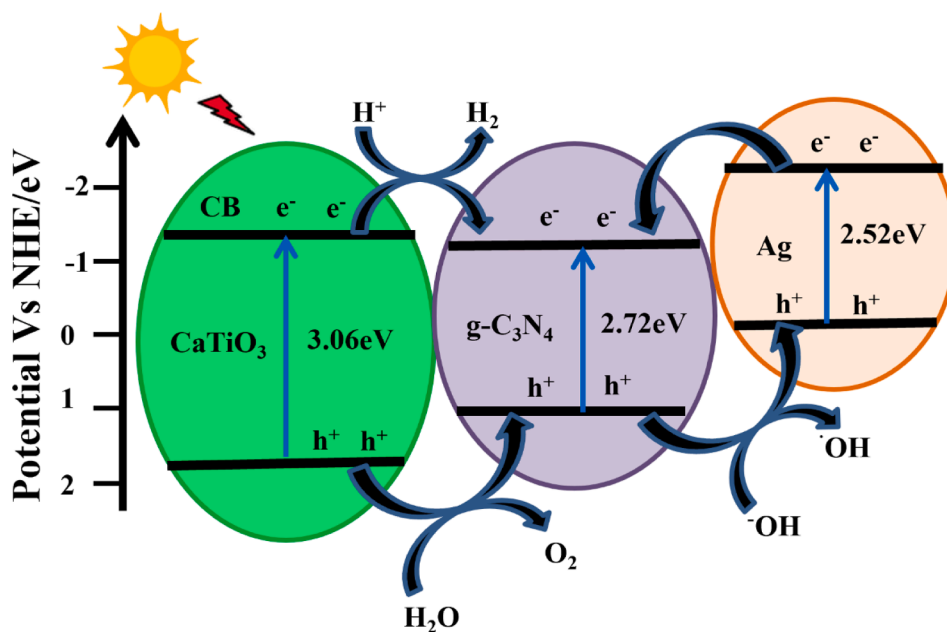


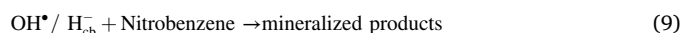
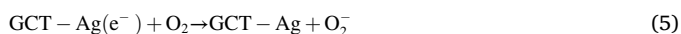
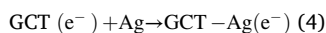
Fig. 8. Proposed process of charge separation in Ag/g-C<sub>3</sub>N<sub>4</sub>/CaTiO<sub>3</sub> photocatalyst.

trend. The minimum initial rate of reaction was observed  $0.85 \times 10^{-3} \text{ molL}^{-1} \text{ min}^{-1}$  at 5 °C and highest  $2.36 \times 10^{-3}$  at 20 °C  $\text{molL}^{-1} \text{ min}^{-1}$ .

The temperature influences primarily to the energy of activation and helps to overcome that. Thus, the oxidation of organic pollutants occurs at higher rate at high reaction temperature conditions [34]. Further, at increased temperature, charge carrier species become more active and shows higher mobility. Photogenerated charged species  $e^-$  and  $h^+$  react with adsorbed oxygen and  $\text{OH}^-$  at greater speed and improve the degradation capacity of the catalyst. However, previous studies reported that photocatalytic activity may get reduced if the temperature is increased after an optimum level. That happens due to more recombination of charge carriers. In this study, we observed an increasing pattern of performance with increase in temperature as reaction temperature applied was 20 °C and below. Fig. 7 (C) demonstrates the plot of natural logarithm of rate constant  $\ln(k)$  as a function of reciprocal temperature ( $1/T$ ). The slope of the plot relates to the apparent activation energy ( $E_a$ ) of the overall reaction, expressed in kilojoules per mole ( $\text{kJ mol}^{-1}$ ). The calculated value for the overall apparent activation energy of the NB degradation process from the data of Table 2 was found to be 41.3 kJ/mol. This value is much higher than the previously reported studies where the activation energy of photocatalytic degradation of NB with P25 was to be around 22 kJ/mol [34]. The Comparative literature of synthesized Ag/g-C<sub>3</sub>N<sub>4</sub>/CaTiO<sub>3</sub> nanocomposite photocatalyst with other similar kind of catalysts is given in Table 3.

## 5. Mechanism approach nitrobenzene degradation

Photocatalytic degradation of organic materials in water can be explained by bandgap model of semiconductors. Semiconductors are composed by band framework, where valence band (VB) and conduction band (CB) are separated with an energy gap ( $E_g$ ). Based on experimental data received, the photocatalytic process and its mechanistic approaches are proposed. The proposed mechanism of NB degradation using metal doped CT is given from Eqs. (3)–(9).



Firstly, synthesized GCT photocatalyst take a photon with energy higher or equal to its band gap and generate  $e^-/h^+$  charge carrier in CB and VB respectively as Eq. (3). These  $e^-$  transfer from GCT to Ag. Further, these  $e^-$  and  $h^+$  react with the reactive oxygen species  $\text{O}_2$  and  $\text{H}_2\text{O}$  to generate superoxide anion ( $\text{O}_2^-$ ), hydroxyl radical ( $\text{OH}^\bullet$ ) and  $\text{H}_2\text{O}_2$  as shown in Equation 5–7. These strong oxidative species that is reactive oxygen species (ROS) further oxidize NB and other organic fragments adsorbed on the photocatalyst, finally convert to the mineralized product  $\text{CO}_2$ ,  $\text{H}_2\text{O}$  and  $\text{NH}_4^+$  as in Eq. (9) [39,40]. The involvement of these major reactive species can be confirmed by application of suitable scavengers during the process [41]. As shown by Fig. 8, bandgap of all CT, g-C<sub>3</sub>N<sub>4</sub> and Ag are suitable for electron and hole transport, and this leads to minimise electron hole recombination which is more suitable for photocatalysis of pollutants.

## 6. Conclusion

In summary, Ag/g-C<sub>3</sub>N<sub>4</sub>/CaTiO<sub>3</sub> (AGCT) heterostructure photocatalysts were synthesized. Compared with bare CT nanoparticles, the photocatalytic activity of AGCT heterostructures was improved for the degradation of nitrobenzene under sunlight irradiation. The enhanced photocatalytic activity of AGCT heterostructure photocatalysts could be ascribed to the formation of heterojunction between CT and g-C<sub>3</sub>N<sub>4</sub>. The Final percentage of degradation was observed 70 % with AGCT5 and 64 % with AGCT1 which were highest among other catalyst applied after 2 h. The final percentage degradation was observed in the range of 34–70 % for all the reaction performed because silver nanoparticle has proven to exhibit excellent electrical conductivity, chemical stability, and catalytic properties. The presence of silver nanoparticles on the surface of GCT can facilitate catalytic reaction by providing active sites for adsorption and reaction. This enhanced catalytic activity makes silver-doped GCT potentially useful for the application such as catalytic

converter for water purification. From the result it was concluded that the doped material increased the efficiency of the catalyst as compared to the without doped material.

### Consent to participate

Not applicable.

### Consent to publish

Not applicable.

### Ethical approval

Not applicable for this work.

### CRedit authorship contribution statement

**Akshima Soni:** Data curation, Investigation, Writing – original draft.  
**Saurav Mishra:** Formal analysis. **Dipti Vaya:** . **Praveen K. Surolia:** .

### Declaration of Competing Interest

The authors declare that they have no known competing financial interests or personal relationships that could have appeared to influence the work reported in this paper.

### Data availability

The data used and/or analysed during the present study are available from the corresponding author on request.

### Acknowledgements

All Authors are thankful to Amity university, Haryana, 'Central Analytical Facilities (CAF)' and 'Sophisticated Analytical Instrument Facility (SAIF)' at Manipal University Jaipur for providing the materials characterization facility and support. DV acknowledges the support provided under the DST-FIST Grant No. SR/FST/PS-I/2018/48 of Govt. of India. PKS acknowledge funding support from Science and Engineering Research Board (SERB), India, under the Grant No. [CRG/2021/002477-G].

### Appendix A. Supplementary material

Supplementary data to this article can be found online at <https://doi.org/10.1016/j.inoche.2023.111862>.

### References

- [1] P.K. Arora, H. Bae, Toxicity and microbial degradation of nitrobenzene, monochloronitrobenzenes, polynitrobenzenes, and pentachloronitrobenzene, *J. Chem.* 2014 (2014), 265140, <https://doi.org/10.1155/2014/265140>.
- [2] R. Emmanuel, C. Karupiah, S.-M. Chen, S. Palanisamy, S. Padmavathy, P. Prakash, Green synthesis of gold nanoparticles for trace level detection of a hazardous pollutant (nitrobenzene) causing Methemoglobinemia, *J. Hazard. Mater.* 279 (2014) 117–124, <https://doi.org/10.1016/j.jhazmat.2014.06.066>.
- [3] S. Majeed, H.M. Junaid, M.T. Waseem, T. Mahmood, U. Farooq, S.A. Shahzad, Receptor free fluorescent and colorimetric sensors for solution and vapor phase detection of hazardous pollutant nitrobenzene; a new structural approach to design AIEE active and piezofluorochromic sensors, *J. Photochem. Photobiol. A Chem.* 431 (2022), 114022, <https://doi.org/10.1016/j.jphotochem.2022.114022>.
- [4] S. Mishra, N. Chakinala, A.G. Chakinala, P.K. Surolia, Photocatalytic performance of Bi/Zn co-doped sol-gel synthesized TiO<sub>2</sub> nanoparticles, *J. Chem. Technol. Biotechnol. n/a (n.d.)*. <<https://doi.org/https://doi.org/10.1002/jctb.7555>>.
- [5] S. Mishra, N. Chakinala, A.G. Chakinala, P.K. Surolia, Photocatalytic degradation of methylene blue using monometallic and bimetallic Bi-Fe doped TiO<sub>2</sub>, *Catal. Commun.* 171 (2022), 106518, <https://doi.org/10.1016/j.catcom.2022.106518>.
- [6] N. Verma, T.S. Chundawat, H. Chandra, D. Vaya, An efficient time reductive photocatalytic degradation of carcinogenic dyes by TiO<sub>2</sub>-GO nanocomposite, *Mater. Res. Bull.* 158 (2023), 112043, <https://doi.org/10.1016/j.materresbull.2022.112043>.
- [7] R. Yadav, T.S. Chundawat, P.K. Surolia, D. Vaya, Photocatalytic degradation of ortho-nitrophenol using ZnO-β-CD nanocomposite, *ChemistrySelect* 7 (2022) e202200394.
- [8] H. Zhang, G. Chen, Y. Li, Y. Teng, Electronic structure and photocatalytic properties of copper-doped CaTiO<sub>3</sub>, *Int. J. Hydrogen Energy.* 35 (2010) 2713–2716, <https://doi.org/10.1016/j.ijhydene.2009.04.050>.
- [9] H. Wang, Q. Zhang, M. Qiu, B. Hu, Synthesis and application of perovskite-based photocatalysts in environmental remediation: a review, *J. Mol. Liq.* 334 (2021), 116029, <https://doi.org/10.1016/j.molliq.2021.116029>.
- [10] P. Kanhere, Z. Chen, A review on visible light active perovskite-based photocatalysts, *Molecules* 19 (2014) 19995–20022, <https://doi.org/10.3390/molecules191219995>.
- [11] D. Vaya, B. Kaushik, P.K. Surolia, Recent advances in graphitic carbon nitride semiconductor: structure, synthesis and applications, *Mater. Sci. Semicond. Process.* 137 (2022), 106181, <https://doi.org/10.1016/j.mssp.2021.106181>.
- [12] T. Sureshkumar, S. Thiripuranthagan, S.M.K. Paskalis, S. Kumaravel, K. Kannan, A. Devarajan, Synthesis, characterization and photodegradation activity of graphitic C<sub>3</sub>N<sub>4</sub>-SrTiO<sub>3</sub> nanocomposites, *J. Photochem. Photobiol. A Chem.* 356 (2018) 425–439, <https://doi.org/10.1016/j.jphotochem.2018.01.027>.
- [13] D. Gogoi, A. Namdeo, A.K. Golder, N.R. Peela, Ag-doped TiO<sub>2</sub> photocatalysts with effective charge transfer for highly efficient hydrogen production through water splitting, *Int. J. Hydrogen Energy.* 45 (2020) 2729–2744, <https://doi.org/10.1016/j.ijhydene.2019.11.127>.
- [14] J. Tao, M. Zhang, X. Gao, H. Zhao, Z. Ren, D. Li, J. Li, R. Zhang, Y. Liu, Y. Zhai, Photocatalyst Co<sub>3</sub>O<sub>4</sub>/red phosphorus for efficient degradation of malachite green under visible light irradiation, *Mater. Chem. Phys.* 240 (2020), 122185, <https://doi.org/10.1016/j.matchemphys.2019.122185>.
- [15] X.J. Huang, X. Yan, H.Y. Wu, Y. Fang, Y.H. Min, W.S. Li, S.Y. Wang, Z.J. Wu, Preparation of Zr-doped CaTiO<sub>3</sub> with enhanced charge separation efficiency and photocatalytic activity, *Trans. Nonferr. Metals Soc. China (English Ed.)*. 26 (2016) 464–471, [https://doi.org/10.1016/S1003-6326\(16\)64097-9](https://doi.org/10.1016/S1003-6326(16)64097-9).
- [16] Y. Zhang, M. Sillanpää, Chapter 5 – modification of photocatalyst with enhanced photocatalytic activity for water treatment, in: M. Sillanpää (Ed.), *Advanced Water Treatment*, Elsevier, 2020, pp. 289–366. <<https://doi.org/https://doi.org/10.1016/B978-0-12-819225-2.00005-3>>.
- [17] A. Kumar, C. Schuerings, S. Kumar, A. Kumar, V. Krishnan, Perovskite-structured CaTiO<sub>3</sub> coupled with g-C<sub>3</sub>N<sub>4</sub> as a heterojunction photocatalyst for organic pollutant degradation, *Beilstein J. Nanotechnol.* 9 (2018) 671–685, <https://doi.org/10.3762/bjnano.9.62>.
- [18] W. Zhang, J. Zhang, F. Dong, Y. Zhang, Facile synthesis of in situ phosphorus-doped g-C<sub>3</sub>N<sub>4</sub> with enhanced visible light photocatalytic property for NO purification, *RSC Adv.* 6 (2016) 88085–88089, <https://doi.org/10.1039/C6RA18349B>.
- [19] J. Zhao, X. Cao, Y. Bai, J. Chen, C. Zhang, Simple synthesis of CaTiO<sub>3</sub>/g-C<sub>3</sub>N<sub>4</sub> heterojunction for efficient photodegradation of methylene blue and levofloxacin, *Opt. Mater. (Amst.)* 135 (2023), 113239, <https://doi.org/10.1016/j.optmat.2022.113239>.
- [20] Y. Yan, H. Yang, Z. Yi, R. Li, T. Xian, Design of ternary CaTiO<sub>3</sub>/g-C<sub>3</sub>N<sub>4</sub>/AgBr Z-scheme heterostructured photocatalysts and their application for dye photodegradation, *Solid State Sci.* 100 (2020), 106102, <https://doi.org/10.1016/j.solidstatesciences.2019.106102>.
- [21] C.W. Chang, C. Hu, Graphene oxide-derived carbon-doped SrTiO<sub>3</sub> for highly efficient photocatalytic degradation of organic pollutants under visible light irradiation, *Chem. Eng. J.* 383 (2020), 123116, <https://doi.org/10.1016/j.cej.2019.123116>.
- [22] P. Akhter, A. Arshad, A. Saleem, M. Hussain, Recent development in non-metal-doped titanium dioxide photocatalysts for different dyes degradation and the study of their strategic factors: a review, *Catalysts* 12 (2022) 1331, <https://doi.org/10.3390/catal12111331>.
- [23] S. Krejčíková, L. Matějová, K. Kočí, L. Obalová, Z. Matěj, L. Čapek, O. Šolcová, Preparation and characterization of Ag-doped crystalline titania for photocatalysis applications, *Appl. Catal. B.* 111–112 (2012) 119–125, <https://doi.org/10.1016/j.apcatb.2011.09.024>.
- [24] S.P. Onkani, P.N. Diagboya, F.M. Mtunzi, M.J. Klink, B.I. Olu-Owolabi, V. Pakade, Comparative study of the photocatalytic degradation of 2-chlorophenol under UV irradiation using pristine and Ag-doped species of TiO<sub>2</sub>, ZnO and ZnS photocatalysts, *J. Environ. Manage.* 260 (2020), 110145, <https://doi.org/10.1016/j.jenvman.2020.110145>.
- [25] S. Preeti, N. Mishra, A.G. Chakinala, P.K. Chakinala, Surolia, Bimetallic Bi/Zn decorated hydrothermally synthesized TiO<sub>2</sub> for efficient photocatalytic degradation of nitrobenzene, *Catal. Commun.* 172 (2022), 106538, <https://doi.org/10.1016/j.catcom.2022.106538>.
- [26] V. Lalan, V.P.M. Pillai, K.G. Gopchandran, Enhanced electron transfer due to rGO makes Ag e CaTiO<sub>3</sub> @ rGO a promising plasmonic photocatalyst, *J. Sci.: Adv. Mater. Devices* 7 (2022), 100468, <https://doi.org/10.1016/j.jsamd.2022.100468>.
- [27] M. Karimipour, S. Khazraei, B.J. Kim, G. Boschloo, E.M.J. Johansson, Efficient and bending durable flexible perovskite solar cells via interface modification using a combination of thin MoS<sub>2</sub> nanosheets and molecules binding to the perovskite, *Nano Energy* 95 (2022), 107044, <https://doi.org/10.1016/j.nanoen.2022.107044>.
- [28] S. Kappadan, S. Thomas, N. Kalarikkal, Enhanced photocatalytic performance of BaTiO<sub>3</sub>/g-C<sub>3</sub>N<sub>4</sub> heterojunction for the degradation of organic pollutants, *Chem. Phys. Lett.* 771 (2021), 138513, <https://doi.org/10.1016/j.cplett.2021.138513>.

- [29] T. Xian, H. Yang, L.J. Di, J.F. Dai, Enhanced photocatalytic activity of BaTiO<sub>3</sub>@g-C<sub>3</sub>N<sub>4</sub> for the degradation of methyl orange under simulated sunlight irradiation 622 (2015) 1098–1104. <<https://doi.org/10.1016/j.jallcom.2014.11.051>>.
- [30] B. Yang, C. Wu, J. Wang, J. Bian, L. Wang, M. Liu, Y. Du, When C<sub>3</sub>N<sub>4</sub> meets BaTiO<sub>3</sub>: ferroelectric polarization plays a critical role in building a better photocatalyst, *Ceram. Int.* 46 (2020) 4248–4255, <https://doi.org/10.1016/j.ceramint.2019.10.145>.
- [31] S.K.K. Aung, A. Vijayan, M. Karimipour, T. Seetawan, G. Boschloo, Reduced hysteresis and enhanced air stability of low-temperature processed carbon-based perovskite solar cells by surface modification, *Electrochim. Acta.* 443 (2023), 141935, <https://doi.org/10.1016/j.electacta.2023.141935>.
- [32] R.P. Singh, K. Sharma, K. Mausam, Dispersion and stability of metal oxide nanoparticles in aqueous suspension: a review, *Mater Today Proc.* 26 (2020) 2021–2025, <https://doi.org/10.1016/j.matpr.2020.02.439>.
- [33] P.K. Surolia, R.V. Jasra, Photocatalytic degradation of p-nitrotoluene (PNT) using TiO<sub>2</sub>-modified silver-exchanged NaY zeolite: kinetic study and identification of mineralization pathway, *Desal. Water Treat.* 57 (2016) 22081–22098, <https://doi.org/10.1080/19443994.2015.1125798>.
- [34] X. Shen, L. Zhu, N. Wang, T. Zhang, H. Tang, Selective photocatalytic degradation of nitrobenzene facilitated by molecular imprinting with a transition state analog, *Catal. Today.* 225 (2014) 164–170, <https://doi.org/10.1016/j.cattod.2013.07.011>.
- [35] S. Iqbal, A. Bahadur, S. Ali, Z. Ahmad, M. Javed, R.M. Irfan, N. Ahmad, M. A. Qamar, G. Liu, M.B. Akbar, M. Nawaz, Critical role of the heterojunction interface of silver decorated ZnO nanocomposite with sulfurized graphitic carbon nitride heterostructure materials for photocatalytic applications, *J. Alloys Compd.* 858 (2021), 158338, <https://doi.org/10.1016/j.jallcom.2020.158338>.
- [36] Q.D. Ho, T.T. Le, G.T. Nguyen, D.H. Nguyen, H.H. Nguyen, H.T.T. Le, L.T.T. Chu, C. Van Tran, P.T.H. Nguyen, M.-J. Um, T.T. Nguyen, D.D. Nguyen, D.D. La, Fabrication of g-C<sub>3</sub>N<sub>4</sub>@porphyrin nanorods hybrid material via CTAB surfactant-assisted self-assembly for photocatalytic degradation of Cr(VI) and methylene blue, *Nano-Struct. Nano-Obj.* 36 (2023), 101063, <https://doi.org/10.1016/j.nanos.2023.101063>.
- [37] P. Ding, H. Ji, P. Li, Q. Liu, Y. Wu, M. Guo, Z. Zhou, S. Gao, W. Xu, W. Liu, Q. Wang, S. Chen, Visible-light degradation of antibiotics catalyzed by titania/zirconia/graphitic carbon nitride ternary nanocomposites: a combined experimental and theoretical study, *Appl. Catal. B.* 300 (2022), 120633, <https://doi.org/10.1016/j.apcatb.2021.120633>.
- [38] L. Tang, C. Feng, Y. Deng, G. Zeng, J. Wang, Y. Liu, H. Feng, J. Wang, Enhanced photocatalytic activity of ternary Ag/g-C<sub>3</sub>N<sub>4</sub>/NaTaO<sub>3</sub> photocatalysts under wide spectrum light radiation: the high potential band protection mechanism, *Appl. Catal. B.* 230 (2018) 102–114, <https://doi.org/10.1016/j.apcatb.2018.02.031>.
- [39] P.K. Surolia, R.J. Tayade, R.V. Jasra, Photocatalytic degradation of nitrobenzene in an aqueous system by transition-metal-exchanged ETS-10 zeolites, *Ind. Eng. Chem. Res.* 49 (2010) 3961–3966, <https://doi.org/10.1021/ie901603k>.
- [40] P.K. Surolia, R.V. Jasra, Degradation and mineralization of aqueous nitrobenzene using ETS-4 photocatalysis, *Desalination, Water Treat.* 57 (2016) 15989–15998, <https://doi.org/10.1080/19443994.2015.1079801>.
- [41] R. Yadav, T.S. Chundawat, P.K. Surolia, D. Vaya, Photocatalytic degradation of textile dyes using β-CD-CuO/ZnO nanocomposite, *J. Phys. Chem. Solid* 165 (2022), 110691, <https://doi.org/10.1016/j.jpcs.2022.110691>.



**Rotary International President**  
Rtn Jennifer Jones

**District Governor**  
Rtn Dr Balwant Singh Chirana

**President**  
PHF Rtn Radhey Shyam Gupta  
D-13, Indra Puri Colony, Lal Kothi,  
Jaipur, Rajasthan 302015 (India)  
Mobile: +91-9414779184  
eMail: rsgupta9414@gmail.com

**Secretary**  
PHF Rtn Meeta Mathur  
G-2, Janpath, Shyam Nagar,  
Jaipur Rajasthan 302019 (India)  
Mobile: +91-9982659532  
eMail: alokmeeta@yahoo.com

**Treasurer**  
Rtn Brajesh Kumar Gupta  
D-28, Indra Puri Colony, Lal Kothi,  
Jaipur, Rajasthan 302015 (India)  
Mobile: +91-9829072271  
eMail: brajeshgupta24@gmail.com

**Club Patron**  
Maj Donor Rtn Dr Sudhir Kumar Calla

**President Elect (2024-25)**  
PHF Rtn CFP Shalini

**Immediate Past President**  
MPHF Rtn Er Narendra Mal Mathur

**Vice Presidents**  
MPHF Rtn Adv Ashok Goyal  
PHF Rtn Desh Deepak Goyal

**Jt. Secretary**  
Rtn Er Nand Kishore Maheshwari

**Director – Club Administration**  
PHF Rtn Rajendra Tiwari

**Director – Service Projects**  
Rtn Er Sudesh Roop Rai

**Director – Environment Service**  
Rtn Shyam Sunder Gupta

**Director – Foundation**  
MPHF Rtn Vipin Bahl

**Director – Literacy & T.E.A.C.H.**  
PHF Rtn Dr Arun Kumar Arya

**Director – Membership**  
PHF Rtn Jwala Prasad Sharma

**Director – Public Image & Fellowship**  
PHF Rtn Chander Mohan Mahajan

**Director – Publications**  
PHF Rtn Basant Jain

**Director – Youth Service**  
Rtn Prof Anil Dutt Vyas

**Executive Secretary - I.T.**  
PHF Rtn Prof Raj Kishor Pareek

**Club Trainer**  
MPHF Rtn Ravi Shanker Sharma

**Sergeant at Arms**  
PHF Rtn Er Satish Goyal

Date: 31 Oct 23

**TO WHOMSOEVER IS CONCERN**

Rotaract Club, Directorate of Students' Welfare along with Rotary Club Jaipur, Bapu Nagar conducted a Awareness on Environmental Protection at Dehmi Kalan Village by planting the 15 plants in village on 31<sup>st</sup> Oct 2023. It was a physical activity involving the students from NSS, DSW and the Rotaract Club MUJ. Event was well coordinated by the Department of Business Administration

We would like to appreciate Rotaract Club, Directorate of Students' Welfare, Manipal University Jaipur for the efforts and express our gratitude towards them.

Regards

Rtn Meeta Mathur  
**Secretary**

**Rotary International President**  
Rtn Jennifer Jones

**President**  
PHF Rtn **Radhey Shyam Gupta**  
D-13, Indra Puri Colony, Lal Kothi,  
Jaipur, Rajasthan 302015 (India)  
Mobile: +91-9414779184  
eMail: rsgupta9414@gmail.com

**Secretary**  
PHF Rtn **Meeta Mathur**  
G-2, Janpath, Shyam Nagar,  
Jaipur Rajasthan 302019 (India)  
Mobile: +91-9982659532  
eMail: alokmeeta@yahoo.com

**Treasurer**  
Rtn **Brajesh Kumar Gupta**  
D-28, Indra Puri Colony, Lal Kothi,  
Jaipur, Rajasthan 302015 (India)  
Mobile: +91-9829072271  
eMail: brajeshkgupta24@gmail.com

**Club Patron**  
Maj Donor Rtn Dr **Sudhir Kumar Calla**

**President Elect (2024-25)**  
PHF Rtn CFP **Shalini**

**Immediate Past President**  
MPHF Rtn Er **Narendra Mal Mathur**

**Vice Presidents**  
MPHF Rtn Adv **Ashok Goyal**  
PHF Rtn **Desh Deepak Goyal**

**Jt. Secretary**  
Rtn Er **Nand Kishore Maheshwari**

**Director – Club Administration**  
PHF Rtn **Rajendra Tiwari**

**Director – Service Projects**  
Rtn Er **Sudesh Roop Rai**

**Director – Environment Service**  
Rtn **Shyam Sunder Gupta**

**Director – Foundation**  
MPHF Rtn **Vipan Bahl**

**Director – Literacy & T.E.A.C.H.**  
PHF Rtn Dr **Arun Kumar Arya**

**Director – Membership**  
PHF Rtn **Jwala Prasad Sharma**

**Director – Public Image & Fellowship**  
PHF Rtn **Chander Mohan Mahajan**

**Director – Publications**  
PHF Rtn **Basant Jain**

**Director – Youth Service**  
Rtn Prof **Anil Dutt Vyas**

**Executive Secretary - I.T.**  
PHF Rtn Prof **Raj Kishor Pareek**

**Club Trainer**  
MPHF Rtn **Ravi Shanker Sharma**

**Sergeant at Arms**  
PHF Rtn Er **Satish Goyal**

Date: 02/10/23

### TO WHOMSOEVER IS CONCERN

Rotaract Club, Directorate of Students' Welfare along with Rotary Club Jaipur, Bapu Nagar conducted a Cleanliness Drive at Dehmi Kalan Village on 2<sup>nd</sup> October 2023. It was a physical activity which is the Swachhtha Abhiyan involving the students from NSS, DSW and the Rotaract Club MUJ.

We would like to appreciate Rotaract Club, Directorate of Students' Welfare, Manipal University Jaipur for the efforts and express our gratitude towards them.

Regards



Rtn Meeta Mathur  
**Secretary**



**Rotary International President**  
Rtn Jennifer Jones

**District Governor**  
Rtn Dr Balwant Singh Chirana

**President**  
PHF Rtn Radhey Shyam Gupta  
D-13, Indra Puri Colony, Lal Kothi,  
Jaipur, Rajasthan 302015 (India)  
Mobile: +91-9414779184  
eMail: rsgupta9414@gmail.com

**Secretary**  
PHF Rtn Meeta Mathur  
G-2, Janpath, Shyam Nagar,  
Jaipur Rajasthan 302019 (India)  
Mobile: +91-9982659532  
eMail: alokmeeta@yahoo.com

**Treasurer**  
Rtn Brajesh Kumar Gupta  
D-28, Indra Puri Colony, Lal Kothi,  
Jaipur, Rajasthan 302015 (India)  
Mobile: +91-9829072271  
eMail: brajeshgupta24@gmail.com

**Club Patron**  
Maj Donor Rtn Dr Sudhir Kumar Calla

**President Elect (2024-25)**  
PHF Rtn CFP Shalini

**Immediate Past President**  
MPHF Rtn Er Narendra Mal Mathur

**Vice Presidents**  
MPHF Rtn Adv Ashok Goyal  
PHF Rtn Desh Deepak Goyal

**Jt. Secretary**  
Rtn Er Nand Kishore Maheshwari

**Director – Club Administration**  
PHF Rtn Rajendra Tiwari

**Director – Service Projects**  
Rtn Er Sudesh Roop Rai

**Director – Environment Service**  
Rtn Shyam Sunder Gupta

**Director – Foundation**  
MPHF Rtn Vipana Bahl

**Director – Literacy & T.E.A.C.H.**  
PHF Rtn Dr Arun Kumar Arya

**Director – Membership**  
PHF Rtn Jwala Prasad Sharma

**Director – Public Image & Fellowship**  
PHF Rtn Chander Mohan Mahajan

**Director – Publications**  
PHF Rtn Basant Jain

**Director – Youth Service**  
Rtn Prof Anil Dutt Vyas

**Executive Secretary - I.T.**  
PHF Rtn Prof Raj Kishor Pareek

**Club Trainer**  
MPHF Rtn Ravi Shanker Sharma

**Sergeant at Arms**  
PHF Rtn Er Satish Goyal

Date: 03/10/23

### TO WHOMSOEVER IS CONCERN

Rotaract Club, Directorate of Students' Welfare along with Rotary Club Jaipur, Bapu Nagar conducted a Plantation Drive at Mahatma Gandhi Government School (English Medium), Begas on 3<sup>rd</sup> October 2023. It was a physical activity involving the students from NSS, DSW and the Rotaract Club MUJ.

We would like to appreciate Rotaract Club, Directorate of Students' Welfare, Manipal University Jaipur for the efforts and express our gratitude towards them.

Regards



Rtn Meeta Mathur  
**Secretary**



**Rotary International President**  
Rtn **Jennifer Jones**

**District Governor**  
Rtn Dr **Balwant Singh Chirana**

**President**  
PHF Rtn **Radhey Shyam Gupta**  
D-13, Indra Puri Colony, Lal Kothi,  
Jaipur, Rajasthan 302015 (India)  
Mobile: +91-9414779184  
eMail: rsgupta9414@gmail.com

**Secretary**  
PHF Rtn **Meeta Mathur**  
G-2, Janpath, Shyam Nagar,  
Jaipur Rajasthan 302019 (India)  
Mobile: +91-9982659532  
eMail: alokmeeta@yahoo.com

**Treasurer**  
Rtn **Brajesh Kumar Gupta**  
D-28, Indra Puri Colony, Lal Kothi,  
Jaipur, Rajasthan 302015 (India)  
Mobile: +91-9829072271  
eMail: brajeshgupta24@gmail.com

**Club Patron**  
Maj Donor Rtn Dr **Sudhir Kumar Calla**

**President Elect (2024-25)**  
PHF Rtn CFP **Shalini**

**Immediate Past President**  
MPHF Rtn Er **Narendra Mal Mathur**

**Vice Presidents**  
MPHF Rtn Adv **Ashok Goyal**  
PHF Rtn **Desh Deepak Goyal**

**Jt. Secretary**  
Rtn Er **Nand Kishore Maheshwari**

**Director – Club Administration**  
PHF Rtn **Rajendra Tiwari**

**Director – Service Projects**  
Rtn Er **Sudesh Roop Rai**

**Director – Environment Service**  
Rtn **Shyam Sunder Gupta**

**Director – Foundation**  
MPHF Rtn **Vipan Bahl**

**Director – Literacy & T.E.A.C.H.**  
PHF Rtn Dr **Arun Kumar Arya**

**Director – Membership**  
PHF Rtn **Jwala Prasad Sharma**

**Director – Public Image & Fellowship**  
PHF Rtn **Chander Mohan Mahajan**

**Director – Publications**  
PHF Rtn **Basant Jain**

**Director – Youth Service**  
Rtn Prof **Anil Dutt Vyas**

**Executive Secretary - I.T.**  
PHF Rtn Prof **Raj Kishor Pareek**

**Club Trainer**  
MPHF Rtn **Ravi Shanker Sharma**

**Sergeant at Arms**  
PHF Rtn Er **Satish Goyal**

Date: 26 Oct 23

**TO WHOMSOEVER IS CONCERN**

Dept of Chemistry and Rotaract Club, Directorate of Students' Welfare along with Rotary Club Jaipur, Bapu Nagar conducted Plantation Drive at Dadar ki Dhani Village. Event was well coordinated by the Department of Chemistry and DSW.

We would like to appreciate Rotaract Club, Directorate of Students' Welfare, Manipal University Jaipur for the efforts and express our gratitude towards them.

Regards

Rtn Meeta Mathur  
**Secretary**

**Rotary International President**  
Rtn Jennifer Jones

**District Governor**  
Rtn Dr Balwant Singh Chirana

**President**  
PHF Rtn Radhey Shyam Gupta  
D-13, Indra Puri Colony, Lal Kothi,  
Jaipur, Rajasthan 302015 (India)  
Mobile: +91-9414779184  
eMail: rsgupta9414@gmail.com

**Secretary**  
PHF Rtn Meeta Mathur  
G-2, Janpath, Shyam Nagar,  
Jaipur Rajasthan 302019 (India)  
Mobile: +91-9982659532  
eMail: alokmeeta@yahoo.com

**Treasurer**  
Rtn Brajesh Kumar Gupta  
D-28, Indra Puri Colony, Lal Kothi,  
Jaipur, Rajasthan 302015 (India)  
Mobile: +91-9829072271  
eMail: brajeshgupta24@gmail.com

**Club Patron**  
Maj Donor Rtn Dr Sudhir Kumar Calla

**President Elect (2024-25)**  
PHF Rtn CFP Shalini

**Immediate Past President**  
MPHF Rtn Er Narendra Mal Mathur

**Vice Presidents**  
MPHF Rtn Adv Ashok Goyal  
PHF Rtn Desh Deepak Goyal

**Jt. Secretary**  
Rtn Er Nand Kishore Maheshwari

**Director – Club Administration**  
PHF Rtn Rajendra Tiwari

**Director – Service Projects**  
Rtn Er Sudesh Roop Rai

**Director – Environment Service**  
Rtn Shyam Sunder Gupta

**Director – Foundation**  
MPHF Rtn Vipin Bahl

**Director – Literacy & T.E.A.C.H.**  
PHF Rtn Dr Arun Kumar Arya

**Director – Membership**  
PHF Rtn Jwala Prasad Sharma

**Director – Public Image & Fellowship**  
PHF Rtn Chander Mohan Mahajan

**Director – Publications**  
PHF Rtn Basant Jain

**Director – Youth Service**  
Rtn Prof Anil Dutt Vyas

**Executive Secretary - I.T.**  
PHF Rtn Prof Raj Kishor Pareek

**Club Trainer**  
MPHF Rtn Ravi Shanker Sharma

**Sergeant at Arms**  
PHF Rtn Er Satish Goyal

Date: 06/09/23

**TO WHOMSOEVER IS CONCERN**

Rotaract Club, Directorate of Students' Welfare along with Rotary Club Jaipur, Bapu Nagar conducted a Plantation Drive at Mahatma Gandhi Government School (English Medium), Begas on 6<sup>th</sup> September 2023. It was a physical activity involving the students from NSS, DSW and the Rotaract Club MUJ. Event was well coordinated, where more than 30 samplings of plants were planted in the schools.

We would like to appreciate Rotaract Club, Directorate of Students' Welfare, Manipal University Jaipur for the efforts and express our gratitude towards them.

Regards



Rtn Meeta Mathur  
**Secretary**



**Rotary International President**  
Rtn **Jennifer Jones**

**District Governor**  
Rtn Dr **Balwant Singh Chirana**

**President**  
PHF Rtn **Radhey Shyam Gupta**  
D-13, Indra Puri Colony, Lal Kothi,  
Jaipur, Rajasthan 302015 (India)  
Mobile: +91-9414779184  
eMail: rsgupta9414@gmail.com

**Secretary**  
PHF Rtn **Meeta Mathur**  
G-2, Janpath, Shyam Nagar,  
Jaipur Rajasthan 302019 (India)  
Mobile: +91-9982659532  
eMail: alokmeeta@yahoo.com

**Treasurer**  
Rtn **Brajesh Kumar Gupta**  
D-28, Indra Puri Colony, Lal Kothi,  
Jaipur, Rajasthan 302015 (India)  
Mobile: +91-9829072271  
eMail: brajeshgupta24@gmail.com

**Club Patron**  
Maj Donor Rtn Dr **Sudhir Kumar Calla**

**President Elect (2024-25)**  
PHF Rtn CFP **Shalini**

**Immediate Past President**  
MPHF Rtn Er **Narendra Mal Mathur**

**Vice Presidents**  
MPHF Rtn Adv **Ashok Goyal**  
PHF Rtn **Desh Deepak Goyal**

**Jt. Secretary**  
Rtn Er **Nand Kishore Maheshwari**

**Director – Club Administration**  
PHF Rtn **Rajendra Tiwari**

**Director – Service Projects**  
Rtn Er **Sudesh Roop Rai**

**Director – Environment Service**  
Rtn **Shyam Sunder Gupta**

**Director – Foundation**  
MPHF Rtn **Vipan Bahl**

**Director – Literacy & T.E.A.C.H.**  
PHF Rtn Dr **Arun Kumar Arya**

**Director – Membership**  
PHF Rtn **Jwala Prasad Sharma**

**Director – Public Image & Fellowship**  
PHF Rtn **Chander Mohan Mahajan**

**Director – Publications**  
PHF Rtn **Basant Jain**

**Director – Youth Service**  
Rtn Prof **Anil Dutt Vyas**

**Executive Secretary - I.T.**  
PHF Rtn Prof **Raj Kishor Pareek**

**Club Trainer**  
MPHF Rtn **Ravi Shanker Sharma**

**Sergeant at Arms**  
PHF Rtn Er **Satish Goyal**

Date: 26 Oct 23

**TO WHOMSOEVER IS CONCERN**

Dept of Chemistry and Rotaract Club, Directorate of Students' Welfare along with Rotary Club Jaipur, Bapu Nagar conducted Plantation Drive at Dadar ki Dhani Village. Event was well coordinated by the Department of Chemistry and DSW.

We would like to appreciate Rotaract Club, Directorate of Students' Welfare, Manipal University Jaipur for the efforts and express our gratitude towards them.

Regards

Rtn Meeta Mathur  
**Secretary**



**Rotary International President**  
Rtn Jennifer Jones

**District Governor**  
Rtn Dr Balwant Singh Chirana

**President**  
PHF Rtn Radhey Shyam Gupta  
D-13, Indra Puri Colony, Lal Kothi,  
Jaipur, Rajasthan 302015 (India)  
Mobile: +91-9414779184  
eMail: rsgupta9414@gmail.com

**Secretary**  
PHF Rtn Meeta Mathur  
G-2, Janpath, Shyam Nagar,  
Jaipur Rajasthan 302019 (India)  
Mobile: +91-9982659532  
eMail: alokmeeta@yahoo.com

**Treasurer**  
Rtn Brajesh Kumar Gupta  
D-28, Indra Puri Colony, Lal Kothi,  
Jaipur, Rajasthan 302015 (India)  
Mobile: +91-9829072271  
eMail: brajeshgupta24@gmail.com

**Club Patron**  
Maj Donor Rtn Dr Sudhir Kumar Calla

**President Elect (2024-25)**  
PHF Rtn CFP Shalini

**Immediate Past President**  
MPHF Rtn Er Narendra Mal Mathur

**Vice Presidents**  
MPHF Rtn Adv Ashok Goyal  
PHF Rtn Desh Deepak Goyal

**Jt. Secretary**  
Rtn Er Nand Kishore Maheshwari

**Director – Club Administration**  
PHF Rtn Rajendra Tiwari

**Director – Service Projects**  
Rtn Er Sudesh Roop Rai

**Director – Environment Service**  
Rtn Shyam Sunder Gupta

**Director – Foundation**  
MPHF Rtn Vipin Bahl

**Director – Literacy & T.E.A.C.H.**  
PHF Rtn Dr Arun Kumar Arya

**Director – Membership**  
PHF Rtn Jwala Prasad Sharma

**Director – Public Image & Fellowship**  
PHF Rtn Chander Mohan Mahajan

**Director – Publications**  
PHF Rtn Basant Jain

**Director – Youth Service**  
Rtn Prof Anil Dutt Vyas

**Executive Secretary - I.T.**  
PHF Rtn Prof Raj Kishor Pareek

**Club Trainer**  
MPHF Rtn Ravi Shanker Sharma

**Sergeant at Arms**  
PHF Rtn Er Satish Goyal

Date: 25 Oct 23

**TO WHOMSOEVER IS CONCERN**

Rotaract Club, Directorate of Students' Welfare along with Rotary Club Jaipur, Bapu Nagar conducted campaign on Swach Bharat Abhiyan on October 25 2023 at Dehmi Kalan. An awareness session is taken by Team MUJ physically involving the students from NSS, DSW and the Rotaract Club MUJ. Event was well coordinated by the Department of Business Administration.

We would like to appreciate Rotaract Club, Directorate of Students' Welfare, Manipal University Jaipur for the efforts and express our gratitude towards them.



Regards

Rtn Meeta Mathur  
**Secretary**



---

# 5E analysis of a novel designed hot water storage header integrated vacuum tube solar water heater

K. Chopra <sup>a d</sup>, V.V. Tyagi <sup>b</sup>  , Sudhir Kumar Pathak <sup>b</sup>, Ravi Kumar Sharma <sup>c</sup>,  
Muhamad Mansor <sup>d e</sup>, Varun Goel <sup>f</sup>, Ahmet Sari <sup>g h</sup>

Show more 

 Share  Cite

---

<https://doi.org/10.1016/j.tsep.2023.101929> 

[Get rights and content](#) 

---

## Highlights

- 5-E analysis of a novel designed hot water storage header integrated system.
- Thermal and exergy outputs of the system varied by 63–74% and 4–10% respectively.
- Hot water cost by designed & electric heater is 0.15 & 0.47 INR/L respectively.

## Abstract

In this study, 5-E analysis of a heat pipe equipped vacuum tube collector system for residential warm water application has been carried out. The issue of overheating in heat pipes and low thermal efficiency is the major key issues associated with heat pipe

vacuum tube collector. This design completely removes the problem of overheating. In addition to this copper fins mounting with condensers of heat pipe enhance the heat transmission rate between the condenser & water stored in a manifold. The results of an experimental investigation reveal that thermal and exergy outputs of the proposed system were obtained almost 63–74% and 4–10% respectively. The average energy gain at the end of the days selected for Run-A, B, and C was calculated to be 7505, 6912, and 6619kJ respectively, whereas the average exergy gain for corresponding runs was found to be 928, 700, and 401 kJ respectively. In addition to this, the proposed system can provide hot water of approximately 125 L, 76 L, and 52 L in temperatures 50°C, 55°C, and 60°C respectively.

Concerning to techno-economic investigation, the per liter cost of warm water generation for the proposed & electric geyser was observed to be 0.15 INR/L & 0.47 INR/L respectively. The levelized energy cost, net present worth, and payback time were found to be 5.48 INR/kWh, 55,819 INR, and 4.12years respectively. The amount of CO<sub>2</sub> mitigation by the developed system was found to be 18.76, 17.28, and 16.54 tCO<sub>2</sub>/lifetime for Run-A, B & C respectively.

---

## Introduction

In today's era, non-conventional energy sources utilization has increased rapidly because of the incessant exhaustion of conservative fuels. Among available renewable power sources, solar energy is quite fascinating and promising energy source due to its huge accessibility in maximum parts of the earth free of cost [1]. Solar energy is mainly harnessed in two forms: (i) solar energy is directly changed into electricity using a photovoltaic device (ii) solar energy is transformed into heat energy using thermal collectors [2], [3], [4]. Solar energy can be utilized in several applications like water/air heating, and crop drying. In all solar thermal applications, water heating is consuming a huge amount of conventional energy that will lead to a rise in greenhouse gas (GHG) emissions. Solar heat collectors, which are mostly utilized for water heating, are called solar water heaters. Generally, two types of collectors: vacuum tube collectors & flat plate collectors (FPCs) are utilized for hot water production [5], [6]. The ETCs are dominating the FPCs due to their higher thermal output in cold regions. Also, the convective heat losses are minimum in evacuated tube collectors. Currently, 80–85% of total installed solar collectors are ETCs. Moreover, the ETCs can warm the water to 90°C comparatively at a low cost. Thus, ETC is a promising technology, which can be implemented for hot water applications in fluctuating weather conditions [7], [8].

Nowadays, different designs of vacuum tube collectors are mainly utilized for hot water production. Among these, heat pipe-based vacuum tube collectors are the most efficient and advanced in technology because heat pipe is an efficient heat exchanger unit. Many

researchers have completed various studies on different designs of heat pipe-based vacuum tube collectors for hot water generation. Işka and Yldzba [9] designed a unique hot water collector tank with a novel finned-type cell construction. The performance of the newly developed tank was compared with a PCM-embedded nonfinned tank & a normal insulated tank. The outcomes reveal that the newly constructed tank's thermal energy storage ability is roughly 10% higher than the normal tank and, almost 4–5% more in comparison to a non-finned water tank. Khani et al. [10] evaluated that the integrated system's three-objective optimization decrease reduces environmental impacts, total costs, and monthly environmental emergency rate by 34.31%, 11.4%, and 6.38%, respectively. Nitsas and Koronaki [11] experimentally investigated U-Tube solar vacuum collector in terms of exergy efficiency, energy efficiency, and heat energy output. The results indicate that collector thermal efficiency was 60% and the system gained the highest heat energy output of 5.60kW at approximately noon. The authors observed the highest exergy gain when the temperature of the working fluid was highest. By utilizing a variety of heat-carrying fluids and variable flow rates, the thermal output of a heat pipe-equipped SWH was improved by Shafieian et al. [12]. The different cases, i.e., a flexible flow of nanofluid (Case-I), a fixed flow of nanofluid (Case-II), and a fixed flow of DI water (Case-III), all performed under similar climatic conditions. The exergy output of Cases I and II was found to be higher than Case III by 2.66% and 1.58%, respectively. Al-Joboory [13] performed experiments with two identical ET-SWHs. The first system employs thermosyphon; the second employs twenty wickless heat pipes filled with methanol (50%) as working fluid and serve as heat conductors from the collector to the storage tank. The test results found that the wickless heat pipe system outperforms the thermosyphon one in terms of overall daily efficiency by 22.5% for zero loads, 42.5% for fluctuating loads, and 32.4% for constant loads. The heat pipe based SWH was more suited to local domestic use because it produced higher temperatures and thermal output under all loads and adverse weather situations. Ozsoy and Corumlu [14] analyzed the energy output of a thermosyphon heat pipe (THP) based ETSC using nanofluid (silver-water) used in viable applications. It was discovered that the THP filled with nanofluid upheld its enhanced heat transmission ability. Nanofluid improved the collector efficiency by 20.7% to 40% more than water. The experiment's findings indicate that the THP ETSC can be marginally improved by using silver-water nanofluid. Maraj et al. [15] performed the energy study of a forced flow SWH with an HP-ETC (area of  $1.476\text{m}^2$ ) in Mediterranean environmental conditions. For a solar collection of 2,212 kWh/year, they determined that the yearly valuable heat gain of the HP-ETC, the valuable energy delivered to the storage tank by the collector, and the delivered energy to the heat consumer were 1,345, 1,311, and 1,009 kWh/year. The forced circulated system had an annual efficiency of 0.516 compared to the HP-ETC's 0.62. Jayanthi et al. [16] performed an experiment to determine the thermal output of a HP-ETSC using DI water and R134a as the heat transfer fluid. The impact of input variables on the thermal output of the



HPSC, such as temperature distribution and time, was looked into, compared, and discussed. The findings revealed that using R134a in place of distilled water increases the HPSC's thermal output. Chopra et al. [17] done the exergy, energy, and financial investigation of the vacuum collector based SWH system for the complex climate of Jammu (India). The system was designed and built for a six-person family. The tests were carried out for six flow rates of a fluid. The highest avg. energy and exergy outputs were 72% and 5.2%, at 20 LPH, while the lowest was 55% and 1.25% at 60 LPH. It was discovered that at 20 and 60 LPH, the max. and min. avg. outlet temperatures were 76.4 and 45 °C, respectively. It was discovered that the cost of producing hot water at the required temperature was 0.12, as opposed to 0.40 and 0.26 INR/L for electric and gas geysers, respectively. The return on investment of the SWH was 4 years, which is a much shorter period. Mehmood et al. [18] created a TRNSYS simulation prototype of an SWH system that uses evacuated tubes fitted with heat pipes and is hybridized with a backup of natural gas to deliver a continuous thermal energy supply. It was discovered that switching from a traditional (gas) water heater to a hybrid solar water heater could save 23% to 56% on backup fuel while also lowering greenhouse gas (GHG) emissions. The results revealed that the hybrid vacuum tubes-based SWH is more effective and eco-friendlier, with a benefit-cost ratio of 1.87, & would result in yearly natural gas savings of 8.79105 kWh, resulting in a reduction of 175.539 tCO<sub>2</sub> emissions. Bhowmik et al. [19] studied the thermal output of serpentine vacuum collector system for different tilt angles. They also validated the experimental results with outcomes obtained from computational fluid dynamics model. The results of CFD depicted that with increasing of diameter of U-Tube from 1/8–3/8" increased the net gain in temperature by 39%. They also concluded that twisted taped with square holes among the various considered geometries observed to be most effective in terms of thermal output in comparison to plain serpentine design. Kuang et al. [20] used convolutional Neural Network technique to forecast the thermal output of vacuum collector system on the basis of collected operational data over many days. Authors concluded that Back Propagation (BP) neural network model having high accuracy than Multiple Linear Regression model. Also Multiple Linear Regression model is not suggested to be used for the evaluation of the performance of vacuum tube collector system because of its inability to handle non-linear problem results in poor accuracy. Modabber and Manesh [21] found that by integrating of solar heating and inlet air cooling system with the existing cogeneration plant (generation of power with hot water), energy performance touch 68% and increase in exergy efficiency was 50%, also reduced the impact of environmental. Haghghi et al. [22] evaluated the thermal performance, environmental and economic aspects of flat plat collector integrated with conventional heating system (run on natural gas). The experimental results revealed that the maximum load of 91.05 and 37.52 kW in cold and warm days respectively can be accomplished by flat plat collector with area of 443.8 and 63.3 m<sup>2</sup> respectively. In addition to this, they determined that deployment of flat plat

collector reduced the carbon dioxide emission of 84.71 and 84.67kg/MWh in warm and cold seasons respectively.

In the present study, a 5-E analysis of the novel designed hot water storage header integrated vacuum tube solar water heater is carried out. On the basis of the previous research work in the concerned field, the authors find the uniqueness of the present work as:

- 6 In this study, the author has uniquely designed the water storage tank cum header of the heat pipe based vacuum collector. An integrated finned heat exchanger is placed inside the header/water tank to increase the rate of heat transfer due to the welding of copper fins over the condenser of the heat pipe.
- 6 Based on the literature studies related to solar water heaters (summarized in Table 1) the energy efficiency of the proposed system fluctuates in the range of 63–74% which is more efficient than the conventional heat pipe system whose thermal efficiency fluctuates in the range of 42–56% [23]. Also, the increment in the energy gain of the designed system fluctuates in the range of 32–50%, which is higher as compared to the increment in energy gain reported in previous studies (Tabulated in Table 1).
- 6 In most of the existing studies, exergy, energy, and heat transfer investigation of vacuum collector have been done. But these methods do not consider the economic and environmental aspects. The economic and environmental exploration clarifies whether utilization of the proposed system is feasible in terms of the environmental and economic points of view or not. These aspects of the analysis of the system are crucial to be considered during its sustainability analysis. Therefore, in this study along with energy and exergy investigation, enviroeconomic, economic, and exergoeconomic analysis is also carried out for the practical implementation of the proposed solar water heater.
- 6 In the current study, modification in the vacuum collector system reduces the issue of overheating, decreases the overall heat losses and the initial financial investment in the vacuum collector system.

---

## Access through your organization

Check access to the full text by signing in through your organization.

Access through your organization

## Section snippets

### Experimental setup & methodology

This section is divided into two sub-sections. Firstly, the design and development of the experiment setup were explained comprehensively. Secondly, the research methodology adopted to perform the experiments has been discussed. ...

### Thermodynamic, enviro-economic, and exergo-economic analysis

The present section is classified into three subsections namely energy and exergy analysis, enviroeconomic analysis, and exergoeconomic analysis. In the first subsection i.e. in section 3.1, the relations of energy and exergy investigation of designed and fabricated solar collector system has been given which is useful to access the quantitative and qualitative analysis of the designed system. In subsection 3.2, the equations which are useful to access the commercial viability of the designed ...

### Experimental error analysis

The uncertainty related to a specific observation is calculated using Holman's Eq. can be

$$\text{given as: } \delta U = \left[ \left( \frac{\partial U}{\partial x_1} \delta w_1 \right)^2 + \left( \frac{\partial U}{\partial x_2} \delta w_2 \right)^2 + \dots + \left( \frac{\partial U}{\partial x_n} \delta w_n \right)^2 \right]$$

Where  $i = 1, 2, \dots, n$  and  $U = U(x_1, x_2, \dots, x_n)$  are the independent variables, the dependent variable is  $x_i$ , and the independent variable's ambiguity is  $w_i$ . For instance, the error in temperature sensors is  $\pm 0.6^\circ\text{C}$ , whereas the solar power error is  $\pm 1.2\%$ , and the rotameter error is  $\pm 1.5\%$  of the standard deviation.

$$\delta \eta_O = \eta_O \times \sqrt{\left( \frac{\delta EN_{u,O}}{EN_{u,O}} \right)^2 + \left( \frac{\delta EN_{inc,O}}{EN_{inc,O}} \right)^2} \quad \delta \eta_{ex, O} = \eta_{ex, O} \times \sqrt{\left( \frac{\delta EX_{u,O}}{EX_{u,O}} \right)^2 + \left( \frac{\delta E}{E} \right)^2} \dots$$

### Result and discussion

The current section provides a compressive discussion of the results of different experiments. In this section, thermal analysis, thermodynamic analysis, financial analysis, enviroeconomic & exergoeconomic analysis of the proposed system for different runs have been presented and discussed. Section 5.1 discuss batch wise hot water temperature, ambient temperature & solar radiation variation with time, Section 5.2 deliberate energy and exergy efficiencies variation, Section 5.3 debate heat ...

## Conclusions

The current study provides a compressive discussion of the results of thermal performance analysis, thermodynamic analysis, financial analysis, enviroeconomic & exergoeconomic analysis of the proposed system for different runs. Based on the analysis following observations have been pointed out which are as:

- a) Integration of novel designed manifold with a vacuum tube collector completely removes the problem of overheating. ...
- b) The copper fins mounting with condensers of the heat pipe enhance the ...

...

## CRedit authorship contribution statement

**K. Chopra:** Conceptualization, Methodology, Writing – original draft, Writing – review & editing. **V.V. Tyagi:** Writing – review & editing, Supervision, Project administration.

**Sudhir Kumar Pathak:** Formal analysis, Writing – review & editing. **Ravi Kumar**

**Sharma:** Formal analysis. **Muhamad Mansor:** Writing – review & editing. **Varun Goel:**

Formal analysis. **Ahmet Sari:** Visualization, Writing – review & editing. ...

## Declaration of Competing Interest

The authors declare that they have no known competing financial interests or personal relationships that could have appeared to influence the work reported in this paper. ...

## Acknowledgments

- This work was supported by Tenaga Nasional Berhad (TNB) and UNITEN through the BOLD Refresh Postdoctoral Fellowships under the project code of J510050002-IC-6 BOLDREFRESH2025-Centre of Excellence. ...
- It was also supported by Shri Mata Vaishno Devi University, Katra (J&K) through the research project with unique ID RP-141 (Japan International Cooperation Agency Project for AUN/SEED-NET and the University of Malaya Malaysia). ...

...

## References (38)

G. Hekimoğlu *et al.*

**Thermal management performance and mechanical properties of a novel cementitious composite containing fly ash/lauric acid-myristic acid as form-stable phase change material**

Constr. Build. Mater. (2021)

S. Kumar Pathak *et al.*

**Recent development in thermal performance of solar water heating (SWH) systems**

Mater. Today Proc. (2022)

M.A. Essa *et al.*

**Experimental and Theoretical Analysis for the Performance of Evacuated Tube Collector Integrated with Helical Finned Heat Pipes using PCM Energy Storage**

Energy. (2020)

N.B. Ziyadanogullari *et al.*

**Thermal performance enhancement of flat-plate solar collectors by means of three different nanofluids**

Therm. Sci. Eng. Prog. (2018)

A.K. Pandey *et al.*

**Energy, exergy, exergoeconomic and enviroeconomic (4-E) assessment of solar water heater with/without phase change material for building and other applications: A comprehensive review**

Sustain. Energy Technol. Assessments. (2021)

S. Faisal Ahmed *et al.*

**Recent progress in solar water heaters and solar collectors: A comprehensive review**

Therm. Sci. Eng. Prog. (2021)

A. Shafieian *et al.*

**Strategies to improve the thermal performance of heat pipe solar collectors in solar systems: A review**

Energy Convers. Manag. (2019)

S. Işık *et al.*

## Improving thermal energy storage efficiency of solar collector tanks by placing phase change materials in novel finned-type cells

Therm. Sci. Eng. Prog. (2020)

N. Khani *et al.*

## Optimal 6E design of an integrated solar energy-driven polygeneration and CO<sub>2</sub> capture system: A machine learning approach

Therm. Sci. Eng. Prog. (2023)

M.T. Nitsas *et al.*

## Experimental and theoretical performance evaluation of evacuated tube collectors under mediterranean climate conditions

Therm. Sci. Eng. Prog. (2018)



[View more references](#)

### Cited by (6)

#### Solar thermal potential of phase change material based U-pipe ETSCs for different climatic zones: Evaluating energy matrices and economic viability

2024, Sustainable Materials and Technologies

[Show abstract](#) 

#### Entropy weighted WASPAS and MACBETH approaches for optimizing the performance of solar water heating system

2024, Case Studies in Thermal Engineering

*Citation Excerpt :*

...Different techniques are now widely employed in SWHS to improve the heat transfer rate from absorber tubes to flowing fluids [15–17]. In this regard, convective heat transfer proved to be most effective and is achieved by placing hindrance promoters (fins, coil springs, twisted tapes, helical spring tabulators, etc.) into the fluid's path that converts laminar to turbulent flow [18–21]. Sarma et al. [22] developed correlations for predicting the heat transfer coefficient and friction factors with twisted tapes in a tube for a wide range of Re and pitch-to-diameter ratios....

[Show abstract](#) 

#### Solar Water Heating System with Absorption Heat Transformer for Annual Continuous Water Heating

2024, Processes

## [Design consideration of a filled layer U-pipe evacuated tubular solar collector with flat diffuse reflector: energy and exergy analysis ↗](#)

2024, International Journal of Ambient Energy

## [Improving the Performance of Unglazed Solar Air Heating Walls Using Mesh Packing and Nano-Enhanced Absorber Coating: An Energy–Exergy and Environmental Economic Assessment ↗](#)

2023, Sustainability (Switzerland)

## [High Pressure Water Solar Collector as Potential of Mini Steam Power Plant in Iraq ↗](#)

2023, ISAS 2023 - 7th International Symposium on Innovative Approaches in Smart Technologies, Proceedings

---

[View full text](#)

© 2023 Published by Elsevier Ltd.



All content on this site: Copyright © 2024 Elsevier B.V., its licensors, and contributors. All rights are reserved, including those for text and data mining, AI training, and similar technologies. For all open access content, the Creative Commons licensing terms apply.



# Upconverted Nanophosphors for Increasing Efficiency in a Dye-Sensitized Solar Cell

Yogendra Nath Chouryal,<sup>#</sup> Rahul Kumar Sharma,<sup>#</sup> Neeraj Tomar, Neelam Yadav, Heera Lal Kewat, Ishfaq Abdullah Wani, Sandeep Nigam, Praveen Kumar Surolia,<sup>\*</sup> Sri Sivakumar, and Pushpal Ghosh<sup>\*</sup>



Cite This: <https://doi.org/10.1021/acsaem.3c00424>



Read Online

ACCESS |

Metrics & More

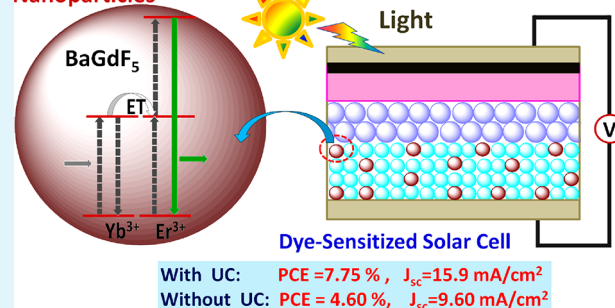
Article Recommendations

Supporting Information

**ABSTRACT:** Upconverting nanoparticles has a significant potential to enhance solar cell efficiency as a “spectral converter”. Here, we report a phase pure, cubic, upconverting BaGdF<sub>5</sub>:Er/Yb-doped nanocrystal accessible via ionic liquids that are combined with TiO<sub>2</sub> to apply as the absorption layer in a dye-sensitized solar cell (DSSC) as a potential technology to harvest solar energy. Bright-green (520 and 540 nm) and red (665 nm) emissions were observed due to transitions of <sup>2</sup>H<sub>11/2</sub> + <sup>4</sup>S<sub>3/2</sub> → <sup>4</sup>I<sub>15/2</sub> and <sup>4</sup>F<sub>9/2</sub> → <sup>4</sup>I<sub>15/2</sub>, respectively. The experimental data for 540 and 665 nm emission bands of BaGdF<sub>5</sub>:Er<sup>3+</sup>/Yb<sup>3+</sup> nanoparticles have been fitted with a straight line with a slope of ~2, which confirms the two-photon absorption process. It is also found that not only the overall upconversion intensity but also the I<sub>G</sub>/I<sub>R</sub> ratio has a significant effect on device efficiency. Under 1 sun illumination, cells fabricated with the BaGdF<sub>5</sub>:Er<sup>3+</sup>(1%)/Yb<sup>3+</sup>(10%)/TiO<sub>2</sub> absorption layer showed the highest photon conversion efficiency (PCE) of 7.75% with current density J<sub>sc</sub> = 15.9 mA/cm<sup>2</sup>. However, when only TiO<sub>2</sub> is used as the absorption layer, a much lesser PCE of 4.60% along with J<sub>sc</sub> = 9.6 mA/cm<sup>2</sup> is obtained. Almost a 68.47% enhancement in photon conversion efficiency and a significant increase in current density (J<sub>sc</sub>) (65.62%) for the BaGdF<sub>5</sub>:Er<sup>3+</sup>(1%)/Yb<sup>3+</sup>(10%)/TiO<sub>2</sub>-based device compared to the bare TiO<sub>2</sub> cells promise the potential use of upconverting materials as a spectral converter in the DSSC and other solar cell devices.

**KEYWORDS:** rare-earth ions, ionic liquid, upconversion, dye-sensitized solar cell, spectral converter

## IL ([C<sub>4</sub>mim][BF<sub>4</sub>])–Assisted Synthesized Upconverting (UC) Nanoparticles



## INTRODUCTION

The creation of sufficient “clean” energy is very important, both for an energy perspective and for the environment. As the population explosion is continuing through the last decade, consumption of conventional energy resources gradually increases, resulting in the release of greenhouse gases like CO<sub>2</sub> and others, which cause a hazardous effect on the flora and fauna.<sup>1–5</sup> To overcome these issues, several renewable sources are explored, among which solar energy is most prominent as abundant solar radiation reaches the earth’s surface. Approximately 120,000 TW solar powers are available due to the irradiation of sunlight on the earth’s surface.<sup>6</sup> However, one pertinent issue is how can we use maximum solar energy required for daily life? Previously, it was reported that not all the photons of the solar spectrum have the sufficient energy to match the band gap in a silicon solar cell, which absorb a maximum of 45% of all photons of the solar spectrum.<sup>7</sup> Therefore, it is utmost important to transform the sub-band gap photons into higher energy photons in a conventional solar cell to get the better efficiency.<sup>8,9</sup> In this regard, upconverting nanomaterials can play a major role as a “spectral converter”. In the upconversion process, photons

with lower energy near-infrared (NIR, higher wavelength) light are converted into higher energy (lower wavelength) ultra-violet (UV) or visible light photons.<sup>10–14</sup> As the photons of lower or lesser band gap energy are not absorbed by a solar cell, spectral mismatch occurs that results in the energy loss in the conversion of solar energy to electricity. By process upconversion, two sub-band gap photons can be converted into one photon of the optimum energy and may help to increase the solar cell efficiency. Such upconverting phosphor absorbs the transmitted sub-band gap photons by sequential ground state absorption/excited state absorption. By this, an excited state is generated in the upconverting phosphor from which photons are emitted, which can then be absorbed in the solar cell to generate electron–hole pairs.

**Received:** February 15, 2023

**Accepted:** April 3, 2023



Upconversion can work by doping of lanthanide ions ( $\text{Ln}^{3+}$ ) such as Yb, Er, Tm, and Ho in different host materials where  $\text{Yb}^{3+}$  ions can act as the sensitizer due to its high absorption cross section ( $10\text{--}20\text{ cm}^{-2}$  at around 980 nm), and  $\text{Er}^{3+}$ ,  $\text{Tm}^{3+}$ , and  $\text{Ho}^{3+}$  ions can work as an emitter or activator.<sup>15</sup> Upconversion efficiency may depend on some important factors like the host lattice, rare-earth ion doping concentration, and donor to acceptor ratio. One of the most promising upconverting materials is sodium ternary tetrafluoride.<sup>16,17</sup> Upconverted materials (UCM) are nowadays extensively used in various photonic and biophotonic applications like drug delivery.<sup>16,18–20</sup> However, their use in solar cell applications is still in its infancy. Ramasamy et al. reported various upconverting nanoparticles for solar cell applications.<sup>6</sup> Shang et al. reviewed enhancement in solar cell efficiency by using photon upconversion materials.<sup>21</sup> Shalav et al. explored the application of erbium-doped  $\text{NaYF}_4$  microcrystals as an upconverter in bifacial c-Si solar cells.<sup>22</sup> Fischer et al. also observed the potential use of erbium-doped  $\text{NaYF}_4$  microcrystals as an upconverter to improve the conversion performance of c-Si solar cells.<sup>7</sup> Liang and their co-workers reported core-shell-shell  $\text{NaYF}_4:\text{Yb}/\text{Er}@/\text{SiO}_2@/\text{TiO}_2$  microplates sandwiched between a counter electrode and a transparent  $\text{TiO}_2$  layer to take full advantage of the scattering and upconverting functions of the microplates, and approximately 30% efficiency enhancement in application for the dye-sensitized solar cell (DSSC) was observed.<sup>23</sup> Currently, DSSC technology plays a crucial role in the harvesting of solar energy to generate the electricity.<sup>24</sup>

Ionic liquid, which is considered as a “green and designer” solvent, can play a major role in nanomaterial synthesis due to its negligible vapor pressure, high viscosity, non-flammability, large electrochemical window, catalytic nature, etc.<sup>25–31</sup> In this article, we report the synthesis of upconverted rare-earth ion(s)-doped (i.e.,  $\text{RE}^{3+} = \text{Yb}^{3+}/\text{Er}^{3+}$ )  $\text{BaGdF}_5$  nanocrystals via the ionic liquid-assisted hydrothermal method where IL  $[\text{C}_4\text{mim}]\text{BF}_4$  can be used as a solvent, reaction partner (fluorinating agent), and templating agent/capping agent, i.e., “all three in one” (Figure 1) and details are given in the

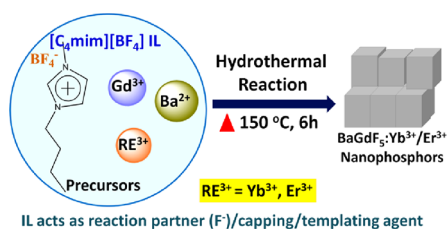


**Figure 1.** Synthesis of  $\text{BaGdF}_5:\text{Yb}^{3+}/\text{Er}^{3+}$  nanophosphors using the ionic liquid (IL)-assisted hydrothermal method.

**Supporting Information.** Analysis reveals that upconversion intensity is influenced by dopant concentrations, and finally, upconverted nanophosphors are used in device application for the DSSC. It is observed that when upconverted  $\text{BaGdF}_5:\text{Er}^{3+}/\text{Yb}^{3+}$  materials are combined with  $\text{TiO}_2$  to apply as the absorption layer in a dye-sensitized solar cell (DSSC), both the photon conversion efficiency (PCE) and current density ( $J_{sc}$ ) significantly increased compared to bare  $\text{TiO}_2$ -based cells. For example, a significant enhancement in PCE (68.47%) and current density (65.25%) for the  $\text{BaGdF}_5:\text{Er}^{3+}(1\%)/\text{Yb}^{3+}(10\%)/\text{TiO}_2$ -based device compared to the bare  $\text{TiO}_2$  cells is noticed. Of particular interest to our research program

is how the upconverted nanoparticle can be efficiently employed as a spectral converter to reduce the sub-band gap losses and enhance the efficiency in solar cells, especially in DSSCs in the present case.

## EXPERIMENTAL SECTION

Chemical details and synthesis of ionic liquids are mentioned in the [Supporting Information](#) file.

**Synthesis of  $\text{BaGdF}_5:\text{Er}^{3+}$  Nanocrystals.** A stoichiometric amount of barium acetate (0.327 g) and gadolinium nitrate hexahydrate (0.579 g) was taken in deionized (DI) water. In another beaker, erbium nitrate pentahydrate (0.0091 g) was taken in deionized (DI) water and mixed properly. After mixing them, a sufficient amount of  $[\text{C}_4\text{mim}]\text{BF}_4$  IL was added. The resultant solution was transferred into a Teflon-lined autoclave (Parr Instruments, Moline, Illinois, USA coated with a stainless-steel jacket) and heated at  $150\text{ }^\circ\text{C}$  for 6 h. Thereafter, the autoclave was cooled at room temperature in ambient conditions and the white product was separated by centrifugation (2000 rpm for 10 min). Then, the as-obtained product was washed with ethanol, methanol, and acetone to remove other impurities. Finally, the obtained white powder product was dried in a hot air oven for 12 h at  $80\text{ }^\circ\text{C}$  (Figure 1). Similar synthesis techniques with adequate dopant concentrations were used for the preparation of  $\text{BaGdF}_5:\text{Er}^{3+}(1\%)/\text{Yb}^{3+}(1\%)$ ,  $\text{BaGdF}_5:\text{Er}^{3+}(1\%)/\text{Yb}^{3+}(5\%)$ , and  $\text{BaGdF}_5:\text{Er}^{3+}(1\%)/\text{Yb}^{3+}(10\%)$ . In all these syntheses,  $[\text{C}_4\text{mim}]\text{BF}_4$  (IL) was used as a solvent, fluorinating agent ( $\text{F}^-$  source in all reactions), and templating agent/capping agent, i.e., as a three in one (Figure 1). Similar methodology was adopted for the synthesis of pure  $\text{BaGdF}_5$  without addition of dopant ions and is mentioned in the [Supporting Information](#).

**DSSC Fabrication and Assembly: Overview of Dye-Sensitized Solar Cell (DSSC) Application.** DSSC devices were fabricated and tested to check the utility of novel upconverting material (UCM),  $\text{BaGdF}_5:\text{Er}^{3+}/\text{Yb}^{3+}$  nanocrystals in solar cell application. The complete device architecture is given in Figure 2. In this experiment, we mixed  $\text{TiO}_2$  nanoparticles with 5% (w/w) UCM materials, further mentioned as  $\text{BG1}/\text{TiO}_2$  to  $\text{BG7}/\text{TiO}_2$  and applied as transparent absorption layers (for the abbreviation of BG, please see the [Supporting Information](#)). The  $\text{BG}/\text{TiO}_2$  powders were first converted into a viscous paste, which is suitable for screen printing.<sup>32</sup> DSSC working electrodes were prepared on a fluorine-doped tin oxide (FTO) conducting transparent glass substrate with a compact blocking layer of  $\text{TiO}_2$ , six layers of a transparent bare  $\text{TiO}_2$  or  $\text{BG}/\text{TiO}_2$  paste, and finally two layers of a  $\text{TiO}_2$  scattering paste.

The screen-printing method as reported was used for layer-by-layer deposition of  $\text{BG}/\text{TiO}_2$ .<sup>33</sup> The nonporous dense blocking layer of  $\text{TiO}_2$  was deposited on the conducting FTO glass substrate via  $\text{TiCl}_4$  treatment to reduce the charge recombination.<sup>34</sup> Prepared  $\text{BG}/\text{TiO}_2$  pastes were then printed on the (pre)  $\text{TiCl}_4$  treated glass using a DR-FSD-1215 (DR Optical Disc India Pvt., Ltd.) automatic screen-printer and repeated in six cycles. Further, two layers were deposited of a commercially available  $\text{TiO}_2$  scattering paste. For the sake of even layers after each layer deposition, the FTO substrate was kept in an ethanol chamber for 6 min followed by drying at  $120\text{ }^\circ\text{C}$  for 6 min. Further, the final sintering involved gradually heating in an oven at  $325\text{ }^\circ\text{C}$  (5 min),  $375\text{ }^\circ\text{C}$  (5 min),  $450\text{ }^\circ\text{C}$  (15 min), and  $500\text{ }^\circ\text{C}$  (30 min). Furthermore, the electrodes were again treated with (post)  $\text{TiCl}_4$  followed by sintering at  $500\text{ }^\circ\text{C}$  for 30 min. The finally printed active area of  $\text{TiO}_2$  was  $0.28\text{ cm}^2$ . The sintered electrodes were placed in a dye bath of N719 dissolved in acetonitrile and *tert*-butyl alcohol (1:1) for 16–20 h. Dyes were procured from commercial suppliers and used without any purification. The platinum (Pt) counter electrode was prepared using a drop of  $\text{H}_2\text{PtCl}_6$  solution (2 mg of Pt in 1 mL of ethanol) deposition on the FTO substrate further heated at  $400\text{ }^\circ\text{C}$  for 15 min to remove the solvent. The dye-coated  $\text{TiO}_2$  electrode and Pt-coated counter electrode were sandwiched together using a  $50\text{ }\mu\text{m}$  Bynel polymer (gasket/spacer). The electrolyte was vacuum-filled between both the electrodes through a small hole that

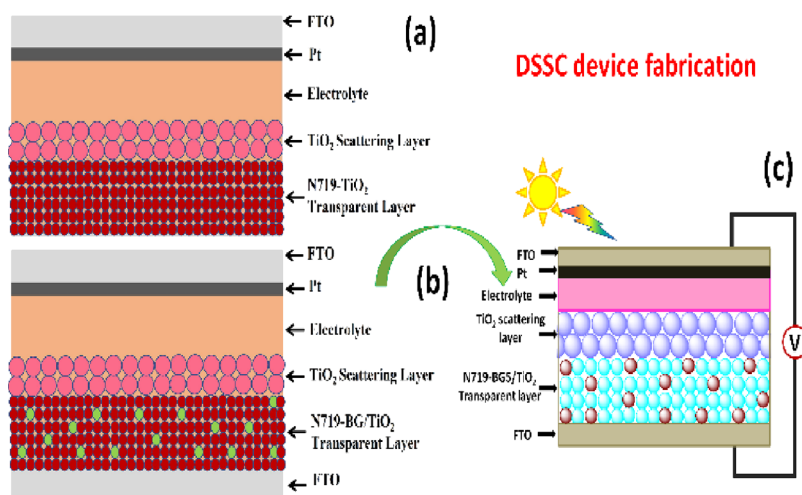


**Figure 2.** Schematic representations of the DSSC devices: (a) device with the scatter layer, (b) device using the  $\text{TiO}_2$  + UCM ( $\text{BaGdF}_5:\text{Er}^{3+}/\text{Yb}^{3+}$ ), and (c) schematic representation of assembly of the dye-sensitized solar cell [BG5 =  $\text{BaGdF}_5:\text{Er}^{3+}(1\%)/\text{Yb}^{3+}(10\%)$ ].

was sealed afterward using hot melting of Bynel and cover glass using soldering iron. The compositions of the electrolyte used were 0.03 M iodine, 0.1 M guanidinium thiocyanate, 0.5 M 4-*tert*-butylpyridine, and 0.06 M 1-butyl-3-methyl imidazolium iodide.

The transparent absorption layer pastes were prepared using  $\text{TiO}_2$  powder with particles of an average size of 20 nm procured from Merck using the standard fabrication procedure reported in ref 35. A “scattering” paste of a particle size of 150–250 nm (WER 2–0), N719 dye, and Bynel spacer were purchased from Dye Sol Ltd. and used as received. Transparent absorption layers and scattering layers were screen-printed with 90T and 43T mesh screens, respectively.

## RESULTS AND DISCUSSION

**Structural Characterizations by Powder X-Ray Diffraction (PXRD) and Scanning and Transmission Electron Microscopy (SEM and TEM).** As-prepared doped and undoped  $\text{BaGdF}_5$  nanoparticles are synthesized at 150 °C for 6 h reaction time using the IL-assisted hydrothermal method. The crystal phase purities of as-prepared  $\text{BaGdF}_5$  NPs (undoped) and  $\text{BaGdF}_5:\text{Er}^{3+}/\text{Yb}^{3+}$  NPs are checked by using powder X-ray diffraction (P-XRD), and all of them match nicely with standard cubic  $\text{BaGdF}_5$  (Figure 3a; JCPDS card no. C24-98). Crystallite sizes are measured using the Debye–Scherer equation, and it is observed that the concentrations of dopant ions have a significant effect on crystallite size (Table S1). In addition, the lattice strain of as-synthesized rare-earth ion-doped nanophosphors is also calculated using the Williamson–Hall equation.<sup>26–30</sup> Tensile strain is obtained in all cases for the as-prepared undoped and ( $\text{Er}^{3+}/\text{Yb}^{3+}$ )-doped  $\text{BaGdF}_5$  nanophosphors (Figures S1 and S2 and Table S1).

The morphologies of undoped  $\text{BaGdF}_5$  (BG1) and doped upconverting  $\text{BaGdF}_5$  nanophosphors (BG2 to BG5) are understood by TEM and SEM images (Figure 3b,d and Figures S3 and S5). Well-dispersed cubic/cuboid morphology is obtained for pure  $\text{BaGdF}_5$  nanoparticles (BG1); however, an agglomerated image is obtained for upconverting  $\text{BaGdF}_5$  nanophosphors (BG2 to BG5). HRTEM images reveal that (111) planes are dominant in all these cases (Figure 3d and Figure S5c,d). The selected area electron diffraction (SAED) pattern confirms the polycrystalline nature of materials (inset of Figure 3d and Figure S5e,f). To confirm the incorporation of dopant ions ( $\text{Er}^{3+}/\text{Yb}^{3+}$ ) in the  $\text{BaGdF}_5$  host lattice, energy-dispersive X-ray analysis (EDAX) and elemental mapping of

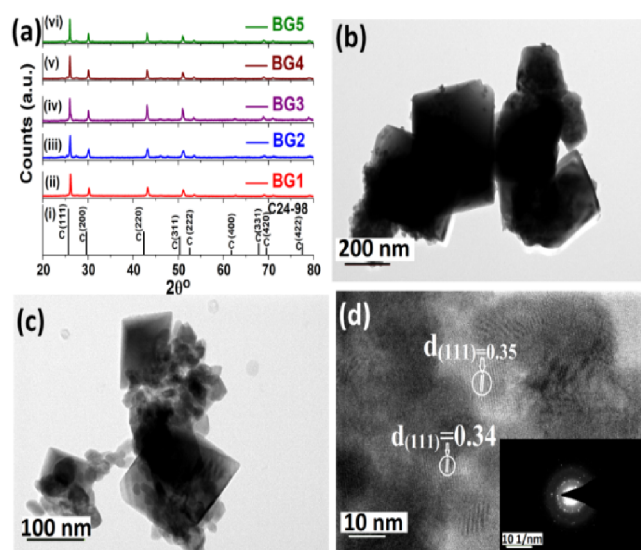


**Figure 3.** PXRD patterns: (a) (i) standard  $\text{BaGdF}_5$  JCPDS card C24-98, (ii)  $\text{BaGdF}_5$  undoped (BG1), (iii)  $\text{BaGdF}_5:\text{Er}^{3+}(1\%)$  [BG2], (iv)  $\text{BaGdF}_5:\text{Er}^{3+}(1\%)/\text{Yb}^{3+}(1\%)$  [BG3], (v)  $\text{BaGdF}_5:\text{Er}^{3+}(1\%)/\text{Yb}^{3+}(5\%)$  [BG4], and (vi)  $\text{BaGdF}_5:\text{Er}^{3+}(1\%)/\text{Yb}^{3+}(10\%)$  [BG5]; (b) low magnification undoped  $\text{BaGdF}_5$  [BG1]; (c, d) low magnification, HRTEM, and inset of  $\text{BaGdF}_5:\text{Er}^{3+}(1\%)/\text{Yb}^{3+}(10\%)$  [BG5]. All these nanocrystals are synthesized using the  $[\text{C}_4\text{mim}]\text{BF}_4$  IL-assisted hydrothermal method.

undoped  $\text{BaGdF}_5$  (BG1) and  $\text{BaGdF}_5:\text{Er}^{3+}(1\%)/\text{Yb}^{3+}(1\%)$  nanophosphors (BG3) are also studied. EDAX results clearly show that  $\text{Yb}^{3+}$  and  $\text{Er}^{3+}$  ion(s) are nicely incorporated in the  $\text{BaGdF}_5$  host lattice (Figure S4a,b). It is also clear that  $\text{Er}^{3+}$  and  $\text{Yb}^{3+}$  ions are doped in this case and are very close to the calculated amount of erbium and ytterbium ions taken during the preparation of nanoparticles. Elemental mapping also confirms homogeneous distribution of dopant ions throughout the lattice.

**Upconversion Measurement.** Figure 4a and Figure S6 depict the upconversion (UC) luminescence of  $\text{Er}^{3+}/\text{Yb}^{3+}$  ion-doped  $\text{BaGdF}_5$  nanophosphors. At present, the most common combinations of dopant ions such as  $\text{Yb}^{3+}/\text{Er}^{3+}$  and  $\text{Yb}^{3+}/\text{Tm}^{3+}$  are used for designing upconverting nanomaterials.<sup>35–45</sup> Herein,  $\text{Yb}^{3+}$  is employed as a sensitizer for  $\text{Tm}^{3+}$  or  $\text{Er}^{3+}$

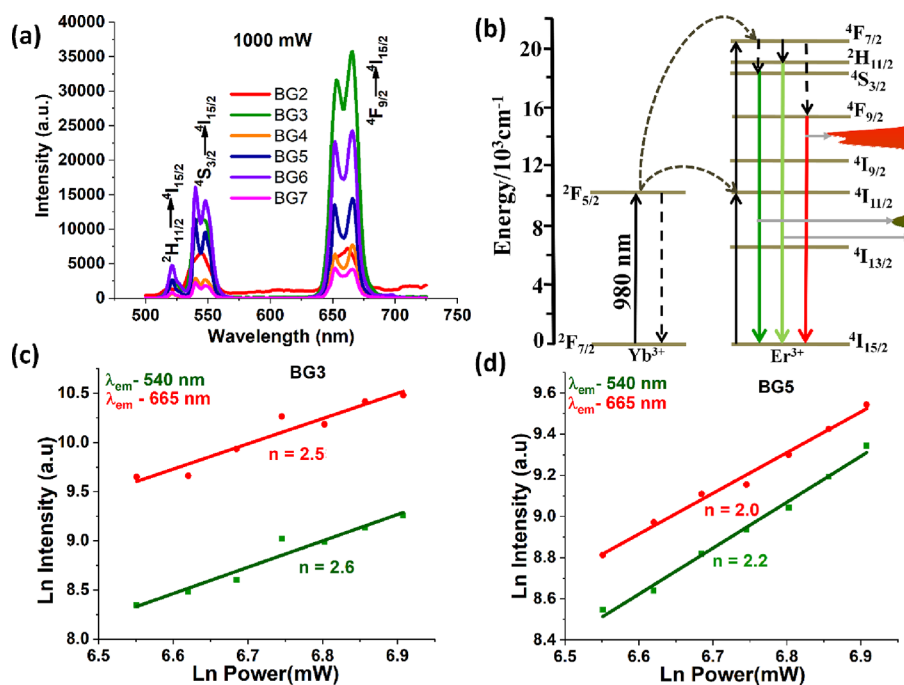


**Figure 4.** (a) Photoluminescence emission spectra of BaGdF<sub>5</sub>:Er<sup>3+</sup>(1%) [BG2], BaGdF<sub>5</sub>:Er<sup>3+</sup>(1%)/Yb<sup>3+</sup>(1%) [BG3], BaGdF<sub>5</sub>:Er<sup>3+</sup>(1%)/Yb<sup>3+</sup>(5%) [BG4], BaGdF<sub>5</sub>:Er<sup>3+</sup>(1%)/Yb<sup>3+</sup>(10%) [BG5], BaGdF<sub>5</sub>:Er<sup>3+</sup>(1%)/Yb<sup>3+</sup>(15%) [BG6] and BaGdF<sub>5</sub>:Er<sup>3+</sup>(1%)/Yb<sup>3+</sup>(20%) [BG7]. (b) Schematic energy level diagram of the Er<sup>3+</sup>/Yb<sup>3+</sup> ions for UC emissions from the Er<sup>3+</sup>/Yb<sup>3+</sup> co-doped BaGdF<sub>5</sub> nanophosphors. (c, d) Number of pump photons of BG3 and BG5 samples.

ions due to its large absorption cross section of Yb<sup>3+</sup> ions and Er<sup>3+</sup> or Tm<sup>3+</sup> ions can act as an activator.<sup>38,42,43</sup> In this process, NIR photons (i.e., 980 nm) are first absorbed by the Yb<sup>3+</sup> ion and then it is transferred to a near activator center (e.g., Er<sup>3+</sup> and Tm<sup>3+</sup>) via the energy transfer upconversion (ETU) process.<sup>38–40</sup> Finally, the excited activator ions emit photons in the visible region via the radiative relaxation process.<sup>36,37</sup>

Figure 4a shows that the highest luminescence intensity is observed for the BaGdF<sub>5</sub>:Er<sup>3+</sup>(1%)/Yb<sup>3+</sup>(1%) [BG3] sample compared to the BaGdF<sub>5</sub>:Er<sup>3+</sup>(1%)/Yb<sup>3+</sup>(20%) [BG7] sample and others, though all are prepared under the same reaction conditions and measured under identical conditions. It is known that, in the host lattice at a low concentration, the ions are distributed randomly and the distances are too far apart, whereas at a higher concentration, the distances between two ions are shortened, causing formation of ion pairs.<sup>42</sup> This clearly indicates that the dopant concentration has a strong effect on luminescence efficiency of Yb<sup>3+</sup>-doped BaGdF<sub>5</sub> nanophosphors.<sup>46</sup>

In addition, a very weak emission intensity is observed in the case of BG2 nanophosphors in which only a 1% Er<sup>3+</sup> ion is doped in BaGdF<sub>5</sub> (Figure 4a). When Yb<sup>3+</sup> ions are incorporated as a sensitizer along with Er<sup>3+</sup> ions in the BaGdF<sub>5</sub> host matrix, good emission is obtained in the case of BG3 to BG7. Among them, the strongest emission is obtained in the case of BG3 [BaGdF<sub>5</sub>:Er<sup>3+</sup>(1%)/Yb<sup>3+</sup>(1%)] compared to other nanophosphors. The red emission peak in the range of 625–700 nm is more intense compared to the green emission peak for samples BG3 to BG7. The intensity of the red emission band was nearly 3.39 times stronger than green emission bands for the BG3 sample. From Figures S6 and S7, it is depicted that the I<sub>G</sub>/I<sub>R</sub> ratios for BG2 to BG7 samples are obtained in the range of 0.29–0.82 (i.e., the maximum is 0.82 for BG2 and BG5 and the minimum is 0.29 for the BG3

sample) (Table S2). The I<sub>G</sub>/I<sub>R</sub> ratio first decreases (0.82–0.29), and then, it increases on increasing dopant ion (Yb<sup>3+</sup>) concentration (0.39–0.82).

This upconversion process is found to be the two-photon process and their detailed schematic energy level diagram of the Er<sup>3+</sup> and Yb<sup>3+</sup> ions, as shown in Figure 4b. The number of pump photons involved in the upconversion process is determined by plotting the ln–ln graph between intensity vs pump power (mW), as shown in Figure 4c,d and Figure S8. The slope of the graphs shows the number of pump photons (*n*). The experimental data for 540 and 665 nm emission bands of BaGdF<sub>5</sub>:Er<sup>3+</sup>/Yb<sup>3+</sup> nanoparticles have been fitted with a straight line with a slope of ~2, which confirms the two-photon absorption process. Various processes like energy transfer (ET), excited state adsorption (ESA), and non-radiative relaxation (NR) are involved in the upconversion process.<sup>38–40,42</sup> Generally, the <sup>4</sup>I<sub>15/2</sub> → <sup>4</sup>I<sub>11/2</sub> and <sup>2</sup>F<sub>7/2</sub> → <sup>2</sup>F<sub>5/2</sub> absorption transitions are obtained for Er<sup>3+</sup> and Yb<sup>3+</sup> ions, respectively, by using a 980 nm pump photon.<sup>38–40</sup> First, on exciting the Yb<sup>3+</sup> ion using the 980 nm pump photon, the <sup>2</sup>F<sub>7/2</sub> → <sup>2</sup>F<sub>5/2</sub> transition occurs.<sup>38</sup> Subsequently, the ground state absorption (GSA) process has taken place including energy transfer from the excited (<sup>2</sup>F<sub>5/2</sub>) level of Yb<sup>3+</sup> ions to Er<sup>3+</sup> ions and simultaneously excitation of Er<sup>3+</sup> ions through the <sup>4</sup>I<sub>15/2</sub> to <sup>4</sup>I<sub>11/2</sub> transition is also taking place.<sup>38–40</sup> The intermediate energy level <sup>4</sup>I<sub>13/2</sub> is populated via the non-radiative relaxation process from intermediate energy level <sup>4</sup>I<sub>11/2</sub>.<sup>38–40</sup> Second, excited state absorption (ESA) processes (<sup>4</sup>I<sub>11/2</sub> to <sup>4</sup>F<sub>7/2</sub> and <sup>4</sup>I<sub>13/2</sub> to <sup>4</sup>F<sub>9/2</sub>) are taking place via another ET process, resulting in the population of <sup>4</sup>F<sub>7/2</sub> and <sup>4</sup>F<sub>9/2</sub> levels.<sup>38–40</sup> When radiative relaxation processes have taken place due to <sup>2</sup>H<sub>11/2</sub> → <sup>4</sup>I<sub>15/2</sub> and <sup>4</sup>S<sub>3/2</sub> → <sup>4</sup>I<sub>15/2</sub> transitions, emissions at 520 and 540 nm are found, respectively.<sup>40,42</sup> Furthermore, red emission at 650 nm wavelength has occurred as the radiative relaxation

process takes place from intermediated energy level  ${}^4F_{9/2}$  to ground state level  ${}^4I_{15/2}$  of the  $\text{Er}^{3+}$  ions. Alternatively, if the excited  ${}^4F_{7/2}$  level is relaxed via the non-radiative process to the  ${}^4F_{9/2}$  level and further relaxed to the  ${}^4I_{15/2}$  level of the  $\text{Er}^{3+}$  ions by the radiative relaxation process, then again, red emission is observed.<sup>38</sup>

**Measuring Photon Conversion Efficiency.** Figure 5 highlights the  $J$ - $V$  characteristics of cells featuring different

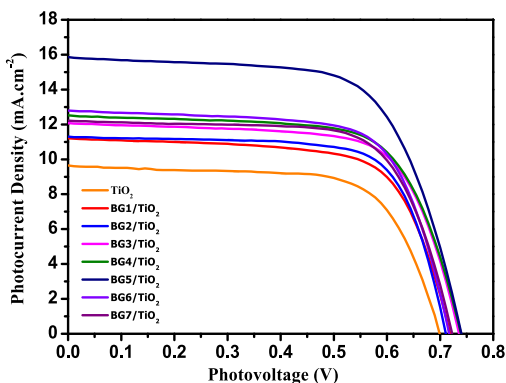


**Figure 5.**  $J$ - $V$  curves for a dye-sensitized solar cell using different photoanode materials measured under standard AM 1.5 conditions.

photoanodes. Under 1 sun illumination, cells fabricated with the BG5/ $\text{TiO}_2$  absorption layer [BG5 =  $\text{BaGdF}_5\text{:Er}^{3+}(1\%)/\text{Yb}^{3+}(10\%)$ ] showed to be the highest with an overall efficiency of 7.75% with  $J_{sc} = 15.9 \text{ mA/cm}^2$ . The current density and performance both were observed to be the highest among all other BG/ $\text{TiO}_2$  and bare  $\text{TiO}_2$  samples. For comparison, the cells fabricated with bare  $\text{TiO}_2$  absorption layers showed a PCE of 4.60% along with a  $J_{sc}$  value of  $9.6 \text{ mA/cm}^2$ . The photovoltaic parameters of DSSC devices made with different photoanodes are shown in Table 1. The results reveal that PCE and  $J_{sc}$  of BG1 to BG7 samples follow a trend wherein PCE and  $J_{sc}$  first increase from BG1 to BG5 and then gradually decrease to BG7. As a result, maximum values of PCE (7.75%) and  $J_{sc}$  ( $15.9 \text{ mA/cm}^2$ ) are found for BG5 sample [BG5 =  $\text{BaGdF}_5\text{:Er}^{3+}(1\%)/\text{Yb}^{3+}(10\%)$ ] whereas minimum (PCE =

**Table 1.** PCE (%) of  $\text{Er}^{3+}/\text{Yb}^{3+}$ -Doped  $\text{BaGdF}_5$  Nanophosphors

sample	PCE (%)	$J_{sc}$ ( $\text{mA/cm}^2$ )	$V_{oc}$ (V)	FF (%)	overall increase (%) <sup>a</sup>
BG1/ $\text{TiO}_2$ + scattering layer	5.51	11.2	0.72	68.34	19.78
BG2/ $\text{TiO}_2$ + scattering layer	5.76	11.3	0.71	71.69	25.20
BG3/ $\text{TiO}_2$ + scattering layer	6.15	12.1	0.73	69.22	33.69
BG4/ $\text{TiO}_2$ + scattering layer	6.33	12.5	0.74	68.35	37.60
BG5/ $\text{TiO}_2$ + scattering layer	7.75	15.9	0.74	65.99	68.47
BG6/ $\text{TiO}_2$ + scattering layer	6.42	12.8	0.72	70.21	39.56
BG7/ $\text{TiO}_2$ + scattering layer	6.17	12.2	0.72	69.85	34.13
bare $\text{TiO}_2$ + scattering layer	4.60	9.6	0.70	68.30	

<sup>a</sup>Overall increased PCE of DSSCs with UCM nanoparticles (BG1 to BG7) compared to the bare DSSC without UCM.

5.51% and  $J_{sc} = 11.2 \text{ mA/cm}^2$ ) is found for BG1 sample that is undoped  $\text{BaGdF}_5$  nanoparticles (as shown in Table 1 and Figure 6). However, the lowest values of PCE and  $J_{sc}$  are observed for the bare  $\text{TiO}_2$  layer (Table 1). Thus, PCE and  $J_{sc}$  of the DSSC have substantially been enhanced in the presence of UCM compared to  $\text{TiO}_2$ .

Figure 6a depicts the effect of the dopant ion concentration on both the PCE and  $J_{sc}$  values. As stated earlier, the  $\text{BaGdF}_5\text{:Er}^{3+}(1\%)/\text{Yb}^{3+}(10\%)$ -based [BG5/ $\text{TiO}_2$ -based DSSC] DSSC device exhibited the highest level of photon-to-current conversion efficiency (Figure 6a). It is observed that with increasing the concentration of the  $\text{Yb}^{3+}$  ion as dopant ions up to 10% for BG5 [ $\text{BaGdF}_5\text{:Er}(1\%)/\text{Yb}(10\%)$ ], maximum PCE (7.75%) and current density ( $J_{sc} = 15.9 \text{ mA/cm}^2$ ) are observed and then it decreases with BG6 and BG7. This might be attributed on increasing the concentration of  $\text{Yb}^{3+}$  dopant ions up to 10%, and effective energy transfer from the  $\text{Yb}^{3+}$  ion to the  $\text{Er}^{3+}$  ion takes place. Thereafter, on further increasing the concentration of  $\text{Yb}^{3+}$  ions above 15%, there might be concentration-based quenching of the energy transfer process from the  $\text{Yb}^{3+}$  to  $\text{Er}^{3+}$  ion. Therefore, less PCE (6.17%) is observed for the DSSC prepared using 20%  $\text{Yb}^{3+}$  and 1%  $\text{Er}^{3+}$ -based upconverting nanophosphors (BG7). In addition, the  $I_G/I_R$  ratio also eventually shows a similar trend like the dopant ion  $\text{Er}^{3+}/\text{Yb}^{3+}$  ratio. For example, as the concentration of the  $\text{Yb}^{3+}$  ion increases, the emission intensity in the green region ( $I_G$ ) increases as compared to the emission intensity in the red region ( $I_R$ ). Although,  $I_G/I_R$  of BG2 is also similar to the BG5 sample; however, emission intensity ( $I_G$ ) of the green region of the BG2 sample is very less as compared to  $I_G$  of the BG5 sample. As a result,  $I_G$  of the  $\text{Er}^{3+}$  ion does not only significantly match with the absorption range of the Ru dye leading (N719) but also efficiently sensitized the dye present in DSSCs. The absorbance spectra of the N719 dye are given in Figure S9 in the Supporting Information. Consequently, PCE of the BG5 sample is substantially enhanced as compared to the other samples. Yang et al. have explained that the increase in emission intensity in the green region ( $I_G$ ) enhances the PCE of the DSSC due to the matching of  $I_G$  with the absorption range of the Ru dye.<sup>47</sup> Figure 6b depicts the overall enhancement or relative enhancement of BG/ $\text{TiO}_2$ -based solar cells with respect to the cell where only  $\text{TiO}_2$  is used as an absorbing layer. Photon conversion efficiency of DSSCs made up of the BG5 sample was found to be 68.47% higher as compared to the bare  $\text{TiO}_2$  made up of the DSSC device, devoid of UPC nanomaterials (Figure 6b and Table 1). This is also maximum among the other UCM-based DSSCs too. For example, for the BG2-based device [BG2 =  $\text{BaGdF}_5\text{:Er}(1\%)$ ], the enhancement in PCE compared to the bare  $\text{TiO}_2$  made device is 25.2% (Table 1 and Figure 6b). It is also observed that by adding upconverting material, PCE and current density increase for the device significantly, indicating reduction of sub-band gap loss of the solar cell device, which is a major issue now. It is worth noting to mention that the  $\text{Yb}^{3+}$  ion contains a higher absorption coefficient than the other rare-earth ions. This maximum efficiency for BG5 may be due to the combination of the optimum concentration of the  $\text{Yb}^{3+}$  ion and upconversion efficiency. In this way, the  $\text{BaGdF}_5\text{:Er}(1\%)/\text{Yb}(10\%)$  [BG5] sample might be a potential nanophosphor for DSSC application.

Furthermore, we have also compared the PCE of  $\text{BaGdF}_5\text{:Er}(1\%)/\text{Yb}(10\%)$  [BG5] with the previously reported  $\text{NaYF}_4\text{:Yb/Er}$  materials that have been extensively employed

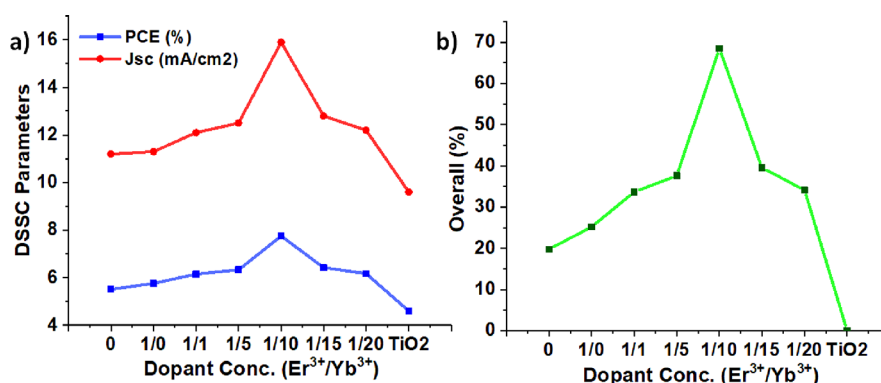


**Figure 6.** Effect of the Er<sup>3+</sup>/Yb<sup>3+</sup> dopant ion concentration on (a) PCE and  $J_{sc}$  and (b) overall increased PCE.

for DSSC applications (Table S3). Our device prepared with the BaGdF<sub>5</sub>:Er(1%)/Yb(10%) nanophosphors shows a significant PCE efficiency of 7.75%, which is higher than bare NaYF<sub>4</sub>:Yb/Er nanophosphors mentioned in Table S3. Performance stability of the prepared DSSC was tested with the best performing device “BG5/TiO<sub>2</sub> + scattering layer” over a period of 4 weeks at an interval of a 1 week period. The results are presented in the Supporting Information as Table S4 and Figure S10. It was observed that the device has reasonable durability for the performance. The major cause of the drop in DSSC performance over time is sealing failure. Thus, the durability of the DSSC can be further extended by applying new sealing materials and technologies available in the market.

## CONCLUSIONS

In summary, we have successfully synthesized upconverting nanomaterials using [C<sub>4</sub>mim]BF<sub>4</sub> IL, which is employed as a solvent, capping/templating agent, and fluoride source, i.e., all three in one. It is observed that the average crystallite size, lattice strain, morphology, and optical properties of nanoparticles are influenced with the doping of upconverting rare-earth ions. The highest upconversion efficiency is obtained for the sample BaGdF<sub>5</sub>:Er(1%)/Yb(10%) [BG3]. Analysis reveals that the pump power dependence of green and red UCM emission is quadratic, indicating that two-photon excitation processes are involved in the upconversion process. A significant increase in photon conversion efficiency (PCE = 7.75%) and current density ( $J_{sc}$ ) is observed for the 10% dopant concentration of the Yb<sup>3+</sup> ion [BaGdF<sub>5</sub>:Er(1%)/Yb(10%)]. A significant enhancement in PCE (68.47%) and current density (65.25%) is noticed for the BG5 [BaGdF<sub>5</sub>:Er(1%)/Yb(10%)]-based device compared to the DSSC device where only TiO<sub>2</sub> is used as the absorbing layer. This enhancement is due to the overall upconversion intensity as well as overlapping of green emission of the Er<sup>3+</sup> ion with the absorption region of the N719 dye. Other devices [BG2 to BG7] where also UCM materials with different dopant concentrations (Er<sup>3+</sup>/Yb<sup>3+</sup>) are combined with TiO<sub>2</sub> as the absorbing layer showed better performances than the device where only TiO<sub>2</sub> is used. These results reveal that the role of UCM material with the combination of TiO<sub>2</sub> has exhibited its potential utility as light-to-current conversion material. More work in this direction is undergoing to optimize the ratio of UCM to TiO<sub>2</sub> and understand the functioning of this combination.

## ASSOCIATED CONTENT

### Supporting Information

The Supporting Information is available free of charge at <https://pubs.acs.org/doi/10.1021/acsaem.3c00424>.

Experimental methods and additional lattice strain, FESEM, EDAX, elemental mapping, TEM, and upconversion characterizations (PDF)

## AUTHOR INFORMATION

### Corresponding Authors

**Praveen Kumar Surolia** – Department of Chemistry, School of Basic Sciences, Manipal University Jaipur, Jaipur 303007, India; Email: [praveenkumar.surolia@jaipur.manipal.edu](mailto:praveenkumar.surolia@jaipur.manipal.edu)  
**Pushpal Ghosh** – School of Chemical Science and Technology, Department of Chemistry, Dr. Harisingh Gour University (A Central University), Sagar 470003 M.P., India; [orcid.org/0000-0002-7596-5056](https://orcid.org/0000-0002-7596-5056); Email: [pushpalghosh27@gmail.com](mailto:pushpalghosh27@gmail.com), [pghosh@dhsgsu.edu.in](mailto:pghosh@dhsgsu.edu.in)

### Authors

**Yogendra Nath Chouryal** – School of Chemical Science and Technology, Department of Chemistry, Dr. Harisingh Gour University (A Central University), Sagar 470003 M.P., India  
**Rahul Kumar Sharma** – School of Chemical Science and Technology, Department of Chemistry, Dr. Harisingh Gour University (A Central University), Sagar 470003 M.P., India; Present Address: Department of Chemistry, Government Shyam Sundar Agrawal PG College, Sihora 483225, Jabalpur, M.P., India (R.K.S.)  
**Neeraj Tomar** – Department of Chemistry, School of Basic Sciences, Manipal University Jaipur, Jaipur 303007, India  
**Neelam Yadav** – Department of Chemical Engineering, IIT Kanpur, Kanpur 208016, India  
**Heera Lal Kewat** – School of Chemical Science and Technology, Department of Chemistry, Dr. Harisingh Gour University (A Central University), Sagar 470003 M.P., India  
**Ishfaq Abdullah Wani** – School of Chemical Science and Technology, Department of Chemistry, Dr. Harisingh Gour University (A Central University), Sagar 470003 M.P., India  
**Sandeep Nigam** – Chemistry Division, Bhabha Atomic Research Centre, Mumbai 400085, India; [orcid.org/0000-0001-9949-4466](https://orcid.org/0000-0001-9949-4466)  
**Sri Sivakumar** – Department of Chemical Engineering, IIT Kanpur, Kanpur 208016, India; [orcid.org/0000-0002-6472-2702](https://orcid.org/0000-0002-6472-2702)

Complete contact information is available at:  
<https://pubs.acs.org/10.1021/acsaem.3c00424>

### Author Contributions

<sup>#</sup>Y.N.C. and R.K.S. contributed equally in this manuscript. The manuscript was written through contributions of all authors. All authors have given approval to the final version of the manuscript.

### Notes

The authors declare no competing financial interest.

## ACKNOWLEDGMENTS

P.G. and P.K.S. appreciate the support from the Science and Engineering Research Board (SERB), Government of India [grant nos. CRG/2018/003751 and EMR/2016/006259, respectively] for funding, Centre for Advanced Research (CAR), Dr. H.S. of Gour Central University, and Departmental Instrumental Facility for measurements. P.G. also acknowledges the Board of Research in Nuclear Sciences (BRNS), Government of India [grant no. 58/14/22/2022-BRNS/37094] for funding.

## REFERENCES

- (1) De Wild, J.; Meijerink, A.; Rath, J. K.; van Sark, W. G. J. H. M.; Schropp, R. E. I. Upconverter solar cells: materials and applications. *Energy Environ. Sci.* **2011**, *4*, 4835–4848.
- (2) Kalyanasundaram, K.; Grätzel, M. Themed issue: nanomaterials for energy conversion and storage. *J. Mater. Chem.* **2012**, *22*, 24190–24194.
- (3) Nozik, A. J.; Miller, J. Introduction to solar photon conversion. *Chem. Rev.* **2010**, *110*, 6443–6445.
- (4) Luna-Rubio, R.; Trejo-Peria, M.; Vargas-Vázquez, D.; Ríos-Moreno, G. J. Optimal sizing of renewable hybrids energy systems: A review of methodologies. *Sol. Energy* **2012**, *86*, 1077–1088.
- (5) Müller-Fürstenberger, G.; Wagner, M. Exploring the environmental Kuznets hypothesis: Theoretical and econometric problems. *Ecol. Econ.* **2007**, *62*, 648–660.
- (6) Ramasamy, P.; Manivasakan, P.; Kim, J. Upconversion nanophosphors for solar cell applications. *RSC Adv.* **2014**, *4*, 34873–34895.
- (7) Fischer, S.; Goldschmidt, J. C.; Löper, P.; Bauer, G. H.; Brüggemann, R.; Krämer, K.; Biner, D.; Hermle, M.; Glunz, S. W. Enhancement of silicon solar cell efficiency by upconversion: Optical and electrical characterization. *J. Appl. Phys.* **2010**, *108*, No. 044912.
- (8) Trupke, T.; Green, M. A.; Würfel, P. Improving solar cell efficiencies by up-conversion of sub-band-gap light. *J. Appl. Phys.* **2002**, *92*, 4117–4122.
- (9) Gibart, P.; Auzel, F.; Guillaume, J. C. G. J. C.; Zahraman, K. Z. K. Below band-gap IR response of substrate-free GaAs solar cells using two-photon up-conversion. *J. Appl. Phys.* **1996**, *35*, 4401.
- (10) Shao, Y.; Liu, B.; Di, Z.; Zhang, G.; Sun, L.-D.; Li, L.; Yan, C.-H. Engineering of upconverted metal–organic frameworks for near-infrared light-triggered combinational photodynamic/chemo–immunotherapy against hypoxic tumors. *J. Am. Chem. Soc.* **2020**, *142*, 3939–3946.
- (11) Liao, J.; Jin, D.; Chen, C.; Li, Y.; Zhou, J. Helix shape power-dependent properties of single upconversion nanoparticles. *J. Phys. Chem. Lett.* **2020**, *11*, 2883–2890.
- (12) Li, D.; Wen, S.; Kong, M.; Liu, Y.; Hu, W.; Shi, B.; Shi, X.; Jin, D. Highly doped upconversion nanoparticles for in vivo applications under mild excitation power. *Anal. Chem.* **2020**, *92*, 10913–10919.
- (13) Safdar, M.; Ghazy, A.; Lastusaari, M.; Karppinen, M. Lanthanide-based inorganic–organic hybrid materials for photon-upconversion. *J. Mater. Chem. C* **2020**, *8*, 6946–6965.
- (14) Kang, D.; Jeon, E.; Kim, S.; Lee, J. Lanthanide-doped upconversion nanomaterials: Recent advances and applications. *BioChip J.* **2020**, *14*, 124–135.
- (15) Zhang, H.; Chen, Z.-H.; Liu, X.; Zhang, F. A mini-review on recent progress of new sensitizers for luminescence of lanthanide doped nanomaterials. *Nano Res.* **2020**, *13*, 1795–1809.
- (16) Yang, B.; Chen, H.; Zheng, Z.; Li, G. Application of upconversion rare earth fluorescent nanoparticles in biomedical drug delivery system. *J. Lumin.* **2020**, *223*, 117226.
- (17) Fischer, S.; Siefe, C.; Swearer, D. F.; McLellan, C. A.; Alivisatos, P.; Dionne, J. A. Bright infrared-to-ultraviolet/visible upconversion in small alkaline earth-based nanoparticles with biocompatible CaF<sub>2</sub> shells. *Angew. Chem., Int. Ed.* **2020**, *132*, 21787–21796.
- (18) Zhao, J.; Jin, D.; Schartner, E. P.; Lu, Y.; Liu, Y.; Zvyagin, A. V.; Zhang, L.; Dawes, J. M.; Xi, P.; Piper, J. A.; Goldys, E. M.; Monro, T. M. Single-nanocrystal sensitivity achieved by enhanced upconversion luminescence. *Nat. Nanotechnol.* **2013**, *8*, 729–734.
- (19) Liu, Q.; Zhang, Y.; Peng, C. S.; Yang, T.; Joubert, L.-M.; Chu, S. Single upconversion nanoparticle imaging at sub-10 W cm<sup>-2</sup> irradiance. *Nat. Photonics* **2018**, *12*, 548–553.
- (20) Tian, B.; Fernandez-Bravo, A.; Najafiaghdam, H.; Torquato, N. A.; Altoe, M. V. P.; Teitelboim, A.; Tajon, C. A.; Tian, Y.; Borys, N. J.; Barnard, E. S.; Anwar, M.; Chan, E. M.; Schuck, P. J.; Cohen, B. E. Low irradiance multiphoton imaging with alloyed lanthanide nanocrystals. *Nat. Commun.* **2018**, *9*, 3082.
- (21) Shang, Y.; Hao, S.; Yang, C.; Chen, G. Enhancing solar cell efficiency using photon upconversion materials. *Nanomaterials* **2015**, *5*, 1782–1809.
- (22) Shalav, A.; Richards, B. S.; Trupke, T.; Krämer, K. W.; Güdel, H. U. Application of NaYF<sub>4</sub>:Er<sup>3+</sup> up-converting phosphors for enhanced near-infrared silicon solar cell response. *Appl. Phys. Lett.* **2005**, *86*, No. 013505.
- (23) Liang, L.; Liu, Y.; Zhao, X.-Z. Double-shell β-NaYF<sub>4</sub>:Yb<sup>3+</sup>, Er<sup>3+</sup>/SiO<sub>2</sub>/TiO<sub>2</sub> submicroplates as a scattering and upconverting layer for efficient dye-sensitized solar cells. *Chem. Commun.* **2013**, *49*, 3958–3960.
- (24) Tomar, N.; Agrawal, A.; Dhaka, V. S.; Surolia, P. K. Ruthenium complexes based dye sensitized solar cells: Fundamentals and research trends. *Solar Energy* **2020**, *207*, 59–76.
- (25) Chouryal, Y. N.; Sharma, R. K.; Lvanovskikh, K.; Ishchenko, A.; Shi, Q.; Lvanov, V.; Nigam, S.; Pandey, A.; Ghosh, P. Temperature dependent quantum cutting in cubic BaGdF<sub>3</sub>:Eu<sup>3+</sup> nanophosphors. *New J. Chem.* **2021**, *45*, 1463–1473.
- (26) Ghosh, P.; Mudring, A. V. Phase selective synthesis of quantum cutting nanophosphors and the observation of a spontaneous room temperature phase transition. *Nanoscale* **2016**, *8*, 8160–8169.
- (27) Sharma, R. K.; Chouryal, Y. N.; Chaudhari, S.; Saravanakumar, J.; Dey, S. R.; Ghosh, P. Adsorption-driven catalytic and photocatalytic activity of phase tuned In<sub>2</sub>S<sub>3</sub> nanocrystals synthesized via ionic liquids. *ACS Appl. Mater. Interfaces* **2017**, *9*, 11651–11661.
- (28) Sharma, R. K.; Chouryal, Y. N.; Nema, S.; Nigam, S.; Bera, S. P.; Bhargava, Y.; Ghosh, P. Green Emitting Ce<sup>3+</sup>/Tb<sup>3+</sup>-Doped BaF<sub>2</sub> Nanocrystals and Their Impact on Skeletal Muscle of Developing Zebrafish Larvae. *ChemistrySelect* **2020**, *5*, 9105–9110.
- (29) Chouryal, Y. N.; Sharma, R. K.; Acharjee, D.; Ganguly, T.; Pandey, A. Ghosh, P. Influence of ionic liquids and concentration of red phosphorous on luminescent Cu<sub>3</sub>P nanocrystals. *J. Chem. Sci.* **2019**, *131*, 93.
- (30) Ghosh, P.; Sharma, R. K.; Chouryal, Y. N.; Mudring, A.-V. Size of the rare-earth ions: a key factor in phase tuning and morphology control of binary and ternary rare-earth fluoride materials. *RSC Adv.* **2017**, *7*, 33467–33476.
- (31) Sharma, R. K.; Chouryal, Y. N.; Slesarev, A. I.; Ivanovskikh, K. V.; Leonidov, I. I.; Nigam, S.; Ghosh, P. A closer look at the defects and luminescence of nanocrystalline fluorides synthesized via ionic liquids: the case of Ce<sup>3+</sup>-doped BaF<sub>2</sub>. *New J. Chem.* **2020**, *44*, 200–209.
- (32) Szymanski, L.; Surolia, P.; Byrne, O.; Thampi, K. R.; Stubenrauch, C. Porous “sponge-like” anatase TiO<sub>2</sub> via polymer

templates: synthesis, characterization, and performance as a light-scattering material. *Colloid Polym. Sci.* **2013**, *291*, 805–815.

(33) Byrne, O.; Ahmad, L.; Surolia, P. K.; Gun'ko, Y. K.; Thampi, K. R. The optimisation of dye sensitised solar cell working electrodes for graphene and SWCNTs containing quasi-solid state electrolytes. *Solar Energy* **2014**, *110*, 239–246.

(34) Ghavre, M.; Byrne, O.; Altes, L.; Surolia, P. K.; Spulak, M.; Quilty, B.; Thampi, K. R.; Gathergood, N. Low toxicity functionalised imidazolium salts for task specific ionic liquid electrolytes in dye-sensitized solar cells: a step towards less hazardous energy production. *Green Chem.* **2014**, *16*, 2252–2265.

(35) Ito, S.; Chen, P.; Comte, P.; Nazeeruddin, M. K.; Liska, P.; Pechy, P.; Gratzl, M. Fabrication of screen-printing pastes from TiO<sub>2</sub> powders for dye-sensitized solar cells. *Progr. Photovolt.: Res. Appl.* **2007**, *15*, 603–612.

(36) Arppe, R.; Hyppänen, I.; Perälä, N.; Peltomaa, R.; Kaiser, M.; Würth, C.; Christ, S.; Resch-Genger, U.; Schäferling, M.; Soukka, T. Quenching of the upconversion luminescence of NaYF<sub>4</sub>:Yb<sup>3+</sup>, Er<sup>3+</sup> and NaYF<sub>4</sub>: Yb<sup>3+</sup>, Tm<sup>3+</sup> nanophosphors by water: the role of the sensitizer Yb<sup>3+</sup> in non-radiative relaxation. *Nanoscale* **2015**, *7*, 11746–11757.

(37) Liu, J.; Huang, L.; Tian, X.; Chen, X.; Shao, Y.; Xie, F.; Chen, D.; Li, L. Magnetic and fluorescent Gd<sub>2</sub>O<sub>3</sub>:Yb<sup>3+</sup>/Ln<sup>3+</sup> nanoparticles for simultaneous upconversion luminescence/MR dual modal imaging and NIR-induced photodynamic therapy. *Int. J. Nanomed.* **2017**, *12*, 1.

(38) Dey, R.; Rai, V. K. Yb<sup>3+</sup> sensitized Er<sup>3+</sup> doped La<sub>2</sub>O<sub>3</sub> phosphor in temperature sensors and display devices. *Dalton Trans.* **2014**, *43*, 111–118.

(39) Kumar, V.; Pandey, A.; Swami, S. K.; Ntwaeaborwa, O. M.; Swart, H. C.; Dutta, V. Synthesis and characterization of Er<sup>3+</sup>-Yb<sup>3+</sup> doped ZnO upconversion nanoparticles for solar cell application. *J. Alloys Compd.* **2018**, *766*, 429–435.

(40) Wujczyk, M.; Watras, A.; Szyszka, K.; Wiglusz, R. J. Influence of vanadium concentration on up-conversion luminescence in Er<sup>3+</sup>-Yb<sup>3+</sup> and Tm<sup>3+</sup>-Yb<sup>3+</sup> ions pair co-doped YVxP<sub>1-x</sub>O<sub>4</sub> solid state solution. *J. Alloys Compd.* **2021**, *884*, 161022.

(41) Mokoena, P. P.; Oluwole, D. O.; Nyokong, T.; Swart, H. C.; Ntwaeaborwa, O. M. Enhanced upconversion emission of Er<sup>3+</sup>-Yb<sup>3+</sup> co-doped Ba<sub>3</sub>(PO<sub>4</sub>)<sub>3</sub>OH powder phosphor for application in photodynamic therapy. *Sens. Actuators, A* **2021**, *331*, 113014.

(42) Ghosh, P.; Oliva, J.; Rosa, E. D. L.; Haldar, K. K.; Solis, D.; Patra, A. Enhancement of upconversion emission of LaPO<sub>4</sub>:Er@Yb core-shell nanoparticles/nanorods. *J. Phys. Chem. C* **2008**, *112*, 9650–9658.

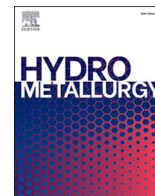
(43) Ghosh, P.; Rosa, E. D. L.; Oliva, J.; Solis, D.; Kar, A.; Patra, A. Influence of surface coating on the upconversion emission properties of LaPO<sub>4</sub>:Yb/Tm core-shell nanorods. *J. Appl. Phys.* **2009**, *105*, 113532.

(44) Deng, X.; Yu, M.; Zhou, X.; Xia, Z.; Chen, X.; Huang, S. Highly bright and sensitive thermometric LiYF<sub>4</sub>:Yb, Er upconversion nanocrystals through Mg<sup>2+</sup> tridoping. *J. Mater. Sci.: Mater. Electron.* **2020**, *31*, 3415–3425.

(45) Maurya, S. K.; Mohan, M.; Poddar, R.; Sanapati, D.; Singh, S.; Roy, A.; Manirathnappa, A. K.; Silva, J. C. G. E. d.; Kumar, K. Synthesis of NaGdF<sub>4</sub>:Er<sup>3+</sup>/Yb<sup>3+</sup> upconversion particles as exogenous contrast agent for swept-source optical coherence tomography: in vitro animal tissue imaging. *J. Phys. Chem. C* **2020**, *124*, 18366–18378.

(46) Patra, A.; Ghosh, P.; Chowdhury, P. S.; Alencar, M. A. R. C.; Lozano, B. W.; Rakov, N.; Maciel, G. S. Red to blue tunable upconversion in Tm<sup>3+</sup>-doped ZrO<sub>2</sub> nanocrystals. *J. Phys. Chem. B* **2005**, *109*, 10142–10146.

(47) Yang, H.; Peng, F.; Zhang, Q.; Liu, W.; Sun, D.; Zhao, Y.; Wei, X. Strong upconversion luminescence in LiYMo<sub>2</sub>O<sub>8</sub>:Er, Yb towards efficiency enhancement of dye-sensitized solar cells. *Opt. Mater.* **2013**, *35*, 2338–2342.



## Investigations into the closed-loop hydrometallurgical process for heavy metals removal and recovery from biosolids via mild acid pre-treatment

Ibrahim Gbolahan Hakeem<sup>a,b</sup>, Pobitra Halder<sup>b,c</sup>, Shefali Aktar<sup>a</sup>, Mojtaba Hedayati Marzbali<sup>a,b</sup>, Abhishek Sharma<sup>b,d</sup>, Aravind Surapaneni<sup>b,e</sup>, Graeme Short<sup>e</sup>, Jorge Paz-Ferreiro<sup>a</sup>, Kalpit Shah<sup>a,b,\*</sup>

<sup>a</sup> Chemical and Environmental Engineering, School of Engineering, RMIT University, Melbourne, VIC 3000, Australia

<sup>b</sup> ARC Training Centre for the Transformation of Australia's Biosolids Resource, RMIT University, Bundoora, VIC 3082, Australia

<sup>c</sup> School of Engineering, Deakin University, VIC 3216, Australia

<sup>d</sup> Department of Chemical Engineering, Manipal University, Jaipur, Rajasthan 303007, India

<sup>e</sup> South East Water Corporation, Frankston, VIC 3199, Australia

### ARTICLE INFO

#### Keywords:

Leachate recycling  
Biosolids treatment  
Heavy metals  
Metal recovery  
Metal extraction

### ABSTRACT

Biosolids contain heavy metals (HMs), restricting their beneficial reuse in agricultural land. However, these metals can be a valuable resource in many applications if recovered efficiently. Therefore, the removal and recovery of HMs and other limiting contaminants in biosolids without degrading the organic nutrients of the resulting treated biosolids demands holistic investigations. A closed-loop hydrometallurgical treatment process for metal removal and recovery from biosolids was developed in this study. Firstly, mild acid treatment using 3% v/v H<sub>2</sub>SO<sub>4</sub> at 25 °C, 600 rpm for 30 min was performed in a 1 L continuous stirred tank reactor to extract common HMs (such as As, Cd, Co, Cr, Cu, Ni, Pb, and Zn) from biosolids into the aqueous phase. The effects of solids concentration and acid types on the HMs extraction efficiency were studied. Then, the primary acid leachate stream was continuously recycled for metal extraction from biosolids until the dissolved metals in the solution reached saturation concentration. After that, the dissolved metals were recovered in staged NaOH precipitation and adsorption. Low solids contents (<5% w/v) using mineral acids having pH <2 and oxidation-reduction potential (ORP) ~500 mV (versus SHE) favoured HMs solubilisation from biosolids with an average extraction efficiency of 70%. The dissolution of ferric iron (Fe<sup>3+</sup>) by H<sub>2</sub>SO<sub>4</sub> and subsequent in-situ formation of ferric sulfate enhanced the metal extraction strength of the spent leachate stream during recycling. However, the solids loading in each leaching process must be kept low to prevent ferric concentration build-up and precipitation as the leachate pH steadily increases above 2 during recycling. Amongst the metal recovery methods investigated, H<sub>2</sub>O<sub>2</sub> oxidation prior to 2-stage NaOH precipitation had the highest efficiency with 75–95% HMs recovery. The clarified stream was used to neutralise the acidic treated biosolids to close the process loop. The complete process flowsheet was developed with mass balances, and the fate of nutrients (mainly C, N, and P) and major *per-* and polyfluoro alkyl substances (PFAS) were overviewed.

### 1. Introduction

Biosolids, also known as stabilised sewage sludge, are the by-product of the wastewater treatment process. Biosolids contain valuable organic and inorganic components (mainly N, P, and K) that constitute important plant nutrients. These nutrients facilitate the application of a substantial volume of biosolids in agricultural soils in many countries, including Australia (Paz-ferreiro et al., 2018). However, heavy metals

(HMs) and other contaminants such as pesticides, microbial pathogens, microplastics, and surfactants are limiting the attractiveness of biosolids for direct land application with increasingly stringent regulations (EPA Victoria, 2004; LeBlanc et al., 2009). Thermochemical treatment of sub-grade biosolids via pyrolysis, gasification, hydrothermal carbonisation/liquefaction or incineration process can effectively degrade the organic and microbial contaminants (Kundu et al., 2021; Ross et al., 2016). However, HMs remain a persistent pollutant in biosolids and their

\* Corresponding author at: Chemical and Environmental Engineering, School of Engineering, RMIT University, Melbourne, VIC 3000, Australia.

E-mail address: [kalpit.shah@rmit.edu.au](mailto:kalpit.shah@rmit.edu.au) (K. Shah).

<https://doi.org/10.1016/j.hydromet.2023.106044>

Received 13 December 2022; Received in revised form 26 February 2023; Accepted 27 February 2023

Available online 2 March 2023

0304-386X/© 2023 Elsevier B.V. All rights reserved.



thermally-derived products due to the low thermal degradation as well as the formidable bioaccumulation and high environmental toxicity of HMs (Feng et al., 2018).

The pre-treatment of biosolids is considered an effective process for removing the HMs before land application or thermal processing. Several pre-treatment methods, including chemical leaching with acids (Gaber et al., 2011; Stylianou et al., 2007), chelating agents (Gheju et al., 2011; Leštan et al., 2008), ferric salts (Bayat and Sari, 2010; Ito et al., 2000), ionic liquids (Abouelela et al., 2022; Yao et al., 2021), surfactants (Guan et al., 2017; Tang et al., 2017), and microbial agents (Pathak et al., 2009; Xiang et al., 2000) have been investigated for this purpose. Amongst all, leaching with acids is the most common, efficient with short operation times, and cost-effective with high industrial maturity (Babel and del Mundo Dacera, 2006; Gunarathne et al., 2020; Hakeem et al., 2022a). The high oxidising potential, as well as the low pH of acids, are favourable for metal dissolution (Ma et al., 2020). In addition, most metal cations are basic and readily ion-exchangeable with protons from acids (Persson et al., 2017). Therefore, acid leaching plays a leading role in hydrometallurgical processes for metals recovery from different materials, including biosolids (Gunarathne et al., 2020; Montenegro et al., 2016). In a typical acid leaching process, a high liquid-to-solid ratio is desired to achieve high HMs dissolution by overcoming thermodynamic equilibrium, which occurs when the solid dissociates to such an extent that the metal species are fully saturated in the solution (Lee et al., 2006). Hence, acid leaching is usually accompanied by a large volume of aqueous waste stream with dilute metal concentrations. Metal recovery from this dilute stream is unattractive and improper disposal poses environmental threats.

One of the potential ways to manage the resulting leachate stream from biosolids pre-treatment is to reuse and recycle the stream for another leaching process until the leachate stream gets saturated with HMs. The heavily concentrated leachate stream can be a precursor for recovering valuable metals. Recycling the aqueous acidic leachate stream can be attractive for metal extraction due to its low pH, high oxidation-reduction potential (ORP), and presence of surrogate leaching components such as dissolved ferric sulfates or chlorides (Beauchesne et al., 2007; Ito et al., 2000; Strasser et al., 1995). In addition, recycling the acidic waste stream can reduce the overall acid solution requirements during the metal extraction process, with the potential to favour the techno-economics of the process. The effect of process variables such as temperature, acid concentration, solids contents, agitation speeds, and contact time on HMs removal efficiency has been elucidated in previous studies (del Mundo Dacera and Babel, 2006; Gaber et al., 2011; Hakeem et al., 2022b; Yang et al., 2021). However, there is a limited investigation on the recyclability of the acidic leachate stream as a solvent for metal extraction from raw biosolids (Shim, 2023). Particularly, the effects of solids loading on the recycling performance of the leachate stream have not been reported in extant literature.

The overall hydrometallurgical process can be grouped into three sequential stages: metal extraction, leachate concentration and purification, and metal recovery (Gunarathne et al., 2020). The growing interest in resource recovery has increased the prospect of critical element extraction and recovery from biosolids via hydrometallurgical operations (Tyagi and Lo, 2013). However, metal recovery from biosolids has not been fully explored in the literature beyond the acid leaching stage, which removes the metals from biosolids to the liquid phase, as described earlier. Therefore, developing a comprehensive hydrometallurgical process chain to understand the feasibility of metal recovery from biosolids through the production of less contaminated biosolids is desired. While the metal extraction stage is the most critical in the overall hydrometallurgical process, leachate purification and metal recovery are the most challenging because acidic solvents have poor selectivity during metal solubilisation. Moreover, biosolids have many metal and non-metal components that elute simultaneously into solution during acid leaching. For example, the co-solubilisation of iron, aluminium, and alkali and alkaline earth metals (AAEMs) alongside HMs

usually complicates the selective recovery of valuable metals from the leachate stream (Lee et al., 2002). In some cases, elements such as carbon (C), nitrogen (N), and phosphorous (P) are dissolved in the acidic stream, interfering with the purification and recovery of desired metals.

The main techniques for metal recovery from aqueous streams are chemical precipitation (Liang et al., 2019; Marchioretto et al., 2005), electrodeposition (Yao et al., 2021), adsorption (Singh et al., 2020), ion exchange (Yoshizaki and Tomida, 2000), and solvent extraction (Montenegro et al., 2016). Chemical precipitation using caustic soda (NaOH) or slaked lime (Ca(OH)<sub>2</sub>) and adsorption are the most common, less laborious, and suitable for multi-components metal streams typical of biosolids leachate (Li et al., 2021; Marchioretto et al., 2005). However, the efficacy of alkali precipitation of HMs is challenged by the amphoteric nature of some metal ions having different optimum hydroxides solubility as well as interferences from other metal species, particularly iron (de Fátima da Silva et al., 2020). Given the number of metal in a biosolids leachate stream, identifying suitable metal recovery methods will depend on the final composition, metal concentration, and pH (Sethurajan et al., 2017). Studies involving the chemical precipitation of multiple metal from real biosolids leach solutions are limited in the literature (Marchioretto et al., 2005). Chemical precipitation and adsorption have only been extensively applied on metal ores leachate or simulated wastewater containing single or dual metal components (Ait Ahsaine et al., 2017; Ni et al., 2019; Xu et al., 2009).

In summary, the full spectrum of chemical treatment of biosolids for HMs removal involving metal extraction, separation of solids from the leach liquor, leachate concentration and purification, and metal recovery is missing in the literature. Hence, this study explored a comprehensive mild acid treatment of biosolids for HMs extraction and the subsequent recovery of the metal from the concentrated leachate stream. The specific objectives of the work were to (i) study the effect of acid solution and solids concentration on the extraction efficiency of metals from biosolids, (ii) investigate the reusability and extraction performance of the primary leachate stream through partial and complete recycling at optimum solids concentrations, (iii) examine the efficacy of staged NaOH co-precipitation, H<sub>2</sub>O<sub>2</sub> oxidation followed by NaOH co-precipitation, and biochar adsorption for the purification and recovery of HMs from the concentrated leachate stream, (iv) understand the fate of dissolved nutrients (mainly C, N, K, and P) and *per*- and poly-fluoro alkyl substance (PFAS) compounds in the process streams, and (v) develop and propose optimum process flow diagrams with mass balances for biosolids metal removal and recovery. This detailed investigation will help to understand the feasibility of developing an in-situ or ex-situ hydrometallurgical process for biosolids HMs decontamination with potential for nutrient and critical metal recovery within the existing wastewater treatment facilities.

## 2. Materials and methods

### 2.1. Biosolids preparation and analyses

Biosolids used in this study were obtained from Mount Martha Water Recycling Plant, South East Water Corporation, Victoria, Australia. The biosolids production process was described in our previous study (Hakeem et al., 2022b). Before use in the pre-treatment experiments, biosolids were dried overnight in an oven at 105 °C and sieved to 100–300 µm particle size. The elemental composition was determined by X-ray Fluorescence (XRF, S4 AXS Bruker), ultimate analysis was performed using a CHNS Series II Perkin Elmer instrument, and the metal concentration was measured using Inductive Coupled Plasma-Mass Spectrometry (ICP-MS 2200 series, Agilent Technologies). The chemicals used in this work were of analytical grades. They include 98% H<sub>2</sub>SO<sub>4</sub> (Chem-Supply Pty Ltd), 65% HNO<sub>3</sub> (Univar Pty Ltd), 35% HCl (Emplura Pty Ltd), 99% glacial acetic acid (Sigma Aldrich), 99.5% citric acid (Sigma Aldrich), 21–23% ferric sulfate pentahydrate (Chem-Supply) and 30% hydrogen peroxide (Rowe Scientific Pty Ltd). Milli-Q

water with a resistivity of 18.2 M $\Omega$  cm was used throughout this study. Table 1 shows the composition of the biosolids. The concentration of some of the HMs, such as Cu, Zn, and Cd, is higher than that prescribed for the least contaminant grade (C1) for unrestricted beneficial reuse of biosolids according to Victoria EPA biosolids guidelines (EPA Victoria, 2004).

## 2.2. Heavy metals fractionation in the biosolids

The efficacy of acid leaching for metal extraction depends on the chemical fractionation of the metal in the biosolids matrix (Geng et al., 2020). Therefore, according to previous literature, a modified three-step Community Bureau of Reference (BCR) sequential extraction technique was used to determine the distribution of metal in the biosolids (Liu et al., 2021, 2018; Wang et al., 2019). This method allows the chemical classification of HMs species in biosolids, soils, and sediments into four major fractions: exchangeable (F-1), reducible (F-2), oxidisable (F-3), and residual (F-4) based on the ease of extraction with standard reagents (Zhao et al., 2018). The F-1 refers to acid-ionisable metals, F-2 are metals bound to carbonates and Fe–Mn oxides, F-3 are metals bound to organic matter and sulfides, and F-4 are bound to silicates and recalcitrant organics. Depending on the severity of the acid leaching conditions, such as acid concentration (or pH), temperature, and time, F-1, F-2, and F-3 metals can be removed at various rates in decreasing order, while F-4 metals are hardly removed via chemical leaching. The result of this analysis is presented in Fig. S1. From Fig. S1, the potential mobility of the metals in the biosolids can be estimated by adding F-1 and F-2 metal percentages (Geng et al., 2020), and this can be ranked as Mn > Zn > Cd  $\approx$  Ni  $\approx$  Co > Cr > As > Pb > Cu  $\approx$  Fe. Copper has the highest F-3 percentage due to the higher affinity of Cu to organic matter (Beauchesne et al., 2007), while Fe and Pb have the highest F-4 percentages. Copper is the most challenging HM to remove in biosolids via acid leaching; this observation has been widely reported in other works (Beauchesne et al., 2007; Blais et al., 2005; Mercier et al., 2002). Therefore, the extraction of Cu under mild acid leaching conditions may be limited.

## 2.3. Biosolids metals extraction

The batch pre-treatment procedure was as described previously (Hakeem et al., 2022b). All leaching experiments were conducted at room temperature (25  $\pm$  2  $^{\circ}$ C) using 3% (v/v) acid concentration under continuous stirring at 600 rpm for 30  $\pm$  2 min in a 1 L continuous stirred tank reactor. These are the optimised conditions from our previous investigation (Hakeem et al., 2022b). The effect of acid types was studied by using three mineral acids (H<sub>2</sub>SO<sub>4</sub>, HCl, HNO<sub>3</sub>) and two organic acids (acetic and citric) to extract HMs (such as As, Cd, Co, Cr, Cu, Ni, Pb, and Zn) from biosolids at 5% (w/v) solids loading using 3% (v/v) acid solution. Similarly, the effect of solids concentration was studied by leaching biosolids at 1, 3, 5, 10, 15 and 20% (w/v) solids using 3% (v/v) H<sub>2</sub>SO<sub>4</sub> solution. At the end of each metal extraction experiment, the slurry was transferred into Eppendorf tubes and centrifuged at 4000 rpm for 30 min. The leachate stream was carefully decanted into sample vials, and the residue (treated biosolids) was dried and stored for further analysis. The pH and ORP of the leachate stream

were measured, and 1 mL aliquot of the well-mixed leachate was filtered, diluted, and quantified for metals by ICP-MS. All leaching experiments were performed in triplicates, and average results were reported with errors expressed as the standard deviation of the measurements. A schematic illustration of the metal extraction process including the downstream separation and metal recovery processes is shown in Fig. 1.

## 2.4. Concentration of the leachate stream

### 2.4.1. Total recycling of the leachate

The recovered aqueous stream from the parent (primary) pre-treatment was reused fully for another extraction process at 5% and 10% (w/v) fresh biosolids loading; all other conditions remain unchanged. The process was repeated for five leaching cycles (after the parent leaching) using 100% spent leachate stream and fresh biosolids in each cycle. The volume of the leachate stream and mass of the fresh biosolids were adjusted to achieve 5% or 10% solids loading in each cycle. It is assumed that the metals dissolved in the leachate will remain in the solution all the time unless the pH  $\geq$  2.5, where ferric precipitation will be initiated. During the recycling, precipitate from poorly soluble metals such as Ca and Pb is partitioned in the treated solids. The parent (primary) leachate stream and leachate stream after each successive recycle are denoted by R0 and Rn, where n = 1, 2, 3 etc., denotes the number of cycles.

### 2.4.2. Partial recycling of the leachate

A constant volume pre-treatment experiment was performed with biosolids to liquid (g/mL) ratio of 1:10 (10% solids) and 1:20 (5% solids) using the recovered leachate. A fixed mass of biosolids (10 g or 5 g) and a solution volume of 100 mL were maintained for this experiment. The recycled stream was topped with fresh 3% (v/v) H<sub>2</sub>SO<sub>4</sub> to maintain the solution volume at 100 mL for each leaching experiment. The added fresh lixiviant (FL) volume replaced the lost solution volume during each leaching cycle, including aliquots taken for analysis. Thus, the make-up ratio (volume of FL to volume of spent leachate) was  $\sim$ 15 vol% and  $\sim$ 20 vol% at 5% and 10% solids, respectively. The number of effective leaching cycles (n) was determined by continuously reusing the spent stream with make-up solution until the solution became saturated with dissolved metals. At the end of each leaching cycle, the recovered leachate stream was filtered to reduce suspended solids carryover before reusing it in another leaching cycle. All pre-treatment experiment with leachate recycling was repeated at least two times, and average data was reported.

## 2.5. Metals recovery

Most HMs precipitate out of solution at a pH range of 7–12 (Fu and Wang, 2011); however, the concentrated leachate stream obtained from the partial leachate recycling experiment was in the acidic pH (2.45). Therefore, an alkaline solution is required to adjust the solution pH to the metal precipitation region. Since each metal has different optimal precipitation pH depending on the metal ion concentration in the solution (Sethurajan et al., 2017), a typical pH of 9 was chosen for the precipitation experiment. A concentrated NaOH (6 M, pH 14) solution

**Table 1**  
Metals composition of biosolids.

Metal type	Source	Metals composition (mg/kg)								
		Ca	Mg	Na	K	Al	Fe	Mn	Mo	Ba
Major and trace metals	This study	35,600	3630	2790	3530	5180	13,440	210	6	185
		Cr	Ni	Pb	Cd	As	Co	Cu	Zn	
Heavy metals	This study	22	14	17	1.3	2	3	825	815	
	C1 grade*	400	60	300	1	20	–	100	200	
	C2 grade*	3000	270	500	10	60	–	2000	2500	

\* Biosolids contaminant grade as prescribed by Victoria EPA biosolids guidelines (EPA Victoria, 2004).

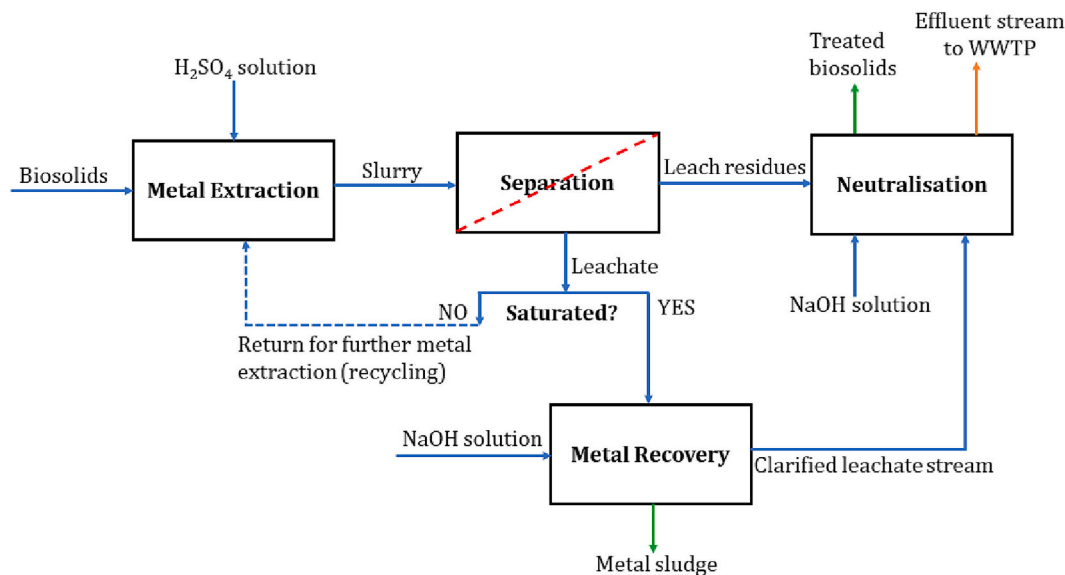


Fig. 1. Schematic of biosolids hydrometallurgical process for metal removal and recovery.

was used for the precipitation of metal ions to reduce the dilution effect on the concentration of the metals. The metal ion precipitation experiment was designed in the following ways to maximise the recovery of the HMs from other metal and non-metal contaminants.

- 1) Two-step NaOH precipitation when Fe/Al precipitation was considered: 20 mL of well-mixed and filtered leachate stream was measured in a conical flask, and 6 M NaOH was added in drops under continuous stirring until the solution pH was  $4.5 \pm 0.2$ . The pH of the solution was monitored via a well-calibrated pH meter, and the amount of NaOH added was noted. The sample was left to stay still for 2 h and centrifuged at 4000 rpm for 30 min to recover the precipitates. Then, 5 mL of the clarified stream was treated in the second step with NaOH in drops until the solution pH was  $9.0 \pm 0.5$ ; the solution was left to settle for 2 h and centrifuged to recover the precipitates. The concentration of metal in the treated liquid after each step was measured by ICP-MS.
- 2) Single-step NaOH precipitation when Fe/Al precipitation was not considered: 10 mL of the leachate stream was treated with NaOH until the final pH was  $9.0 \pm 0.5$ . The presence of Fe and Al in the stream may help in the co-precipitation reaction with HMs since  $\text{Fe}^{3+}$  and  $\text{Al}^{3+}$  salts are common coagulants used in the wastewater treatment process.
- 3) Fenton reaction by adding  $\text{H}_2\text{O}_2$  when oxidation of Fe and dissolved organics were considered: Ferric iron is known to precipitate at low pH  $<4$ , whereas ferrous has a high precipitation pH  $>8.5$ , so  $\text{H}_2\text{O}_2$  can oxidise ferrous to ferric for recovery at stage 1 (pH 4.5). Moreover, dissolved organics in the form of COD (chemical oxygen demand) can limit HMs recovery, so the oxidation of dissolved organic by  $\text{H}_2\text{O}_2$  was considered before NaOH precipitation. Briefly, a few drops of 30% v/v  $\text{H}_2\text{O}_2$  ( $<0.5$  mL) were added to 10 mL of well-filtered leachate stream. Then, the pH of the stream was adjusted to 4.5 with the addition of NaOH in drops to recover Fe/Al. The clarified stream was treated in a second stage to co-precipitate all other metals at pH 9.0 by adding NaOH.
- 4) Adsorption: An attempt to use biochar for adsorption when the leachate stream was at acidic pH (2.45) caused the leaching of metals from the biochar to the liquid, so adjustment of the leachate pH is necessary. Ten mL of clarified leachate (pH 4.5) obtained after the first step of Fe/Al precipitation was used for the adsorption experiment. Biochar produced from raw biosolids at 500 °C for 3 h residence time in a muffle furnace was used as the adsorbent and

charged at a dose of 0.05 g per mL leachate (0.048 g/g leachate). The adsorption was carried out at room temperature overnight under a constant agitation speed of 250 rpm. The mixture was filtered to separate the biochar and the aqueous stream, which was analysed for metal contents by ICP-MS. It should be noted that the presence of HMs in biosolids-biochar is a major concern only for land application of biochar. Metal-loaded biochar can have many valuable applications in catalysis and energy storage (Shen and Chen, 2022; Wang et al., 2017). Besides, biochar adsorption could be an effective and cheaper alternative than alkali precipitation for recovering dissolved metals from the acidic leachate stream.

## 2.6. Process configurations and the fate of nutrients and PFAS

The process flow diagram was developed to capture the entire hydrometallurgical treatment chain from metal extraction via acid leaching to metal recovery via alkali precipitation and, finally, the neutralisation of treated solids. Material balances were performed assuming a steady-state operation. The flow of C, N, and P in the process streams from the biosolids feed to the leachate stream and treated biosolids was overviewed. Similarly, twenty-eight compounds of PFAS (per- and polyfluoroalkyl substances) were measured in the raw biosolids, neutralised treated biosolids, the acidic leachate, and the final liquid effluent. The change in pH of both solid and liquid streams along the treatment chain might influence the leachability and the final fate of PFAS compounds (Kabiri et al., 2022). The C and N content in the raw and treated biosolids was determined using a CHN Series II Perkin Elmer instrument, while P content was measured by XRF analysis. Total organic carbon dissolved in the leachate stream was measured using TOC-L (Shimadzu Corporation). Total N representing the sum of total Kjeldahl nitrogen (TKN) and  $\text{NO}_x$  and total P analysis, as well as PFAS analysis, were performed externally at ALS Water Resource Group, Melbourne, Australia.

## 3. Results and discussions

### 3.1. Effect of acid types

The efficiency of three mineral acids (sulfuric, nitric and hydrochloric) and two organic (acetic and citric) acids at the same volume concentration of 3% (v/v) and 5% (w/v) solids were studied on HMs extraction (Fig. 2). Mineral acids outperformed organic acids, and

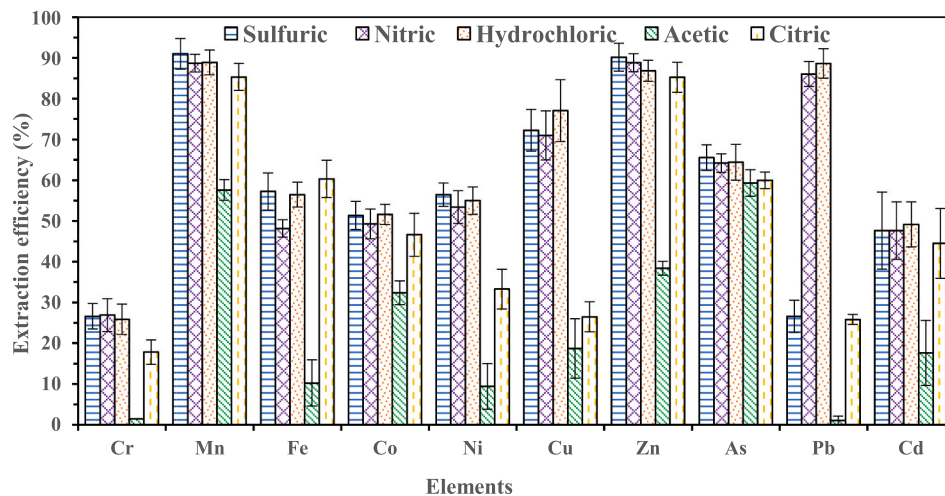


Fig. 2. Effect of mineral and organic acid solutions on the metal extraction efficiency from biosolids (conditions: 5% (w/v) solids, 3% (v/v) acid concentration, 25 °C, 30 min, and 600 rpm).

except for Pb, all mineral acids perform similarly in the metal extraction process. The high ionising power and extremely low pH of the mineral acids (~1.7) compared to the organic acids (~2.7) favoured the solubilisation of HMs (Gaber et al., 2011). Most sulfate, nitrate, and chloride salts are highly soluble in water and dilute acids, which may explain the similar metal extraction efficiencies of the three mineral acids. Sulfuric acid performed poorly in removing Pb owing to the low solubility (0.038 g/L) of  $\text{PbSO}_4$  in water ( $K_{sp@298\text{ K}} 1.6 \times 10^{-8}$ ). Generally, organic acids are considered weak acids ( $\text{pK}_a > 1$ ) as the ionised hydrogen concentration is typically lower than strong acids ( $\text{pK}_a < 0$ ) at the same molar concentration. For instance, the ionised hydrogen concentration of nitric acid is 100% of the acid concentration, whereas the ionised hydrogen concentration of citric acid is equivalent to 1.3–2.1% of nitric acid concentration (Lee et al., 2005). Therefore, it is expected that both organic acids have weaker ionic strength to desorb HMs ions in the biosolids, especially at low acid concentrations. However, of the two organic acids, citric acid was competitive with mineral acids despite having a similar pH to acetic acid in the metal extraction process. Citric acid is a natural chelating agent, and citrate ions form soluble complexes with cations of metals (Ma et al., 2020). Moreover, acetic acid is dicarboxylic while citric acid is tricarboxylic; the presence of an extra carboxylic group in citric acid also favours the number of available chelating sites for metal extraction (Gheju et al., 2011). Therefore, the chelating mechanism of citric acid was responsible for the high metal extraction rather than the acidolysis (reaction with  $\text{H}^+$ ) mechanism for the mineral acid-based leaching. Studies have demonstrated that the oxidation-reduction potential (ORP) of the leaching solvents can affect their metal extraction ability since metal solubilisation usually involves an ion-exchange reaction with protons from acid (Babel and del Mundo Dacera, 2006; Bayat and Sari, 2010; Blais et al., 2005; Pathak et al., 2009). In this work, 3% nitric acid had the highest ORP of 611 mV, followed by sulfuric acid (590 mV) and hydrochloric acid (473 mV). This ORP value can be related to the amount of dissolved oxygen each solvent can donate to participate in redox reactions involving metal ions and  $\text{H}^+$ . However, there is no obvious difference in the removal efficiency of the three mineral acids for all metal ions (except Pb), irrespective of the ORP of the slurry/solution. Hence, the metal leaching process observed in this study can be stated to be largely controlled by the solution pH. This observation is contrary to a few studies reporting that both the leaching solution pH and ORP influence HMs solubilisation in biosolids (Beauchesne et al., 2007; Blais et al., 2005; Mercier et al., 2002). In particular, Cu dissolution was found to be driven by the redoxolysis mechanism rather than acidolysis due to the higher affinity of Cu to organic matter in sludge (Blais et al., 2005; Strasser et al., 1995). Based on this, the

leaching of biosolids was further tested with strong oxidising solutions such as 3% acidified ferric sulfate (670 mV) and ferric sulfate added hydrogen peroxide (603 mV). However, no significant improvement in metal extraction was observed, particularly for Cu and Cr, compared to mineral acids (data not shown). A previous study has reported that there was an optimum pH at which ORP of slurry becomes influential on HMs extraction efficiency (Beauchesne et al., 2007). Also, different washing agents may have various degrees of affinity and selectivity for different HMs. The removal efficiencies of multiple HMs in biosolids can be greatly improved by composite or sequential treatment (Shi et al., 2020). From these results, sulfuric acid was selected for subsequent experiments due to the relatively low cost of  $\text{H}_2\text{SO}_4$ , industrial maturity, and lesser toxicity of sulfates of HMs than their corresponding nitrates or chlorides salts at the same molar concentration (Erichsen Jones, 1934; Nie et al., 2015).

### 3.2. Effect of solids concentration

The effect of solids concentration on the metal extraction from biosolids using 3% v/v  $\text{H}_2\text{SO}_4$  at 25 °C, 600 rpm for 30 min was investigated, and the results are presented in Fig. 3. The solids concentration significantly influenced the extraction of the metals ( $p < 0.05$ ). The extraction of all metals (except Pb and Cr) at lower solids contents (1–3%) achieved ~60–95% removal compared to 30–80% removal at higher solids content (5–15%). This behaviour is expected from the stoichiometry of the leaching/desorption reaction. Notably, Mn and Zn had the least variation in extraction efficiency with the change in solids concentration because they have the highest proportion (75–90%) of acid-leachable metal fractions (F-1 + F-2) in the biosolids used in this study (Fig. S1). The change in solids concentration was largely inconsequential on Cr and Pb extraction. The consistent low solubilisation of Cr in biosolids can be attributed to the poor mobility of Cr; the trivalent metal ions such as Fe and Cr are more difficult to extract than the divalent ions such as Zn, Ni, and Cd due to the competitive uptake of protons by the more reactive species. Lead has the highest residual (inert) fraction (F-4) of all metals in the biosolids (Fig. S1); therefore, its extraction is usually limited by common acids (Gheju et al., 2011; Xiao et al., 2015). Moreover,  $\text{H}_2\text{SO}_4$  is not a suitable lixiviant for Pb extraction due to the low solubility of  $\text{PbSO}_4$  in water (see Fig. 2). The removal efficiencies of all other metals increased with decreasing solid/liquid ratio, and the maximum extraction efficiency for all metals was observed at the lowest solids content (1%). The result agrees with previous literature on the effect of solids concentration on metal extraction (Bayat and Sari, 2010; Kuan et al., 2010; Wu et al., 2009). Low solids content is

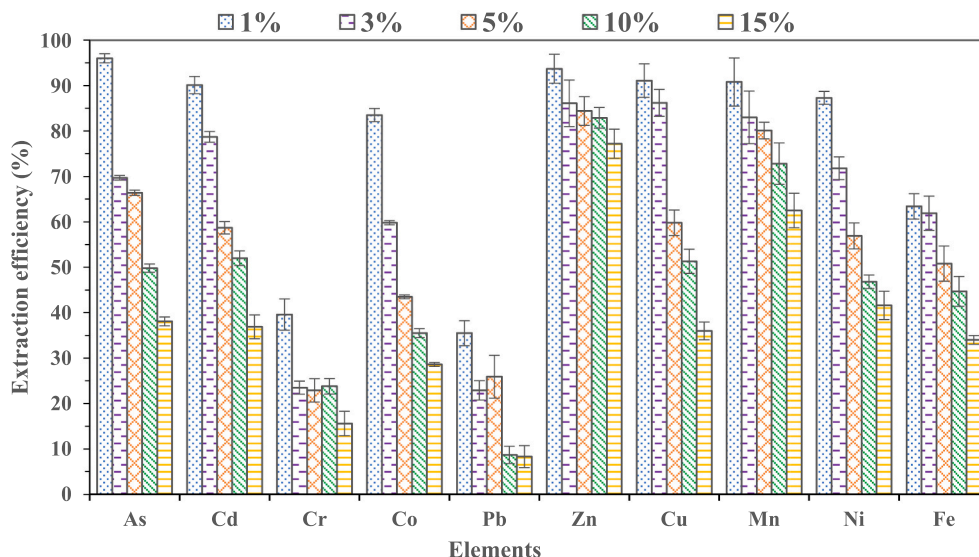


Fig. 3. Effect of solids concentration (w/v) on metal extraction efficiency from biosolids (conditions: 3% (v/v) H<sub>2</sub>SO<sub>4</sub>, 25 °C, 30 min, and 600 rpm).

associated with a higher volume of lixiviant and higher proton (H<sup>+</sup>) concentration, benefiting the dissolution of acid-exchangeable HMs fraction (F-1) in the biosolids. Since there are more H<sup>+</sup> than available surface chelating sites on the biosolids, the excess H<sub>2</sub>SO<sub>4</sub> can penetrate the biosolids pores and react with more metal ions, particularly the reducible (F-2) and oxidisable (F-3) HMs fractions, leading to overall higher extraction efficiency (Yang et al., 2021).

Table S1 shows the dissolved metal ion concentration in the leachate at different solids loading. The dissolved metal ion concentration in mg/

L liquid increased with increasing solids contents, while the metal ion concentration in mg/kg solids decreased with increasing solids contents (Table S1). Treatment using 1% (w/v) solids concentration produced cleaner biosolids, while the 15% (w/v) solids produced a highly concentrated metal-laden leachate stream which can make the recovery of metals more attractive. On the other hand, lower solid loading produced a dilute liquor stream. Moreover, 1% solids concentration appears unrealistic in practical scenarios in wastewater treatment plants (WWTPs). Besides, lower solids concentration is associated with higher

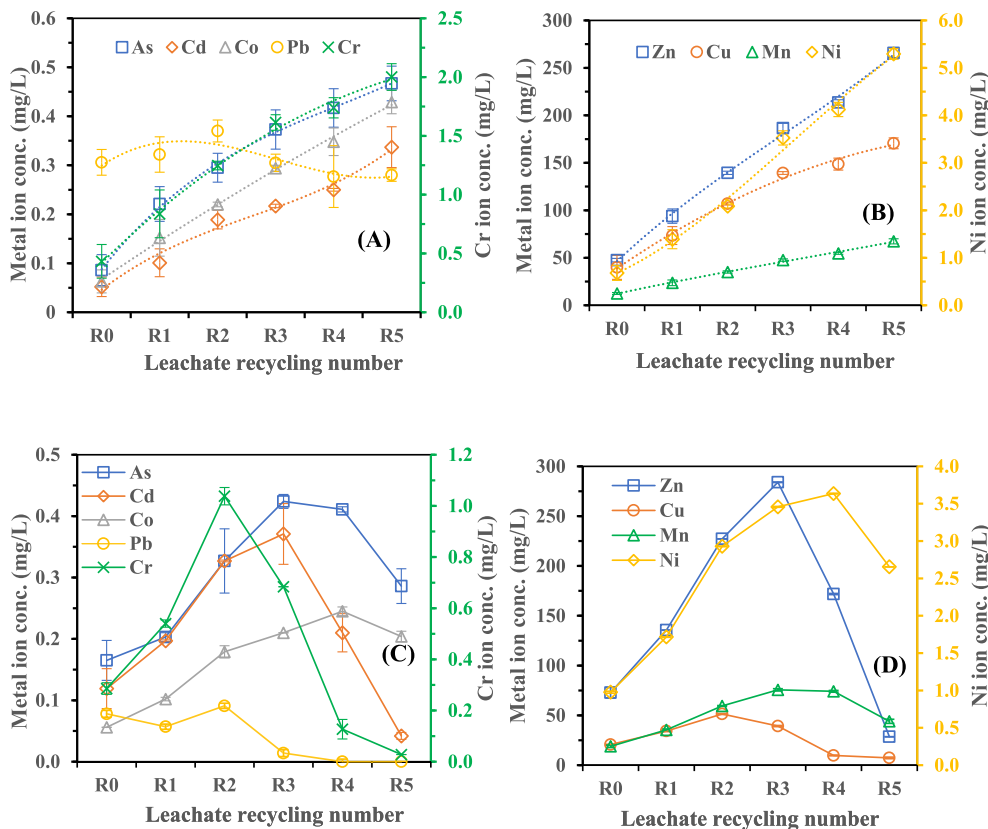


Fig. 4. Effect of fresh biosolids concentration on 100% recycling of the leachate stream (A) & (B) 5% solids (C) & (D) 10% solids (conditions: 3% (v/v) H<sub>2</sub>SO<sub>4</sub>, 25 °C, 30 min, and 600 rpm).

lixiviant consumption, and dewaterability can be challenging (Vesilind and Hsu, 1997). Similarly, at 15% solids, the mass transfer limitation was significant, negatively impacting mixing and liquid recovery, and the overall metal ion removal efficiency was the lowest. In fact, at 20% solids, mixing and separation became difficult, and the leaching process was not successful (data not reported). Hence, a moderate 5–10% solids loading may be a good balance and are the typical value in most biosolids leaching operations (Gheju et al., 2011; Wang et al., 2015; Wu et al., 2009).

### 3.3. Recyclability of the leachate stream

#### 3.3.1. Metal saturation concentration and the leachate recycling efficiency

The cumulative metal concentration in the leachate stream after five successive leaching cycles at 5% and 10% solids using 3% v/v H<sub>2</sub>SO<sub>4</sub> solution, 25 °C, 30 min, and 600 rpm is presented in Fig. 4(A–D). It is obvious that the primary leachate stream (R0) from the parent leaching experiment has not reached its maximum extraction capacity as more metals were extracted from fresh biosolids using the R0 stream five times. At 5% solids, the R0 stream had higher extraction strength than that at 10% because of the higher liquid-to-solid ratio and the dilute concentration of the dissolved metal. A higher liquid-to-solid ratio slowed the attainment of thermodynamic equilibrium between the dissolved metal species and the acidic solution (Lee et al., 2006). The leachate streams obtained at 10% solids were saturated faster compared to 5% solids. The primary leachate at 5% solids was recycled up to five times without reaching saturation point (Fig. 4(A&B)), while the leachate at 10% solids can only be reused up to three times, beyond which a rapid decline in cumulative concentration was observed (Fig. 4(C&D)). There was at least a 3-fold increase in the concentration of all metals (except Pb) by completely reusing the primary leachate stream from R0 to R5 (Fig. 4(A&B)). At 5% solids, the percentage increase in metal ion concentration in the leachate from R0 to R3 can be ranked as Cu(II) (249) < Cr(III) (273) < Mn(II) (284) < Zn(II) (293) < Cd(II) (317) < As(III) (334) < Co(II) (367) < Ni(II) (419). However, at 10% solids (Fig. 4(C&D)), there was a lesser increase in the cumulative concentration from R0 to R3, and the percentage increase was Cu(II) (90) < Cr(III) (139) < As(III) (157) < Cd(II) (212) < Ni(II) (254) < Co(II) (275) < Zn(II) (290) < Mn(II) (300). The percentage increase in cumulative concentration for Mn and Zn was similar at 5% and 10% solids, whereas there was a substantial decrease in the accumulation of other metals at 10% solids compared to 5% solids. Expectedly, higher solids loading limited the efficiency of metal accumulation during leachate recycling at the same extraction cycle with 5% solids. In particular, the cumulative Cu loading during recycling was severely impacted at 10% solids, possibly due to the dominant redox reaction between soluble Cu(II) and iron(II) sulfate, the mechanism which has been elucidated in previous literature (Matocha et al., 2005). The 100% recycling of the leachate stream at 10% solids performed competitively with 5% solids only in removing easily leachable metal fractions (F-1 and F-2) such as Zn and Mn, while the removal of other metal species dominant in F-3 was largely difficult. The removal of metal ions in F-3 fractions will require abundant protons from fresh H<sub>2</sub>SO<sub>4</sub> solution as well as harsh oxidising conditions to break the organometallic bond (Beauchesne et al., 2007). The monotonic decline in the extraction efficiency after the third recycling at 10% solids (Fig. 4(C&D)) was due to Al/Fe-induced co-precipitation of metal from the leachate to the solid phase as the solution pH approaches 3, which is conducive for ferric precipitation (Marchiorretto et al., 2005). The pH of the R5 stream at 10% solids was 4.5, while it was 2.4 at 5% solids.

Furthermore, it was observed that all metal extraction profiles followed closely that of Fe, and the improved extraction of HMs using the spent leachate stream can be attributed to the role of ferric sulfate hydrates in the metal desorption process. The iron source in the biosolids is the ferric salt coagulant used during the wastewater treatment process. Sulfuric acid solution can partly dissolve ferric-containing salts (such as

FeCl<sub>3</sub> or FeOOH), and then dissolved ferric ion can form ferric sulfate through ion exchange reaction with SO<sub>4</sub><sup>2-</sup> or HSO<sub>4</sub><sup>-</sup> from H<sub>2</sub>SO<sub>4</sub> (Demol et al., 2022). Ferric sulfate is a well-known leaching agent which acidifies by hydrolysis (Fe<sup>3+</sup> + H<sub>2</sub>O = FeOH<sup>2+</sup> + H<sup>+</sup>) and increases the elution efficiency of HMs from soils and biosolids (Bayat and Sari, 2010; Ito et al., 2000; Shi et al., 2020; Strasser et al., 1995). X-ray photoelectron spectra of the metal precipitates confirmed the presence of ferric sulfate (Fig. S2). The effective extraction of HMs by dissolved Fe<sup>3+</sup> is due to its ability to oxidise metal sulfides to soluble metallic ions and the release of more protons through the hydrolysis of ferric hydrates (Pathak et al., 2009). The dissolution of inherent ferric-containing components in biosolids and the subsequent formation of ferric sulfates extended the overall extraction strength of the leachate stream during recycling. The presence of native ferric salts was beneficial for the reuse of the leachate stream; however, there is a critical Fe<sup>3+</sup> concentration beyond which it counteracts the HMs extraction as Fe<sup>3+</sup> precipitates at a low pH value (<4). It was observed that the higher the concentration of Fe in the stream, the better the extraction efficiency of other metals up to a certain Fe concentration (~1400 mg/L). This is consistent with the study of Ito et al. (2000), who observed that the higher the amount of ferric iron added, the lower the pH of the lixiviant and the higher the extraction efficiency of HMs (~80%) from digested biosolids at low solids concentration (2% w/w). In other studies, leaching at pH 2 with acidified ferric iron outperformed H<sub>2</sub>SO<sub>4</sub> in extracting common HMs from biosolids (Bayat and Sari, 2010; Ito et al., 2000). The combination of ferric sulfate and acid solutions at different dosage had positive synergistic interactions for the solubilisation of multiple HMs from biosolids and soils (Beauchesne et al., 2007; Shi et al., 2020).

#### 3.3.2. Effect of make-up solution on the leachate recyclability

The cumulative metal ion concentration in the leachate stream after ten successive cycles with the addition of make-up lixiviant between each cycle is shown in Fig. 5. A constant feed rate of 5 g or 10 g of dry biosolids per 100 mL liquid for a 30 min leaching cycle was maintained. Contrary to the observation at 100% leachate recycling, without adding make up lixiviant (Fig. 4), the continuous addition of 3% H<sub>2</sub>SO<sub>4</sub> as FL prolonged the extraction strength of the spent leachate until R8 stage (Fig. 5). At 5% solids (Fig. 5), there was a substantial increase (at least 250%) in the cumulative metal ion concentration (except for Pb) from R0 to R10. For instance, Ni(II) was concentrated from 0.5 to 3.5 mg/L, Zn(II) from 38.9 to 277 mg/L, Cu(II) from 11.5 to 100 mg/L, As(III) from 0.14 to 0.51 mg/L, Cd(II) from 0.04 to 0.34 mg/L, Cr(III) from 0.12 to 1.2 mg/L, Co(II) from 0.04 to 0.22 mg/L, and Mn(II) from 10.3 to 71.5 mg/L. There was a steady increase in the cumulative metal ion concentration from R0 to R4 due to the low make-up ratio of the FL in the total leachate stream (<25%). The addition of FL to the leachate stream possibly aided the dilution of the metal ion concentration and hence enhanced the extraction strength (and capacity) of the stream. Up to R7, the increase in the metal ion concentration far outweighed the dilution effect of the added fresh solution. Nevertheless, adding FL was not beneficial beyond R6 as the leachate had been fully saturated with the metal ions. This observation was due to the similar extent of metal ions dilution and extraction efficiency in the stream by the added FL beyond R6. At R6, increasing the make-up ratio above 15 vol% would likely enhance the metal extraction strength of the stream further. The overall extraction trend of the HMs was largely governed by Fe, which reached saturation at R6. Contrary to the observation for 100% leachate recycling without adding make up lixiviant (Fig. 4), the continuous addition of the FL and the acidifying effect of Fe<sup>3+</sup> kept the pH of the leachate stream at <2 throughout the process, limiting ferric precipitation.

The addition of make-up acid lixiviant was less beneficial in enhancing the recyclability of the leachate stream at 10% solids compared to 5% solids (Fig. S3). There was no monotonic increase in the concentration of metal ions, and the irregular increase and decrease in the cumulative concentration across the ten leaching cycles can be

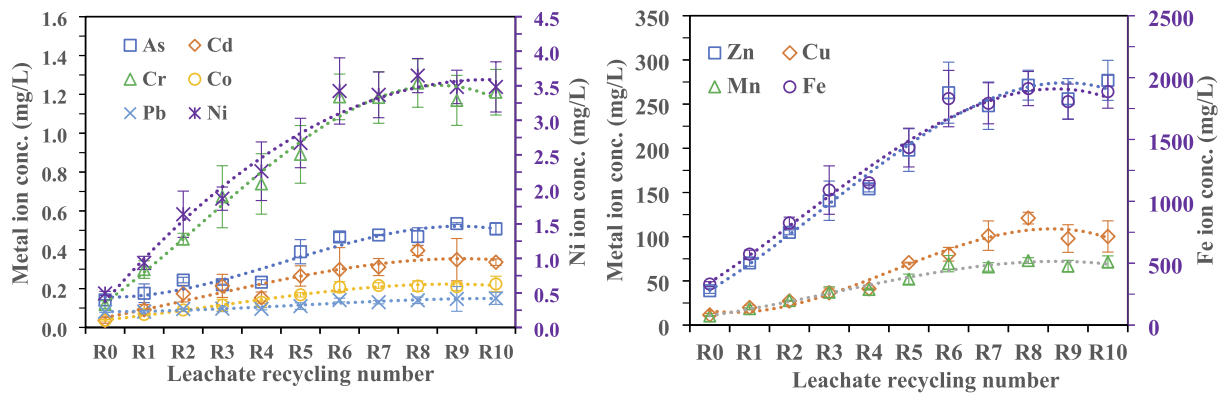


Fig. 5. Effect of make-up lixiviant on the recyclability strength of the leachate stream at 5% fresh biosolids concentration (conditions: 3% (v/v) H<sub>2</sub>SO<sub>4</sub>, 25 °C, 30 min, and 600 rpm).

attributed to Fe(III) precipitation. The leachate at 10% solids saturated faster than at 5% solids, and pH increased rapidly, thus facilitating Fe (III) precipitation much earlier. Iron(III) co-precipitated other metals in the stream. Contrary to the observation at 5% solids, adding FL between successive leaching could not suppress Fe precipitation (Fig. S3) at 10% solids. The dilution and acidifying effect of the FL on the metal ion concentration in the leachate stream were minimal at higher solids loading. The sharp rise in solution pH rather than the increase in Fe concentration stimulated Fe co-precipitation reaction at 10% solids. For instance, at 10% solids, Fe precipitation began at a maximum concentration of ~1400 mg/L (pH 2.45), whereas, at 5%, no Fe precipitation occurred even at the maximum concentration of 1830 mg/L (pH 1.85). At low pulp density (5% solids), the overall extraction efficiency of the spent stream was competitive with the FL, and the performance improved with increasing Fe concentration in the stream. Acidified ferric salt leaching is optimally performed at low solids concentration (<5% w/v) to avoid a rapid increase in pH and minimise ferric precipitation, which is counterproductive for HMs solubilisation (Bayat and Sari, 2010; Ito et al., 2000).

Leachate recycling could bring significant cost savings for H<sub>2</sub>SO<sub>4</sub> lixiviant besides environmental benefits. The 100% recycling of the spent leachate at 5% solids loading for five leaching cycles (Fig. 4) could save 4.5 times the required H<sub>2</sub>SO<sub>4</sub> volume at 90% liquid recovery per leaching cycle. Similarly, for the partial recycling of the leachate with 15% make-up lixiviant at 5% solids for six leaching cycles (Fig. 5), there

could be ~5 times reduction in the volume of H<sub>2</sub>SO<sub>4</sub>. Assuming a linear relationship between H<sub>2</sub>SO<sub>4</sub> volume and cost, around 400% cost savings can be achieved with leachate recycling with make-up lixiviant, which may substantially lower the cost of acid leaching.

### 3.4. Metal recovery from the concentrated leachate stream

A single-step or two-step NaOH co-precipitation and biochar adsorption were investigated for recovering HMs from the saturated leachate stream. Metals like Cr, Cu, Pb, and Zn do not form hydroxide precipitates at pH <6, allowing the separation from ferric iron and aluminium, which precipitate at pH <5 (Marchioretto et al., 2005). Table S2 shows the metal ion composition of the leachate stream used for the metal recovery experiments. It was observed that the concentration of Zn, Mn, and Cu in the leachate was up to 100 mg/L. Concentrations of all other HMs were < 5 mg/L, while Fe, Al, and alkali and alkaline earth metals (AAEMs: Na, K, Mg, and Ca) were highly concentrated in the stream (>500 mg/L). The metal recovery at each precipitation stage is shown in Table 2, while the overall metal recovery from the different methods is shown in Fig. 6.

The single-stage NaOH precipitation at pH 9 recovered about 9–99% of the HMs. The recovery efficiency of the metals can be ranked as Zn (99%) ≈ Cd (99%) > Cr (97%) > Pb (79%) > Co (33%) > Ni (31%) > As (11%) > Cu (9%). The precipitation of these HMs was accompanied by the precipitation of >90% for Fe, Al, Ca, Mg, and Mn. The precipitation

Table 2  
Metals recovery from the leachate stream under different methods.

Description	Metals	NaOH consumption, pH, and metal removal efficiency in different methods					
		Single-stage co-precipitation	2-stage co-precipitation		H <sub>2</sub> O <sub>2</sub> pre-2-stage co-precipitation	Biochar sorption	
Stages	–	One stage	1st	2nd	1st	2nd	One stage
NaOH (g/mL) <sup>a</sup>	–	0.11	0.04	0.08	0.05	0.06	0.04
pH range	–	2.5–9.0	2.5–4.5	4.5–9.0	2.5–4.5	4.5–9.0	2.5–4.5
Heavy metals (%) <sup>b</sup>	As	11.4	20.4	8.4	13.0	60.6	19.0
	Cd	98.9	32.7	94.3	35.5	97.2	46.8
	Co	32.9	3.2	32.3	13.4	51.5	32.1
	Cr	97.4	72.7	85.5	82.6	57.3	47.1
	Cu	9.30	15.1	31.3	24.5	49.0	56.0
	Ni	30.7	3.50	33.2	33.2	73.8	70.5
	Pb	78.7	34.0	78.7	80.9	26.6	3.80
	Zn	99.3	35.5	96.3	50.0	99.0	56.8
Other metals (%) <sup>b</sup>	Al	97.4	91.4	77.9	95.4	96.6	95.8
	Ca	91.0	2.30	88.9	23.8	76.9	20.9
	Fe	98.5	99.0	59.5	99.1	96.1	46.6
	K	18.7	16.8	22.3	24.7	46.2	22.6
	Mg	98.0	3.40	99.0	13.3	92.2	29.6
	Mn	99.3	11.4	99.2	22.1	94.4	35.6

<sup>a</sup> 6 M NaOH consumed (g/mL leachate).

<sup>b</sup> The metal removal efficiency in the second stage refers to the percentage removal of the remaining metal in solution after the first stage.

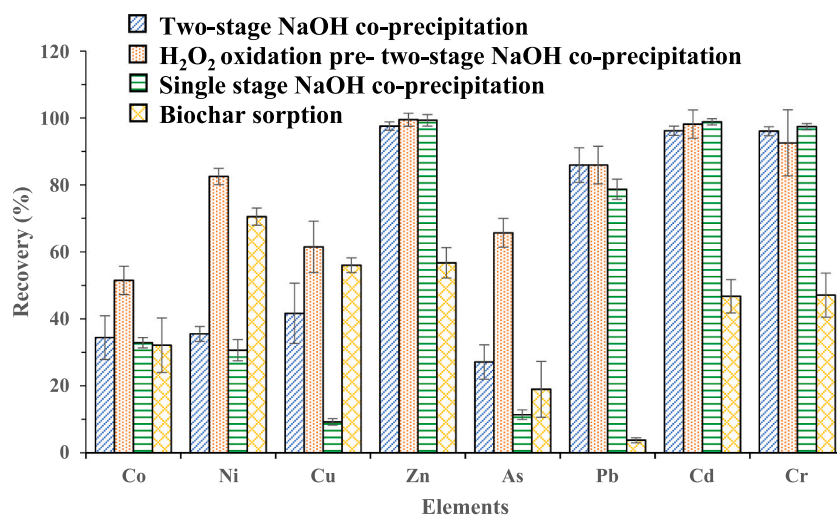


Fig. 6. Overall removal efficiency of HMs under different recovery techniques.

of Co, Ni, As, and Cu was low under this condition due to the high solubility of their respective metal hydroxide at pH 9 (see Fig. S4). It was hypothesised that the presence of Fe and Al would facilitate the precipitation of HMs in the stream. However, the presence of both metal salts did not improve HMs recovery at the basic pH 9 relative to the observation at acidic pH 4.5. The co-precipitating effect of Fe and Al on the other metals cannot be observed under the single-stage recovery, and only the solubility of the various metal hydroxides at pH 9 can be assessed. The single-stage precipitation resulted in a low recovery efficiency of some HMs and, at the same time, produced a highly contaminated HMs sludge stream. This may reduce the attractiveness of the recovered metal sludge for downstream separation and subsequent applications in catalysis or smelting.

The staged recovery of the metals at pH 4.5 (stage 1) and pH 9.0 (stage 2) effectively precipitated Fe and Al from the leachate stream in the first stage, while most of the HMs were recovered in the second stage (Table 2). About 99% Fe and 91% Al were recovered in the first stage (pH 4.5); however, 3–73% of some HMs were co-precipitated. For example, 73% Cr, 36% Zn, 34% Pb, 33% Cd, 20% As, 15% Cu, 4% Ni and 3% Co were co-precipitated with Fe/Al at pH 4.5. The removal of these HMs at pH 4.5 was due to the sorption capacity and co-precipitating ability of Fe and Al hydroxides (Lee et al., 2002). No precipitation of these metals was observed at pH 4.5 in the absence of Fe and Al when the solution of their pure salts was treated with NaOH (data not shown). Only Cd and Zn had the highest removal efficiency of >94% in the second stage. In comparison, other HMs' removal efficiency was 8–79%, similar to the single-stage precipitation from solutions of same pH value of 9 (Table 2). The recovery of As was minimal in the staged NaOH co-precipitation; the highest recovery of 20% occurred at pH 4.5, which could be attributed to the formation of ferric arsenate (Hao et al., 2018). The major benefit of the dual-stage precipitation, aside from the selective recovery of Al, Fe and Cr, was the improvement in Cu recovery from 9% in the single-stage to 31% in the two-stage at pH 9. The mechanism involving the precipitation of ferric iron and the associated Cu loss from solution has been elucidated elsewhere (Javed and Asselin, 2020). The chosen pH 9 is a compromise for the recovery of all the HMs; further optimisation studies are required to identify the optimum recovery pH for each metal species in the solution. From the theoretical solubility curve for metal hydroxides (Fig. S4), Cu has the lowest solubility (<0.1 mg/L) at pH 9 relative to other HMs. However, this theoretical solubility behaviour contradicts the low recovery of Cu (<50%) at pH 9 with a solubility concentration of 36 mg/L. Probable explanations for this include the affinity of Cu(II) to dissolved organic ligands making complexes and the crystal growth vs (super)saturation level of the various metals in the solution (Weng et al., 2002). Moreover, the leachate

stream contains many metal and non-metal species, which may cause significant deviation from the theoretical solubility behaviour of pure metal in aqueous systems.

Adding H<sub>2</sub>O<sub>2</sub> prior to NaOH precipitation improved the recovery of some HMs from the leachate. For example, without adding H<sub>2</sub>O<sub>2</sub>, the overall recovery of As was 27%; however, it increased to 66% when H<sub>2</sub>O<sub>2</sub> was added. Similarly, Cu recovery increased by 47%, Co recovery improved by 53%, and Ni recovery increased by 130%. In fact, increasing the amount of H<sub>2</sub>O<sub>2</sub> added by a unit volume before the staged NaOH precipitation further increased the recovery of As, Co, Cu, and Ni by 48%, 22%, 18%, and 68%, respectively (Fig. S5). The addition of H<sub>2</sub>O<sub>2</sub> had no improvement on the recovery of Zn, Pb, Cd, and Cr compared to the sole 2-stage NaOH co-precipitation. The oxidation of dissolved organics by H<sub>2</sub>O<sub>2</sub> enhanced the desorption of metal species. The biosolids used in this study contain organically bonded HMs (F-3 fraction; Fig. S1), where the bonding strength can be ranked as Cu > As > Co > Ni. The complexation of HMs with dissolved organic matter in aqueous solutions has been reported to influence the solubility and mobility of metals (Weng et al., 2002).

The removal efficiency of the HMs via biochar adsorption was poor compared to the alkali precipitation and did not follow any specific trend. Only a modest 3–70% uptake was achieved, with the highest for Ni and the lowest for Pb. The performance of biochar adsorption for HMs uptake from aqueous solutions is influenced by many factors, including the adsorbent properties, pH, adsorbate concentration, temperature, and solution chemistry of the metal species (Ni et al., 2019). Most of these factors have not been optimised in this study and may contribute to the relatively poor removal efficiency of the biochar sorption process. The FTIR spectra of the biochar before and after the sorption (Fig. S6) confirmed the non-depletion of the surface functional group of the biochar, suggesting the dominance of physisorption. Chemisorption usually involves the chemical reaction between the charged surface functional group of the biochar adsorbent and the metal ions via electrostatic precipitation, organo-metallic complexation, and deprotonation phenomena (Yang et al., 2021).

### 3.5. Process configurations and mass balances

The various unit operations were put together in a process flow diagram (Fig. 7) to provide an insight into the materials requirement of the treatment process demonstrated in this work. Based on our findings, leachate recycling is only attractive at 5% solids which can considerably lower acid and alkali consumption. However, processing 10% solids with no leachate recycling may be favourable commercially. Fig. 7(A) shows the mass balance for processing 10% solids with no leachate



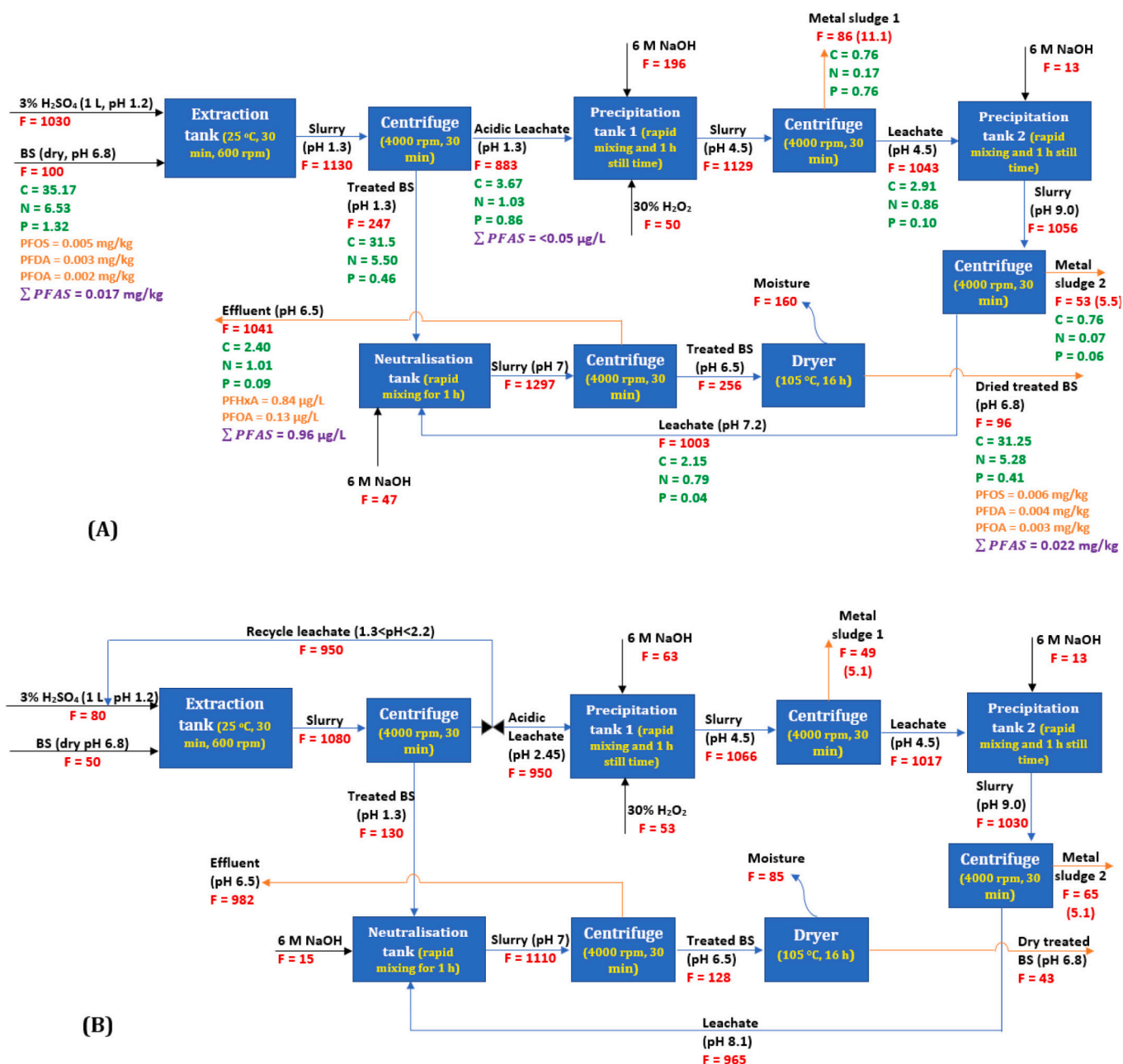


Fig. 7. Process block flow diagram for HMs removal and recovery from biosolids. (A) for processing 10% solids with no leachate recycling (B) for processing 5% solids with leachate recycling (with top-up lixiviant). Red font (F) denotes mass flow in grams; the flowrate in parenthesis corresponds to the dry weight of the metal sludge; green font (C, N, and P) denotes carbon, nitrogen, and phosphorous mass flows in grams, while the purple font denotes total PFAS concentration in the major streams. (For interpretation of the references to colour in this figure legend, the reader is referred to the web version of this article).

recycling, while Fig. 7(B) shows the balance for processing 5% solids with leachate recycling with make-up lixiviant. The separation of solids from the leachate produced acidic treated biosolids (pH 1.3), which cannot be used directly for land application or thermal processing without prior neutralisation or conditioning. A considerable volume of water is required to wash off residual acid in the treated biosolids and raise the pH to near neutral values. It is proposed that the clarified alkali stream be used to neutralise the acidic treated biosolids in an attempt to close the process loop and reduce the volume of aqueous waste generated. In Fig. 7, the total mass flow of streams (grams) in and out of each unit operation is denoted as F, and carbon, nitrogen and phosphorous mass flows (in grams) are denoted as C, N, and P, respectively. For a 1:10 w/v (biosolids to H<sub>2</sub>SO<sub>4</sub> solution ratio) feed rate (Fig. 7(A)), the

overall liquid recovery was 77%, while overall solids recovery was 96% (dry biosolids basis). When the feed ratio was changed to 1:20 w/v (5% solids) with leachate recycling, the mass balance is shown in Fig. 7(B). Overall liquid and solids recovery was 84% and 86%, respectively. Notably, the leachate recycling yielded about a 92% and 43% decrease in H<sub>2</sub>SO<sub>4</sub> and NaOH consumption, respectively. The lixiviant consumption changes remarkably when processing 5% solids with no leachate recycling (Fig. S7). The total H<sub>2</sub>SO<sub>4</sub> consumption (g/g biosolids) doubled, and total NaOH consumption increased by 25% relative to processing 10% solids. The overall results with respect to solids and liquid recovery, metal sludge recovery as well as H<sub>2</sub>SO<sub>4</sub> and NaOH consumption at different process configurations are summarised in Table 3. At 10% solids processing, the major composition (wt%) of

**Table 3**  
Summary of process performance at different configurations.

Indicators	Unit	Process configurations		
		10% solids with no leachate recycling	5% solids with no leachate recycling	5% solids with leachate recycling with make-up lixiviant
Overall solids recovery	wt% dry basis	96	87.6	85.8
Overall liquid recovery	wt%	76.7	80.3	82.4
Total metal sludge recovery	g/g dry biosolids	0.17	0.19	0.21
H <sub>2</sub> SO <sub>4</sub> consumption <sup>a</sup>	g/g dry biosolids	0.57	1.14	0.09
NaOH consumption <sup>b</sup>	g/g dry biosolids	0.50	0.63	0.36

<sup>a</sup> H<sub>2</sub>SO<sub>4</sub> stock solution (98% Assay, SG = 1.84).

<sup>b</sup> NaOH (Analytical reagent grade pellets, SG = 2.13).

recovered metal sludge 1 is 10.7% Fe, 8.8% Na, 8.2% S, 7.9% P, and 5.5% Al while that of metal sludge 2 is 13.1% Na, 12.5% S, 12.4% Ca, 6.0% P, and 3.3% Mg. The detailed composition is provided in Table S3, and the thermal stability profile of the recovered metal sludge is shown in Fig. S8. The recovered metal can be employed in a number of potential applications in catalysis, smelting, and materials production, such as metal-based adsorbents/nanomaterials depending on the required purity and properties (Tawalbeh et al., 2021; Yu et al., 2022).

### 3.6. Fate of nutrients and PFAS

Considering the processing of 10% solids with no leachate recycling, the balance around organic nutrients (C, N, and P) is presented in Fig. 7 (A). The overall process modestly preserved the organic matter in the biosolids as the reduction in C, N, and P contents from raw biosolids to treated biosolids was 11%, 19%, and 65% (w/w), respectively. This observation on nutrient dissolution is comparable to other studies. For example, Mercier et al. (2002) reported about 19% decrease in dissolved organic carbon in treated sludge compared to raw sludge. Similarly, Beauchesne et al. (2007) and Shiba and Ntuli (2017) observed about 77% P and 82% P solubilisation, respectively, from biosolids treatment using H<sub>2</sub>SO<sub>4</sub> (pH <2). The excessive dissolution of P in biosolids is a typical limitation of mineral acid leaching. The joint use of ferric salts and/or H<sub>2</sub>O<sub>2</sub> with H<sub>2</sub>SO<sub>4</sub> has been reported to enhance P retention in biosolids as ferric phosphate (Beauchesne et al., 2007). However, unlike C and N, which largely remain in the dissolved form in the liquid streams, >90% of the total dissolved P was recovered at the metal precipitation stages. Phosphorous has a high affinity for metal ions (particularly Fe) in aqueous media which can be recovered as metal phosphate precipitates (Vardanyan et al., 2018). The dissolution and recovery of P is more sensitive to pH compared to C and N. In the neutralisation stage, where the acid-leached biosolids are treated with NaOH, about 1% C, 4% N and 11% P were further lost from the solids to the liquid phase. The final effluent stream contains about 0.23% C, 0.10% N and 0.009% P (w/w). The guideline for the disposal of this effluent stream as trade wastewater was assessed with respect to the organic and metal concentration load (Table S4). All the metals and organic nutrient concentrations (except for N) are within the acceptable criteria set by South East Water Recycling Corporation, Melbourne, Australia. The excess nitrogen can be removed from the effluent stream by adsorption, and the final liquid can be safely discharged.

Per- and poly-fluoroalkyl substances (PFAS) are rapidly becoming a limiting contaminant for biosolids reuse in agricultural land. Therefore, there is interest in understanding the fate of the plethora of PFAS compounds during the hydrometallurgical treatment process. Twenty-eight common PFAS compounds, the major ones being PFOA (C<sub>8</sub>HF<sub>15</sub>O<sub>2</sub>), PFOS (C<sub>8</sub>HF<sub>17</sub>O<sub>3</sub>S), PFDA (C<sub>10</sub>HF<sub>19</sub>O<sub>2</sub>), PFBS (C<sub>4</sub>HF<sub>9</sub>O<sub>3</sub>S), and PFHxA (C<sub>6</sub>HF<sub>11</sub>O<sub>2</sub>), were measured in the raw biosolids, treated biosolids (with leachate neutralisation), acidic leachate, and the final effluent stream. The representative PFAS compounds detected in the

selected process streams and the total sum of PFAS are shown in Fig. 7 (A). The overall PFAS result is presented in Table S5. The acid extraction (at pH <2) did not leach out the PFAS compounds in the raw biosolids (0.0165 mg/kg), as the concentration of the PFAS in the acidic leachate stream was <0.05 µg/L. However, there appears to be an increase in the leachability of PFAS compounds with a carboxylic head group (particularly PFHxA and PFOA) at the neutralisation stage at pH > 7. The leaching of these PFAS compounds from the acidic treated biosolids (pH 1.3) slightly increased the concentration of the PFAS compounds in the final effluent to 0.96 µg/L. Nevertheless, the PFAS compounds reaching the liquid stream are substantially negligible (<1 µg/L), and the PFAS are largely retained in the treated biosolids (0.0221 mg/kg). Further investigations into the mechanisms controlling the mobility and the final fate of the diverse PFAS compounds during biosolids acid pre-treatment are needed.

Lastly, the viability of the developed closed-loop process with respect to residual nutrients and HMs concentration in the treated biosolids was briefly assessed. The concentration of nutrients and HMs in the treated biosolids with leachate neutralisation was compared with treated biosolids obtained under two different neutralisation washing scenarios at the same pre-treatment conditions. The neutralisation washing scenarios were (i) treated biosolids with leachate neutralisation, (ii) treated biosolids with no neutralisation, and (iii) treated biosolids with deionised water neutralisation. The concentration of the residual nutrients, HMs, and PFAS in the three treated biosolids streams are presented in Table 4. The concentrations are further benchmarked with EPA Victoria prescribed concentration for contaminant-grade biosolids (C1-grade and C2-grade) (EPA Victoria, 2004). The C1-grade refers to the least contaminant grade biosolids with respect to HMs concentration which can be applied to land unrestrictedly. Except for Cu in all scenarios, all other HMs concentrations met the requirements of C1-grade biosolids, with the lowest concentration obtained in treated biosolids with water neutralisation step. Most metal sulfates are soluble in water; therefore, water neutralisation washing helped in the dissolution of metal sulfate salts as well as the removal of H<sub>2</sub>SO<sub>4</sub>-insoluble metal species. Hence it is proposed that the treated biosolids obtained with the leachate neutralisation step be neutralised in a second step with deionised water to reduce the residual metal concentration load further, particularly for Cu. There is largely an inconsequential difference in residual nutrient concentration in the treated biosolids with respect to neutralisation washing scenarios.

## 4. Conclusions

This work provided a detailed investigation into the hydrometallurgical process for extracting and recovering HMs from biosolids. The extraction performance of mineral acids (H<sub>2</sub>SO<sub>4</sub>, HNO<sub>3</sub> and HCl) was similar and only citric acid performed competitively with mineral acids in achieving ~70% extraction of HMs at 5% solids loading. Low solids content (1–5% w/v) favoured HMs extraction and produced a leachate

**Table 4**

Concentration of residual nutrients, metals, and PFAS in biosolids streams obtained under different neutralisation washing scenarios by processing 10% solids.

Content	Elements/ abbreviations	Streams, pH, and concentration					
		Raw biosolids	Treated biosolids (no washing) <sup>a</sup>	Treated biosolids (leachate washing) <sup>b</sup>	Treated biosolids (water washing) <sup>c</sup>	C1-grade biosolids <sup>d</sup>	C2-grade biosolids <sup>d</sup>
	pH	6.8	2.0	6.5	7.0	7.0	7.0
Nutrients (% w/w dry feed basis)	C	35.4	32.9	35.2	36.4	–	–
	N	5.6	5.5	6.2	5.6	–	–
	K	1.1	0.4	0.3	0.2	–	–
	P	1.3	0.5	0.4	0.5	–	–
Major metals (% w/w dry feed basis)	Na	0.1	BDL <sup>e</sup>	1.5	BDL	–	–
	Mg	0.5	0.1	0.1	0.1	–	–
	Al	0.7	0.6	0.4	0.5	–	–
	Ca	10.2	8.5	6.8	5.4	–	–
	Fe	4.2	2.3	2.9	4.1	–	–
Trace metals (mg/kg dry feed basis)	As	<5	<5	<5	<5	20	60
	Cd	1.3	0.5	0.4	0.3	1	10
	Co	<5	<5	<5	<5	–	–
	Cu	690	380	420	220	100	2000
	Cr	20	16	14	14	400	3000
	Hg	0.7	0.9	0.9	0.9	1	5
	Mn	210	53	39	17	–	–
	Mo	8	8	8	9	–	–
	Ni	18	12	14	8	60	270
	Pb	20	17	18	18	300	500
	Se	5	4	4	3	3	50
Zn	850	160	160	48	200	2500	
Major PFAS <sup>f</sup> (mg/kg dry feed basis)	PFBS	0.0005	–	0.0003	–	–	–
	PFDA	0.0028	–	0.0040	–	–	–
	PFHxA	0.0014	–	0.0014	–	–	–
	PFOS	0.0048	–	0.0060	–	–	–
	PFOA	0.0019	–	0.0029	–	–	–
	∑PFAS	0.0165	–	0.0221	–	–	–

<sup>a</sup> Refers to the as-obtained acidic treated biosolids.<sup>b</sup> Refers to the treated biosolids obtained from the closed-loop process developed in this study (see Fig. 7(A)).<sup>c</sup> Refers to treated biosolids obtained from deionised water washing post the acid treatment step until neutral pH.<sup>d</sup> Refers to contaminant-grade biosolids as prescribed in Victoria EPA biosolids management guidelines (EPA Victoria, 2004).<sup>e</sup> BDL- Below detection limit.<sup>f</sup> Abbreviations and chemical formulae–PFBS: Perfluorobutanesulfonic acid, C<sub>4</sub>HF<sub>9</sub>O<sub>3</sub>S.PFDA: Perfluorodecanoic acid, C<sub>10</sub>HF<sub>19</sub>O<sub>2</sub>.PFHxA: Perfluorohexanoic acid, C<sub>6</sub>HF<sub>11</sub>O<sub>2</sub>.PFOS: Perfluorooctanesulfonic acid, C<sub>8</sub>HF<sub>17</sub>O<sub>3</sub>S.PFOA: Perfluorooctanoic acid, C<sub>8</sub>HF<sub>15</sub>O<sub>2</sub>.

stream with dilute metal concentration suitable for recycling, whereas high solids content >5% w/v produced a highly concentrated leachate stream attractive for metal recovery. The leachate stream produced at 5 and 10% solids can be completely recycled at least two times to reach saturation levels of metal ion concentration. However, the recycling of the leachate stream was only attractive at 5% solids; the rapid build-up of ferric iron concentration and increase in solution pH limit the recycling performance of the leachate stream at 10% solids loading. The continuous addition of fresh H<sub>2</sub>SO<sub>4</sub> solution as a make-up lixiviant during the partial recycling (85%) of the spent leachate stream enhanced the dilution of the metal ion concentration and suppressed the precipitation of ferric from the solution at 5% solids. The oxidation of dissolved organics by H<sub>2</sub>O<sub>2</sub> before the 2-stage NaOH precipitation achieved the optimum metal recovery of ~75% from the concentrated leachate stream. The developed process modestly preserved the organic nutrient to a larger extent in the treated biosolids with about 11% loss of carbon and 19% loss of nitrogen. The leaching of PFAS from biosolids into the aqueous phase was limited under the investigated conditions. The findings of this work provide a framework for developing a hydrometallurgical process for biosolids treatment which may be implemented within the existing wastewater treatment facilities.

#### CRediT authorship contribution statement

**Ibrahim Gbolahan Hakeem:** Conceptualization, Methodology,

Formal analysis, Investigation, Software, Writing – original draft. **Pobitra Halder:** Validation, Visualization, Data curation, Writing – review & editing. **Shefali Aktar:** Formal analysis. **Mojtaba Hedayati Marzbali:** Validation, Writing – review & editing. **Abhishek Sharma:** Writing – review & editing. **Aravind Surapaneni:** Resources, Supervision, Writing – review & editing. **Graeme Short:** Methodology, Supervision. **Jorge Paz-Ferreiro:** Supervision, Writing – review & editing. **Kalpiti Shah:** Conceptualization, Validation, Supervision, Project administration.

#### Declaration of Competing Interest

The authors declare that they have no known competing financial interests or personal relationships that could have appeared to influence the work reported in this paper.

#### Acknowledgements

This work is supported through Top-up scholarships from the School of Engineering, RMIT University and the ARC Training Centre for the Transformation of Australia's Biosolids Resources at RMIT University, Australia. The first author acknowledges the postgraduate scholarship received from RMIT University, Australia.

## Appendix A. Supplementary data

Supplementary data to this article can be found online at <https://doi.org/10.1016/j.hydromet.2023.106044>.

## References

- Abouelela, A.R., Mussa, A.A., Talhami, M., Das, P., Hawari, A.H., 2022. Industrial sludge valorization and decontamination via lipid extraction and heavy metals removal using low-cost protic ionic liquid. *Sci. Total Environ.* 835, 155451 <https://doi.org/10.1016/j.scitotenv.2022.155451>.
- Ait Ahsaine, H., Zbair, M., El Haouti, R., 2017. Mesoporous treated sewage sludge as outstanding low-cost adsorbent for cadmium removal. *Desalin. Water Treat.* 85, 330–338. <https://doi.org/10.5004/dwt.2017.21310>.
- Babel, S., del Mundo Dacera, D., 2006. Heavy metal removal from contaminated sludge for land application: a review. *Waste Manag.* 26, 988–1004. <https://doi.org/10.1016/j.wasman.2005.09.017>.
- Bayat, B., Sari, B., 2010. Comparative evaluation of microbial and chemical leaching processes for heavy metal removal from dewatered metal plating sludge. *J. Hazard. Mater.* 174, 763–769. <https://doi.org/10.1016/j.jhazmat.2009.09.117>.
- Beauchesne, I., Cheikh, R. Ben, Mercier, G., Blais, J.F., Ouarda, T., 2007. Chemical treatment of sludge: in-depth study on toxic metal removal efficiency, dewatering ability and fertilizing property preservation. *Water Res.* 41, 2028–2038. <https://doi.org/10.1016/j.watres.2007.01.051>.
- Blais, J.-F., Meunier, N., Sasseville, J.-L., Tyagi, R.D., Mercier, G., Hammy, F., 2005. Hybrid chemical and biological process for decontaminating sludge from municipal sewage. *US 6,855,256 B2*.
- de Fátima da Silva, M., de Sousa Oliveira, M.R., dos Santos, I.D., Radino-Rouse, P., Mansur, M.B., 2020. Iron precipitation strategies from nickel laterite ore sulfuric acid leach liquor. *Miner. Process. Extr. Metall. Rev.* 1–12 <https://doi.org/10.1080/08827508.2020.1809392>.
- del Mundo Dacera, D., Babel, S., 2006. Use of citric acid for heavy metals extraction from contaminated sewage sludge for land application. *Water Sci. Technol.* 54, 129–135. <https://doi.org/10.2166/wst.2006.764>.
- Demol, J., Ho, E., Soldenhoff, K., Karatchevseva, I., Senanayake, G., 2022. Beneficial effect of iron oxide/hydroxide minerals on sulfuric acid baking and leaching of monazite. *Hydrometallurgy* 211, 105864. <https://doi.org/10.1016/j.hydromet.2022.105864>.
- EPA Victoria, 2004. *Guidelines for Environmental Management: Biosolids Land Application*. Southbank, Victoria 3006, Australia.
- Ericksen Jones, J., 1934. *The Toxic Action of Heavy Metal Salts on the Three-Spined Stickleback (Gasterosteus Aculeatus)*. Aberystwyth, Wales.
- Feng, J.J., Jia, L., Liu, Q.Z., Chen, X.L., Cheng, J.P., 2018. Source identification of heavy metals in sewage sludge and the effect of influent characteristics: a case study from China. *Urban Water J.* 15, 381–387. [https://doi.org/10.1080/1573062X.2018.1483525/SUPPL\\_FILE/NURW\\_A\\_1483525\\_SM7700.PDF](https://doi.org/10.1080/1573062X.2018.1483525/SUPPL_FILE/NURW_A_1483525_SM7700.PDF).
- Fu, F., Wang, Q., 2011. Removal of heavy metal ions from wastewaters: a review. *J. Environ. Manag.* 92, 407–418. <https://doi.org/10.1016/j.jenvman.2010.11.011>.
- Gaber, S., Rizk, M., Yehia, M., 2011. Extraction of certain heavy metals from sewage sludge using different types of acids. *Biokemistri* 23, 41–48. <https://doi.org/10.4314/biokem.v23i1>.
- Geng, H., Xu, Y., Zheng, L., Gong, H., Dai, L., Dai, X., 2020. An overview of removing heavy metals from sewage sludge: achievements and perspectives. *Environ. Pollut.* 266, 115375 <https://doi.org/10.1016/j.envpol.2020.115375>.
- Gheju, M., Pode, R., Manea, F., 2011. Comparative heavy metal chemical extraction from anaerobically digested biosolids. *Hydrometallurgy* 108, 115–121. <https://doi.org/10.1016/j.hydromet.2011.03.006>.
- Guan, R., Yuan, X., Wu, Z., Wang, H., Jiang, L., Li, Y., Zeng, G., 2017. Functionality of surfactants in waste-activated sludge treatment: a review. *Sci. Total Environ.* 609, 1433–1442. <https://doi.org/10.1016/j.scitotenv.2017.07.189>.
- Gunarathe, V., Rajapaksha, A.U., Vithanage, M., Alessi, D.S., Selvasembian, R., Naushad, M., You, S., Oleszczuk, P., Ok, Y.S., 2020. Hydrometallurgical processes for heavy metals recovery from industrial sludges. *Crit. Rev. Environ. Sci. Technol.* 1–42 <https://doi.org/10.1080/10643389.2020.1847949>.
- Hakeem, I.G., Halder, P., Dike, C.C., Chiang, K., Sharma, A., Paz-Ferreiro, J., Shah, K., 2022a. Advances in biosolids pyrolysis: roles of pre-treatments, catalysts, and co-feeding on products distribution and high-value chemical production. *J. Anal. Appl. Pyrolysis* 166, 105608. <https://doi.org/10.1016/j.jaap.2022.105608>.
- Hakeem, I.G., Halder, P., Marzbali, M.H., Patel, S., Rathnayake, N., Surapaneni, A., Short, G., Paz-Ferreiro, J., Shah, K., 2022b. Mild sulphuric acid pre-treatment for metals removal from biosolids and the fate of metals in the treated biosolids derived biochar. *J. Environ. Chem. Eng.* 10, 107378 <https://doi.org/10.1016/j.jece.2022.107378>.
- Hao, L., Liu, M., Wang, N., Li, G., 2018. A critical review on arsenic removal from water using iron-based adsorbents. *RSC Adv.* 8, 39545–39560. <https://doi.org/10.1039/C8RA08512A>.
- Ito, A., Umata, T., Aizawa, J., Takachi, T., Morinaga, K., 2000. Removal of heavy metals from anaerobically digested sewage sludge by a new chemical method using ferric sulfate. *Water Res.* 34, 751–758. [https://doi.org/10.1016/S0043-1354\(99\)00215-8](https://doi.org/10.1016/S0043-1354(99)00215-8).
- Javed, T., Asselin, E., 2020. Fe(III) precipitation and copper loss from sulphate-chloride solutions at 150 °C: a statistical approach. *Metals (Basel)* 10, 669. <https://doi.org/10.3390/MET10050669>.
- Kabiri, S., Tucker, W., Navarro, D.A., Bräunig, J., Thompson, K., Knight, E.R., Nguyen, T. M.H., Grimison, C., Barnes, C.M., Higgins, C.P., Mueller, J.F., Kookana, R.S., McLaughlin, M.J., 2022. Comparing the leaching behavior of per- and polyfluoroalkyl substances from contaminated soils using static and column leaching tests. *Environ. Sci. Technol.* 56, 368–378. [https://doi.org/10.1021/ACS.EST.1C06604/ASSET/IMAGES/LARGE/ESI06604\\_0005.JPEG](https://doi.org/10.1021/ACS.EST.1C06604/ASSET/IMAGES/LARGE/ESI06604_0005.JPEG).
- Kuan, Y.C., Lee, I.H., Chern, J.M., 2010. Heavy metal extraction from PCB wastewater treatment sludge by sulfuric acid. *J. Hazard. Mater.* 177, 881–886. <https://doi.org/10.1016/j.jhazmat.2009.12.115>.
- Kundu, S., Patel, S., Halder, P., Patel, T., Hedayati Marzbali, M., Pramanik, B.K., Paz-Ferreiro, J., De Figueiredo, C.C., Bergmann, D., Surapaneni, A., Megharaj, M., Shah, K., 2021. Removal of PFASs from biosolids using a semi-pilot scale pyrolysis reactor and the application of biosolids derived biochar for the removal of PFASs from contaminated water. *Environ. Sci. Water Res. Technol.* 7, 638–649. <https://doi.org/10.1039/d0ew00763c>.
- LeBlanc, R.J., Matthews, P., Richard, R.P., 2009. *Global atlas of excreta, wastewater sludge, and biosolids management: Moving forward the sustainable and welcome uses of a global resource*. United Nations Human Settlements Programme, UN-HABITAT, P.O. Box 30030, Nairobi 00100, Kenya.
- Lee, G., Bigham, J.M., Faure, G., 2002. Removal of trace metals by coprecipitation with Fe, Al and Mn from natural waters contaminated with acid mine drainage in the Ducktown Mining District, Tennessee. *Appl. Geochem.* 17, 569–581. [https://doi.org/10.1016/S0883-2927\(01\)00125-1](https://doi.org/10.1016/S0883-2927(01)00125-1).
- Lee, I.H., Wang, Y.J., Chern, J.M., 2005. Extraction kinetics of heavy metal-containing sludge. *J. Hazard. Mater.* 123, 112–119. <https://doi.org/10.1016/j.jhazmat.2005.03.035>.
- Lee, I.H., Kuan, Y.C., Chern, J.M., 2006. Factorial experimental design for recovering heavy metals from sludge with ion-exchange resin. *J. Hazard. Mater.* 138, 549–559. <https://doi.org/10.1016/j.jhazmat.2006.05.090>.
- Leštan, D., Luo, C., Ling, Li, X., Dong, 2008. The use of chelating agents in the remediation of metal-contaminated soils: a review. *Environ. Pollut.* 153, 3–13. <https://doi.org/10.1016/j.envpol.2007.11.015>.
- Li, Y., Yu, Han, Liu, L., Yu, Hongbing, 2021. Application of co-pyrolysis biochar for the adsorption and immobilization of heavy metals in contaminated environmental substrates. *J. Hazard. Mater.* 420, 126655 <https://doi.org/10.1016/j.jhazmat.2021.126655>.
- Liang, S., Chen, H., Zeng, X., Li, Z., Yu, W., Xiao, K., Hu, J., Hou, H., Liu, B., Tao, S., Yang, J., 2019. A comparison between sulfuric acid and oxalic acid leaching with subsequent purification and precipitation for phosphorus recovery from sewage sludge incineration ash. *Water Res.* 159, 242–251. <https://doi.org/10.1016/j.watres.2019.05.022>.
- Liu, T., Liu, Z., Zheng, Q., Lang, Q., Xia, Y., Peng, N., Gai, C., 2018. Effect of hydrothermal carbonization on migration and environmental risk of heavy metals in sewage sludge during pyrolysis. *Bioresour. Technol.* 247, 282–290. <https://doi.org/10.1016/j.biortech.2017.09.090>.
- Liu, L., Huang, L., Huang, R., Lin, H., Wang, D., 2021. Immobilization of heavy metals in biochar derived from co-pyrolysis of sewage sludge and calcium sulfate. *J. Hazard. Mater.* 403, 123648 <https://doi.org/10.1016/j.jhazmat.2020.123648>.
- Ma, D., Su, M., Qian, J., Wang, Q., Meng, F., Ge, X., Ye, Y., Song, C., 2020. Heavy metal removal from sewage sludge under citric acid and electroosmotic leaching processes. *Sep. Purif. Technol.* 242, 116822 <https://doi.org/10.1016/j.seppur.2020.116822>.
- Marchioretto, M.M., Bruning, H., Rulkens, W., 2005. Heavy metals precipitation in sewage sludge. *Sep. Sci. Technol.* 40, 3393–3405. <https://doi.org/10.1080/01496390500423748>.
- Matocha, C.J., Karathanasis, A.D., Rakshit, S., Wagner, K.M., 2005. Reduction of copper (II) by iron(II). *J. Environ. Qual.* 34, 1539–1546. <https://doi.org/10.2134/jeq2005.0002>.
- Mercier, G., Blais, J.F., Hammy, F., Lounès, M., Sasseville, J.L., 2002. A decontamination process to remove metals and stabilise Montreal sewage sludge. *Sci. World J.* 2, 1121–1126. <https://doi.org/10.1100/tsw.2002.201>.
- Montenegro, V., Agatzini-Leonardou, S., Oustadakis, P., Tsakiridis, P., 2016. Hydrometallurgical treatment of EAF dust by direct sulphuric acid leaching at atmospheric pressure. *Waste Biomass Valorization* 7 (7), 1531–1548. <https://doi.org/10.1007/S12649-016-9543-Z>.
- Ni, B.J., Huang, Q.S., Wang, C., Ni, T.Y., Sun, J., Wei, W., 2019. Competitive adsorption of heavy metals in aqueous solution onto biochar derived from anaerobically digested sludge. *Chemosphere* 219, 351–357. <https://doi.org/10.1016/j.chemosphere.2018.12.053>.
- Nie, J., Pan, Y., Shi, J., Guo, Y., Yan, Z., Duan, X., Xu, M., 2015. A comparative study on the uptake and toxicity of nickel added in the form of different salts to maize seedlings. *Int. J. Environ. Res. Public Health* 12, 15075–15087. <https://doi.org/10.3390/IJERPH121214972>.
- Pathak, A., Dastidar, M.G., Sreekrishnan, T.R., 2009. Bioleaching of heavy metals from sewage sludge: a review. *J. Environ. Manag.* <https://doi.org/10.1016/j.jenvman.2008.11.005>.
- Paz-Ferreiro, J., Nieto, A., Méndez, A., Askeland, M.P.J., Gasco, G., 2018. Biochar from biosolids pyrolysis: a review. *Int. J. Environ. Res. Public Health* 15, 1–16. <https://doi.org/10.3390/ijerph15050956>.
- Persson, H., Kantarelis, E., Evangelopoulos, P., Yang, W., 2017. Wood-derived acid leaching of biomass for enhanced production of sugars and sugar derivatives during pyrolysis: in fl uence of acidity and treatment time. *J. Anal. Appl. Pyrolysis* 127, 329–334. <https://doi.org/10.1016/j.jaap.2017.07.018>.
- Ross, J.J., Zitomer, D.H., Miller, T.R., Weirich, C.A., Mcnamara, P.J., 2016. Emerging investigators series: pyrolysis removes common microconstituents trichloroan, triclosan, and nonylphenol from biosolids. *Environ. Sci. Water Res. Technol.* 2, 282–289. <https://doi.org/10.1039/C5EW00229J>.

- Sethurajan, M., Lens, P.N.L., Horn, H.A., Figueiredo, L.H.A., van Hullebusch, E.D., 2017. Leaching and recovery of metals. In: Rene, E.R. (Ed.), *Sustainable Heavy Metal Remediation*. Springer International Publishing AG, pp. 161–206. [https://doi.org/10.1007/978-3-319-61146-4\\_6](https://doi.org/10.1007/978-3-319-61146-4_6).
- Shen, Y., Chen, L., 2022. Catalytic pyrolysis of cellulose with biochar modified by Ni–Co–Mn cathode material recovered from spent lithium-ion battery. *Chemosphere* 305, 135430. <https://doi.org/10.1016/J.CHEMOSPHERE.2022.135430>.
- Shi, J., Pang, J., Liu, Q., Luo, Y., Ye, J., Xu, Q., Long, B., Ye, B., Yuan, X., 2020. Simultaneous removal of multiple heavy metals from soil by washing with citric acid and ferric chloride. *RSC Adv.* 10, 7432–7442. <https://doi.org/10.1039/C9RA09999A>.
- Shiba, N.C., Ntuli, F., 2017. Extraction and precipitation of phosphorus from sewage sludge. *Waste Manag.* 60, 191–200. <https://doi.org/10.1016/J.WASMAN.2016.07.031>.
- Shim, M.J., 2023. Recycling of washing agents for heavy metal removal from digested sewage sludge. *Int. J. Environ. Sci. Technol.* 1–12 <https://doi.org/10.1007/S13762-023-04757-4/FIGURES/9>.
- Singh, S., Kumar, V., Dhanjal, D.S., Datta, S., Bhatia, D., Dhiman, J., Samuel, J., Prasad, R., Singh, J., 2020. A sustainable paradigm of sewage sludge biochar: valorization, opportunities, challenges and future prospects. *J. Clean. Prod.* 269, 122259 <https://doi.org/10.1016/J.JCLEPRO.2020.122259>.
- Strasser, H., Brunner, H., Schinner, F., 1995. Leaching of iron and toxic heavy metals from anaerobically-digested sewage sludge. *J. Ind. Microbiol.* 14, 281–287. <https://doi.org/10.1007/BF01569940>.
- Stylianou, M.A., Kollia, D., Haralambous, K.J., Inglezakis, V.J., Moustakas, K.G., Loizidou, M.D., 2007. Effect of acid treatment on the removal of heavy metals from sewage sludge. *Desalination* 215, 73–81. <https://doi.org/10.1016/j.desal.2006.11.015>.
- Tang, J., He, J., Liu, T., Xin, X., 2017. Removal of heavy metals with sequential sludge washing techniques using saponin: optimization conditions, kinetics, removal effectiveness, binding intensity, mobility and mechanism. *RSC Adv.* 7, 33385–33401. <https://doi.org/10.1039/C7RA04284A>.
- Tawalbeh, M., Al-Othman, A., Salamah, T., Alkasrawi, M., Martis, R., El-Rub, Z.A., 2021. A critical review on metal-based catalysts used in the pyrolysis of lignocellulosic biomass materials. *J. Environ. Manag.* 299, 113597 <https://doi.org/10.1016/J.JENVMAN.2021.113597>.
- Tyagi, V.K., Lo, S.L., 2013. Sludge: a waste or renewable source for energy and resources recovery? *Renew. Sust. Energ. Rev.* <https://doi.org/10.1016/j.rser.2013.05.029>.
- Vardanyan, A., Kafa, N., Konstantinidis, V., Shin, S.G., Vyrides, I., 2018. Phosphorus dissolution from dewatered anaerobic sludge: effect of pHs, microorganisms, and sequential extraction. *Bioresour. Technol.* 249, 464–472. <https://doi.org/10.1016/J.BIORTECH.2017.09.188>.
- Vesilind, P.A., Hsu, C.C., 1997. Limits of sludge dewaterability. *Water Sci. Technol.* 36, 87–91. [https://doi.org/10.1016/S0273-1223\(97\)00673-2](https://doi.org/10.1016/S0273-1223(97)00673-2).
- Wang, Xuejiang, Chen, J., Yan, X., Wang, Xin, Zhang, J., Huang, J., Zhao, J., 2015. Heavy metal chemical extraction from industrial and municipal mixed sludge by ultrasound-assisted citric acid. *J. Ind. Eng. Chem.* 27, 368–372. <https://doi.org/10.1016/J.JIEC.2015.01.016>.
- Wang, Y., Zhang, Y., Pei, L., Ying, D., Xu, X., Zhao, L., Jia, J., Cao, X., 2017. Converting Ni-loaded biochars into supercapacitors: implication on the reuse of exhausted carbonaceous sorbents. *Sci. Report.* 71 (7), 1–8. <https://doi.org/10.1038/srep41523>.
- Wang, X., Chi, Q., Liu, X., Wang, Y., 2019. Influence of pyrolysis temperature on characteristics and environmental risk of heavy metals in pyrolyzed biochar made from hydrothermally treated sewage sludge. *Chemosphere* 216, 698–706. <https://doi.org/10.1016/J.CHEMOSPHERE.2018.10.189>.
- Weng, L., Temminghoff, E.J.M., Lofts, S., Tipping, E., Van Riemsdijk, W.H., 2002. Complexation with dissolved organic matter and solubility control of heavy metals in a sandy soil. *Environ. Sci. Technol.* 36, 4804–4810. [https://doi.org/10.1021/ES0200084/SUPPL\\_FILE/ES0200084\\_S.PDF](https://doi.org/10.1021/ES0200084/SUPPL_FILE/ES0200084_S.PDF).
- Wu, C.H., Kuo, C.Y., Lo, S.L., 2009. Recovery of heavy metals from industrial sludge using various acid extraction approaches. *Water Sci. Technol.* 59, 289–293. <https://doi.org/10.2166/wst.2009.859>.
- Xiang, L., Chan, L.C., Wong, J.W.C., 2000. Removal of heavy metals from anaerobically digested sewage sludge by isolated indigenous iron-oxidizing bacteria. *Chemosphere* 41, 283–287. [https://doi.org/10.1016/S0045-6535\(99\)00422-1](https://doi.org/10.1016/S0045-6535(99)00422-1).
- Xiao, Z., Yuan, X., Li, H., Jiang, L., Leng, L., Chen, X., Zeng, G., Li, F., Cao, L., 2015. Chemical speciation, mobility and phyto-accessibility of heavy metals in fly ash and slag from combustion of pelletized municipal sewage sludge. *Sci. Total Environ.* 536, 774–783. <https://doi.org/10.1016/J.SCITOTENV.2015.07.126>.
- Xu, Y., Xie, Y., Liu, J., Yan, L., Yang, R., 2009. Enrichment of valuable metals from the sulfuric acid leach liquors of nickeliferous oxide ores. *Hydrometallurgy* 95, 28–32. <https://doi.org/10.1016/J.HYDROMET.2008.04.003>.
- Yang, Z., Wang, D., Wang, G., Zhang, S., Cheng, Z., Xian, J., Pu, Y., Li, T., Jia, Y., Li, Y., Zhou, W., Xu, X., 2021. Removal of Pb, Zn, Ni and Cr from industrial sludge by biodegradable washing agents: Caboxyethylthiosuccinic acid and itaconic-acrylic acid. *J. Environ. Chem. Eng.* 9, 105846 <https://doi.org/10.1016/J.JECE.2021.105846>.
- Yao, J.G., Tan, S.Y., Metcalfe, P.I., Fennell, P.S., Kelsall, G.H., Hallett, J.P., 2021. Demetallization of sewage sludge using low-cost ionic liquids. *Environ. Sci. Technol.* 55, 5291–5300. <https://doi.org/10.1021/acs.est.0c03724>.
- Yoshizaki, S., Tomida, T., 2000. Principle and process of heavy metal removal from sewage sludge. *Environ. Sci. Technol.* 34, 1572–1575. <https://doi.org/10.1021/es990979s>.
- Yu, H., Naidu, G., Zhang, C., Wang, C., Razmjou, A., Han, D.S., He, T., Shon, H., 2022. Metal-based adsorbents for lithium recovery from aqueous resources. *Desalination* 539, 115951. <https://doi.org/10.1016/J.DESAL.2022.115951>.
- Zhao, B., Xu, X., Zeng, F., Li, H., Chen, X., 2018. The hierarchical porous structure biochar assessments produced by co-pyrolysis of municipal sewage sludge and hazelnut shell and Cu(II) adsorption kinetics. *Environ. Sci. Pollut. Res.* 25, 19423–19435. <https://doi.org/10.1007/S11356-018-2079-Y>.

RESEARCH ARTICLE | MAY 31 2023

# Characterization of AgNPs biosynthesized from stem and leaf extracts of *Cissus quadrangularis* and *C. rotundifolia* ✓

Smita Purohit; Divya Pancholi; Niranjan Kunwar; ... et. al

Check for updates

*AIP Conference Proceedings* 2752, 030003 (2023)

<https://doi.org/10.1063/5.0136566>

View Online

Export Citation

CrossMark

## Articles You May Be Interested In

Determination of fruit maturation and ripening potential on postharvest quality of *Passiflora quadrangularis* L.

*AIP Conference Proceedings* (July 2021)

Phenetic analysis of *Passiflora* in Probolinggo-East Java based on generative characteristic

*AIP Conference Proceedings* (May 2021)

Effects of High Intensity Sound upon *Micrococcus pyogenes*, var. *aureus*

*J Acoust Soc Am* (June 2005)

Downloaded from [http://pubs.aip.org/aip/acp/article-pdf/doi/10.1063/5.0136566/17910206030003\\_1\\_5.0136566.pdf](http://pubs.aip.org/aip/acp/article-pdf/doi/10.1063/5.0136566/17910206030003_1_5.0136566.pdf)

## AIP Advances

Why Publish With Us?

- 25 DAYS**  
average time to 1st decision
- 740+ DOWNLOADS**  
average per article
- INCLUSIVE**  
scope

[Learn More](#)

# Characterization of AgNPs Biosynthesized from Stem and Leaf Extracts of *Cissus quadrangularis* and *C. rotundifolia*

Smita Purohit<sup>1</sup>, Divya Pancholi<sup>1</sup>, Niranjana Kunwar<sup>1</sup>, Rajpal Choudhary<sup>2</sup> and Rohit Jain<sup>2, a)</sup>

## Author Affiliations

<sup>1</sup>Department of Botany, The IIS University, Jaipur, Rajasthan, India, 302020

<sup>2</sup>Department of Biosciences, Manipal University Jaipur, Rajasthan, India, 303007

## Author Emails

<sup>a)</sup> Corresponding author: rohit.jain@jaipur.manipal.edu

**Abstract.** Antimicrobial activity of silver nanoparticles biosynthesized from leaf and stem extracts of *Cissus quadrangularis* and *C. rotundifolia* was assessed against two pathogenic microbes (*Micrococcus*, *Proteus vulgaris*). Methanolic extracts of both stem and leaves of *C. quadrangularis* and *C. rotundifolia* were prepared using soxhlet method. Qualitative profiling of secondary metabolites confirmed the presence of saponins in *C. quadrangularis* extracts, while tannins and flavonoids were present in extracts of both the plants. AgNPs biosynthesized from both leaf and stem extracts were characterized using SEM and FTIR. Antimicrobial assays of all the four crude extracts and NPs derived from leaf and stem extract revealed that none of the crude extracts of *C. quadrangularis* showed antimicrobial activity against either *P. vulgaris* or *Micrococcus*, while nanoparticles derived from stem extracts exhibited higher (~2.5 times) activity against *P. vulgaris* than that against *Micrococcus*. In contrast, both the extracts of *C. rotundifolia* and AgNPs derived from stem extract showed similar inhibitory effect on growth of both tested microorganisms. Nanoparticles biosynthesized from leaf extract of *C. rotundifolia* showed higher activity (~1.6 times) against *P. vulgaris* than that against *Micrococcus*. AgNPs derived from *C. quadrangularis* stem extract exhibited ~1.5 times higher activity than that of *C. rotundifolia* derived AgNPs against *P. vulgaris*. This study therefore indicates that the rich phytochemical profile and antimicrobial potential of *Cissus* sp. can further be used to develop non-toxic herbal formulations with multiple medicinal properties.

## INTRODUCTION

Fast evolving nature of microbial pathogens and increasing toll of nosocomial infections has been one of the frontline challenges in development of efficient antimicrobial drugs [1]. Moreover, emergence of multidrug resistant variants due to excessive use of antibiotics has further made the need for identification of novel antimicrobial agents of paramount importance [2, 3].

Nanotechnology has emerged as a powerful tool in past few decades due to their vast applications in clinical imaging & detection, targeted drug delivery, biomedicines and cancer treatment therapies [4]. Various metal nanoparticles have effectively been used against various microbial pathogens due to their small size, higher surface area to volume ratio, which enables their close interaction with the microbial membranes [5]. Further, the pathogens are unlikely to develop resistance against these metals, as metal nanoparticles attack the microbes by targeting multiple regions, thus for developing resistance, the pathogens would have to mutate all the targeted sites [6].

Silver and its salts have been used as antimicrobial agents for ages, infact it has been one of the popular treatment/remedy for microbial infections since ancient times. Applications of silver-containing or silver-coated materials as antimicrobial agents has been well established over decades and has been used as an excellent anti-bacterial growth control agent in prostheses, catheters, burn wounds, dental materials and vascular grafts [7]. In recent decade, silver nanoparticles (AgNPs) have emerged as efficient nanomedicine against infectious agents due to

their unique chemical, optical, electromagnetic, and mechanical properties [8]. Among all known antibacterial metal nanoparticles, AgNPs have been reported to have highest bactericidal activity & biocompatibility and has been reported to be highly effective not only against bacteria, but also against fungal and viral pathogens [6, 9]. AgNPs also exhibit other therapeutic activities including anti-cancer, anti-inflammatory, anti-angiogenesis and many more [9].

Synthesis of AgNPs using conventional physico-chemical methods such as electrochemical reduction, thermal evaporation, beam electron irradiation and vapor condensation has declined in recent past due to use of toxic chemicals, time consuming & difficult to scale up process, complicated downstream processing, which also makes the process cost expensive [9, 10]. Biological synthesis of nanoparticles using microorganisms, enzymes and plants enables fast, high yields and cost-effective downstream processing, and thus have been widely used for synthesis of AgNPs based nanomedicines. Synthesis of silver nanoparticles using plant extracts have gained lot of impetus in past few decades due to faster synthesis rate, higher stability, more diversity in size and shape, lower synthesis cost, and environment friendly approach [11]. Some of the common plants that have been used for green synthesis of silver nanoparticles include *Moringa oleifera*, *Azadirachta indica*, *Xanthium strumarium*, *Tinospora cordifolia*, *Brassica rapa* and Red onion [12-18].

*Cissus*, member of grape family Vitaceae is known as natural reservoir of an important medicinal compound, resveratrol. This compound has been well reported to exhibit wide range of pharmaceutical properties including cardioprotection, chemoprotection, and many more (Bertelli and Das 2009; Das et al. 2011).

*C. quadrangularis* L. and *C. rotundifolia* (Forsk.) Vahl are two important medicinal plants of the grape family known for their diverse medicinal applications in Indian medicinal system. These are known as natural bone healing plants and have been used for the purpose since ancient times [19]. Different plant parts of both the plants have been reported to exhibit therapeutic properties against various disorders including asthma, syphilis, tumors, haemorrhoids, menorrhagia, leucorrhoea, scurvy, obesity and gout [20-24]. Apart from being used as nutritional supplement, *Cissus* sp. also exhibit pharmaceutical properties including antioxidant, anti-inflammatory, analgesic, anti-diabetic, anti-neurodegenerative, analgesic, gastroprotective and antimicrobial [25-27]. Till date, there are no significant reports on antimicrobial activity of *C. rotundifolia* and even that for *C. quadrangularis* are scarce.

*Proteus vulgaris* and *Micrococcus luteus* are amongst the most opportunistic bacterial pathogens and are major among causative agents of hospital borne infections. Despite of various antibacterial agents available, the fast-evolving nature and increasing fatality of nosocomial infections it has become imperative to develop more efficient drugs against these pathogens.

Therefore, in the present study, antimicrobial potential of AgNPs biosynthesized from methanolic leaf and stem extracts of *C. quadrangularis* and *C. rotundifolia* against *P. vulgaris* and *Micrococcus* has been reported for the first time. This study provides new insights into some important medicinal properties and phytochemical composition of these two invaluable medicinal plants.

## MATERIALS & METHODS

### Plant sample collection & preparation

Plant samples (leaf & stem) of *C. quadrangularis* (CQ) and *C. rotundifolia* (CR) were collected from Smriti Kulish Van Biodiversity Park, Jaipur, Rajasthan, India, thoroughly washed under running tap water, air dried, pulverised into fine powder and stored at 4°C till further use.

### Metabolite extraction & qualitative profiling

Leaf & stem powder were subjected to Soxhlet extraction method [22]. Briefly, dried powder (20 g) was extracted with 500 ml methanol (HiMedia, India) using Soxhlet apparatus (Borosil, India) for 24h. The resulting extracts were filtered using Whatmann filter paper No. 1, concentrated upto 1 ml volume in rotary evaporator (Sigma, India) and stored at 4°C till further use. All the four extracts (CRS, CRL, CQS, CQL) were analysed for the presence of alkaloids, flavonoids, saponins, tannins and phenols using Hager's test, lead acetate solution test, foam test and ferric chloride test, respectively.



## AgNPs synthesis and characterization

5 ml of extract was mixed with equal volume of 0.1 M AgNO<sub>3</sub> solution (HiMedia, India) and the mixture was incubated at RT for 20 min or until the color of the mixture changed from green to dark brown. The nanoparticles were extracted from the mix by centrifugation at 8000 rpm for 30 min. The pellet was resuspended in double distilled water and stored at 4°C till further use. The chemical composition and shape of the synthesized AgNPs was determined using FTIR (Bruker, USA) and SEM (Jeol, USA), respectively as per method reported by [28].

### Antimicrobial activity

Standard strains of *Micrococcus luteus* (MTCC 106) and *Proteus vulgaris* (MTCC 426) were procured from MTCC, Institute of Microbial Technology, Chandigarh, India. Antimicrobial activity of all the crude extracts and biosynthesized AgNPs was performed using disc diffusion method. Briefly, sterilized filter paper discs of 6 mm diameter were dipped in different extracts and AgNP solution and were transferred onto sterilised nutrient agar petri plates pre-inoculated with 24 h old broth culture of *M. luteus* and *P. vulgaris*. Methanol was used as control, and the strains were inoculated using spread plate technique. The plates were then incubated at 37°C for 24 h and the zone of inhibition was recorded.

## RESULTS & DISCUSSION

### Extract yield & composition

Yield of *C. rotundifolia* stem (CRS) and *C. quadrangularis* leaf (CQL) extracts was maximum, producing ~1.53 g and 1.08 g extract per 20 g sample, respectively. CRL and CQS extracts yielded about 0.67 g and 0.87 g extract per 20 g sample, respectively. The difference in the extract yields could be attributed to the different phytochemical composition and their differential solubility in methanol. The higher yield indicates presence of more methanol soluble compounds, or in other words more polar compounds. It can be assumed that CQL and CRS are richer in polar metabolites as compared to their stem and leaf counterparts, respectively. Murthy [22] reported higher CQ stem extract yield in polar solvents with maximum in water followed by methanol. Higher solubility of CQ extracts in polar solvents has also been confirmed by [29].

Phytochemical composition of both plants was similar, such that presence of flavonoids & tannins was confirmed in leaf extracts of both plants, while that of flavonoids, tannins and saponins was confirmed in both stem extracts (CQS & CRS). Alkaloids were not detected in either of the four extracts. Further, in a similar study presence of polyphenols and ascorbic acid has been reported in methanolic stem extract of CQ [22].

### Characterization of AgNPs

Change in color of solution from green to brown after addition of AgNO<sub>3</sub> solution was observed. Change in color of the extract has been reported as visible indicator of reduction of silver ions, excitation of surface plasmon resonance and formation of small nano-sized particles [30, 31]. AgNPs synthesised from all the four extracts were spherical and ~100 - 200 nm in size (Figure 1). The nanoparticles formed aggregates and were present in the form of large agglomerates. However, these aggregates when mixed in appropriate solvent, formed a uniform suspension. The AgNPs biosynthesised with plant extracts often round in shape and form aggregates [30].

The FTIR spectrum of the biosynthesized AgNPs from different extracts were almost similar. The peaks at 1624 cm<sup>-1</sup> and 1521 cm<sup>-1</sup> represents C=O (carbonyl group) and C-N groups, respectively. Presence of peak at 1748 cm<sup>-1</sup> confirms presence of medium stretch from C=O bond due to dimer formation. Wavenumber 2851 cm<sup>-1</sup> corresponds to weak carbonyl (C=O) vibrations, wherein 1458 cm<sup>-1</sup> & 2851 cm<sup>-1</sup> corresponds to C=C vibrations. Further, presence of peak at 1248 cm<sup>-1</sup> and 791 cm<sup>-1</sup> confirmed presence of N-H bond. The C-N bond stretching represented by peak at 1035 cm<sup>-1</sup> is probably due to aliphatic amines. A downward shift in the FTIR spectra of AgNPs indicates binding functional groups at their surface. Such downward shift was recorded in C=O and C-N peaks and an upward shift was recorded in O-H peak.

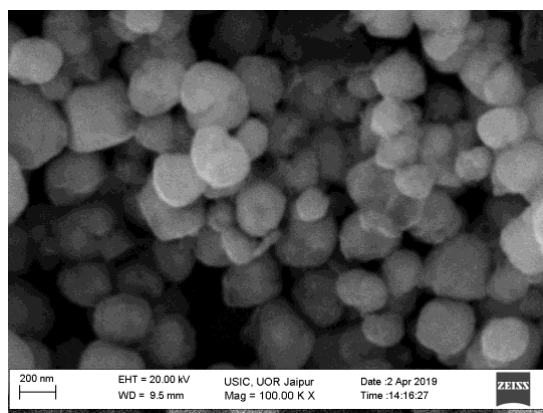


**FIGURE 1.** Scanning electron microscopic image of AgNPs synthesized using *Cissus* extracts

### Antibacterial activity of AgNPs

Crude extracts of CQ did not showed any inhibitory effect against either of the tested pathogens, while the nanoparticles synthesised from these extracts showed significant activity. Absence of activity from CQ stem and leaf crude extracts indicates that the antimicrobial activity exhibited by its nanoparticles is most likely due to the silver, which is a well known bactericidal agent. In contrast, both extracts of CR showed good inhibitory activity against both pathogens. Moreover, the nanoparticles derived from CR extracts showed enhanced inhibitory effect, and igher inhibition was recorded for CRL extracts. All the nanoparticles showed greater inhibitory activity against *P. vulgaris*, which could be attributed to the greater biocompatibility for *P. vulgaris*. Though AgNPs synthesised from both CQ & CR extracts showed enhanced antibacterial activity, yet higher activity was shown by CQS AgNPs, which however was not considered as a good candidate for formulation of antibacterial nanomediicne, as its crude extracts did nt showed any inhibition, thus the inhibition was most likely only due to the silver. CQ stem stem extracts have been reported to be effective against gram positive bacteria (*Bacillus subtilis*, *B. cereus*, *Staphylococcus aureus*) than gram negative bacteria (*Pseudomonas aeruginosa*, *E. coli*), and thus have been rendered relatively resistant to the CQ stem extracts [22]. Inactivity or lower activity of crude CQ extracts has also been reported against *K. penumoniae*, *E. faecalis*, *V. cholerae* and *S. typhi* [31]. Ethnol & aqueous extracts of CQ have been reported to show significant inhibitory effect against *P. mirabilis* [32].

### CONCLUSION

The present study was aimed to explore the potential of *C. quadrangularis* and *C. rotundifolia* as bioactive ingredient in antibacterial nanomedicinal formulations. Phytochemical profiling of the extracts confirmed the presence of flavonoids and tannins in all the extracts. Antimicrobial assays of all the crude extracts of CQ and NPs derived from leaf and stem extract revealed that none of the crude extracts showed antimicrobial activity, whereas nanoparticles derived from stem extracts showed significant antimicrobial potential, with higher (~2.5 times) activity against *P. vulgaris* than that against *M. luteus*. On the contrary, all extracts of *C. rotundifolia* exhibited antimicrobial activity against both pathogens. Nanoparticles biosynthesized from leaf and stem extracts of *C. rotundifolia* exhibited higher activity than the crude extracts against *P. vulgaris*, while it was similar to the crude extracts against Micrococcus. This study therefore indicates that the rich phytochemical profile and antimicrobial potential of *C. rotundifolia* extracts can further be used to develop efficient and non-toxic herbal drugs formulations against various pathogenic microbes.

### ACKNOWLEDGEMENT

Authors would like to acknowledge the Department of Botany, IIS University for providing all the laboratory facilities that were required to conduct the experiments related to this work.

## REFERENCES

1. H. Charkhian, A. Bodaqlouie, E. Soleimannezhadbari, L. Lotfollahi, N. Shaykh-Baygloo, R. Hosseinzadeh, N. Yousefi and M. Khodayar, *Curr. Microbiol.* **77**, 2674-2684 (2020).
2. A. Singh, J. Kumar, V. Sharma, D. Singh, P. Kumari, J. Nishad, V. Gautam and R. Kharwar, *S. Afr. J. Bot.* **140**, 87-94 (2021).
3. B. Al-Sum and A. Al-Arfaj, *Sci. J. Clin. Med.* **2**, 110-113 (2013).
4. H. Zulfiqar, A. Zafar, M. Rasheed, Z. Ali, K. Mehmood, A. Mazher, M. Hasan and N. Mahmood, *Nanoscale Adv.* **1**, 1707-1713 (2019).
5. J. J. Ramyadevi, K. A. Marikani, G. Rajakumar and A. Rahuman, *Mat. Letters* **71**, 114-116 (2012).
6. B. Chudasama, A. Vala, N. Andhariya, R. Mehta and R. Upadhyay, *J. Nanoparticle Res.* **12**, 1677-1685 (2010).
7. K. Szczepanowicz, J. Stefanska, R. Socha and P. Warszynski, *Physicochem. Prob. Min. Process.* **45**, 85-98 (2010).
8. D. Suárez, J. Colón, W. García-Mercado, D. Piñero-Cruz and S. Bailón-Ruiz, *MRS Adv.* **5**, 975-984 (2020).
9. R. Hamouda, M. Abd El-Mongy and K. Eid International, *J. Pharm.* **14**, 359-368 (2018).
10. G. Marslin, R. Selvakesavan, G. Franklin, B. Sarmento and A. Dias, *Int. Journal of Nanomedicine* **10**, 5955 (2015).
11. S. Iravani, *Green Chem* **13**, 2638-2650 (2011).
12. J. Mittal, A. Batra, A. Singh and M. M. Sharma, *Adv. Nat. Sci. Nanosci. Nanotech.* **5**, 043002 (2014).
13. J. Mittal, R. Jain and M. M. Sharma, *Adv. Nat. Sci. Nanosci. Nanotech.* **8**, 025011 (2017).
14. J. Mittal, U. Pal, L. Sharma, A. Verma, M. Ghosh and M. Sharma, *IET Nanobiotech.* **14**, 230-238 (2020).
15. H. Mehewish, M. Rajoka, Y. Xiong, H. Cai, R. Aadil, Q. Mahmood, Z. He and Q. Zhu, *J. Environ. Chem. Eng.* **9**, 105290 (2021).
16. H. Abdullah, S. Asseri, W. Mohamad, S. Kan, A. Azmi, F. Julius and P. Chia, *Environ. Pollut.* **271**, 116295 (2021).
17. S. Ahmed, Saifullah, M. Ahmad, B. Swami and S. Ikram, *J Rad. Res. App. Sci.* **9**, 1-7 (2016).
18. K. B. Narayanan and H. H. Park, *Eur. J. Plant Path.* **140**, 185-192 (2014).
19. S. Stohs and S. Ray, *Phytother. Res.* **27**, 1107-1114 (2013).
20. M. Sen and B. Dash, *Int. J. Green Pharm.* **6**, 169-173 (2012).
21. S. Chanda, Y. Baravalia and K. Nagani, *J. Pharmacogn. Phytochem.* **2**, (2013).
22. K. Murthy, A. Vanitha, M. Swamy and G. Ravishankar, *J. Med. Food* **6**, 99-105 (2003).
23. G. Mishra, S. Srivastava and B. Nagori, *Int. J. Pharmtech. Res.* **2**, 1298-1310 (2010).
24. S. Kumar, A. Anandan and M. Jegadeesan, *Arch. Appl. Sci. Res.* **4**, 1782-1787 (2012).
25. M. Jainu and C. Devi, *Chem.-Biol. Interact.* **161**, 262-270 (2006).
26. G. Mate, N. Naikwade, C. Magdum, A. Chowki and S. Patil, *Int. J. Green Pharm.* **2**, 118-121 (2008).
27. G. Vijayalakshmi, O. Aysha and S. Valli, *World J. Pharm. Pharm. Sci.* **4**, 1702-1713 (2015).
28. S. Gupta, S. Kachhwaha, S. Kothari, M. Bohra and R. Jain, *ACS Omega* **5**, 29189-29198 (2020).
29. S. Srivastava, I. Seethalakshmi and L. Rebecca, *J. Chem. Pharmaceut. Res.* **5**, 131-134 (2013).
30. P. Agarwal, V. Bairwa, S. Kachhwaha and S. Kothari, *Int. J. Nanotech. App.* **4**, 1-8 (2014).
31. K. Renugadevi, D. Inbakandan, M. Bavaniatha and V. Poornima, *Int. J. Pharma Bio Sci.* **3**, 437-445 (2012).
32. A. Raj, A. Selvaraj, V. Gopalakrishnan and S. Dorairaj, *J. Herb. Med. Toxicol.* **4**, 177-180 (2010).



Alexandria University  
Alexandria Engineering Journal

[www.elsevier.com/locate/aej](http://www.elsevier.com/locate/aej)  
[www.sciencedirect.com](http://www.sciencedirect.com)



# Removal of congo red from water by adsorption onto activated carbon derived from waste black cardamom peels and machine learning modeling

Rameez Ahmad Aftab<sup>a</sup>, Sadaf Zaidi<sup>b,\*</sup>, Aftab Aslam Parwaz Khan<sup>c,\*</sup>,  
Mohd Arish Usman<sup>d</sup>, Anees Y. Khan<sup>d</sup>, Muhammad Tariq Saeed Chani<sup>c</sup>,  
Abdullah M. Asiri<sup>c</sup>

<sup>a</sup> Department of Chemical Engineering, Zakir Husain College of Engineering and Technology, Aligarh Muslim University, Aligarh 202002, Uttar Pradesh, India

<sup>b</sup> Department of Post Harvest Engineering and Technology, Faculty of Agricultural Sciences, Aligarh Muslim University, Aligarh 202002, Uttar Pradesh, India

<sup>c</sup> Center of Excellence for Advanced Materials Research, King Abdulaziz University, Jeddah 21589, Saudi Arabia

<sup>d</sup> Department of Chemical Engineering, Manipal University Jaipur, Dehmi Kalan, Off. Jaipur-Ajmer Expressway, Jaipur 303007, Rajasthan, India

Received 19 October 2022; revised 12 January 2023; accepted 12 March 2023

## KEYWORDS

Black cardamom;  
Activated carbon;  
Machine learning modeling;  
Support vector regression;  
Langmuir isotherm

**Abstract** The present work utilizes waste black cardamom (BC) as an inexpensive and environmentally friendly adsorbent for sequestering the Congo Red (CR) dye from aqueous media for the first time. Following a carbonization process at 600 °C, chemical activation with KOH was carried out for waste BC and subsequent black cardamom activated carbon (BCAC) was employed as an adsorbent for CR eradication. The effect of experimental factors, including pH, adsorption time, dose and CR initial concentration, was investigated. 96.21 % of CR dye removal was achieved at pH 6 for 100 mg/L of CR concentration having 0.1 g dose at 30 °C. Maximum Langmuir adsorption capacity of BCAC was found to be 69.93 mg/g at 30 °C. The kinetic analyses showed that the CR adsorption over BCAC behaved in accordance with a pseudo-second order kinetic model as high  $R^2$  values (0.997–1) were obtained. Thermodynamic parameters ( $\Delta H^\circ$ ,  $\Delta S^\circ$ , and  $\Delta G^\circ$ ) demonstrated that the CR adsorption over BCAC was feasible, spontaneous and exothermic in nature. In addition, the state-of-the-art machine learning (ML) approaches namely, support vector regression (SVR) and artificial neural network (ANN) were employed for modeling the BCAC adsorbent for CR removal. The statistical analysis revealed high prediction performance of SVR model with AARE value of 0.0491 and RMSE value of 0.4635 while the corresponding values for the ANN model were 0.0781 and 0.5395,

*Abbreviations:* BC, Black Cardamom; BCAC, Black cardamom activated carbon; CR, Congo Red; ML, Machine Learning; ANN, Artificial neural networks; SVR, Support vector regression; AARE, Average absolute relative error;  $R^2$ , Coefficient of determination; RMSE, Root mean square error; SEM, Scanning Electron Microscopy; FTIR, Fourier Transform Infra-Red

\* Corresponding authors.

E-mail addresses: [sadaf63in@yahoo.com](mailto:sadaf63in@yahoo.com) (S. Zaidi), [draapk@gmail.com](mailto:draapk@gmail.com) (A. Aslam Parwaz Khan).

Peer review under responsibility of Faculty of Engineering, Alexandria University.

<https://doi.org/10.1016/j.aej.2023.03.055>

1110-0168 © 2023 The Authors. Published by Elsevier B.V. on behalf of Faculty of Engineering, Alexandria University  
This is an open access article under the CC BY-NC-ND license (<http://creativecommons.org/licenses/by-nc-nd/4.0/>).

**Nomenclature**

$C_o$	Initial dye concentration ( $\text{mg L}^{-1}$ )	$K_L$	Langmuir constant ( $\text{L mg}^{-1}$ )
$C_e$	Dye concentration at equilibrium ( $\text{mg L}^{-1}$ )	qm	Maximum adsorption capacity ( $\text{mg g}^{-1}$ )
$q_e$	Adsorption capacity at equilibrium ( $\text{mg g}^{-1}$ )	$R_L$	Separation factor
m	Mass of Adsorbent (g)	$K_F$	Freundlich adsorption constant ( $\text{mg g}^{-1}$ ) ( $\text{L mg}^{-1}$ ) <sup>1/n</sup>
V	Volume (L)	n	Freundlich exponent ( $\text{g L}^{-1}$ )
$\varepsilon$	Loss function	A	Temkin constant for binding energy ( $\text{L/g}^{-1}$ )
w	Weight vector	B	Temkin constant for heat of adsorption ( $\text{J mol}^{-1}$ )
$\lambda(c_i)$	High dimensional feature function for input vector c	$\chi^2$	Chi-squared error
$\alpha$ and $\alpha^*$	Lagrange multipliers	$K_1$	Pseudo-first-order rate constant ( $\text{min}^{-1}$ )
f(c)	Regression function	$K_2$	Pseudo-second-order rate constant ( $\text{g mg}^{-1} \text{min}^{-1}$ )
b	Bias term	$K_{id}$	Intra particle diffusion constant ( $\text{mg g}^{-1} \text{min}^{-1}$ )
$K(c_i, c_j)$	Kernel function	I	Intra particle constant
L	Dual form of the Lagrangian function	$K_C$	Equilibrium constant
$c_i$	Input vector	$\Delta G^\circ$	Standard Free energy change ( $\text{kJ mol}^{-1}$ )
$d_i$	Output vector	$\Delta H^\circ$	Standard Enthalpy change ( $\text{kJ mol}^{-1}$ )
$P_i$	PRedicted value	$\Delta S^\circ$	Standard Entropy change ( $\text{kJ mol}^{-1} \text{K}^{-1}$ )
$E_i$	Experimental value	T	Absolute temperature (K)
N	Total data points	t	Time (min)
$R^2$	Coefficient of determination		

respectively. Furthermore, the plots between experimental CR data and ML forecasted data were closely matched ( $R^2 > 0.99$ ). Thus, it can be concluded that BC, an agro waste could be utilized for CR removal and that the adoption of ML approaches can benefit users by providing them with a tool to enhance the design and performance of wastewater treatment operations.

© 2023 The Authors. Published by Elsevier B.V. on behalf of Faculty of Engineering, Alexandria University This is an open access article under the CC BY-NC-ND license (<http://creativecommons.org/licenses/by-nc-nd/4.0/>).

**1. Introduction**

Water contamination is one of the main issues of our time as a result of the uncontrolled urbanization, population expansion, and industry that has occurred rapidly [1]. Although strict laws and regulations have been promulgated but proper wastewater treatment and its disposal has not been applied [2]. Particularly, a significant volume of polluted water has been released into the environment directly, harming the water resources. An important class of pollutants is synthetic dyes, which are utilized in a variety of sectors including the textile, dyeing, paper, leather tanning, cosmetics, and others [3,4].  $> 7 \times 10^5$  tons of dyes are generated yearly of which about 10% are released into the environment by the textile and associated sectors [5]. Dyes are categorised according to their chemical structures, which influence their characteristics and are divided as cationic or anionic dyes [6]. It is highly challenging to handle wastewater from the dyeing industry because dyes contain complicated molecular structures that prevent biodegradation and make them resilient to light, heat, and oxidising agents [7]. Colored dyes are aesthetically pleasing, cancer-causing, and block light from entering aquatic systems. Additionally, the hazardous and cancer-causing nature of dyeing wastewaters has an impact on both the aquatic ecology and human health [8]. Therefore, it is crucial to remove dye from wastewater or effluents before releasing them into the environment. In this study, the removal of Congo Red (CR) is considered.

Anionic CR dye is very soluble in water which causes disagreeable color changes that endanger water species [9]. CR is an azo dye that metabolizes to benzidine which poses grave risk to human health, including skin, ocular, and gastrointestinal irritation [10]. The removal of CR dye from wastewater has been accomplished using a variety of methods, including coagulation, membrane separation, adsorption, reverse osmosis and ion exchange [11]. Adsorption is rapidly rising to the forefront of treatment technologies as a means of handling dye contaminated aqueous effluent due to its affordability, procedural simplicity, efficacy, and practicality [12]. Due to its porous nature and thermal durability, activated carbon is most frequently utilized as an adsorbent on a large scale [13]. Because it is more expensive and difficult to produce, activated carbon made from non-renewable sources has fewer uses overall [14]. However, various agricultural based materials have been looked at as advantageous raw materials for the production of activated carbon, due to their abundance and non-toxic makeup [15]. Several adsorbents namely, coconut fibre [16], celery residue [7], cabbage waste [12], *Cornulaca monacantha* stem [17], Antigonon leptopus leaf [18] kenaf fibre [19], Casuarina empty fruit [20], *Teucrium polium* L.[10], Eucalyptus leaf powder [21] walnut shell [22], *Eichhornia* shoots [23], pine bark[24], Arjuna seed [25], mango leaves [26], jujube shell [27] *Phoenix dactylifera* seeds [8], apricot stone [28], powder *Bombax Buonopozense* bark [29], teak leaf [30], pineapple stem [31], litchi seed [32] have been utilized for CR removal. Thus, it is observed that efficient adsorbents have been

obtained from agricultural sources. In view of the encouraging development, an effort was made to identify some locally available, cost-effective, and novel bio-waste for scavenging of CR dye from water. It was discovered that black cardamom waste, which is usually discarded in the open or dumped in landfills, aggravates pollution and impinges upon the availability of arable land. It is estimated that nearly 400 kg of black cardamom waste is generated annually in the small Indian town of Aligarh alone. Hence, it was planned to carry out the present study by converting the BC into BCAC and estimate its performance as an adsorbent in the removal of CR dye from water by adsorption.

Modeling of any system or a process is a significant and challenging task in engineering. The challenge may be due to the physical complexity of the natural phenomenon or our limited knowledge of mathematics. Recently, ML has been found to be a very powerful tool in helping to overcome those challenges, by building basic models from the observed patterns as well as assisting decision makers in facing real world problems. Since ML is able to map causal factors and consequent outcomes from the observed patterns (experimental data), without deep knowledge of the complex physical process, these modeling techniques are becoming popular among engineers. Recently, a wide range of applications have benefited greatly from the extensive use of ML techniques for the predictive modeling of the many engineering problems in areas such as air pollution monitoring [33], heat exchanger performance analysis [34], breakthrough mechanism [35], circulation rate in thermosiphon reboiler [36], energy resources forecasting [37] and reservoir properties [38], to name a few. These computational methods accurately forecast complicated processes and quickly give an understanding of how these systems work [39]. The model eliminates the requirement for completing a pilot experiment and aids in developing adsorption apparatus [40].

The main goals of the current study were two-fold. The first was dedicated to the investigation of the efficacy of waste black cardamom based activated carbon (BCAC) to remove CR from aqueous solutions, and generate experimental data. The second was to use this data to develop ML models namely, support vector regression (SVR) and artificial neural network (ANN) for the first time to forecast the uptake capacity of the BCAC adsorbent. Study was done on the variables that affected the CR removal, including temperature, starting dye concentration and pH of the dye water. To verify the performance of the developed ML models, statistical parameters namely, coefficient of determination ( $R^2$ ), average absolute relative error (AARE), root mean squared error (RMSE), and chi-square ( $\chi^2$ ) were employed. It was observed that the BCAC adsorbent was a promising adsorbent for CR removal from aqueous media and the novel application of ML techniques to model the dye removal efficiency of BCAC may be widely employed as a practical tool to enhance treatment procedures for the removal dyes from aqueous solutions.

## 2. Materials and methods

### 2.1. Black cardamom and reagents

Black cardamom waste was collected from local herbal medicine manufacturing plant in Aligarh. Congo Red dye was purchased from Sigma Aldrich. Salts namely, potassium

hydroxide (KOH), hydrochloric acid (HCl) and sodium hydroxide (NaOH) used in the experiments were of analytical grade. Deionized water was utilized in carrying out all the studies. One gram of CR was dissolved in one litre of deionized water to create a stock solution (1000 PPM), which was then diluted with deionized water to the precise concentrations needed.

### 2.2. Preparation of BCAC

The waste black cardamom pods were washed with water to eliminate dust particles and then dried in the sun for two days. Furthermore, all of these BC pods were oven dried for 24 h at 70 °C. Now the dried BC was pre-carbonised at 300 °C for 1.5 h. The pre-carbonized BC samples were then weighed and blended with a KOH solution (impregnation ratio of 1.5). The impregnated sample were dried in oven and further activated in furnace for 2 hrs at 600 °C. The obtained material was repeatedly refluxed with water. The sample material was then dried and kept before being used.

### 2.3. Characterization of BCAC

Scanning electron microscope (SEM) was employed for structural pattern and surface morphology of BCAC. SEM (JEOL JSM-7610 FPLUS model) was used to acquire the electron micrographs of gold-coated BCAC prior and post CR dye adsorption. The Fourier transform infra-Red (FTIR) analysis was performed using Bruker ALPHA FTIR Spectrophotometer in KBr pellets (spectroscopic grade) in the wavelength range of 500–4000  $\text{cm}^{-1}$ . This approach could be useful in describing potential surface functional differences between feedstock and BCAC. The concentrations of CR dye were analysed by visible – spectrophotometer (Electronics India). The solid addition technique was used to determine the pH values of the adsorbent at the (pH<sub>pzc</sub>). The pH of solutions was ascertained by Labman pH meter (India).

### 2.4. Adsorption experiments

The effect on the CR adsorption mechanism was studied by adjusting operational conditions such dose, pH (6–10), beginning CR dye concentration (50–200 mg/L), and temperature (30 °C – 50 °C) and interaction time (0–120 min) of CR dye and BCAC. The CR batch adsorption investigations were conducted using the temperature-controlled water bath shaker (REMI CIS 24). In a 250-ml conical flask, an aliquot of 0.2 g of BCAC was assorted with 20 ml of CR required concentration solution and flask was put at 150 rpm agitation speed of water bath until equilibrium was attained. The spectrophotometer (Electronics India) was used to determine the final concentration of the filtered sample. The pollutant removal percentage (% R) of CR dye and quantity of adsorption at equilibrium  $Q_e$  (mg/g), was determined at time (t) using equation (1) and (2) respectively.

$$\%R = \left( \frac{C_o - C_e}{C_o} \right) \times 100 \quad (1)$$

$$q_e = \left( \frac{C_o - C_e}{m} \right) \times V \quad (2)$$

Where, Co and Ce are the CR concentrations at the start and end of the experiment, respectively. The number V represents the volume of CR aqueous solution (in litres), whereas m symbolizes the BCAC adsorbent mass (in grams).

The effect of solution pH on the removal effectiveness of CR using BCAC was explored by regulating pH in the range of 6–10 for CR and utilising 0.01 M HCl and 0.01 M NaOH solution as adjusting medium. The point-of-zero charges ( $pH_{PZC}$ ) is a property that establishes the pH level at which the adsorbent surface achieves net electrical neutrality and offers important details on the electrostatic interactions between the adsorbent and adsorbate. The  $pH_{PZC}$  is determined by solid addition method. At a constant temperature of 30 °C, adsorption isotherm studies were carried out with starting CR concentrations ranging from 50 to 200 mg/L. The kinetic tests were performed, with residual dye concentrations measured at specified time intervals at five different starting CR concentrations of 50, 70, 100, 150 and 200 mg/L, respectively.

## 2.5. Desorption studies

To conduct the reusability test, 0.1 g of CR loaded BCAC adsorbent was placed into 10 ml of 0.05 M NaOH for 24 hrs. The regenerated adsorbent was then removed and properly cleaned with deionized water before being dried at 55 °C for the subsequent cycle.

## 2.6. Machine learning modelling

### 2.6.1. Artificial neural network

The building of ANN intelligent models is based on a variety of straightforward simulations of the biological processes in the human brain that enable learning, remembering, and problem-solving [41]. The neurons of ANN are core processing units, capable of acquiring complex relationship between input and output variables [42]. The mathematical neuron's output is often represented as:

$$Y_n = F(I) = F\left(b + \sum_{n=1}^N w_n X_n\right) \quad (3)$$

In the multi layered (input, hidden and output layers) network fit the data during training, these algorithms modify the weights of the neurons based on the discrepancy between the actual output values and the desired output [43]. The best ANN architecture and training method for a particular job are discovered through a process of trial and error [44]. One of the popular ANN architecture is a first order gradient descent approach called back-propagation which is used to train an algorithm to minimise error [38]. The nodes modified their weights, and the process iterates until error is reduced to a low-est value.

### 2.6.2. Support vector regression (SVR)

Many literatures provides a detailed explanation of SVMs [45]. The support vector regression makes use of data sets  $P = \{(c_1, d_1), (c_2, d_2), \dots, (c_n, d_n)\}$ , such that each input  $c_i$  has its output  $d_i$ . The goal of epsilon SVR model is to adjust the function,  $d = f(c)$ , so that when it is evaluated with unknown input data  $\{c_i\}$ , it can predict the output values  $\{d_i\}$ . The regression function can be expressed as:

$$f(c, w) = (w \cdot \lambda(c) + b) \quad (4)$$

Where  $\lambda(c)$  is the high dimensional input function and the dot product ( $w \cdot \lambda(c)$ ).

The regression function represented in equation (4) can be minimized as follows:

$$\text{Minimize : } Q(f) = C \frac{1}{N} L_\epsilon(d, f(c, w)) + \frac{1}{2} \|w^2\| \quad (5)$$

The aforementioned equation has two components. The first is the empirical error, which may be assessed using the following insensitive loss function:

$$L_\epsilon(d, f(c, w)) = \begin{cases} 0 & \text{if } |d - f(c, w)| \leq \epsilon \\ |d - f(c, w)| - \epsilon & \text{otherwise} \end{cases} \quad (6)$$

The second term in the equation stands in for the function flatness. The trade-off between training error and model function flatness is provided by parameter C. With the addition of slack variables ( $\xi_i, \xi_i^*$ ), the SVR problem is transformed into a dual optimization problem as follows:

$$\text{Minimize : } \frac{1}{2} \|w^2\| + C \sum_{i=1}^N \xi_i + \xi_i^* \quad (7)$$

Subjected to

$$(d_i - w \cdot \lambda(c) - b) \leq \epsilon + \xi_i$$

$$(w \cdot \lambda(c) + b - d_i) \leq \epsilon + \xi_i^*, \quad \xi_i \text{ and } \xi_i^* \geq 0 \quad (8)$$

The introduction of Lagrangian multiplier  $\alpha_i$  and  $\alpha_i^*$  in the above convex optimization equation transforms it into dual form expressed as:

$$f(c, \alpha_i, \alpha_i^*) = \sum_{i=1}^{N_{SV}} (\alpha_i - \alpha_i^*) (\lambda(c_i) \cdot \lambda(c_j)) + b \quad (9)$$

The non-zero values of coefficients ( $\alpha_i, \alpha_i^*$ ) and their input vectors  $c_i$  create the support vectors (SVs). The basic expression for SVR is finally got after applying the kernel function as follows:

$$f(c, \alpha_i, \alpha_i^*) = \sum_{i=1}^{N_{SV}} (\alpha_i - \alpha_i^*) k(c_i, c_j) + b \quad (10)$$

The Karush-Kuhn Tucker (KKT) conditions are used to evaluate the constant b.

### 2.6.3. ML Models' formulation

The computational ML models (ANN and SVR) were created with five inputs, namely starting CR concentration (50–200 mg/L), dosage (0.04–0.12 g), pH of solution (6–10), Temperature (30 °C –50 °C) and time (2–120 mins), and adsorption capacity of CR as an output, in order to forecast the performance of BCAC for CR batch adsorption. Following the identification of independent – dependent variables, random normalised data was separated into train and test sets. In this study, the ANN toolbox component of the software package MATLAB (2019b) software was adopted. Three layers in feed forward sequence make up the ANN design, with the hidden layer and output layer each having a different transfer function of tansig and purelin respectively. For little to medium-sized data, one of the most effective back propagation methods is Levenberg-Marquardt optimization. Twelve neu-

rons at hidden layer resulted in lowest prediction error of the formulated ANN model.

The SVR model to predict CR removal over BCAC was programmed by implementing `fitsvm` in MATLAB (2019b). Since just a few settings needed to be changed and the RBF kernel has a high general efficiency, it was chosen for this study out of all the available kernels [46]. To Reduce the five-fold cross-validation loss, the optimal hyperparameter combination was determined via Bayesian optimization [47]. It is possible to compare the performance of these developed models equitably since all models are trained and evaluated using the same data sets. Statistical assessment metrics such as  $R^2$ , AARE, RMSE and Chi-square value were used to verify the performance standard of the developed models as follows:

$$AARE = \frac{1}{N} \sum_{i=1}^N \left| \frac{p_i - E_i}{E_i} \right| \quad (11)$$

$$RMSE = \sqrt{\frac{\sum_{i=1}^N \left( \frac{E_i - p_i}{p_i} \right)^2}{N}} \quad (12)$$

$$\text{Chi-squared value, } \chi^2 = \sum \frac{(E_i - p_i)^2}{p_i} \quad (13)$$

Where,  $E_i$  and  $p_i$  represent experimental and predicted data points respectively. Whereas,  $N$  denotes total data points. The  $R^2$  values were obtained using its command in M. S. Excel (2010).

### 3. Results and discussion

#### 3.1. BCAC characterization

The SEM micrographs of BCAC and CR laden BCAC at 1  $\mu\text{m}$  are depicted in Fig. 1 (a)-(b). By the pictures from the SEM examination, the structural characteristic of the BCAC adsorbent demonstrates a interconnected porous structure that provides effective CR dye adsorption. Before adsorption, empty spherical holes indicated that there was a substantial surface area available for dye uptake [48]. As from Fig. 1(b) after CR interacted with BCAC, the surface shape changes to become smoother and acquire flaky patches. These modifications show that the CR dye has effectively been loaded onto the adsorbent surface.

The FTIR spectra of BCAC can be seen in Fig. 2 indicating the existence of functional groups and bonds on the BCAC adsorbent. The band at 3438 ( $\text{cm}^{-1}$ ) was shifted after CR accumulation over BCAC to 3425 ( $\text{cm}^{-1}$ ) due to stretching vibrations of -OH group. The peak appear at 2886 ( $\text{cm}^{-1}$ ) may be attributed to -CH stretching [49]. The alkyne group located band at 2310 ( $\text{cm}^{-1}$ ) was moved to 2311 ( $\text{cm}^{-1}$ ) on CR adsorption [50]. The pronounced peak at 1428 ( $\text{cm}^{-1}$ ) changes to 1437 ( $\text{cm}^{-1}$ ) suggest bending  $\text{CH}_2$  and  $\text{CH}_3$  deformation vibrations [51]. The presence of the C-N length of the aliphatic amines was confirmed by the peak at 1034  $\text{cm}^{-1}$  which shifted to 1032 after CR treatment [26]. Following the application of

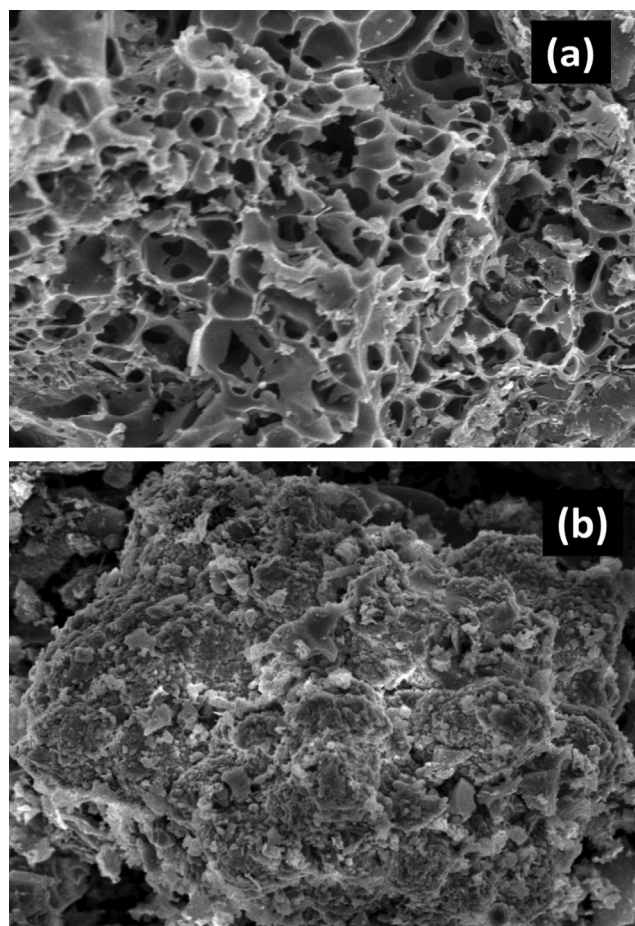


Fig. 1 SEM images of BCAC (a) Prior to CR adsorption and (b) after adsorption of CR at (Magnification: 6000 X; scale: 1  $\mu\text{m}$ ).

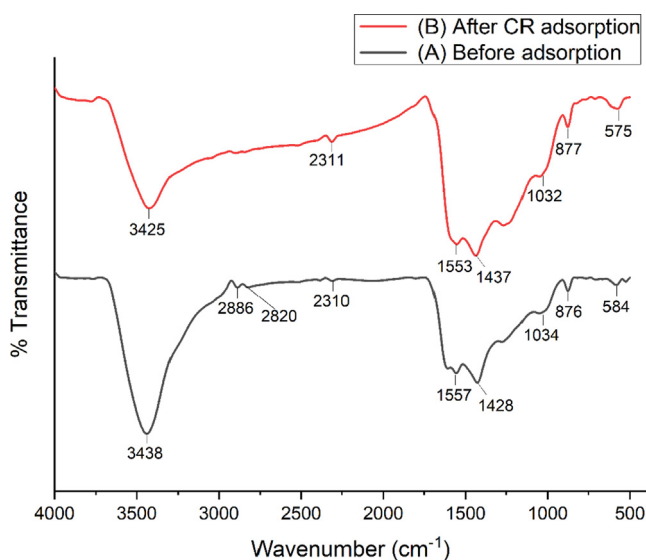


Fig. 2 FTIR spectra of BCAC.



CR dye, there were changes in peak positions, indicating that the CR dye had been successfully adhered onto the BCAC surface. The bands between 400 cm and 800 cm were due to presence of stretch vibrations of C-O and C-H.

### 3.2. Influence of pH

The pH exhibits a key characteristic throughout the adsorption process by regulating the adsorbent charge and ionisation level of the adsorbate in the solution. It is recognised that pH has an impact on CR's structural stability, which in turn affects the intensity of its hue. When the pH is acidic (pH 3.0–5.0), CR turns blue, whereas between pH 10.0 and 12.0, it turns to different shade of red color compared to original of CR dye [52]. It is stable in the pH range of 6 to 10. Fig. 3 illustrates the outcomes of altering the pH from 6 to 10 in order to investigate the impact of initial pH on CR adsorption. The 96.21 percent of CR dye removal was achieved at

pH 6 for 100 mg/L of CR concentration at 30 °C. Fig. 3A demonstrates that when the solution pH rose to 10, the adsorption effectiveness of BCAC for CR fell to 39.44 percent. This impact of pH change can be explained based on obtained PZC value of 7.54 (Fig. 3B). The  $pH_{PZC}$  was determined by salt addition method. The surface of the BCAC is negatively charged below this value [53]. Since CR is an azo anionic dye, removing it was facilitated by a pH value lower than  $pH_{PZC}$  because of the stronger electrostatic attraction between the anionic dye molecules and the positive adsorbent surface [40]. Thus, optimum CR uptake on BCAC was obtained at pH 6. In line with our findings, maximum adsorption of CR by bio magnetic composite was occurRed at pH 6.95 [52]; nevertheless, another published study also shows that at pH 6 maximum CR was adsorbed over coffee husk [54].

A detailed description of possible adsorption mechanisms between CR onto BCAC is proposed and described schemati-

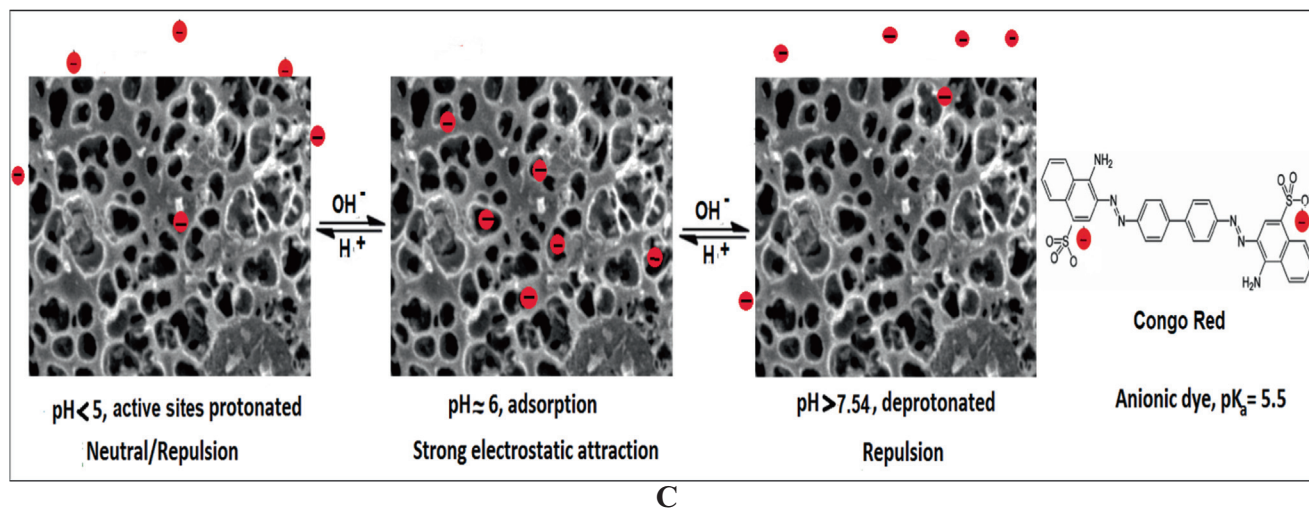
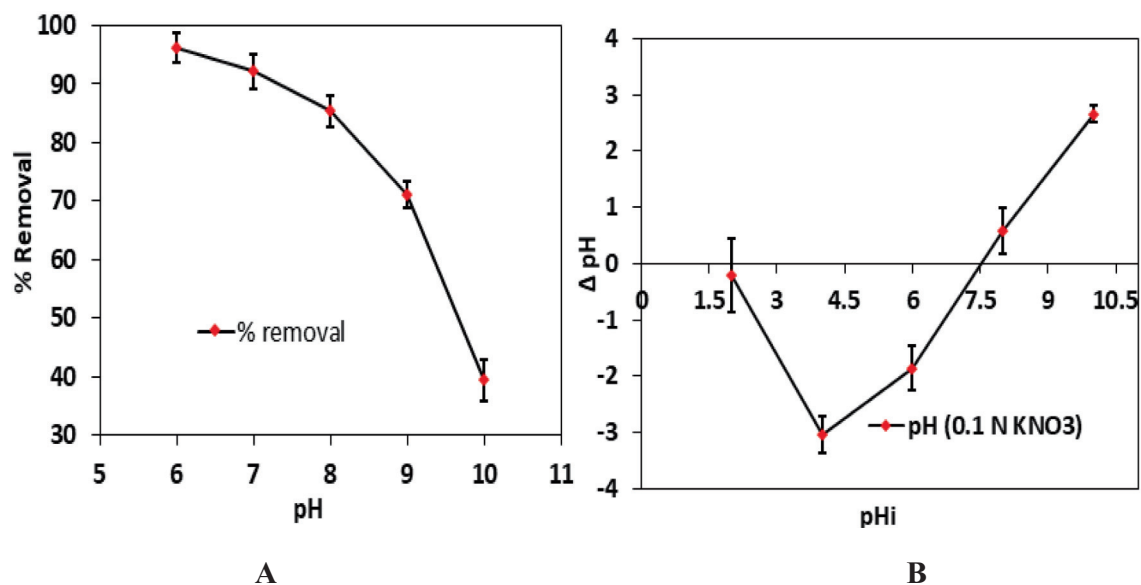


**Fig. 3** (A) Outcome of pH change on CR adsorption on BCAC (B) Point of zero charge of BCAC. (C) Possible adsorption mechanism for the adsorption of CR onto BCAC.

cally in Fig. 3(C). The effect of pH on the adsorption of CR on BCAC can be explained based on the surface charges of both the sorbent and the dye in the aqueous medium and also on the basis of  $pK_a$  values of major constituents [55]. At high solution  $pH > 7.54$ , active sites of BCAC are completely deprotonated; at neutral  $pH (\sim 7)$  active sites are primarily protonated; while at low  $pH < 4$ , most of the active sites are protonated [55]. Typically, CR is negatively charged when  $pH > 5.5$  ( $pK_a = 5.5$ ) [55] as can be seen in Fig. 3 (C). When the solution  $pH$  is 6 (above  $pK_a$  values of CR), dye molecules are negatively charged, while adsorbent sites of BCAC are relatively highly protonated (because of  $pH$  is much lower than 7.54). This leads to a strong electrostatic attraction between  $SO_3^-$  groups of CR and positively charged BCAC (as shown in Fig. 3(C)), thus resulting in a higher adsorption capacity for CR. However, when  $pH$  increases, the  $OH^-$  ions increase gradually, which compete with anionic dye molecules for penetrating the positively charged adsorbent. Hence adsorption capacity decreases for CR at higher  $pH$ . Therefore, based on the above-mentioned results, it is evident that the surface charge of the adsorbent surface and dye governs the adsorption behavior towards anionic dye CR.

### 3.3. Variation of concentration with time

Fig. 4 displays the relationship between the contact time (0–120 mins) and the CR adsorption capability of BCAC at  $pH$  6 for initial CR concentration range (50–200 mg/L). The CR adsorption capacity increased quickly for brief time periods before settling towards equilibrium although the quantity varied for each concentration. This can be explained as at early stage of experiment many vacant spots were present and due to passage of time these active pores were get saturated [56]. The shorter equilibrium period (10, 15 and 30 mins) were attained for lower (50, 70 and 100 mg/L) initial concentration of CR. Similarly, for raised initial CR concentrations of 150 mg/L and 200 mg/L, the equilibrium times were found to be 60 and 90 mins. A similar pattern was observed in literature where equilibrium was attained within 100 mins for CR dye over pine powder adsorbent [57].

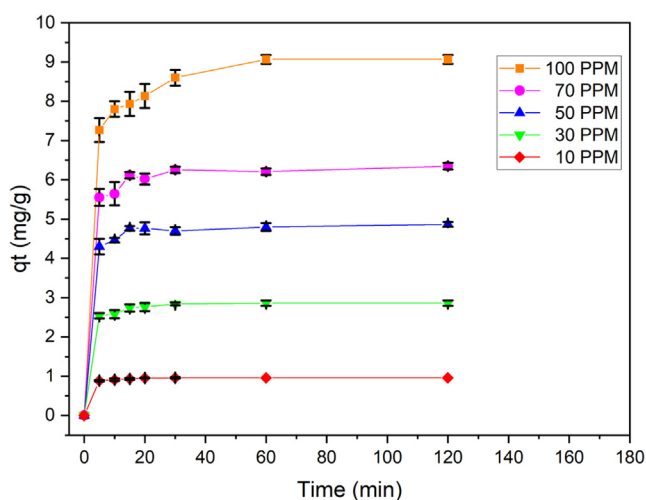


Fig. 4 The concentration vs. time graph for CR adsorption on BCAC.

### 3.4. Variation of dose

Fig. 5 shows how adsorbent dosage affects the amount of CR that can be adsorbed onto BCAC. Increases in BCAC dosage of 0.04, 0.06, 0.08, 0.1 and 0.12 g, respectively, resulted in increases in CR removal percentage of 84.3, 88.65, 91.33, 95.89 and 96.35 % as depicted in Fig. 5. This might be attributed to the rise in the total aggregate surface area of the BCAC particles and the number of accessible active adsorption sites [7]. At 0.1 g and 0.12 g loading of dose, there was no discernible difference in elimination of CR that may be due aggregation of adsorbent particles [8]. Thus for all experiments, BCAC of 0.1 g was discovered to be the best dosage when taking CR removal percentage values into account.

### 3.5. Adsorption isotherms

Adsorption isotherm investigations are crucial because they describe the distribution of the adsorbed molecules between the adsorbent and the liquid solutions at equilibrium. As it serves a useful purpose in the analysis and design of adsorption systems, it is vital to establish the most suitable correlation for equilibrium data and empirical equations. The Langmuir, Freundlich, and Temkin models were utilised to evaluate the data in order to determine which isothermal model is most appropriate for delivering the CR adsorption over BCAC. The linear forms of aforementioned isotherm models are presented in Table 1 and values of corresponding parameters were analysed from Fig. 6.

#### 3.5.1. Langmuir isotherm

The Langmuir isotherm model, state that adsorption happens at specified homogenous sites on the adsorbent through monolayer adsorption [58]. It is also hypothesised that once a sorbate molecule fills a space, no further sorption may occur there. The adsorbate draws to all of the active vacant sites of the adsorbent using the same amount of energy [59]. In Table 1,  $q_e$  is the dye amount per unit weight of BCAC (mg/g) and  $C_e$  is remaining CR concentration at equilibrium (mg/L). The con-

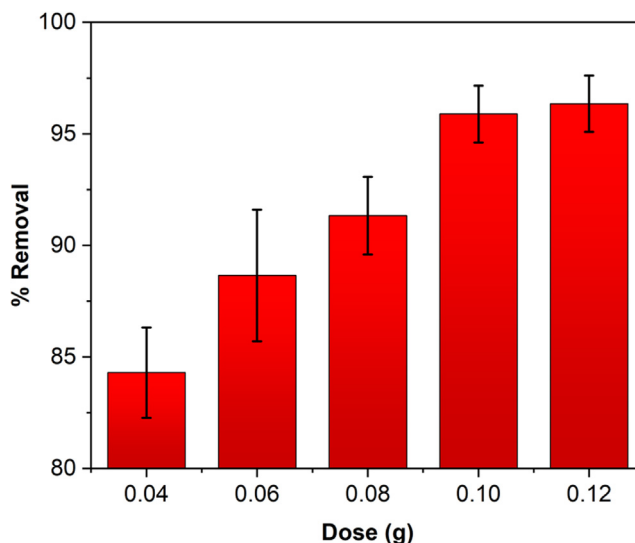
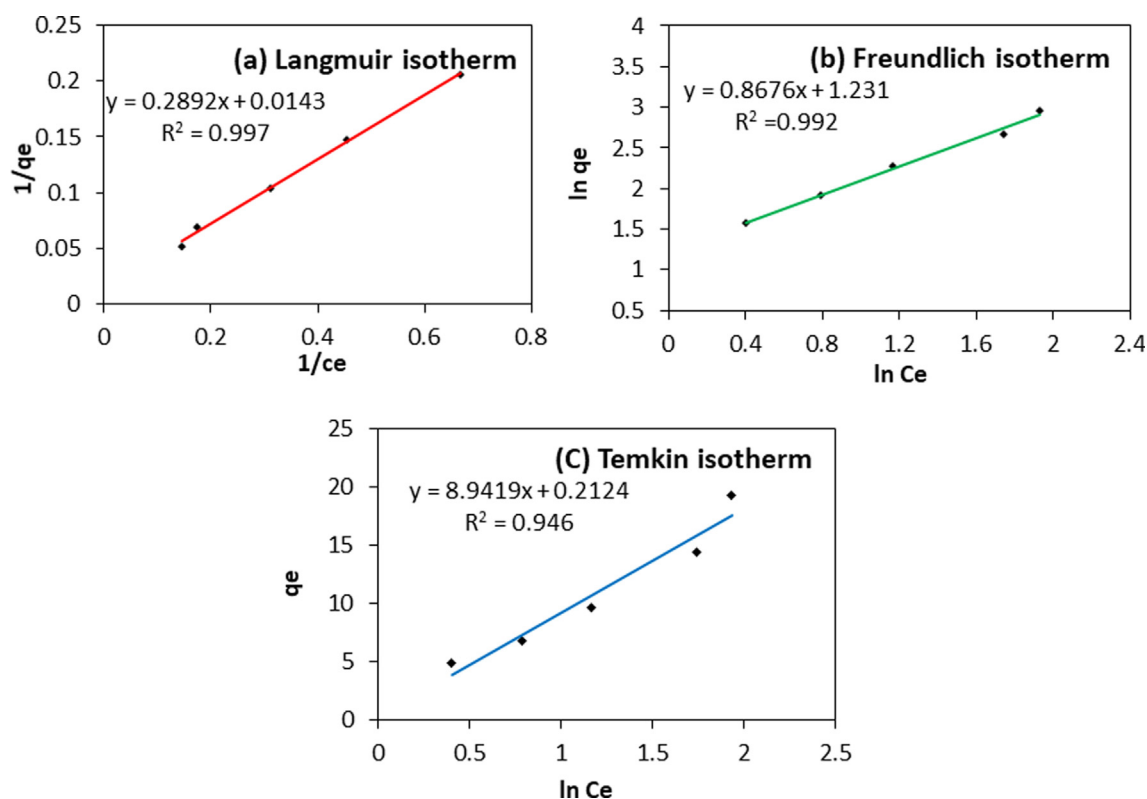


Fig. 5 Impact of changing the BCAC dose on CR adsorption.

**Table 1** Isotherm's equations and constants for CR adsorption on BCAC.

Isotherms	Equations	Parameters	Values
Langmuir	$\frac{1}{q_e} = \left( \frac{1}{q_m} \times \frac{1}{b} \times \frac{1}{C_e} \right) + \frac{1}{q_m}$	$q_m$ (mg g <sup>-1</sup> )	69.93
		$b$ (L mg <sup>-1</sup> )	0.049
		$R_L$	0.091–0.287
		$R^2$	0.997
Freundlich	$\ln q_e = \ln K_F + \frac{1}{n} \ln C_e$	$K_F$ (mg g <sup>-1</sup> ) (L mg <sup>-1</sup> ) <sup>1/n</sup>	3.424
		$n$	1.152
		$R^2$	0.992
Temkin	$q_e = B \ln A + B \ln C_e$	$A$ (L g <sup>-1</sup> )	1.024
		$B$ (J mol <sup>-1</sup> )	8.941
		$R^2$	0.946

**Fig. 6** Adsorption isotherm for CR uptake on BCAC (Temp = 30 °C, pH = 6 and contact time 120 min).

stant  $q_{\max}$  is related to the sites filled by a dye monolayer and reflects the adsorption capacity (mg/g).  $K_L$  is a constant related to adsorption energy (L/mg). Plotting the adsorption curve;  $1/q_e$  vs  $1/C_e$  gives the value of  $q_{\max}$  and  $K_L$ . The graph showed that the Langmuir adsorption capacity was 69.93 mg/g, and an excellent  $R^2$  of 0.997 was observed suggesting monolayer coverage of sites by CR dye molecules (Fig. 6). Separation factor ( $R_L$ ), is another dimensionless measure which provides information on how favourable is the adsorption process. The adsorption is indicated by  $R_L$ , which can be either unfavourable ( $R_L > 1$ ), favourable ( $0 < R_L < 1$ ), irreversible ( $R_L = 0$ ), or linear ( $R_L = 1$ ) [60]. The separation factor values for the present study lie in order (0.091–0.287), which ranges

from 0 to 1, indicates favourable adsorption [60]. In conformity to our results, several investigations have demonstrated that the Langmuir model best describes the sorption of CR onto agro-based adsorbent [17,32].

### 3.5.2. Freundlich isotherm

The Freundlich model, which is frequently used in heterogeneous systems and denotes multilayer adsorption with unstable distribution of enthalpies and affinities between adsorbent and adsorbate [61]. Freundlich sorption equilibrium constant  $K_F$  is expressed in (mg/g). (L/mg)<sup>1/n</sup>, and  $n$  stands for distinctive surface heterogeneity. The linear graph  $\log q_e$  vs  $\log C_e$  is used to estimate the model parameters. The result of correlation

coefficient of this model is represented in Table 1. Due to lower  $R^2$  value than Langmuir model indicate that this model does not adequately account for the variation in the experimental data.

### 3.5.3. Temkin isotherm

According to the above isotherm, all molecules' adsorption heat decreases in a linear manner, proving that the binding energy is homogeneous [62,63]. The constants  $A$  (g/L) and  $B$  (J/mol) corresponding to the maximal equilibrium binding energy and heat of adsorption respectively, were calculated

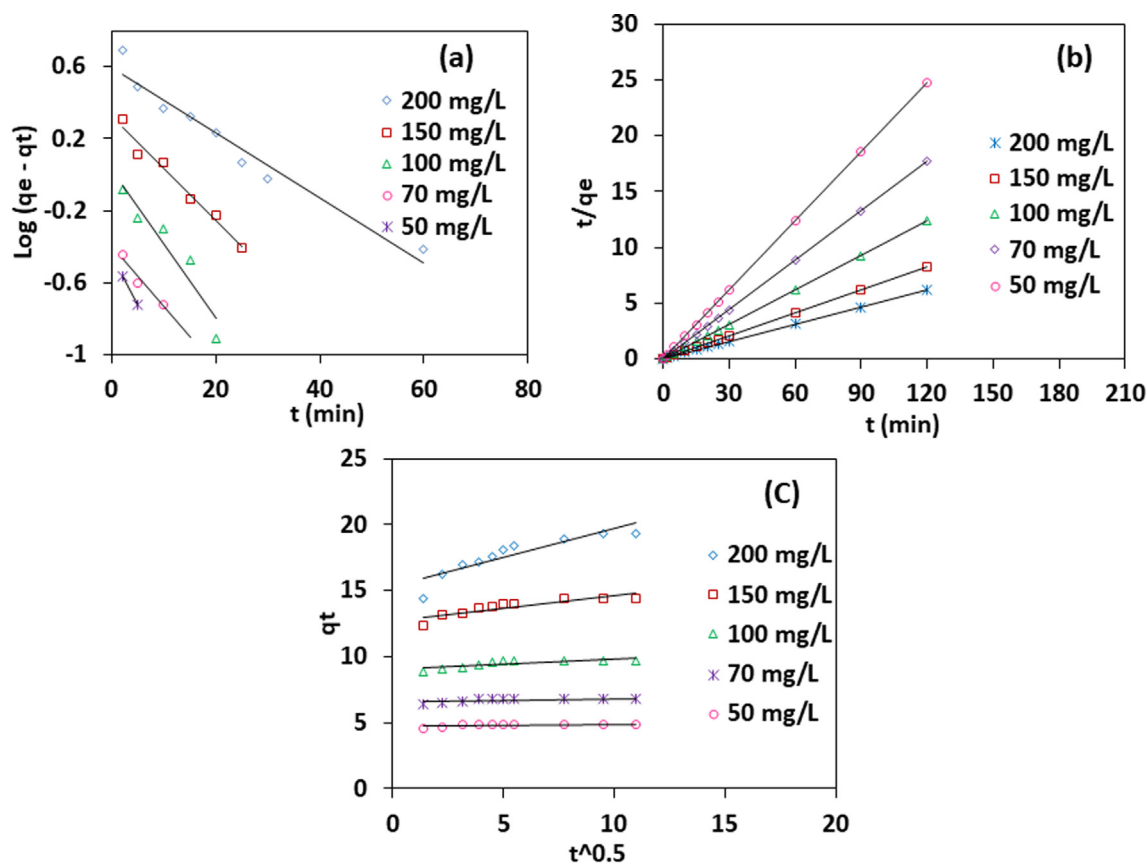
using the linearized Temkin equation. The obtained values of  $A$  and  $B$  are given in the following Table 1. The computed  $R^2$  value (0.94) for Temkin isotherm in the case of CR adsorption is less than those for the Langmuir and Freundlich isotherms. This finding suggests that the Temkin model does not provided an adequate fit for the experimental data.

### 3.6. Adsorption kinetics

The process by which a solute bind to a sorbent can be expressed using a variety of models. Studies on adsorption rate

**Table 2** Kinetic parameters for CR removal on BCAC at different initial concentration.

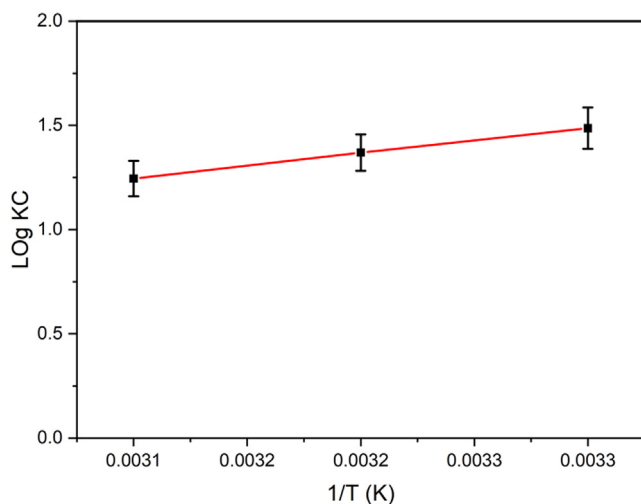
Kinetic models & Equations	Parameters	Concentrations (mg L <sup>-1</sup> )				
		50	70	100	150	200
Pseudo-first order $\log(q_e - q_t) = \log q_e - \left(\frac{K_1}{2.303}\right) \times t$	$q_e$ (exp)	4.849	6.777	9.678	14.428	19.308
	$q_e$ (calc)	0.346	0.401	1.058	2.102	3.908
	$K_1$	0.120	0.0778	0.094	0.066	0.041
	$R^2$	1	0.952	0.903	0.974	0.953
Pseudo-second order kinetics $\frac{t}{q_t} = \left(\frac{1}{K_2 q_e^2}\right) + \left(\frac{1}{q_e}\right) \times t$	$q_e$ (exp)	4.849	6.777	9.678	14.428	19.308
	$q_e$ (calc)	4.852	6.784	9.708	14.513	19.493
	$K_2$	4.045	1.633	0.392	0.108	0.038
	$R^2$	1	1	0.999	0.999	0.997
Intra-particle diffusion model $q_e = k_{id} \times t^{1/2} + I$	$K_{id}$	0.019	0.030	0.077	0.188	0.441
	$I$	4.699	6.534	9.025	12.753	15.271
	$R^2$	0.362	0.484	0.639	0.779	0.806



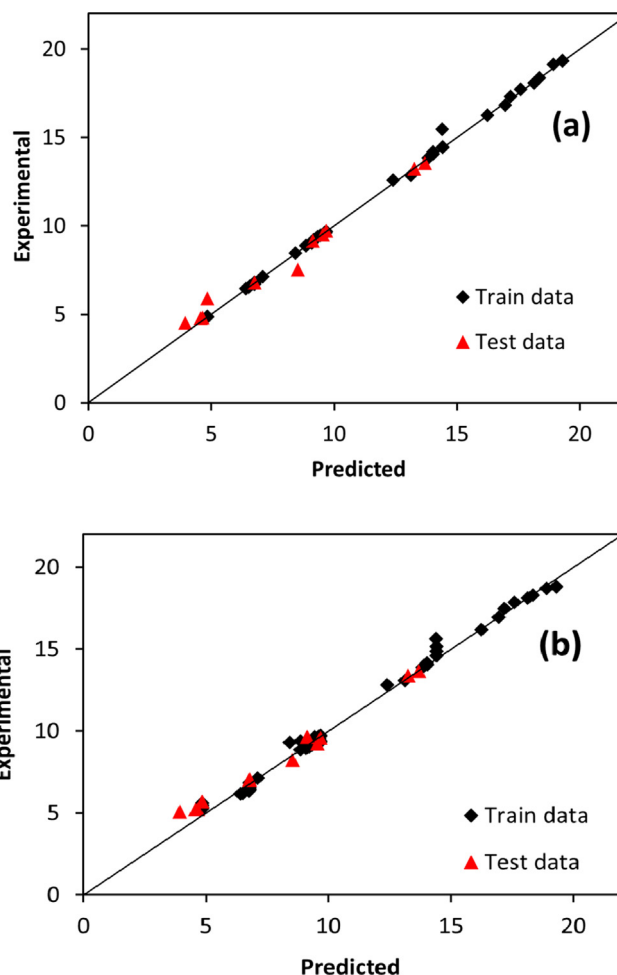
**Fig. 7** Adsorption Kinetics for CR dye onto BCAC (a) pseudo-first order, (b) pseudo-second order and (c) Intra-particle diffusion (at pH = 6, temp = 30 °C and dose = 0.1 g).

**Table 3** Thermodynamic variables for CR adsorptions on BCAC.

Temperature (K)	$\Delta G^\circ$ (kJ mol <sup>-1</sup> )	$\Delta H^\circ$ (kJ mol <sup>-1</sup> )	$\Delta S^\circ$ (kJ mol <sup>-1</sup> K <sup>-1</sup> )
303	-8.621	-22.697	-0.046
313	-8.202		
323	-7.696		

**Fig. 8** A graph of  $\log K_c$  plotted against  $1/T$  for CR adsorption on BCAC.

were conducted in order to quickly and effectively construct a model. Adsorption kinetics demonstrates how the rate of dye uptake is time-dependent and aids in calculating the residence time for the purpose of optimising the size of the adsorption device [64]. The uptake of CR over BCAC was established by fitting data into kinetic models namely, pseudo-first order, pseudo-second order and intra-particle diffusion kinetics. The linear expressions and coefficients of these kinetic models are described in Table 2. According to Fig. 7 (a-c) for adsorption of CR dye by BCAC, pseudo-second order rate kinetics had an  $R^2$  value of 0.998, which was higher than first order rate kinetics. Additionally, the  $q_e$  values for the pseudo-first-order equation varied considerably with the experimental ones. As opposed to that,  $q_e$  values estimated by pseudo-second order rate kinetics were closely matched with experimental data. According to the intraparticle diffusion model, the value of constant (I) provides information about the boundary layer impact [3]. As  $qt$  vs  $t^{1/2}$  plot show divergence from the origin pointed that the CR adsorption over BCAC comprise intra particle diffusion, in addition to the rate control step and other ways such film diffusion, surface adsorption, and pore diffusion [65]. Similar findings for the kinetics of CR uptake over kenaf activated carbon [19] and litchi seed powder [32]

**Fig. 9** ML-modelling of CR adsorption on BCAC for (a) SVR model and (b) ANN model.

that follows pseudo-second order kinetics were reported recently.

### 3.7. Adsorption thermodynamics

An investigation of the thermodynamics was done at three different temperatures (30 °C, 40 °C and 50 °C) for CR uptake on BCAC. The following equations (14–16) were used to compute the thermodynamic characteristics of the process, including the change in Gibbs free energy ( $\Delta G^\circ$ ), change in enthalpy ( $\Delta H^\circ$ ), and change in entropy ( $\Delta S^\circ$ ).

$$K_c = \frac{C_{AC}}{C_e} \quad (14)$$

$$\Delta G = -RT \ln K_c \quad (15)$$

**Table 4** Optimized hyperparameters for the SVR Model.

Model	Box constraint	Kernel Scale	Epsilon	Type of Kernel	Loss Function
CR-SVR Model	927.902	2.7123	0.0126	RBF	$\epsilon$ -insensitive

$$\log K_c = \frac{\Delta S^\circ}{2.303 \times R} - \frac{\Delta H^\circ}{2.303 \times R \times T} \quad (16)$$

Here,  $R$  stands for the universal gas constant ( $8.314 \text{ J K}^{-1} \text{ mol}^{-1}$ ), and  $T$  stands for the temperature on the Kelvin scale.  $C_a$  and  $C_e$  represent the equilibrium concentrations of CR on the BCAC and in the solution, respectively. Table 3 lists the computed thermodynamic parameters obtained from Fig. 8. The process is more impulsive as  $\Delta G^\circ$  becomes more negative [66]. The CR adsorption process is spontaneous, as evidenced by the negative values of total free energy changes during the process. In light of the computed  $\Delta G^\circ$  values, which ranged between  $-7.696$  and  $-8.621 \text{ kJ mol}^{-1}$ , the thermodynamic investigation came to the conclusion that the adsorption happened by a physical sorption process as  $\Delta G^\circ < 20 \text{ kJ mol}^{-1}$  [67]. Since, the negative values  $\Delta H^\circ$  and  $\Delta G^\circ$  represents exothermic and spontaneous process [68]. Thus, the findings demonstrated that the negative values of  $\Delta H^\circ$  and  $\Delta S^\circ$  establish the exothermic nature of CR dye adsorption onto BCAC and Reduction in randomness. Several investigations that have been conducted for the elimination of CR reported similar thermodynamic results [23,32].

### 3.8. Desorption and regeneration

Regeneration of the adsorbent is a crucial consideration when evaluating the process's viability in terms of both practical use

and economics. During desorption process dye molecules are liberated from the carbon surface. Experiments with Congo Red-loaded BCAC for desorption study have been carried out by using NaOH solution. The interaction bonds between the surface sites of BCAC and adsorbed CR become weaker in an alkaline NaOH solution, making regeneration simple. According to the regeneration data, the CR percentage adsorption by BCAC was decreased in the third cycle to 84.77 % from 96.81 %. Moreover, desorption percentage was seen to diminish with an increase in the number of regeneration cycles, remaining at 88.31 % of its initial level after the first cycle and falling to 72.58% after the third. As a result, the adsorbent can be successfully employed for up to three cycles. Similar desorption studies were performed utilizing NaOH to recover Congo Red dye from jujube shell [27] and methyl orange from pumpkin seed powder adsorbent [69].

### 4. Simulation of machine leaning models

In order for the ML-based SVR model to function properly, the model parameters must be chosen correctly. The optimised hyperparameters are listed in Table 4. The results showed that the optimal ANN design was created using the tansig-purelin transfer functions, trainlm as the back-propagation technique, and 10 neurons in a single hidden layer. The models' output was employed, in order to create parity graphs between the

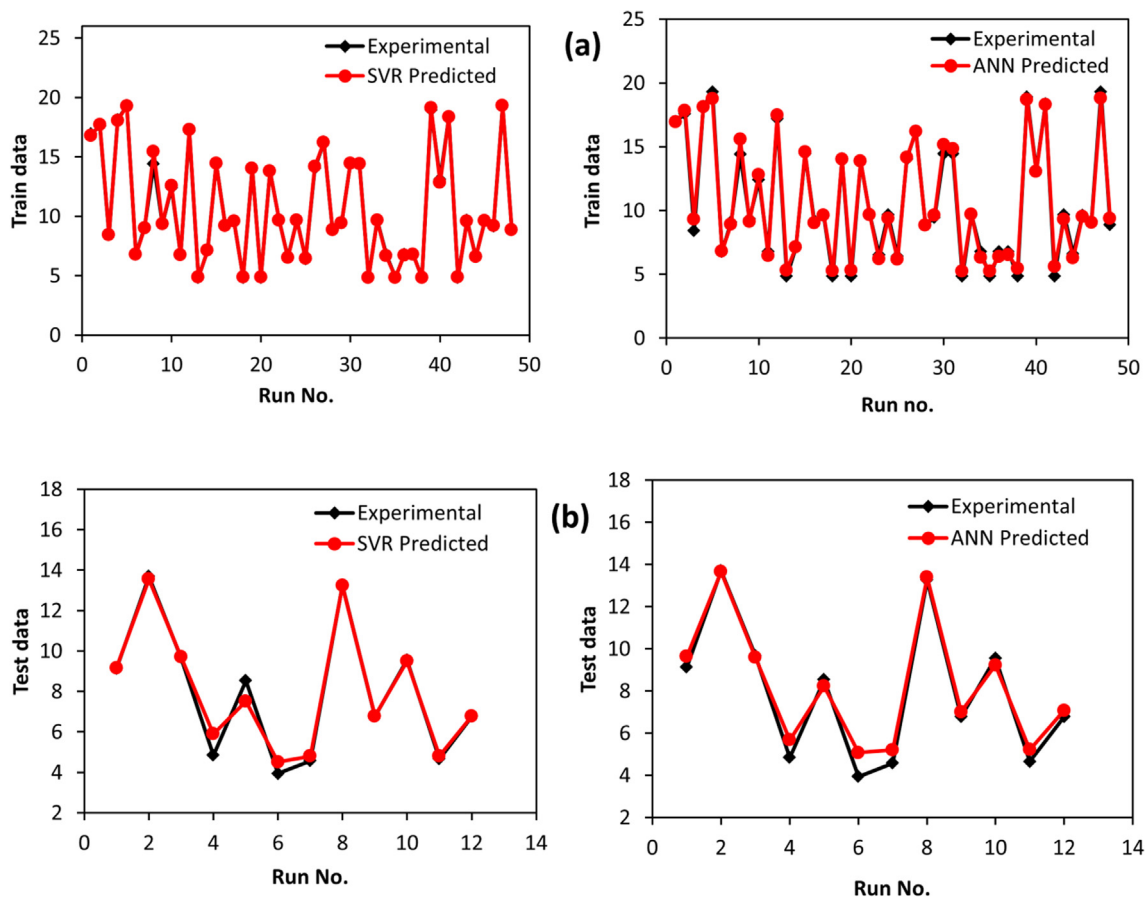


**Fig. 10** Plots of Congo Red ML models during (a) training course and (b) testing course. (For interpretation of the references to color in this figure legend, the reader is referred to the web version of this article.)

**Table 5** SVR model performance evaluation.

Parameter	Train data	Test data
R <sup>2</sup>	0.9987	0.9816
AARE	0.0053	0.0491
RMSE	0.1686	0.4635
Chi-squared	0.0913	0.4165

**Table 6** ANN model performance evaluation.

Parameter	Train data	Test data
R <sup>2</sup>	0.9931	0.9884
AARE	0.0365	0.0781
RMSE	0.3855	0.5395
Chi-squared	0.8131	0.5797

actual adsorption capacity of CR over BCAC and those predicted by the ML-based models as represented in Fig. 9 (a-b). It is obvious that the anticipated train and test data both fall very near the optimum fit line, signifying that the two ML-based models performed effectively. Fig. 10 (a) - (b) demonstrates the training process and testing phase for ML-SVR and ML-ANN models respectively. It is noted that the forecasted results closely match the experimentally determined values of adsorption capacity for almost all sample runs. The two constructed ML-models produce good results, with high R<sup>2</sup> values of 0.9978 for SVR and 0.9931 for the ANN model obtained during training. These ML models were generalised since, during testing, they functioned effectively for even anonymous data, with R<sup>2</sup> for the SVR and ANN models being equivalent to 0.9816 and 0.9884, respectively. Furthermore, as depicted in Tables 5 and 6, low AARE values in ranges (0.0053–0.0491) for SVR and (0.0365–0.0781) for ANN, whereas evaluated RMSE values were found to be in ranges (0.1686–0.4635) for SVR and (0.3855 – 0.5395) for ANN were close to ideal error value of zero, confirms ML models' capacity for prediction CR removal onto BCAC. The results of the ML approach for present adsorption study were found to be consistent with previously reported literature where prediction of Chromium adsorption over Medlar seed by SVR and ANN models have R<sup>2</sup> of 0.981 and 0.958 respectively [70]. Similar

trend was also noted in ANN modelling of Basic Red 46 dye and Cu (II) with R<sup>2</sup> in between 0.98 and 0.99 [71].

## 5. Comparison with other adsorbents

Table 7 shows that the BCAC has a notable capacity for CR adsorption when compared to the other adsorbents that are being used. It has been determined how well various adsorbents can remove the CR dye when compared to the maximal adsorption capacity of BCAC for CR.

## 6. Conclusion

The herbal waste derived BCAC was discovered through this investigation to be a potential material for the elimination of harmful CR dye in water systems. Increases in initial dye concentration (50–200 mg/L), contact time (0–120 mins), and dose (0.04–0.12) were shown to enhance the amount of Congo Red dye uptake on BCAC, whereas increases in solution pH (6–10) and temperature (30–50 °C) were found to decrease it. The reported negative values for  $\Delta H^\circ$  (–22.697 kJ mol<sup>–1</sup>) and  $\Delta G^\circ$  (–8.621 kJ mol<sup>–1</sup>), respectively, show that adsorption is exothermic and spontaneous in nature. The provided results (R<sup>2</sup> > 0.9) demonstrate that ML models are potential forecasting techniques that can be applied successfully and have adequate accuracy for the prediction of the CR dye removal. Thus, ML prediction can help in the planning and development of a more efficient treatment for removing dye from waste effluent.

## Declaration of Competing Interest

The authors declare that they have no known competing financial interests or personal relationships that could have appeared to influence the work reported in this paper.

## Acknowledgements

This research work was funded by Institutional Fund Projects under grant no. (IFPIP: 1820-961-1443). The authors gratefully acknowledge technical and financial support provided by the Ministry of Education and King Abdulaziz University, DSR, Jeddah, Saudi Arabia.

**Table 7** Comparison of CR adsorption over various adsorbents.

Adsorbent	Adsorption Isotherm	Adsorption Kinetic	Optimum pH	Max Adsorption (mg/g)	Reference
Mango Leaves	Freundlich	Pseudo-second order	7	21.28	[26]
Dactylifera seeds	Langmuir	Pseudo-second order	2	61.72	[8]
Kenaf-based activated carbon	Freundlich	Pseudo-second order	4	14.20	[19]
	Langmuir				
Coconut fiber based activated carbon	–	Pseudo-second order	3	22.10	[16]
Litchi seed	Freundlich	Pseudo-second order	2	20.49	[32]
	Langmuir				
<i>Acacia auriculiformis</i> biochar	Freundlich	Pseudo-second order	2	130.0	[72]
Apricote stone	Langmuir	Pseudo-second order	13	32.68	[28]
	Dubinini-Radushkevich				
Black Cardamom activated carbon	Langmuir	Pseudo-second order	6	69.93	Present study

## References

- [1] M. Danish, K.B. Ansari, M. Danish, A. Khatoon, R. Ali Khan Rao, S. Zaidi, R. Ahmad Aftab, A comprehensive investigation of external mass transfer and intraparticle diffusion for batch and continuous adsorption of heavy metals using pore volume and surface diffusion model, *Sep. Purif. Technol.* 292 (2022), <https://doi.org/10.1016/j.seppur.2022.120996> 120996.
- [2] M.A. Usman, A.Y. Khan, Selective adsorption of anionic dye from wastewater using polyethyleneimine based macroporous sponge: Batch and continuous studies, *J. Hazard. Mater.* 428 (2022), <https://doi.org/10.1016/j.jhazmat.2022.128238> 128238.
- [3] M.A. Fawzy, M. Gomaa, Use of algal biorefinery waste and waste office paper in the development of xerogels: A low cost and eco-friendly biosorbent for the effective removal of congo red and Fe (II) from aqueous solutions, *J. Environ. Manage.* 262 (2020), <https://doi.org/10.1016/j.jenvman.2020.110380> 110380.
- [4] M.T. Yagub, T.K. Sen, S. Afroze, H.M. Ang, Dye and its removal from aqueous solution by adsorption: A review, *Adv. Colloid Interface Sci.* 209 (2014) 172–184, <https://doi.org/10.1016/j.cis.2014.04.002>.
- [5] S. Parvin, B.K. Biswas, A. Rahman, Chemosphere Study on adsorption of Congo red onto chemically modified egg shell membrane 236 (2019), <https://doi.org/10.1016/j.chemosphere.2019.07.057>.
- [6] Y.H. Chiu, T.F.M. Chang, C.Y. Chen, M. Sone, Y.J. Hsu, Mechanistic insights into photodegradation of organic dyes using heterostructure photocatalysts, *Catalysts* 9 (2019), <https://doi.org/10.3390/catal9050430>.
- [7] S. Mohebbi, D. Bastani, H. Shayesteh, Equilibrium, kinetic and thermodynamic studies of a low-cost biosorbent for the removal of Congo red dye: acid and CTAB-acid modified celery (*Apium graveolens*), *J. Mol. Struct.* 1176 (2018) 181–193, <https://doi.org/10.1016/j.molstruc.2018.08.068>.
- [8] D. Pathania, A. Sharma, Z. Siddiqi, Removal of congo red dye from aqueous system using Phoenix dactylifera seeds, *J. Mol. Liq.* 219 (2016) 359–367, <https://doi.org/10.1016/j.molliq.2016.03.020>.
- [9] M.A. Adebayo, J.M. Jabar, J.S. Amoko, E.O. Openiyi, O.O. Shodiya, Coconut husk-raw clay-Fe composite: preparation, characteristics and mechanisms of Congo red adsorption, *Sci. Rep.* 12 (2022) 1–12, <https://doi.org/10.1038/s41598-022-18763-y>.
- [10] N.A. Alamrani, Elimination of Congo Red Dye from Industrial Wastewater Using *Teucrium polium L.* as a Low-Cost Local Adsorbent, *Adsorpt. Sci. Technol.* (2021) 12.
- [11] S. Mishra, L. Cheng, A. Maiti, The utilization of agro-biomass/byproducts for effective bio-removal of dyes from dyeing wastewater: A comprehensive review, *J. Environ. Chem. Eng.* 9 (2021), <https://doi.org/10.1016/j.jece.2020.104901> 104901.
- [12] J.N. Wekoye, W.C. Wanyonyi, P.T. Wangila, M.K. Tonui, Kinetic and equilibrium studies of Congo red dye adsorption on cabbage waste powder, *Environ. Chem. Ecotoxicol.* 2 (2020) 24–31, <https://doi.org/10.1016/j.enceco.2020.01.004>.
- [13] A. Kumar, H.M. Jena, Removal of methylene blue and phenol onto prepared activated carbon from Fox nutshell by chemical activation in batch and fixed-bed column, *J. Clean. Prod.* 137 (2016) 1246–1259, <https://doi.org/10.1016/j.jclepro.2016.07.177>.
- [14] A. Sharma, G. Sharma, M. Naushad, A.A. Ghfar, D. Pathania, Remediation of anionic dye from aqueous system using bio-adsorbent prepared by microwave activation, *Environ. Technol. (United Kingdom)* 39 (2018) 917–930, <https://doi.org/10.1080/09593330.2017.1317293>.
- [15] R.A.K. Rao, U. Khan, Adsorption of Ni(II) on alkali treated pineapple residue (*Ananas comosus L.*): Batch and column studies, *Groundw. Sustain. Dev.* 5 (2017) 244–252, <https://doi.org/10.1016/j.gsd.2017.08.002>.
- [16] L. Zhang, L.Y. Tu, Y. Liang, Q. Chen, Z.S. Li, C.H. Li, Z.H. Wang, W. Li, Coconut-based activated carbon fibers for efficient adsorption of various organic dyes, *RSC Adv.* 8 (2018) 42280–42291, <https://doi.org/10.1039/c8ra08990f>.
- [17] A. Sharma, Z.M. Siddiqui, S. Dhar, P. Mehta, D. Pathania, Adsorptive removal of congo red dye (CR) from aqueous solution by *Cornulaca monacantha* stem and biomass-based activated carbon: isotherm, kinetics and thermodynamics, *Sep. Sci. Technol.* 54 (2019) 916–929, <https://doi.org/10.1080/01496395.2018.1524908>.
- [18] V.S. Devi, B. Sudhakar, K. Prasad, P. Jeremiah Sunadh, M. Krishna, Adsorption of Congo red from aqueous solution onto *Antigonon leptopus* leaf powder: Equilibrium and kinetic modeling, *Mater. Today Proc.* 26 (2019) 3197–3206, <https://doi.org/10.1016/j.matpr.2020.02.715>.
- [19] S. Mandal, J. Calderon, S.B. Marpu, M.A. Omary, S.Q. Shi, Mesoporous activated carbon as a green adsorbent for the removal of heavy metals and Congo red: Characterization, adsorption kinetics, and isotherm studies, *J. Contam. Hydrol.* 243 (2021), <https://doi.org/10.1016/j.jconhyd.2021.103869> 103869.
- [20] F. Amran, M.A.A. Zaini, Sodium hydroxide-activated Casuarina empty fruit: Isotherm, kinetics and thermodynamics of methylene blue and congo red adsorption, *Environ. Technol. Innov.* 23 (2021), <https://doi.org/10.1016/j.eti.2021.101727> 101727.
- [21] R. Kumari, J. Mohanta, B. Dey, S. Dey, Eucalyptus leaf powder as an efficient scavenger for Congo red from water: Comprehensive batch and column investigation, *Sep. Sci. Technol.* 55 (2020) 3047–3059, <https://doi.org/10.1080/01496395.2019.1670208>.
- [22] Z. Li, H. Hanafy, L. Zhang, L. Sellaoui, M. Schadeck Netto, M. L.S. Oliveira, M.K. Seliem, G. Luiz Dotto, A. Bonilla-Petriciolet, Q. Li, Adsorption of congo red and methylene blue dyes on an ashitaba waste and a walnut shell-based activated carbon from aqueous solutions: Experiments, characterization and physical interpretations, *Chem. Eng. J.* 388 (2020), <https://doi.org/10.1016/j.cej.2020.124263> 124263.
- [23] T.K. Roy, N.K. Mondal, Potentiality of *Eichhornia* shoots ash towards removal of Congo red from aqueous solution: Isotherms, kinetics, thermodynamics and optimization studies, *Groundw. Sustain. Dev.* 9 (2019), <https://doi.org/10.1016/j.gsd.2019.100269> 100269.
- [24] K. Litefti, M.S. Freire, M. Stitou, J. González-Álvarez, Adsorption of an anionic dye (Congo red) from aqueous solutions by pine bark, *Sci. Rep.* 9 (2019) 1–11, <https://doi.org/10.1038/s41598-019-53046-z>.
- [25] M. Goswami, P. Chaturvedi, R. Kumar Sonwani, A. Dutta Gupta, R. Rani Singhania, B. Shekher Giri, B. Nath Rai, H. Singh, S. Yadav, R. Sharan Singh, Application of *Arjuna* (*Terminalia arjuna*) seed biochar in hybrid treatment system for the bioremediation of Congo red dye, *Bioresour. Technol.* 307 (2020), <https://doi.org/10.1016/j.biortech.2020.123203> 123203.
- [26] O.A. Adelaja, A.C. Bankole, M.E. Oladipo, D.B. Lene, Biosorption of Hg(II) ions, Congo red and their binary mixture using raw and chemically activated mango leaves, *Int. J. Energy Water Resour.* 3 (2019) 1–12, <https://doi.org/10.1007/s42108-019-00012-0>.
- [27] N. El messaoudi, M. Elkhomri, A. Dbik, S. Bentahar, A. Lacherai, B. Bakiz, Biosorption of Congo red in a fixed-bed column from aqueous solution using jujube shell: Experimental and mathematical modeling, *J. Environ. Chem. Eng.* 4 (2016) 3848–3855, <https://doi.org/10.1016/j.jece.2016.08.027>.
- [28] M. Abbas, M. Trari, Kinetic, equilibrium and thermodynamic study on the removal of Congo Red from aqueous solutions by adsorption onto apricot stone, *Process Saf. Environ. Prot.* 98 (2015) 424–436, <https://doi.org/10.1016/j.psep.2015.09.015>.



- [29] Y. Achour, L. Bahsis, E.H. Ablouh, H. Yazid, M.R. Laamari, M. El Haddad, Insight into adsorption mechanism of Congo red dye onto Bombax Buonopozense bark Activated-carbon using Central composite design and DFT studies, *Surfaces and Interfaces*. 23 (2021), <https://doi.org/10.1016/j.surfin.2021.100977>.
- [30] V.V. Gedam, P. Raut, A. Chahande, P. Pathak, Kinetic, thermodynamics and equilibrium studies on the removal of Congo red dye using activated teak leaf powder, *Appl. Water Sci.* 9 (2019) 1–13, <https://doi.org/10.1007/s13201-019-0933-9>.
- [31] S.L. Chan, Y.P. Tan, A.H. Abdullah, S.T. Ong, Equilibrium, kinetic and thermodynamic studies of a new potential biosorbent for the removal of Basic Blue 3 and Congo Red dyes: Pineapple (*Ananas comosus*) plant stem, *J. Taiwan Inst. Chem. Eng.* 61 (2016) 306–315, <https://doi.org/10.1016/j.jtice.2016.01.010>.
- [32] J.N. Edokpayi, E. Makete, Removal of Congo red dye from aqueous media using Litchi seeds powder: Equilibrium, kinetics and thermodynamics, *Phys. Chem. Earth*. 123 (2021), <https://doi.org/10.1016/j.pce.2021.103007>.
- [33] W.C. Leong, R.O. Kelani, Z. Ahmad, Prediction of air pollution index (API) using support vector machine (SVM), *J. Environ. Chem. Eng.* 8 (2020), <https://doi.org/10.1016/j.jece.2019.103208>.
- [34] J. Huang, T. Jin, M. Liang, H. Chen, Prediction of heat exchanger performance in cryogenic oscillating flow conditions by support vector machine, *Appl. Therm. Eng.* 182 (2021), <https://doi.org/10.1016/j.applthermaleng.2020.116053>.
- [35] R.A. Aftab, S. Zaidi, M. Danish, K.B. Ansari, M. Danish, Novel Machine Learning (ML) Models for Predicting the Performance of Multi-Metal Binding Green Adsorbent for the Removal of Cd (II), Cu (II), Pb (II) and Zn (II) ions, *Environ. Adv.* 9 (2022), <https://doi.org/10.1016/j.envadv.2022.100256>.
- [36] S. Zaidi, Development of support vector regression (SVR)-based model for prediction of circulation rate in a vertical tube thermosiphon reboiler, *Chem. Eng. Sci.* 69 (2012) 514–521, <https://doi.org/10.1016/j.ces.2011.11.005>.
- [37] A. Zendejboudi, M.A. Baseer, R. Saidur, Application of support vector machine models for forecasting solar and wind energy resources: A review, *J. Clean. Prod.* 199 (2018) 272–285, <https://doi.org/10.1016/j.jclepro.2018.07.164>.
- [38] D.A. Otchere, T.O.A. Ganat, R. Gholami, S. Ridha, Application of supervised machine learning paradigms in the prediction of petroleum reservoir properties: Comparative analysis of ANN and SVM models, *J. Pet. Sci. Eng.* 200 (2020), <https://doi.org/10.1016/j.petrol.2020.108182>.
- [39] M. Danish, K.B. Ansari, R.A. Aftab, M. Danish, S. Zaidi, Q.T. Trinh, gPROMS-driven modeling and simulation of fixed bed adsorption of heavy metals on a biosorbent: benchmarking and case study, *Environ. Sci. Pollut. Res.* (2021), <https://doi.org/10.1007/s11356-021-13207-y>.
- [40] M.A. Usman, R.A. Aftab, S. Zaidi, S.M. Adnan, R.A.K. Rao, Adsorption of aniline blue dye on activated pomegranate peel: equilibrium, kinetics, thermodynamics and support vector regression modelling, *Int. J. Environ. Sci. Technol.* (2021), <https://doi.org/10.1007/s13762-021-03571-0>.
- [41] A.M. Ghaedi, A. Vafaei, Applications of artificial neural networks for adsorption removal of dyes from aqueous solution: A review, *Adv. Colloid Interface Sci.* 245 (2017) 20–39, <https://doi.org/10.1016/j.cis.2017.04.015>.
- [42] R.A. Aftab, S. Zaidi, M. Danish, S.M. Adnan, K.B. Ansari, M. Danish, Support vector regression-based model for phenol adsorption in rotating packed bed adsorber, *Environ. Sci. Pollut. Res.* (2021), <https://doi.org/10.1007/s11356-021-14953-9>.
- [43] P.R. Souza, G.L. Dotto, N.P.G. Salau, Artificial neural network (ANN) and adaptive neuro-fuzzy interference system (ANFIS) modelling for nickel adsorption onto agro-wastes and commercial activated carbon, *J. Environ. Chem. Eng.* 6 (2018) 7152–7160, <https://doi.org/10.1016/j.jece.2018.11.013>.
- [44] S. Ullah, M.A. Assiri, A.G. Al-Sehemi, M.A. Bustam, M. Sagir, F.A. Abdulkareem, M.R. Raza, M. Ayoub, A. Irfan, Characteristically Insights, Artificial Neural Network (ANN), Equilibrium, and Kinetic Studies of Pb(II) Ion Adsorption on Rice Husks Treated with Nitric Acid, *Int. J. Environ. Res.* 14 (2020) 43–60, <https://doi.org/10.1007/s41742-019-00235-3>.
- [45] A.J. Smola, B. Scholkopf, A tutorial on support vector regression, *Stat. Comput.* 14 (2004) 199–222, <https://doi.org/10.1023/B:STCO.0000035301.49549.88>.
- [46] H. Peng, X. Ling, Predicting thermal – hydraulic performances in compact heat exchangers by support vector regression, *Int. J. Heat Mass Transf.* 84 (2015) 203–213, <https://doi.org/10.1016/j.ijheatmasstransfer.2015.01.017>.
- [47] I. Olanrewaju, M. Amiruddin, A. Rahman, T.A. Saleh, An approach to predict the isobaric specific heat capacity of nitrides / ethylene glycol-based nanofluids using support vector regression, *J. Energy Storage*. 29 (2020) 1–10.
- [48] M.K. Uddin, A. Nasar, Walnut shell powder as a low-cost adsorbent for methylene blue dye: isotherm, kinetics, thermodynamic, desorption and response surface methodology examinations, *Sci. Rep.* 10 (2020) 1–13, <https://doi.org/10.1038/s41598-020-64745-3>.
- [49] R. Ahmad, R. Kumar, Adsorptive removal of congo red dye from aqueous solution using bael shell carbon, *Appl. Surf. Sci.* 257 (2010) 1628–1633, <https://doi.org/10.1016/j.apsusc.2010.08.111>.
- [50] N. Hoc Thang, D. Sy Khang, T. Duy Hai, D. Thi Nga, P. Dinh Tuan, Methylene blue adsorption mechanism of activated carbon synthesised from cashew nut shells, *RSC Adv.* 11 (2021) 26563–26570, <https://doi.org/10.1039/d1ra04672a>.
- [51] Q. Du, J. Sun, Y. Li, X. Yang, X. Wang, Z. Wang, L. Xia, Highly enhanced adsorption of congo red onto graphene oxide/chitosan fibers by wet-chemical etching off silica nanoparticles, *Chem. Eng. J.* 245 (2014) 99–106, <https://doi.org/10.1016/j.ccej.2014.02.006>.
- [52] G. Akkaya Saygılı, Synthesis, characterization and adsorption properties of a novel biomagnetic composite for the removal of Congo red from aqueous medium, *J. Mol. Liq.* 211 (2015) 515–526, <https://doi.org/10.1016/j.molliq.2015.07.048>.
- [53] F. Gündüz, B. Bayrak, Biosorption of malachite green from an aqueous solution using pomegranate peel: Equilibrium modelling, kinetic and thermodynamic studies, *J. Mol. Liq.* 243 (2017) 790–798, <https://doi.org/10.1016/j.molliq.2017.08.095>.
- [54] P. Vairavel, N. Rampal, G. Jeppu, Adsorption of toxic Congo red dye from aqueous solution using untreated coffee husks: kinetics, equilibrium, thermodynamics and desorption study, *Int. J. Environ. Anal. Chem.* 00 (2021) 1–20, <https://doi.org/10.1080/03067319.2021.1897982>.
- [55] B. Huang, Y. Liu, B. Li, H. Wang, G. Zeng, Adsorption mechanism of polyethyleneimine modified magnetic core-shell Fe<sub>3</sub>O<sub>4</sub>@SiO<sub>2</sub> nanoparticles for anionic dye removal, *RSC Adv.* 9 (2019) 32462–32471, <https://doi.org/10.1039/c9ra06299h>.
- [56] O. Paşka, R. Ianoş, C. Păcurariu, A. Brădeanu, Magnetic nanopowder as effective adsorbent for the removal of Congo Red from aqueous solution, *Water Sci. Technol.* 69 (2014) 1234–1240, <https://doi.org/10.2166/wst.2013.827>.
- [57] S. Dawood, T.K. Sen, Removal of anionic dye Congo red from aqueous solution by raw pine and acid-treated pine cone powder as adsorbent: Equilibrium, thermodynamic, kinetics, mechanism and process design, *Water Res.* 46 (2012) 1933–1946, <https://doi.org/10.1016/j.watres.2012.01.009>.
- [58] P.C. Bhomick, A. Supong, M. Baruah, C. Pongener, D. Sinha, Pine Cone biomass as an efficient precursor for the synthesis of activated biocarbon for adsorption of anionic dye from aqueous solution: Isotherm, kinetic, thermodynamic and regeneration

- studies, *Sustain. Chem. Pharm.* 10 (2018) 41–49, <https://doi.org/10.1016/j.scp.2018.09.001>.
- [59] I. Langmuir, The adsorption of gases on plane surfaces of glass, mica and platinum, *J. Am. Chem. Soc.* 40 (1918) 1361–1403, <https://doi.org/10.1021/ja02242a004>.
- [60] M. Dirbaz, A. Roosta, Adsorption, kinetic and thermodynamic studies for the biosorption of cadmium onto microalgae *Parachlorella sp.*, *J. Environ. Chem. Eng.* 6 (2018) 2302–2309, <https://doi.org/10.1016/j.jece.2018.03.039>.
- [61] H.M.F. Freundlich, Over the adsorption in solution, *J. Phys. Chem.* 57 (1906) 385–471, <https://doi.org/10.4161/epi.6.7.16250>.
- [62] S.J. Allen, G. Mckay, J.F. Porter, Adsorption isotherm models for basic dye adsorption by peat in single and binary component systems, *J. Colloid Interface Sci.* 280 (2004) 322–333, <https://doi.org/10.1016/j.jcis.2004.08.078>.
- [63] H. Shayesteh, A. Rahbar-kelishami, R. Norouzbeigi, Treatment Adsorption of malachite green and crystal violet cationic dyes from aqueous solution using pumice stone as a low-cost adsorbent : kinetic, equilibrium, and thermodynamic studies, *Desalin. Water Treat.* (2015) 12822–12831, <https://doi.org/10.1080/19443994.2015.1054315>.
- [64] A. Dutta, Y. Diao, R. Jain, E.R. Rene, S. Dutta, Adsorption of Cadmium from Aqueous Solutions onto Coffee Grounds and Wheat Straw : Equilibrium and Kinetic Study, *J. Environ. Eng.* 142 (2016) 1–6, [https://doi.org/10.1061/\(ASCE\)EE.1943-7870.0001015](https://doi.org/10.1061/(ASCE)EE.1943-7870.0001015).
- [65] F. Zhang, B. Ma, X. Jiang, Y. Ji, Dual function magnetic hydroxyapatite nanopowder for removal of malachite green and Congo red from aqueous solution, *Powder Technol.* 302 (2016) 207–214, <https://doi.org/10.1016/j.powtec.2016.08.044>.
- [66] H.S. AL-Shehri, E. Almudaifer, A.Q. Alorabi, H.S. Alanazi, A. S. Alkorbi, F.A. Alharthi, Effective adsorption of crystal violet from aqueous solutions with effective adsorbent: equilibrium, mechanism studies and modeling analysis, *Environ. Pollut.* Bioavailab. 33 (2021) 214–226, <https://doi.org/10.1080/26395940.2021.1960199>.
- [67] M.A. Ahmad, N.A. Ahmad Puad, O.S. Bello, Kinetic, equilibrium and thermodynamic studies of synthetic dye removal using pomegranate peel activated carbon prepared by microwave-induced KOH activation, *Water Resour. Ind.* 6 (2014) 18–35, <https://doi.org/10.1016/j.wri.2014.06.002>.
- [68] A.T. Ojedokun, O.S. Bello, Kinetic modeling of liquid-phase adsorption of Congo red dye using guava leaf-based activated carbon, *Appl. Water Sci.* 7 (2017) 1965–1977, <https://doi.org/10.1007/s13201-015-0375-y>.
- [69] M.V. Subbaiah, D.S. Kim, Adsorption of methyl orange from aqueous solution by aminated pumpkin seed powder: Kinetics, isotherms, and thermodynamic studies, *Ecotoxicol. Environ. Saf.* 128 (2016) 109–117, <https://doi.org/10.1016/j.ecoenv.2016.02.016>.
- [70] M. Solgi, T. Najib, S. Ahmadnejad, B. Nasernejad, Synthesis and characterization of novel activated carbon from Medlar seed for chromium removal: Experimental analysis and modeling with artificial neural network and support vector regression, *Resour. Technol.* 3 (2017) 236–248, <https://doi.org/10.1016/j.refit.2017.08.003>.
- [71] M. Dolatabadi, M. Mehrabpour, M. Esfandyari, H. Alidadi, M. Davoudi, Modeling of simultaneous adsorption of dye and metal ion by sawdust from aqueous solution using of ANN and ANFIS, *Chemom. Intell. Lab. Syst.* 181 (2018) 72–78, <https://doi.org/10.1016/j.chemolab.2018.07.012>.
- [72] D.L.T. Nguyen, Q.A. Binh, X.C. Nguyen, T.T. Huyen Nguyen, Q.N. Vo, T.D. Nguyen, T.C. Phuong Tran, T.A. Hang Nguyen, S.Y. Kim, T.P. Nguyen, J. Bae, I.T. Kim, Q. Van Le, Metal salt-modified biochars derived from agro-waste for effective congo red dye removal, *Environ. Res.* 200 (2021), <https://doi.org/10.1016/j.envres.2021.111492> 111492.